

Edited by Paolo Samorì

WILEY-VCH

Scanning Probe Microscopies Beyond Imaging

Manipulation of Molecules and Nanostructures



**Scanning Probe
Microscopies Beyond
Imaging**

*Edited by
Paolo Samori*

Scanning Probe Microscopies Beyond Imaging. Manipulation of Molecules and Nanostructures.
Edited by Paolo Samori
Copyright © 2006 WILEY-VCH Verlag GmbH & Co. KGaA, Weinheim
ISBN: 3-527-31269-2

Related Titles

M. Köhler, W. Fritzsche

Nanotechnology

An Introduction to Nanostructuring Techniques

284 pages with 143 figures and 9 tables

2004

Hardcover

ISBN 3-527-30750-8

C. M. Niemeyer, C. A. Mirkin (eds.)

Nanobiotechnology

Concepts, Applications and Perspectives

491 pages with 193 figures and 9 tables

2004

Hardcover

ISBN 3-527-30658-7

S. Roth, D. Carroll

One-Dimensional Metals

Conjugated Polymers, Organic Crystals, Carbon Nanotubes

264 pages with 249 figures and 6 tables

2004

Hardcover

ISBN 3-527-30749-4

P. Gómez-Romero, C. Sanchez (eds.)

Functional Hybrid Materials

434 pages with 212 figures and 12 tables

2004

Hardcover

ISBN 3-527-30484-3

F. Caruso (ed.)

Colloids and Colloid Assemblies

Synthesis, Modification, Organization and Utilization of Colloid Particles

621 pages with 273 figures and 8 tables

2004

Hardcover

ISBN 3-527-30660-9

Balzani, V., Credi, A., Venturi, M.

Molecular Devices and Machines

A Journey into the Nanoworld

511 pages with 290 figures, 4 in color

2003

Hardcover

ISBN 3-527-30506-8

Scanning Probe Microscopies Beyond Imaging

Manipulation of Molecules and Nanostructures

Edited by Paolo Samorì



WILEY-
VCH

WILEY-VCH Verlag GmbH & Co. KGaA

The Editor

Dr. Paolo Samori
Istituto per la Sintesi Organica e la
Fotoreattività
Consiglio Nazionale delle Ricerche
via Gobetti 101
40129 Bologna
Italy
and
Institut de Science et d'Ingénierie
Supramoléculaires (ISIS)
Université Louis Pasteur
8 allée Gaspard Monge
67083 Strasbourg
France

■ All books published by Wiley-VCH are carefully produced. Nevertheless, authors, editors, and publisher do not warrant the information contained in these books, including this book, to be free of errors. Readers are advised to keep in mind that statements, data, illustrations, procedural details or other items may inadvertently be inaccurate.

Library of Congress Card No.: applied for
British Library Cataloguing-in-Publication Data:

A catalogue record for this book is available from the British Library.

**Bibliographic information published by
Die Deutsche Bibliothek**

Die Deutsche Bibliothek lists this publication in the Deutsche Nationalbibliografie; detailed bibliographic data is available in the Internet at <http://dnb.ddb.de>.

© 2006 WILEY-VCH Verlag GmbH & Co.
KGaA, Weinheim

All rights reserved (including those of translation into other languages). No part of this book may be reproduced in any form – by photoprinting, microfilm, or any other means – nor transmitted or translated into a machine language without written permission from the publishers. Registered names, trademarks, etc. used in this book, even when not specifically marked as such, are not to be considered unprotected by law.

Printed in the Federal Republic of Germany.
Printed on acid-free paper.

Printing Strauss GmbH, Mörlenbach
Binding Litges & Dopf GmbH, Heppenheim
Typesetting Asco Typesetters, Hong Kong
Cover Design 4T Matthes + Traut GmbH,
Darmstadt

ISBN-13: 978-3-527-31269-6

ISBN-10: 3-527-31269-2

To Cristiana

Foreword

Nanoscience and nanotechnology are interdisciplinary fields involving functional objects and materials whose components and structures, due to their nanoscale size, have unusual or enhanced properties. The processing and the manipulation of complex assemblies on the nanoscale as well as the fabrication of devices with new sustainable approaches have a paramount importance in view of a technology based on intelligent materials. The invention of scanning probe microscopies (SPMs) truly boosted the development of nanoscience and nanotechnology. SPMs are key tools for mapping the topography of surfaces as well as for unveiling a variety of physical and chemical properties of molecule-based structures at scales ranging from hundreds of micrometers down to the subnanometer regime. The flexibility of their modes makes it possible to single out static and dynamic processes under different environmental conditions, including gaseous, liquid, and ultra-high vacuum. Moreover, SPMs allow the manipulation of objects with a nanoscale precision, thereby making it possible to nanopattern a surface or to elucidate the nanomechanics of complex artificial and natural assemblies. Thus, they can offer decisive insight for the optimization of functional nanomaterials and nanodevices. This book brings together contributions of experts from different fields, with the aim of casting light on the potential of SPMs to explore as many physico-chemical properties of single molecules and of larger objects as possible, so as to foster a greater understanding of surface properties both for unraveling the basic rules operating at nanoscale level and for the construction of miniaturized devices with “market potential.”

This book provides timely summaries of the present status of the applications of scanning probe microscopies beyond imaging, with a specific emphasis on soft nanomaterials. The judicious combination of chapters covering technical aspects of various modes of SPM to gain insight into structural, electrical, and mechanical properties of nanoscale architectures offers a wide panorama to the reader by highlighting stimulating examples of exploitation of these powerful tools. Various future applications can be foreseen and surely will involve researchers operating in different disciplines, including physics, chemistry, biology, and materials and polymer sciences, as well as engineering. The areas that will benefit from these approaches are countless; among them catalysis, self-assembly of (bio)hybrid architectures, molecular recognition, and optical, electrical, and mechanical studies of nanostructures, as well as more technological issues such as nanopatterning, nano-

VIII | *Foreword*

construction of functional materials, and nanodevice fabrication. Overall, this book will be a valuable tool for both beginners and more expert scientists interested in the fascinating realm of scanning probe microscopies and more generally in the nanoworld.

Jean-Marie Lehn
ISIS-ULP, Strasbourg, France

Contents

	Foreword	VII
	Preface	XIX
	List of Authors	XXI
I	Scanning Tunneling Microscopy-Based Approaches	1
	Nanoscale Structural, Mechanical and Electrical Properties	3
1	Chirality in 2D	3
	<i>Steven De Feyter and Frans C. De Schryver</i>	
1.1	Introduction	3
1.2	Chirality and STM: From 0D to 2D	4
1.2.1	Determination of Absolute Chirality	4
1.2.2	Expression of 2D Chirality by Enantiopure Molecules	6
1.2.3	Racemic Mixture of Chiral Molecules	12
1.2.4	Achiral Molecules	14
1.2.5	Systems with Increased Complexity	21
1.2.6	Multicomponent Systems	23
1.2.6.1	Mixed Systems	23
1.2.6.2	Cocrystals	26
1.2.7	Chemisorption versus Physisorption	26
1.2.8	The Effect of Molecular Adsorption on Substrates: Toward Chiral Substrates	28
1.2.9	Chirality and AFM	29
1.3	Conclusion	33
	Acknowledgements	33
	References	33
2	Scanning Tunneling Spectroscopy of Complex Molecular Architectures at Solid/Liquid Interfaces: Toward Single-Molecule Electronic Devices	36
	<i>Frank Jäckel and Jürgen P. Rabe</i>	
2.1	Introduction	36

2.2	STM/STS of Molecular Adsorbates	37
2.3	An Early Example of STS at the Solid/Liquid Interface	38
2.4	Ultrahigh Vacuum versus Solid/Liquid Interface	40
2.5	Probing π -Coupling at the Single-Molecule Level by STS	41
2.6	Molecular Diodes and Prototypical Transistors	47
2.7	Conclusions	51
	Acknowledgements	51
	References	51
3	Molecular Repositioning to Study Mechanical and Electronic Properties of Large Molecules	54
	<i>Francesca Moresco</i>	
3.1	Introduction	54
3.2	Specially Designed Molecules	55
3.3	STM-Induced Manipulation	58
3.3.1	Manipulation of Single Atoms	58
3.3.2	Repositioning of Molecules at Room Temperature	61
3.3.3	Manipulation in Constant Height Mode	61
3.4	Mechanical Properties: Controlled Manipulation of Complex Molecules	63
3.5	Inducing Conformational Changes: A Route to Molecular Switching	67
3.6	The Role of the Substrate	68
3.7	Electronic Properties: Investigation of the Molecule–Metal Contact	71
3.8	Perspectives	74
	Acknowledgements	74
	References	74
4	Inelastic Electron Tunneling Microscopy and Spectroscopy of Single Molecules by STM	77
	<i>Jose Ignacio Pascual and Nicolás Lorente</i>	
4.1	Introduction	77
4.1.1	Working Principle	78
4.2	Experimental Results	80
4.2.1	C ₆₀ on Ag(110)	82
4.2.2	C ₆ H ₆ on Ag(110)	85
4.3	Theory	88
4.3.1	Extension of Tersoff–Hamman Theory to IETS–STM	88
4.3.2	Some Model Systems	90
4.3.3	Acetylene Molecules on Cu(100)	90
4.3.4	Oxygen Molecules on Ag(110)	92
4.3.5	Ammonia Molecules on Cu(100)	92
4.4	Conclusion	96
	References	96

II	Scanning Force Microscopy-Based Approaches	99
	Patterning	101
5	Patterning Organic Nanostructures by Scanning Probe Nanolithography	101
	<i>Cristiano Albonetti, Rajendra Kshirsagar, Massimiliano Cavallini, and Fabio Biscarini</i>	
5.1	Importance of Patterning Organic Nanostructures	101
5.2	Direct Patterning of Organic Thin Films	102
5.2.1	Fabrication of Nanostructures by a Local Modification	103
5.2.1.1	Nanorecording for Memory Storage	104
5.2.1.2	Local Probe Photolithography	106
5.2.1.3	Nanorubbing	107
5.2.2	Self-Organization of Molecular Nanostructures Triggered by SPM	109
5.3	Assembly of Organic Structures on Nanofabricated Patterns	111
5.3.1	Replacement Nanolithography on Self-Assembly Monolayers (SAMs)	112
5.3.2	Template Growth of Molecular Nanostructures	114
5.3.2.1	Nanopatterns by Local Oxidation Nanolithography	114
5.3.2.2	Nanopatterns on SAMs	119
5.3.3	Constructive Nanolithography	121
5.3.3.1	Nanolithography by Local Electrochemical Oxidation	122
5.3.3.2	Nanolithography by Local Electrochemical Reduction	124
5.3.3.3	Additional Examples of Patterning by CNL	124
5.3.4	Catalytic Probe Nanolithography	126
5.3.5	Nanografting	128
5.4	Outlook and Conclusions	135
	Acknowledgements	136
	References	136
6	Dip-Pen Nanolithography	141
	<i>Seunghun Hong, Ray Eby, Sung Myung, Byung Yang Lee, Saleem G. Rao, and Joonkyung Jang</i>	
6.1	Introduction	141
6.1.1	History of Writing	141
6.1.2	The Age of Microfabrication	142
6.1.3	New Building Blocks in the Era of Nanotechnology	144
6.2	Basics of Dip-Pen Nanolithography	144
6.2.1	Basic Concepts	144
6.2.2	Ink and Pen	146
6.2.3	DPN Writing Procedure	150
6.3	Lithographic Capability of Dip-Pen Nanolithography	153
6.3.1	Resolution	153
6.3.2	Overcoming Speed Limits via Multiple-Pen Writing	155

6.3.3	Patterning Extreme Materials: Biomaterials and Conducting Polymers	157
6.3.4	Unconventional DPN	158
6.3.5	New Pens and Hardware	161
6.4	Other Applications	162
6.4.1	Etching Resist Patterning	162
6.4.2	Nanoassembly	163
6.5	Nanoscale Statistical Physics Inspired by DPN	166
6.5.1	DPN Theory	166
6.5.2	Nanoscale Water Condensation	168
6.5.3	Anomalous Surface Diffusion	170
6.6	Conclusions	170
	Acknowledgements	171
	References	171

Mechanical Properties 175

7 Scanning Probe Microscopy of Complex Polymer Systems: Beyond Imaging their Morphology 175

Philippe Leclere, Pascal Viville, Mélanie Jeusette, Jean-Pierre Aimé, and Roberto Lazzaroni

7.1	Introduction	175
7.2	Microscopic Morphologies of Multicomponent Polymer Systems	176
7.3	Methodology	185
7.3.1	Intermittent Contact versus Noncontact Atomic Force Microscopy	185
7.3.2	Modeling the Oscillating Behavior	186
7.3.2.1	Conservative Interaction	186
7.3.2.2	Dissipative Interaction	187
7.3.2.3	Stationary States and Transient States: Error and Phase Signal	192
7.3.2.4	Influence of the Quality Factor upon the Sensitivity	194
7.3.2.5	Approach–Retract Curve (ARC) Analysis	196
7.4	Combined Analysis of Height and Phase Images	198
7.4.1	Pure Topographic Contribution	198
7.4.2	Pure Mechanical Contribution	200
7.4.3	Mixed Contributions	203
7.5	Concluding Remarks	205
	Acknowledgements	205
	References	205

8 Pulsed Force Mode SFM 208

Alexander Gigler and Othmar Marti

8.1	Introduction	208
8.2	Modes of SPM Operation	208
8.2.1	Static Modes	210

8.2.1.1	Constant Height Mode	210
8.2.1.2	Constant Deflection Mode	211
8.2.2	Dynamic Modes	211
8.2.2.1	Resonant Modes	212
8.2.2.2	Force Modulation Mode	213
8.2.2.3	Nanoindentations	213
8.3	Pulsed Force Mode	213
8.3.1	Technical Implementation of Pulsed Force Mode	216
8.3.2	Analogies and Differences between PFM, JM, and Force–Volume Mode	217
8.3.3	Extending PFM to CODYMode for Full Mechanical Characterization of Samples	217
8.4	Theoretical Description of Contact Mechanics	218
8.4.1	Hertzian Modeling	218
8.4.2	Sneddon’s Extensions to the Hertzian Model	222
8.4.3	Models Incorporating Adhesion	223
8.5	AFM Measurements Using Pulsed Force Mode	227
8.5.1	Force Curves	227
8.5.2	Data Evaluation	229
8.6	Applications of Pulsed Force Mode	233
8.6.1	Examination of Dewetting Polymer Blends	235
8.6.2	Excimer Laser Ablation of PMMA and Adhesion Measurements by PFM	235
8.6.3	Temperature-Dependent PFM Investigations of Crystalline PTFE	235
8.6.4	Conducting PFM of Lithographically Structured Circuitry	238
8.6.5	Investigation of Very Thin Layers of Poly(vinyl alcohol) in PFM	239
8.6.6	PFM in Liquids with Chemically Modified Tips	239
8.6.7	Electric Double Layer – PFM in Liquids	239
8.6.8	Measuring Biological Samples in Liquids	242
8.6.9	Combined Mechanical Measurements – CODYMode	242
8.7	Conclusions	245
	Acknowledgements	246
	References	246
9	Force Spectroscopy	250
	<i>Phil Williams</i>	
9.1	Introduction	250
9.2	Basic Experiments	251
9.3	Theory	252
9.4	The Ramp-of-Force Experiment	255
9.5	Multiple Transition States	258
9.6	Multiple Bonds	258
9.7	Distributions	259
9.8	Simulations	260
9.8.1	An Example: The Streptavidin–Biotin Interaction	263

9.9	The Future	266
	References	267
	Appendix	272

Bond Strength and Tracking Chemical Reactions 275

10 Chemical Force Microscopy: Nanometer-Scale Surface Analysis with Chemical Sensitivity 275

Holger Schönherr and G. Julius Vancso

10.1	Introduction: Mapping of Surface Composition by AFM Approaches	275
10.2	Chemical Force Microscopy: Basics	277
10.2.1	Surface Modification Procedures for Tip Modification	278
10.2.1.1	Thiol-Based Self-Assembled Monolayers (SAMs) on Gold	278
10.2.1.2	SAMs on Hydroxylated Silicon and Si ₃ N ₄	280
10.2.1.3	Modified Carbon Nanotube Probes	281
10.2.2	Force Measurements and Mapping in CFM	281
10.2.2.1	Normal Forces	282
10.2.2.2	Lateral Forces	285
10.2.2.3	Intermittent Contact Mode Phase Imaging	285
10.2.3	AFM Using Chemically Modified Tips	286
10.2.3.1	Stability of SAMs and Modified Tips	286
10.2.3.2	Imaging with Optimized Forces	287
10.2.3.3	Distinguishing Different Functional Groups on Surfaces by CFM	287
10.2.3.4	Artifacts and Experimental Difficulties	289
10.3	Applications of CFM	293
10.3.1	Surface Characterization by CFM	293
10.3.1.1	Tip-Sample Forces and Interfacial Free Energies	293
10.3.1.2	Acid-Base Titrations	298
10.3.1.3	Following Surface Chemical Reactions in SAMs	300
10.3.2	Compositional Mapping of Heterogeneous Surfaces	301
10.3.2.1	Micro- and Nanometer-Scale Patterned SAMs	301
10.3.2.2	Heterogeneous and Multiphase Systems	303
10.3.2.3	Surface-Treated Polymers	305
10.4	Outlook	309
	Acknowledgements	310
	References	310

11 Atomic Force Microscopy-Based Single-Molecule Force Spectroscopy of Synthetic Supramolecular Dimers and Polymers 315

Shan Zou, Holger Schönherr, and G. Julius Vancso

11.1	Introduction	315
11.2	Supramolecular Interactions	318
11.2.1	Hydrogen Bonds	319

11.2.2	Coordinative Bonds	321
11.2.3	π -Electron Stacking	322
11.3	AFM-Based Single-Molecule Force Spectroscopy (SMFS)	323
11.3.1	SMFS Experiments	323
11.3.2	Rupture Forces of Molecular Bonds	325
11.3.2.1	Rupture of Single Bonds	325
11.3.2.2	Crossover from Near-Equilibrium to Far-from-Equilibrium Unbinding and Effect of Soft Polymer Linkages on Strengths	327
11.3.2.3	Rupture of Multiple Bonds	328
11.4	SMFS of Synthetic Supramolecular Dimers and Polymers	330
11.4.1	Host–Guest Interactions in Inclusion Complexes	330
11.4.1.1	β -CD-Based Inclusion Complexes	330
11.4.1.2	Inclusion Complexes of Resorc[4]arene Cavitands	335
11.4.1.3	Inclusion Complexes of Crown Ethers	336
11.4.2	Host–Guest Interactions via H-bonds: Quadruple H-bonded UPy Complexes	338
11.4.3	Metal-Mediated Coordination Interactions	344
11.4.3.1	Interactions Between Histidine and Nickel Nitrilotriacetate	344
11.4.3.2	Metallo-Supramolecular Ruthenium(II) Complexes	344
11.4.4	Charge-Transfer Complexes	346
11.5	Conclusions and Outlook	347
	Acknowledgments	349
	References	350
	<i>Electrical Properties of Nanoscale Objects</i>	355
12	Electrical Measurements with SFM-Based Techniques	355
	<i>Pedro. J. de Pablo and Julio Gómez-Herrero</i>	
12.1	Introduction	355
12.2	SFM Tips	358
12.3	Setups for Short Molecules	359
12.4	Experiments with Molecular Wires (MWs)	364
12.4.1	Contact Experiments on Long Molecules	365
12.4.1.1	Contact Experiments in Single-Walled Carbon Nanotubes	366
12.4.1.2	The Influence of Buckling on the Electrical Properties of SWNTs	371
12.4.1.3	Radial Electromechanical Properties of SWNTs	371
12.4.1.4	Three Electrodes plus a Gate Voltage	374
12.4.1.5	Contact Experiments on Single DNA Molecules	374
12.4.1.6	Electrical Maps of SWNTs	376
12.4.1.7	Electrical Maps of V ₂ O ₅ Nanofibers with Jumping Mode	377
12.4.1.8	Using Tunneling Current to Obtain Current Maps of SWNTs	378
12.5	Noncontact Experiments	379
12.5.1	Carbon Nanotubes	381
12.5.2	Single DNA Molecules	384
	References	387

13	Electronic Characterization of Organic Thin Films by Kelvin Probe Force Microscopy	390
	<i>Vincenzo Palermo, Matteo Palma, and Paolo Samori</i>	
13.1	Introduction	390
13.2	Kelvin Probe Scanning Force Microscopy	392
13.3	Interpretation of the Signal in KPFM Measurements	396
13.4	Electronic Characterization of Organic Semiconductors	400
13.5	KPFM of Conventional Inorganic Materials	403
13.6	KPFM on Organic Monolayers, Supramolecular Systems, and Biological Molecules	407
13.7	KPFM on Organic Electronic Devices	413
13.8	Conclusions and Future Challenges	422
	Acknowledgements	422
	References	423
	Appendix: Practical Aspects of KPFM	426
III	Other SPM Methodologies	431
14	Scanning Electrochemical Microscopy Beyond Imaging	433
	<i>François O. Laforge and Michael V. Mirkin</i>	
14.1	Introduction	433
14.2	SECM Principle of Operation	434
14.2.1	Feedback Mode	434
14.2.2	Tip Generation/Substrate Collection	436
14.2.3	Substrate Generation/Tip Collection Mode	437
14.3	Instrumentation	438
14.3.1	Tip	438
14.3.2	Positioning	439
14.3.3	Potentiostat	439
14.4	Theory	439
14.4.1	Analytical Approximations for Steady-State Responses	440
14.4.1.1	Diffusion-Controlled Heterogeneous Reactions	440
14.4.1.2	Finite Kinetics at the Tip or Substrate	443
14.4.1.3	SG/TC Mode	444
14.5	Applications	445
14.5.1	Heterogeneous Electron Transfer	445
14.5.1.1	Electron Transfer Kinetics at Solid/Liquid Interfaces	445
14.5.1.2	Liquid/Liquid ET Kinetics	447
14.5.2	Experiments Employing Nanoelectrodes	450
14.5.3	Surface Reactions: Corrosion and Dissolution of Ionic Crystals	452
14.5.4	Biological Systems	454
14.5.4.1	Single-Cell Measurements	454
14.5.4.2	Redox Enzymes	456
14.5.5	Surface Patterning	459

	Acknowledgements	464
	References	464
IV	Theoretical Approaches	469
15	Theory of Elastic and Inelastic Transport from Tunneling to Contact	471
	<i>Nicolas Lorente and Mads Brandbyge</i>	
15.1	Introduction	471
15.2	Theory of Tunneling Conductance	472
15.2.1	Introduction	472
15.2.2	Tunneling Calculations with Bardeen's Transfer Hamiltonian	472
15.2.3	Extension of the Bardeen Approach to the Many-Body Problem	474
15.3	Theory of Inelastic Processes in Electron Transport	475
15.3.1	Linear Model for the Electron-Vibration Coupling	476
15.3.2	Tunneling Regime	477
15.3.2.1	Approaches Based on Scattering Theory	478
15.3.3	Approaches Based on Conductance Calculations	479
15.3.4	Inelastic Approach Based on Bardeen's Approximation	480
15.4	Elastic High-Transmission Regime	484
15.4.1	The Orbital-Based DFT-NEGF Method	485
15.5	Inelastic High-Transmission Regime	492
15.6	Conclusions and Outlook	497
	Acknowledgements	499
	References	499
	Appendix A	502
	Appendix B	504
16	Mechanical Properties of Single Molecules: A Theoretical Approach	508
	<i>Pasquale De Santis, Raffaella Paparcone, Maria Savino, and Anita Scipioni</i>	
16.1	Introduction	508
16.2	DNA Curvature	509
16.3	DNA Flexibility	511
16.4	The Worm-Like Chain Model	513
16.5	DNA Persistence Length in Two Dimensions	514
16.6	A Model for Predicting the DNA Intrinsic Curvature and Flexibility	515
16.7	Mapping Sequence-Dependent DNA Curvature and Flexibility from Microscopy Images	518
16.8	The Ensemble Curvature and the Corresponding Standard Deviation for a Segmented DNA	519
16.9	The Symmetry of Palindromic DNA Images	521
16.10	Experimental Evidence of DNA Sequence Recognition by Mica Surfaces	523

xviii | *Contents*

16.11	Comparison between Theoretical and Experimental DNA Curvature and Flexibility	525
16.12	Sequence-Dependent DNA Dynamics from SFM Time-Resolved DNA Images	529
16.13	Conclusions	531
	Acknowledgements	532
	References	532
	Index	534

Preface

Following the invention of scanning tunneling microscopy (STM), and later of atomic force microscopy (AFM), in the early 1980s a terrific effort has been addressed to the study of morphology and structures of surfaces and interfaces. Immediately, very fascinating and artistically excellent images have been generated, providing a direct view into the nanoworld. Chemists, physicists, and engineers quickly realized the potential of these techniques and started to bestow more and more information on nanoscale objects, expanding their researches beyond imaging, thereby exploring physico-chemical properties of matter in a quantitative manner, and triggering actions that can highlight specific characteristics of the molecular nanosystems under investigation. Such fertile application of scanning probe microscopies (SPMs) takes great advantage of the unique versatility of these tools. Moreover, the simplicity in the different modes as well as their applicability to different kinds of samples provides direct access to new realms at the interface between diverse disciplines, and opens up a vast range of applications that foster materials science in the nanoscale world.

By bringing together the contributions of pre-eminent scientists operating in the field, this book aims at providing a wide overview of different applications of SPM beyond imaging, in particular exploiting STM- and AFM-based approaches, primarily on soft (nano)materials comprising organic, supramolecular, polymeric, and biological architectures adsorbed on inorganic and metallic surfaces. Particular attention is paid to fundamental studies on the interactions governing various nanoscale processes in both biological and artificial supramolecular systems, and to mechanical and electrical properties of molecules and macromolecules, as well as to controlled nanopatterning of soft matter. Moreover, STM examples of chirality in 2D and single-molecule manipulations, as well as STM spectroscopies at the single-molecule level, are highlighted, enabling unprecedented insight to be gained into individual nano-entities. Most importantly, as highlighted in this book, nowadays there are already quite a few groups employing SPM beyond imaging; nevertheless this field is still in its infancy. New applications can be envisioned which surely will be boosted by the implementation of new SPM modes.

I would like to acknowledge all the colleagues who enthusiastically contributed to this book. I am grateful to Martin Ottmar and Eva E. Wille for their invitation to edit this book, and to Waltraud Wüst, who has been working closely with me to

make it a reality. Finally I am thankful to Jean-Marie Lehn for his support in writing the foreword.

ISOF-CNR Bologna
Italy & ISIS-ULP
Strasbourg, France

Paolo Samorì

List of Authors

Jean-Pierre Aimé

CPMOH, Université de Bordeaux I
351 Cours de la Libération
33405 Talence cédex
France

Cristiano Albonetti

CNR – Istituto per lo Studio dei Materiali
Nanostrutturati (ISMN)
Via P. Gobetti 101
40129 Bologna
Italy

Fabio Biscarini

CNR – Istituto per lo Studio dei Materiali
Nanostrutturati (ISMN)
Via P. Gobetti 101
40129 Bologna
Italy

Mads Brandbyge

Department of Micro and Nanotechnology
Technical University of Denmark
Ørstedes Plads, Bldg. 345E
2800 Lyngby
Denmark

Massimiliano Cavallini

CNR – Istituto per lo Studio dei Materiali
Nanostrutturati (ISMN)
Via P. Gobetti 101
40129 Bologna
Italy

Steven De Feyter

Katholieke Universiteit Leuven
Department of Chemistry
Celestijnenlaan 200 F
3001 Leuven
Belgium

Pasquale De Santis

Dipartimento di Chimica
Università di Roma “La Sapienza”
P. le A. Moro 5
00185 Roma
Italy

Frans C. De Schryver

Katholieke Universiteit Leuven
Department of Chemistry
Celestijnenlaan 200 F
3001 Leuven
Belgium

Ray Eby

NanoInk
Inc. 215 E. Hacienda Avenue
Campbell
CA 95008
USA

Alexander Gigler

Department of Experimental Physics
University Ulm
89069 Ulm
Germany

Julio Gómez-Herrero

Departamento de Física de la Materia
Condensada C-III
Universidad Autónoma de Madrid
28049 Madrid
Spain

Seunghun Hong

Physics and NANO Systems Institute
Seoul National University
San 56-1
Sillim-dong
Kwanak-gu
Seoul 151-747
Korea

Frank Jäckel

Department of Physics
Humboldt University Berlin
Newtonstr. 15
12489 Berlin
Germany

Joonkyung Jang

School of Nano Science and Technology
Pusan National University
San 30
Jangjeon-dong
Geumjeong-gu
Busan 609-735
Korea

Mélanie Jeusette

Service de Chimie des Matériaux Nouveaux
Materia Nova/Université de Mons-Hainaut
Place du Parc 20
7000 Mons
Belgium

Rajendra Kshirsagar

CNR – Istituto per lo Studio dei Materiali
Nanostrutturati (ISMN)
Via P. Gobetti 101
40129 Bologna
Italy

François O. Laforge

Department of Chemistry & Biochemistry
Queens College–CUNY
Flushing, NY 11367
USA

Roberto Lazzaroni

Service de Chimie des Matériaux Nouveaux
Materia Nova/Université de Mons-Hainaut
Place du Parc 20
7000 Mons
Belgium

Philippe Leclere

Service de Chimie des Matériaux Nouveaux
Materia Nova/Université de Mons-Hainaut
Place du Parc 20
7000 Mons
Belgium

Byung Yang Lee

School of Physics
Seoul National University
San 56-1
Sillim-dong
Kwanak-gu
Seoul 151-747
Korea

Nicolás Lorente

Laboratoire Collisions
Agrégats, Réactivité
UMR5589, Université Paul Sabatier
118 route de Narbonne
31062 Toulouse cédex 4
France

Othmar Marti

Department of Experimental Physics
University Ulm
89069 Ulm
Germany

Michael V. Mirkin

Department of Chemistry & Biochemistry
Queens College–CUNY
Flushing, NY 11367
USA

Francesca Moresco

Institut für Experimentalphysik
Freie Universität Berlin
Arnimallee 14
14195 Berlin
Germany

Sung Myung

School of Physics
Seoul National University
San 56-1
Sillim-dong
Kwanak-gu Seoul 151-747
Korea

Pedro J. de Pablo

Departamento de Física de la Materia
Condensada C-III
Universidad Autónoma de Madrid
28049 Madrid
Spain

Vincenzo Palermo

Istituto per la Sintesi Organica e la
Fotoreattività
Consiglio Nazionale delle Ricerche
via Gobetti 101
40129 Bologna
Italy

Matteo Palma

Institut de Science et d'Ingénierie
Supramoléculaires (ISIS)
Université Louis Pasteur
8 allée Gaspard Monge
67083 Strasbourg
France

Raffaella Paparcone

Dipartimento di Chimica
 Università di Roma “La Sapienza”
 P. le A. Moro 5
 00185 Roma
 Italy

José I. Pascual

Institut für Experimentalphysik
 Freie Universität Berlin
 Arnimallee 14
 14195 Berlin
 Germany

Jürgen P. Rabe

Department of Physics
 Humboldt University Berlin
 Newtonstr. 15
 12489 Berlin
 Germany

Saleem G. Rao

Department of Physics
 Florida State University
 315 Keen Building
 Tallahassee
 FL 32306
 USA

Paolo Samori

Istituto per la Sintesi Organica e la
 Fotoreattività –
 Consiglio Nazionale delle Ricerche
 via Gobetti 101
 40129 Bologna
 Italy

and

Institut de Science et d'Ingénierie
 Supramoléculaires (ISIS)
 Université Louis Pasteur
 8 allée Gaspard Monge
 67083 Strasbourg
 France

Maria Savino

Dipartimento di Genetica e Biologia
 Molecolare
 Fondazione Pasteur-Cenci Bolognetti
 Università di Roma “La Sapienza”
 P. le A. Moro 5
 00185 Roma
 Italy

Holger Schönherr

University of Twente
 MESA⁺ Institute for Nanotechnology and
 Faculty of Science and Technology
 Department of Materials Science and
 Technology of Polymers
 7500 AE Enschede
 The Netherlands

Anita Scipioni

Dipartimento di Chimica
 Università di Roma “La Sapienza”
 P. le A. Moro 5
 00185 Roma
 Italy

G. Julius Vancso

University of Twente
 MESA⁺ Institute for Nanotechnology and
 Faculty of Science and Technology
 Department of Materials Science and
 Technology of Polymers
 7500 AE Enschede
 The Netherlands

Pascal Viville

Service de Chimie des Matériaux Nouveaux
 Materia Nova/Université de Mons-Hainaut
 Place du Parc 20
 7000 Mons
 Belgium

Phil Williams

Laboratory of Biophysics and Surface Analysis
 School of Pharmacy
 University of Nottingham
 Nottingham NG7 2RD
 UK

Shan Zou

MESA⁺ Institute for Nanotechnology and
 Materials Science and Technology of Polymers
 University of Twente
 7500 AE Enschede
 The Netherlands

Part I
Scanning Tunneling Microscopy-Based
Approaches

Nanoscale Structural, Mechanical and Electrical Properties

1 Chirality in 2D

Steven De Feyter and Frans C. De Schryver

1.1 Introduction

The existence and induction of chirality are among the most intriguing and inspiring phenomena in nature. Chirality can be defined as a geometric property which dictates that an object and its mirror image are non-superimposable by any translation or rotation. A chiral object therefore has no inverse symmetry elements (i.e., center of inversion or reflection planes). In fact, it is easier to create chirality in two dimensions than in three: a surface does not have a center of inversion, and reflection mirror symmetry is only allowed normal to the surface [1–3]. In many cases even the simple adsorption of a single molecule, chiral or achiral, on a substrate leads to the formation of a chiral entity. Often, its two-dimensional self-assembled structures are chiral too.

One of the main reasons why this particular field of research, expression of chirality at surfaces, has only been burgeoning in the last couple of years is the difficulty in evaluating the chiral nature of molecules on surfaces. In Langmuir and Langmuir–Blodgett films, pressure–area isotherms and epifluorescence microscopy were traditionally used to evaluate 2D chirality. However, these techniques do not provide direct insight into the molecular interactions at play. With grazing incidence X-ray diffraction measurements one can achieve information on the ordering of the molecules with near-atomic resolution though, as this is a diffraction technique, data are averaged over a macroscale area [4].

The ability of scanning probe microscopy techniques to investigate the adsorption and ordering of single molecules, clusters, fibers, and complete monolayers, both under UHV and ambient conditions, and at the liquid/solid interface has stimulated the activities in this particular field of research. Expression of chirality upon adsorption can be evaluated, ranging from the submolecular level to extended monolayers. The level of detail these techniques are able to reveal is amazing and over the last few years a wealth of data has been gathered.

1.2

Chirality and STM: From 0D to 2D

1.2.1

Determination of Absolute Chirality

With scanning tunneling microscopy (STM), it is possible to determine the absolute chirality of molecules, for instance of individual adsorbed molecules. The geometric configuration (*cis* or *trans*) of several simple alkenes chemisorbed on the silicon (100) surface has been determined under UHV conditions, through the ability of the STM to identify individual methyl groups [5]. Because both the position and the orientation of those groups could be seen, the absolute configuration (*R* or *S*) for each of the chiral centers formed on chemisorption could be determined. On the Si(100) surface, each surface atom has two “back bonds” to the substrate below, shares in one dimer bond, and has one unsatisfied or “dangling” bond. Those dimers form rows that appear as bars in STM images. Achiral alkenes adsorb molecularly on the silicon dimers forming two Si–C bonds with the dangling bonds on each dimer. Upon adsorption of molecules such as propylene, *trans*-2-butene and *cis*-2-butene on Si(100), small protrusions are observed that are associated with the adsorbed molecules. The butenes show paired protrusions which are associated with the methyl groups. In the STM images, the methyl groups of the *cis* isomer define a line that is at a right angle to the dimer rows. In contrast, the methyl units of the *trans* isomer define a line that is angled at $\sim 30^\circ$ to the dimer row (Fig. 1.1). The alkenes become alkane-like on adsorption as each carbon atom rehybridizes from sp^2 to sp^3 , forming a bond to one silicon atom (of the same dimer) and thereby satisfying the dimer dangling bonds. As a result, two chiral centers are induced upon chemisorption. The reaction of *trans*-2-butene leads to two chiral products (either *R,R* or *S,S*) whereas the reaction of *cis*-2-butene results in a nonchiral product (*R,S* or *S,R*). As both sites of *trans*-2-butene react with equal probability, an equal number of *R,R*- and *S,S* enantiomers are formed. This is a clear example of how the superior resolution provided by STM allows identification of the chiral nature of individual adsorbed molecules.

The direct determination of the absolute configuration has also been demonstrated for a larger organic molecule with a single chiral carbon atom, i.e., (*R*)/(*S*)-2-bromohexadecanoic acid, $(\text{CH}_3(\text{CH}_2)_{13}\text{CHBrCOOH})$, which forms 2D crystals at the liquid/solid interface [6]. In the high-resolution images, the relative position of the bromine atom (bright) and the carboxyl group (dark) can be discerned, from which the orientation of the rest of the alkyl chain is also determined (Fig. 1.1). The long alkyl chain of the molecule must lie on the opposite side of the bromine atom from the carboxyl group. Given that three of the four groups attached to the chiral carbon atom have been determined directly, the fourth, which is a hydrogen atom, is right underneath the bromine atom. Therefore, the atomic resolution enables direct determination of the absolute configuration of a single organic molecule.

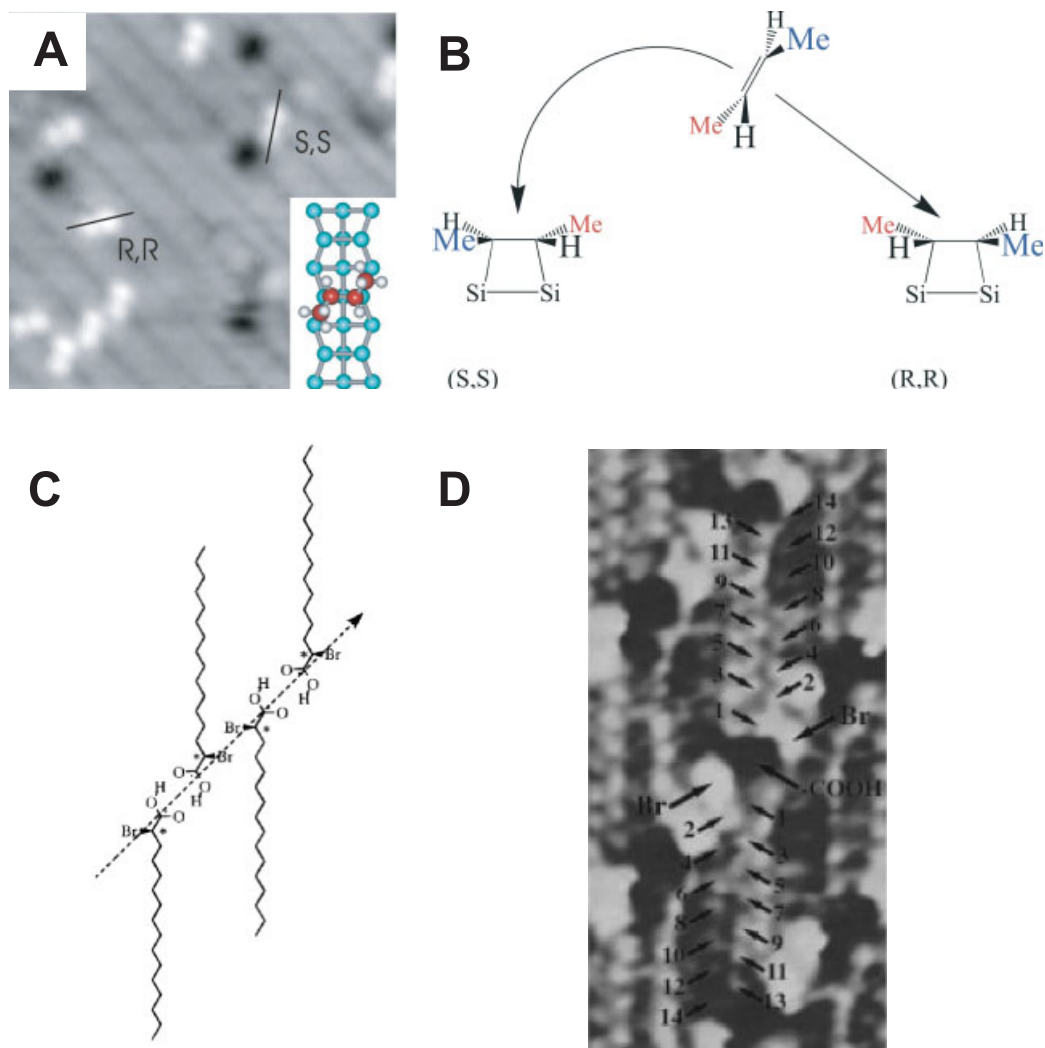


Fig. 1.1 (A) STM image of *trans*-2-butene on Si(100). The bar-like structures are the dimer rows of the silicon substrate. The protrusions are the methyl groups of the adsorbed molecules. Image area 7.5 nm \times 7.5 nm. The black lines are drawn through the methyl groups to show the orientation of these with respect to the substrate. (B) Scheme explaining the two ways *trans*-2-butene can approach the surface. Reprinted with permission from

ref. 5. (C) Schematic of the molecular structure of (*R*)-2-bromohexadecanoic acid physisorbed on graphite. Detailed assignment of individual atoms on a zoom of an STM image of a chiral pair of (*R*)-2-bromohexadecanoic acid molecules. The numbers 1–14 point to the positions of 14 hydrogen atoms on the 14 methylene groups. Reprinted with permission from ref. 6.

Though in both cases the absolute chirality has been determined, the systems differ significantly. In the first example individual molecules are chemisorbed, while in the second case physisorbed molecules form a 2D crystal. Chemisorption can strongly affect the nature of the adsorbed molecule, for instance by creating chiral centers as a result of a change in the state of hybridization of the carbon atoms. In contrast, physisorption does not affect the molecular properties substantially upon adsorption.

1.2.2

Expression of 2D Chirality by Enantiopure Molecules

Enantiomers always form mirror image structures on a surface as long as the presence of the chiral center effectively influences the adsorption of the molecules, because the interaction with the surface leads to the formation of diastereomeric adsorbed states. Kühnle et al. reported on the chiral recognition in the dimerization of adsorbed cysteine, a natural amino acid, under UHV conditions [7]. Pure cysteine enantiomers are adsorbed as pairs on the gold surface (Figs. 1.2A(a) and 1.2A(b)). D-Cysteine pairs are the mirror image of L-cysteine pairs with respect to the symmetry of the gold surface. The molecules are chemisorbed on the gold surface; the carboxylic acids form hydrogen bonds. Most amino acids bind to metal surfaces by the amino and carboxylic acid groups, though cysteine ($\text{HS-CH}_2\text{-CH(NH}_2\text{)-COOH}$) also has a thiol group which is known to interact strongly with gold. The chiral recognition in this system can be explained by a three-point contact model (sulfur-gold, amino-gold, carboxylic-carboxylic). At higher coverages, the molecules form small clusters composed of eight cysteine molecules. The cluster consists of a central part composed of two subunits centered on a close-packed gold row, surrounded by three smaller subunits on each side on top of neighboring close-packed rows (Fig. 1.2A(d)) [8]. The upper left and lower right corner units appear higher than the other four side units. The clusters formed by the two enantiomers are identical, except that they are mirror images. The appearance of the dimers is chiral with respect to the substrate, while for the clusters their internal structure is chiral too.

Raval et al. reported on the extended surface chirality from supramolecular assemblies of adsorbed chiral molecules, which are of relevance to heterogeneous enantioselective catalysis [9]. The STM images reveal that the (*R,R*)-bitartrate molecules on Cu(110) are self-assembled in rows of three, each row stacking in parallel with others to form long chains (Fig. 1.2B). The growing direction does not coincide with one of the symmetry directions of the underlying metal surface, which implies the creation of a chiral surface that is non-superimposable on its mirror image. This self-assembly was attributed to the close proximity of the hydroxy groups on neighboring bitartrate molecules, leading to intermolecular hydrogen-bonding interactions that extend across the surface. (*R,R*)-Tartaric acid and (*S,S*)-tartaric acid form identical 2D patterns. However, the respective patterns are related by mirror symmetry. The mirror positions of the OH groups in the two enantiomers lead to a switch in supramolecular assembly directions. In the case of

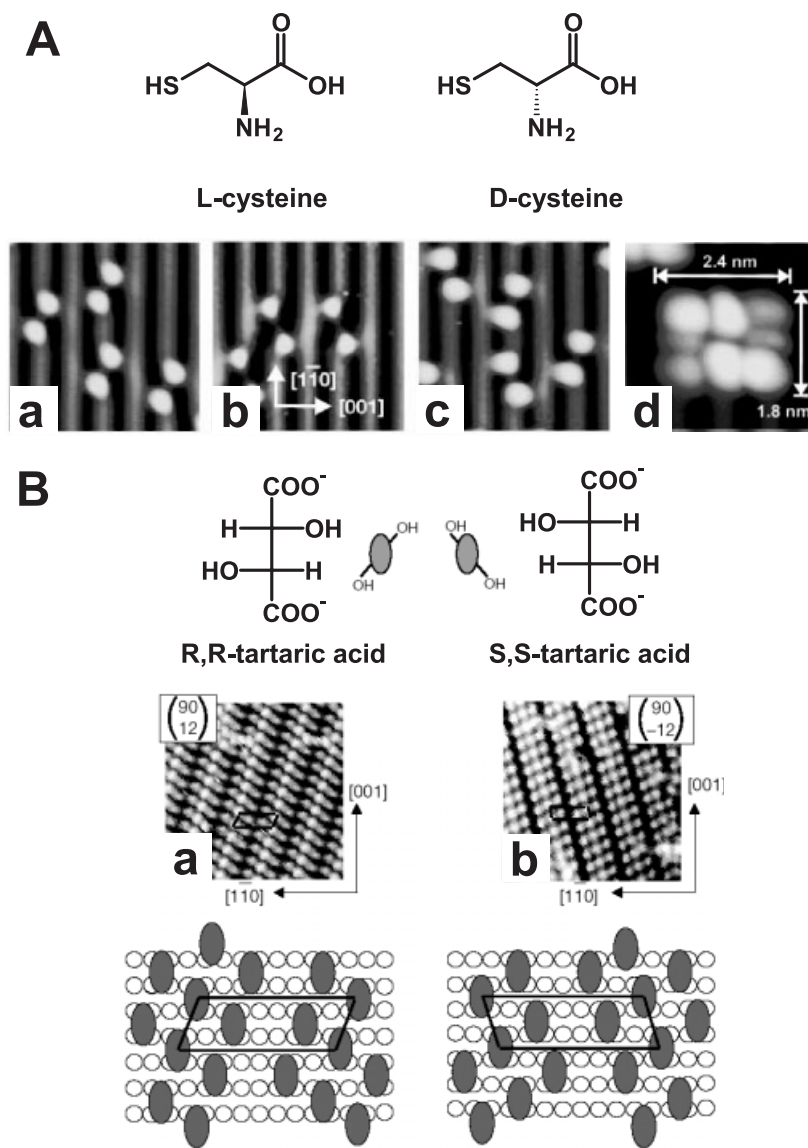


Fig. 1.2 (A) STM images on an Au(110) surface of (a) L-cysteine pairs; (b) D-cysteine pairs; (c) molecular pairs formed from DL-cysteine. Image size is 49 Å × 53 Å; (d) close-up of an L-cysteine nanocluster. Image size

32 Å × 32 Å. (B) STM images on Cu(110) of (a) (R,R)-tartaric acid monolayers; (b) (S,S)-tartaric acid monolayers. Image size 108 Å × 108 Å. Reprinted with permission from Refs. 7, 8, and 9.

tartaric acid, the formation of a chiral array does not depend only on the adsorption phase but also on the substrate. Tartaric acid does not form chiral arrays on Ni(110) [10] but it does on Ni(111) [11]. Of interest is the fact that when the doubly deprotonated species attaches to Ni(110), a chiral rearrangement of four Ni atoms occurs and the adsorption site possesses an electronic structure composed of chiral single-electron wavefunctions [12].

Chemisorbed 2D chiral layers are formed not only under UHV conditions but also under ambient conditions. (*R*)- and (*S*)-1,1'-Binaphthalene-2,2'-dithiol, which are the two enantiomers of an atropisomeric compound, form ordered monolayer domains on an Au(111) surface upon dipping the substrate in an ethanol solution, via the formation of the sulfur-gold bonds. The twisted aryl groups enable the detection of the shape of the molecule in the STM observations. The monolayer was described by a rhombic unit cell and, as expected, both enantiomers form mirror-type monolayer structures. In addition, the data also show evidence that the chiral surface is commensurate with the structure of the underlying Au(111) surface [13].

When enantiopure heptahelicene molecules are forced under UHV conditions into a close-packed monomolecular layer, molecular chirality is transformed into monolayer chirality (Fig. 1.3) [14]. When the molecules are squeezed together repulsive forces dominate the lateral interaction. The self-assembly is obviously governed not only by the interaction between the molecules but also by adsorbate-substrate interactions which determine the mobility of the molecules on the surface. On Ni(111) and Ni(100) the low mobility of the helicenes did not allow the observation of chiral effects. On Cu(111) the molecules are observed to diffuse readily at coverages below 95%. At 95% coverage, a long-range ordered structure is observed, apparently built up from clusters containing six molecules and clusters containing three molecules. At 100% surface coverage, the unit cell of the adsorbate lattice contains a group of three molecules. The observed adsorbate lattice structures show enantiomorphism: adsorption of the *P* enantiomer of the helicene leads to structures which are mirror images of those observed for the *M* enantiomer. In addition to the chiral shape of the unit cell, the arrangement of the molecules within the unit cell is also chiral. The hexamer (95% coverage) has a pinwheel-like shape and the pinwheel's wings point either anticlockwise, as found for (*M*)-heptahelicene, or clockwise, as found for (*P*)-heptahelicene. In the case of the trimers (100% coverage) the mirror symmetry is expressed by tilts of the three-molecule cloverleaf units in opposite directions with respect to the adsorbate lattice vectors.

Walba et al. were the first to report on the ordering of chiral molecules and the expression of 2D chirality [15]. They highlighted the direct observation of enantiomorphous monolayer crystals from liquid-crystalline (smectic A phase) enantiomers by STM on highly oriented pyrolytic graphite (HOPG) at room temperature. The images of monolayer crystals grown from both enantiomers exhibited well-defined rows of tilted, rod-shaped bright regions, but with the bright rods tilted in opposite directions for the enantiomers. However, the formation of quasi-enantiomorphous images from a single enantiomer also has been reported, i.e., domains which are chiral and apparently of opposite handedness. Clearly, two

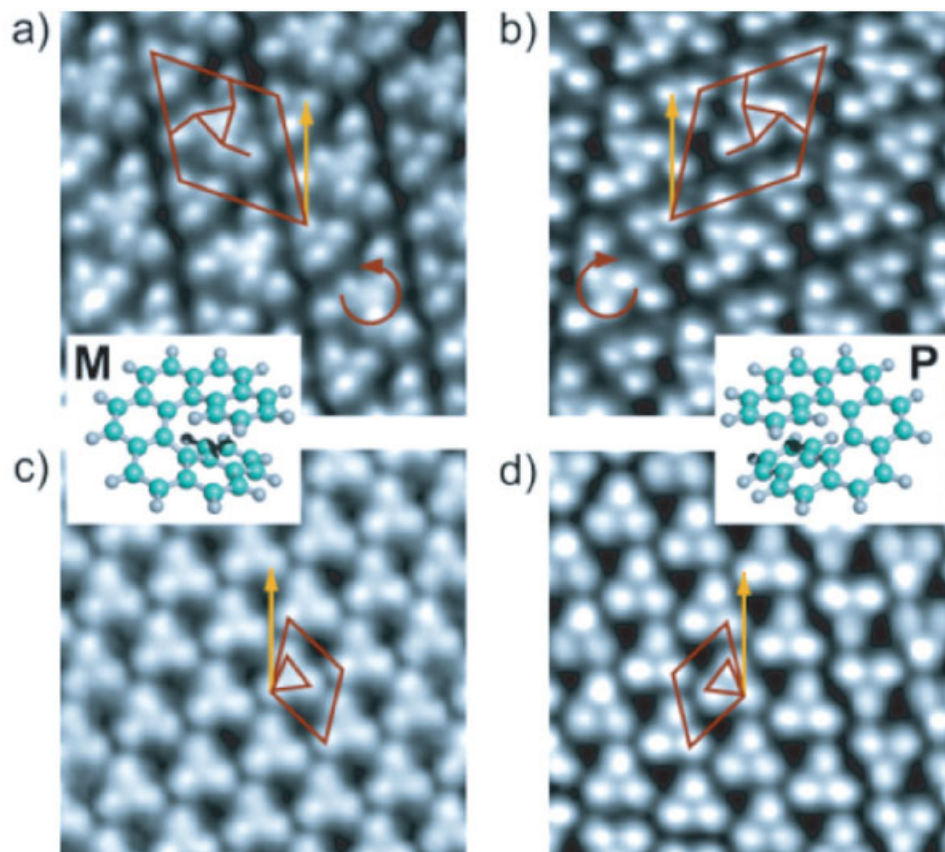
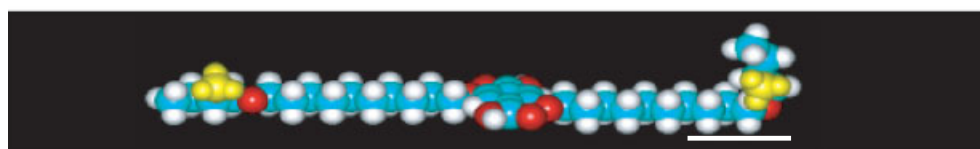
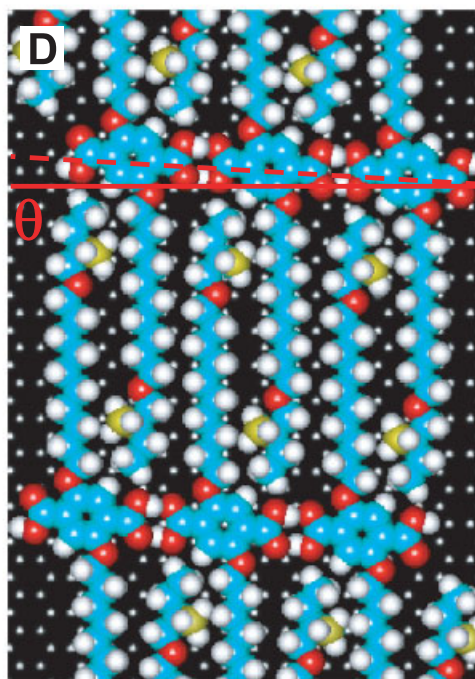
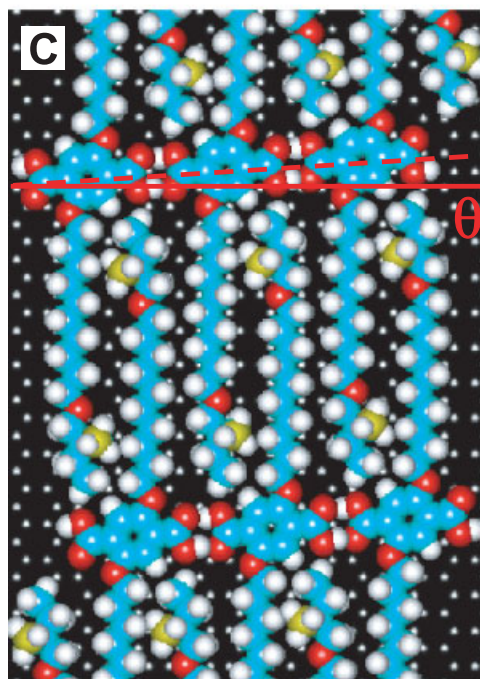
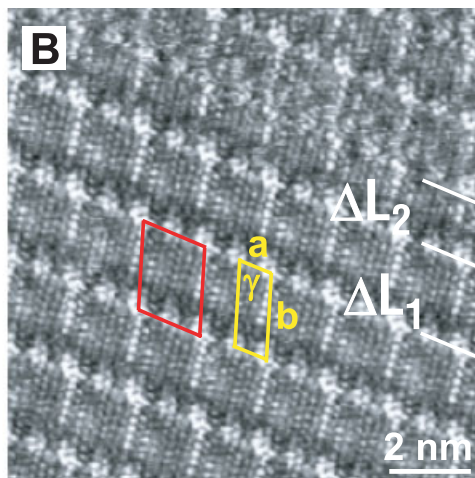
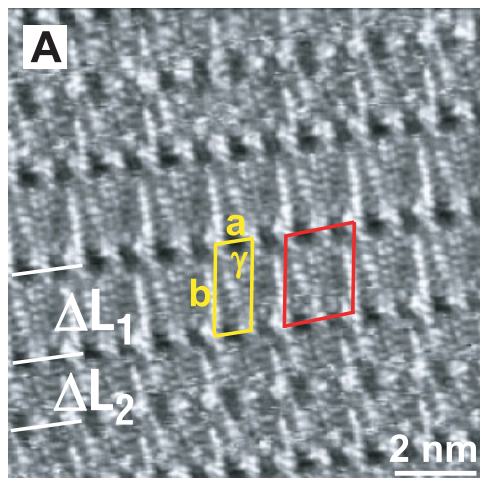
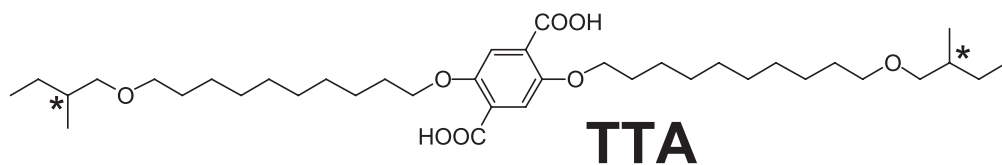


Fig. 1.3 STM images of (a, c) (M)- and (b, d) (P)-heptahelicene (10 nm \times 10 nm). Monolayer coverage is 0.95 (a, b) and 1.00 (c, d). Both enantiomers clearly form mirror-image structures. Reproduced with permission from ref. 14.

such crystal domains cannot be enantiomeric because they are composed of the same enantiomer. In fact, they appear in the images as only enantiomorphous. Such domains, which apparently form mirror images, are diastereomeric. The exact orientation of the molecules with respect to each other or to the substrate is different in both cases [16].

At the liquid/solid interface also, molecules express their chirality. Examples include terephthalic acid derivatives [17], carboxylic acid derivatives [18], dihydroxyalkanes [19], *p*-phenylene-vinylene oligomers [20–23], and many others. In all these systems, the enantiomers form enantiomorphous monolayers. Figures 1.4(A) and 1.4(B) represent respective STM images of physisorbed monolayer structures of the *S* and *R* enantiomers of a chiral terephthalic acid derivative, 2,5-



bis[10-(2-methylbutoxy)decyloxy]terephthalic acid, with two identical stereogenic centers. The aromatic terephthalic acid groups appear as the larger bright spots. The monolayers are characterized by two different spacings between adjacent rows of (*R*)-TTA or (*S*)-TTA terephthalic acid groups. For both enantiomers, the width of the broader lamellae ($\Delta L_1 = 2.54 \pm 0.05$ nm) corresponds to the dimension of fully extended alkoxy chains, which are lying flat on the graphite surface and almost parallel to a main graphite axis. The width of the narrow lamellae ($\Delta L_2 = 1.9 \pm 0.1$ nm) indicates that the terminal 2-methylbutoxy groups are bent away from the surface, while the decyloxy groups are lying flat on the graphite surface adopting an all-*anti* conformation. For this system, monolayer chirality is expressed in several ways. In regions of the monolayer where the alkoxy chains are fully extended, the unit cells for the *S* and *R* enantiomers are clearly chiral. Moreover, the STM images exhibit a clear modulation of the contrast along the lamellae. This superstructure (Moiré pattern) is attributed to the incommensurability of the monolayer with the underlying graphite lattice. The unit cells of this contrast modulation, indicated in red, are mirror images for both enantiomers, which means that each enantiomer forms its characteristic enantiomorphous monolayer structure. This enantiomorphism is also expressed by the orientation of the lamella axes with respect to the graphite lattice: the angle θ between a lamella axis (any line parallel to a row formed by terephthalic acid groups) and a graphite reference axis, which is (nearly) perpendicular to the alkoxy chains, takes a value of $-3.7 \pm 0.3^\circ$ and $+3.7 \pm 0.3^\circ$ for the *S* and *R* enantiomer, respectively. In addition to the effect of chirality on the 2D ordering of these monolayers outlined above, monolayer images reveal elongated discontinuous feature both in narrow and wide lamellae. In the narrow lamellae, the position of those features can be identified with the location of 2-methylbutoxy groups, which are pointing away from the graphite surface. The discontinuous fuzzy character of the observed features is due to the mobility of the non-adsorbed chain ends and the interaction with the STM tip during the scanning process. However, these streaky features are also observed in the wide lamellae, and are attributed to the interaction between the scanning tip and the protruding methyl unit on the chiral carbon atom, which allows the visualization of the location of stereogenic centers in a direct way. Further support was provided by the observation that an increase in the bias voltage which results in a slight retraction of the tip leads only to the disappearance of the spots correlated with the stereogenic centers, while the spots related to the 2-methylbutoxy groups are still visible.

Compounds with more than two identical chiral centers have also been investigated, such as different classes of chiral *p*-phenylene-vinylenes. They all carry (*S*)-2-

←
Fig. 1.4. STM images at the solid (HOPG)/liquid interface and models of (A, C) (*R,R*)-TTA; (B, D) (*S,S*)-TTA. Both enantiomers form mirror-image type patterns. Bottom: alkyl chains are not always extended; the 2-methylbutoxy group is often raised up from the HOPG surface (ΔL_2). The monolayer unit cell (for the fully extended alkyl chains (ΔL_1)) is indicated in yellow. The red unit cell refers to the epitaxy with the HOPG surface. Adapted with permission from ref. 17.

methylbutoxy groups along the backbone. In the first type, oligo-*p*-phenylene-vinylene enantiomers which are functionalized with three dodecyl chains at both termini (Fig. 1.5A) self-assemble in highly organized enantiomorphous 2D crystals on graphite by spontaneous self-assembly. They form stacks and the bright features correspond to the conjugated backbones, of which one is indicated by a white oval [20]. Alkyl chains are interdigitated. In the second and the third types, the molecules are functionalized by hydrogen-bonding groups such as ureido-*s*-triazine (type 2) (Fig. 1.5B) or 2,5-diaminotriazine groups (type 3) (Fig. 1.5C). The ureido-*s*-triazine-derivatized oligo-*p*-phenylene-vinylenes show linear dimerization via self-complementary hydrogen bonding, as expected [21]. The molecules are indeed stacked in parallel, though not equidistant, rows. These compounds show exclusively enantiomorphous monolayer formation: the long axis of the conjugated backbones of their dimers are rotated counterclockwise with respect to the normal on the lamella axis. In contrast to the stacked arrangement of these molecules, the 2,5-diaminotriazine-derivatized oligo-*p*-phenylene-vinylenes show cyclic hexamer formation [22, 23]. Hydrogen bonding between the triazine moieties drives the cyclic pattern formation. The chiral (*S*)-2-methylbutoxy groups on the oligo-*p*-phenylene-vinylene units determine the handedness of the rosette. It is surprising that the handedness of the rosettes reverses upon lengthening the oligo-*p*-phenylene-vinylene unit by one monomer. This has been attributed to the balance between substrate coverage and steric interactions, not at the level of an individual rosette but at the monolayer level.

Determination of 2D chirality has been targeted by electrochemical STM also [24–26].

The details of the chirality induction mechanism differ from compound to compound. In the case of compounds with the chiral center in the alkyl chain, i.e., a methyl group instead of a hydrogen atom, calculations show that the most stable configuration is the one with the methyl group directed away from the substrate, in order to maximize the interactions between the alkyl chains and substrate [27].

1.2.3

Racemic Mixture of Chiral Molecules

The question of whether a racemic mixture of chiral molecules undergoes spontaneous separation into enantiopure domains on a solid surface is of special interest. Will a racemate form or will the molecules undergo spontaneous spatial resolution, leading to racemic conglomerate formation? In 3D systems the formation of these so-called conglomerates is rather the exception than the rule: most racemic mixtures crystallize as racemates with the unit cell composed of an equal number of molecules with opposite handedness, or as random solid solutions. Due to the confinement of the molecules in a plane and the interaction with the substrate, conglomerate formation becomes more likely on a solid surface. Indeed, in most cases spontaneous resolution occurs, on the cluster level as well as on the monolayer level.

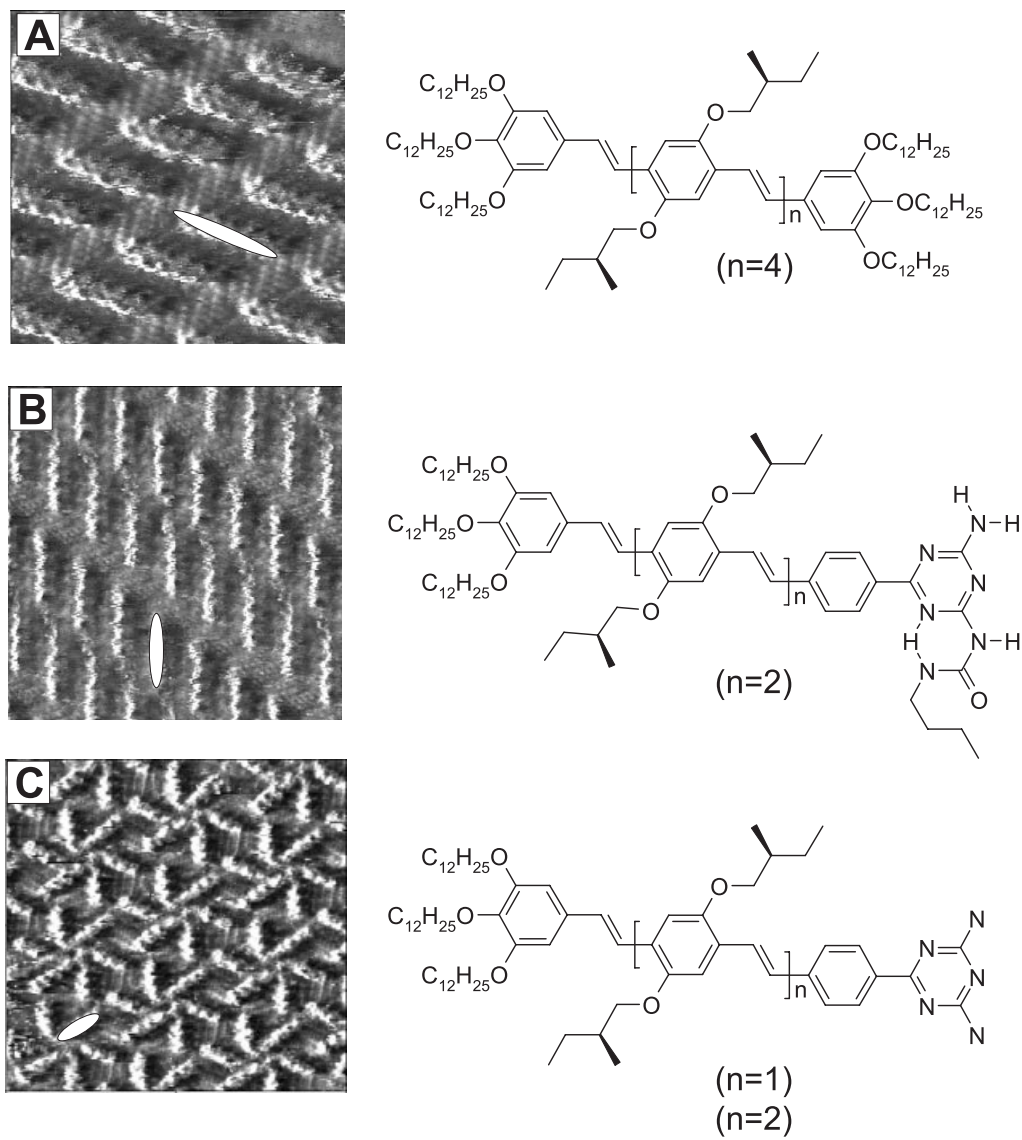


Fig. 1.5 STM images and chemical structures of chiral *p*-phenylene-vinylenes: (A) $n = 4$ (image size: 10.7 nm \times 10.7 nm); (B) $n = 2$ (image size: 12.1 nm \times 12.1 nm); (C) $n = 2$ (image size: 18.4 nm \times 18.4 nm) at the liquid/

HOPG interface. Hydrogen bonding has a strong effect on the supramolecular architecture. The white ovals indicate a conjugated backbone. Reprinted with permission from Refs. 20, 21, and 22.

Pseudo-racemate formation has been reported in only a few cases. In the STM images of PB (Fig. 1.6) physisorbed at the 1-phenol/octane/ or 1-heptanol/graphite interface, the phenyl benzoate moieties show up as the bright structures corresponding to a high tunneling current through the aromatic groups [28, 29]. The alkyl chains are located in between the rows of the phenyl benzoate groups, and sometimes their orientation can be discerned. The location and orientation of a number of phenyl benzoate groups are indicated by sticks. The molecules form chains which in turn form dimers. The X-ray data of their 3D crystals indicate hydrogen-bonding interactions along the chains and between them through the formamide groups. The molecular chirality of the pure enantiomers of PB is expressed at the 1-heptanol/solid interface at two different levels: (a) at the level of the monolayer structure as expressed by the orientation of the phenyl benzoate moieties (α) with respect to the lamella normal; (b) at the level of the orientation of the adlayer with respect to the underlying graphite lattice as expressed by the direction of the lamella axis of the monolayer with respect to the symmetry axes of graphite (θ) (Fig. 1.6B,C). The latter correlation can be made because after imaging a monolayer each time, the graphite lattice is recorded under identical experimental conditions except for the lowering of the bias voltage which allows imaging of the graphite surface underneath the monolayer. The histograms in Fig. 1.6(D) represent the number of domains of which the lamella axis is rotated a given angle θ with respect to the reference axis of the graphite; they reflect this second level of expression of chirality for (*R*)-PB, (*S*)-PB, and *rac*-PB, respectively. Despite the considerable spread, in none of the three cases is the orientation of the lamella axis completely random with respect to the substrate symmetry. (*R*)-PB has a strong tendency to form domains with $\theta > 0$ (Fig. 1.6D(a)) whereas (*S*)-PB preferentially forms domains with $\theta < 0$ (Fig. 1.6D(b)). In addition, both enantiomers form a substantial fraction of domains for which the angle θ is close to zero (Fig. 1.6D(a,b)). In contrast to the enantiopure forms, the racemate exclusively forms domains with the angle θ_1 close to zero (Fig. 1.6D(c)). So, the patterns formed by the racemate are not a mere reflection of the adsorbate layers formed by the pure enantiomers. Therefore no racemic conglomerate formation takes place. The exclusive formation of $\theta = 0$ domains for the racemate suggests that there is a preferred interaction between the two enantiomers, as opposed to the formation of homochiral domains.

1.2.4

Achiral Molecules

Molecules which are achiral in the gas or solution phase are described as prochiral, so one desymmetrizing step away from chirality, if they become two-dimensionally chiral when they are constrained to a surface. Why do achiral molecules form chiral 2D structures? Many achiral molecules are prochiral, as adsorption can lead to two mirror-type structures: rotation or translation of the molecule within the plane of the substrate does not convert the molecules into each other.

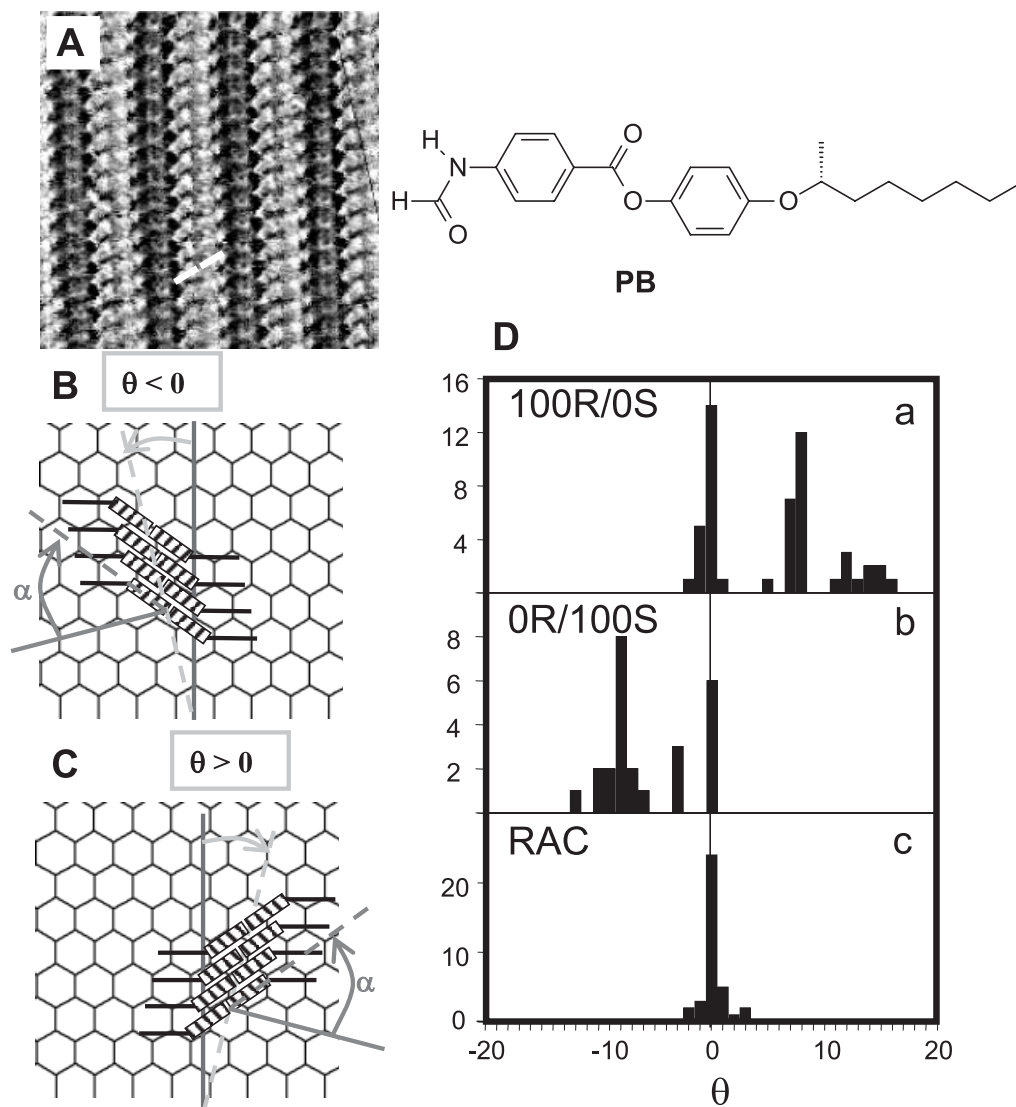


Fig. 1.6 (A) STM image of (*R*)-PB at the 1-heptanol/graphite interface. Image size: 11.0 nm \times 11.0 nm. Two phenyl benzoate groups are indicated by a white bar. (B, C) Schematic representations of the orientation of “dimers” of PB on graphite. The reference axis of graphite is indicated as a solid line. The broken light gray represents a lamella axis.

θ = angle between the reference axis and the lamella axis; α = angle between the normal on the lamella axis and the (*R*)-PB dimer. (D) Histograms of the angle θ observed for physisorbed monolayers of (a) (*R*)-PB; (b) (*S*)-PB; (c) *rac*-PB. Reprinted with permission from ref. 29.

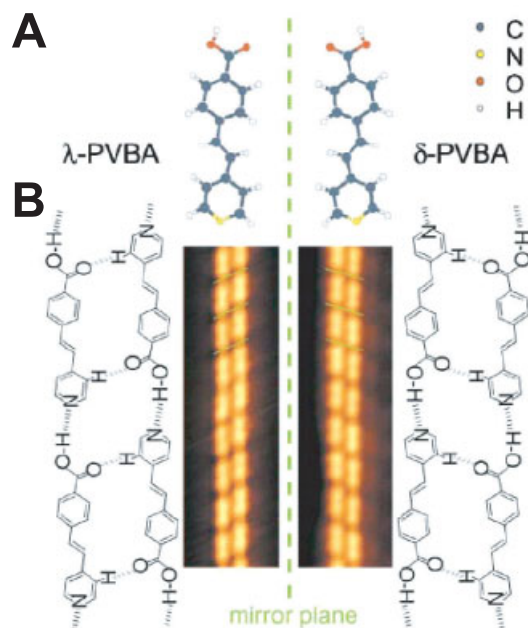


Fig. 1.7 (A) Mirror image relationship between the two possible adsorption geometries of PVBA. (B) Models and STM images of the chiral twin chains. Adapted with permission from ref. 30.

Consider for instance 4-*trans*-2-(pyrid-4-ylvinyl)benzoic acid (PVBA): this molecule can be placed in two different ways on a surface: it cannot be superimposed by any in-plane translation or rotation and is 2D-chiral because of the kink in the middle of the molecule [30]. Figure 1.7 shows that the constituent molecular rows of the twin chains can have two relative displacements, related by mirror symmetry. Therefore, the twin chains display supramolecular chirality. Molecular dynamics simulations indicate that all the molecules in a twin chain have the same 2D chirality, suggesting real spontaneous chiral resolution.

A detailed comparison of tartaric acid with achiral succinic acid informs us that the bisuccinate phase produces domains which consist of rows of three bisuccinate molecules that assemble into long chains at the surface [31]. These chains lie along nonsymmetry directions and are chiral, similarly to tartaric acid, leading overall to a racemic conglomerate of coexisting mirror domains. For both compounds, the two COO–Cu bonding interactions constitute the primary factor determining the nature, ordering, density, and chirality of the superstructures formed. The OH groups in tartaric acid do not dictate the supramolecular ordering – succinic acid forms a similar supramolecular organization – however, they break the degeneracy by molecular distortion/metal substrate reconstruction effects. The formation of chiral patterns from the achiral succinic acid is intimately related to the nature of the molecule–metal bonding.

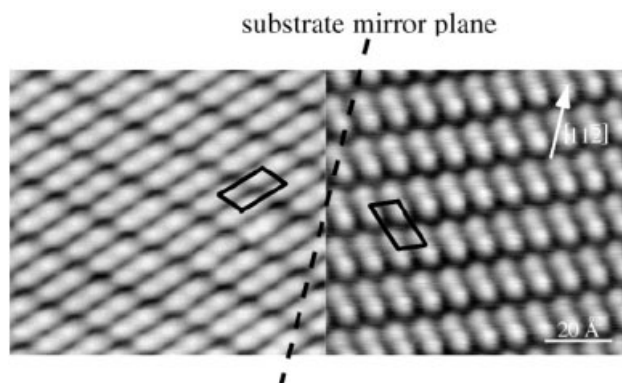


Fig. 1.8 Enantiomorphism of PEBA islands on Ag(111). Two mirror domains together with their respective unit cells are shown. Printed with permission from ref. 32.

An interesting case is provided by comparison with the supramolecular patterns (islands) formed by 4-[(pyrid-4-ylethynyl)]benzoic acid (PEBA) [32]. Although the molecule is 2D-achiral (the asymmetry of the carboxylic acid group is disregarded as the hydrogen atom is expected to move freely from one oxygen atom to the other on the surface), the islands represent a pair of enantiomorphic supramolecular structures because of a distinct shift of adjacent molecular chains in the islands, and consequently are not simply rotational domains. In contrast to PVBA, where 2D enantiomers assemble in supramolecular chiral structures because of resolution of a racemic mixture, in the PEBA case enantiomorphic structures result from the distinct packing of a 2D achiral species (Fig. 1.8).

The formation of supramolecular clusters by nitronaphthalene (NN) forms another interesting case [33, 34]. STM images of the NN-covered Au(111) surface at about 70 K reveal that molecular aggregates of distinct size and geometry have self-assembled. About 85% of these structures are composed of ten molecules arranged in a modified pinwheel structure (Fig. 1.9). Two related kinds of decamers are observed, which behave in a similar manner to an object and its mirror image and cannot be transformed into one another by rotation and translation within the surface plane. Note that the mirror symmetry does not mean that a decamer consists exclusively of one of the 2D enantiomers, as one might think: however, the inversion of symmetry implies that they are composed of an even number of both 2D enantiomers. Molecular dynamics calculations performed by these authors (Böhlinger et al.) suggest an 8:2 ratio (2:8 for the opposite chirality). Moreover, they demonstrated most elegantly the manipulation capabilities of STM. By adjusting the experimental tunneling parameters, they achieved lateral movement of the clusters over the surface, without affecting the chirality and the supramolecular arrangement of the clusters. These experiments indicate that the decamers behave as supermolecules whose stability, structure, and chirality are determined by intermolecular interactions. Böhlinger et al. achieved separation of R and L clusters in

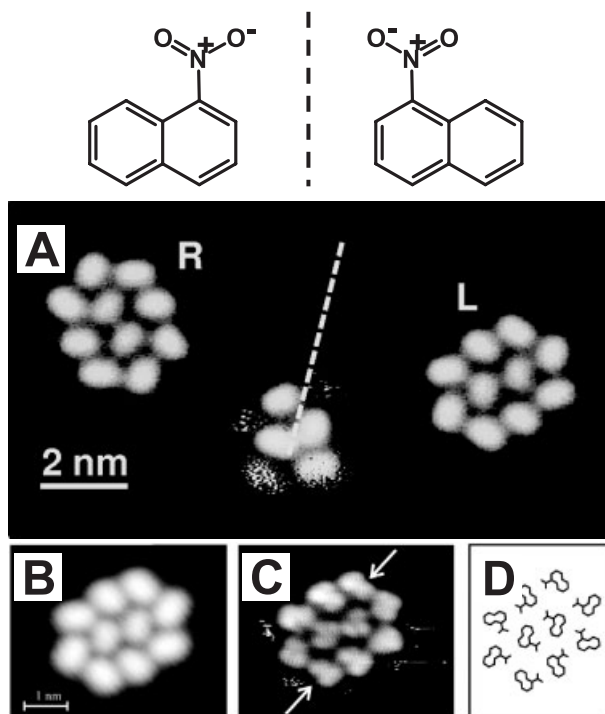


Fig. 1.9 Mirror-image relationship between the two possible adsorption geometries of NN. (A) Two-dimensional chiral decamers (denoted L and R) formed by NN molecules on the Au(111) surface. The broken line is the mirror plane. (B, C) High-resolution images of a decamer. (D) A molecular model obtained by molecular dynamics simulations. Decamers comprise of an even number of both 2D enantiomers in an 8:2 ratio (or vice versa). Adapted with permission from Refs. 34 and 33.

separate domains on the surface. This “2D” experiment is similar to the famous one performed more than 150 years ago by Pasteur. In analogy with tweezers and a magnifier which Pasteur needed to mechanically resolve enantiomorphous crystals obtained from a solution of racemic sodium ammonium tartrate, these authors used the STM tip to identify the enantiomorphous clusters and to separate them.

Coordination chemistry can also be involved in the expression of chirality at surfaces. The assembly of achiral molecules and metal centers at a metal surface can lead to the formation of chiral complexes [35]. Following codeposition of iron atoms and trimesic acid (TMA) on Cu(100), the molecules react with the metal centers to form chiral complexes stabilized by metal–ligand interactions (Fig. 1.10). Upon annealing of the sample which was formed by evaporating Fe atoms and TMA molecules in a 1:4 ratio, flower-shaped arrangements with a central protrusion decorated by four TMA molecules were observed by codeposition at low concentrations. These flower-shaped structures were identified as compounds

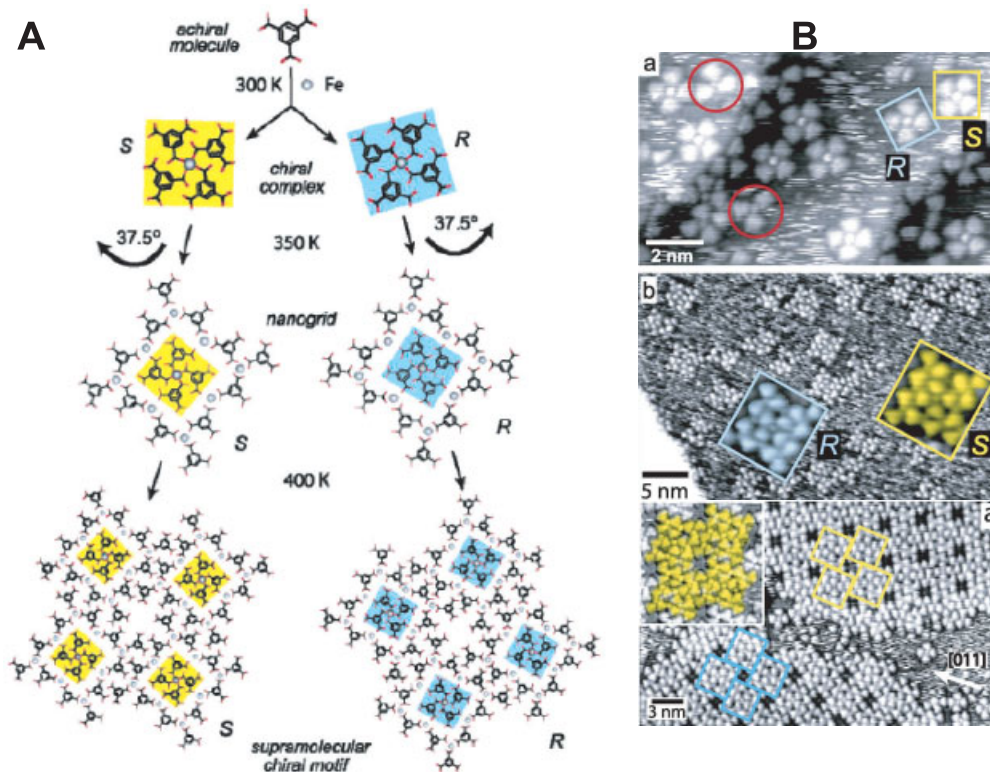


Fig. 1.10 (A) Scheme of the formation of chiral complex of supramolecular chiral motifs based on metal–ligand interactions on Cu(100) (UHV). (B) Corresponding STM images. Reprinted with permission from ref. 36.

from a central Fe atom surrounded by four TMA molecules. High-resolution images show that the TMA molecules do not point straight to the central Fe atom. The triangular envelope is rotated by 22.5° clockwise or counterclockwise with respect to the principal axis of the complex, which can be attributed to the mode of interaction between TMA and Fe: due to the unidentate Fe–carboxylate bond, one of the oxygen atoms of the carboxylate group involved in the bonding is significantly closer to the central Fe atom than the other. In addition, the angle between the high-symmetry direction of the substrate and the principal axis of the complexes is $+75^\circ$ or -75° . A strict relationship exists between the orientation of the complexes with respect to the substrate symmetry and the apparent rotation direction of the TMA molecules in the complexes. In a complex rotated by $+75^\circ$ (-75°) relative to the substrate direction, each individual TMA molecule rotates counterclockwise (clockwise). Of special interest is the fact that complex formation is only the first step in a hierarchical assembly toward the formation of homochiral nano-

cavity arrays. Upon further annealing of samples containing the flower-leaf type of complexes described, polynuclear assemblies which typically consist of 16 TMA molecules arranged in square-like molecular 4×4 nanogrids are formed. The attachment of the extra TMA molecules is mediated by the incorporation of further metal atoms forming a second coordination shell. The central cloverleaf complexes are rotated by 37.5° with their chiral nature persisting. The chiral arrangement of the secondary core units induces dissymmetric tertiary nanogrids. The final stage of the complexation, which is achieved upon further annealing, leads to the formation of extended regular metal–organic superstructures, giving rise to nanocavities by the interlocking of four nanogrids which were formed in the previous annealing process. The interlocked nanogrids are of the same chirality, associated with the fact that only homochiral species match. As a consequence, two sets of different chirality coexist at the surface, though in different domains [36].

Some other examples of chiral patterns formed by achiral molecules include supramolecular assemblies of “lander” molecules [37], discotic [38], and smectic [39] liquid crystals, and achiral purine molecules [40].

Similarly to chiral molecules, most achiral systems which become 2D-chiral upon adsorption on a surface show conglomerate formation: packing of one stereoisomer with copies of itself is thermodynamically more favorable (or kinetically faster) than packing with other molecules [41]. Adsorption of a prochiral molecule to an achiral surface creates a racemic adlayer if the adsorption geometry establishes different interactions between the two (formerly) enantiotopic groups on the surface. Chiral domains with chiral unit cells form when interactions between identical 2D enantiomorphs are more favorable than between opposite 2D enantiomorphs. Mixed domains with unit cells containing both enantiomorphous forms should be formed when interactions between opposite isomers are more favorable. An elegant system has been presented where the stereochemical morphology of monolayers formed from alkylated prochiral molecules on HOPG switches from a 2D racemate to a 2D conglomerate by the addition of a single methylene unit to each side chain. The two anthracene derivatives (1,5-bis(3'-thiaalkyl)anthracenes) contain linear alkyl chains on the anthracene in 1 and 5 positions; the alkyl chains of the longer analogue contain one additional CH_2 . A striking difference is observed between the two compounds. For the smaller compound ($n = 11$) the orientation of the anthracene moieties alternates from row to row, leading to a racemic monolayer with pg plane group symmetry, while for the longer analogue ($n = 12$) the orientation of the anthracene units remains constant within a given domain, reflecting the formation of a 2D conglomerate monolayer with $p2$ plane group symmetry. Isolated mirror-image 2D enantiomers have identical energy whereas pairs of interacting 2D isomers are diastereomeric and have distinct energies. For both compounds, the lowest-energy row contains molecules of identical 2D chirality. However, the difference between the two compounds occurs between adjacent rows. What determines this difference? The monolayer structure is determined both by molecule–molecule and molecule–substrate interactions. Alkyl chains tend to align along one of the main symmetry axes of graphite and methylene groups of adjacent chains align in registry so as to maximize intermolecular van

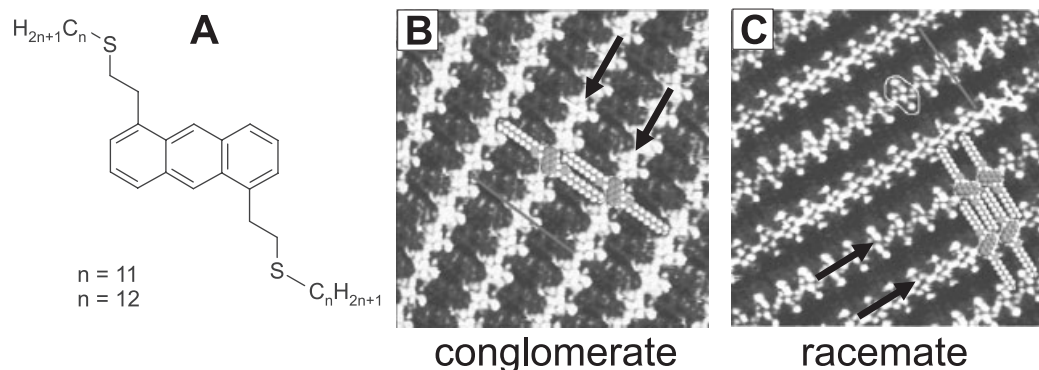


Fig. 1.11 (A) Structure of the anthracene derivatives. (B) STM-image (11 nm \times 11 nm) of the longer alkyl chain compound ($n = 12$) adsorbed on HOPG. From row to row, the anthracene units are parallel. A 2D conglomerate is formed. (C) STM image (12

nm \times 12 nm) of the shorter alkyl chain compound ($n = 11$) adsorbed onto HOPG. From row to row, the anthracene units (indicated by arrows) are twisted. A 2D racemate is formed. Reproduced with permission from ref. 41.

der Waals interactions. The different stereomorphologies arise from the different relative orientation of the $\text{CH}_2\text{-CH}_3$ and the C-aryl-C1' bonds within the same side chain (see Fig. 1.11). For the shorter compound the two bonds are parallel, whereas for the longer compound these bonds make an angle of about 110° within the same chain. Optimizing the interchain van der Waals interactions, in combination with the all-*trans* conformation of the alkyl chains, leads to the difference between inter-row orientations of the anthracenes. This illustrates an odd/even effect on the expression of 2D chirality, comparable with the ordering of *n*-alkanoic acids [42]. Acids with even numbers of carbon atoms form conglomerate domains constructed from a single 2D enantiomer. Acids with an odd number of carbons form racemic domains with both 2D enantiomers in the same unit cell.

1.2.5

Systems with Increased Complexity

Though racemate formation and especially racemic conglomerate formation are most commonly observed when a racemic mixture is applied to the surface, sometimes more complex manifestations of the transfer of molecular chirality to surfaces may be observed [43]. (*9R,10R*)-9,10-Diiodooctadecan-1-ol and (*9S,10S*)-9,10-diiodooctadecan-1-ol are relatively flat molecules and when they approach the surface, they could expose two different phases (Fig. 1.12). In these molecules, the two iodine atoms are on the same side of the backbone chain. As a consequence, upon adsorption, the two iodine atoms are facing up, above the alkyl chain, or they are facing down, buried underneath the alkane chain. Due to the presence of the chiral centers, for a given enantiomer the interaction of one of the faces with the

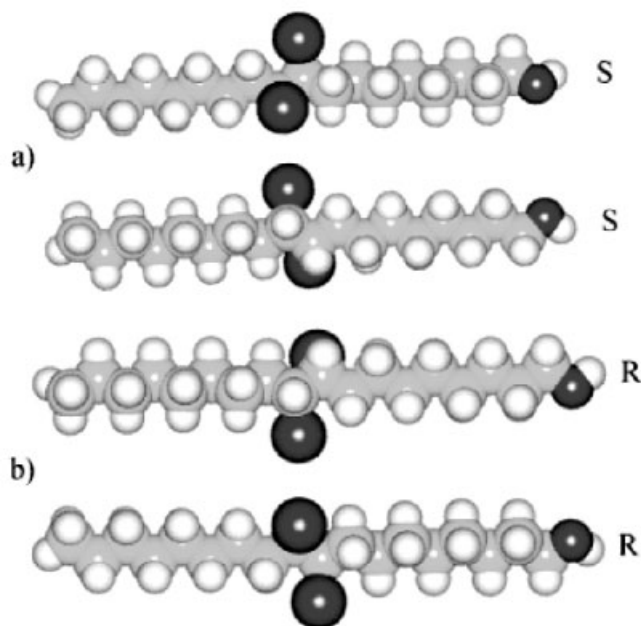


Fig. 1.12 Models of (a) (9*S*,10*S*)-9,10-diiodooctadecan-1-ol and (b) (9*R*,10*R*)-9,10-diiodooctadecan-1-ol, showing different faces of the two molecules. Reprinted with permission from ref. 43.

substrate will be favored. The molecules assemble in rows and each row is composed of only one type of optical isomer. Molecules in adjacent rows are the opposite optical isomers. Despite the fact that *R* and *S* rows appear in an alternating fashion, adjacent rows do not form mirror images, because for one enantiomer both iodine atoms are facing up, while for the other optical enantiomer in the adjacent row both iodine atoms are facing down. The entire domain, although composed of both the *S* and *R* enantiomers, is chiral.

Another peculiar example is the formation of an asymmetric assembly, adsorption-induced, from an achiral adsorbate [44]. Octadecanol molecules are achiral. Upon adsorption on highly oriented pyrolytic graphite, the alkane chain undergoes distortion which is due to a slight mismatch between the octadecanol molecules and the substrate: the HOPG lattice unit is 2.46 Å, compared with the H–H distance on adjacent methylene groups (2.52 Å) in the hydrogen–carbon chain. This is observed as a change in contrast (height profile) along the molecular axis in the STM experiments. Moiré patterns have been ruled out as the origin of the contrast differences observed. Two types of conformations are observed: slightly u-shaped or slightly n-shaped. In the u-shaped molecules the termini of the molecules point slightly to the solution phase, while the termini of the n-shaped molecules are directed toward the substrate (Fig. 1.13). Within a given

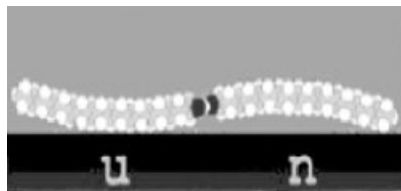


Fig. 1.13 Shape of a dimer of two 1-octadecanol molecules upon adsorption on graphite. Reprinted with permission from ref. 44.

row, all molecules are u-shaped or n-shaped. Interestingly, the “u” rows and the “n” rows do not appear in a random way. A strict alternation is observed which is attributed to the requirements set by hydrogen bonding to have the C–O–H units of both interacting molecules in the same plane. Molecules paired by hydrogen bonding are asymmetrically bent, giving rise to an asymmetric distortion of the octadecanol unit cell pair.

However, in not all cases is molecular chirality clearly expressed on the 2D ordering. In the case of nonacosan-10-ol, no differences could be observed in the STM images between the monolayers formed of the pure enantiomers and of a racemic mixture [45].

1.2.6

Multicomponent Systems

The systems reported so far were composed of one component, or two at the maximum (racemic mixtures). However, the study of mixtures of chiral and achiral mixtures has been reported also. Mainly, the mixtures give rise to mixed 2D crystals where (a) the chiral component fits in the 2D crystal of the achiral one, or (b) the chiral and achiral components form 2D cocrystals which are different from the 2D adlayers of the individual components.

1.2.6.1 Mixed Systems

A study of 1:1 mixtures of hexadecanoic acid with racemic 2-bromohexadecanoic acid physisorbed onto a graphite surface shows that these compounds coadsorb onto the surface, and the mixed monolayer film resolves into domains of hexadecanoic acid with either (*R*)- or (*S*)-2-bromohexadecanoic acid [46]. As observed for other fatty acid molecules with an even number of carbon atoms, achiral hexadecanoic acid forms domains exhibiting nonsuperimposable mirror image domains – enantiomorphous domains. The molecular axis is oriented perpendicular to the lamella axis. As demonstrated by the random appearance in the images of bright spots, which are assigned to bromo groups, the 2-bromohexadecanoic acid molecules sporadically appear in the monolayer. The relative orientation of the bromine atoms relative to the carboxylic groups remains consistent throughout the STM im-

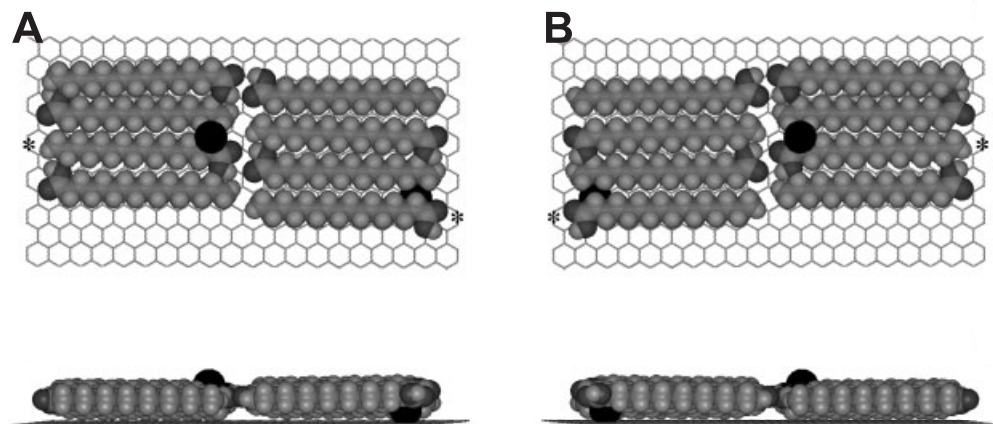


Fig. 1.14 (A) Top and side views of a possible model for a domain consisting of both (*R*)- and (*S*)-2-bromohexadecanoic acid mixed with hexadecanoic acid molecules physisorbed on graphite. In A (B), the conformer on the left-hand side indicated with a star is an *R* enantiomer (*S* enantiomer), and the one on the right-hand side is an *S* enantiomer (*R* enantiomer). In A (B), the *R* enantiomer (*S* enantiomer) has a bromine protruding up and away from the graphite substrate, while the *S* enantiomer (*R* enantiomer) has the bromine pushing into the surface. This last configuration is energetically unfavorable and is therefore rejected as a model for the mixed monolayer. Reprinted with permission from ref. 46.

ages of a single domain which is mainly composed of achiral hexadecanoic acid molecules. In a given domain, all of the bromine atoms lie either above and to the left of the carboxyl group or below and to the right of the carboxyl group. This means that racemic 2-bromohexadecanoic acid coadsorbed with hexadecanoic acid segregates into separate chiral domains (Fig. 1.14). The formation of enantiomorphous domains by hexadecanoic acid and the segregation of 2-bromohexadecanoic acid in hexadecanoic acid domains were explained in the following way. As in hexadecanoic acid the 2D self-assembly is controlled by hydrogen bonding, and the hexadecanoic acid molecules appear as chiral pairs on the substrate. As a consequence, the domains composed of these chiral pairs are also chiral. Assuming that the most stable interaction of a 2-bromohexadecanoic unit has the bromine groups directed toward the liquid phase instead of toward the substrate, (*R*)-2-bromohexadecanoic acid fits only in an “A” domain (Fig. 1.14A) and (*S*)-2-bromohexadecanoic acid coadsorbs in an “B” domain (Fig. 1.14B).

To investigate the presence of an odd/even effect, similar experiments have been carried out but now in the presence of heptadecanoic acid [47]. Determination of the absolute configuration of the racemic 2-bromohexadecanoic acid molecules coadsorbed in the heptadecanoic acid matrix suggests that each lamella is composed of alternating coadsorbed (*R*)- and (*S*)-2-bromo-hexadecanoic acid molecules. These experiments indicate a clear odd/even effect: even-numbered acids induce domains

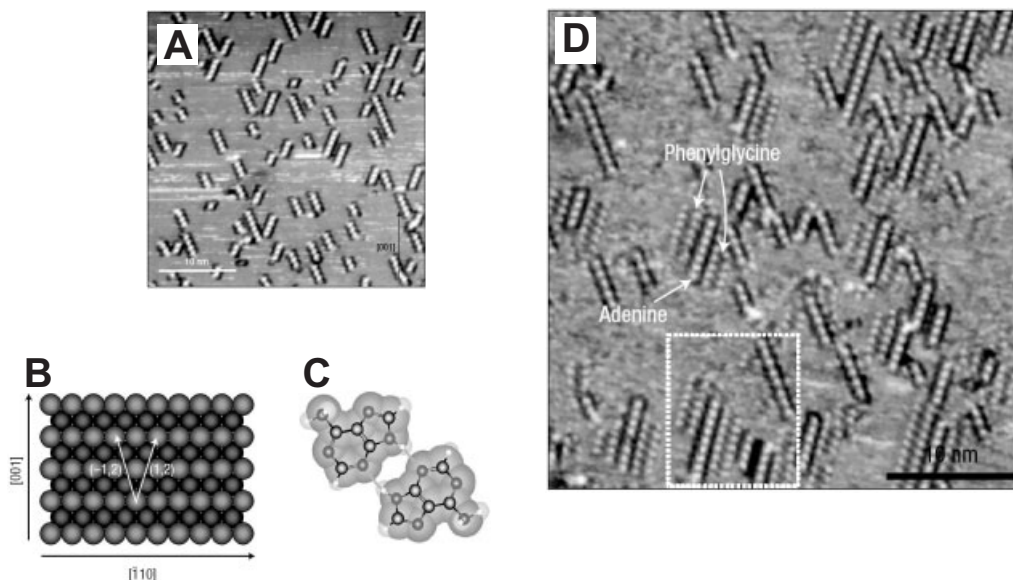


Fig. 1.15 (A) STM image of Cu(110) surface with sub-monolayer coverage of adenine obtained in UHV at room temperature. (B) Model of the surface. (C) Homodimer of adenine molecules. (D) STM-image with

a low coverage of preadsorbed adenine, subsequently exposed to (*S*)-phenylglycine, showing decoration of adenine chains in the (1,2) direction by (*S*)-phenylglycine molecules. Reprinted with permission from ref. 48.

of enantiomeric purity while odd-numbered acids cause coadsorption of both enantiomers within both domains.

Adenine is a planar achiral molecule and adsorbs on Cu(110) in a flat-lying orientation through the delocalized π orbitals of the ring system and the lone pair on the nitrogen atom. By this event, this prochiral molecule becomes chiral, and the adsorbed molecules exist as left- and right-handed forms. Because of the energetic equivalence of these two forms, the adsorption leads to the formation of a racemic mixture. Under the appropriate experimental conditions, adenine molecules diffuse on the achiral surface and dimers are formed which self-assemble into chains about 6.5 nm long (Fig. 1.15) [48]. These chains do not appear along random directions with respect to the symmetry of the Cu(110) lattice: they are rotated 19.5° clockwise or anticlockwise with respect to the high-symmetry [001] direction. This suggests that molecules adsorbed along one given direction have the same chirality. The correspondence between chirality and chain direction is believed to be driven by hydrogen bonding in the formation of the dimers and chains, and by the preference of the nitrogen atoms to adsorb directly above a copper atom. Upon exposure of these surfaces, covered with 15–20% of adenine chains, under UHV conditions at room temperature to (*S*)-phenylglycine, it was observed that the (*S*)-phenylglycine molecules decorate the adenine chains, but only those run-

ning clockwise with respect to the high-symmetry [001] direction. This supports the homochirality of the chains, which was suggested by their orientation. The preference of (*S*)-phenylglycine for one of the adenine rows indicates enantiomeric interactions between the two molecules. In line with these results (*R*)-phenylglycine associates exclusively with those adenine rows which are rotated anticlockwise with respect to the [001] direction. The chiral preference in the interaction of phenylglycine with adsorbed adenine points to specific interactions between the amino acid and the nucleic acid base, keeping in mind that the substrate plays an important role.

1.2.6.2 Cocrystals

Mixtures of chiral and achiral molecules have also been investigated at the liquid/solid interface. In contrast to the systems described in Section 1.2.6.1, the different molecules form 2D cocrystals. Figures 1.16(A) and 1.16(B) represent STM images of a monolayer of the (*S*)- and (*R*)-enantiomers ((*S*)-ISA and (*R*)-ISA, respectively), of a chiral isophthalic acid derivative (5-[10-(2-methylbutoxy)decyloxy]isophthalic acid) (ISA) physisorbed from 1-heptanol [49]. As far as the packing of the isophthalic acid molecules is concerned, each enantiomer forms its characteristic enantiomorphous lamella structure. The orientation of each enantiomer with respect to the graphite surface is shown in Figures 1.16(C) and 1.16(D). The orientation of the coadsorbed 1-heptanol molecules depends on the enantiomeric character of the domain in which those molecules are coadsorbed. For (*S*)-ISA, the alcohol molecules are rotated clockwise with respect to the normal on the isophthalic acid lamellae, while for (*R*)-ISA monolayers this rotation is counterclockwise. Thus the orientation of achiral coadsorbed molecules expresses the chiral character of the domains. Coadsorption of alkylated alcohols (1-heptanol, 1-octanol, 1-undecanol) is a typical phenomenon in the presence of 5-alkyl(oxy)isophthalic acid derivatives. The investigation of the racemic solution indicates conglomerate formation.

Self-assembled monolayers of stearic acid, (*R,S*)- and (*S*)-16-methyloctadecanoic acid ion-paired with 4,4'-bipyridine in a 2:1 ratio have been observed at the liquid/graphite interface too. Spontaneous resolution takes place [50].

1.2.7

Chemisorption versus Physisorption

Both chemisorbed (on metal substrates) and physisorbed (mainly on HOPG) systems show expression of chirality. The chemisorbed species are most often investigated under UHV conditions whereas the physisorbed systems mainly appear under ambient conditions or at the liquid/solid interface. The question arises of whether this makes a difference with respect to the expression of 2D chirality. In fact, it does not. Both types of interactions lead to surface chirality, with some nuances. Due to the weak nature of physisorption, physisorbed molecules often show considerable mobility. As a result, successful STM imaging requires that those molecules form 2D adlayers: clusters and isolated molecules are hardly observed,

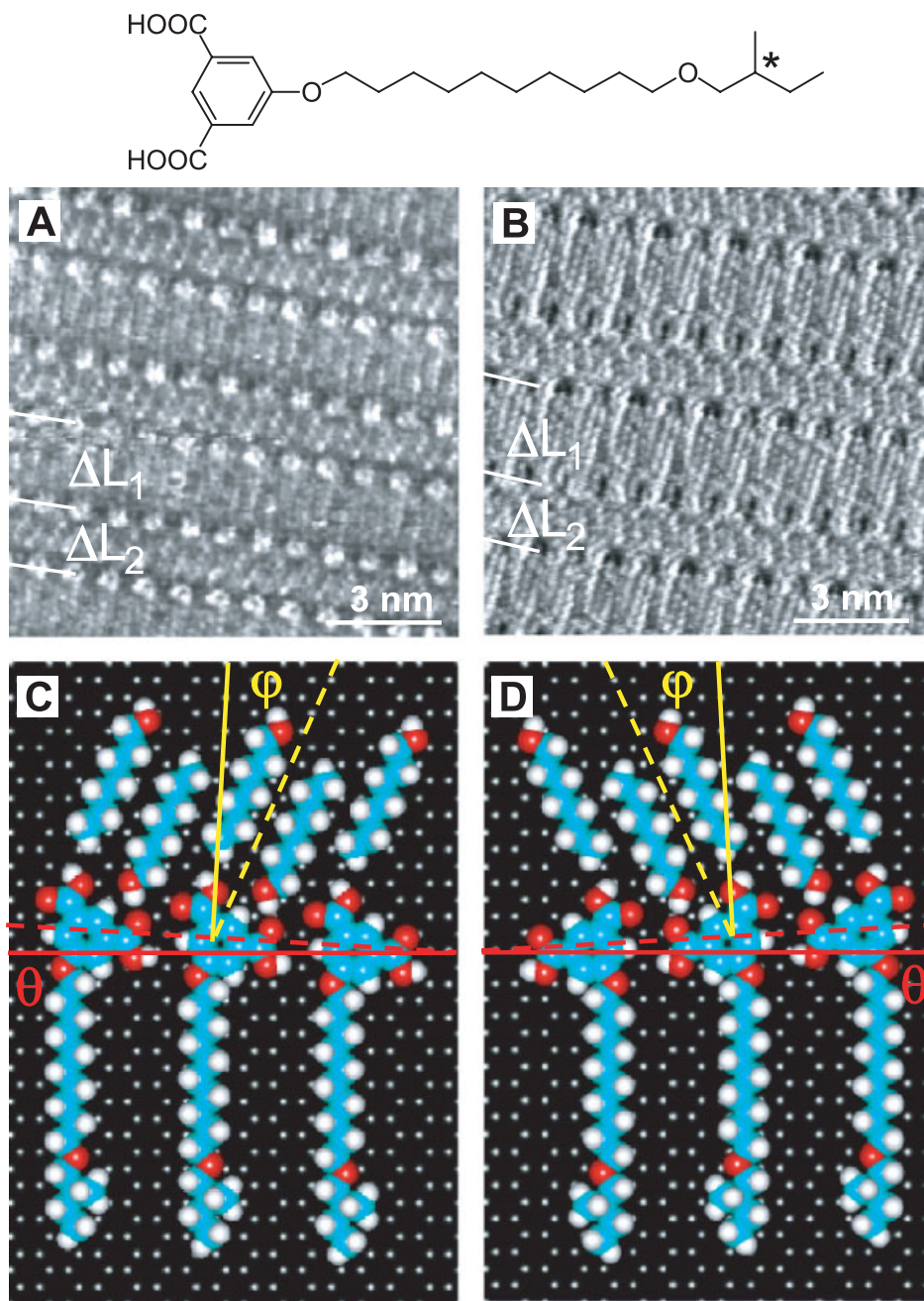


Fig. 1.16 Monolayer image and model of (S)-ISA (A and C) and (R)-ISA (B and D). ΔL_1 and ΔL_2 indicate lamellae composed of ISA and 1-octanol molecules, respectively. θ is the angle between the lamella axis and the graphite reference axis. φ is the angle between the 1-octanol axis and the normal on the lamella axis of ISA. Reprinted with permission from ref. 49.

in contrast to UHV conditions (at low temperature), where chiral clusters can be observed.

1.2.8

The Effect of Molecular Adsorption on Substrates: Toward Chiral Substrates

The adsorption of chiral molecules may also affect the substrate. Annealing of a sample of L-lysine on Cu(001), imaged by STM under UHV conditions, leads to the formation of homochiral facets which have never been observed in the absence of L-lysine. Chiral kink sites are formed at the step edges. Therefore, there should also be a difference in the adsorption energies of L-lysine on bare *R* and *S* facets. Chiral transition-metal surfaces are able to exhibit enantioselectivity [51, 52].

The adsorption of molecules can bestow chirality on the extended flat terraces of a single-crystal surface, which is caused by a pronounced surface restructuring induced chemically by the adsorption of achiral molecules, as revealed by UHV STM [53]. This could be visualized as moving adsorbed molecules aside and exposing the substrate. With the adsorption of large molecules, such as hexa-*tert*-butyldecacyclene (Fig. 1.17) on a Cu(110) surface, metal atoms can be dug out of the surface, resulting in a “trench base” for anchoring of the molecules. In the

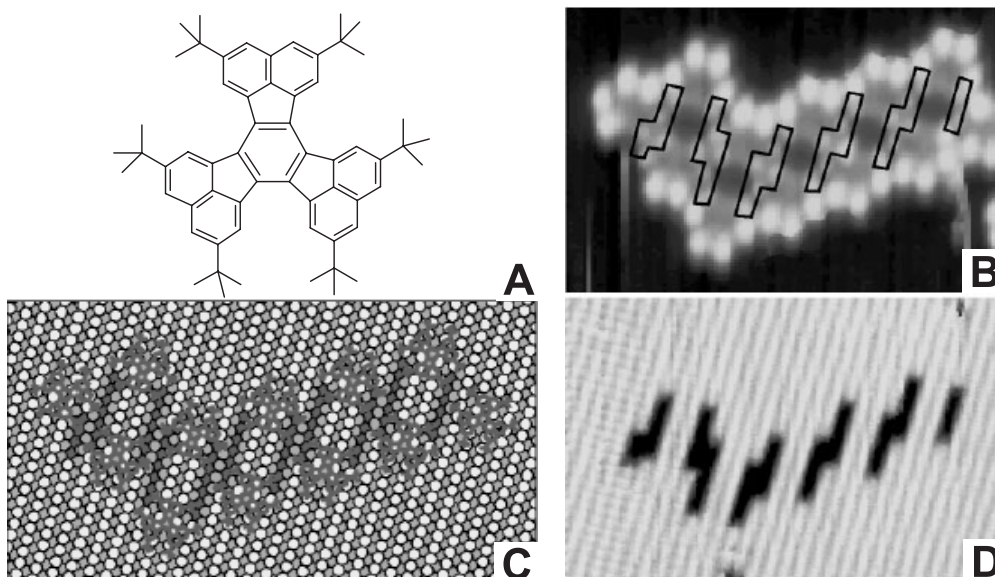


Fig. 1.17 (A) Chemical structure of hexa-*tert*-butyldecacyclene. (B, D) Constant-current images ($10.5 \text{ nm} \times 6.9 \text{ nm}$). (B) Double row structure. The trenches in the underlying surface are sketched in. (C) The trenches in the surface layers are disclosed after

manipulating the molecules aside. Ball model of the double row structure. The substrate atoms are more darkly shaded, the deeper the layers lie. The molecules are shown in gray. (D) STM image. Reproduced with permission from ref. 53.

case of the single, individual molecules, all six *tert*-butyl lobes appear to have nearly the same height. For molecules within a double row, the three lobes at the rim of the row are have much brighter images than the three lobes pointing toward the interior of the double row. The molecules in the double rows appear to be tilted. After moving the adsorbed molecules aside, images showed that 14 Cu atoms were expelled from the surface in two adjacent rows, creating a chiral hole in the surface. The three more dimly imaged *tert*-butyl lobes of each molecule are located on top of the missing Cu atoms, increasing molecule–substrate interactions. In the case of *tert*-butyl-free decacyclene molecules, no ordered structures are observed at low coverage and no restructuring of the Cu(110) surface is induced; this is attributed to the strong interaction of the aromatic π system with the substrate.

Adsorption of molecules can lead not only to the formation of chiral kinks and “defects”. Some metal surfaces are intrinsically chiral or can be made chiral. Studies on the adsorption of molecules on this kind of chiral substrate by STM are very rare, though it is clear that STM will be one of techniques which will help in understanding the adsorbate–substrate interactions on these interesting chiral surfaces [54].

1.2.9

Chirality and AFM

Not only with STM is it possible to probe the expression of chirality at surfaces. Though STM has been used most extensively for these studies, this approach is not sufficient if the electron tunneling through an ordered layer becomes impossible due to the thickness of the layer and/or the limited “conductivity.” High-resolution atomic force microscopy (AFM) provides an elegant alternative technique with which to investigate the 2D chirality. Spontaneous chiral symmetry breaking by achiral molecules in a Langmuir–Blodgett (LB) film has been reported [55] as well as the separation of chiral phases in monolayer crystals of racemic amphiphiles in LB films (Figs. 1.18A and 1.18B) [56]. The conclusions were based upon the observation of chiral unit cells, as revealed by the atomic resolution images. On a larger scale also, 2D chiral effects can be observed by AFM. An achiral barbituric acid derivative can form a chiral Langmuir–Blodgett film through the air/water interface: spiral nanofibers were observed which wound in a clockwise or an anticlockwise direction (Fig. 1.18C) [57]. Some molecules self-assemble into aggregates upon adsorption on a substrate which can give rise to the formation of chiral fiberlike structures, as observed for a sexithiophene derivative enantiomer on silicon which formed left-handed helices exclusively (Fig. 1.18D) [58].

The spontaneous resolution by AFM of a racemic mixture of helical self-assembled tetra-rosettes into enantiopure domains in 2D supramolecular assemblies on HOPG has been reported (Fig. 1.19) [59]. It is unique to this system that the well-defined chiral nanostructures, composed of 3 melamine-substituted calix[4]arenes and 5,5-diethylbarbiturate molecules, are stable in solution. Because there are no elements of chirality in the building blocks, the rosette assemblies form as a racemic mixture of P and M enantiomeric helices in solution. The depo-

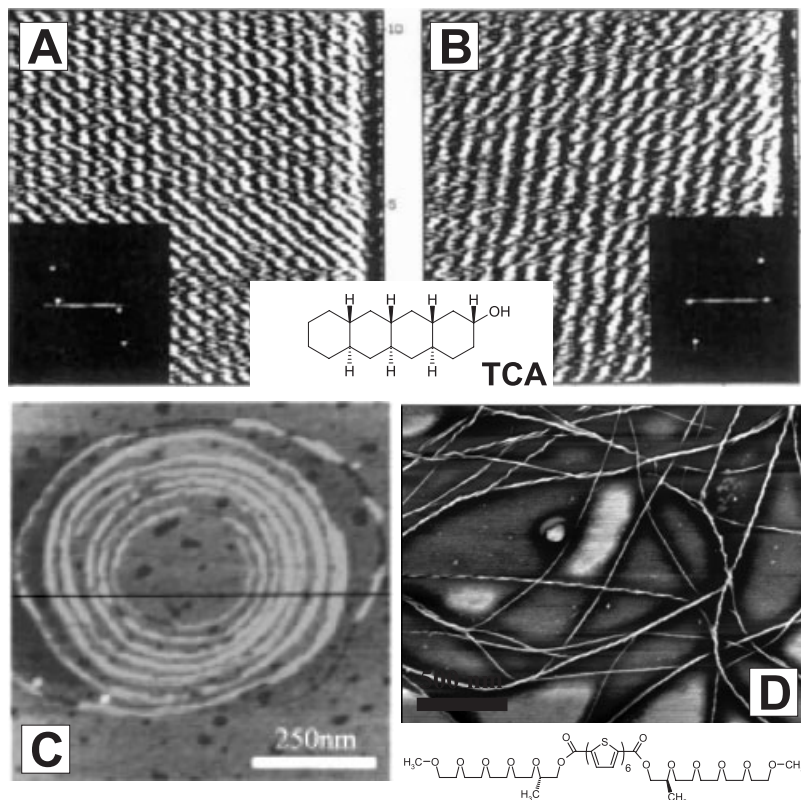


Fig. 1.18 (A, B) AFM images ($10 \text{ nm} \times 10 \text{ nm}$) with corresponding Fourier pattern inserts of a TCA racemate monolayer on mica, recorded at different locations, suggesting spontaneous chiral resolution. Reprinted with permission from ref. 56. (C) AFM image of a

one-layer LB film of an achiral barbituric acid derivative on mica. Reprinted with permission from ref. 57. (D) AFM phase image on silicon, showing left-handed helical aggregates (image kindly provided by P. Leclère, Université de Mons).

sition of tetra-rosettes from solution onto HOPG leads to the formation of characteristic domains. The rosettes are stacked in an approximately face-to-face arrangement. Due to the size of the individual nanostructures, they are too high to be measured by STM. Though submolecular resolution cannot be achieved with AFM, supramolecular resolution is possible under carefully controlled conditions in intermittent contact mode. The domains formed by self-organization of the tetra-rosette on HOPG are characterized by an inter-row spacing of $4.6 \pm 0.1 \text{ nm}$. Three distinct orientations which differ by an angle of 60° appear to be related to the symmetry of the underlying HOPG substrate. In addition, certain domains are oriented at approximately 46° to the orientation of the surrounding domain and

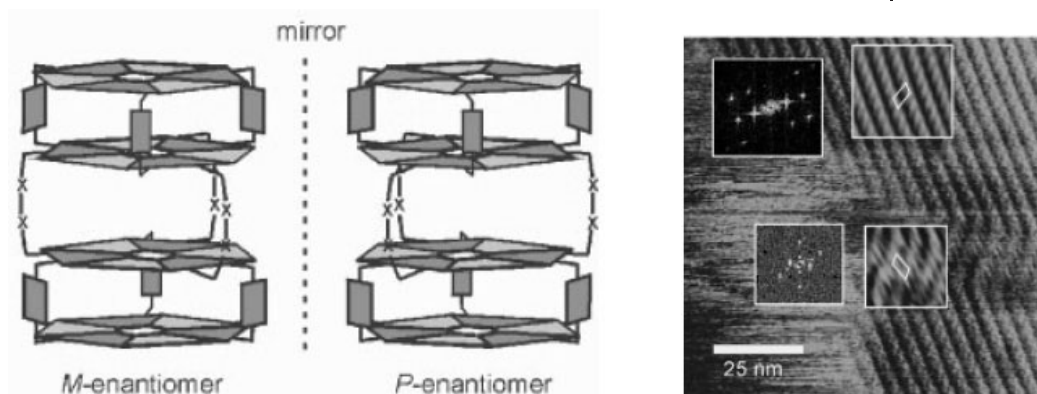


Fig. 1.19 Left: Models of the self-assembled M and P enantiomers. Right: Tapping-mode AFM phase image of tetra-rosettes on HOPG. Insets: Left: 2D FFTs; right: Fourier-filtered sections. Reprinted with permission from ref. 59.

there are approximately equally abundant sets of domains with different orientations with respect to HOPG. In those high-resolution AFM images where the lattice structure is resolved for two domains that are oriented at 46° to each other, the ordering of the supramolecules can be described by an oblique lattice, which contains one tetra-rosette suprastructure. The presence of a chiral arrangement of the rosettes within the domains and the presence of two types of arrangements with mirror symmetry suggest that P and M tetra-rosette enantiomers have been spontaneously resolved into enantiopure domains in 2D. The observations of mirror symmetry and two sets of domains that differ in orientation by 46° – each set exists in domains with mutual angles of 60° – are consistent with an orientation of the domains of 23° with respect to the orientation of the underlying HOPG.

It has been shown that AFM is capable of chiral discrimination [60, 61]. Chemical force microscopy is a technique that combines chemical discrimination with AFM by chemical derivatization of the scanning probe tip. Measurement of the adhesion force between the tip and the surface gives information on the binding energy between the small number of molecules on the tip and those on the surface under the tip. Knowledge of the local adhesion on the surface may be combined with topographic and friction images to give functional maps of the surface. The tips were coated with an acylated phenylglycine modified with an alkanethiol so that they could be attached to a gold-coated probe by chemisorption. Mandelic acid was attached to the surface as an ether, with three groups attached to the chiral center – an acid, a phenyl ring, and a hydrogen atom – allowing hydrogen-bonding and π -stacking interactions complementarily to the chiral ligand attached to the probe. The adhesion force experiments reveal that the interaction between the *S* enantiomer of the compound covalently bound to the tip and the *R* form of

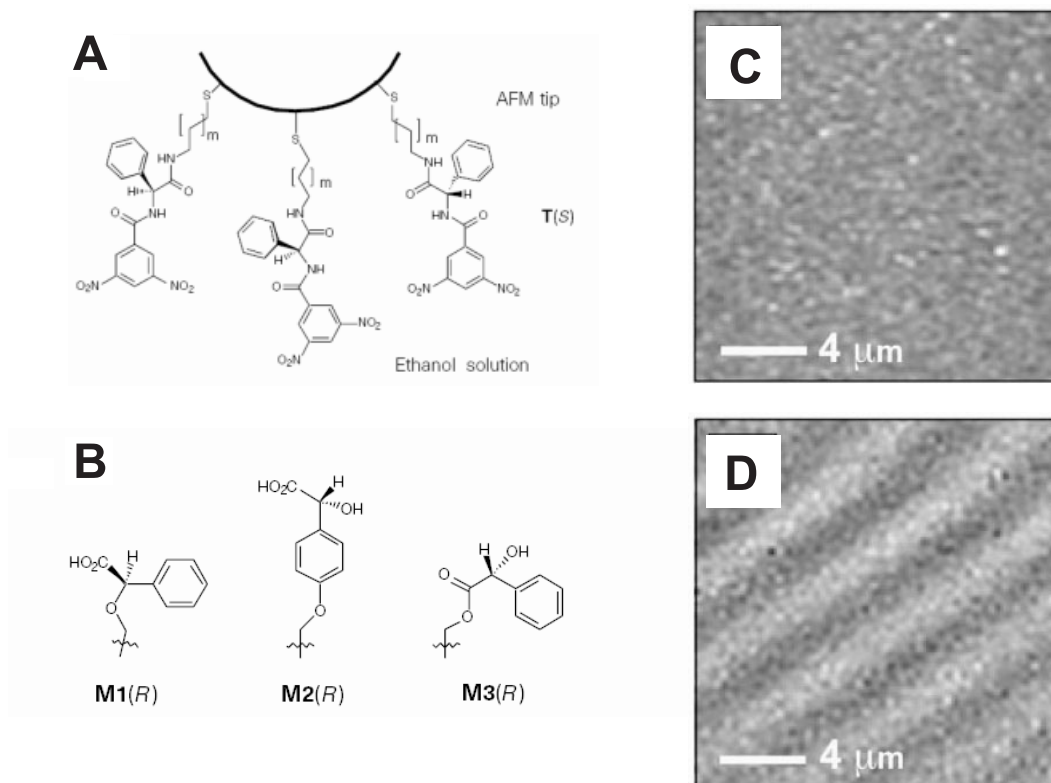


Fig. 1.20 (A) Structure of the *S* enantiomer of the chiral ligand T attached to the tip; (B) structure of the *R* enantiomer of each of the mandelic acid thiols; (C) topographic and (D) friction maps obtained simultaneously of an M1 surface with a tip functionalized with T(*S*). Reprinted with permission from ref. 60.

the surface is more than twice that for the *S* surface. This result is mirrored by a stronger interaction between the *R* form of the tip and the *S* form of the surface. A racemic tip gives adhesion values intermediate to those of the *R* or *S* tip for a given surface. Friction experiments on patterned surfaces or (*R*)- and (*S*)-mandelic acid derivatives using a chirally functionalized tip (*R* or *S*) shows clear evidence of a surface pattern in the friction map, whereas there is no evidence for this in the raw topography images (Fig. 1.20). No contrast was found for tips functionalized with a racemic mixture, which implies that there are equal numbers of *R* and *S* molecules of the resin on top of the tip within the contact region. So, the results show that chemical force microscopy is sufficiently sensitive to permit discrimination between enantiomers of simple chiral molecules. The chiral discrimination observed must arise from the different diastereomeric complexes formed transiently between the chiral molecule on the tip and either the (*R*)- or the (*S*)-mandelic acid on the surface.

1.3

Conclusion

The implementation of scanning probe microscopy techniques has provided important insight into the way in which molecules, chiral and achiral, order on surfaces and how the ordering is affected by their symmetry. STM and AFM are not the only techniques which help to unravel the complexity of molecular interactions with surfaces, though they are the only ones which do so locally on the nanometer scale in a noninvasive manner.

Acknowledgements

The authors thank the Federal Science Policy through IUAP-V03, the Institute for the Promotion of Innovation by Science and Technology in Flanders (IWT), and the Fund for Scientific Research – Flanders (FWO). We also thank the Marie-Curie RTN “CHEXTAN” (Chiral Expression and Transfer at the Nanoscale) for financial support. S.D.F. is a postdoctoral fellow of FWO. We are very grateful to the colleagues who have provided original artwork.

References

- 1 L. PEREZ-GARCIA, D. B. AMABILINO, *Chem. Soc. Rev.* **2002**, *31*, 342–356.
- 2 V. HUMBLLOT, S. M. BARLOW, R. RAVAL, *Prog. Surf. Sci.* **2004**, *76*, 1–19.
- 3 S. M. BARLOW, R. RAVAL, *Surf. Sci. Rep.* **2003**, *50*, 201–341.
- 4 I. WEISSBUCH, I. RUBINSTEIN, M. J. WEYGAND, K. KJAER, L. LEISEROWITZ, M. LAHAV, *Helv. Chim. Acta* **2003**, *86*, 3867–3874.
- 5 G. P. LOPINSKI, D. J. MOFFATT, D. D. M. WAYNER, R. A. WOLKOW, *Nature* **1998**, *392*, 909–911.
- 6 H. FANG, L. GIANCARLO, G. W. FLYNN, *J. Phys. Chem. B* **1998**, *102*, 7311–7315.
- 7 A. KÜHNLE, T. R. LINDERTOH, B. HAMMER, F. BESENBACHER, *Nature* **2001**, *415*, 891–893.
- 8 A. KÜHNLE, T. R. LINDEROTH, F. BESENBACHER, *J. Am. Chem. Soc.* **2003**, *125*, 14680–14681.
- 9 M. O. LORENZO, C. J. BADDELEY, C. MURYN, R. RAVAL, *Nature* **2000**, *404*, 376–379.
- 10 V. HUMBLLOT, S. HAQ, C. MURYN, W. A. HOFER, R. RAVAL, *J. Am. Chem. Soc.* **2002**, *124*, 503–510.
- 11 T. E. JONES, C. J. BADDELEY, *Surf. Sci.* **2002**, *519*, 237–249.
- 12 W. A. HOFER, V. HUMBLLOT, R. RAVAL, *Surf. Sci.* **2004**, *554*, 141–149.
- 13 B. OHTANI, A. SHINTANI, K. UOSAKI, *J. Am. Chem. Soc.* **1999**, *121*, 6515–6516.
- 14 R. FASEL, M. PARSCHAU, K.-H. ERNST, *Angew. Chem. Int. Ed.* **2003**, *42*, 5178–5181.
- 15 F. STEVENS, D. J. DYER, D. M. WALBA, *Angew. Chem. Int. Ed. Engl.* **1996**, *35*, 900–901.
- 16 D. M. WALBA, F. STEVENS, N. A. CLARK, D. C. PARKS, *Acc. Chem. Res.* **1996**, *29*, 591–597.
- 17 S. DE FEYTER, A. GESQUIÈRE, C. MEINERS, M. STEFFERT, K. MÜLLEN, F. C. DE SCHRYVER, *Langmuir* **1999**, *15*, 2817–2822.
- 18 D. G. YABLON, J. S. GUO, D. KNAPP, H. B. FANG, G. W. FLYNN, *J. Phys. Chem. B* **2001**, *105*, 4313–4316; and references therein.

- 19 P. QIAN, H. NANJO, T. YOKOYAMA, T. M. SUZUKI, *Chem. Lett.* **1998**, 1133–1134.
- 20 A. GESQUIÈRE, P. JONKHEIJM, A. P. H. J. SCHENNING, E. MENA-OSTERITZ, P. BÄUERLE, S. DE FEYTER, F. C. DE SCHRYVER, E. W. MEIJER, *J. Mater. Chem.* **2003**, *13*, 2164–2167.
- 21 A. GESQUIÈRE, P. JONKHEIJM, F. J. M. HOEBEN, A. P. H. J. SCHENNING, S. DE FEYTER, F. C. DE SCHRYVER, E. W. MEIJER, *Nano Lett.* **2004**, *4*, 1175–1179.
- 22 P. JONKHEIJM, A. MIURA, M. ZDANOWSKA, F. J. M. HOEBEN, S. DE FEYTER, A. P. H. J. SCHENNING, F. C. DE SCHRYVER, E. W. MEIJER, *Angew. Chem. Int. Ed.* **2004**, *43*, 74–78.
- 23 A. MIURA, P. JONKHEIJM, S. DE FEYTER, A. P. H. J. SCHENNING, E. W. MEIJER, F. C. DE SCHRYVER, *Small* **2005**, 131–137.
- 24 Q.-M. XU, D. WANG, L.-J. WAN, C. WANG, C.-L. BAI, G.-Q. FENG, M.-X. WANG, *Angew. Chem. Int. Ed.* **2002**, *41*, 3408–3411.
- 25 Q.-M. XU, D. WANG, M.-J. HAN, L.-J. WAN, C.-L. BAI, *Langmuir* **2004**, *20*, 3006–3010.
- 26 M.-J. HAN, D. WANG, J.-M. HAO, L.-J. WAN, Q.-D. ZENG, Q.-H. FAN, C.-L. BAI, *Anal. Chem.* **2004**, *76*, 627–631.
- 27 M. YONEYA, H. YOKOYAMA, *J. Chem. Phys.* **2001**, *114*, 9532–9538.
- 28 S. DE FEYTER, A. GESQUIÈRE, K. WURST, D. B. AMABILINO, J. VECIANA, F. C. DE SCHRYVER, *Angew. Chem. Int. Ed.* **2001**, *40*, 3217–3220.
- 29 W. MAMDOUH, H. UJI-I, A. GESQUIÈRE, S. DE FEYTER, D. B. AMABILINO, M. M. S. ABDEL-MOTTALEB, J. VECIANA, F. C. DE SCHRYVER, *Langmuir* **2004**, *20*, 9628–9635.
- 30 J. WECKESSER, A. DE VITA, J. V. BARTH, C. CAI, K. KERN, *Phys. Rev. Lett.* **2001**, *87*, 096101-1–4.
- 31 V. HUMBLLOT, M. ORTEGA LORENZO, C. J. BADDELEY, S. HAQ, R. RAVAL, *J. Am. Chem. Soc.* **2004**, *126*, 6460–6469.
- 32 J. V. BARTH, J. WECKESSER, G. TRIMARCHI, M. VLADIMIROVA, A. DE VITA, C. CAI, H. BRUNE, P. GÜNTER, K. KERN, *J. Am. Chem. Soc.* **2002**, *124*, 7991–8000.
- 33 M. BÖHRINGER, K. MORGENSTERN, W.-D. SCHNEIDER, R. BERNDT, F. MAURI, A. DE VITA, R. CAR, *Phys. Rev. Lett.* **1999**, *83*, 324–327.
- 34 M. BÖHRINGER, K. MORGENSTERN, W.-D. SCHNEIDER, and R. BERNDT, *Angew. Chem. Int. Ed.* **1999**, *38*, 821–823.
- 35 P. MESSINA, A. DMITRIEV, N. LIN, H. SPILLMAN, M. ABEL, J. V. BARTH, K. KERN, *J. Am. Chem. Soc.* **2002**, *124*, 14000–14001.
- 36 H. SPILLMANN, A. DMITRIEV, N. LIN, P. MESSINA, J. V. BARTH, K. KERN, *J. Am. Chem. Soc.* **2003**, *125*, 10725–10728.
- 37 J. KUNTZE, X. GE, R. BERNDT, *Nanotechnology* **2004**, *15*, 337–340.
- 38 F. CHARRA, J. COUSTY, *Phys. Rev. Lett.* **1998**, *80*, 1682–1685.
- 39 D. P. E. SMITH, *J. Vac. Sci. Technol. B* **1991**, *9*, 1119–1125.
- 40 S. J. SOWERBY, W. M. HECKL, G. B. PETERSEN, *J. Mol. Evol.* **1996**, *43*, 419–424.
- 41 Y. WEI, K. KANNAPPAN, G. W. FLYNN, M. B. ZIMM, *J. Am. Chem. Soc.* **2004**, *126*, 5318–5322.
- 42 M. HIBINO, A. SUMI, H. TSUCHIYA, I. HATTA, *J. Phys. Chem. B* **1998**, *102*, 4544–4547.
- 43 Y. CAI, S. L. BERNASEK, *J. Am. Chem. Soc.* **2003**, *125*, 1655–1659.
- 44 Y. G. CAI, S. L. BERNASEK, *J. Am. Chem. Soc.* **2004**, *126*, 14234–14238.
- 45 C. LE POULENNEC, J. COUSTY, Z. X. XIE, C. MIOSKOWSKI, *Surf. Sci.* **2000**, *448*, 93–100.
- 46 D. G. YABLON, L. C. GIANCARLO, G. W. FLYNN, *J. Phys. Chem. B* **2000**, *104*, 7627–7635.
- 47 D. G. YABLON, D. WINTGENS, G. W. FLYNN, *J. Phys. Chem. B* **2002**, *106*, 5470–5475.
- 48 Q. CHEN, N. V. RICHARDSON, *Nat. Mat.* **2003**, *2*, 324–328.
- 49 S. DE FEYTER, P. C. M. GRIM, M. RÜCKER, P. VANOPPEN, C. MEINERS, M. SIEFFERT, S. VALIYAVEETIL, K. MÜLLEN, F. C. DE SCHRYVER, *Angew. Chem. Int. Ed.* **1998**, *37*, 1223–1226.

- 50 P. QIAN, H. NANJO, T. YOKOYAMA, T. M. SUZUKI, K. AKASAKA, H. ORHUI, *Chem. Commun.* **2000**, 2021–2022.
- 51 X. ZHAO, *J. Am. Chem. Soc.* **2000**, *122*, 12 584–12 585.
- 52 X. ZHAO, R. ZHAO, W. S. YANG, *Langmuir* **2000**, *16*, 9812–9818
- 53 M. SCHUNACK, L. PETERSEN, A. KÜHNLE, E. LÆGSGAARD, I. STENSGAARD, I. JOHANNSEN, F. BESENBACHER, *Phys. Rev. Lett.* **2001**, *86*, 456–459.
- 54 R. M. HAZEN, D. S. SHOLL, *Nature Materials* **2003**, *2*, 367–374.
- 55 R. VISWANATHAN, J. A. ZASADZINSKI, D. K. SCHWARZ, *Nature* **1994**, *368*, 440–443.
- 56 C. J. ECKHARDT, N. M. PEACHY, D. R. SWANSON, J. M. TAKACS, M. A. KHAN, X. GONG, J.-H. KIM, J. WANG, R. A. UPHAUS, *Nature* **1993**, *362*, 614–616.
- 57 X. HUANG, C. LI, S. JIANG, X. WANG, B. ZHANG, M. LIU, *J. Am. Chem. Soc.* **2004**, *126*, 1322–1323.
- 58 A. P. H. J. SCHENNING, A. F. M. KILBINGER, F. BISCARINI, M. CAVALLINI, H. J. COOPER, P. J. DERRICK, W. J. FEAST, R. LAZZARONI, Ph. LECLÈRE, L. A. MCDONELL, E. W. MEIJER, S. C. J. MESKERS, *J. Am. Chem. Soc.* **2002**, *124*, 1269–1275.
- 59 H. SCHÖNHERR, M. CREGO-CALAMA, C. JULIUS VANCISO, D. N. REINHOUDT, *Adv. Mater.* **2004**, *16*, 1416–1420.
- 60 R. MCKENDRY, M.-E. THEOCLITOU, T. RAYMENT, C. ABELL, *Nature* **1998**, *391*, 566–568.
- 61 R. MCKENDRY, M.-E. THEOCLITOU, C. ABELL, T. RAYMENT, *Jpn. J. Appl. Phys.* **1999**, *38*, 3901–3907.

2 Scanning Tunneling Spectroscopy of Complex Molecular Architectures at Solid/Liquid Interfaces: Toward Single- Molecule Electronic Devices

Frank Jäckel and Jürgen P. Rabe

2.1 Introduction

The last decade has witnessed rapid progress in the application of large π -conjugated molecules in organic electronic devices such as organic field-effect transistors [1–3], organic light emitting diodes [4–6] and organic solar cells [7–9]. This progress is mainly based on an improved understanding of the electronic properties of the materials in ultrathin films as well as at the interface with the substrate which determine the device function. Since the interaction of the molecules with the substrate differs in general significantly from that between the molecules, the molecular arrangements at the interface differ from those in the bulk. On the other hand, the charge carrier mobilities in organic thin films, for instance, depend strongly on the molecular order of the film, and determine to a large extent the performance of organic transistors and light-emitting diodes. Moreover, in light-emitting devices a balanced injection of electrons and holes into the device is desired which renders the organic/electrode interface, and in particular the energy-level alignment at the interface, a crucial parameter to be optimized.

The interfacial arrangement of molecular layers adsorbed onto conducting substrates can be studied with submolecular, i.e., subnanometer, resolution with scanning tunneling microscopy (STM), including studies at solid/liquid interfaces [10]. Combining STM imaging with the measurement of current–voltage-characteristics (I – V s), i.e., scanning tunneling spectroscopy (STS), at similar resolution [11] makes it possible in principle to obtain a detailed map of the electronic structure at the interface. It is noteworthy that STS data provide information on occupied *and* unoccupied electronic states at the interface. Considering the high spatial resolution, combined STM/STS studies represent a complementary technique to ultraviolet, inverse and two-photon photoelectron spectroscopy. Although the latter techniques offer less spatial resolution, they also probe either occupied or unoccupied electronic states.

Exploiting the exceptional spatial resolution of STM/STS enables one even further to study the behavior of single molecules in prototypical electronic devices. The so-called bottom-up approach to molecular electronics [12–15] is at present

considered a potential alternative to inorganic semiconductor-based nanoelectronics, since potentially lower processing and fabrication costs may be expected. It should be mentioned that in the field of molecular electronics a number of other techniques have been developed and applied in order to study the electron transport properties of single molecules or small ensembles thereof, including conducting probe scanning force microscopy [16], metal/Langmuir–Blodgett film/metal structures [17, 18], mechanically controlled break junctions [19–22], or nanopores [23, 24]. The major shortcoming of all these techniques is the lack of control of the number of molecules investigated and their conformation. Both of these parameters may be verified and controlled in STM [11, 25].

In this chapter, we will focus on studies aiming at a deeper understanding of how molecular interactions, in particular π – π -interactions, influence electronic properties on the few-molecules (or single-molecule) level, as well as on work targeted on self-assembled molecular architectures serving as prototypical electronic single-molecule devices. We will focus on studies at the solid/liquid interface with an emphasis on the authors' own work. Related work under ultrahigh vacuum (UHV) conditions will be discussed for one example in order to demonstrate the differences and to compare advantages and drawbacks of the respective conditions, i.e., solid/liquid versus vacuum. Investigations at the solid/liquid interface appear in particular attractive for complex architectures of large molecules with different chemical functions which are otherwise difficult to crystallize. On substrates such as highly oriented pyrolytic graphite (HOPG) crystallization is facilitated by alkylation of the molecules, which additionally allows for solution processing.

2.2 STM/STS of Molecular Adsorbates

For a simple STM junction without a molecule, the tunneling current can be described in a perturbation theory approach, using the transfer Hamiltonian of Bardeen [26], and assuming a flat surface and a locally spherical tip. The result is a tunneling current, which is proportional to the local density of states at the tip position and at the energy of the tunneling electrons [27, 28]. More complex theoretical approaches consider multiple pathways for the tunneling electrons [29, 30] or inelastic effects such as electron–electron scattering or electron–phonon scattering.

STM of molecular adsorbates can be explained in a resonant tunneling picture (Fig. 2.1), where the frontier orbitals of the adsorbate give rise to an increase in tunneling current if they are energetically close to the electrode states involved in the tunneling, since they open new pathways for the tunneling electrons in the former empty STM junction [31]. Alternatively, it has been attributed to a modification of the local density of states of the substrate by the adsorbed species [32].

The tunneling current through an STM junction with a molecule between the tip and substrate certainly depends on the local density of states of the tip, substrate, and molecular adsorbate, their relative energetic and spatial positions, and

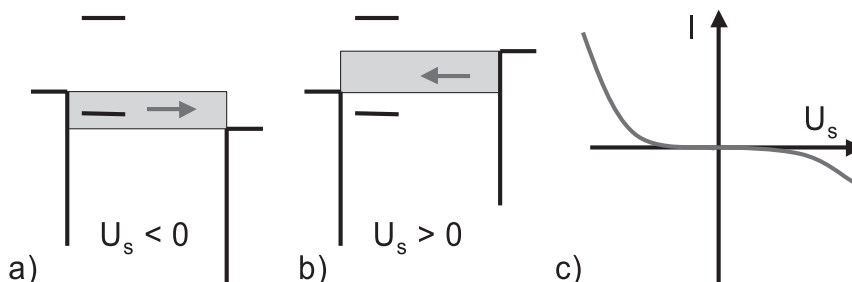


Fig. 2.1 Schematic illustrating the tunneling process for an adsorbed molecule with its HOMO closer to the Fermi level of the substrate than its LUMO: (a) resonant contributions from the HOMO at sufficiently large negative sample bias U_s ; (b) no resonant contribution from the LUMO at the same opposite bias; (c) the resulting asymmetric I - V plot. Copyright with the authors.

the bias voltage. The measurements of current–voltage characteristics (I - V s) at fixed positions of the tip relative to the sample provide direct access to the electronic properties of the molecule on the substrate. In the picture of resonantly enhanced tunneling [31] the symmetry (or asymmetry) of the I - V s can be explained simply by the energy-level alignment between molecular orbitals (HOMO, highest occupied molecular orbital; LUMO, lowest unoccupied molecular orbital) and the Fermi level of the substrate. Figure 2.1 illustrates the case where the HOMO of the adsorbed molecule is much closer to the Fermi level of the substrate than its LUMO. At sufficiently large negative sample bias (Fig. 2.1a) a resonant contribution from the HOMO will be observed as an increase in tunneling current, while at the same opposite bias (Fig. 2.1b) no contributions from the LUMO are detected yet. Consequently an asymmetric I - V with larger currents at negative sample bias can be expected (Fig. 2.1c). This simple picture will be sufficient to explain a number of phenomena detailed below.

Alternatively, electronic properties may be characterized by recording current images at different biases. In yet another method the tunneling bias is modulated, and with a lock-in amplifier differential conductance curves (dI/dV s as functions of the tunneling bias V) are measured, which can be displayed as normalized differential conductance curves $dI/dV/(I/V)$, accounting for the linear dependence of the tunneling current at low bias.

2.3 An Early Example of STS at the Solid/Liquid Interface

The first example demonstrating reproducible STS at the solid/liquid interface with submolecular resolution was reported in 1995 by the author's (JPR) group [11].

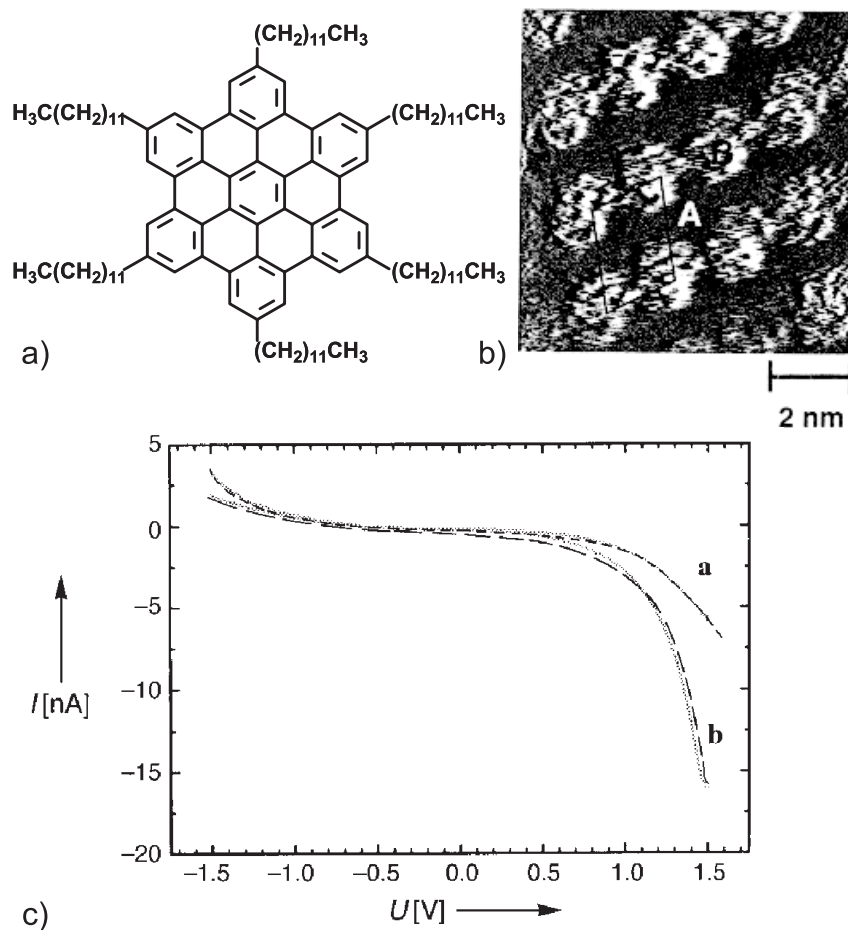


Fig. 2.2 (a) Chemical formula of an alkylated hexa-*peri*-hexabenzocoronene (HBC-C₁₂) derivative; (b) STM current image of this derivative at the solid/liquid interface on HOPG ($U_t = 0.9$ V; $I_t = 500$ pA); (c) I/V characteristics through alkyl chains (a) and through the aromatic cores (b). Note that here current is plotted versus tip, not sample bias. Reprinted with permission from ref. 11. Copyright (1995) Wiley-VCH Verlag GmbH & Co. KG.

In this work the self-assembly and electronic properties of an alkylated hexa-*peri*-hexabenzocoronene (HBC-C₁₂, Fig. 2.2a) derivative were studied by both STM and STS. At the solid/liquid interface between HOPG and a solution of the molecules in 1,2,4-trichlorobenzene, the HBC-C₁₂ molecules self-assemble into highly ordered two-dimensional crystals with domain sizes exceeding $100 \text{ nm} \times 100 \text{ nm}^2$ and unit cell parameters of $a = 1.94 \text{ nm}$, $b = 2.64 \text{ nm}$ and $\gamma = 80^\circ$. The small bright features, reflecting high tunneling probability, have been attributed to the aromatic cores of individual HBC-C₁₂ molecules, while the darker areas were at-

tributed to (locally mobile) alkyl chains. This attribution is justified since the size of the bright features corresponds well with the aromatic core size and additional larger contributions to the tunneling current are expected from molecules with smaller HOMO–LUMO-gaps [33].

Figure 2.2(c) displays the I – V s measured through the different areas attributed to saturated and unsaturated subunits of HBC- C_{12} . The significant difference between the symmetric alkyl-chain I – V s and the diode-like I – V s through the conjugated cores provides evidence that STS with at least 1 nm resolution is possible at the solid/liquid interface. The two different characteristics can be interpreted in the model of resonant tunneling: the rather symmetric curve for the alkyl chains reflects the lack of resonant contributions to the tunneling current from the alkyl chains. This is further supported by the fact that these curves are indistinguishable from those measured on bare, only solvent-covered, graphite. The asymmetry of the curves through the aromatic cores with a higher tunneling probability at positive tip bias can then be explained by resonant contributions of the HBC's HOMO.

2.4

Ultrahigh Vacuum versus Solid/Liquid Interface

Hexa-*peri*-hexabenzocoronene (HBC) without any peripheral substituents (Fig. 2.3a) can also be deposited by sublimation under ultrahigh vacuum conditions onto various substrates. Toerker et al. [34] studied HBC films nominally two monolayers thick on Au(100) substrates with STM and scanning tunneling spectroscopy (STS). Figure 2.3(b) displays an STM current image of a nominal double layer of HBC deposited on Au(100) which gives evidence for the formation of highly ordered domains. A detailed model, however, of how the molecules in the second layer are arranged with respect to first could not be derived in this study. From the I – V s measured on these nominal double layers (Fig. 2.3c) $(dI/dV)/(I/V)$ curves, reflecting the local density of states, could be calculated numerically (Fig. 2.3d). Four peaks at -2.0 , -1.4 , 1.8 , and 2.2 V sample bias can be clearly recognized which were attributed to electronic states derived from the HOMO $- 1$, HOMO, LUMO, and LUMO $+ 1$ of the molecular stack in the tunneling junction.

This example shows that under UHV conditions molecular frontier orbitals can be observed as peaks in differential conductance curves. In contrast, the experience in the authors' laboratory showed that at the solid/liquid interface resonant situations between the Fermi level of the tip and the molecular orbitals frequently lead to unstable imaging probably due to electrochemical reactions in the solution or at the interface which make the imaging unstable. This limits the accessible bias range for STS at the solid/liquid interface. Thus the direct determination of the precise energetic positions of molecular states with respect to the Fermi level of the substrate is often not possible at the solid/liquid interface since the limited bias range does not make it possible to “access” the molecular orbitals. Under UHV conditions the accessible bias range, which is usually larger, is limited by the strength of the interaction between the molecule and substrate which defines

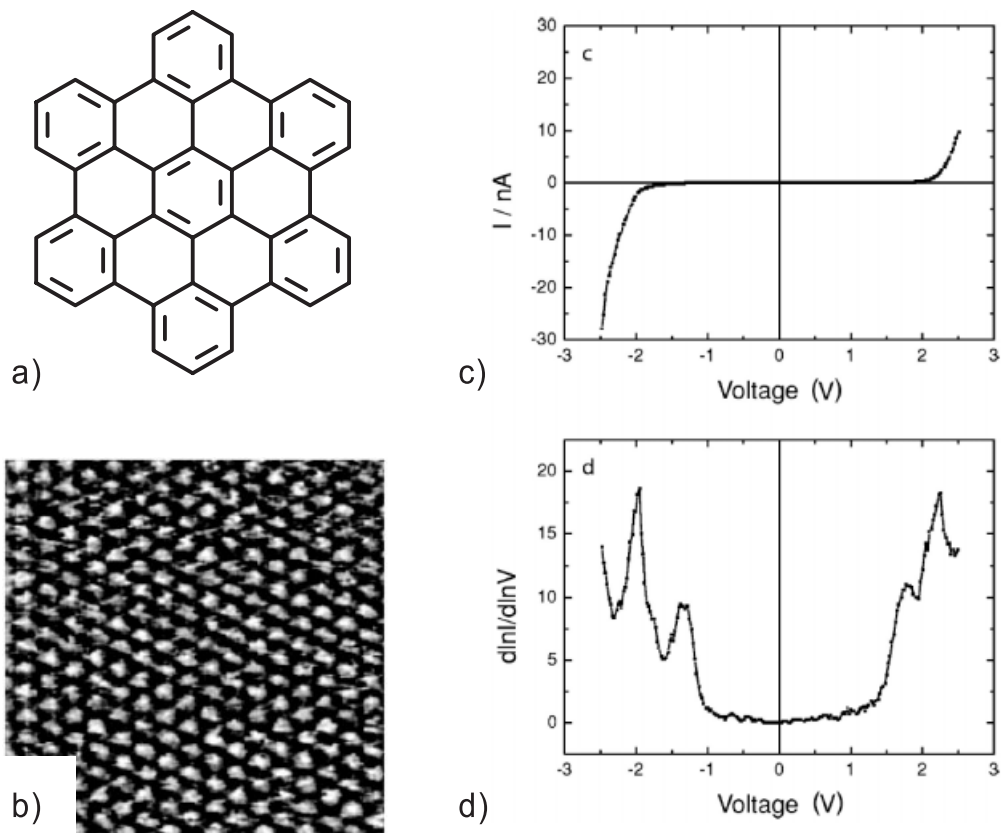


Fig. 2.3 (a) Chemical formula of hexa-*peri*-hexabenzocoronene (HBC); (b) $20 \text{ nm} \times 20 \text{ nm}^2$ STM current image of a nominal double layer of HBC on Au(100): $U = 0.7 \text{ V}$, $I = 50 \text{ pA}$; (c) I - V measured through HBCs in layers such

as those depicted in (a); (d) normalized differential conductance curves calculated from the data in (c). Reprinted with permission from ref. 34. Copyright (2002) by the American Physical Society.

thresholds for desorption and conformational changes of the molecule. On the other hand, as outlined above, the solid/liquid interface enables study of molecules that are otherwise difficult to crystallize. Furthermore, the dynamic nature of that interface, i.e., exchange of adsorbed and solubilized molecules, adds an additional degree of freedom not present under UHV conditions.

2.5 Probing π -Coupling at the Single-Molecule Level by STS

For a number of highly ordered films or single crystals of organic materials charge transport can be described in band-like models similar to those of inorganic semi-

conductors [35]. For π -conjugated materials the corresponding valence and conduction bands are derived from π -coupled HOMO and LUMO levels of the interacting molecules. Consequently, a number of STM studies have been performed to gain deeper insight into π -coupling at the single-molecule or few-molecules level.

Gesquière et al. studied a series of oligothiophene derivatives (Fig. 2.4a) at solid/liquid interfaces [36, 37]. These bis(urea)-substituted thiophene derivatives form

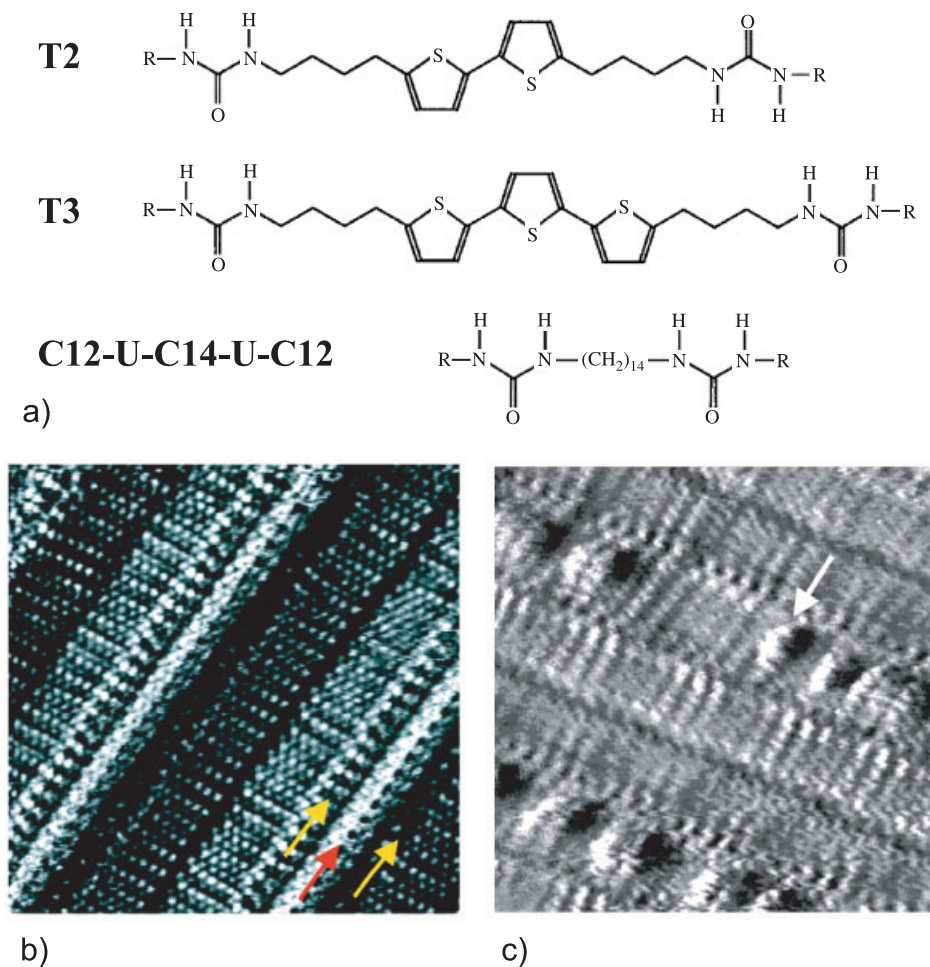


Fig. 2.4 (a) Chemical formulae of bis(urea)-substituted thiophene derivatives **T2** and **T3** and a matrix molecule **C12-U-C14-U-C12**; (b) $10 \text{ nm} \times 10 \text{ nm}$ STM image of an ordered layer of **T2** at the 1-octanol/graphite interface ($U_t = 0.6 \text{ V}$, $I_t = 1.0 \text{ nA}$). Red and yellow arrows indicate urea groups and thiophene

rings respectively. (c) $10 \text{ nm} \times 10 \text{ nm}$ STM image of a mixed layer of **T2** and **C12-U-C14-U-C12** at the 1-phenyloctane/graphite interface ($U_t = 0.6 \text{ V}$, $I_t = 1.0 \text{ nA}$). The arrow indicates an isolated **T2** molecule. Reprinted with permission from refs. 36 and 37. Copyright (2000 and 2001) by the American Chemical Society.

extended domains of lamellar structures at the solid/liquid interfaces, as exemplified for **T2** by the STM image in Fig. 2.4(b). The bright features within the lamellae have been attributed to the thiophene units. From the Moiré pattern observed in these layers the authors determined an intermolecular spacing along the lamella of 0.462 ± 0.005 nm which led to the conclusion that the packing is controlled by intermolecular hydrogen bonds between the urea groups. Interestingly, this dense packing does not allow for the thiophene units to lie flat on the substrate; instead, they must be tilted with respect to the surface which provides electronic coupling between the thiophene rings along the lamella. For this reason these arrangements are promising candidates for the study of π - π -interactions. In order to be able to compare STS data with those of isolated molecules, **T2** was coadsorbed in a matrix of C12-U-C14-U-C12, a molecule of similar length and with the urea groups in similar positions. In these mixed layers single **T2** molecules could be identified, as depicted in Fig. 2.4(c).

Current-voltage characteristics measured through π -stacked **T2** (Fig. 2.5a) or **T3** (no data shown here) were attributed to a semiconductor-like behavior with a band gap around zero bias. Interestingly, this observed gap reduces from 0.45 ± 0.08 eV for **T2** to 0.30 ± 0.05 eV for **T3** which has been attributed to an increase in the effective conjugation length, both intramolecular and along the π -stacked ribbons. However, the reduction of the observed gap by π - π -interactions along the ribbons was most convincingly demonstrated by comparing I - V s of single **T2** molecules in a matrix (see Fig. 2.4c) with those of stacked **T2** as displayed in Fig. 2.5. For single **T2** molecules a considerably larger gap of 0.65 ± 0.11 eV was observed, consistently with the expectation that for π -stacked molecules the HOMO-LUMO-gaps should narrow due to the HOMO and LUMO splittings of the interacting molecules, though the gaps observed here are, surprisingly, significantly smaller than the band gaps reported for polythiophene bulk semiconductors.

A very similar observation has been reported by Uji-i et al. [38, 39]. For 1-pyrenehexadecanoic acid two different structures were observed in self-assembled monolayers at the solid/liquid interface for the pure system and in mixtures with 4,4'-bipyridyl. For the pure system the pyrene units were lying flat on the substrate while in the mixtures lamellar structures similar to the above-mentioned case of **T2** and **T3** were observed. Along the lamellae the pyrenes are likely to be π -stacked with a tilt angle of $\sim 30^\circ$ with respect to the surface. The STS data revealed an approximately 0.15 V earlier onset of the (possibly) resonantly enhanced tunneling current in the π -stacked pyrenes than for the isolated molecules. Notably, the authors found a shift of the energy levels of pyrenes in the aggregates of about 0.06 to 0.11 eV based on a model analogously to J-aggregates, using their previously suggested packing structure.

While the above described studies demonstrate the impact of π -coupling on the electronic properties of the molecules involved in the interaction, they all deal with extended aggregates with a single specific geometry. However, theoretical calculations [35] predict that the changes in the electronic properties, i.e., the HOMO and LUMO splittings, will depend sensitively on the details of the relative positions of the molecules in the aggregates.

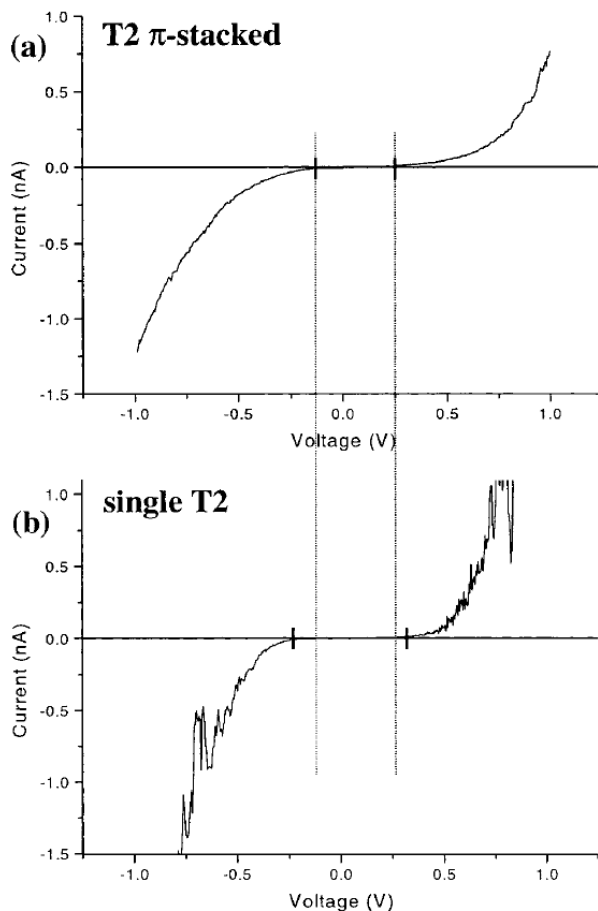


Fig. 2.5 (a) I - V s of **T2** molecules in ribbons from layers of pure **T2**, compared with (b) those of single **T2** molecules in a C12-U-C14-U-C12 matrix. Reprinted with permission from ref. 37. Copyright (2001) by the American Chemical Society.

In order to address this problem we investigated previously characterized [40] double layers of HBC (Fig. 2.6a) at the solid/liquid interface. These double layers offer the additional advantage that the disk-like molecules lie flat, and that charge transport along – not perpendicular to – the stacking direction can be investigated: this is more relevant from a device-oriented point of view.

HBC, previously studied under ultrahigh vacuum (UHV) conditions [34, 41], exhibits enough solubility in hot 1,2,4-trichlorobenzene to be studied at solid/liquid interfaces [40]. Figure 2.6(b) displays an STM image obtained at quite a small impedance of the tunneling junction below $10^9 \Omega$. A periodic hexagonal pattern, identical to the one observed for the same molecule on HOPG under UHV conditions

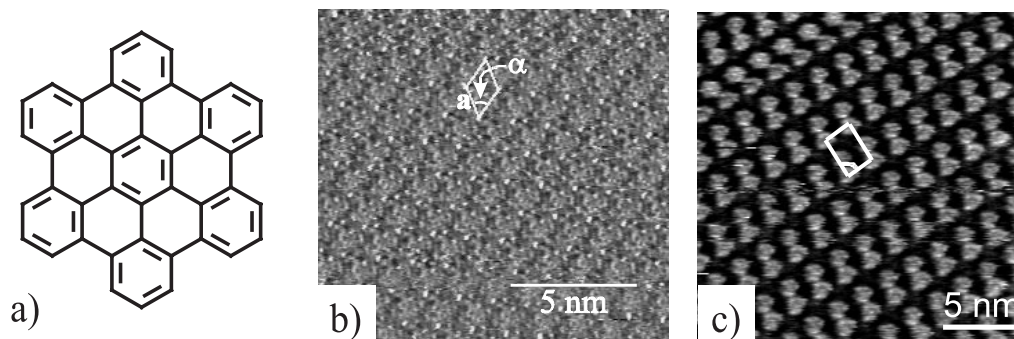


Fig. 2.6 (a) Chemical formula of HBC. STM images of (b) the hexagonal arrangement in the first layer; (c) the dimer structure of the second layer. Tunneling parameters were (a) $U_t = -0.351$ V; $I_t = 0.636$ nA and (b)

$U_t = -1.2$ V; $I_t = 0.1$ nA. Reprinted with permission from ref. 40. Copyright (2002) by the American Chemical Society (b). Reprinted with permission from ref. 42. Copyright (2006) by the American Physical Society (c).

(lateral spacing 1.4 ± 0.1 nm) can be recognized. Though it is difficult to assign single molecules to the contrast observed, we attribute the pattern to a hexagonally close-packed layer of HBC.

Increasing the tip-sample separation by adjusting the tunneling parameters to junction impedances larger than $10^9 \Omega$ makes it possible to visualize a different packing. Now, the HBCs take up an arrangement in an array of dimers with unit cell parameters of $a = 3.3 \pm 0.2$ nm, $b = 1.8 \pm 0.2$ nm and $\alpha = 86 \pm 5^\circ$. The two arrangements can be visualized alternatively by simply adjusting the tunneling junction impedance, causing different tip-sample separations. We suggest a double-layer architecture where the first layer is hexagonally close-packed and the second exhibits a dimer arrangement. It is noteworthy that the reduced symmetry of the second layer and its lattice constants does *not* allow for all HBCs in the second layer to occupy equivalent positions with respect to the first in a crystallographic sense, as reflected by the model as depicted in Fig. 2.7(b) [42]. Arguments supporting the details of this model will be discussed below.

The first indication that the two HBCs forming a dimer are not equivalent is found from STM images (not shown here) simultaneously recorded at opposite sample bias [42]: at positive sample bias one HBC in each dimer appears very bright while the other one is almost invisible; this is in contrast to the equal brightness of the HBCs at negative sample bias (Fig. 2.6c). This unequivalence is also reflected in the STS curves, where the spectra take into account the HBC's position within the dimer as depicted in Fig. 2.7(b). Notably, the I - V s through HBC appearing dim at positive sample bias are indistinguishable from those of the related cyclophanes [43], which can be considered a covalent model for stacked HBCs.

As mentioned above, the electronic properties, i.e. HOMO and LUMO splittings, of conjugated molecules depend sensitively on the details of the stacking geometry [35]. In particular the intermolecular distance and the lateral displacement need to

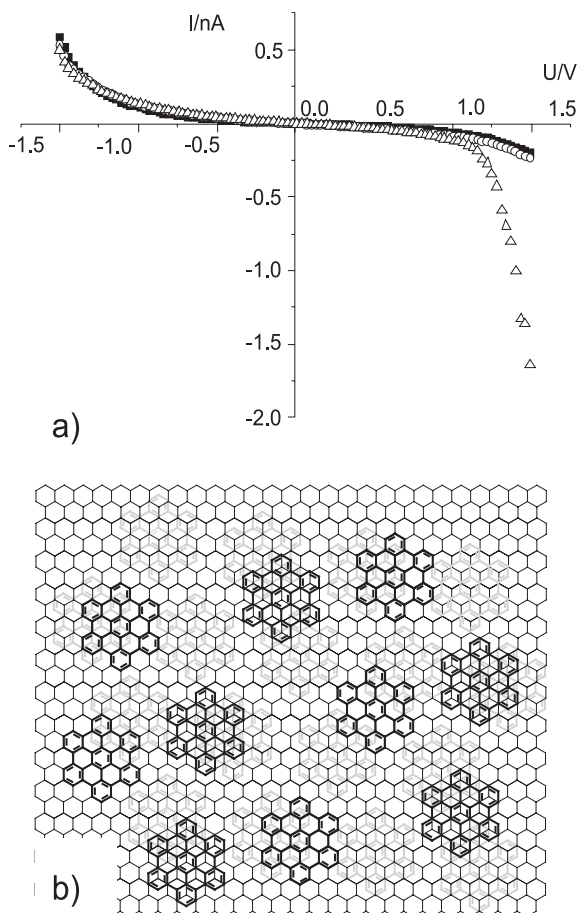


Fig. 2.7 (a) I - V s recorded through the unequivalently positioned HBCs (open symbols, circles for dim and triangles for bright HBCs at positive sample bias, solid squares for cyclophanes) constituting a dimer [42] in the arrangement of the second layer compared with those of HBC-cyclophanes [43]

in the respective monolayers. (b) Packing model for the double-layer architecture of HBC [42]. First and second layers are depicted in gray and black respectively. With permission from ref. 42. Copyright (2006) by the American Physical Society.

be considered. For a perfect cofacially stacked HBC dimer (intermolecular distance 0.35 nm) HOMO and LUMO splittings of 1.0 and 0.6 eV have been reported. Allowing for lateral displacements as present in single crystals of this material [44], these values, reduced by 50%, are still significant. We consequently attribute the different electronic properties of the HBCs in the dimer to differences in HOMO and LUMO splitting caused by a different coupling to the first layer at the different positions that are occupied by the HBCs in the second layer. It should be noted here that for the HBC-cyclophanes that appear electronically equivalent to the dim

HBCs in the second layer, a lateral offset not greater than the bulk value of 0.38 nm was concluded from NMR measurements [43]. Since π - π -interactions become more repulsive at smaller lateral displacements [45], we assume the dim HBCs to be positioned on top of an HBC of the first layer with exactly this lateral offset. The other HBCs are consequently expected to exhibit larger displacements. With this additional lesson learned from the spectroscopic data we can now construct a packing model with justified atomic precision.

The model depicted in Fig. 2.7(b) was constructed as follows [42]: the HBCs of the first layer were positioned on the HOPG substrate in an A-B-type adsorption, i.e., like the next graphene sheet, such that the experimentally observed lattice is reproduced (1.4 nm, 60° and 9° with respect to the HOPG lattice). For the second layer also, the lattice parameters have been reproduced (1.9 nm, 3.2 nm, 82°) but the precise positions with respect to the first layer were determined by using the additional above-mentioned spectroscopic information. One row of molecules in the dimers (the right-hand ones in Fig. 2.7b) was positioned with a lateral offset of 0.38 nm, which matches the bulk value. The resulting lateral displacement for the other molecules in the dimer is then found to be 0.62 nm. As expected, this is substantially larger. Interestingly the positions of the HBCs along one row are electronically equivalent, while in a crystallographic sense only every second position is the same. Moreover, the HBCs with the larger displacement couple to two underlying disks, instead of one. Since these HBCs exhibit a higher tunneling probability at positive sample bias, one is led to conclude that this particular coupling leads to a stronger narrowing of the HOMO-LUMO-gap than the coupling to one disk.

As an alternative to hot 1,2,4-trichlorobenzene, HBC may be solubilized at room temperature in mixtures with electron acceptors such as coronenediimide derivatives. In this case one also observes double-layer architectures with coadsorbed electron acceptors [40]. STS on these double layers reveals an intermediate tunneling probability at positive sample bias compared with the two cases observed for pure HBC, and similarly a consistent model with intermediate lateral displacements can be constructed [42].

2.6 Molecular Diodes and Prototypical Transistors

The suggestion of a molecular diode by Aviram and Ratner in 1974 [12] is often considered the birth of molecular electronics. The rectification in their proposal arises from a built-in asymmetry of an electron-donor/isolating bridge/electron-acceptor molecule which translates into different probabilities for electrons to be transferred in opposite directions across the molecule sandwiched between two metallic electrodes. However, asymmetric electron transmission through molecules with respect to the applied bias has also been observed for symmetric molecules, as exemplified above for HBC-C₁₂ [11]. Here the asymmetry is believed to be induced by an asymmetric spatial position of the molecule in the junction and an asymmetric alignment of the frontier orbitals (HOMO and LUMO) with respect

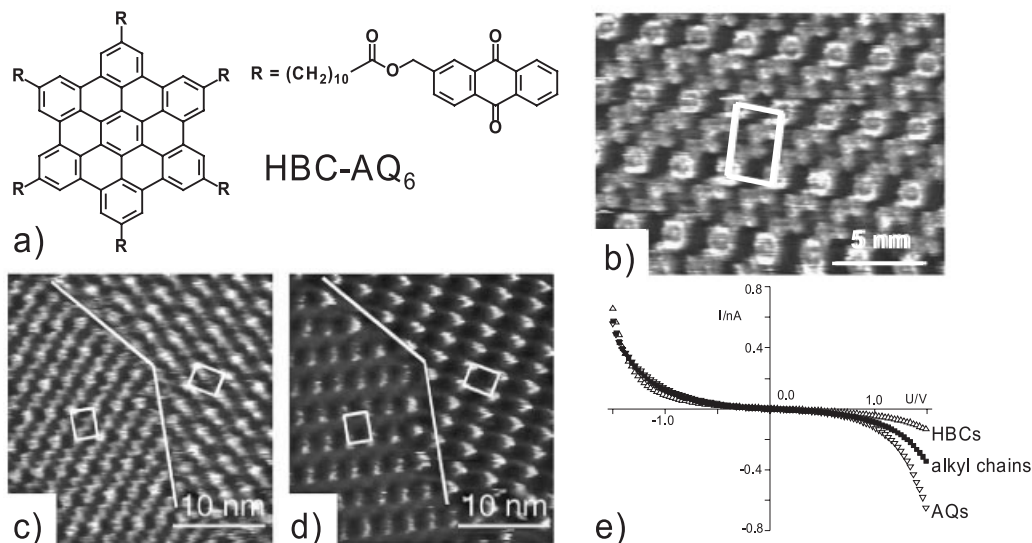


Fig. 2.8 (a) Chemical formula of HBC-AQ₆. (b) STM image of a highly ordered monolayer of HBC-AQ₆. (c), (d) Simultaneously recorded STM images with positive and negative sample bias respectively for the two scan directions. (e) I -Vs through HBC cores, AQs, and alkyl chains recorded in monolayers of HBC-AQ₆.

Tunneling parameters were: (b) $U_t = +1.4$ V, $I_t = 0.300$ nA, (c) $U_t = +1.4$ V, $I_t = 0.300$ nA and (d) $U_t = -1.4$ V, $I_t = 0.300$ nA. Reprinted with permission from refs. 47 and 49.

Copyright (2004) by Elsevier (c, d, e) and the American Physical Society (b).

to the Fermi level of the substrate. In particular, higher tunneling probabilities at negative sample bias were attributed to resonant contributions of the HOMO. Consequently, suitable design of the frontier orbitals of the molecule in the junction should make it possible to control the orientation of the diode, i.e., the bias sign for its forward and backward direction.

To address this question we studied covalently linked electron-donor-acceptor multiads such as the HBC derivative HBC-AQ₆ decorated with six electron-accepting anthraquinones (AQs) on the periphery (Fig. 2.8a) [46, 47]. In the STM current image of HBC-AQ₆ at the HOPG/solution interface in Fig. 2.8(b), the bright circular features at the corners of the indicated unit cell are attributed to the conjugated cores of the HBC, while the slightly less bright features are attributed to AQ molecules. Due to spatial constraints of the unit cell, only four of the six AQs do pack on the surface while the remaining two, which are probably attached in *para* positions, are likely to be solubilized in the supernatant solution. Figures 8(c) and 8(d) provide evidence for an interesting bias-dependent relative contrast between HBCs and AQs. These images have been recorded simultaneously with different tunneling parameters for forward and backward scan directions and therefore they do not suffer from a changing quality of the tip in subsequently recorded images. At positive sample bias (tunneling into empty sample

states) HBC and AQ moieties appear almost equally bright while at negative sample bias (probing occupied sample states) the tunneling probability is much higher for HBCs than for AQs. A similar observation has been reported for triads from a perylene and two oligo-*para*-phenylene-vinylenes [48]. In this case also the electron donors, i.e., oligo-*para*-phenylene-vinylenes, appeared much brighter at negative sample bias while the opposite was true for positive sample bias. The bias dependence of the relative contrast is also reflected in the I - V s through the respective molecules in Fig. 2.8(e). Compared with the resonant-free case of the alkyl-chains, HBC exhibits significantly higher tunneling probabilities at negative sample bias, while for AQ an increased tunneling current is observed at positive sample bias. Consequently these opposite asymmetries are attributed to resonant contributions of the HOMO of HBC and the LUMO of AQ.

Thus it was shown that by going from an electron acceptor to an electron donor the orientation of a molecular diode, i.e., the forward and backward directions, can be changed. Notably, the self-assembly of HBC-AQ₆ demonstrates a possible, more general approach toward a major challenge in molecular electronics, namely the integration of different functional modules on the nanoscale. While for binary mixtures a phase segregation on meso- or macroscopic length scales is frequently observed, the covalent connection of the two components used here prevents such segregation. Instead it promotes the formation of highly ordered arrays in which the two components are separated on the molecular scale and still addressable separately, a situation we called “nanophase segregation”. In yet another step we tried to use the nanophase segregation of HBC-AQ₆ at solid/liquid interfaces in order to achieve control over the electronic properties of the HBC-core at the interface [49].

To this extent 9,10-dimethoxyanthracene (DMA; Fig. 2.9a), an electron donor known to form charge-transfer complexes (CTCs) with AQ, was added to the HBC-AQ₆ solution. STM current images obtained from such mixtures are depicted in Figs. 2.9(b) and 2.9(c). Two arrangements with different unit cells can be observed, as demonstrated in Fig. 2.9(b). The arrangement with the smaller unit cell is indistinguishable from that of neat HBC-AQ₆ discussed above. In the other arrangement six additional bright spots per unit cell can be recognized in the high-resolution image in Fig. 2.9(c) which we attributed to charge-transfer complexes between AQ and DMA. Depending on whether or not charge-transfer complexes are coadsorbed next to the HBC, two different I - V s through the HBCs are observed. Interestingly enough, the two I - V s are superimposed by shifting the one in the presence of CTCs by 120 mV to more positive sample bias and normalizing with an appropriately chosen constant (Fig. 2.9d, inset).

Several control experiments were performed in order to exclude a number of possible origins for the two kinds of I - V s, such as the presence of DMA or CTCs in solution, the formation of DMA-HBC complexes, etc., thereby insuring that the effect is indeed due to the presence of oriented CTCs, i.e., electrical dipoles. These dipoles will give rise to an interface dipole which causes a potential drop at the interface. For resonantly tunneling electrons this potential drop shifts the molecular orbitals of the adsorbate with respect to the Fermi level of the substrate. In a continuum approximation the strength of the potential drop is related to the dipole

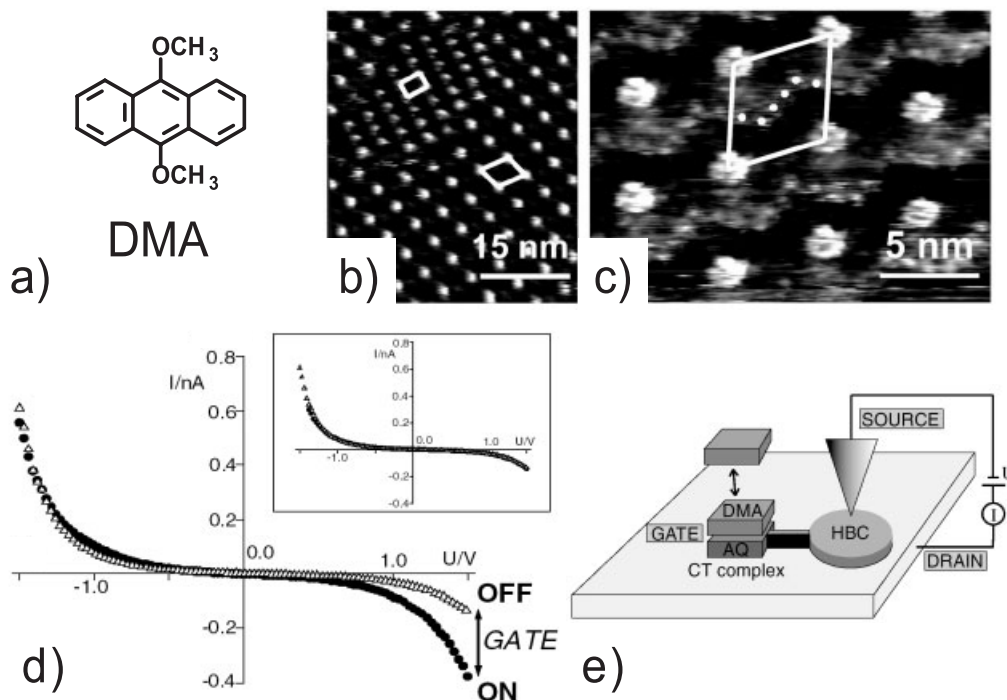


Fig. 2.9 (a) Chemical formula of 9,10-dimethoxyanthracene (DMA). STM images of monolayers from mixed solutions of HBC-AQ₆ and DMA: (b) overview; (c) small-scale high-resolution. (d) I - V s through HBC cores in domains in which DMA is coadsorbed (solid symbols) and in domains where no DMA is coadsorbed (open symbols). Inset: the same

data after normalization. (e) Schematic of the prototypical Chem-FET with nanogates.

Tunneling parameters were: (b) $U_t = -1.4$ V; $I_t = 0.108$ nA; (c) $U_t = -1.2$ V, $I_t = 0.270$ nA. Reprinted with permission from ref. 49.

Copyright (2004) by the American Physical Society.

density N at the interface, the strength of the dipoles μ , the dielectric constant ϵ_0 , and ϵ_r via the Helmholtz equation [Eq. (1)].

$$\Delta\phi = \frac{eN\mu}{\epsilon_0\epsilon_r} \quad (1)$$

With a dipole strength of 3 D (from ab initio calculations), a dipole density determined from the STM images, and a dielectric constant of 3, a relative shift of 130 meV is found, in good agreement with the experimental value of 120 meV. The model allows for several predictions that may be tested: the effect should scale linearly with, firstly, the dipole density, which can be controlled via the spacer length between HBC and the acceptor; and secondly, with the dipole strength, which may be varied by different donor-acceptor pairs. Thirdly, the orientation of the dipole moment is relevant. By now, it has been demonstrated that dipoles ori-

ented parallel to the interface do not show significant impact on the observed $I-V$ s [50, 51].

More generally, the set-up can be viewed as prototypical single-molecule chemical field-effect transistor (Chem-FET, Fig. 2.9e), since the change in the $I-V$ s is induced by the formation of a charge-transfer complex of which the acceptor is covalently bound to the channel (HBC) and the donor comes from the ambient fluid. In particular the gate is of true molecular size and integrated in the molecule itself, which is considered a major step toward monomolecular electronics [13].

2.7

Conclusions

In this chapter the power of submolecularly resolved STS combined with STM has been exemplified. On the one hand, π - π -interactions have been investigated at the single-molecule level and have been used to solve the structures of complex molecular architectures of derivatives of hexa-*peri*-hexabenzocoronene at solid/liquid interfaces, which to our knowledge is impossible today with any other technique. On the other hand, the electronic functions of prototypical electronic devices have been demonstrated, including rectifiers and transistors based on single molecules. Again, this could not be achieved by any other technique; also, it indicates that molecular electronics based on single molecules appears feasible at ambient conditions.

Acknowledgements

This work has been partially supported by the Collaborative Research Center Sfb658 “Elementary processes in molecular switches at surfaces”. Moreover, it is a pleasure to acknowledge the long-standing and fruitful collaboration with the group of Klaus Müllen from the Max-Planck Institute for Polymer Research in Mainz, Germany.

References

- 1 G. HOROWITZ, *J. Mater. Chem.* **9**, 2021 (1999).
- 2 H. E. KATZ, Z. BAO, S. L. GILAT, *Acc. Chem. Res.* **34**, 359 (2001).
- 3 A. HEPP, H. HEIL, W. WEISE, M. AHLES, R. SCHMECHEL, H. VON SEGGERN, *Phys. Rev. Lett.* **91**, 157 406 (2003).
- 4 J. H. BURROUGHES, D. D. C. BRADLEY, A. R. BROWN, R. N. MARKS, K. MACKAY, R. H. FRIEND, P. L. BURNS, A. B. HOLMES, *Nature* **347**, 539 (1990).
- 5 R. H. FRIEND, R. W. GYMER, A. B. HOLMES, J. H. BURROUGHES, R. N. MARKS, C. TALIANI, D. D. C. BRADLEY, D. A. DOS SANTOS, J. L. BRÉDAS, M. LÖGLUND, W. SALANECK, *Nature* **397**, 121 (1999).
- 6 U. MITSCHKE, P. BÄUERLE, *J. Mater. Chem.* **10**, 1471 (2000).

- 7 H. HOPPE, N. S. SARICIFTCI, *J. Mater. Res.* **19**, 1924 (2004).
- 8 P. PEUMANS, A. YAKIMOV, S. R. FORREST, *J. Appl. Phys.* **93**, 3693 (2003).
- 9 A. GÖTZBERGER, C. HEBLING, H.-W. SCHOCK, *Mater. Sci. Engng. R* **40**, 1 (2003).
- 10 (a) J. P. RABE, S. BUCHHOLZ, *Science* **253**, 424 (1991); (b) J. P. RABE, S. BUCHHOLZ, *Phys. Rev. Lett.* **66**, 2096 (1991).
- 11 A. STABEL, P. HERWIG, K. MÜLLEN, J. P. RABE, *Angew. Chem. Int. Ed.* **34**, 1609 (1995).
- 12 A. AVIRAM, M. A. RATNER, *Chem. Phys. Lett.* **29**, 277 (1974).
- 13 C. JOACHIM, J. K. GIMZEWSKI, A. AVIRAM, *Nature* **408**, 541 (2000).
- 14 R. L. CARROLL, C. B. GORMAN, *Angew. Chem. Int. Ed.* **41**, 4378 (2002).
- 15 G. MARUCCIO, R. CINGOLANI, R. RINALDI, *J. Mater. Chem.* **14**, 542 (2004).
- 16 T. W. KELLEY, E. L. GRANSTROM, C. D. FRISBIE, *Adv. Mater.* **11**, 261 (1999).
- 17 G. J. ASHWELL, J. R. SAMBLES, A. S. MARTIN, W. G. PARKER, M. SZABLIEWSKI, *Chem. Soc. Chem. Comm.* **19**, 1374 (1990).
- 18 R. M. METZGER, B. CHEN, U. HÖPFNER, M. V. LAKSHMIKANTHAM, D. VUILLAUME, T. KAWAI, X. WU, H. TACHIBANA, T. V. HUGHES, H. SAKURAI, J. W. BALDWIN, C. HOSCH, M. P. CAVA, L. BREHMER, G. J. ASHWELL, *J. Am. Chem. Soc.* **119**, 10455 (1997).
- 19 M. A. REED, C. ZHOU, C. J. MULLER, T. P. BURGİN, J. M. TOUR, *Science* **278**, 292 (1997).
- 20 A. I. YANSON, I. K. YANSON, J. M. VAN RUITENBEEK, *Nature* **400**, 144 (1999).
- 21 C. KERGUERIS, J. P. BOURGOIN, S. PALACIN, D. ESTEVE, C. URBINA, M. MAGOGA, C. JOACHIM, *Phys. Rev. B* **59**, 12505 (1999).
- 22 J. REICHERT, R. OCHS, D. BECKMANN, H. B. WEBER, M. MAYOR, H. v. LÖHNESEN, *Phys. Rev. Lett.* **88**, 176804 (2002).
- 23 C. ZHOU, M. R. DESHPANDE, M. A. REED, L. JONES, J. M. TOUR, *Appl. Phys. Lett.* **71**, 611 (1997).
- 24 M. A. REED, C. ZHOU, M. R. DESHPANDE, C. J. MULLER, T. P. BURGİN, L. JONES, J. M. TOUR, *Ann. N. Y. Acad. Sci.* **852**, 133 (1998).
- 25 L. GRILL, F. MORESCO, P. JIANG, C. JOACHIM, A. GOURDON, K.-H. RIEDER, *Phys. Rev. Lett.* **69**, 035416 (2004).
- 26 J. BARDEEN, *Phys. Rev. Lett.* **6**, 57 (1961).
- 27 J. TERSOFF, D. R. HAMANN, *Phys. Rev. Lett.* **50**, 1998 (1983).
- 28 J. TERSOFF, D. R. HAMANN, *Phys. Rev. B* **31**, 805 (1985).
- 29 M. BÜTTIKER, Y. IMRY, R. LANDAUER, S. PINHAS, *Phys. Rev. B* **31**, 6207 (1985).
- 30 Y. MEIR, N. S. WINGREEN, *Phys. Rev. Lett.* **68**, 2512 (1992).
- 31 W. MIZUTANI, M. SHIGENO, K. KAJIMURA, M. ONO, *Ultramicroscopy* **42–44**, 236 (1992).
- 32 J. K. SPONG, H. A. MIZES, L. J. LA COM, M. M. DOVEK, J. E. FROMMER, J. S. FOSTER, *Nature* **338**, 137 (1989).
- 33 R. LAZZARONI, A. CALDERONE, J. L. BRÉDAS, J. P. RABE, *J. Chem. Phys.* **107**, 99 (1997).
- 34 M. TOERKER, T. FRITZ, H. PROEHL, R. GUTIERREZ, F. GROSMANN, R. SCHMIDT, *Phys. Rev. B* **65**, 245422 (2002).
- 35 J. L. BRÉDAS, J. P. CALBERT, D. A. DA SILVA FILHO, J. CORNIL, *Proc. Natl. Acad. Sci.* **99**, 5804 (2002).
- 36 A. GESQUIÈRE, M. M. S. ABDEL-MOTTALIB, S. DE FEYTER, F. C. DE SCHRYVER, F. SCHOONBEEK, J. VAN ESCH, R. M. KELLOG, B. L. FERİNGA, A. CALDERONE, R. LAZZARONI, J. L. BRÉDAS, *Langmuir* **16**, 10385 (2000).
- 37 A. GESQUIÈRE, S. DE FEYTER, F. C. DE SCHRYVER, F. SCHOONBEEK, J. VAN ESCH, R. M. KELLOG, B. L. FERİNGA, *Nano Lett.* **1**, 201 (2001).
- 38 H. UJI-I, M. YOSHIDOME, J. HOBLEY, K. HATANAKA, H. FUKUMURA, *Phys. Chem. Chem. Phys.* **5**, 4231 (2003).
- 39 H. UJI-I, S. NISHIO, H. FUKUMURA, *Chem. Phys. Lett.* **408**, 112 (2005).
- 40 P. SAMORÍ, N. SEVERIN, C. D. SIMPSON, K. MÜLLEN, J. P. RABE, *J. Am. Chem. Soc.* **124**, 9454 (2002).
- 41 T. SCHMITZ-HÜBSCH, F. SELLAM, R.

- STAUB, M. TÖRKER, T. FRITZ, C.
KÜBEL, K. MÜLLEN, K. LEO, *Surf. Sci.*
445, 358 (2000).
- 42 F. JÄCKEL, M. D. WATSON, K. MÜLLEN,
J. P. RABE, *Phys. Rev.* **B73**, 04 54 23
(2006).
- 43 M. D. WATSON, F. JÄCKEL, N. SEVERIN,
J. P. RABE, K. MÜLLEN, *J. Am. Chem.*
Soc. **126**, 1402 (2004).
- 44 R. GODDARD, M. W. HAENEL, W. C.
HERNDON, C. KRÜGER, M. ZANDER,
Mater. Sci. Engng R **117**, 30 (1995)
- 45 C. A. HUNTER, K. R. LAWSON, J.
PERKINS, C. J. URCH, *J. Chem. Soc.,*
Perkin Trans 1, 651, (2001).
- 46 P. SAMORÍ, X. YIN, N. TCHEBOTAREVA,
Z. WANG, T. PAKULA, F. JÄCKEL, M. D.
WATSON, A. VENTURINI, K. MÜLLEN,
J. P. RABE, *J. Am. Chem. Soc.* **126**,
3567 (2004).
- 47 F. JÄCKEL, Z. WANG, M. D. WATSON,
K. MÜLLEN, J. P. RABE, *Chem. Phys.*
Lett. **387**, 372 (2004).
- 48 A. MIURA, Z. CHEN, H. UJI-I, S. DE
FEYTER, M. ZDANOWSKA, P. JONKHEJM,
A. P. H. J. SCHENNING, E. W. MEIJER,
F. WÜRTHNER, F. C. DE SCHRYVER,
J. Am. Chem. Soc. **125**, 14 968 (2003).
- 49 F. JÄCKEL, M. D. WATSON, K. MÜLLEN,
J. P. RABE, *Phys. Rev. Lett.* **92**, 188 303
(2004).
- 50 F. JÄCKEL, Z. WANG, M. D. WATSON,
K. MÜLLEN, J. P. RABE, *Synth. Met.*
146, 269 (2004).
- 51 F. JÄCKEL, Self-Assembly and
Electronic Properties of Conjugated
Molecules: Toward Mono-molecular
Electronics, PhD thesis, Humboldt
University Berlin (2005).

3

Molecular Repositioning to Study Mechanical and Electronic Properties of Large Molecules

Francesca Moresco

3.1

Introduction

The investigation of single molecules as electrical and nanomechanical devices has come in recent years to be an important and well established research field, both in terms of technological development and also in the context of fundamental research. The application of molecules as electronic devices can allow a high grade of miniaturization and permit exploitation of the quantum mechanical properties of molecules in systems where electrons are confined to dimensions comparable with their wavelength.

The idea that a single molecule could be embedded between electrodes in order to perform the basic functions of digital electronics was first suggested by Aviram and Ratner in 1974 [1]. They proposed that a molecule with a donor–spacer–acceptor structure would behave as a diode when placed between two electrodes. An example of this type of molecule has recently been synthesized [2]. Assemblies consisting of such molecules embedded between several electrodes constitute a first example of the so-called hybrid molecular electronic (HME) devices. More recently, a different approach to molecular electronics was proposed, known as mono-molecular electronics (MME): it suggested that all elementary functions and interconnections required for computation could be integrated into a single molecule [3].

However, several fundamental problems have to be solved before the ideas of HME or MME can be applied. In this context, scanning tunneling microscopy at low temperature (LT-STM) is an important experimental technique. Besides imaging surfaces with atomic resolution, it enables manipulation of single molecules and controlled two-terminal conductance measurements. Important work on the way to single-molecule devices were the electrical single-atom switch realized by Eigler et al. [4] using a single Xe atom, and the first experimental determination of the electrical contact point of a C₆₀ molecule by Joachim et al. [5]. In the latter case a single-molecule electromechanical amplifier was obtained, using the tip of an STM to deform the C₆₀ molecule, thereby shifting the molecular orbitals [6]. Moreover, the conductance of single- and multi-wall carbon nanotubes electrically

interconnected in a fully planar geometry was measured [7, 8], and carbon nanotube transistors have been realized [9, 10]. Recently, current–voltage characteristics of single (or a few) molecules have been measured by break junction experiments [11–14]. However, the number of interconnected molecules, the molecular conformation, and the geometry of the molecule–metal junction is inaccessible in such experiments [12].

Self-organization of molecules appears to be a practical strategy for fabricating ensembles of molecular nanostructures in a parallel geometry and understanding the delicate balance between molecule–substrate and intramolecular interaction is fundamental to learning how to drive the ordering of molecules on surfaces. For this reason, the adsorption of large organic molecules on metal surfaces is being investigated intensively (as reviewed in refs. 15 and 16).

Low-temperature scanning tunneling microscopy (LT-STM) is at present the only experimental method which allows both precise submolecular imaging of a single molecule and the possibility of manipulation and measurement of the electronic properties in clean and controlled conditions. In this chapter, recent LT-STM investigations of the mechanical and electronic properties of single molecules deposited on metal surfaces are reviewed. In particular, some recent experiments are described, starting from the study of the internal mechanics of a molecule during its movement on a surface, going through the realization of a conformational molecular switch working under the action of the STM tip, and concluding with the characterization of the controlled contact of a molecular wire with a metallic nanoelectrode.

The experiments that are reported have been performed in ultra-high vacuum (UHV) conditions on copper substrates. Low Miller-index surfaces have been chosen because of their symmetry properties, and vicinal surfaces like Cu(211) because their stepped geometry forms natural railways for manipulation experiments. Moreover, the strong interaction of the copper surfaces with the adsorbed molecules is especially interesting, producing conformational changes in the adsorbed molecules and molecularly induced restructuring of the substrate.

3.2 Specially Designed Molecules

In order to apply manipulation methods to complex molecules and therefore to investigate their electronic and mechanical properties, it is first of all important to design specifically, for each type of experiment, suitable molecular systems. A few common features are desirable to obtain model systems for molecular mechanical and electronic devices, which can be manipulated by STM at low temperature. To allow STM imaging, the molecules should first of all have a planar design, with the active part parallel to the substrate. Then, some rigidity is required to reduce the number of possible conformations. Moreover, to allow conductance or contact measurements, contacting groups are needed. Finally, it is necessary to decouple the active part of the molecule electronically from the metallic surface. One of the

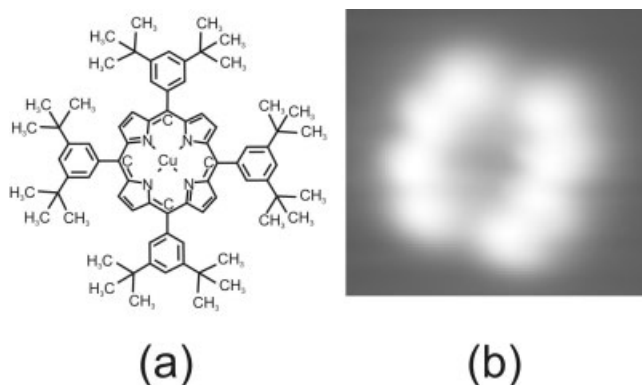


Fig. 3.1 (a) Chemical structure of a TBPP molecule; (b) STM image of a TBPP molecule adsorbed on a Cu(111) surface. The molecule has a diameter of about 2.5 nm and an apparent height of 0.2 nm. On Cu(111) TBPP molecules are adsorbed with the spacer groups flat on the surface.

possible solutions is to use molecular spacers, able to keep the central part of the molecule separate from the metallic substrate and to increase the mobility of the molecule, allowing STM manipulation even at low temperature. The molecules described below have been specially designed to be investigated by STM and to study the effects of LT-STM manipulation on the internal conformation of the molecules. They can be considered model systems for molecular switches and conducting wires kept isolated from metallic surfaces.

Cu-tetra[(3,5-di-*tert*-butyl)phenyl]porphyrin (TBPP) is a porphyrin-based molecule with four phenyl-based spacer groups. Its chemical structure is shown in Fig. 3.1(a). The spacers are di(*tert*-butyl)phenyl (TBP) groups. These bulky groups lift the central porphyrin and are poorly coupled to the surface. In the gas phase the spacers are oriented perpendicular to the central ring, but are able to rotate around the σ bond connecting each of them to the porphyrin, assuming different conformations. As one can see in the STM image of Fig. 3.1(b), the molecule shows bright lobes corresponding to the spacers, while the central ring is not visible because its π orbitals are electronically decoupled from the metal surface. The adsorption geometry of TBPP on Cu(111), Cu(100), and Cu(211) has been investigated in detail by LT-STM, to determine the angular rotations of the lateral groups in the different cases [17]. Previous experiments at room temperature have already made it possible to observe different conformations of the molecule on different substrates [18].

The molecular lander ($C_{90}H_{98}$) [19], proposed by analogy with the “Mars Landers” spacecrafts, consists of a long rigid polyaromatic mainboard (a molecular wire), maintained above the surface by four TBP spacer groups (exactly the same as the spacers already described for the TBPP). The design of the lander guarantees the separation of the board from the metal surface to preserve its electronic

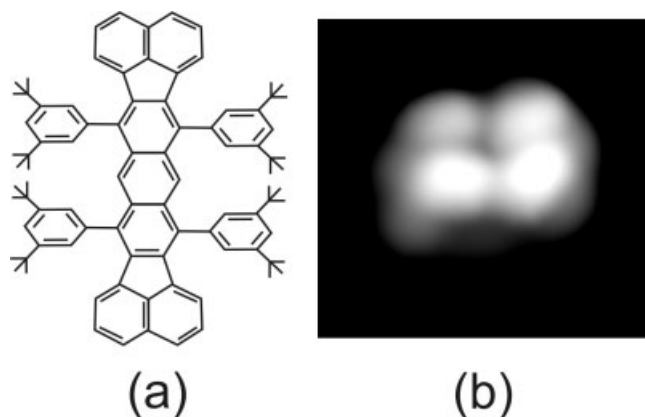


Fig. 3.2 (a) Chemical structure of a lander molecule; (b) STM image of a lander adsorbed on a Cu(111) surface. The spacer groups are in parallel conformation. Image size: 3.4 nm \times 3.4 nm.

integrity and to allow its manipulation with the STM tip. Moreover, the mainboard has a rigid aromatic platform projected beyond the last spacer, which is useful to study the electrical contact with a terrace or a nanostructure on a metal surface. The chemical structure of the molecule is shown in Fig. 3.2(a). As in the case of TBPP, the spacer groups of the lander are oriented perpendicular to the central board in the gas phase, but adapt themselves to the surface structure, showing different orientations [20–23]. On all the copper surfaces investigated, the molecule appears as four bright lobes in STM images (an example is shown in Fig. 3.2b). In fact the tunneling occurs primarily via the lateral TBP groups, while the central molecular wire contributes very little. Due to the symmetry of the σ bond between the TBP groups and the central wire, the spacer legs can rotate around the bond axis. When the molecule is adsorbed on a surface, due to steric hindrance the legs positioned on the same side of the central molecular wire always rotate in the same direction, resulting in two qualitatively different conformations. In one case, the two legs on each of the two sides of the central wire rotate in the same direction. This is called the parallel-leg conformation and it leads to a square shape of the molecule in STM images. In the second case, the legs on each of the two sides rotate in opposite directions. This is called the crossed-leg conformation. It leads to a rhombic shape in the STM images.

In order to improve the molecular conductance and allow efficient long-distance electron transport, new families of molecular landers with smaller HOMO–LUMO gaps [24] have been designed. These landers comprise a central oligo-perinaphthalene known for a vanishing gap with increasing oligomerization and also excellent chemical and structural stability. Further examples of landers have been designed to study 2D ribbons or plates and to investigate the tunnel transport in larger structures which can be required in single-molecule computing. Along these

lines, a series of hexabenzocoronene (HBC) [25] derivatives have been prepared. These molecules are being studied intensively at present because they show interesting properties such as high charge-carrier mobility along the π -stacked columns in the bulk mesogenic phases [26], stabilized triplet and quartet states, and ability to take up six electrons [27]. Submonolayer adsorption of these molecules on copper surfaces has been investigated recently [28] and manipulation experiments are being performed currently.

3.3

STM-Induced Manipulation

3.3.1

Manipulation of Single Atoms

The idea of using the tip of an STM to move adsorbates on a surface was applied for the first time to the positioning of atoms and small molecules by Don Eigler's group at IBM–Almaden in the early 1990s [29], followed by Gerhard Meyer at the FU Berlin [30]. To manipulate an atom it is first of all necessary to work at cryogenic temperatures, where the diffusion of adsorbates is strongly reduced and the mechanical stability of the STM is increased. The tip should be precisely positioned on a particle; then, the short-range forces between the tip and the particle can be used to manipulate it with atomic precision [31].

There are two basic manipulation techniques: the lateral manipulation method, where a single particle is moved on a surface without losing the contact to it; and the vertical manipulation method, where the particle is picked up and deposited at the desired location. For lateral manipulation at atomic scale, the interaction forces between tip and atom, i.e., van der Waals or chemical forces, are sufficient to move atoms, and no electric field or tunneling current has to be applied. For vertical manipulation, however, field and current effects are necessary. Vertical manipulation was first performed in Don Eigler's group [4], demonstrating that a Xe atom could be reversibly transferred between the tip and the surface by the application of a voltage pulse.

Lateral manipulation allows positioning of adsorbates with great precision and can be used to build nanostructures starting from single adsorbed particles [32], as can be seen in the example in Fig. 3.3. Additionally, by lateral manipulation it is possible to record in real time the tunnel signal during the manipulation process. This manipulation signal makes it possible to understand the details of the particle's movement and the interaction between the adsorbate and the tip. During manipulation, the tip height can be recorded as a function of the lateral movement. It is therefore possible to distinguish between different forms of lateral manipulation and to gain information about the interaction between the tip, the adsorbate, and the surface [33]. Typical manipulation signals are shown schematically in Fig. 3.4 and correspond to three different "manipulation modes." In the pulling mode (Fig. 3.4a), attractive forces, normally van der Waals interactions, force the adsor-

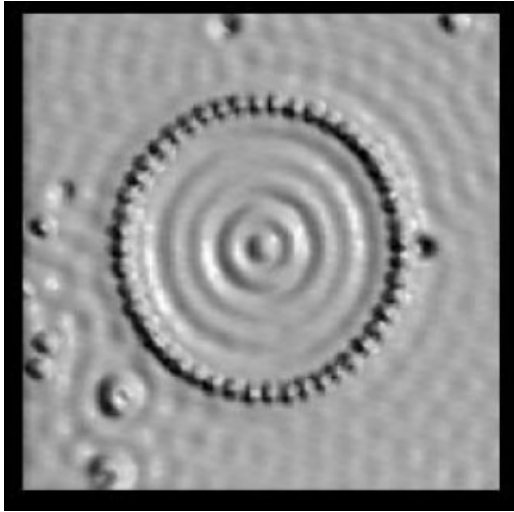


Fig. 3.3 Quantum corral built from 48 Fe adatoms on Cu(111) by means of lateral STM manipulation. Confined electron states give rise to standing wave patterns. Reprinted with permission from ref. 32.

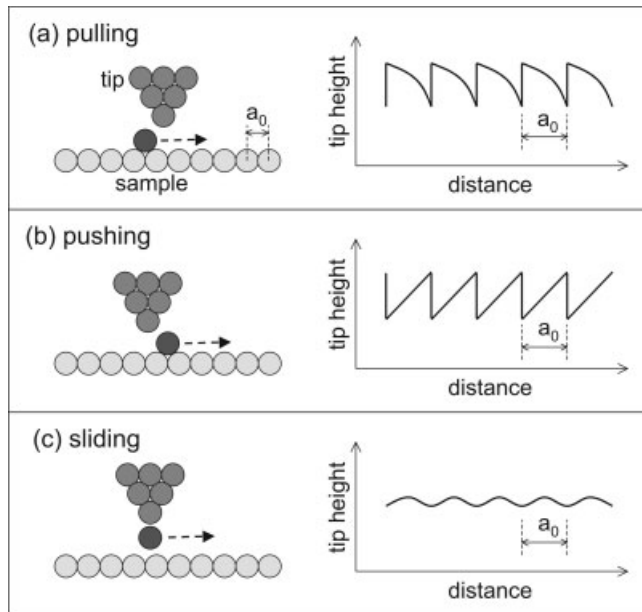


Fig. 3.4 Schematic representation of the different manipulation modes and their typical manipulation signals: (a) pulling; (b) pushing; (c) sliding.

bate to follow the motion of the tip. When the tip approaches the molecule, the tip height immediately rises because the adsorbate jumps under it. Then, when the tip moves away from the adsorption site of the molecule, the tip height drops with finite slope following the contour of the adsorbate until the particle jumps again to an adsorption position underneath the tip (and the tip again retracts). The periodicity of the signal corresponds to that of the substrate. In the pushing mode (Fig. 3.4b), repulsive interactions between the STM tip and the adsorbate force the molecule to jump away from the tip. In this case, the manipulation signal has the form of a sawtooth, but inverted with respect to the case of manipulation in pulling mode. The tip height rises with a finite slope when the tip is approaching the molecule. Then it suddenly drops when the molecule jumps away. Finally, the sliding mode (Fig. 3.4c) takes place when the tip–particle interaction is so strong that tip and the particle move together on the surface. In this case the adsorbate–tip distance remains nearly constant during the manipulation process. The manipulation signal is smooth and reflects the corrugation of the surface.

Recently, lateral manipulation of single atoms or small molecules was applied to the investigation of more complex problems. As shown in Fig. 3.5, Niluis et al. [34] have used lateral manipulation to study the development of the one-dimensional band structure in gold chains on a NiAl(110) surface. Heinrich et al. [35] have shown how CO molecules can be arranged by lateral manipulation to form “molecular cascades”, where the motion of one molecule causes the consequent motion of the others. Moreover, the combined application of different manipulation techniques has shown the possibility of inducing the steps of a complex chemical reaction with the STM tip. Specifically, the synthesis of biphenyl from iodobenzene on copper (Ullmann reaction) has been induced on a Cu(111) substrate using the

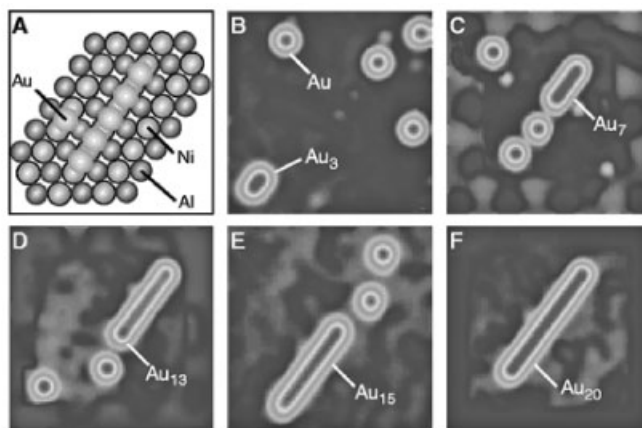


Fig. 3.5 (A) Structural model of an Au_5 chain and an Au atom on NiAl(110); (B–F) STM images showing intermediate stages of building an Au_{20} chain. Reprinted with permission from ref. 34.

STM tip [36]. Other examples of chemical reactions induced by the STM tip are the dissociation of pyridine and of benzene, proven by vibrational spectroscopy, performed by Lauhon and Ho [37], and the controlled chain polymerization reported by Okawa and Aono [38]. Very recently, Lastapis et al. [39] have shown that tunneling electrons from the STM tip can be used to control the molecular dynamics of individual biphenyl molecules adsorbed on a Si(100) surface.

3.3.2

Repositioning of Molecules at Room Temperature

The repositioning of particles with the STM-tip at room temperature on metal surfaces is especially difficult because of the high amount of diffusion of adsorbates and substrate atoms. At room temperature, metal surfaces, step-edges, and the tip can be considered “fluid” at the nanoscale. The high thermal energy requires a strong bond between an isolated molecule and the metal surface to prevent its diffusion. However, this bond must be not so strong that it hinders the movement of the molecule with the tip. It is therefore necessary to design special molecules if one wants to succeed in repositioning single molecules at room temperature on metal surfaces. The first molecular manipulation at room temperature was performed by Jung et al. at IBM-Zurich [40], who were able to move single TBPP molecules (already described in Section 3.2) on a Cu(100) surface. The controlled positioning of TBPP at room temperature was possible because of the special architecture of the molecule: the lateral spacer groups permit a sufficiently strong interaction of the molecule with the surface, preventing thermally activated diffusion, and, on the other hand, decouple the central part of the molecule from the substrate, allowing its controlled translation. The repositioning experiment shows that, after lateral approach and retraction of the STM tip, the repulsion between the tip and the molecule is responsible for the translation, suggesting that a pushing mechanism takes place. Simulations demonstrate that the tip produces a substantial adjustment of the molecular conformation and that flexure during the positioning process plays a crucial role. Moreover, different conformations of TBPP molecules on different substrates have been observed for the first time [18], leading to the conclusion that the changes in conformation occur predominantly by rotations around the π bonds to the spacer TBP groups.

The lateral manipulation of molecules strongly bonded to a semiconductor substrate has been achieved very recently at room temperature [41]. C_{60} was manipulated on Si(100). In this case the molecules are covalently bound to the substrate and the movement is achieved by bond breaking. Manipulation curves have been recorded and explained by a combined rotational and translational movement.

3.3.3

Manipulation in Constant Height Mode

As discussed in Section 3.3.2, special functionalized molecules can be repositioned successfully at room temperature. However, to obtain experimentally quantitative

information on the details of the process, the stability and the low noise level achievable at cryogenic temperatures are necessary. In the case of complex molecules, the tunneling signal recorded during lateral manipulation contains fundamental information for an understanding of the manipulation process itself and for a study of the internal mechanics of the molecule when it moves under the action of the tip. Molecular flexure and reorientation of the internal conformation play an important role, and one expects a different translational movement than in the case of atoms or simple molecules. However, due to the complicated structure of the molecules and to the increased diffusion barrier with decreasing temperature, the traditional lateral manipulation modes are in most cases unable to move large molecules like TBPP or lander. The main problem of the normal manipulation technique is that the feedback loop keeping the current constant remains active, so that the tip retracts when it approaches the molecule, giving rise to instabilities in the vertical position of the tip. To manipulate large, complex molecules successfully, it is necessary to move the tip on the molecule in “constant height mode.”

The idea is to keep the tip at a fixed distance from the surface when it is moved laterally across the molecule [42]. Such a technique makes the interaction between the tip and the molecule stronger and provides the molecule enough energy to overcome the diffusion barrier. To keep the tip height constant, the feedback loop is switched off. The current signal can then be recorded and contains information about the mechanism of the manipulation process.

In a lateral manipulation at constant height, a first scan in constant current mode over the molecule is necessary to determine the local angle of inclination of the surface. Then the feedback loop is switched off and the height of the tip decreased by a selected amount Δz , as shown schematically in Fig. 3.6. The tip then moves along the chosen manipulation path and both tip height and current signal are recorded. The tip height signal remains constant in this case, while the information on the manipulation process details is now carried by the tunneling current signal.

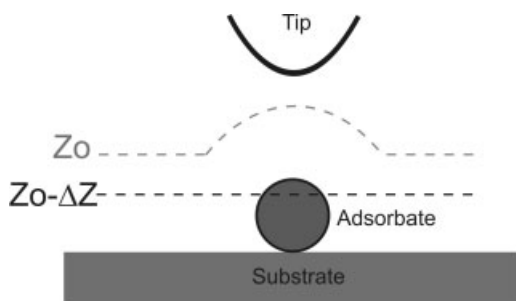


Fig. 3.6 Lateral manipulation in constant height mode. Z_0 is the initial tip-surface distance.

3.4

Mechanical Properties: Controlled Manipulation of Complex Molecules

An important prerequisite to the use of single molecules as active devices in molecular electronics is to understand and control their conformations when adsorbed on a surface. The molecular conformation determines to a large extent the conductance properties of a molecule and the possibility of performing conformational changes therefore opens very interesting perspectives. For these reasons, the interest of research is focusing on the manipulation and on the controlled positioning of large organic molecules with the aim of studying deformations and conformational changes. The tunneling signal recorded during a manipulation is a fundamental experimental tool to understand the internal mechanics of a molecule and permits the molecular deformations induced by the tip apex and by the surface atomic corrugation to be followed in real time.

By working at low temperature, we have applied the technique of lateral manipulation at constant height [42] to investigate the internal mechanics of a TBPP molecule moving on a Cu(100) surface, inducing motion and deformation of the molecule with the STM tip and monitoring it in real time [43]. This experiment represents the first step toward the realization of a molecular nanomachine, where a physical link between the molecule and the STM tip apex can be established by their direct electronic interaction. To extract from an STM image the exact conformation of an adsorbed molecule and to determine the details of its mechanics when moved on a surface by the STM tip, a suitable theoretical method is necessary. In the manipulation experiments with TBPP and lander molecules, a molecular mechanics (MM) optimization of the geometry of the molecule on the surface followed by elastic scattering quantum chemistry (ESQC) calculations of the STM images [44], developed by Joachim's group in Toulouse, was used.

A submonolayer amount of TBPP molecules was deposited onto a Cu(100) surface. An individual TBPP molecule is imaged as four bright lobes (Fig. 3.7a). The porphyrin ring is hardly visible. MM-ESQC calculations of the STM image show that each lobe corresponds to a leg oriented nearly perpendicular to the surface, at an angle of about 80° [43]. The height of the tip above the surface was reduced step by step and the manipulation was performed at the height at which the molecule starts to move. In order to manipulate the TBPP we have chosen a pushing mode performed on a single leg, as shown by the arrow in Fig. 3.7(a).

An example of a manipulation curve recorded during this manipulation experiment is presented in Fig. 3.7(b). The sequence reflects first of all the Cu(100) lattice periodicity. However, details in each period do not resemble the regular sawtooth signals recorded during STM manipulations of atoms and diatomic molecules (see Fig. 3.4). Magnified parts of the signal show a specific intra-period signature, peculiar to this specific type of manipulation.

Details of the intramolecular mechanics occurring during a manipulation sequence have been extracted from the manipulation curves by ESQC and molecular mechanics calculations, with the conclusion that the main contribution to the sig-

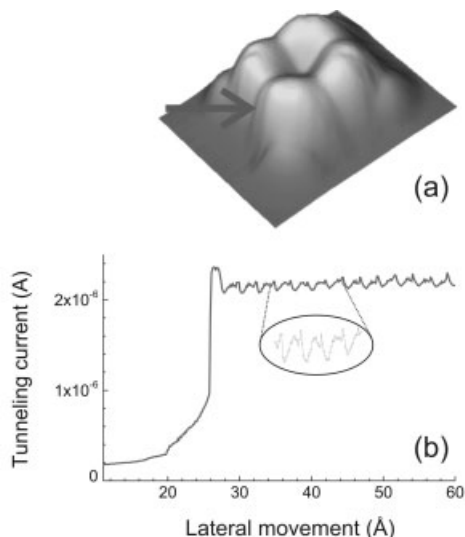


Fig. 3.7 (a) STM image (in 3D) of a single TBPP molecule adsorbed on Cu(100); (b) current curve recorded during the manipulation of a TBPP molecule on Cu(100). The inset shows details of the signal.

nal comes from the movement of the molecular group directly interacting with the tip apex. A contribution from lateral groups not directly in contact with the tip can be extracted. The recorded movements are very small, however, on the one hand showing the high grade of precision reached by this kind of experiment and, on the other hand opening the quest for new molecules where larger internal movements and deformations are possible.

Similarly to TBPP, the lander molecule presents internal degrees of freedom and shows different conformations when adsorbed on metallic surfaces. It is therefore possible to investigate its internal movements starting from the manipulation curves. An interesting example is given by the manipulation of landers on the stepped Cu(211) surface [33, 45]. Cu(211) is formed by (111) facets separated by (100) steps. The manipulation of landers perpendicularly to the intrinsic steps is quite difficult because of the high diffusion barrier and no regular manipulation curves can be observed. However, successful manipulations are possible in the direction parallel to the intrinsic steps even if the configuration of the spacer groups of the lander often changes. In the case considered here, the before the manipulation molecules show a crossed-leg conformation. After this manipulation, performed by pushing over a single rear spacer group, the molecule is still in its crossed-leg conformation, with the board parallel to the intrinsic steps of the Cu(211), but the orientations of the legs pair is inverted. An overview image of lander molecules on Cu(211) is shown in Fig. 3.8(a).

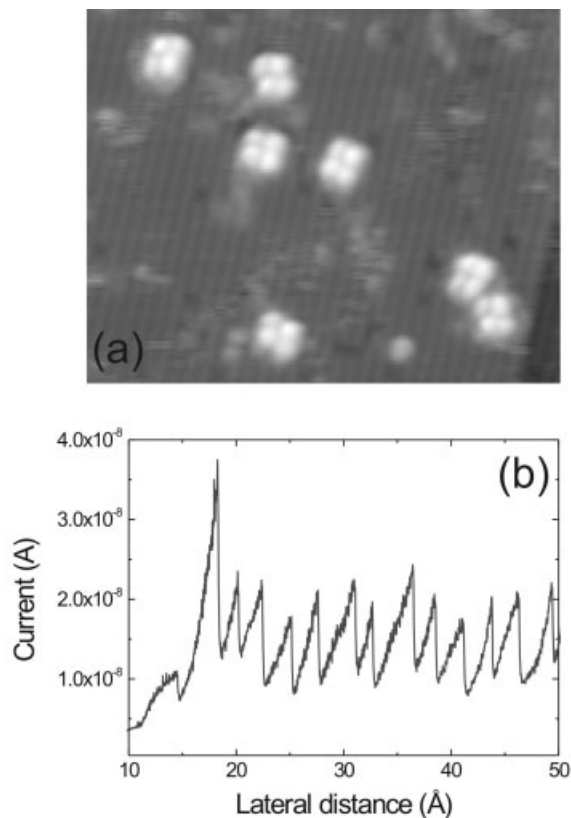


Fig. 3.8 (a) Overview STM image of lander molecules on Cu(211); (b) example of a manipulation curve of a lander on Cu(211) in the direction parallel to the intrinsic steps.

In the investigation described, we have attempted over 303 manipulations of single lander molecules. The molecules were manipulated 219 times along an intrinsic Cu(211) step. Of these manipulations 67% were successful, while in the remaining cases the molecule was either destroyed (4%), or jumped to the tip (5%), or did not move at all (24%). Notably, the rate of success of a manipulation experiment is limited by the form and composition of the tip apex and is therefore never completely controllable.

In the example of a manipulation curve in the direction parallel to the intrinsic steps shown in Fig. 3.8(b), the curve has a quite regular sawtooth form. However, as shown by MM-ESQC simulations, it contains information on the mechanical movements of parts of the molecule that do not interact directly with the tip apex during the manipulation sequence [45]. This is because the intramolecular deformation induced by the tip can open other tunneling paths, which are not directly located on the part of the molecule in close contact with the tip apex. Specif-

ically, the manipulation signal is sensitive to the movements of the central board of the molecule, even if the tip pushes the legs. The mechanical deformations of the central board, which cannot be imaged by STM in standard conditions, dominate the manipulation signal.

The manipulation of lander molecules along the step edges of Cu(211) can be used to align three lander molecules, forming molecular chains. This can be done both at natural steps and at restructured steps (which will be described in Section 3.6). In the case of lateral manipulation along the step edges, the molecules always remain in the same conformation, with the board at the step edge and oriented parallel to the step. Therefore the step edge acts as a rail on which the lander molecules are kept oriented and positioned along a straight line. This guidance guarantees atomic precision in orientation and position (perpendicular to the direction of manipulation) during an STM manipulation of a molecule. In Fig. 3.9 a chain of three landers built by lateral manipulation is shown. The distance between the molecules is 20 Å (measured from center to center), matching the van der Waals bonding distance. This is the closest distance that can be achieved by lateral manipulation. If a molecule is tentatively pushed closer to the next one, both molecules move simultaneously.

Recently, we have investigated a nanoscale molecular barrow [46, 47]. This molecule integrates two wheels, legs, and handles along a polyaromatic platform. The investigation of its adsorption on Cu(100) shows, however, that the interaction with

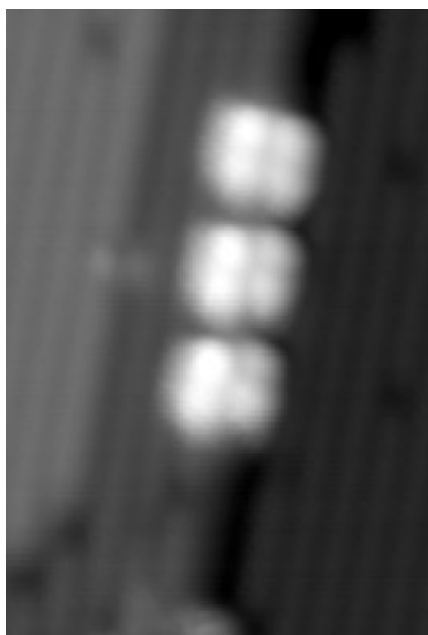


Fig. 3.9 Chain formed by three lander molecules manipulated on Cu(211) along a step.

the metallic substrate is too strong to allow the lateral repositioning of the molecule and the rotation of the wheels.

3.5

Inducing Conformational Changes: A Route to Molecular Switching

Conformational changes induced in a complex molecule by manipulation can be used for controlled modification of its electronic properties. An example is the principle of a conformational molecular switch realized by manipulating a TBPP molecule on a Cu(211) surface [48]. To demonstrate the principle of such a switch, we have investigated quantitatively the interaction between the tip apex and a spacer group of the molecule during a vertical manipulation sequence. In particular, we have measured the current passing through this rotating group in real time during its conformational change, demonstrating that the tunneling current depends strongly on the extent of the rotation.

TBPP molecules on Cu(211) normally show eight lobes, (Fig. 3.10a), corresponding to the four spacer groups oriented nearly flat on the surface [48]. In a few cases, a single brighter lobe appears among the double lobes, indicating that one spacer group is rotated nearly perpendicular to the plane of the substrate (Fig. 3.10b). MM-ESQC calculations confirm that the spacer groups form an angle of 10° relative to the surface when they are flat on the surface, whereas otherwise they are rotated by 55° .

Manipulation techniques have been used to reversibly modify the molecular conformation. The rotation of a single leg from the rotated to the flat conformation, i.e., from the “on” to the “off” state of the switch, is possible by both lateral and vertical manipulation methods, without however moving the molecule from its original adsorption position. To demonstrate the principle of the molecular switch, we have measured the current passing through a single leg in real time during its

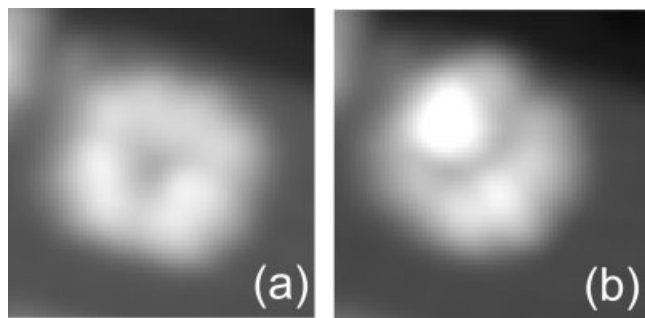


Fig. 3.10 (a) STM image of a TBPP molecule deposited on Cu(211) lying flat on the surface; (b) STM image of a TBPP molecule on Cu(211) showing one leg rotated out of the plane of the porphyrin.

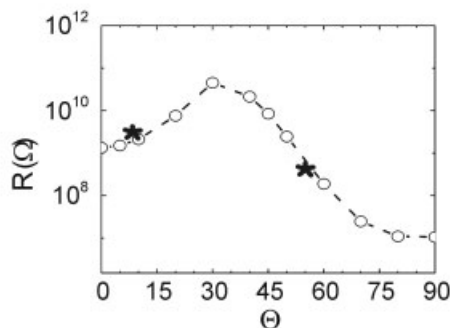


Fig. 3.11 Calculated variation of the tunnel resistance (R) for the molecular switch given by the rotation of a leg of a TBPP molecule vs. the rotational angle Θ of one leg, as obtained by ESQC. The tip apex is kept fixed at a distance $z_0 = 7 \text{ \AA}$ from the surface. The stars indicate the two experimental points.

rotation. We are able to demonstrate in this way that the tunneling current through one leg depends strongly on the extent of its conformational change. Specifically, a factor of nearly 10 in current is measured between the “on” and “off” configurations. ESQC calculations of the tunnel resistance given by the rotation of a leg between 0 and 90° have been performed (Fig. 3.11); the two experimental points corresponding to rotational angles of 10° and 55° are well reproduced by the calculations.

The energy required to operate such a switch, i.e., to manipulate a leg between the “on” and the “off” configurations cannot be determined by STM measurements. However, a very recent noncontact atomic force microscopy experiment [49] has shown that the energy required to perform the rotation of the leg requires an energy of less than $(10\text{--}21) \times 100 \text{ J}$, which is four orders of magnitude lower than state-of-the-art field-effect transistors.

3.6 The Role of the Substrate

The strong interaction between a large polyaromatic molecule and the metallic substrate has the important consequence that functionalities and conformations of molecules in vacuum or in solution cannot be transferred a priori to the situation of a molecule adsorbed on a surface. The interaction with the substrate compresses the molecule on the surface, so that some conformations not observed in vacuum or in solution are stabilized. Moreover, the strong interaction between the aromatic board and the metal induces important distortions such as bending of the board–spacer bonds or rippling of the polyaromatic board when the molecule is adsorbed on a step edge [50], greatly modifying the molecular conductance.

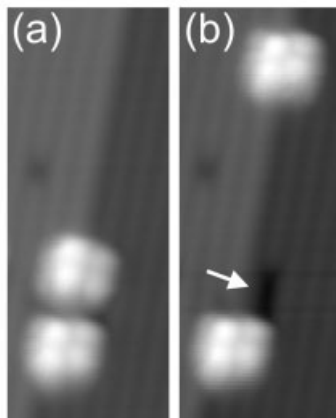


Fig. 3.12 Lander on Cu(211) after evaporation, keeping the substrate at 330 K. Between (a) and (b) a molecule has been manipulated along the step edge, revealing the restructuring of the underlying surface. The arrow shows the restructured step edge.

However, it is important to note that the molecule–substrate interaction is a dual process that not only perturbs the conformation of a molecule, and therefore its electronic properties, but also has an impact on the substrate, leading in some cases to the modification of its structure. It has been shown recently that the substrates cannot be considered as static templates and that molecules can induce surface restructuring such as interfacial roughening, vacancy trapping, and molding. To relax the distortions of the molecule and reduce the board–metal distances, a molecule can block diffusing vacancies, creating ditches, or conversely it can trap diffusing atoms, forming nanostructures.

The first evidence of the anchoring of a molecule by modification of the substrate has been reported for hexa(*tert*-butyl)decacyclene (HtBDC), associated with a trough in the Cu(110) surface underneath [51]. The HtBDC molecule has some properties similar to those of the lander; for example, it has a large rigid polyaromatic platform lifted by six *tert*-butyl spacers.

A similar effect has been observed for lander molecules on Cu(211) [22]. If deposited on a surface kept at room temperature, the lander molecules diffuse and are found at terrace steps. The board of the molecule is always aligned with the step edge, whereas the internal conformation may again differ between crossed legs and parallel legs. When the molecules are moved away from their adsorption site by lateral manipulation, ditches on the lower side of the step edge become visible, showing a surface restructuring induced by the lander molecules, as shown in Fig. 3.12. The trapping of vacancies by molecular lander-type molecules therefore seems to be a very general phenomenon, which is probably common to most molecules comprising unsaturated chemical groups.

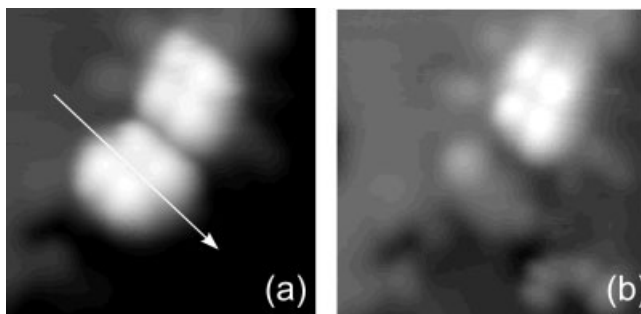


Fig. 3.13 Manipulation sequence of the lander molecules from a step edge on Cu(110). The arrow in (a) shows the manipulation direction. The nanowire formed under the molecule is visible in (b).

On the other hand, landers can also behave as molecular molds to stabilize metallic patterns on a substrate. The adsorption of lander molecules on Cu(110) has been studied by Rosei et al. [21], who found that the molecule acts as a template, restructuring the surface at the step edges and forming metallic nanostructures that are adapted to the dimensions of the molecule. Upon submonolayer deposition of the lander at room temperature, the molecules diffuse toward the steps. If one then removes a molecule from the step edge by pushing it away with the STM tip, an underlying restructuring induced by the molecule is revealed (Fig. 3.13). The nanostructure so obtained forms a copper nanowire with a width of two atomic copper rows and a length of about seven copper atoms. Investigations of this system by LT-STM [52] reveal details of the molecular conformations and enable controlled manipulation of the molecule along the nanostructure. A similar effect was also observed for other molecules of the lander series, such as the violet lander [53] or the reactive lander [54].

Specific information on the electronic interaction between the board of a lander-type molecule and the metallic substrate on Cu(111) has been obtained by studying the standing wave patterns produced by the surface-state electrons when scattered by the molecules [55]. The experiment demonstrates that the central molecular wire, although decoupled from the surface by spacer groups and not visible in STM topographic images, is the main one responsible for the scattering of surface-state electrons. By comparing three different, suitably modified lander-type molecules, the dominant role of the aromatic π system in molecule–substrate interaction is revealed. The analysis of electronic standing wave patterns produced by molecules on metallic surfaces show up as new and promising method to characterize, with a submolecular resolution, the electronic interactions of a complex molecule with a metallic surface.

3.7

Electronic Properties: Investigation of the Molecule–Metal Contact

The characterization of the electronic contact between a molecular unit and a metallic electrode is one of the central problems for the development of molecular electronics. An electronic contact is defined unambiguously when the edges of the electrodes are atomically ordered and clean, and when the geometry and conformation of the contacted molecule are under control at the atomic scale. It has been shown theoretically that the conductance of individual molecules connected to a metal electrode is very sensitive to the presence of impurities adsorbed near the same electrode [56]. Moreover, the electronic properties of atomic-scale electrodes are modified by even a single atom of impurity [57].

Two different experiments have been performed recently to study with atomic precision the contact between a molecular wire and a metallic nanoelectrode [58]. In the first, the molecular wire part of a lander molecule lying on a Cu(111) terrace was contacted by lateral manipulation to a monoatomic step edge. In the second case, on Cu(110), a lander that had molded its nanowire was manipulated a few steps along the structure to reach the final contact position. In both cases, the electronic contact was characterized by the increased tunneling current at the contact location.

To investigate the contact between a molecular wire and a metallic electrode, we have first contacted the wire part of a lander to a step edge of Cu(111) [59]. A stable and extremely clean monoatomic step (0.21 nm in height) was obtained by a controlled crash of the tip into the surface. To bring the molecular wire in contact with the step, a lander lying flat was manipulated laterally by the STM tip in constant height mode to reach the position shown schematically in Fig. 3.14(a).

After the contact was made, an increased tunneling signal corresponding to the contact position could be observed. The STM-ESQC extraction of the molecular conformation from the experimental image confirmed that the terminal naphtha-

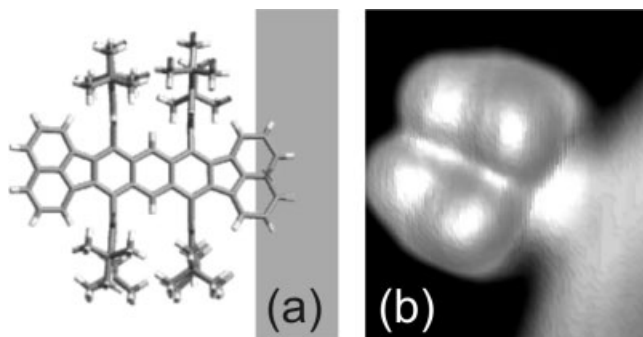


Fig. 3.14 Contacting a lander to a step edge on Cu(111): (a) schematic view; (b) STM image in 3D.

lene group of the wire was on top of the step edge and electronically coupled to the upper terrace. As a consequence, this naphthalene end group was now visible in the STM image of the step edge (Fig. 3.14b).

The apparent height of the contact position in the STM images is related to the electronic interaction between the naphthalene end group of the molecule and the copper atoms of the upper terrace, and also depends on the geometry of the system. It varies as a function of both lateral distance between the naphthalene end group and the step edge and vertical distance between this end group and the upper terrace. At the experimental contact position, a calculated value of the contact maximum of 13 pm (in agreement with an experimental value of about 15 pm) was obtained.

Another way to characterize the contact of the molecular wire end with the Cu(111) step edge is to investigate its effect on the standing wave patterns formed by the surface-state electrons when scattered by adsorbates and steps. When a lander is contacted with its board perpendicular to the step edge, a striking modification of the parallel standing wave patterns due to the step is observed on the upper terrace (Fig. 3.15). Compared with case of the clean step edge, the amplitude of the wave is reduced at the naphthalene contact location. This effect extends a few tens of nanometers away from the contact in a characteristic triangular shape. To reproduce the pattern caused by the contacted lander, we used the scattering formalism of Heller et al. [60]. A simple arrangement of scatterers was used to model the contact and confirms that the observed perturbation of the standing wave patterns on the upper terrace is caused by the naphthalene end group of the molecular wire. The good agreement between STM experiment and numerical simulation

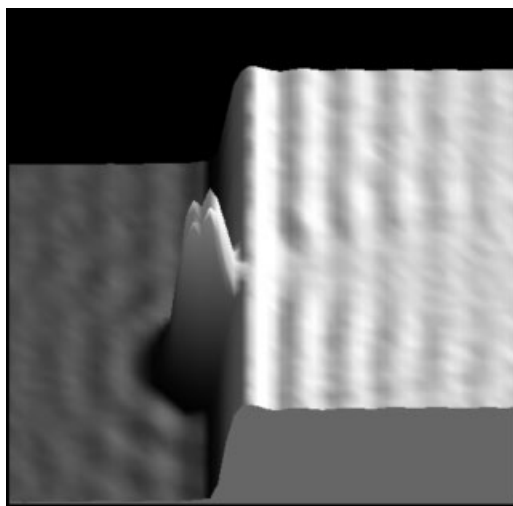


Fig. 3.15 3D representation of the standing wave patterns produced on Cu(111) by a lander contacted to a monoatomic step edge.

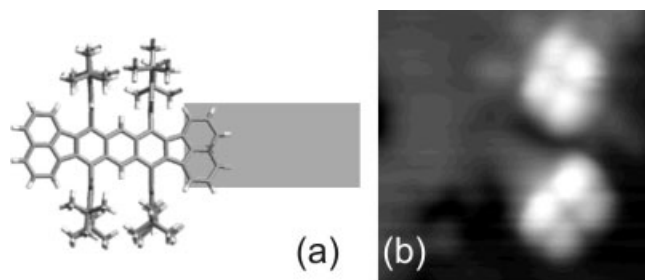


Fig. 3.16 Contacting a lander to a nanowire on Cu(110): (a) schematic view; (b) STM image.

shows that the molecular π orbitals of the wire interact with the upper terrace surface state through their coupling via the naphthalene end.

The possibility of contacting the molecular wire part of a lander to a metallic nanowire, fitting exactly the dimensions of the molecule, comes from the ability, already described, of the lander to behave like molecular molds stabilizing metallic patterns on the substrate [21]. This ability can be used to investigate the electronic contact between the molecular wire part and the metallic nanowire [52], as shown schematically in Fig. 3.16(a).

On Cu(110), we have already seen (Section 3.6) that the molecule restructures the substrate, forming a nanowire two atoms wide under the molecular wire board. In this case the central board is in a good position to interact with the metallic copper wire underneath. To observe the small contribution to the tunneling signal due to the contacting board, one should choose a conformation of the molecule where the legs contribute as little as possible towards the STM tunneling current. This means that the legs have to be oriented to the opposite end of the central wire in order to allow the tip access to this molecular wire end.

This conformation has been obtained by moving a lander step by step to the end of its copper nanowire, by manipulating the whole molecule to the end of the wire with the STM tip. STM images of the lander have been taken at each manipulation step. When the molecule reaches the end of the wire (Fig. 3.16b) the contact position becomes visible in the STM image. In this case the legs have a favorable conformation, so that the tip has access to the naphthalene end group of the central wire. The contacted end group of the molecular wire is clearly visible and has an apparent relative height of about 20 pm. Moreover, weaker shoulders are visible in the STM images for intermediate positions. ESQC calculations confirm that an electronic interaction between the board and the metallic Cu atomic wire underneath takes place, making the central molecular wire of the lander visible in the STM images.

The contact experiments reported demonstrate that LT-STM is a fundamental experimental technique for bringing a molecule into contact with a metallic nanoelectrode and for characterizing the electronic contact by means of the increased tunneling signal at the contact position. Moreover, on surfaces like Cu(111), the

analysis of the standing wave patterns of the surface-state electrons has made it possible to gain further information about the geometry of the contact itself.

3.8 Perspectives

The remarkable growth of fundamental studies connected with molecular electronics in the last few years is mainly due to the recent advances in chemical synthesis and to the possibilities arising from surface functionalization and bonding of molecules at metallic nanostructures. The use of scanning tunneling microscopy is of fundamental importance in this respect, as it allows both measurements and manipulation on a single molecule. Recent investigations such as those described in this chapter have allowed understanding some important behaviors of single molecules concerning their electronic and mechanical properties. At the present state-of-the-art, it is nearly possible to perform measurements inside a junction contacting exactly one molecule. When this fundamental milestone is achieved, there will be new conceptual and experimental challenges for us to confront on the way to the technological realization of molecular devices. These challenges concern first of all the architecture of molecules and therefore a combination of chemistry and theoretical modeling. From a more applied point of view, interconnections, nanocommunication schemes, and finally nanofabrication and nanopackaging techniques will be required.

Acknowledgements

The experiments described have been possible thanks to the collaboration with Gerhard Meyer (at present at IBM–Zürich), Leo Gross, Leonhard Grill, Micol Alemani, and Karl-Heinz Rieder at the FU-Berlin. The fruitful collaboration with the CEMES-CNRS “NanoSciences Group” in Toulouse is acknowledged, where André Gourdon has synthesized the molecules and Christian Joachim, together with Hao Tang, Ping Jiang, Sladjana Stojkovic, and Xavier Bouju, has performed the theoretical calculations.

Financial support from the EU-TMR network “AMMIST” and the Volkswagen-stiftung project “Single Molecule Synthesis” is acknowledged.

References

- 1 AVIRAM, A.; RATNER, M. *Chem. Phys. Lett.*, **1974**, *29*, 277–283.
- 2 PEREPICHKA, D. F.; BRYCE, M. R.; PEARSON, C.; PETTY, M. C.; MCINNES, E. J. L.; ZHAO, J. P. *Angew. Chem. Int. Ed.*, **2003**, *42*, 4636–4639.
- 3 JOACHIM, C.; GIMZEWSKI, J. K.; AVIRAM, A. *Nature*, **2000**, *408*, 541–548.
- 4 EIGLER, D. M.; LUTZ, C. P.; RUDGE, W. E. *Nature*, **1991**, *352*, 600–603.
- 5 JOACHIM, C.; GIMZEWSKI, J. K.;

- SCHLITTLER, R. R.; CHAVY, C. *Phys. Rev. Lett.*, **1995**, *74*, 2102–2105.
- 6 JOACHIM, C.; GIMZEWSKI, J. K. *Chem. Phys. Lett.*, **1997**, *265*, 353–357.
- 7 TANS, S. J.; DEVORET, M. H.; GROENEFELD, R. J. A.; DEKKER, C. *Nature*, **1998**, *394*, 761–764.
- 8 COLLINS, P. G.; ARNOLD, M. A.; AVOURIS, P. *Science*, **2001**, *292*, 706–709.
- 9 MARTEL, R.; SCHMIDT, T.; SHEA, H. R.; HERTEL, T.; AVOURIS, P. *Appl. Phys. Lett.*, **1998**, *73*, 2447–2449.
- 10 TANS, S. J.; VERSCHUEREN, A. R. M.; DEKKER, C. *Nature*, **1998**, *393*, 49–52.
- 11 REED, M. A.; ZHOU, C.; MULLER, C. J.; BURGIN, T. P.; TOUR, J. M. *Science*, **1997**, *278*, 252–254.
- 12 KERGUERIS, C.; BOURGOIN, J.-P.; PALACIN, S.; ESTEVE, D.; URBINA, C.; MAGOGA, M.; JOACHIM, C. *Phys. Rev. B*, **1999**, *59*, 12 505–12 513.
- 13 SMIT, R. M. H.; NOAT, Y.; UNTIEDT, C.; LANG, N. D.; v. HERMERT, M. C.; v. RUITENBEEK, J. M. *Nature*, **2002**, *419*, 906–909.
- 14 REICHERT, J.; OCHS, R.; BECKMANN, D.; WEBER, H. B.; MAYOR, M.; v. LÖHNESEN, H. *Phys. Rev. Lett.*, **2002**, *88*, 176 804, 1–4.
- 15 FORREST, S. R. *Chem. Rev.*, **1997**, *97*, 1793–1896.
- 16 BARLOW, S. M.; RAVAL, R. *Surf. Sci. Rep.*, **2003**, *50*, 201–341.
- 17 MORESCO, F.; MEYER, G.; RIEDER, K.-H.; PING, J.; TANG, H.; JOACHIM, C. *Surf. Sci.*, **2002**, *499*, 94–102.
- 18 JUNG, T. A.; SCHLITTLER, R. R.; GIMZEWSKI, J. K. *Nature*, **1997**, *386*, 696–698.
- 19 GOURDON, A. *Eur. J. Org. Chem.*, **1998**, 2797–2801.
- 20 KUNTZE, J.; BERNDT, R.; JIANG, P.; TANG, H.; GOURDON, A.; JOACHIM, C. *Phys. Rev. B*, **2002**, *65*, 233405, 1–4.
- 21 ROSEI, F.; SCHUNACK, M.; JIANG, P.; GOURDON, A.; LAEGSGAARD, E.; STENSGAARD, I.; JOACHIM, C.; BESENBACHER, F. *Science*, **2002**, *296*, 328–331.
- 22 GROSS, L.; MORESCO, F.; ALEMANI, M.; TANG, H.; GOURDON, A.; JOACHIM, C.; RIEDER, K.-H. *Chem. Phys. Lett.*, **2003**, *371*, 750–756.
- 23 SCHUNACK, M.; ROSEI, F.; NAITOH, Y.; JIANG, P.; GOURDON, A.; LAEGSGAARD, E.; STENSGAARD, I.; JOACHIM, C.; BESENBACHER, F. *J. Chem. Phys.*, **2002**, *117*, 6259–6265.
- 24 GHOSH, S. C.; ZHU, X.; SECCHI, A.; SADHUKHAN, S. K.; GIRDHAR, N. K.; GOURDON, A. *Ann. N.Y. Acad. Sci.*, **2003**, *1000*, 82–93.
- 25 SADHUKHAN, S. K.; C. VIALA; GOURDON, A. *Synthesis*, **2003**, *10*, 1521–1525.
- 26 FISCHBACH, I.; PAKULA, T.; MINKIN, P.; FECHTENKOTTER, A.; MULLEN, K.; SPIESS, H. W.; SAALWACHTER, K. *J. Phys. Chem. B*, **2002**, *106*, 6408.
- 27 GHERGHEL, L.; BRAND, J. D.; BAUMGARTEN, M.; MULLEN, K. *J. Am. Chem. Soc.*, **1999**, *121*, 8104–8105.
- 28 GROSS, L.; MORESCO, F.; RUFFIEUX, P.; GOURDON, A.; JOACHIM, C.; RIEDER, K.-H. *Phys. Rev. B*, **2005**, *71*, 165 428–1–7.
- 29 EIGLER, D. M.; SCHWEIZER, E. K. *Nature*, **1990**, *344*, 524–526.
- 30 MEYER, G.; NEU, B.; RIEDER, K.-H. *Appl. Phys. A*, **1995**, *60*, 343–345.
- 31 AVOURIS, P. *Acc. Chem. Res.*, **1995**, *28*, 95–102.
- 32 CROMMIE, M. F.; LUTZ, C. P.; EIGLER, D. M. *Science*, **1993**, *262*, 218–220.
- 33 BARTELS, L.; MEYER, G.; RIEDER, K.-H. *Phys. Rev. Lett.*, **1997**, *79*, 697–700.
- 34 NILIUS, N.; WALLIS, T. M.; HO, W. *Science*, **2002**, *297*, 1853–1856.
- 35 HEINRICH, A. J.; LUTZ, C. P.; GUPTA, J. A.; EIGLER, D. M. *Science*, **2002**, *298*, 1381–1387.
- 36 HLA, S. W.; BARTELS, L.; MEYER, G.; RIEDER, K.-H. *Phys. Rev. Lett.*, **2000**, *85*, 2777–2780.
- 37 LAUHON, L. J.; HO, W. *J. Phys. Chem.*, **2000**, *104*, 2463–2467.
- 38 OKAWA, Y.; AONO, M. *Nature*, **2001**, *409*, 683–684.
- 39 LASTAPIS, M.; MARTIN, M.; RIEDEL, D.; HELLNER, L.; COMTET, G.; DUJARDIN, G. *Science*, **2005**, *308*, 1000–1003.
- 40 JUNG, T. A.; SCHLITTLER, R. R.; GIMZEWSKI, J. K.; TANG, H.; JOACHIM, C. *Science*, **1996**, *271*, 181–184.
- 41 KEELING, D. L.; HUMPHRY, M. J.; FAWCETT, R. H. J.; BETON, P. H.; HOBBS, C.; KANTOROVICH, L. *Phys. Rev. Lett.*, **2005**, *94*, 146104, 1–4.

- 42 MORESCO, F.; MEYER, G.; RIEDER, K.-H.; TANG, H.; GOURDON, A.; JOACHIM, C. *Appl. Phys. Lett.*, **2001**, *78*, 306–308.
- 43 MORESCO, F.; MEYER, G.; RIEDER, K.-H.; TANG, H.; GOURDON, A.; JOACHIM, C. *Phys. Rev. Lett.*, **2001**, *87*, 088302–1–4.
- 44 SAUTET, P.; JOACHIM, C. *Chem. Phys. Lett.*, **1991**, *185*, 23–30.
- 45 ALEMANI, M.; GROSS, L.; MORESCO, F.; RIEDER, K.-H.; WANG, C.; BOUJU, X.; GOURDON, A.; JOACHIM, C. *Chem. Phys. Lett.*, **2005**, *402*, 180–185.
- 46 JOACHIM, C.; TANG, H.; MORESCO, F.; RAPENNE, G.; MEYER, G. *Nanotechnology*, **2002**, *13*, 330–335.
- 47 GRILL, L.; RIEDER, K.-H.; MORESCO, F.; IMENEZ-BUENO, G.; WANG, C.; RAPENNE, G.; JOACHIM, C. *Surf. Sci.*, **2005**, *584*, L153–L158.
- 48 MORESCO, F.; MEYER, G.; RIEDER, K.-H.; TANG, H.; GOURDON, A.; JOACHIM, C. *Phys. Rev. Lett.*, **2001**, *86*, 672–675.
- 49 LOPPACHER, C.; GUGGISBERG, M.; PFEIFFER, O.; MEYER, E.; BAMMERLIN, M.; LÜTHI, R.; SCHLITZER, R.; GIMZEWSKI, J. K.; TANG, H.; JOACHIM, C. *Phys. Rev. Lett.*, **2003**, *90*, 066107–1–4.
- 50 ZAMBELLI, T.; TANG, H.; LAGOUTE, J.; GAUTHIER, S.; GOURDON, A.; JOACHIM, C. *Chem. Phys. Lett.*, **2001**, *348*, 1–6.
- 51 SCHUNACK, M.; PETERSEN, L.; KUHNLE, A.; LAEGSGAARD, E.; STENSGAARD, I.; JOHANNSEN, I.; BESENBACHER, F. *Phys. Rev. Lett.*, **2001**, *86*, 456–459.
- 52 GRILL, L.; MORESCO, F.; JIANG, P.; JOACHIM, C.; GOURDON, A.; RIEDER, K.-H. *Phys. Rev. B*, **2004**, *69*, 035416, 1–7.
- 53 OTERO, R.; ROSEI, F.; NAITOH, Y.; JIANG, P.; THOSTRUP, P.; GOURDON, A.; LAEGSGAARD, E.; STENSGAARD, I.; JOACHIM, C.; BESENBACHER, F. *Nano Lett.*, **2004**, *4*, 75–78.
- 54 GRILL, L.; MORESCO, F.; RIEDER, K.-H.; STOJKOVIC, S.; GOURDON, A.; JOACHIM, C. *Nano Lett.*, **2005**, *5*, 859–863.
- 55 GROSS, L.; MORESCO, F.; SAVIO, L.; GOURDON, A.; JOACHIM, C.; RIEDER, K.-H. *Phys. Rev. Lett.*, **2004**, *93*, 056103–1–4.
- 56 LANG, N. D.; AVOURIS, P. *Nano Lett.*, **2002**, *2*, 1047–1050.
- 57 MEHREZ, H.; WLASENKO, A.; LARADE, B.; TAYLOR, J.; GRÜTTER, P.; GUO, H. *Phys. Rev. B*, **2002**, *65*, 195419–1–13.
- 58 MORESCO, F. *Phys. Rep.*, **2004**, *399*, 175–225.
- 59 MORESCO, F.; GROSS, L.; ALEMANI, M.; RIEDER, K.-H.; TANG, H.; GOURDON, A.; JOACHIM, C. *Phys. Rev. Lett.*, **2003**, *91*, 036601, 1–4.
- 60 HELLER, E. J.; CROMMIE, M. F.; LUTZ, C. P.; EIGLER, D. M. *Nature*, **1994**, *369*, 464–466.

4 Inelastic Electron Tunneling Microscopy and Spectroscopy of Single Molecules by STM

Jose Ignacio Pascual and Nicolás Lorente

4.1 Introduction

The exceptional ability of scanning tunneling microscopy (STM) to resolve structural and electronic information on surfaces and adsorbates with atomic resolution has been greatly reinforced by the demonstration of its ability to measure molecular vibrations also [1]. These carry the chemical information, which STM had been previously lacking. In combination with its very high spatial resolution STM can measure atom-specific information, resolve local aspects of adsorption as the effect of intermolecular interaction or site-dependent phenomena, and when inducing single-molecule reactions, characterize the nature of reaction products.

The use of STM as a tool to excite and measure vibrations was soon an objective after the first development of the STM. In 1985, Binnig and coworkers [2] proposed a strategy to obtain the vibrational structure of a single molecule based on a traditional vibrational spectroscopy technique called inelastic electron tunneling spectroscopy (IETS) [3]. IETS had been developed in 1966, when Jacklevic and Lambe observed that tunneling electrons were able to excite vibrational modes of a thin layer of molecules buried between two metallic electrodes and an oxide layer [4]. The oxide represents a tunneling barrier for electronic transport between the metallic electrodes. The excitation of vibrations was a consequence of inelastic scattering processes taking place in the tunnel junction. Such inelastic processes induced a slight increase in the tunnel conductance due to the opening of those additional transport channels mediated by the inelastic scattering processes. Thus, the detection of the energy threshold to excite a vibrational mode was used to investigate the vibrational structure of the buried molecular layer.

The configuration of an STM junction is similar. Here, the oxide layer is substituted by the tip-sample vacuum gap. The advantages are that the molecules under investigation are adsorbed on an atomically clean metal surface with a well-defined geometry, and can be investigated without interaction with any other object. The adsorption geometry and orientation of the adsorbate can be well known. Thus STM works under the same controlled conditions as other classical surface chemistry techniques, but with a large gain regarding the spatial resolution of the adsorbate's vibrational structure.

However, there are important differences between inelastic electron tunneling spectroscopy with STM (IETS–STM) and traditional IETS, basically related to the nature of the excitation mechanism. In the STM configuration the majority of the electron current tunnels through the adsorbate itself, therefore having a strong component of molecule-derived resonances [5]. This results in a local inelastic scattering mechanism mediated by the molecular electronic configuration. In IETS, however, the tunneling current is less focused on the adsorbate. Therefore, the excitation mechanism is predominantly a nonlocal mechanism like, for example, dipolar interaction between electron and molecule.

Since the first clear demonstration of IETS–STM [1] several theoretical and experimental works have concentrated on unraveling the peculiarities of inelastic tunneling spectroscopy, such as the nature of the excitation mechanisms and the sensitivity of detection. Besides, the investigation of inelastic processes have revealed valuable information about several molecular-scale elementary processes such as intramolecular energy transfer via intermode coupling [6–8], conformational changes [9, 10] or fundamental pathways of chemical reactions [8, 11–13]. Reference 14 is an interesting recent review of the progress of IETS–STM.

Here, we present a combined experimental and theoretical overview of the fundamentals of single-molecule vibrational spectroscopy, in order to draw an overall picture of resonant mechanisms of excitation and detection of the inelastic signal.

4.1.1

Working Principle

Single-molecule vibrational spectroscopy uses a measurable change in conductance across the threshold of a vibrational excitation of an adsorbed molecule to identify the onset of inelastic scattering processes. The tip of an STM is placed on top of a molecule and the voltage is ramped up. When the electrons' energy matches a quantum of vibration, the conductance changes abruptly: the STM has detected the mode frequency of an adsorbed molecule.

The resolution of these inelastic effects depends on two fundamental processes: excitation and detection. These are not equivalent and both have to be treated to understand the origin of active modes in the spectra [15]. The excitation is based on inelastic scattering processes, thus connecting initial and final states with different energies. Instead of an excitation cross-section for the scattering processes we usually refer to the fraction of tunneling current, which follows the inelastic channel (or the inelastic fraction, f_i). As we shall see later in this chapter, this inelastic fraction is intrinsically connected with the nature and alignment of electronic resonances associated with the molecule/surface system. Therefore, it is very sensitive to the chemical interaction between the adsorbate and the surface.

The detection relies on the effect of the new (inelastic) channel on experimentally observable magnitudes, i.e., the junction differential conductivity ($G = dI/dV_s$, with V_s the sample voltage). The inelastic channel acts in addition to those scattering (transport) processes in which initial and final electronic states have equal energy, i.e., the elastic channels. Hence, as a first approximation, the

effect of the vibrational excitations will be a slight increment $\Delta G \sim f_i \times G$. On a very first order, the effect of the opening of the inelastic channel on the differential conductivity (dI/dV_s) may be understood by using a water analogy, as in ref. [3]. The water flow (tunneling current) through a water pipe increases steadily with the water pressure (voltage). If at a certain pressure a crack in the pipe opens (inelastic channel), a sudden increase in the rate of water flow will take place. The opening of the crack is an additional channel for the flow of water, producing a decrease in the tube's resistance.

In practice, the inelastic fraction is a small number, typically smaller than 0.1, therefore producing a change of the total conductance of at most 10%. This change can be detected only under very extreme conditions of stability and energy resolution. To help with the detection of such a small signal, the second derivative of the tunneling current, $d^2I/dV_s^2 = dG/dV$, is usually measured. In principle this magnitude should show peaked features at energies corresponding to the opening of an inelastic channel (Fig. 4.1b). The inelastic channel can be opened indistinguishably by tunneling electrons traveling from every electrode. Therefore, a fingerprint of vibrational signal is that peaks appear at roughly the same bias values, independently of the sample polarity [17].

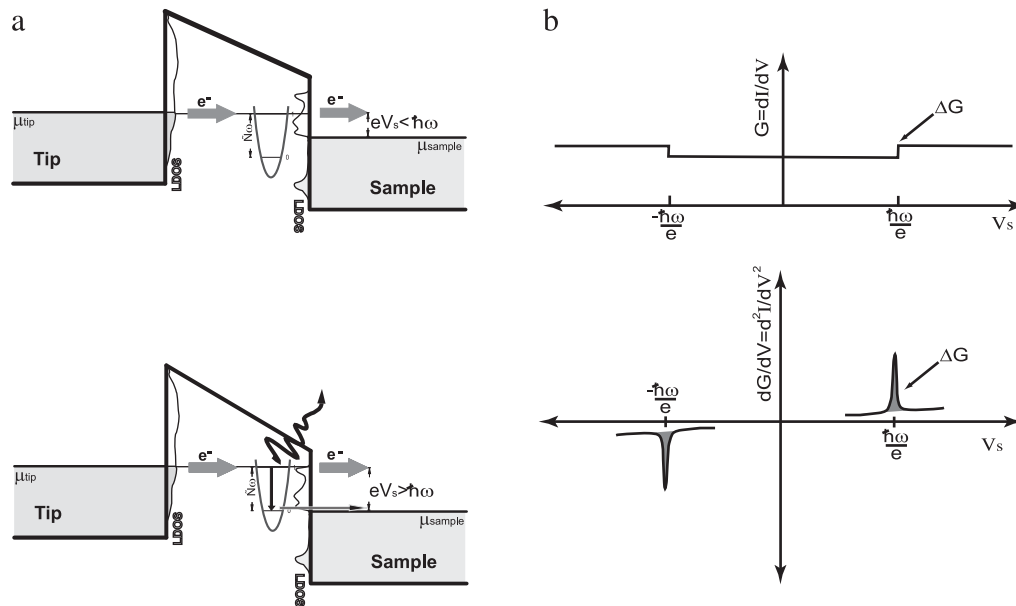


Fig. 4.1 (a) Model potential energy diagram of a tunneling junction with an adsorbed molecule in it. The vibrational degrees of freedom of the adsorbate are included as a simple harmonic potential. Only when the final state becomes accessible by the tunneling

electrons (i.e., when it is above the surface electrochemical potential) is the inelastic channel open. (b) The effect of the inelastic channels is ideally a slight stepwise increase in the tunneling conductance. This induces a peak in a d^2I/dV_s^2 vs. V_s plot.

To detect the weak d^2I/dV_s^2 signal lock-in techniques are usually employed. These techniques are implemented by adding a small AC modulation with frequency ω to the bias voltage and by detecting the response of the molecular tunneling junction. Nonlinearities in the current versus bias (I - V) plot give rise to higher harmonics in the response of the tunneling current to an AC voltage. The magnitude of the response oscillating with frequency 2ω yields a value proportional to d^2I/dV_s^2 . This value is outputted by modern lock-in instruments, which can measure a large number of different harmonics of the modulation frequency ω . To acquire a spectrum, the DC sample bias is scanned along the energy window of interest, searching for sharp variations of the d^2I/dV_s^2 magnitude. One of the major drawbacks is that, due to the small magnitude of the inelastic signal, measurements usually have to be performed very slowly in order to maximize the temporal averaging of the measurements. Since the measurements are performed with the STM feedback open, the stability of the STM junction is an important issue. Usually, the measurement of one spectrum takes from tens of seconds to minutes. Such stability can be reached only when working at very low temperatures as, for example, with the STM head in thermal equilibrium with a liquid-helium reservoir.

Working at low temperatures is also an imposed requirement for reaching the appropriate energy resolution in STS. The intrinsic width of a vibrational mode is less than 1 meV. In order to detect the inelastic signal, high resolution in energy is required. Since we are working with tunneling electrons, such resolution may be accomplished only by working at cryogenic temperatures. Thermal broadening of the vibrational peaks is in the order of 5 kT; at 10 K this corresponds to ~ 4 meV. Although there is no fixed temperature limit for the detection of the inelastic signal, it becomes extremely difficult to resolve the peaks from the background above some tens of degrees. Thermal drift worsens this upper limit considerably. Lauhon et al. [17] succeeded in detecting the signal of the C-H stretch mode in acetylene at temperatures up to 60 K. A detailed description of experimental methods for acquiring the inelastic signal can be found in refs. 16 and 17.

Figure 4.2 reproduces typical vibrational spectra of three different adsorbate systems, and summarizes the extents and limitations of this spectroscopy. As is shown in the figure, IETS-STM can resolve internal vibrations, as is the case of the C-H stretch mode of acetylene (Fig. 4.2a), external (hindered) vibrations, as for example the external modes of CO on Cu(110) (Fig. 4.2b), and even collective modes, illustrated by the breathing mode of a icosahedral fullerene cavity shown in Fig. 4.2c. In every case, the signal can be resolved in space with sub-nanometer resolution, and in energy with millielectronvolt resolution.

4.2 Experimental Results

The first successful detection of a vibrational mode using an STM was the C-H stretch mode of acetylene adsorbed on Cu(100) [1]. Since then, C-H stretch has

been detected with higher or lower intensity in several hydrocarbons by Ho's group (as reviewed in ref. 18) and by Kawai's group 13, 19, 20. The experimental database, albeit reduced, has been extended to other internal and external modes, without a previous understanding of which modes were going to be active in the excitation/detection processes.

A major drawback of IETS–STM is the lack of sensitivity for many of the molecular modes of a molecular-surface system which remain inactive or undetected. Furthermore, there is no relationship with excitation selection rules from other techniques (IR, Raman, EELS, etc.). The initial results of IETS–STM point to the fact that active modes depend on the symmetry and configuration of the adsorption geometry. Although the exact origin of excitation/detection selection rules are unknown, there is general agreement that they lie behind the resonant mechanism for excitation, proposed first by Persson and Baratoff [5]. The main conclusion of this model is that the excitation depends strongly on the electronic configuration of the adsorbate–surface complex at the Fermi energy. This implies that to understand excitation processes, the adsorption process itself has to be known perfectly, and to predict the excitation, a good model for tunneling transport has to be used. A strong combination of experimental measurements and theoretical modeling must be used to understand the fundamentals of IETS–STM.

In this section we present two examples which illustrate the advantages and disadvantages of IETS–STM: on one hand the possibility of resolving the inelastic signal with submolecular resolution; and on the other, the small number of active modes, which has limited the initial experimental and theoretical efforts to gain understanding on the fundamentals of the excitation itself.

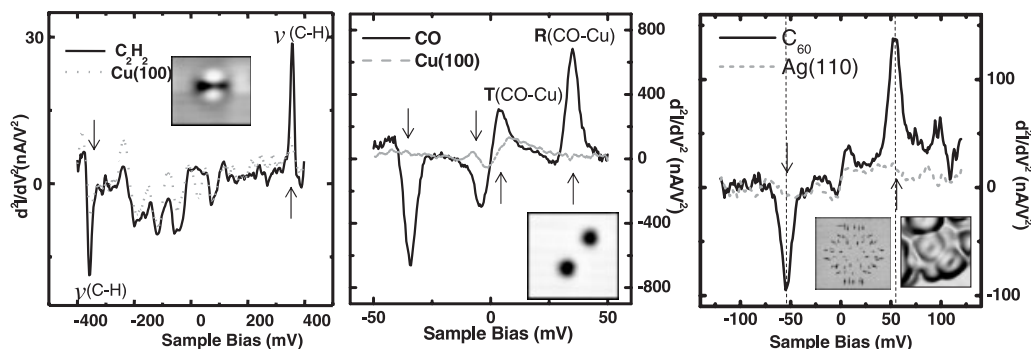


Fig. 4.2 Vibrational spectra of several adsorbate systems. The insets show the topography of the corresponding molecules. (a) C_2H_2 on $Cu(100)$: the peak at 356 mV is due to excitation of the C–H stretch vibration. (b) External vibrations of CO on $Cu(100)$: the peaks at 5 mV and 35 mV are due to excitation

of the CO frustrated rotation ($R(CO-Cu)$) and translation ($T(CO-Cu)$) with respect the $Cu(110)$ surface. (c) C_{60} on $Ag(110)$: two peaks at 55 mV are associated with a breathing mode of the fullerene cavity ($H_u(2)$ mode, shown in the inset).

4.2.1

C₆₀ on Ag(110)

In order to understand the role of the molecular and electronic-structure symmetries in the inelastic signal, the study of fullerene molecules on a highly anisotropic surface, Ag(110), aims at comparing excitation and detection of vibrations between different molecular/surface configurations. C₆₀ was used because of its cage structure with icosahedral (*I_h*) symmetry. The high symmetry of its atomic structure causes high degeneration of both its electronic and vibrational states. Also, its rigid three-dimensional structure remains highly unperturbed upon adsorption. Thus, when C₆₀ is adsorbed on a surface the structure of the free-molecule orbitals remains fairly unaltered [21]. Adsorbed on noble metal surfaces, fullerenes behave as electrophilic species, their interaction being usually described by a predominantly ionic charge transfer to unoccupied, LUMO-derived resonances. Figure 4.3 shows STM compared with photoemission and inverse photoemission spectra. The STM spectrum is measured on a single molecule forming part of a small island.

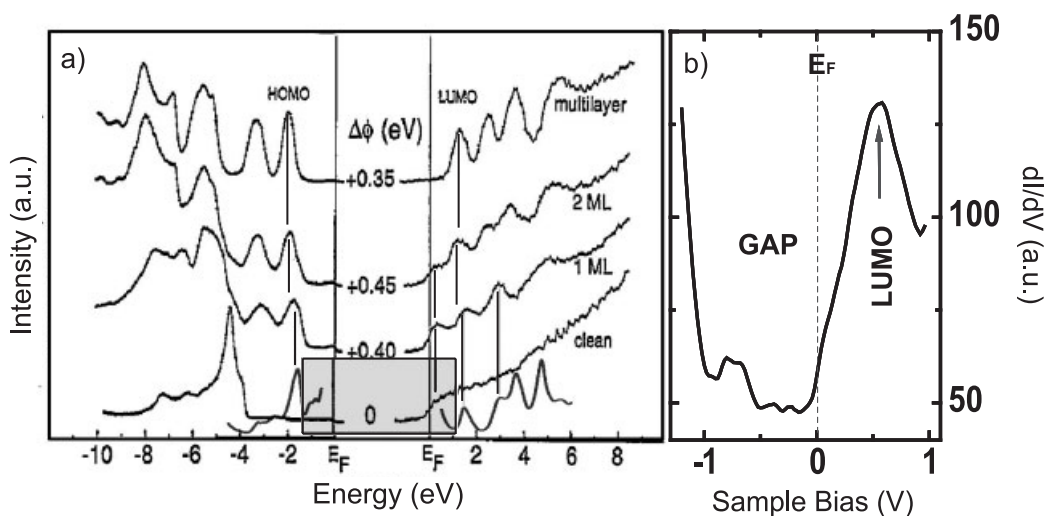


Fig. 4.3 (a) Comparison of electronic structure of C₆₀ on Ag(110) as obtained by STM on a single molecule forming part of a domain (lower plot) and by photoemission and inverse photoemission for different coverage values (four upper plots, reprinted from ref. 22 with permission from Elsevier). To be able to explore a wider energy range, the STS data are measured with the feedback loop closed, and modulating the bias voltage at a frequency of 2 kHz, larger than the response of the feedback. The LUMO peak cannot be resolved in the STS

data; however, peaks HOMO and LUMO+1 to LUMO+4 are seen below the vacuum level at position compatible with the photoemission results for the first and second molecular layers (1 ML, 2 ML). The yellow square locates the energy range of the zoomed data, shown in (b). There, the dI/dV vs. V_s plot, measured now under open feedback loop conditions, is shown for electron energies around the substrate Fermi level: now the LUMO and gap features are clearly resolved and indicated in the figure.

The others are measured on both submonolayer and multilayer regimes. STM reaches a better resolution, and seems to reveal more information, especially in the region of unoccupied states, where the spectroscopy is more sensitive to the electronic structure of the surface electrode.

The position of the HOMO- and LUMO-derived resonances for the first molecular layer coincides in both measurements, giving a HOMO–LUMO gap of 2.3 eV. The electrophilic behavior of the fullerene molecule causes the closer alignment of the LUMO resonance with the Fermi energy level, as a consequence of a partial filling of the molecules' empty levels. As a consequence of this, a small tail of the unoccupied resonance crosses the Fermi energy (Fig. 4.3b). This behavior is consistent with the intramolecular structure as resolved by the STM.

STM has proven its ability to resolve the molecular orientation [21, 23] and its electronic configuration [24] at the single-molecular level, relating it with fundamental aspects of the local molecular adsorption properties [25] such as adsorption site, coordination, symmetry/orientation, and intermolecular interactions. Figure 4.4(a) shows an example of a typical molecular island found on Ag(110) after depositing the molecules with the substrate at room temperature. In contrast with the case of post-deposition annealing, where a $c(2 \times 4)$ molecular superstructure arises [26] the island does not present a clear ordered structure, and besides, molecules within it show different orientations, as can be seen by inspecting the intramolecular structure. Figures 4.4(b,c) show a zoom on two of these molecules,

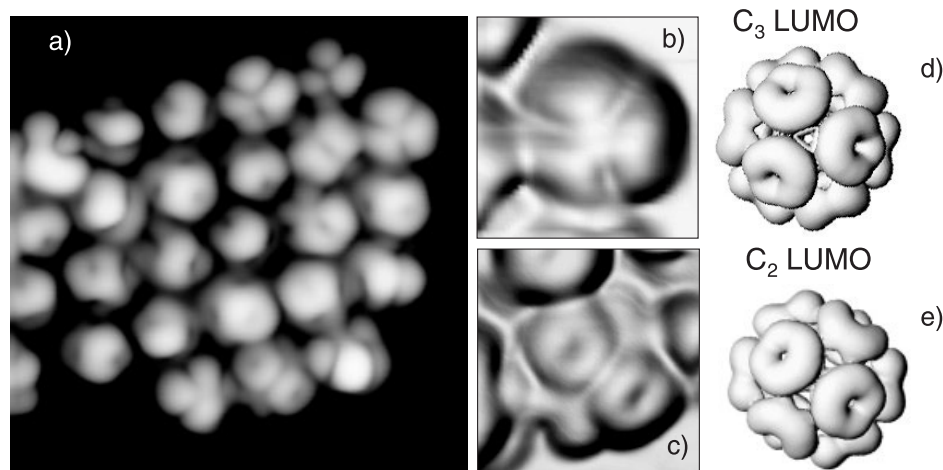


Fig. 4.4 (a) STM image of a C_{60} island on Ag(110). The intramolecular structure reveals the multiple molecular orientations. Only a small number of molecules show intramolecular structure with symmetry in agreement with the expected symmetries of the C_{60} cage. In (b) and (c) a zoom on two of these molecules is shown for comparison with

constant charge isosurfaces of the LUMO orbitals, as seen along the (d) three-fold and (e) two-fold symmetry axis. The calculations were performed with the SIESTA program [27, 28], based on density-functional theory. In the free molecule, the LUMO is three-fold degenerate.

whose internal structure has a well-defined symmetry. These correspond to fullerenes adsorbed with one of their symmetry axes perpendicular to the surface, and therefore probably keeping some degree of degeneracy in their electronic and vibrational states upon adsorption.

It is interesting to compare the internal structure with calculations of the spatial shape of their molecular orbitals. Since the perturbation of the C_{60} molecule at the surface is small, this comparison can be done successfully by simply calculating the charge density $\rho(r)$ for the free molecule. Constant- ρ surfaces will, therefore, simulate what the STM sees in those cases in which interference of multiple molecular resonances does not play a role [21]. The comparison is quite good, both methods resolving rings of charge centered at the pentagons of the icosahedral cage. This comparison confirms that essentially LUMO molecular orbitals (in the free molecule having three-fold degeneracy) dominate the transport of electrons with energy close to the Fermi level. This result leads to the conclusion that the LUMO-originating resonances will have an important role in the molecular vibrational excitation. At the same time, the molecular gap below the Fermi level makes quite it improbable that HOMO-derived states present any significant contribution to the excitation mechanism. As we shall see later for smaller molecules such as benzene, this is not the case.

The vibrational structure of a free C_{60} molecule consists of 46 distinct excitations with energies ranging from 33 to 195 meV, which account for the 174 internal vibrations of a molecular cage with icosahedral symmetry. Figure 4.5 shows the char-

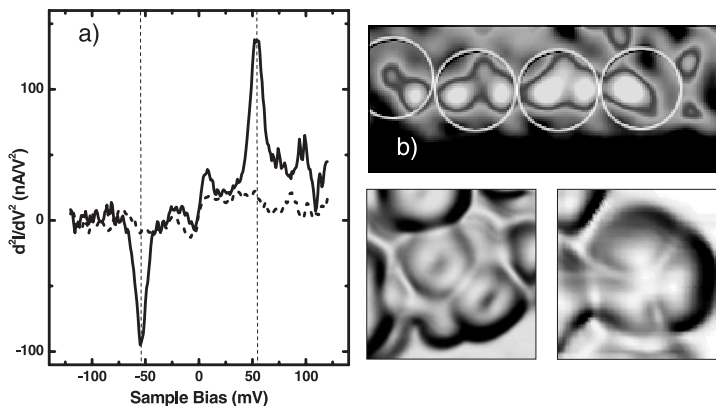


Fig. 4.5 (a) d^2I/dV_s^2 vs. V_s spectrum of an adsorbed fullerene. The spectrum is compared with that measured on the nearby bare Ag(110) surface. The peak at 54 mV (-54 mV) represents a normalized change in conductance of 9% (8%). ($I = 1.6$ nA, $V_s = 0.1$ V, $V_{ac} = 5$ mV rms at $f_{ac} = 341$ Hz) (b) d^2I/dV_s^2 maps on part of a C_{60} island measured at 56 mV. A critical enhancement of

the signal is observed on some small locations within the molecular cage. White circles help to locate the position of the molecules in the corresponding topography image. ($I = 1.6$ nA, $V_{ac} = 6$ mV rms at $f_{ac} = 941$ Hz). The inelastic maps compare with the shape of LUMO orbitals (STM images are shown for comparison).

acteristic d^2I/dV_s^2 spectra measured on top of a C_{60} molecule. A narrow peak at a bias value of 54 mV appears at both polarities. Such a symmetric position with respect to the zero bias point is a signature of its vibrational origin, since the corresponding inelastic channel is similarly open for electrons tunneling in both directions. The peak is probably associated with the H_g mode corresponding to an even breathing of the molecular cage with a larger radial component along the C_{5v} symmetry axis [29]. In the free molecule, this mode is five-fold degenerate. At the surface, it is expected that the degree of degeneracy changes depending on the specific orientation of the molecule.

The resonant character of the excitation mechanism can be demonstrated by analyzing the spatial distribution of the inelastic signal within the molecular cage. This measurement is done by tuning the sample bias to the value of the inelastic peak, and performing a slow STM image while plotting the d^2I/dV_s^2 signal. This microscopy approach is quite powerful for the localization of the inelastic signal within the molecular cage. Here, it can be used to understand the origin of excitation by comparing it with the topography images of Fig. 4.4.

Figure 4.5 shows one such map acquired at a DC sample bias of 56 mV. The inelastic signal has a maximum excitation only at specific locations within the fullerene cavity. Such positions are usually randomly located within the cage, which is consistent with a lack of orientational order. However, some of the molecular species show lobes of maximum inelastic signal at positions arranged with the expected symmetry of the fullerene cavity; in particular, their arrangement fits with the location of the molecular pentagons. This map thus resembles the shape of the LUMO shown in Fig. 4.3 for some orientations, revealing the active role of the LUMO resonance in the excitation process.

4.2.2

C_6H_6 on Ag(110)

A smaller molecular system, benzene (C_6H_6) on Ag(110), was also employed to investigate the role of the molecular orientation in the excitation of vibrations. Benzene populates two adsorption states with very different growth, stability, and shape in the STM topography [30, 31]. Each state dominates in a different temperature range. Benzene trapped in the weakest state is imaged as protrusions. This state appears only when the adsorption occurs at sample temperatures below 20 K, which is characteristic of an adsorption process with an activated barrier for chemisorption. Dosing benzene on samples above that temperature leads to molecular chemisorption, in which benzene is imaged as depressions. The STM image of Fig. 4.6 shows molecules populating every adsorption state; the depressions labelled “T” and “S” correspond to chemisorbed benzene. The protrusions at the step edge are physisorbed molecules. Inelastic spectroscopy resolves some of the external modes of each state [30, 31]. A different vibrational fingerprint in the IETS–STM spectra was found as a consequence of the different nature of their interaction with the surface. Furthermore, rather than mode–energy shifts, the spectra show different modes in every case. This exemplifies the difficulty in con-

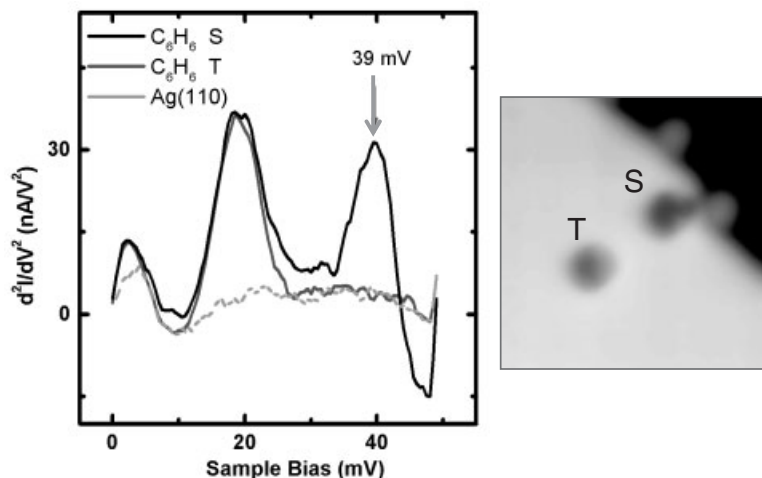


Fig. 4.6 d^2I/dV_s^2 vs. V_s spectra of adsorbed benzene molecules. The plot compares a spectrum of a flat-lying molecule on the terrace, marked “T” in the STM image, with that of a molecule close to a kink site (“S” in the image). The proximity of the step disrupts

the molecular feature as seen in the STM image, presumably corresponding to a slight tilting of the molecular plane. For this distorted molecule, an additional peak, indicated in the figure with an arrow, is found. ($I = 2$ nA, $V_s = 0.1$ V, $V_{ac} = 4$ mV rms at $f_{ac} = 641$ Hz).

structuring a set of general selection rules, since different minima in the adsorption potential surface may show different modes in the spectra.

Let us concentrate on the chemisorbed species shown in Fig. 4.6. An inelastic spectra measured on top of them is also shown in the figure. Peaks at 4 and 19 meV were found on both of them, and tentatively associated with the hindered translational and rotational vibrations. However, on the molecule close to a step edge, the reduced symmetry of the environment led to an additional peak at 39 meV, which was associated with the stretching of the molecule with respect to the surface. The other two peaks were not affected, remaining the same shape. The origin of this new peak is attributed to the change in the electronic resonance configuration when the molecular structure, even for the same adsorption state, changes due to the presence of a step. The observation of a vibration when the adsorption geometry is changed was also detected for benzene on Cu(100) [32, 19]. In this case, the molecular structure changes from flat-lying to perpendicular to the surface when one or two hydrogen atoms are removed from the benzene ring.

For a small molecule such as benzene, molecular orbitals are considerably broadened upon chemisorption. They form broad resonances extending over a large energy window with a tail crossing the Fermi energy level. Several molecular resonances may have a non-negligible weight at the Fermi energy, and to some extent, they all participate in the transport. It is thus interesting to analyze the distribution of the inelastic signal measured on a single benzene molecule.

Figure 4.7 plots the d^2I/dV_s^2 signal as a function of the energy (vertical axis) and

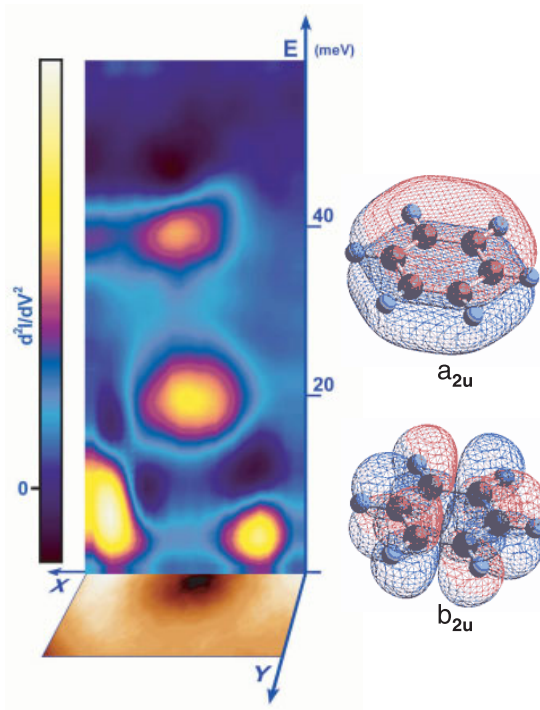


Fig. 4.7 2D color scale representation of the d^2I/dV_s^2 signal as a function of the energy and the distance along one line crossing the “S” benzene molecule in Fig. 4.6. The line is perpendicular to a [100]-oriented step edge, which is located on the left side. For clarity, in the bottom image we represent the scaled topography of the molecule. ($I = 2$ nA,

$V_s = 0.1$ V, $V_{ac} = 4$ mV rms at $f_{ac} = 641$ Hz). For comparison, the figure also shows the spatial shape of the two π orbitals of a free benzene molecule: the lowest orbital, a_{2u} , has no nodal point at the center. Higher-lying orbitals (the probably unoccupied b_{2u} orbital is shown here) present nodal planes.

as a function of the position along the diagonal of the molecule (horizontal axis). This bidimensional representation loses one spatial dimension but gains a direct view of the energy dependence of the inelastic signal. The three modes shown in Fig. 4.6 appear here as bright features, with a spatial extent slightly smaller than the molecular structure. The two higher-energy modes are centered with a bell-shaped distribution in the molecular structure. The spatial width at half maximum is 4.2 Å and 3.4 Å for the 19 mV and 39 mV peaks respectively. The distributions of the inelastic signal contrast with that of the lowest energy mode. In this case, the vibrational signal is very weak at the center of the topographic feature, representing a value of d^2I/dV_s^2 smaller than 1%, but has stronger intensity at both sides of the molecule up to about $d^2I/dV_s^2 \sim 10\%$. The distance between the two maxima is 6.4 Å and thus the maximal intensity is obtained with the tip outside the molecular ring.

The interpretation of such different distributions of the signal follows the resonant model for excitation. As in the case of C_{60} on Ag(110) shown above, or in the previously reported work by Hahn et al. [33] for O_2 on Ag(110), inelastic maps may reflect directly the shape of the resonances involved in the excitation. Free benzene orbitals are well known. The bell-shaped distribution of the higher-energy inelastic peaks resembles the lowest-energy π state of a free benzene molecule, with symmetry a . The shape of the lowest peak resembles a resonance with a nodal point at the center of the molecule. These are characteristic for the a and b orbitals. In general, the inelastic maps are consistent with the spatial distribution of the resonances, supporting the general picture of a resonant mechanism of vibrational excitation. Here it is also remarkable that vibrational modes which lie only 15 meV apart are activated by different electronic resonances, which are usually several electronvolts wide.

The nature of the coupling between vibrational and electronic states is thus behind the “selection” rules for the activation of vibrations. Besides, the detection of the inelastic channels relies on the effect of a molecular vibration on the tunneling conductance. The problem is not simple, and probably there is no way of extracting a list of rules, but, instead, detailed simulations must be produced for every adsorption system. Therefore, the establishment of a reliable theoretical understanding of both excitation and detection is of great interest.

4.3 Theory

4.3.1 Extension of Tersoff–Hamann Theory to IETS–STM

The conduction process can be computed by using Bardeen’s transfer Hamiltonian, which is basically a perturbation approach to the influence of the tip on the substrate’s wavefunctions; for a summary of this approach please refer to Chapter 16. For the case of adsorbates this procedure is very reliable due to the accurate electronic-structure calculations available nowadays. Tersoff and Hamann [34] used the wavefunction of a spherical tip and obtained that the tunneling conductance, σ , is proportional to the local density of states (LDOS), ρ , evaluated at the Fermi level (chemical potential of the substrate) according to Eq. (1).

$$\sigma \propto \sum_{\mu} |\psi_{\mu}(r_0)|^2 \delta(E_F - \varepsilon_{\mu}) = \rho(r_0, \varepsilon_F) \quad (1)$$

The LDOS is a density of states ($\delta(E_F - \varepsilon_{\mu})$) weighted by the spatial information of each state contributing ($|\psi_{\mu}(r_0)|^2$). This quantity is evaluated at the tip’s center of curvature (r_0) and at the Fermi level (E_F). A first success of such a result is that the STM is interpreted as a probe to read the electronic structure of the substrate at a certain distance from the surface (r_0) and at the substrate’s Fermi level. This

last result is a consequence of linear-response theory, which is justified in the limit of low bias voltage. In the case of molecules adsorbed on metal surfaces, this approach yields a very good description of the STM constant-current image when the substrate's electronic structure (eigenvalue ε_μ and wavefunction $\psi_\mu(r)$) is evaluated within DFT.

In refs. 35 and 37 the many-body extension of Tersoff–Hamann theory to the treatment of IETS–STM is presented. Briefly, the inelastic contribution to the change in conductance, $\Delta\sigma$, will be caused by the change in the LDOS due to the vibration. Now, the problem is complicated by the many-body aspects of the theory. There is a first term that can be traced back to an energy transfer from the impinging electron to a quantum of vibration. This is called the inelastic contribution to the change in conductance [15, 36]. The relative change in differential conductance, η_{ine} , is then given by Eq. (2).

$$\eta_{\text{ine}}(r_0) = \frac{\Delta\sigma}{\sigma} \quad (2)$$

To leading order in electron–vibration coupling and using Eq. (1), this term is given by Eq. (2).

$$\eta_{\text{ine}}(r_0) = \frac{1}{\rho(r_0, \varepsilon_F)} \times \sum_{\mu} \left| \sum_{\lambda} \frac{\langle \psi_{\lambda} | \delta H | \psi_{\mu} \rangle \psi_{\lambda}(r_0)}{\varepsilon_{\mu} - \varepsilon_{\lambda} + i0^+} \right|^2 \delta(\varepsilon_F - \varepsilon_{\mu}) \quad (3)$$

Here we have taken the quasi-static limit, $\hbar\omega_i \rightarrow 0$. $|\psi_{\lambda}\rangle$ are the unperturbed one-electron states appearing naturally in the lowest-order perturbation theory (LOPT) and ε_{λ} the corresponding eigenenergies. The perturbing potential, δH , is obtained Chapter 16. References 15, 36, and 37 give detailed accounts of the numerical implementation of these equations.

Equation (3) says that there is an increase of conductance due to the modulation of the wavefunction by the vibration, because the squared term is just the square of the perturbed electronic wavefunction. The spatial dependence of the wavefunction carries the information of the exponential decay in vacuum of the tunneling probability. Hence, during the vibration this tunneling probability will be modulated in a way given by the change of the wavefunction.

The second contribution to the change in conductance at the same order in the electron–vibration coupling has been termed the elastic contribution. The name originates from the fact that the initial and final electron states are at the same energy; they do not differ in a quantum of vibration. The physical origin of this term is the many-body character of electron transport in the presence of vibrations. In the absence of vibrations one can approximate the many-body wavefunctions in terms of one-electron wavefunctions, which are solutions of an effective one-body Hamiltonian. When the electron–vibration coupling is included, the one-electron wavefunctions are no longer eigenstates of the Hamiltonian. The vibration mixes them up. The complexity appears because the full wavefunction is antisymmetric

under electron exchange, i.e., two electrons cannot be in the same quantum state. This exchange term gives a negative contribution to the change in conductance due to the antisymmetric character of the many-body wavefunction under exchange of two electrons. This elastic contribution is given by Eq. (4).

$$n_{\text{ela}}(r_0) = \frac{-2\pi^2}{\rho(r_0, \varepsilon_F)} \times \sum_{\mu} \left| \sum_{\lambda} \langle \psi_{\lambda} | \delta H | \psi_{\mu} \rangle \psi_{\lambda}(r_0) \delta(\varepsilon_{\mu} - \varepsilon_{\lambda}) \right|^2 \delta(\varepsilon_F - \varepsilon_{\mu}). \quad (4)$$

The notation is the same as in Eq. (3). There are two fundamental differences between Eqs. (3) and (4). The first one is the sign: the elastic contribution, Eq. (4), is negative. It is the term responsible for the decrease in conductance, as we stated. The second difference is the range of evaluation of the inner summation over electronic states: in Eq. (4) this summation is restricted to states at the Fermi level, while in Eq. (3) it extends over all energies. Hence, the elastic contribution, Eq. (4), will become particularly important when the density of states is very high at the Fermi level: that is, in the case of a sharp resonance at the Fermi level.

The results obtained to date are in good agreement with the experimental data and have made it possible to discuss and analyze the molecular modes excited with the STM.

4.3.2

Some Model Systems

In this section, we analyze two paradigmatic cases: (a) the IETS–STM of acetylene molecules on Cu(100) [1, 35], where the excitation of the C–H stretch gives a purely inelastic contribution to the conductance; (b) the case of oxygen chemisorbed on Ag(110) [33], where the O–O stretch gives a purely elastic contribution to the conductance. We will see that the electronic structure of both molecules is extremely important. In the case of acetylene a large molecular resonance straddles the Fermi level of the substrate. The oxygen molecule presents a sharp resonance at the Fermi level. A third case is exemplified by the ammonia molecule. The ammonia molecule chemisorbed on Cu(100) does not present any resonance at the Fermi level. Accordingly we find a small inelastic signal, undetectable experimentally [36].

4.3.3

Acetylene Molecules on Cu(100)

The change of conductance recorded over an acetylene molecule on Cu(100) shows a maximum at 358 mV [1]. The total change in conductance across the voltage threshold of 358 mV is in the range of 10%. The above theory in the Tersoff and Hamann limit [35, 37] predicts correctly that the detected mode is the antisymmetric C–H stretch mode, and it shows large cancellations in the rest of the modes. The electronic structure of the acetylene molecule on Cu(100) presents a large resonance originating in the π^* orbitals of the free molecule [37, 40]. The electronic

structure with π^* character extends from -7.5 eV below the Fermi level, to 2.5 eV above the Fermi level. The density of states at the Fermi level is dominated by electronic states with a large π^* component, which basically explains the constant-current image [1, 39, 40].

The C–H stretch mode contribution is purely inelastic; however, for the rest of the mode, the two contributions analyzed above become important. Due to their opposite sign in the global change of conductance, large cancellations take place, rendering the detection of the rest of the modes very difficult. The reason for this behavior can be traced back to the way in which the π^* -like electronic structure is strongly perturbed by the C–H stretch mode. This leads to a large modulation of the tunneling amplitude. The tunneling amplitude is responsible for the constant-current image, which for acetylene on copper originates in the π^* orbital of free acetylene. The rest of the modes also perturb the π^* -like electron structure. Large inelastic contributions are also found for the rest of the acetylene modes [35]. But these other modes affect the electronic structure due to the complex hybridization of the different molecular orbitals with the surface electronic structure. Equation (4) yields a large change in the absolute value of the conductance, because of the perturbation of the vibrations on the electronic structure about the Fermi level. However, the C–H stretch mode does not modify orbitals other than the π^* orbital at the Fermi energy, so its relative contribution to Eq. (4) is thus smaller than the one to Eq. (3), where it extends to all energies.

There are two C–H stretch modes: an antisymmetric mode, in which the two H move in phase opposition (one contracts when the other expands); and a symmetric mode. The calculation yields the correct value of the change in conductance if the antisymmetric mode is the only one detected [37]. This symmetry selectivity is due to the tip's and sample's electronic structure. We have assumed a totally symmetric tip wavefunction (s type, due to the Tersoff–Hamman approach), and the wavefunctions at the Fermi level are antisymmetric with respect to the plane perpendicular to the C–C axis (the same plane that defines the mode symmetry). Thus the only way to couple a symmetric with an antisymmetric wavefunction is by exciting an antisymmetric vibration [37].

The inelastic C–H stretch signal is large because there is a wide molecular resonance across the Fermi level that is directly affected by the C–H motion. This resonance is so short-lived that one can barely talk of a negative ion resonance. The theory uses the “sudden approximation”: the lifetime of the molecular resonances is short enough for the negative ion resonance not really to be formed, and the mechanism leading to the vibration excitation is barely impact scattering of an electron. This impact mechanism is purely quantal and bears no relation to a momentum transfer mechanism. In the same way, in the C–H stretch the induced dipole is negligible. Dipole scattering mechanisms can thus be neglected. In the impact mechanism, the modes perturbing the molecular orbitals with an important contribution to the density of states at the Fermi level may yield sizable conductance changes. Otherwise large cancellations appear on metal surfaces, where many-body effects become important. The broadening of the vibrational thresholds due to voltage modulation in the lock-in detection plus the natural broadening due

to temperature effects render the observation of conductance changes in the presence of elastic/inelastic cancelations very difficult.

4.3.4

Oxygen Molecules on Ag(110)

Oxygen on Ag(110) presents a sharp resonance at the Fermi level due to the hybridization of the molecular π_g orbital with the surface electronic states [41]. One of the consequences of this sharp resonance is that O_2 keeps part of its total magnetic moment on the surface. This is in stark contrast with the acetylene case. As a result the detected modes present a decrease in the conductance [33] due to the overwhelming elastic contribution [Eq. (4)]. In the case of O_2 the experimental change in conductance is reproduced when the simulation of the IETS, using Eq. (4), takes into account the true, spin-polarized, electronic structure of the molecular chemisorption. This result shows that (a) the elastic contribution in the quasi-static approximation, Eq. (4), explains the experimental findings; (b) the decrease in conductance is due to the elastic contribution that dominates when a sharp resonance is located at the Fermi level [42]. Hence, the existence of magnetic adsorbates does not automatically lead to decreases in the conductance, because the prevailing electronic-structure element is the existence of a sharp resonance at the Fermi level. The electronic structure giving rise to this resonance needs to have a large electron–vibration coupling, or otherwise the electron conduction will not decrease because the vibration will not be excited. Finally, we would like to note that the excitation of a vibration by an electron current may yield no detectable signal, despite the fact that the molecule has been efficiently excited.

4.3.5

Ammonia Molecules on Cu(100)

The third type of system is represented by the ammonia molecule. This system is especially interesting because every mode presents a very small inelastic fraction, far below the level of experimental detection. Its origin can be easily understood from the lack of resonances close to the Fermi level of the molecule.

Figure 4.8 shows that the Fermi level is between the HOMO and the LUMO. Hence there is not a definite molecular character at the Fermi level. The HOMO has less weight at E_F . However, both experimental and calculated constant-current STM images reveal that the HOMO contribution suffices to explain the overall features of the image. The HOMO is centered on the molecule and extends further into the vacuum. The antibonding (LUMO) states, although with more weight at E_F , are more localized in the N–H bonds. Hence we are dealing with a system in which the molecular state contributing to tunneling lies far from the Fermi level. The result is that the change in conductance due to the excitation of the different modes of the molecule is positive and very small.

In Fig. 4.8 the contribution of the different molecular orbitals to the full electronic structure of the chemisorbed system is shown. DFT calculations were per-

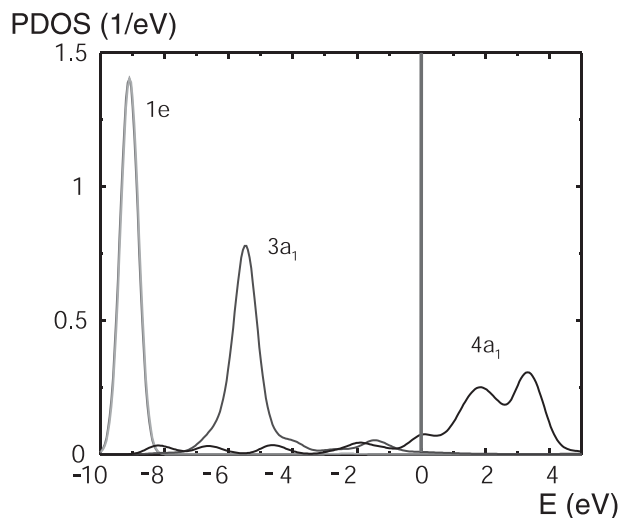


Fig. 4.8 Projected density of states (PDOS) of NH_3 on $\text{Cu}(100)$. The electronic wavefunctions of the full system are projected onto three different molecular orbitals: the $1e$, the HOMO $3a_1$ and the LUMO $4a_1$. The vertical red line indicates the Fermi level. Electronic states on the left are occupied, on the right empty.

formed in the GGA PW'91 for a 3×3 cell, a four-atom slab using the Dacapo code [43]. The molecule chemisorbs on the top site, with an energy of 602 meV in good agreement with experiments [44]. The gas-phase four higher-lying molecular modes are: the asymmetric N–H stretch (E symmetry), the doubly degenerate mode (experimental frequency: 427 meV); the symmetric stretch (A_1 at 414 meV); the scissors modes (E at 202 meV); and the umbrella or inversion mode (A_1 at 118 meV). Upon chemisorption these modes shift: charge transfer slightly weakens the N–H modes, the different symmetry of the surface splits up degeneracies, and the umbrella mode stiffens due to the absence of inversion symmetry. The calculated frequencies of the new modes are respectively 464 and 422 meV (asymmetric stretch), 408 meV (symmetric stretch), 200 and 198 meV (scissors), and 139 meV (umbrella).

The change in conductance is small because the electronic structure with molecular information is poorly represented at the Fermi level (Fig. 4.8). This result means that the actual efficiency in exciting the different modes of ammonia molecules on Cu is very small. The elastic contribution is more than an order of magnitude smaller than the inelastic one in all modes. This is because the density of states at the Fermi level is small and the evaluation of Eq. (4) includes only states at the Fermi level in opposition to the inelastic contribution (Eq. (3)). Nevertheless the small interaction of the ammonia molecule with the surface leads to small changes in conductance. When the STM is located on top of the center of the ammonia molecule, the asymmetric and symmetric stretches give a change in con-

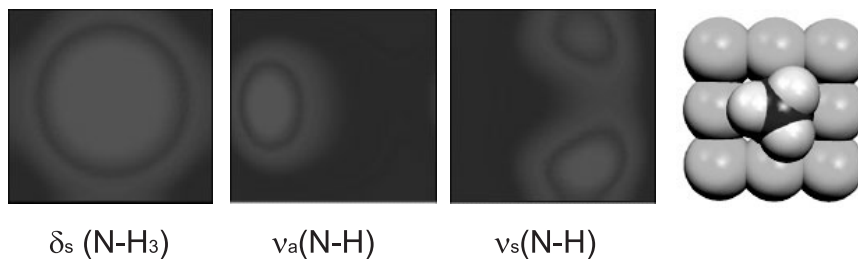


Fig. 4.9 Simulated inelastic maps for the umbrella and for the N–H stretch modes of $\text{NH}_3/\text{Cu}(100)$. The latter correspond to the breaking of three-fold degeneracy of the free-molecule N–H stretch symmetric mode. Calculations follow the procedure from refs. 35 and 36. The umbrella mode is symmetric, while the symmetric stretch mode in the free molecule loses its three-fold symmetry upon adsorption. For the stretch modes, the regions of maximum f_i are located on top of the N–H bonds. A ball model is added for comparison.

ductance of 0.08% (Fig. 4.9). For the scissors mode this value drops to 0.02%, while the umbrella modes presents its maximum at the center of the molecule and attains 0.4% of the conductance change.

The symmetry of the calculated inelastic images or distribution of the change in conductance can be understood by looking at the coupling matrix elements of Eqs. (3) and (4). If we use a symmetric wavefunction for the tip electrons, as is the case in the present calculations within the Tersoff and Hamann framework (s wave), then the image is created by the set of tip points that probe the information given by the sample wavefunction ψ_μ of Eqs. (3) and (4). In the case of a different tip symmetry, the inelastic images would change. Other ingredients that determine the inelastic image are the electron–vibration coupling symmetry, solely fixed by the mode’s symmetry, and the electronic symmetry of the sample at the Fermi level.

The asymmetric mode consists of a large elongation of the left-hand H atom of Fig. 4.9. This mode has a plane of symmetry along the N–H plane corresponding to the main elongation. From the study of the constant-current images of this system we know that the electron mainly tunnels into $3a_1$ -like functions of the substrate. The electron–vibration coupling is symmetric with respect to the N–H plane. Hence, the sample’s state giving rise to the image is also symmetric; otherwise the coupling would be zero.

Figure 4.9 (right-hand panel) shows the inelastic image for the symmetric stretch mode. Due to the actual geometry of the molecule on the surface, the two maxima are not equivalent. They are concentrated on top of the H atoms that are moving, and the character of the electronic states creating the image are of $4a_1$ character. The symmetry arguments are the same as for the asymmetric mode.

The umbrella or inversion mode is totally symmetric, so it couples the tunneling $3a_1$ with a mixture of $3a_1$ and $4a_1$ states. The image is then totally symmetric (Fig. 4.9, left-hand panel).

The changes in the conductance through $\text{NH}_3/\text{Cu}(100)$ are so small that both

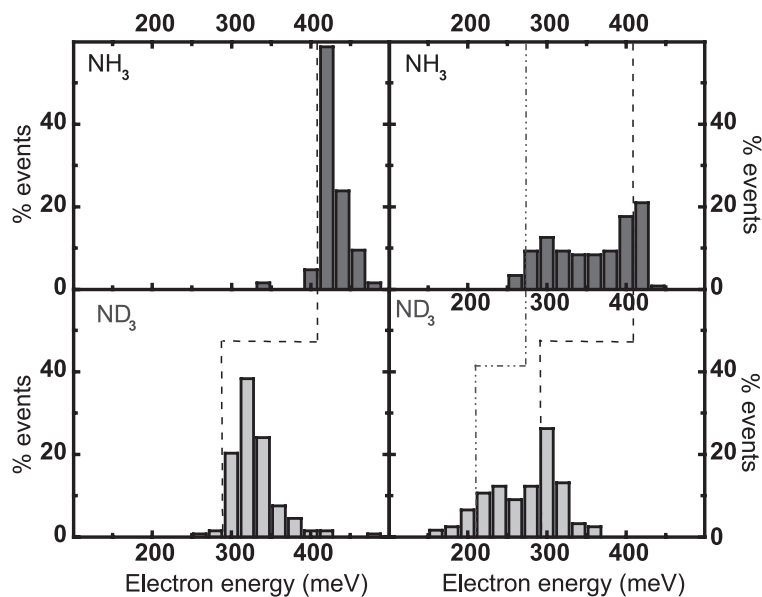


Fig. 4.10 Thresholds of electron energy for inducing ammonia desorption or translation on a Cu(100) surface. They are statistically probed by fixing the tip above a molecule with $V_s = 100$ mV, and slowly increasing the bias magnitude. A sudden current drop reveals the induction of motion. The panels show the distribution of electron energy (eV) reached when the reaction occurs (left) for low tunneling currents ($I_t < 0.5$ nA) and (right) for

$I_t > 1$ nA. The top panels correspond to experiments on NH_3 , and the lower panels to ND_3 . The thresholds together with their isotopic softening reveal the vibrational origin of such electron-induced motion. Furthermore, the umbrella and N–H stretch modes are responsible for the thresholds for the high and low current cases, respectively. Adapted from ref. 8.

modes are only detected thanks to the induced molecular motion. Figure 4.10 shows the statistics of electron energy values for inducing ammonia translation or desorption. A clear onset is found at 400 meV, which softens down to ~ 300 meV for ND_3 (left-hand panels in Fig. 4.10). For larger currents (i.e., excitation rate) the threshold moves down to ~ 270 meV (~ 200 meV for ND_3), in agreement with a second process activated by excitation of two umbrella modes in a coherent fashion [8].

In ref. 8 the excitation of the N–H stretch mode and of the umbrella mode is revealed by the different evolution of the molecule on the surface at the voltage threshold needed to excite each mode. The threshold to produce desorption of the molecule is linked to the excitation of the umbrella mode [45], and translation about the surface is effected by the excitation of the N–H stretch mode [45]. Indirectly, inducing the motion via mode excitation shows that a given mode can be excited even if the change in conductance is so small that it cannot be detected.

Hence, other changes of the system need to be sought in order to reveal mode excitation by tunneling electrons.

4.4

Conclusion

The method of performing vibrational spectroscopy with an STM, IETS–STM, introduced in this chapter gives the chemical sensitivity that STM could not reach merely by investigating electronic structure. Its development and use on a daily routine basis will favor the use of STM to investigate chemical problems at surfaces. At the moment, we are just starting to understand a few concepts regarding its operating principles.

The excitation of vibrations by tunneling electrons is strongly dependent on the electronic configuration of the adsorbate/surface complex, on the coupling of the electronic states at the Fermi level with molecular vibrations, and on the effect of these vibrations on the tunneling conductivity. The three concepts have to be taken into account to understand the nature of the modes detected and their signals. Besides, many-body effects may dominate the inelastic scattering of electrons by vibrations. We show how the effect of an inelastic channel can be canceled by elastic processes. In many cases this can explain the missing modes in experimental spectra. In other cases, the absence of molecule-induced electronic structure at the Fermi level leads to very small changes in the tunneling conductance at the vibration threshold. Finally, only in a few cases can the change in the tunneling conductance be larger than 10%.

Unfortunately, our main conclusion is that it is not possible to extract a general set of selection rules which could predict which modes we can expect. This means that precise simulations of the molecular resonances and transport properties are required. Instead of a drawback, these properties make IETS–STM an extraordinary method of probing fundamental physical-chemical concepts of molecular adsorption processes.

References

- 1 B. C. STIPE, M. A. REZAEI, and W. HO, *Science* **280**, 1732 (1998).
- 2 G. BINNIG, N. GARCA, and H. ROHRER, *Phys. Rev. B* **32**, 1336 (1985).
- 3 *Tunneling Spectroscopy: Capabilities, Applications, and New Techniques*, ed. P. K. HANSMA (Plenum Press, New York, 1982).
- 4 R. C. JACKLEVIC and J. LAMBE, *Phys. Rev. Lett.* **17**, 1139 (1966).
- 5 B. N. J. PERSSON and A. BARATOFF, *Phys. Rev. Lett.* **59**, 339 (1987).
- 6 B. C. STIPE, M. A. REZAEI, and W. HO, *Phys. Rev. Lett.* **81**, 1263 (1998).
- 7 T. KOMEDA, Y. KIM, M. KAWAI, B. N. J. PERSSON, and H. UEBA, *Science* **295**, 2055 (2002).
- 8 J. I. PASCUAL, N. LORENTE, Z. SONG, H. CONRAD, and H.-P. RUST, *Nature* **423**, 525 (2003).
- 9 J. GAUDIOSO, L. J. LAUHON, and W. HO, *Phys. Rev. Lett.* **85**, 1918 (2000).
- 10 J. GAUDIOSO and W. HO, *J. Am. Chem. Soc.* **123**, 10 095 (2001).

- 11 B. C. STIPE, M. A. REZAI, and W. HO, *Phys. Rev. Lett.* **78**, 4410 (1997).
- 12 B. C. STIPE, M. A. REZAI, and W. HO, *Science* **279**, 1907 (1998).
- 13 Y. KIM, T. KOMEDA, and M. KAWAI, *Phys. Rev. Lett.* **89**, 126 104 (2002).
- 14 T. KOMEDA, *Prog. Surf. Sci.* **78**, 41 (2005).
- 15 J. I. PASCUAL and N. LORENTE in *Properties of Single Molecules on Crystal Surfaces*, ed. P. GRÜTTER, F. ROSEI, and W. HOFER (Imperial College Press, London, in press).
- 16 B. C. STIPE, M. A. REZAEI, and W. HO, *Rev. Sci. Inst.* **70**, 137 (1999).
- 17 L. J. LAUHON and W. HO, *Rev. Sci. Inst.* **72**, 216 (2001).
- 18 W. HO, *J. Chem. Phys.* **117**, 11 033 (2002).
- 19 T. KOMEDA, Y. KIM, Y. FUJITA, Y. SAINOO, and M. KAWAI, *J. Chem. Phys.* **120**, 5347 (2004).
- 20 Y. SAINOO, Y. KIM, T. KOMEDA, and M. KAWAI, *J. Chem. Phys.* **120**, 7249 (2004).
- 21 J. I. PASCUAL, J. GMEZ-HERRERO, C. ROGERO, A. M. BAR, D. SNCHEZ-PORTAL, E. ARTACHO, P. ORDEJN, and J. M. SOLER, *Chem. Phys. Lett.* **321**, 78 (2001).
- 22 D. PURDIE, H. BERNHOFF, and B. REIHL, *Surf. Sci.* **364**, 279 (1996).
- 23 J. G. HOU, J. L. YANG, H. Q. WANG, Q. X. LI, C. G. ZENG, H. LIN, W. BING, D. M. CHEN, and Q. S. ZHU, *Phys. Rev. Lett.* **83**, 3001 (1999).
- 24 H. Q. WANG, C. G. ZENG, Q. X. LI, B. WANG, J. L. YANG, J. G. HOU, and Q. S. ZHU, *Surf. Sci.* **442**, L1024 (1999).
- 25 C. ROGERO, J. I. PASCUAL, J. GOMEZ-HERRERO, and A. M. BARO, *J. Phys. Chem.* **116**, 832 (2002).
- 26 T. DAVID, J. K. GIMZEWSKI, D. PURDIE, L. B. REIHL, and R. R. SCHLITTLER, *Phys. Rev. B* **50**, 5810 (1994).
- 27 P. ORDEJÓN, E. ARTACHO, J. M. SOLER, *Phys. Rev. B* **53**, R10441 (1996).
- 28 D. SAÑCHEZ-PORTAL, P. ORDEJON, A. GARCIA, and J. M. SOLER, *Int. J. Quantum Chem.* **65**, 453 (1997).
- 29 *Science of Fullerenes and Carbon Nanotubes*, ed. M. S. DRESSELHAUS, G. DRESSELHAUS, and P. EKLUND (Academic Press, New York, 1996).
- 30 J. I. PASCUAL, J. J. JACKIW, Z. SONG, P. S. WEISS, H. CONRAD, and H. P. RUST, *Phys. Rev. Lett.* **86**, 1050 (2001).
- 31 J. I. PASCUAL, J. J. JACKIW, Z. SONG, P. S. WEISS, H. CONRAD, and H. P. RUST, *Surf. Sci.* **502–503**, 1 (2002).
- 32 L. J. LAUHON and W. HO, *J. Phys. Chem. A* **104**, 2463 (2000).
- 33 J. R. HAHN, H. J. LEE, and W. HO, *Phys. Rev. Lett.* **85**, 1914 (2000).
- 34 J. TERSOFF and D. R. HAMANN, *Phys. Rev. Lett.* **50**, 1998 (1983); *Phys. Rev. B* **31**, 805 (1985).
- 35 N. LORENTE and M. PERSSON, *Phys. Rev. Lett.* **85**, 2997 (2001).
- 36 N. LORENTE, *Appl. Phys. A* **78**, 799 (2004).
- 37 N. LORENTE and M. PERSSON, *Faraday Discuss.* **117**, 277 (2000).
- 38 N. LORENTE, M. PERSSON, L. J. LAUHON, and W. HO, *Phys. Rev. Lett.* **86**, 2593 (2001).
- 39 N. MINGO and K. MAKOSHI, *Phys. Rev. Lett.* **84**, 3694 (2000).
- 40 F. OLSSON, N. LORENTE, M. PERSSON, L. J. LAUHON, and W. HO, *J. Phys. Chem. B* **106**, 8161 (2002).
- 41 F. OLSSON, N. LORENTE, and M. PERSSON, *Surf. Sci.* **522**, L27 (2003).
- 42 B. N. J. PERSSON and A. BARATOFF, *Phys. Rev. Lett.* **59**, 339 (1987).
- 43 Freely available at <http://www.fysik.dtu.dk/campos/ASE/>.
- 44 K. J. WU and S. D. KEVAN, *J. Chem. Phys.* **94**, 7494 (1991); T. J. CHUANG, H. SEKI, and I. HUSSLA, *Surf. Sci.* **158**, 525 (1985).
- 45 N. LORENTE and J. I. PASCUAL, *Phil. Trans. R. Soc.* **362**, 1227 (2004).

Part II
Scanning Force Microscopy-Based
Approaches

Patterning

5 Patterning Organic Nanostructures by Scanning Probe Nanolithography

*Cristiano Albonetti, Rajendra Kshirsagar, Massimiliano Cavallini,
and Fabio Biscarini*

5.1 Importance of Patterning Organic Nanostructures

The control of the properties of materials by size is one of the main goals of nanotechnology. This has motivated a research effort on micro- and nanoscale fabrication techniques specifically aimed at multifunctional materials, such as conjugated molecules and polymers, supramolecular assemblies, block copolymers and blends, biomolecular probes, nanoparticles, clusters, and coordination compounds, whose properties, interactions motifs, and functionality can be chemically designed. Multifunctional materials are attractive as building blocks for developing a bottom-up technological platform: they can be processed under mild conditions owing to their relatively low energy barriers for organization; can be endowed with complementary interactions for the assembly and the recognition of molecules and surfaces; and can undergo self-organization across multiple length scales into hierarchically organized architectures.

Nanoscale patterning of multifunctional materials is a prelude to applications in emerging technological fields: organic electronics, sensors, spintronics, memory storage, photovoltaic cells, adaptive surfaces, smart textiles, bio-arrays, micro- and nanofluidics, and regenerative medicine. Downscaling the charge/energy transport channels is a route to enhancing the response of electronic and photovoltaic devices; multiple length scale patterning greatly improves the sensitivity of bio-arrays for pathology; wetting, crystallization, thin-film growth, flow and deposition, and growth of viable cells and tissues can be spatially directed by a suitable patterning.

We have decided to devote this chapter to scanning probe nanolithography (SPnL) techniques specifically applied to patterning organic semiconductors, self-assembly monolayers, and molecular actuators. Our choice is motivated by the role and the diffusion that scanning probe microscopies have in research laboratories nowadays, and by the fact that SPnL represents the most versatile technique [1–10] for fabricating nanostructures. SPnL has many advantages: it exploits a variety of local tip–surface interactions, i.e., mechanical [11–13], electrical [14, 15],

and optical [16, 17]; it makes it possible to directly pattern the materials of interest with a resolution down to the nanometer scale in standard operating conditions [18], and without the use of masks or stamp prototyping; it does not require special infrastructures, clean rooms, vacuum, or aggressive atmospheres. On the other hand, as for most of the serial techniques, its limitations come from the low throughput and patternable area, as well as the long processing times [19]. SPnL should operate at scan rates three orders of magnitude faster (hundreds of millimeters per second) than the current ones in order to become viable for a real technology. Although an effort has been made to increase the fabrication speed by means of self-actuating/self-sensing cantilever arrays and large two-dimensional parallel arrays of probes [20–22], SPnL remains largely restricted to a tool for proof-of-concept experiments.

This chapter will not survey the vast field of SPM-based fabrication techniques. Its aim is rather to provide an overview of the applications of SPM to pattern molecular nanostructures. SPnL techniques are especially suited to soft materials, since the perturbation exerted on the system can be accurately controlled and extensive damage to the organic material avoided. The chapter will be focused on those fabrication approaches based on the localization of morphological/structural/chemical transformations, growth phenomena, self-organization, and self-assembly, in the proximity of the scanning probe. In this way, we want to bridge the interests of researchers in the field of multifunctional materials with those of the scientists involved in advanced SPM techniques.

Patterning approaches of organic nanostructures by SPnL can be classified according to three general schemes:

- a local modification or a transformation induced by the probe on a continuous organic thin film (Fig. 5.1a)
- a local chemical and/or topographical modification on a substrate (can be inorganic or an organic thin film) which then acts as a template for the growth of molecular assemblies (Fig. 5.1b)
- the local deposition of molecules or clusters from the probe to the substrate (additive manufacturing) (Fig. 5.1c).

Dip-pen nanolithography and field-induced desorption of molecules fall into the third of these schemes. Since they are discussed in detail in chapter 6 and chapter 4, we will not cover them here.

Sections 5.2 and 5.3 review the results from the approaches outlined in the first two schemes listed above. Section 5.4 is an outlook for the SPnL techniques applied to multifunctional organic materials.

5.2 Direct Patterning of Organic Thin Films

The most direct patterning method is a local modification of an organic thin film by applying a controlled interaction with an SPM probe. As the strength of the in-

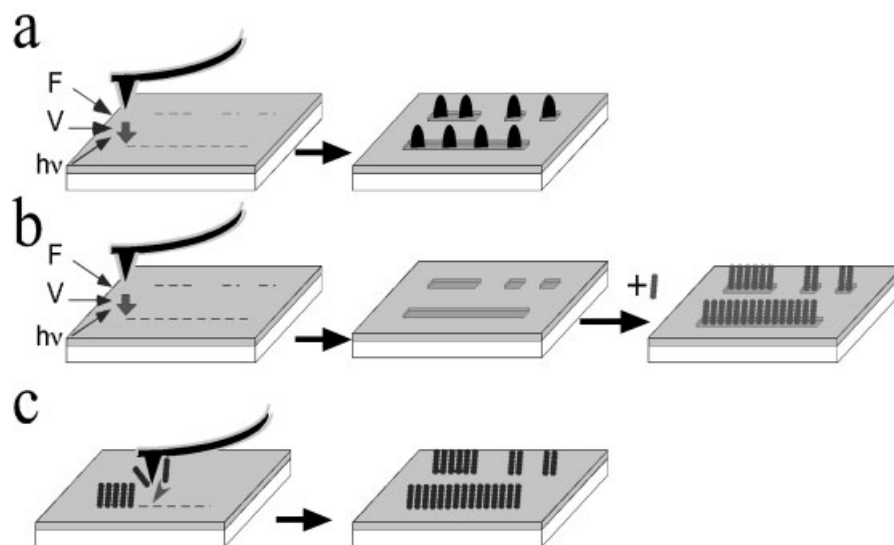


Fig. 5.1 General SPL schemes for fabricating surface patterns. Exploiting probe – sample interactions [Force (F), Bias voltage (V) or Photons ($h\nu$)], the surface can be modified morphologically (a) or chemically (b); in a second stage of (b) molecular assemblies can be deposited or self-organized on the patterns exploiting preferential or specific interactions with the modified regions of the substrate. In (c) the nanostructures are fabricated by releasing molecules or their aggregates from the tip (c).

teraction is changed or raised above a threshold, a nanostructure is fabricated on the thin film in the area where the perturbation acted. As the operation is repeated at different locations, the thin film is patterned with a motif of nanostructures, typically lines and dots, either separated one from another or joined to form the basic structures for any pattern.

5.2.1

Fabrication of Nanostructures by a Local Modification

The simplest nanostructures that are patterned on a smooth thin film are either holes or dots (hillocks). The holes can be formed by various mechanisms: indentation [23, 24], displacement of molecules from the thin film [25, 26], or re-orientation of standing anisotropic molecules [27]. The dots can be formed by a local structural change expanding the out-of-plane crystal axes, else by triggering either a roughening or a wetting/dewetting transition. The nanostructures have a low aspect ratio so they are not easy to “read” by other techniques whose topographical sensitivity is not comparable with that of an SPM. A nanostructure on a smooth continuous substrate raises the possibility of coding bits of information on a *tabula rasa*, and of devising new schemes for ultrahigh-density information storage.

5.2.1.1 Nanorecording for Memory Storage

The advantage of this approach is that the nanostructures have lateral and vertical sizes within the resolution limits of the SPM [28], so the same probe can be used both to write the bits of information *one by one* at predefined positions, and later to read them by changing the operating conditions. SPM techniques have been extensively used to prototype different types of write-once-read-many (WORM) memories and to assess the intrinsic limits of memory storage due to cross-talking. In some cases, it has also been possible to erase the information previously written using a different interaction, and to rewrite on the thin film [21].

The scanning tunneling microscope (STM) has been used to pioneer this type of writing/reading approach. The typical operating bias voltage for imaging in STM is of the order of a few millivolts. If a pulse of a few volts is applied to the STM tip for a short time (nano-seconds to seconds), it produces a beam of low-energy electrons which can modify the substrate surface by either removing material from the substrate [29] or depositing material onto it [30]; this is the basic concept behind STM nanolithography. In the writing approaches, the effect of the sign of the applied bias voltage has been an unsettled issue, with conflicting reports from well-known groups in the field. Thus, Reifenberger and coworkers [31] reported formation of mostly holes but also occasional mounds with a positive bias voltage on a flat gold surface. Hammers and coworkers [32] found that on a flat gold surface, smaller voltages sometimes produce mounds but holes are more common for larger voltages, irrespective of the sign of the bias voltage. Applying the pulses while moving the tip in a predetermined position allows one to “write” on the surface and this has been used to fabricate structures with nanometer feature size. With the added advantage of ultra-fine resolution, being an inherently low-energy technique (<500 eV), STM is an attractive alternative to electron beam lithography (EBL) or focused ion beam lithography (FIB), which both involve high-energy charged particles (in the region of several thousand electronvolts). In the last decade, several groups have explored STM nanolithography for many systems in different environments (UHV, air, and liquids) [33–35]. Different physical phenomena have been invoked to explain the occurrence of surface lithographical modification, including mechanical contact, field evaporation, and anodic oxidation.

Yu and coworkers [36] fabricated hole arrays on different types of 7,7,8,8-tetracyanoquinodimethane (TCNQ) charge-transfer complexes by applying a pulse of 8 V for 100 μs (Fig. 5.2a). This so-called hole-burning process produced holes of sizes in the tenths of nanometer lengthscale corresponding to a storage density of 1 Gbit cm^{-2} . It was found that the threshold voltage required to produce the dots depended on the pulse width (Fig. 5.2b).

Gao and coworkers [37] were able to pattern thin films of a radical molecule, NBMN-pDA (3-nitrobenzal malonitrile and 1,4-phenylenediamine), deposited on highly oriented pyrolytic graphite (HOPG) by producing holes (marks) on an otherwise smooth film. The marks were generated by applying voltage pulses of 3.5–4 V lasting for 1–2 μs , and were erased either by heating the sample *in situ* above 423 K or by applying reverse polarity pulses. The formation of marks was attributed to a conductance transition induced by the local electric field, and the

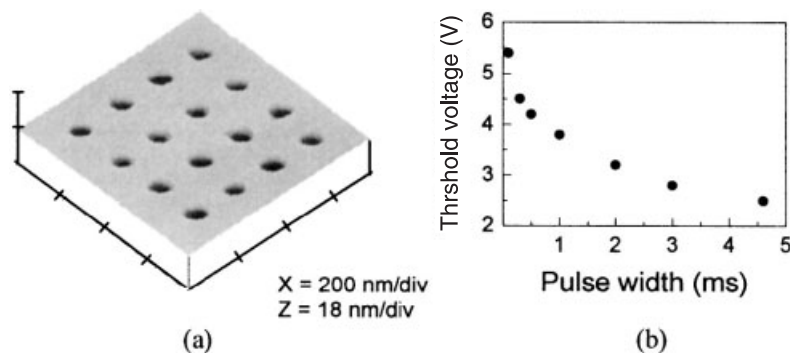


Fig. 5.2 (a) STM three-dimensional image of a 4×4 hole array formed by applying a voltage pulse of 8 V under a pulse width of 100 ms on a IPrDMA-I-TCNQ crystal surface. (b) Dependence of threshold voltage on pulse width (ref. 36, reproduced with the permission of the AIP).

distance between individual marks, viz., the resolution, was 1.7 nm. In subsequent studies [38] on *p*-nitrobenzonitrile (PNBN) films, the resolution was improved to 0.6 nm, corresponding to a data-storage density of about 10 Tbits cm^{-2} . I–V measurements can be performed in the STM configuration to yield a map of the density of states of the surface [39]. This can be useful in determining conductivity variations of the nanostructures produced with respect to the surface [40, 41]. For PNBN nanostructures, I–V measurements showed a great increase in the conductance transition in the recorded regions after the voltage pulses.

Feng and coworkers [41] performed nanorecording on thin films of electroactive rotaxane using either an STM or a conductive AFM probe. Rotaxanes are a novel class of molecular actuators that will be discussed in more detail in Section 5.2.2. Nanostructures such as those shown in Fig. 5.3 resulted from the application of voltage pulses of 2.2 V for 5 ms. The I–V characteristics revealed that conductance increases at the site of the dots.

Feng et al.'s experiment suggests the possibility of an irreversible electrical switching of rotaxane thin films, supporting indirectly some controversial results of Stoddart et al. [42], obtained with metallic crossbars sandwiching a rotaxane monolayer.

One of the major drawbacks of memory storage using scanning probe techniques is that the speed of reading and writing data is orders of magnitude slower than conventional memory devices. The main reason is the serial nature of reading/writing data by SPnL. In order to overcome this difficulty, Binnig and coworkers [43] proposed working with an array of AFM tips reading and writing in parallel, thus increasing the speed. The IBM project, known as Millipede, began with small arrays of 32×32 AFM cantilever array chips (Fig. 5.4).

Thermomechanical writing and reading were employed in ultrathin poly(methyl methacrylate) (PMMA) polymer films. A third-generation prototype consisting of 4096 cantilevers in a 64×64 array was demonstrated in 2003 [44].

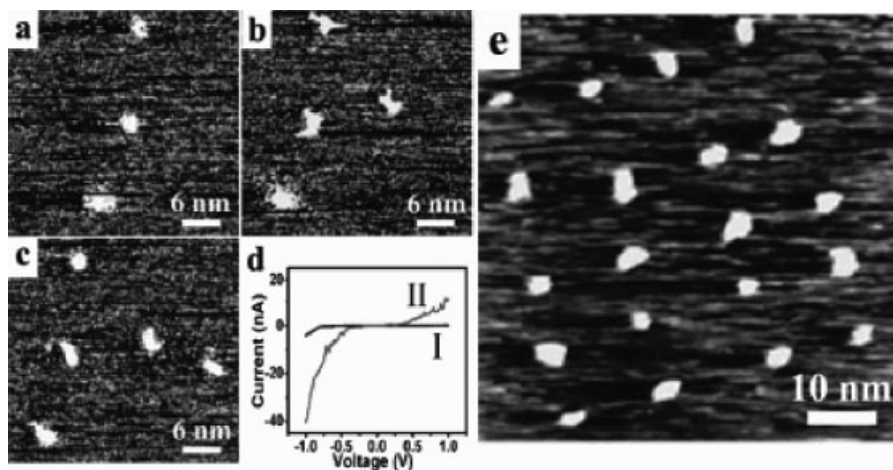


Fig. 5.3 STM images of nanorecording on rotaxane thin films. (a)–(c) Recording of dots one by one. (d) I–V curves performed on films (I) and dots (II), showing different conductivities. (e) Array of 5×4 dots (ref. 41, reproduced with the permission of the American Chemical Society).

5.2.1.2 Local Probe Photolithography

Patterning conjugated polymer films at the nanometer scale is fundamental for applications of organic electronics. Polymer patterning on poly(phenylene vinylene) (PPV) films, one of the most important materials for organic light-emitting diodes, has been demonstrated by Gränstorm [45] using AFM, where patterns with line-widths of ~ 20 nm were generated. DeAro and coworkers [46] used scanning near-

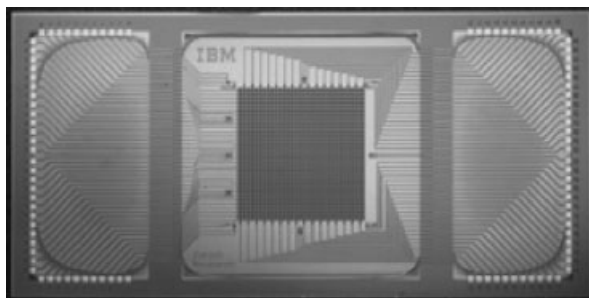


Fig. 5.4 Millipede chip ($7 \text{ mm} \times 14 \text{ mm}$), showing the electrical wiring for addressing the 1024 tips etched out in a square of $3 \text{ mm} \times 3 \text{ mm}$ (center). (Reproduced from and with the permission of the IBM website <http://www.zurich.ibm.com/st/storage/millepede.html>).

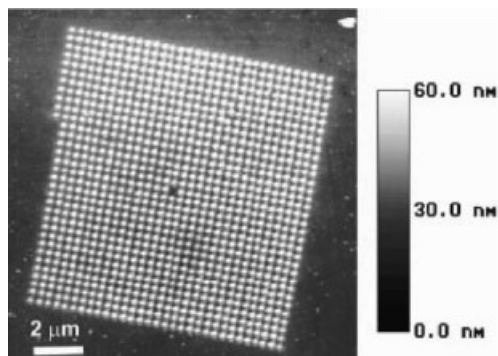


Fig. 5.5 AFM image of a two-dimensional photonic PPV crystal. The fully converted PPV pillars are about 32 nm tall, and have a full-width-at-half-maximum of 200 nm. One pillar

in the middle was intentionally missed to demonstrate the ability to integrate deliberately defects in the photonic structure (ref. 47, reproduced with the permission of AIP).

field optical microscopy (NSOM) to combine high spatial resolution of near-field optics with the process of photo-oxidation to produce patterns with 100 nm resolution on poly[2-methoxy,5-(2'-ethylhexoxy)-1,4-phenylenevinylene] (MEH-PPV) films. The films were patterned using the NSOM tip with a high-power illumination argon ion laser ($\sim 1 \text{ kW cm}^{-2}$). The overall size of the photodamaged region was found to be strongly dependent on exposure.

Using a different approach, Riehn and Cacialli [47] utilized NSOM under UV light (325 nm line of a HeCd laser with power $< 0.2 \text{ mW}$) to partially eliminate the labile groups in the soluble precursor of PPV. The unexposed material was washed off with methanol and the patterned precursor was heated to $220 \text{ }^\circ\text{C}$ for 5 h at low pressure ($< 10^{-5} \text{ mbar}$), resulting in a two-dimensional photonic crystal of fully conjugated PPV with a periodicity of 333 nm and a defect (Fig. 5.5).

This patterning process is “direct”, since it does not require a sacrificial photoresist, and creates polymer features surrounded by empty regions.

5.2.1.3 Nanorubbing

Liquid crystal displays (LCDs) and optical waveguides require control of the anisotropy in terms of orientational order parameters and anchoring of molecular domains at the solid interfaces. In LC technology, this is achieved by orienting the mesogenic molecules on a rubbed polymer layer. Güntherodt and coworkers [48] have demonstrated that by shearing an LC film with an SFM tip operated at a loading force in the range of 10^{-7} – 10^{-5} N a local change of orientation can be induced. They fabricated an optical waveguide ($6 \text{ } \mu\text{m}$ wide and 5 mm long) demonstrating the possibility of patterning higher refractive index regions.

Using a similar approach, Kim and coworkers [49] fabricated tri-stable surface-aligned symmetric patterns of nematic LC (Fig. 5.6). These consisted of locally rubbed parallelograms having corner angles of 60° and 120° so that three of them,

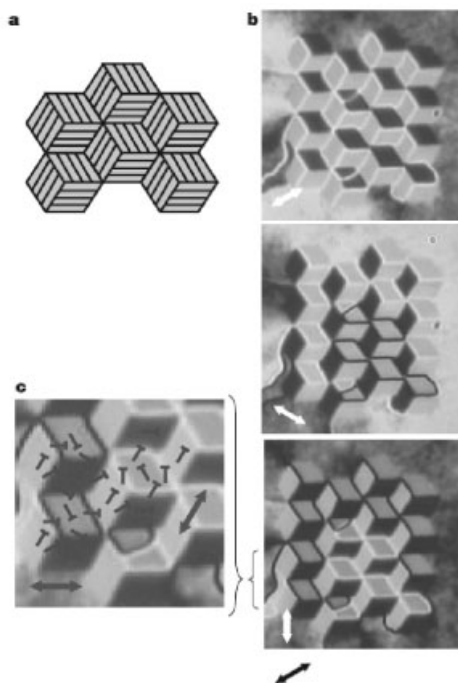


Fig. 5.6 (a) Schematic of the pattern: an array of identical hexagons, consisting of three parallelograms each having a different orientation. (b) The LC texture on the patterned alignment layer under a rotating analyzer in the optical polarizing microscope. The slight contrast of brightness indicates that the patterned region is divided globally into two regions of different macroscopic orientations. Black and white arrows indicate the directions of polarizer and analyzer. Each parallelogram has $10\ \mu\text{m}$ sides. (c) Orientations of surface directors in individual domains and at boundaries (ref. 49, reproduced with the permission of the Nature Publishing Group).

mutually rotated by $\pm 60^\circ$, made a hexagon. The orientations were mutually switched by an in-plane electric field, demonstrating the potential for demanding flexible display applications.

Recently, Derue and coworkers [50] have applied nanorubbing to regioregular polythiophene (P3HT) thin films, across $10\ \mu\text{m} \times 10\ \mu\text{m}$ areas (Fig. 5.7). When examined with tapping mode AFM, the rubbed areas were visible only in phase contrast images and not in height images. Based on the support of GIXRD (grazing incidence X-ray diffraction), they showed that nanorubbing induces a change in the local chain orientation and polymer crystallization [51]. P3HT is an important conjugated material widely studied for applications in organic field-effect transistors. The control of the orientation across device channels by nanorubbing appears to be a promising route for enhancing charge mobility, conductivity, and refraction index, and for tailoring light emission from light-emitting diodes or transistors [51].

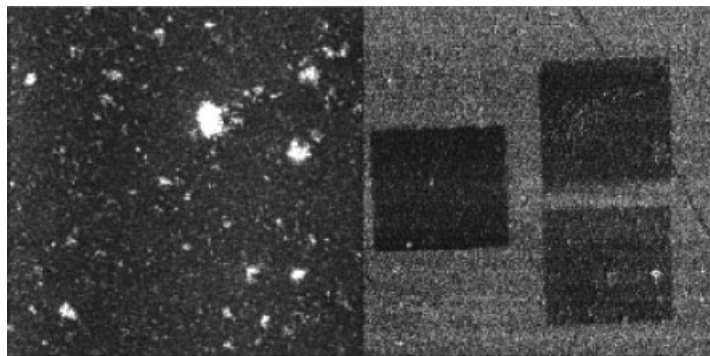


Fig. 5.7 $30 \times 30 \mu\text{m}^2$ tapping mode AFM height (left) and phase (right) images of a nanorubbed P3HT film. The vertical gray scale is 30 nm for the height image and 15° for the phase image (ref. 50, reproduced with the permission of the American Chemical Society).

5.2.2

Self-Organization of Molecular Nanostructures Triggered by SPM

A different approach to patterning of arrays of nanostructures was pioneered by Cavallini and coworkers [52]. It exploits the spatial confinement of a collective molecular reorganization in a thin film triggered by an AFM probe. The peculiarity of this approach is that the molecules self-organize themselves into nanostructures whose size and positions emerge as characteristic length scales of the transformation [53]. The AFM probe does not write the nanostructures one by one; it simply supplies the energy for the transformation to a local region of the thin film. This self-organization phenomenon has been observed and then controlled on thin films made of benzylic amide rotaxanes [54]. Rotaxanes are bistable molecules in which a macrocycle is interlocked mechanically on a “thread.” Two bulky “stoppers” prevent the macrocycle from sliding away from the thread (Fig. 5.8). The bistability arises from two or more (quasi-)degenerate co-conformations that correspond to energy minima in the intramolecular hydrogen bond interactions between the macrocycle and the thread.

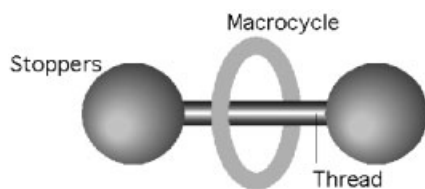


Fig. 5.8 Schematic structure of rotaxanes.



Fig. 5.9 Schematic of the patterning mechanism of rotaxane thin films upon mechanical perturbation of an AFM tip.

Rotaxanes have been used to devise switchable surfaces [54], because the interconversion in the solid state changes the intermolecular interactions and the interactions with the surface. The modified interactions can trigger an instability that propagates across length scales (e.g., wetting/dewetting transitions).

The reorganization phenomenon [53] occurs when the AFM tip scans the thin film just above a threshold force of about 2 nN. Rotaxane thin films (3–35 nm thick) were grown by drop-casting on graphite or mica. The films were imaged by AFM in contact mode using a set-point force below the threshold value. The films exhibit a homogeneous morphology over a square-centimeter area and are stable over a period of months. As the tip is scanned at a load force just above the 2 nN threshold, a string of regularly spaced dots appears collectively along the line. The dots emerge upon repeating the linescan a number of times (between four and 20) depending on the scan rate (typically 1–2 Hz). The process is shown schematically in Fig. 5.9.

Scanning a series of lines results in a regular array of dots of uniform width, height, and pitch (Fig. 5.10a). The number of dots is proportional to the length of each scan line (Fig. 5.10b), so any predetermined number of dots can be fabricated reliably on the surface. The film thickness controls dot size and spacing, and hence the density of dots per unit line; the thinner the film, the denser and smaller are the dots. The transformation can be induced over a large area (Fig. 5.10c) and also across surface steps and terraces. The linear dependence on the scan length allows one to write information as strings of bits (Fig. 5.10d). Different rotaxanes have been tested, giving similar responses, whereas no effect was observed when scanning thin films made of the thread or the macrocycle alone, or thin films of conjugated materials with high packing energies (e.g., sexithienyl, pentacene, tris(hydroxyquinoline)-Al^{III}).

The effect of the mechanical perturbation on the film appears as a roughening of the topographical profile, with the position of the dots fixed at early stages. Peculiarly, the transformation can be interrupted and restarted by turning off and on the perturbation. No sign of scraping or wear of the film is observed, ruling out trivial plowing with the AFM tip, which instead occurs as the set-point force exceeds 3–4 nN.

The collective fabrication of dots arises from coupled nucleation and recrystallization favored by the ease of intercomponent mobility in the solid state [55]. The scanning AFM tip gives energy to the molecules along the line to reorganize into nuclei. As nuclei coarsen by ripening, a characteristic distance emerges, and stable

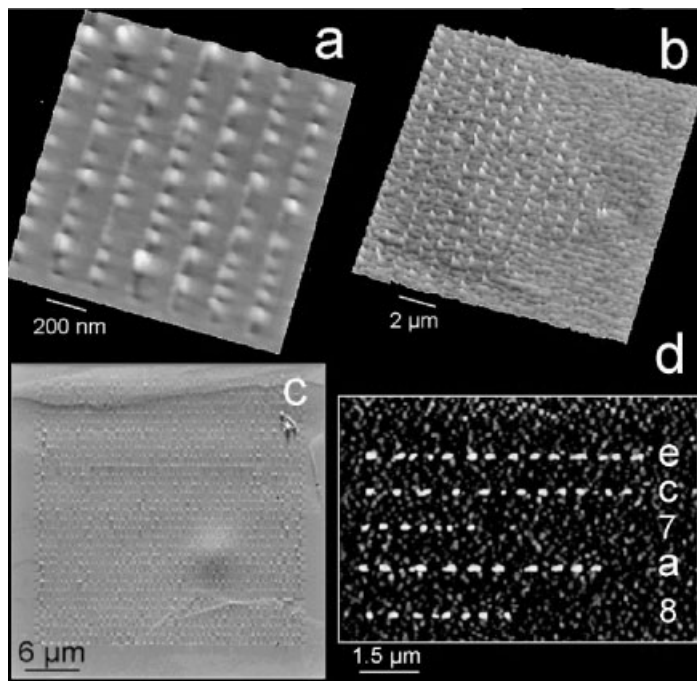


Fig. 5.10 (a) Array of dots fabricated by individual line scans of the AFM tip on a film 5 nm thick deposited on highly oriented pyrolytic graphite (HOPG). (b) For a given thickness (here 20 nm) the number of dots is linearly proportional to the scan length. The number of dots can be determined with an accuracy of at least 2%. Film thickness controls the characteristic size. When the film thickness is varied in the range between 3 and 35 nm,

interdot distance increases from 100 to 500 nm, the dot full-width-at-half-maximum from 40 to 250 nm, and the dot height from 1 to 20 nm, with a dispersion of 10–20%. (c) Pattern composed of 31 lines with 45 dots each on a $\approx 30 \times 30 \mu\text{m}^2$ area on a thicker film. (d) Proof-of-concept for information storage. The sequence: “e-c-7-a-8” in the hexadecimal base corresponds to the number 968616 [ref. 52, reproduced with the permission of AAAS].

nuclei grow due to the incorporation of mobile molecules on the surface. Extending this reorganization process over a two-dimensional region, the final result is a pattern of dots that does not change its morphology upon further mechanical perturbation. The detailed mechanism has been described in an extensive study [53].

5.3 Assembly of Organic Structures on Nanofabricated Patterns

The local chemical modification of a substrate, either bare or coated with a self-assembly monolayer, by SPnL can be exploited to generate a template pattern to

which other molecules are preferentially adsorbed. The approach relies on either preferential or specific interactions, and sometimes on the modification of nucleation density and surface diffusivity. The result is a molecular pattern conformal with the template. The resolution of this approach is comparable with that in the fabrication of the template by SPnL, i.e., a few nanometers. This implies that these approaches have the capability to control interactions and chemical recognition events at a surface down to length scales comparable with the molecular size.

5.3.1

Replacement Nanolithography on Self-Assembly Monolayers (SAMs)

The high structural order, perfect thickness homogeneity, and chemical stability of SAMs make them effective ultrathin resist layers. Patterned SAMs, whose specific components have a controlled spatial distribution on the surface, have been demonstrated to be suitable for fabricating sophisticated nanoscale architectures and for providing well-defined supports for physicochemical and biochemical processes [56, 57]. The first report of scanning probe nanolithography on alkanethiol-type SAMs was by Biebuyck and coworkers [58]. More recently, Kleineberg and coworkers [59] applied UHV-STM to write on different thiol–substrate combinations. A pattern of cross-grating was written onto a *N*-biphenylthiol (N-BPT)–Au system with parameters 1 V and 1 nA, and was transferred by using cyanide etch to the underlying 30 nm-thick gold film. The feasibility of 10 nm resolution demonstrated in this work competes with the best resolution possible for e-beam lithography to date. Since SPM can operate in liquids, a new type of nanolithography, termed replacement lithography, has been devised where molecules from a solution replace molecules in a SAM that are either removed or chemically modified. As demonstrated by Gorman and coworkers [60], the process consists of removing thiolates from defined Au regions with the scanning tip and replacing them with a different type of thiols. A schematic is shown in Fig. 5.11.

The tip–sample system is immersed in the solution of replacement thiols. Initially, (Fig. 5.11a) the SAM is imaged under normal bias conditions to locate an area free from defects and suitable for patterning. A high bias voltage (~ 3 V) causes the thiolates to be desorbed from the gold surface in the proximity of the tip and the replacement thiols then assemble on the exposed gold area (Fig. 5.11b). The pattern is then imaged under normal bias conditions (Fig. 5.11c). Figure 5.12 shows two examples of patterns written by replacement lithography.

The lateral resolution of this nanolithographic process has been tested by drawing two parallel lines of replaced thiols. Generally, the half-height linewidth is about 8–10 nm; thus two lines drawn 10 nm apart are unresolved, but two lines drawn 15 nm apart can be resolved. The ultimate limit of the lateral resolution depends critically on both the applied bias and the scanning rate. This process can be extended to the replacement of multi-thiols by changing the solution environment while the tip is withdrawn.

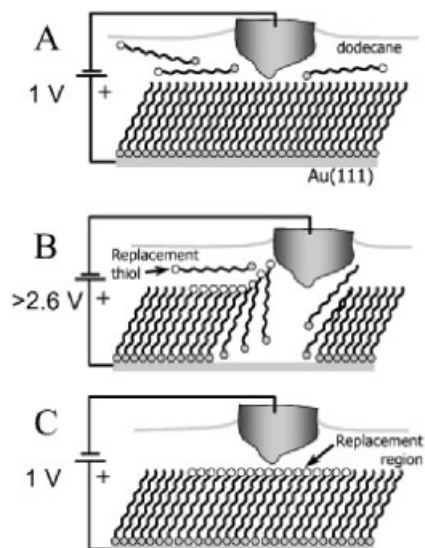


Fig. 5.11 Schematic diagram showing STM replacement lithography. (a) SAM imaged at normal bias. (b) Application of a high-voltage pulse (~ 3 V) produces desorption of the original thiols in the area in the proximity of

the tip. The replacement thiols assemble on the exposed gold area, thus completing the replacement. (c) The replacement pattern is imaged under normal bias (ref. 60a, reproduced with the permission of Wiley-VCH).

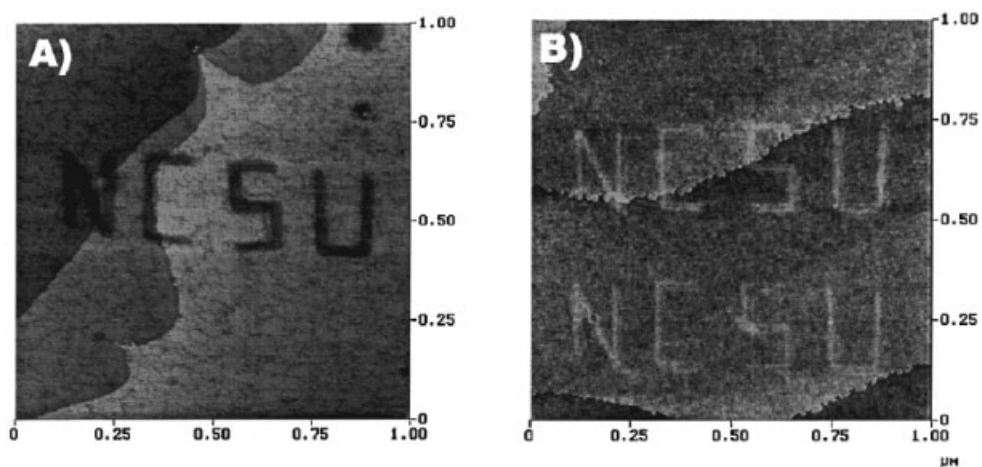


Fig. 5.12 STM images of patterns generated by (A) dodecanethiol replacing decanethiolate ($V_{\text{write}} = 3.8$ V, $V_{\text{read}} = 1.0$ V, $I_{\text{set}} = 6.0$ pA) and (B) decanethiol replacing dodecanethiolate

($V_{\text{write}} = 3.6$ V, $V_{\text{read}} = 1.0$ V, $I_{\text{set}} = 8.0$ pA) (ref. 60b, reproduced with the permission of the American Chemical Society).

Replacement by molecules other than thiols is also possible. Chen and coworkers [61] performed lithographic SAM patterning on a dodecanethiol SAM on an Au(111) surface (pulse voltage 1.8–3.6 V for 0.5 μ s to 0.5 s). The patterned sites were then replaced with more conductive conjugated oligomer molecules that were chemisorbed on the exposed Au surface, thus producing an array of oligomer molecules embedded in an alkanethiol matrix. The authors argued that the sharpness of the tip plays an important role in this process, and therefore that by using a carbon nanotube as the STM tip it might be possible to pursue replacement down to the level of a single molecule.

5.3.2

Template Growth of Molecular Nanostructures

Consolidated thin film growth techniques, such as spin-casting and organic molecular beam deposition (OMBD), do not allow one to control the position and the lateral size of the molecular domains. Growth is a complex phenomenon involving random nucleation, molecular diffusion, and uncorrelated coalescence of domains [62]. To date there is not an established fabrication approach for conjugated organic materials that presets the position, size, and shape of domains.

For these reasons, in recent years there have appeared methods of growth of molecular domains on a surface patterned with nanofabricated structures that acts as a template. The template can be fabricated by a local (electro)chemical reaction confined by the tip. An example is the local anodic oxidation of silicon oxide with a conductive SPM tip [63], to yield nanostructures with a rather modest out-of-plane topography, but a sufficient change in the local stoichiometry/redox state to yield a templating effect.

5.3.2.1 Nanopatterns by Local Oxidation Nanolithography

Local oxidation (or field-induced oxidation) of semiconductor, metallic, and organic surfaces by atomic force microscopy (AFM) is the most robust, reliable, and versatile lithographic method for fabrication of nanometric- and micrometric-scale structures and devices [64–70]. This technique has been used successfully to pattern tunnel junctions [71] and field-effect devices on thin metallic or silicon oxide films [72]. The strong activity developed around this nanolithography technique takes advantage of the simplicity of achieving nanometer-range resolution and of imaging the resulting patterns with the same equipment. We refer the reader to a recent review by Garcia and coworkers [63] for an extensive discussion on the mechanism, the resolution issues, and the applications of local oxidation nanolithography. Here we briefly introduce the principles.

Local oxidation is produced by applying an electric field between the sample and the AFM tip. Figure 5.13 shows a typical experimental scheme illustrating the process of scanning probe oxidation. A positive sample bias is applied between the sample and the grounded probe. The electrolysis within the water meniscus formed between the tip (cathode) and the sample surface (anode) supplies the necessary oxidant anions (mainly OH^- ions). The sample bias applied also provides

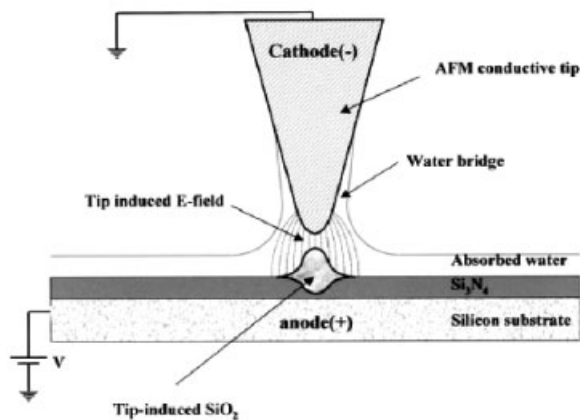


Fig. 5.13 Schematic drawing of the local electric-field induced oxidation using a conductive-probe atomic force microscope in air. The microscope can be operated in contact, noncontact, and tapping mode. The applied sample bias can be either static or

dynamically modulated. The anodic reaction at the sample surface is initiated when the amplitude of the positive sample bias is above a threshold value (ref. 92, reproduced with the permission of Elsevier).

the strong electric field (on the order of magnitude of 10^7 V cm⁻¹) for ion migration into the sample.

The first experiments of anodic oxidation were performed with STM [73, 74] on H-Si passivated surfaces. Then, atomic force microscopy has become the preferred tool for surface nano-oxidation due to its ability to operate with conductive and nonconductive samples. Initially, contact mode AFM was used for local oxidation nanolithography [75, 76] and, more recently, both intermittent contact mode AFM [77, 78] and voltage-modulation techniques [79–82] have been employed. The latter methods yield a higher spatial resolution as well as improving the aspect ratio of the AFM-induced oxide features. Intermittent contact mode AFM oxidation, unlike contact mode AFM, minimizes the dependence of the tip-induced water meniscus on the size of the tip apex, while the voltage modulation technique can be applied to both contact and intermittent contact modes. Modulated pulses with variable peak-to-peak voltage (negative or positive), duty cycles, and frequencies, instead of a static DC voltage pulse, are applied to improve the aspect ratio of the probe-induced oxide. This enhancement is ascribed to a better control of the size of the water meniscus and the decreased charge trapping near the oxide/sample interface.

With these techniques, a variety of materials have been locally oxidized, such as silicon [83], silicon nitride [68], GaAs [84], titanium [85], niobium [86], and aluminum [87]; surface features shaped as dots [88] and patterned parallel lines [89] have been fabricated. These SiO_x motifs have been used for selective growth of inorganic nanostructures: Ge [90] and InGaAs quantum dots [91]; Si [92] and Au [93] nanoparticles.

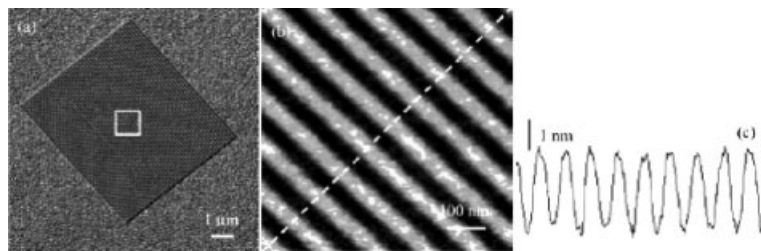


Fig. 5.14 (a) AFM images of a parallel array of silicon oxide lines fabricated by local oxidation nanolithography. The lines are 106 nm apart with an average width of 50 nm. (b) High-resolution image of the region marked in (a). (c) Cross-section along the line shown in (b). The lines protrude 2.6 nm from the substrate baseline (ref. 69, reproduced with the permission of the American Chemical Society).

The first attempts to grow organic nanostructures on SiO_x templates were proposed by Biscarini and García [69]. SiO_x patterns nanofabricated by local oxidation were used as templates to direct the growth of organic molecules on them (Fig. 5.14).

Sexithienyl (T6) molecules were sublimed on an SiO_x surface patterned with 2D array structures made of parallel lines 30–50 nm wide, else on stripes up to 400 nm wide. Biscarini and García [69] showed that the molecules sublimed on the template arranged in monolayer domains of the same shape as the template, but maintaining their molecular orientation as on the substrate outside the template, with their long axis normal to the substrate. The conformal growth of T6 on the template is driven by the interplay between the kinetics of growth and the preferential interactions with the patterned structures. The result is a monolayer film of organic molecules, whose shape reproduces that of the fabricated features (Fig. 5.15).

Template growth has two advantages: it offers the possibility of tailoring the relevant properties of organic devices by controlling the lateral size of the active material to a few tens of nanometers, and it allows one to minimize the amount of active material by defining precisely the transport-active regions [94–96]. Since the length scales of transport phenomena in conjugated materials are in the nanometer range, optimizing the organization at the nanometer scale would lead to an enhancement of the transport properties. As a drawback, there is the extreme sensitivity to the growth conditions that causes the template effect not to be extremely robust to fluctuations in the growth conditions.

Sugimura and coworkers [97] reported other examples of *ex-situ* deposition using an SiO_x template. They fabricated an SiO_x template structure, plowing an octadecylsilyl monolayer (ODS)-SAM grafted on a Si surface by the AFM probe and applying a bias during the plow motion. Where the ODS-SAM is removed, SiO_x grows, creating the template structure. Upon deposition of heptadecafluoro-1,1,2,2-tetrahydrodecyl-1-trimethoxysilane (FAS) by CVD, a chemical reaction occurs only on the oxidized structures, causing FAS to graft only on the template. The samples were monitored before and after by AFM and Kelvin probe force

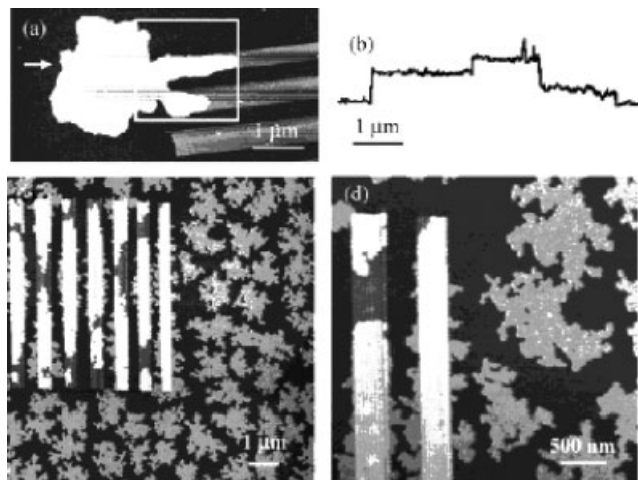


Fig. 5.15 Dynamic AFM images of T6 molecules grown on a parallel set of oxide stripes. (a) Template growth of T6 on local oxide patterns. (b) Cross-section along the line marked in (a). (c) Anisotropic T6 growth on silicon oxide stripes arranged as an array. (d) High-resolution AFM image of the region

marked in (c). The remarkable morphological differences between the T6 nanostructures on the stripes and those T6 islands grown on the bare silicon substrate illustrate the template growth process [ref. 69, reproduced with the permission of the American Chemical Society].

microscopy (KPFM). The large molecular dipole of FAS contributed to surface potentials that were 50 mV higher in the patterned lines than in the surrounding ODS-SAM, as shown clearly in the KPFM images (Fig. 5.16).

Patterns generated by anodic oxidation transferred into the oxide layer by a wet chemical process served as a template for the electroless plating of Au [98]. Here, the plating proceeded selectively on the Si surface due to the galvanic displacement between Si and Au ions, while the ODS-SAM surface remained free of deposits. The line resolution achieved for the electroless plating was 200 nm, which was confirmed with SEM and Auger spectroscopy.

Zheng and coworkers [99] fabricated, by local oxidation, lines 40 nm wide on a silicon wafer surface on which Au nanoparticles were preferentially adsorbed. After SPnL patterning (ca. 8 V, $4 \mu\text{m s}^{-1}$) of a SAM prepared from octadecyltrichlorosilane (OTS) on silica, amine-terminated silanes were self-assembled on the oxidized, patterned areas. Then, 12 nm diameter gold nanoparticles were electrostatically bound to these amine-terminated SAM regions. SEM images showed that the particles were exclusively immobilized on the predefined patterns. Using a methodology similar to that described above, Li and coworkers [100] described the fabrication of lithographic patterns that could trap single gold colloidal particles (Fig. 5.17).

The roles of the humidity, pulse duration, and pulse voltage on the diameter

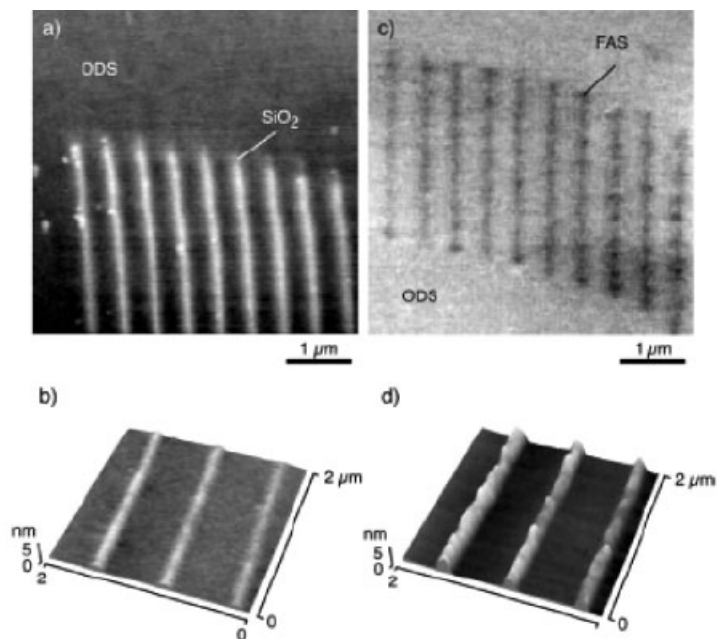


Fig. 5.16 Surface potential and topographic images of fabricated nanostructures with ODS and FAS. KPFM (a, c) and AFM (b, d) images of a nanoscale pattern on ODS-SAM and FAS-

treated sample surfaces. Both KPFM images were taken in air with an applied voltage of 10 V (ref. 97, reproduced with the permission of Wiley-VCH).

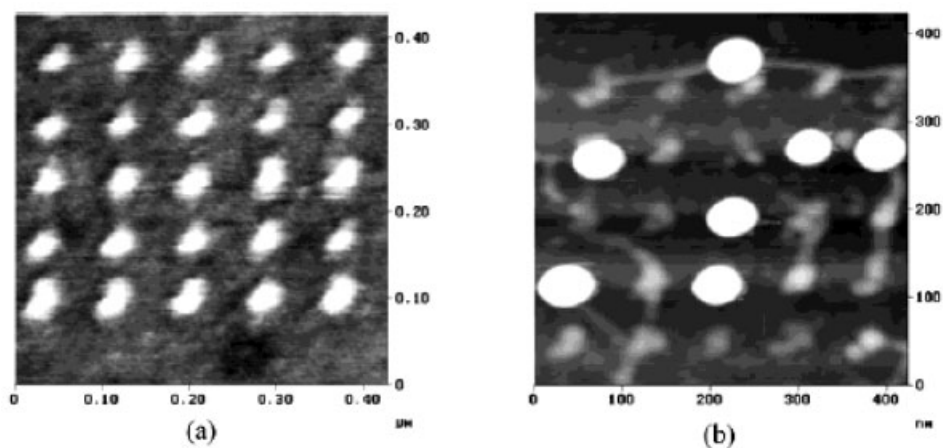


Fig. 5.17 Tapping mode AFM height images of (a) an oxide dot array with a dot diameter of 28 nm (height range: 10 nm) and (b) the corresponding gold nanoparticle array (height range: 30 nm) (ref. 100, reproduced with the permission of the American Chemical Society).

of the oxidized (patterned) dots were studied. Before patterning, OTS-SAMs were incubated in the presence of small silane molecules (phenyltrichlorosilane or 3-(chloropropyl)trichlorosilane) to avoid colloidal binding to the defect sites of the SAM when exposed to the gold nanoparticle (AuNP) solution. The size of the SPnL patterned feature controls the number of particles adsorbed. With a dot diameter of 100 nm, the efficiency for binding 15 nm particles was determined to be 100%. When the diameter was decreased to 28 nm, only 30% of the oxidized/functionalized dots on the surface were found to bind a colloid. The authors estimate that the effective area where the adsorption took place was smaller than the measured diameter of the oxidized area due to an inhomogeneous degradation of the OTS layer. As the dot diameters became smaller, the number of OTS molecules remaining in the patterned region increased, effectively decreasing the number of binding possibilities for the gold nanoparticles. The nonplanar shapes of the oxidized silicon patterns were also believed to contribute to the lower efficiency for binding. Nevertheless, the authors demonstrated the ability to control the number of particles down to the binding of a single Au particle in a single oxidized dot. Fig. 5.17(a) shows an AFM image of the original oxide patterns, and Fig. 5.17(b) depicts AuNP (15 nm diameter) adsorbed onto this structure.

5.3.2.2 Nanopatterns on SAMs

Self-assembled monolayers (SAMs) have emerged as prominent substrates for fabrication of chemically defined nanopatterns [101–104]. Sugimura and coworkers [105, 106] report a method by which a number of molecules can be arranged at one time in positions spatially defined on the near-molecular scale. This approach consists of two steps: fabrication of a template by SPnL and deposition of a monolayer of organosilane molecules. First, a trimethylsilyl $[(\text{CH}_3)_3\text{Si}-(\text{TMS})]$ monolayer is grafted on a native silicon oxide substrate from a precursor $[(\text{CH}_3)_3\text{Si}-\text{NH}-\text{Si}(\text{CH}_3)_3]$, HMDS). The TMS monolayer, (thickness < 1 nm, measured by both AFM and ellipsometry) transforms the silicon oxide substrate from hydrophilic into hydrophobic. The template structure was fabricated with the AFM probe by applying a bias voltage to the probe–sample junction. The electric field generated between the tip and the sample removes the TMS layer locally, transforming the scanned regions into hydrophilic while the regions not scanned remain hydrophobic [107]. Anodization of the Si surface occurs on the patterned regions; therefore these regions are most likely terminated with OH groups and are reactive to organosilane molecules. A (3-aminopropyl)triethoxysilane $(\text{H}_2\text{N}(\text{CH}_2)_3\text{Si}(\text{OC}_2\text{H}_5)_3)$, APS) monolayer was then deposited and expected to react with the template structure. The APS monolayer was labeled with aldehyde-modified fluorescent latex nanoparticles so that the sample could be observed on a fluorescence optical micrograph (Fig. 5.18a).

Figure 5.18(b) shows a magnified image obtained by scanning electron microscopy (SEM) in which the fluorescent nanoparticles are spatially arranged on a submonolayer along the probe-scanned lines. Since specific adsorption was not observed on a sample untreated with the APS solution, the authors concluded that this adsorption is based on the chemical reaction between the APS monolayer and

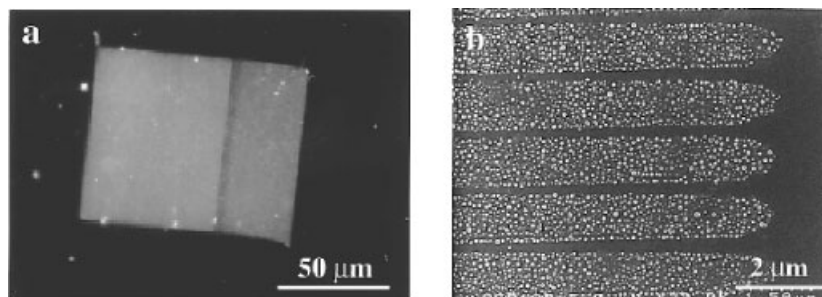


Fig. 5.18 (a) Fluorescence optical and (b) scanning electron images of fluorescent nanoparticles immobilized on an SPM-generated pattern (ref. 105, reproduced with the permission of the American Chemical Society).

surface groups and, furthermore, that this is evidence of the area-selective growth of an APS monolayer on the template structure.

Sugimura and coworkers also reported selective growth of peptides on these template structures (Fig. 5.19). Horseradish peroxidase (HRP) has been selectively assembled on a patterned APS surface using glutaraldehyde as a crosslinker between the APS monolayer and the protein molecules. Figure 5.19(a) shows a topographic image of the sample acquired in the intermittent contact mode. The brighter regions represent 4–5 nm protrusions with respect to the surrounding area. Since this protrusion height is greater than the sum of the substrate anodization thickness and the thickness of the APS monolayer, the authors infer that HRP protein adsorption has taken place onto these regions. The phase contrast image acquired simultaneously with the topographic image confirms the occurrence of

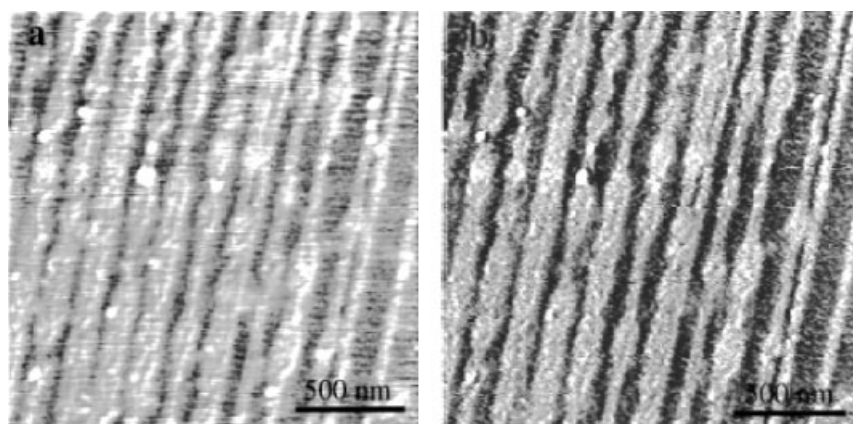


Fig. 5.19 AFM topography (a) and phase (b) images of an APS-treated sample modified with HRP (ref. 112, reproduced with the permission of the American Chemical Society).

protein adsorption (Fig. 5.19b). It is known that adsorbed organic molecules exhibit a larger phase lag than a rigid substrate due to the difference in softness and/or viscosity between them [108]. As may be clearly seen in Fig. 5.19(b), the protruding region in Fig. 5.19(a) exhibits a larger phase lag than the surrounding region, where there were no adsorbates.

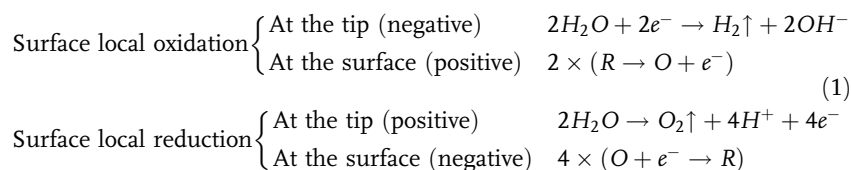
5.3.3

Constructive Nanolithography

In constructive nanolithography (CNL), introduced by Jacob Sagiv [109], an electrically conducting AFM tip operating in contact mode is used to write chemical information nondestructively on the exposed surface of a self-assembly monolayer. The initial nanopattern can be developed further in a controlled manner, by the application of post-patterning surface chemical functionalization [110]. By applying an appropriate positive (or negative) bias voltage during the scan, the conductive tip oxidizes (or reduces) the surface of a highly ordered monolayer (Fig. 5.20a). As for the local oxidation of silicon, to oxidize (or reduce) the monolayer a conductive substrate is needed.

Scanning the surface in a predetermined path with the biased AFM probe results in a pattern of oxidized (reduced) regions. This pattern acts as a superficial template for molecules that have complementary interactions with the modified end groups, so a second organized monolayer conformal with the fabricated pattern is formed (Fig. 5.20b). Playing with the surface chemical activation, different chemical reactions can be exploited and different molecules can be organized.

The pattern fabrication on the monolayer depends on the applied bias and the ambient relative humidity. Either humidity or the vapour of other electrolytes is necessary in order to form the water bridge between the AFM tip and the surface. As in local oxidation, this bridge acts as a nanosized electrochemical cell between the tip and the surface. Negative tip bias is applied for the process of surface oxidation; in this case, the AFM tip, works as the cathode (i.e., the electrochemical reduction occurs at the tip). Positive tip bias is applied for the process of surface reduction; in this case the AFM tip works as the anode (i.e., the electrochemical oxidation occurs at the tip). In order to make the tip conductive, it is coated with a noble metal (such as Au or Pt) with a redox potential higher than water, so that water is oxidized instead of the tip coating. Using water as electrolyte, the products of the chemical reaction are gas and soluble species (Eqs. (1), where O, R and \uparrow indicate the oxidized, the reduced, and the gas species respectively). A higher bias voltage is required in case of low humidity conditions, though the optimal experimental parameters must be searched specifically for each system.



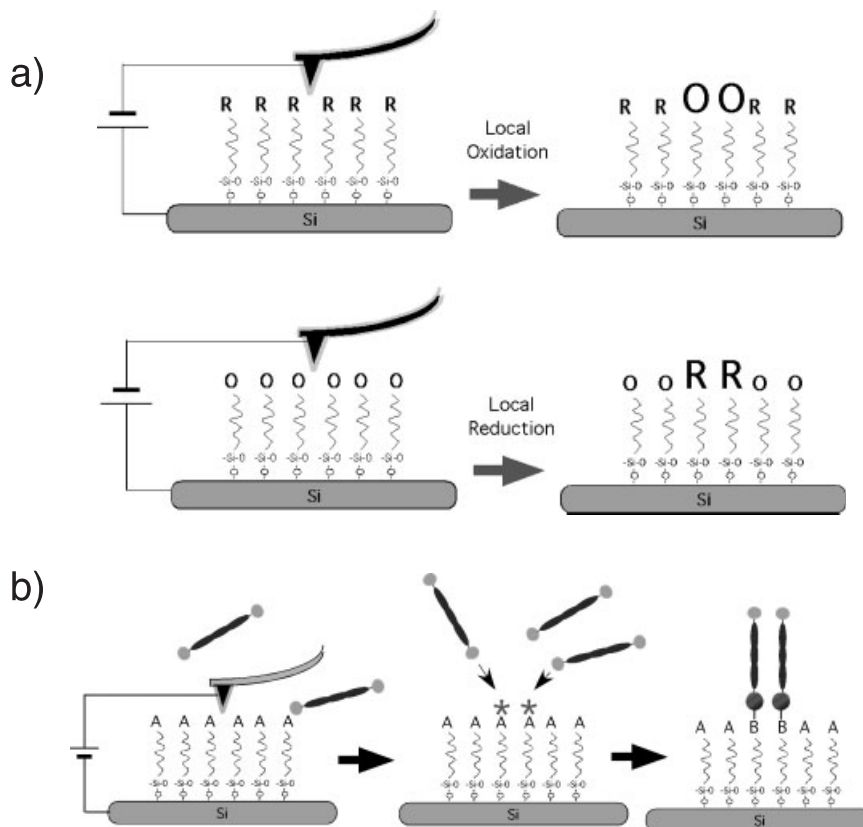


Fig. 5.20 (a) Scheme for the local electro-oxidation and local electroreduction of two possible monolayers. **O** and **R** stand for the oxidized and reduced groups respectively. (b)

Generic schematics of the CNL process. After local oxidation (reduction) the pattern can be developed further by surface chemical functionalization.

5.3.3.1 Nanolithography by Local Electrochemical Oxidation

A representative example of the local electrochemical oxidation is the oxidation of *n*-octadecyltrichlorosilane (OTS) monolayers. OTS is very important in organic electronics where it is used to prime the gate dielectric of organic field-effect transistors (OFETs).

Compared with other methods, CNL allows the control of the chemical species produced, by the applied bias. Maoz and coworkers [111] demonstrated how, at constant humidity, the application of three bias levels gives rise to three distinct modes of pattern formation (Fig. 5.21).

The experiment was performed on an OTS monolayer, oxidized by CNL and again immersed in OTS solution to enhance the effect of bias voltage in CNL. When a moderate positive bias is applied at the surface, between +8.5 and

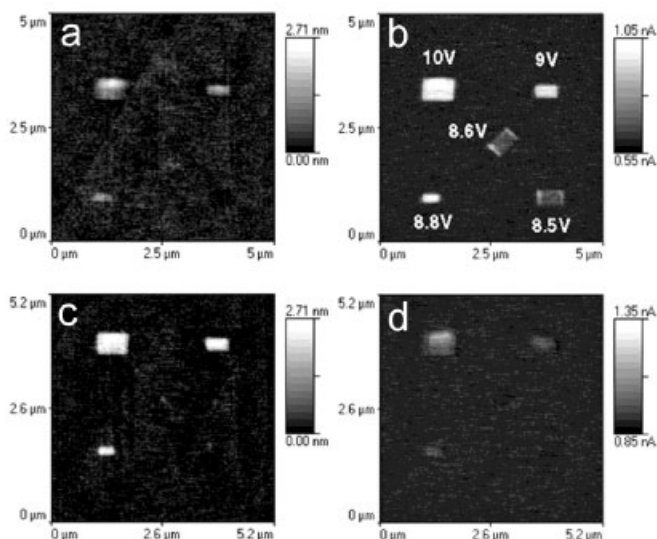


Fig. 5.21 Simultaneously recorded topography and friction in contact mode AFM images, demonstrating three distinct modes of nanoelectrochemical pattern formation in a self-assembled OTS monolayer on silicon, as a function of the bias voltage applied between the surface and the tip (see text). (a), (b) After pattern inscription. (c), (d) After treatment of the patterned surface with a 5 mM solution of

OTS in bicyclohexyl (BCH). Nondestructive patterning gives rise to features initially characterized by high friction contrast and low topography contrast (in (a) and (b)), the contrast being reversed (as with the +9 V and +8.8 V rectangles) after OTS treatment (ref. 111, reproduced with the permission of Wiley-VCH).

+8.6 V, the AFM images do not show any appreciable contrast in topographic mode (Fig. 5.21a). The contrast became visible only in lateral force mode (Fig. 5.21b), which is sensitive to the friction between the AFM tip and the surface [112]. Upon OTS treatment (Fig. 5.21b), the friction contrast disappeared. The explanation of this behavior is that, in the bias range between +8.5 and +8.6 V, some molecules of the OTS monolayer are removed without being oxidized. In the subsequent OTS solution treatment, new molecules replace them as a result of tip-induced cleavage of the siloxane bonds responsible for intralayer and layer-to-surface bonding. This explanation accounts also for the effect of a higher bias. In the range between +8.8 and +9.0 V (relative to the tip), very small changes in topography (Fig. 5.21) were observed with respect to the native surface, whereas a strong contrast appears in the lateral force map.

Upon exposure of the sample to an OTS solution (Figs. 5.21c,d) a topographic contrast of thickness about 2.4 nm was observed, but the contrast in the lateral force disappeared. The step height was consistent with the OTS length. This shows that only the outer surface of the OTS monolayer was modified by electrochemical oxidation of $-\text{CH}_3$ groups under these conditions. The exposure to the OTS solu-

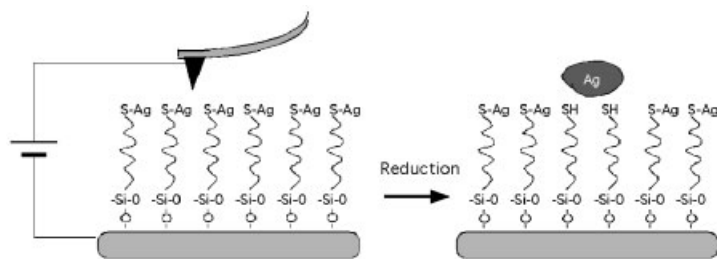


Fig. 5.22 Silver ions chemisorbed on a TFSM electrochemically reduced.

tion resulted in the self-assembly of a second OTS monolayer on top of the pattern. Finally, upon application of a bias of more than +10 V, besides the marked change in surface friction (Fig. 5.21b) a distinct topographic spot became visible (Fig. 5.21a), which remained partially visible after the exposure to the OTS solution. This behavior suggests that excessive bias induces underlayer growth of silicon oxide, in addition to the oxidation of the top methyl groups with possible structural damage to the organic monolayer.

5.3.3.2 Nanolithography by Local Electrochemical Reduction

Similarly to the local electrochemical oxidation concept, Maoz and coworkers [113] have been using CNL to create patterns by chemical reduction of the SAM surface. They have reduced the surface of a thiol-top-functionalized silane monolayer (TFSM) locally by AFM and then chemisorbed silver ions on it (Ag^+ -TFSM). The scheme of the process is shown in Fig. 5.22.

By this nanolithographic process, patterns of metallic silver nanoparticles can be fabricated at selected surface sites, simply by the electrochemical reduction of the surface-bound metal ions by an AFM tip. Figure 5.23 shows representative AFM images of metal particles generated by tip-induced nanoelectrochemical reduction of TFSM-bound silver ions. The clusters of nanoparticles have typical height of 2–3 nm and are composed of single particles with diameters of 20–30 nm (Fig. 5.23b). Isolated particles exhibit 5–6 nm height and lateral size of about 30 nm. The resulting particles from the electrochemical reduction reflect the interplay between tip (size and shape) and reduction pattern.

5.3.3.3 Additional Examples of Patterning by CNL

The CNL approach has been exploited for specific applications with prepatterned surfaces. Schmid and coworkers [114–116] have demonstrated that a layer of Au nanoparticles from a water-soluble precursor ($[\text{Au}_{55}(\text{Ph}_2\text{PC}_6\text{H}_4\text{SO}_3\text{Na})_{12}\text{C}_{16}]_2$) can be assembled on bilayer template patterns functionalized by thiol ($-\text{SH}$). The chemical mechanism exploited is ligand exchange, which favors the specific binding of the clusters to the thiol-terminated sites [116]. The general scheme of the process is shown in Fig. 5.24.

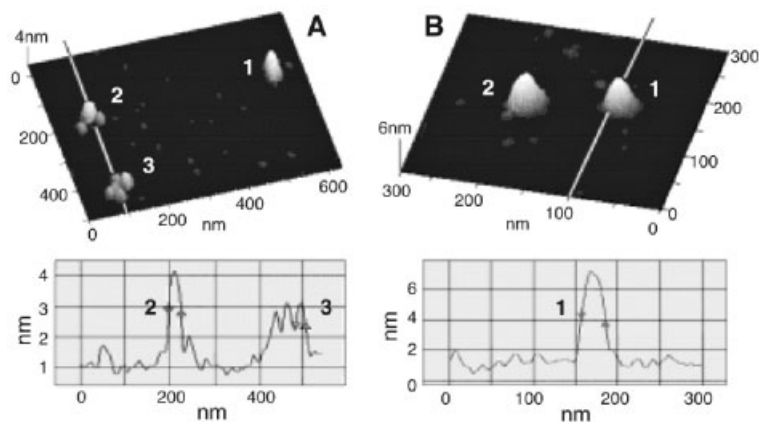


Fig. 5.23 AFM images of Ag^+ on a TFSM template. The images consist of three and two features chemisorbed on the same TFSM, but with two different tips. The pattern was fabricated in contact mode with a pulsing bias

of about 5 V and pulse lengths of 40–150 ms. The particle dimensions are evident in the profiles (along the marked lines) shown below (ref. 113, reproduced with the permission of Wiley-VCH).

Similarly, Sagiv and coworkers [110, 117] patterned gold lines starting from an OTS monolayer. The tip oxidizes the OTS to carboxylic acid (COOH) groups on the top surface of the OTS (C_{18} , *n*-octadecyltrichlorosilane) monolayer self-assembled on the surface of a silicon substrate. Subsequently the patterned OTS

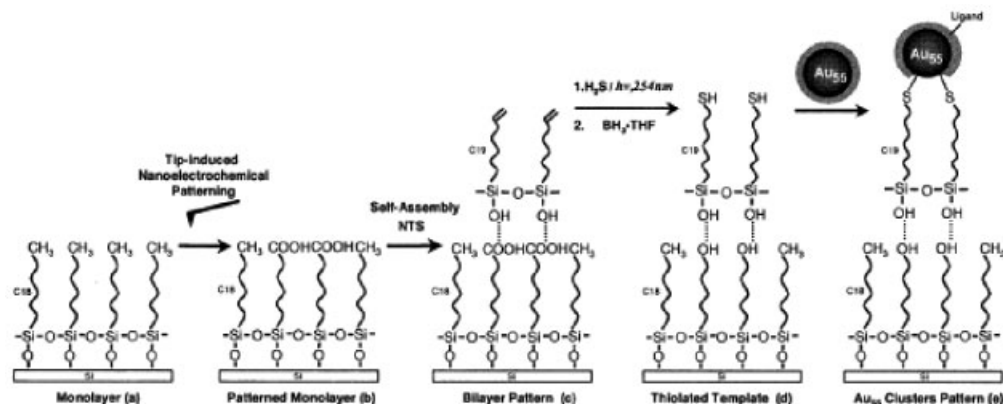


Fig. 5.24 Schematic representation of the fabrication of an organosilane template pattern with top thiol functionality and the selective self-assembly of Au nanoclusters on the template (ref. 119, reproduced with the permission of the American Chemical Society).

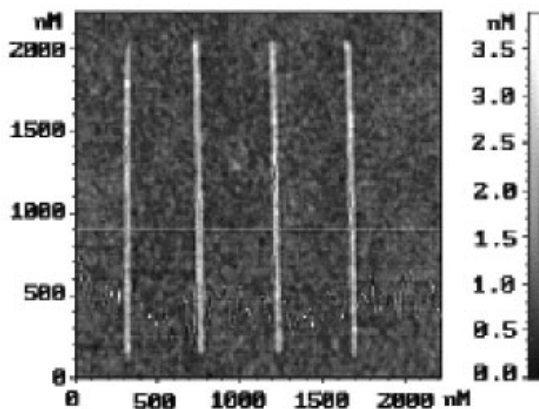


Fig. 5.25 AFM topographic images of a pattern of parallel lines after the assembly of Au nanoclusters on the bilayer pattern (ref. 126, reproduced with the permission of the American Chemical Society).

surface is exposed to a solution of NTS (C_{19} , nonadecyltrichlorosilane), resulting in the selective self-assembly of a monolayer with terminal ethylenic functions ($-\text{CH}=\text{CH}_2$) on the tip-inscribed sites [118].

Photochemical radical addition of H_2S follows a chemical reduction of the fraction of disulfide ($-\text{S}-\text{S}-$) groups produced in the process, and transforms the NTS to a thiolated overlayer. Since only the carboxylic acid groups can react with NTS, the final thiol pattern corresponds to the initial pattern of carboxylic acid groups. If the patterned surface is immersed in a solution of Au nanoclusters, these will be adsorbed on the exposed thiol groups. Figure 5.25 shows an example of patterned lines of gold clusters, fabricated by this method [119].

In conclusion, CNL appears to be an extremely versatile technique for nanofabrication of functional patterns. It combines the resolution and ease of SPnL with the chemical concepts of self-assembly, specific interactions, and reactivity.

5.3.4

Catalytic Probe Nanolithography

Scanning catalytic probe lithography (SCPL), introduced by Müller and coworkers [120], defines a surface pattern exploiting the reactivity of molecules deposited on a surface. By a catalyst-functionalized AFM tip, it activates the surface locally without applying any voltage.

Fig. 5.26 is a schematic illustration of SCPL. The tip activates the chemical end group of a reactive monolayer grafted onto a surface. The activated molecules on the surface react with chemicals present in the environment.

In the first attempt of this technique Müller, used an AFM tip coated with Pt to

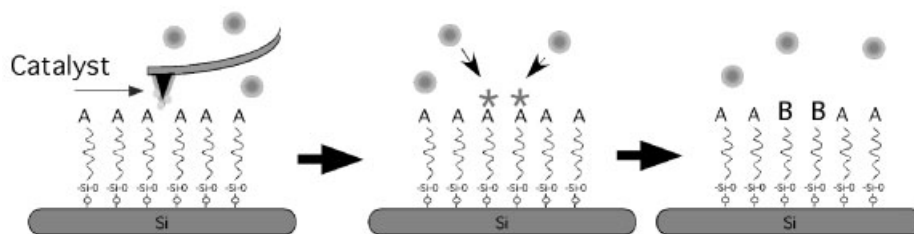


Fig. 5.26 Scheme of scanning catalytic probe lithography.

reduce the terminal azide groups of a monolayer to amino groups. More recently, Reinhoudt and coworkers [121] used SCPL successfully to nanofabricate patterns of reactive adsorbates on self-assembled monolayers. Catalytic writing was carried out by scanning over bis(*tert*-butyldimethylsiloxyundecyl) disulfide self-assembled monolayers using 2-mercapto-5-benzimidazole sulfonic acid-functionalized gold-coated AFM tips (Fig. 5.27). In this example, the acidic tips induced local hydrolysis of the silyl ether groups in the contacted areas, creating a patterned surface.

The smallest lines drawn by this technique were about 25 nm wide, corresponding to the size of actual contact of the tip. Often, as in the case of constructive nanolithography, the chemical transformations are not topographically sizable. Lateral force microscopy (LFM), which is sensitive to the friction, turns out to be the best method for imaging the SAM transformations. Structures with well-defined shapes and sizes were created using SCPL in TBDMS SAMs (Fig. 5.28).

SCPL is a technique with a potential impact in several applications, including the upscaling from serial to parallel methods. Examples are:

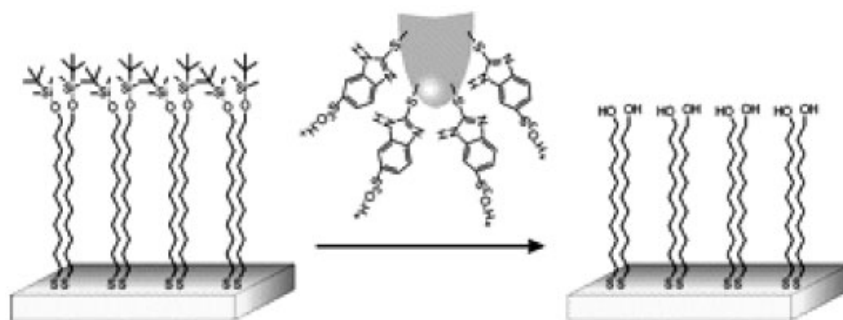


Fig. 5.27 Hydrolysis of bis(*tert*-butyldimethylsiloxyundecyl)disulfide SAMs using 2-mercapto-5-benzimidazole sulfonic acid-functionalized gold-coated AFM tips (ref. 121, reproduced with the permission of the American Chemical Society).

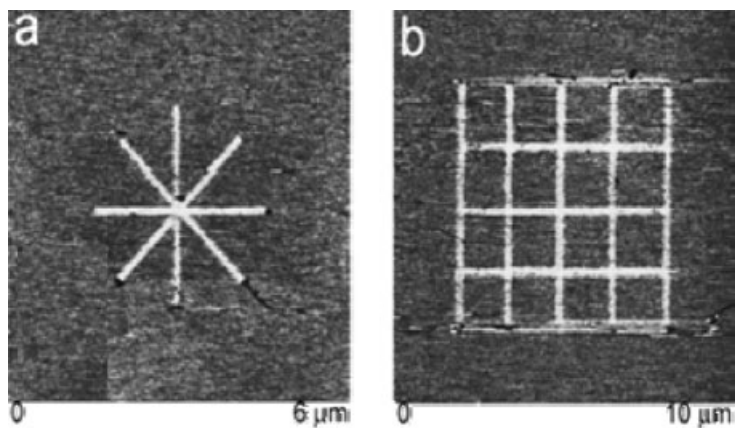


Fig. 5.28 AFM friction images (z range 0.2 V) of nanostructures created on TBDMS SAMs by catalytic probe lithography. Scan size: (a) $6 \times 6 \mu\text{m}^2$; (b) $10 \times 10 \mu\text{m}^2$ (ref. 121, reproduced with the permission of the American Chemical Society).

- selective reduction of a monolayer of imines formed from the reaction of cystamine molecules with cyclopentanone to their corresponding secondary amines within a well-defined region [122];
- tip-assisted base hydrolysis of an ester-terminated alkanethiolate monolayer on Au(111), where the contact between the AFM tip and the surface accelerates the base hydrolysis of a dithiobis(succinimidoundecanoate) monolayer relative to the surrounding area. It been proposed that tip-assisted base hydrolysis starts with the mechanical disruption of the neighboring adsorbates by the tip changing their steric barrier, facilitating the access of hydroxide ions near the buried acyl carbons in the adlayer. Finally, the surface area scanned by the tip is hydrolytically transformed by this disruption. This process is controlled by the SFM imaging conditions [123];
- chemical reactions of terminal functional groups of organosiloxane surface assemblies [124]. The chemical reactions induced by a catalytically active palladium-coated tip result in a lithographed pattern with minimum measured line widths of 33 nm.

The limitations of SCPL are due to the use of catalytically active AFM tips, which are not easy to prepare, and the need of reactive thin films [125, 126].

5.3.5

Nanografting

The SPnL techniques described above exploit AFM with an applied voltage to create the lithographic pattern. Alternatively, the pattern can be created *in-situ* by re-

moving mechanically the molecules from the region of a SAM. This mechanical plowing was developed by Xu and coworkers [127] and termed “nanoshaving.” SAMs were first imaged with a low force to find a suitable area, and then plowed. In “nanografting,” nanoshaving is performed in a solution containing a second thiol so that, as the molecules are removed from the first SAM, they are replaced simultaneously by the thiol molecules in the solution.

Taking advantage of the sharpness of the tip and the localized tip–surface interactions, features with lateral size much smaller than any other SAM-based lithographic technique (i.e., microcontact printing) can be fabricated.

Nanografting includes three steps (Fig. 5.29). The first is the characterization of the matrix SAM to select the area for fabrication. During this process, the surface structure of the matrix SAM is imaged by AFM under a low load force below 1 nN (Fig. 5.29a). The second step is the fabrication of the desired patterns in the selected region of the SAM. In this step, SAMs molecules are removed by scanning these areas with an AFM tip at a force greater than the threshold displacement force.

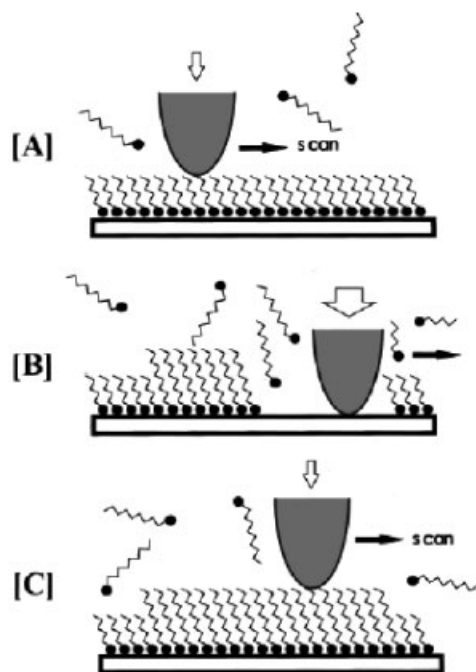


Fig. 5.29 Schematic diagram of the nanografting process. (A) Matrix SAM imaged at a low imaging force in a 2-butanol solution of another thiol. (B) At a force greater than the threshold, the AFM tip displaces the adsorbates on the desired areas, and the thiol

molecules in the contacting solution self-assemble onto the exposed gold sites. (C) The nanopattern is imaged at a reduced imaging force (ref. 133, reproduced with the permission of the American Chemical Society).

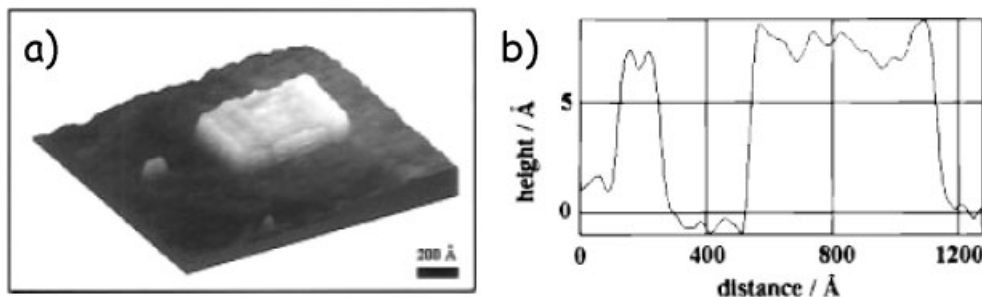


Fig. 5.30 (a) Topographic 3D image of two fabricated $C_{18}S$ nanoislands (brighter areas) inlaid in the matrix $C_{10}S$ monolayer. As shown in the line profile (b), the $C_{18}S$ islands are 8.8 Å

higher than the surrounding $C_{10}S$ monolayer (ref. 127, reproduced with the permission of the American Chemical Society).

As the molecules are removed from, new alkanethiol molecules from the contacting solution are immediately adsorbed onto these areas, following the scanning track of the AFM tip (Fig. 5.29b). The final step is to characterize the patterned SAMs using the same AFM tip at a reduced imaging force (Fig. 5.29c). The geometry of the resulting patterns is defined by the scanning trajectory while the lateral resolution and the feature size depend on the sharpness of the AFM tip, as well as the thermal and mechanical stability of the AFM. The dimensions of patterns are typically 20 nm for the lateral size and 1 nm for the height of the patterns (Fig. 5.30) [127].

To obtain compact ordered structures within the SAM it is important to take into account sample parameters such as interactions between molecules and substrates, SAM stability, crosslinking among molecules of the nearest neighbors [128] packing energy, and the long/short-range order of the SAM [129, 130].

Due to these experimental compromises, Liu and coworkers [131] had been studying the influence of experimental parameters, such as the fabrication force, the scanning speed, the solvent, and the concentration of the thiol solution, on the final patterns. Since the geometry and chemical nature of AFM tips vary, the corresponding threshold force must be determined for each tip before starting the fabrication process. The threshold is determined by monitoring the changes in surface structure as a function of increasing load force. The structural changes are preferably monitored from the molecular resolution images taken across relatively small scanning areas (typically, 3×3 – 25×25 nm²). Under low imaging forces, topographic images reveal the molecular packing within the SAM. Figure 5.31(a–c) shows an ordered octadecanethiol monolayer on gold (abbreviated as $C_{18}S/Au$) and a disordered octadecyltriethoxysilane layer on mica (OTE/mica), respectively. As the load force increases, the images remain unchanged at first and become increasingly distorted at higher forces.

A continuous increase in the imaging force results in a transition in the AFM image from the SAM lattice to that of the substrate. Figure 5.31(b,d) reveals that

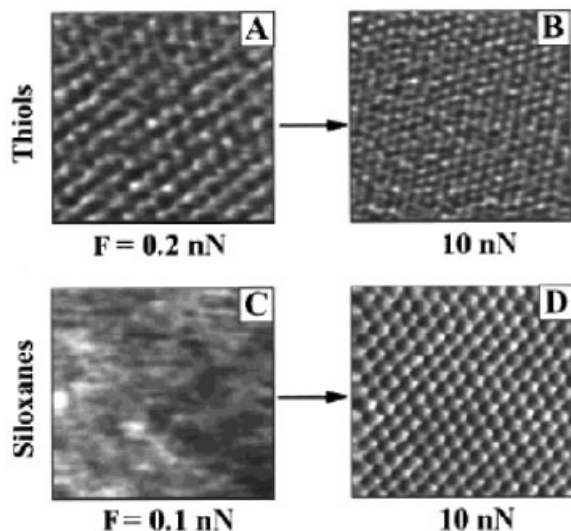


Fig. 5.31 Determination of threshold force. Topographic images ($5 \times 5 \text{ nm}^2$) of (A) $\text{C}_{18}\text{S}/\text{Au}(111)$ and (C) OTE/mica taken in 2-butanol. At a load of 10 nN, images A and C changed to the periodicity of (B) Au(111) and (D) mica(0001), respectively. The threshold forces are 9.5 and 9.6 nN, respectively, which correspond to a pressure of 0.4 GPa based on the Hertzian model (ref. 131, reproduced with the permission of the American Chemical Society).

both Au(111) and mica(0001) have hexagonal symmetry with lattice constants of 2.88 and 5.18 Å, respectively. The load force at which the transition occurs is referred to as the displacement threshold. In the experiments shown in Fig. 5.31, the displacement thresholds for $\text{C}_{18}\text{S}/\text{Au}$ and OTE/mica are 9.5 and 9.6 nN, respectively.

The concentration of thiol-functionalized molecules in solution does not represent a critical parameter because nanografting can be achieved successfully in concentration ranges between 2 μM and 2 mM. Instead, the order of the SAM and the displacement of the molecules on the surface depend on the solvent used.

Finally, the results of nanografting are sensitive to the scan rate, as slow scans often produce pattern distortion due to thermal drifts while fast scans do not produce patterns with high coverage. Scan rates ranging from 100 to 2000 nm s^{-1} result in the rapid and reproducible formation of patterns with well-defined geometry and sharp edges.

The chain length of the thiol molecules plays a role in creating positive or negative patterns. It does not affect the nanografting process because the islands are well ordered and densely packed but, depending upon the relative chain length between the new and matrix adsorbates, islands that are protruding or depressed [132, 133] can be fabricated. Figure 5.32a shows two C_{18}S nanoislands fabricated in a matrix of $\text{C}_{10}\text{S}/\text{Au}(111)$. It is important to point out that the newly grafted

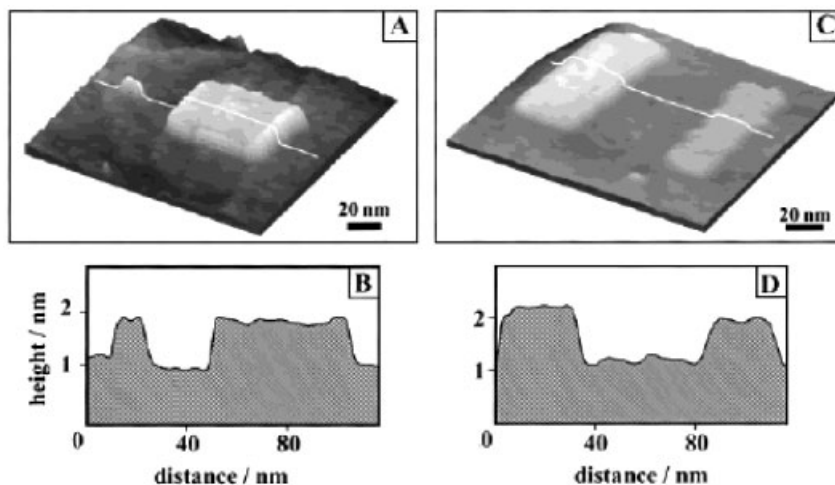


Fig. 5.32 (A) Fabrication of two $C_{18}S$ nanoislands (3×5 and $50 \times 50 \text{ nm}^2$) in the matrix of a $C_{10}S$ monolayer using nanografting. As shown in the cursor profile (B), the $C_{18}S$ islands are 8.8 \AA higher than the surrounding $C_{10}S$ monolayer, consistently with the theoretical value for crystalline-phase SAMs. (C) Fabrication of multicomponent patterns using nanografting. The dimensions of the

$C_{22}S$ (left) and $C_{18}S$ (right) islands are 30×60 and $20 \times 60 \text{ nm}^2$, respectively. (D) The corresponding cursor profile shows that the $C_{18}S$ and $C_{22}S$ islands are (7.5 ± 1.0) and $(12.0 \pm 1.5) \text{ \AA}$ taller than the $C_{10}S/Au$ matrix monolayer, respectively (ref. 131, reproduced with the permission of the American Chemical Society).

$C_{18}S$ nanoislands not only exhibit an ordered and close-packed lattice but also have fewer defects such as pinholes or uncovered areas. During the time frame of nanofabrication experiments (hours to tens of hours), there were no observable exchange or desorption reactions. The absence of pinhole defects and exchange reactions is critical for a reliable pattern transfer when the patterned SAMs are used as masks. Using the same procedure, Xu and coworkers [133] have successfully patterned thiols with various chain lengths from 2 to 37 carbons (C_2SH , C_6SH , $C_{16}SH$, $C_{22}SH$, and $C_{18}OC_{19}SH$). The observed heights and high-resolution images of these nanopatterns indicate that the thiols are close-packed within the patterns.

By changing the thiol solution above the matrix layer before each nanografting experiment, it has been possible to fabricate multiple nanopatterns with desired arrangements and compositions of thiols. Figure 5.32(c) shows two patterns of different heights. First, a rectangular $C_{18}S$ pattern ($20 \times 60 \text{ nm}^2$) was grafted within a $C_{10}S$ matrix SAM. The solution was then replaced with a 0.2 mM $C_{22}S$ solution, and a second rectangular pattern ($30 \times 70 \text{ nm}^2$) of $C_{22}S$ was grafted near the $C_{18}S$ islands. The $C_{18}S$ and $C_{22}S$ patterns were parallel to each other and were $(0.80 \pm 0.05) \text{ nm}$ and $(1.17 \pm 0.03) \text{ nm}$ higher than the surrounding $C_{10}S$ matrix (Fig. 5.32d), respectively. Molecular resolution images of the two nanoislands indicated that the chains were closely packed within the nanoislands.

The ability to produce multiple patterns regiospecifically from different adsorbates satisfies a basic requirement for fabrication of various nanoelectronic devices and sensor arrays, e.g., biochips. In this technological application field, nanografting has proven its potential to fabricate well-ordered nanostructures of typical elements useful for biosensors (e.g., single-stranded DNA (ssDNA) [134], proteins [135] and metalloproteins).

For proteins and metalloproteins, Scoles and coworkers¹³⁶ have used nanografting to pack and orient out-of-plane a three-helix bundle of metalloproteins on a Au(111) surface. They have removed a small area of octadecanethiol SAMs and exchanged it with the proteins. The resulting “nanografted” metalloproteins were imaged and measured. The height of the octadecanethiol monolayer was 2.2 nm and the mean height above this of the grafted metalloprotein layer was 3.1 nm; thus the total height of the grafted metalloprotein was 5.3 nm, in good agreement with the theoretically predicted height. Later, Scoles and coworkers applied the same process to a 4-helix bundle termed S-824-C [137]. Conversely to the previous experiment, they found that the average height of the grafted protein patterns was somewhat greater than expected height. Compression of the nanografted patches by an external force (below 10 nN) was reversible but showed some hysteresis. Interestingly, both the energy required to deform the immobilized protein patterns and the energy extracted from the force hysteresis loop were found to be of the same order as the energy required to unfold the monomer protein in solution (Fig. 5.33). The authors have attributed this behaviour to a different structure in which the protein folds upon adsorption to the gold substrate.

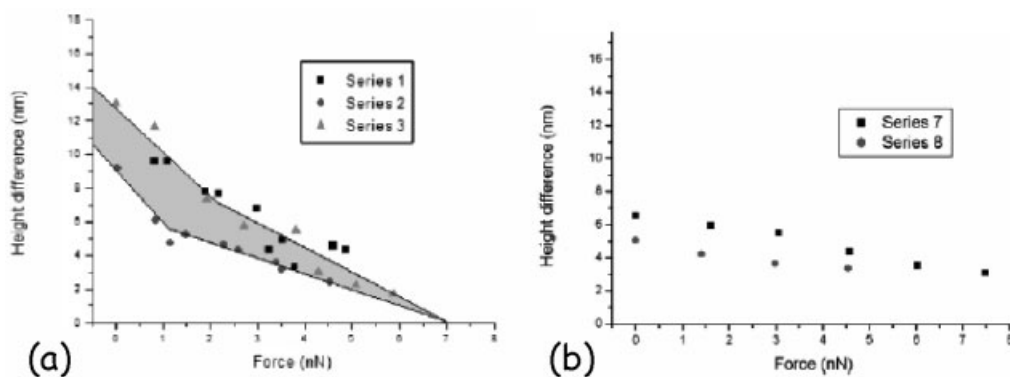


Fig. 5.33 Height differences between grafted protein patches and the C_{18} matrix were measured as a function of the imaging force. (a) Series 1–3 are sequential studies of the same pattern. All scans were obtained starting at low force values, which were increased gradually to their maxima. Series 1 and 2 were obtained within a 30 min time span, whereas series 3 was obtained 3 h later (a single scan

lasts 1.5 min). The shaded area between the two curves represents the energy stored in the proteins compressed by the tip. (b) Series 7 and 8 show similar measurements on another protein patch. Both series were obtained in a 16 min time span (ref. 137, reproduced with the permission of the American Chemical Society).

For DNA, the variations of the fabrication parameters, such as the concentration of ssDNA or lines per frame, allowed one to control the density of ssDNA molecules within the nanostructures, while the immobilization of three proteins (lysozyme, rabbit IgG, and bovine carbonic anhydrase II) was studied by Zhou and coworkers [135] using an approach that combines electrostatic immobilization and specific protein–protein interactions, demonstrating that the combination of nanografting, electrostatic immobilization, and specific protein interaction is a powerful tool for construction of novel 3D protein surface nanostructures (Fig. 5.34).

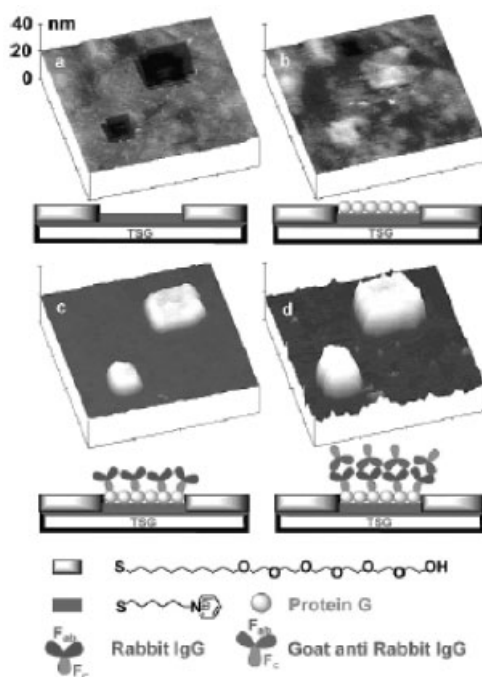


Fig. 5.34 3D AFM topographic images showing the process of creating and growing the 3D protein nanostructures by electrostatic immobilization and biospecific interaction. The schematics underneath each image show the fabrication process of the 3D protein nanostructures. All of the images have the same scan areas ($2 \times 2 \mu\text{m}^2$) and the same z scale. (a) Two nanopatches (200×200 and $400 \times 400 \text{ nm}^2$) created by nanografting of MHP Br (*N*-(6-acetylthiohexyl)pyridinium bromide) into the SAM of C_{11}EG_6 had a depth of 2 nm. The curious features in the image

were the results of piezo drift during the nanografting process. (b) After incubation of the surface with protein G, the patches were completely filled by protein G and transformed into plateaus with an average height of ca. 1 nm. (c) After a treatment of the surface with rabbit IgG, the height of the protein features increased to 8–9 nm. (d) After subsequent treatment of the surface with goat anti-rabbit IgG, the height of the protein features increased to 19–20 nm ref. 135, reproduced with the permission of the American Chemical Society).

5.4 Outlook and Conclusions

Scanning probe nanoithography (SPnL) has been demonstrated to be a powerful method for patterning molecular nanostructures because of the feature size and the resolution that can be achieved at the nanometer scale, together with sustainable processing requirements. This makes SPnL possibly the most versatile technique for nanopatterning molecules, polymers, and soft matter in general. SPnL is a unique technique also because it allows us to quantify the energetics involved in the formation of the nanostructures as well as in the roles of specific/preferential interactions. This information is extremely valuable for exploring the scaling behaviour of intermolecular interactions and other physicochemical properties (mechanical, electronic, and optical), but especially for devising novel patterning approaches. The relevance of SPnL for upscaling nanofabrication methods to technologically viable techniques based, e.g., on multiple tips or protrusions, is definitely unparalleled. Upscaling SPnL seems nowadays the most promising route, in view of the fact that the improvement of factors such as scan rate and area accessible to a single probe is extremely challenging, if not problematic, to fulfill.

If upscaling is a major challenge nowadays, the downscaling of fabrication by SPnL, and especially the ease with which multiple length scales can be fabricated and studied by SPnL, are features of major relevance. By the use ultrasharp probes, e.g., nanotubes with diameters up to a few nanometers, it can be imagined that patterning down to the size of one or a few molecules can be achieved. This may lead to a convergence between fabrication and manipulation of individual molecules, with the result of tailoring properties not only by the size, but also by imparting a defined shape or organization of hybrid architectures at surfaces. An example

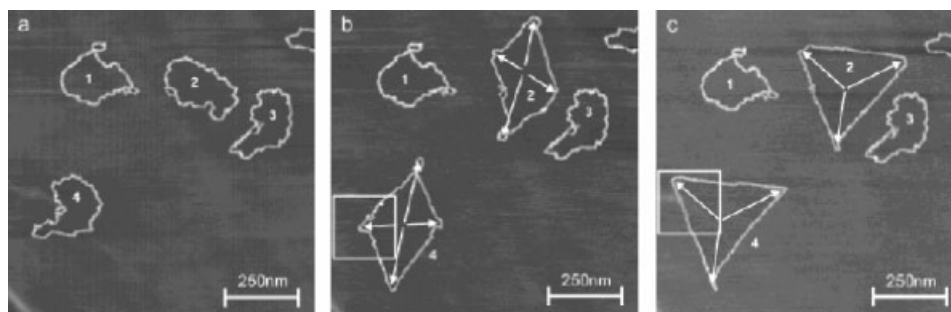


Fig. 5.35 SFM images of double-stranded (ds) DNA adsorbed on a graphite surface modified with $\text{CH}_3(\text{CH}_2)_{11}\text{NH}_2$ molecules. Manipulation was performed by bringing the tip into contact with the surface and moving it in the desired direction, using homemade manipulation hardware and software: (a) ds-plasmid DNA molecules as deposited; (b) after stretching two of them (nos. 2 and 4) along the white arrows; (c) after manipulation of the same molecules into triangles (ref. 138, reproduced with the permission of the American Chemical Society).

which may illustrate a potentially interesting trend is the work of Rabe and co-workers [138] who were able to change the geometry of plasmid DNA molecules from their “natural” quaternary structure on the surface to regular objects such as squares and triangles. This transformation was achieved by bending and stretching molecular segments to remove defects and to overstretch double-stranded DNA into two parallel single strands (Fig. 5.35). By the same approach, the same authors were able to connect polymer strands, then linking them covalently by a photochemical reaction, to create a new single-polymer chains starting from two smaller units [139].

In general, the emerging trend of SPnL is indeed linked to the control of a variety of phenomena confined in nanosized domains, from chemical reactions to self-assembly, from self-organization to biochemical recognition. SPnL will become increasingly more pervasive in all those fields in which the construction of nano-sized architectures at will from soft matter plays a central role.

Acknowledgements

The authors acknowledge financial support from the EU under project no. EU-NMP4-CT-2004-500355 (NAIMO) and EU-NMP3-STREP-013684 Force Tool. We thank Paolo Samorì, Ricardo García, Enzo Palermo, and Jean François Moulin for useful comments.

References

- 1 C. R. K. MARRIAN, F. K. PERKINS, S. L. BRANDOW, T. S. KOLOSKI, E. A. DOBISZ and J. M. CALVERT, *Appl. Phys. Lett.* **64**, 390 (1994).
- 2 K. WILDER, H. T. SOH, A. ATALAR and C. F. QUATE, *J. Vac. Sci. Technol. B* **15**, 1811 (1997).
- 3 H. T. SOH, K. WILDER and C. F. QUATE, *Scanning Probe Lithography*, Kluwer Academic Publishers, Massachusetts, 2001, pp. 37–130.
- 4 M. CALLEJA, J. ANGUIA, R. GARCIA, K. BIRKELUND, F. PÉREZ-MURANO and J. A. DAGATA, *Nanotechnology* **10**, 34 (1999).
- 5 E. S. SNOW, P. M. CAMPBELL and P. J. McMARR, *Appl. Phys. Lett.* **63**, 749 (1993).
- 6 S. SUN and G. J. LEGGETT, *Nano Lett.* **2**, 1223 (2002).
- 7 S. HONG, J. ZHU and C. A. MIRKIN, *Science* **286**, 523 (1999).
- 8 J. T. JONES, P. M. BRIDGER, O. J. MARSH and T. C. MCGILL, *Appl. Phys. Lett.* **75**, 1326 (1999).
- 9 J. J. KOPANSKI and S. MAYO, *Appl. Phys. Lett.* **72**, 2469 (1998).
- 10 H. DAI, N. FRANKLIN and J. HAN, *Appl. Phys. Lett.* **73**, 1508 (1998).
- 11 D. M. EIGLER and E. K. SCHWEIZER, *Nature* **344**, 524 (1990).
- 12 T. SUMOMOGI, T. ENDO, K. KUWAHARA and R. KANEKO, *J. Vac. Sci. Technol. B* **13**, 1257 (1995).
- 13 C. F. QUATE, *Surf. Sci.* **386**, 259 (1997).
- 14 K. SCHOER, F. P. ZAMBORINI and R. M. CROOKS, *J. Chem. Phys.* **100**, 11 086 (1996).
- 15 K. SCHOER and R. M. CROOKS, *Langmuir* **13**, 2323 (1997).
- 16 S. WEGSCHEIDER, A. KIRSCH, J. MLYNEK and G. KRAUSCH, *Thin Solid Films* **264**, 264 (1995).
- 17 J. MOYER, K. WALZER and M. HIETSCHOLD, *Appl. Phys. Lett.* **67**, 2129 (1995).

- 18 S. GINGER, H. ZHANG and C. A. MIRKIN, *Angew. Chem. Int. Ed.* **43**, 30 (2004).
- 19 A. D. L. HUMPHRIS, M. J. MILES and J. K. HOBBS, *Appl. Phys. Lett.* **86**, 034 106 (2005).
- 20 P. VETTIGER, G. CROSS, M. DESPONT, U. DRECHSLER, U. DÜRIG, B. GOTSMANN, W. HÄBERLE, M. A. LANITZ, H. E. ROTHUIZEN, R. STUTZ and G. K. BINNIG, *IEEE Trans. Nanotechnol.* **1**, 39 (2002).
- 21 H. POZIDIS, W. HABERLE, D. WIESMANN, U. DRECHSLER, M. DESPONT, T. R. ALBRECHT and E. ELEFTHERIOU, *IEEE Trans. Magn.* **40**, 2531 (2004).
- 22 M. CAVALLINI, P. MEI, F. BISCARINI and R. GARCIA, *Appl. Phys. Lett.* **83**, 5286 (2003).
- 23 B. CAPPELLA and H. STURM, *J. Appl. Phys.* **91**, 506 (2002).
- 24 J. L. HUANG, Y. E. SUNG and C. M. LIEBER, *Appl. Phys. Lett.* **61**, 1528 (1992).
- 25 M. HEYDE, K. RADEMANN, B. CAPPELLA, M. GEUSS, H. STURM, T. SPANGENBERG and H. NIEHUS, *Rev. Sci. Instrum.* **72**, 136 (2001).
- 26 C. B. GORMAN, R. L. CARROLL, Y. F. HE, F. TIAN and R. FUJERER, *Langmuir* **16**, 6312 (2000).
- 27 M. HEYDE, B. CAPPELLA, H. STURM, C. RITTER and K. RADEMANN, *Surf. Sci.* **476**, 54 (2001).
- 28 C. BUSTAMANTE and D. KELLER, *Physics Today* **48**, 32 (1995).
- 29 T. R. ALBRECHT, M. M. DOVEK, M. D. KIRK, C. A. LANG, C. F. QUATE and D. P. E. SMITH, *Appl. Phys. Lett.* **55**, 1727 (1989).
- 30 H. J. MAMIN, P. H. GUETHNER and D. RUGAR, *Phys. Rev. Lett.* **65**, 2418 (1990).
- 31 Y. Z. LI, L. VAZQUEZ, R. PINER, R. P. ANDRES and R. REIFENBERGER, *Appl. Phys. Lett.* **54**, 1424 (1989).
- 32 J. SCHNEIR, R. SONNERFIELD, O. MARTI, P. K. HANSAMA, J. E. DEMUTH and R. J. HAMMERS, *J. Appl. Phys.* **63**, 717 (1988).
- 33 R. F. W. PEASE, *J. Vac. Sci. Technol.* **B10**, 278 (1992).
- 34 C. F. QUATE, *Surf. Sci.* **386**, 259 (1997).
- 35 A. A. BASKI, *Advanced Semiconductor and Organic Nano-Techniques, Part 3*, Academic Press, New York, 2002.
- 36 X. YU, H. PENG, C. RAN, L. SUN, R. ZHANG and Z. LIU, *Appl. Phys. Lett.* **86**, 133 105 (2005).
- 37 H. J. GAO, K. SOHLBERG, Z. Q. XUE, H. Y. CHEN, S. M. HOU, L. P. MA, X. W. FANG, S. J. PANG and S. J. PENNYCOOK, *Phys. Rev. Lett.* **84**, 1780 (2000).
- 38 D. SHI, Y. SONG, D. ZHU, H. ZHANG, S. XIE, S. PANG and H. GAO, *Adv. Mater.* **13**, 1103 (2001).
- 39 R. M. FEENSTRA, *Surf. Sci.* **299**, 965 (1994).
- 40 G. JIANG, Y. SONG, Y. WEN, W. YUAN, H. WU, Z. YANG, A. XIA, M. FENG, S. DU, H. GAO, L. JIANG and D. ZHU, *ChemPhysChem*, **6**, 1478 (2005).
- 41 M. FENG, X. GUO, X. LIN, X. HE, W. JI, S. DU, D. ZHANG, D. ZHU and H. GAO, *J. Am. Chem. Soc.* **127**, 15 338 (2005).
- 42 C. P. COLLIER, G. MATTERSTEIG, E. W. WONG, Y. LUO, K. BEVERLY, J. SAMPAIO, F. M. RAYMO, J. F. STODDARD and J. R. HEATH, *Science* **289**, 1172 (2000).
- 43 P. VETTIGER, J. BRUGGER, M. DESPONT, U. DRECHSLER, U. DURIG, W. HABERLE, M. LUTWYCHE, H. ROTHUIZEN, R. STUZ, R. WIDMER and G. BINNIG, *Microelectronic Engineering* **46**, 11 (1999).
- 44 P. VETTIGER and G. BINNIG, *Sci. Am.* **288**, 46 (2003).
- 45 M. GRÄNSTORM, *Acta Polym.* **49**, 514 (1998).
- 46 J. A. DEARO, R. GUPTA, A. J. HEEGAR and S. K. BURATTO, *Synth. Met.* **102**, 865 (1999).
- 47 R. RIEHN, A. CHARAS, J. MORGADO and F. CACIALLI, *Appl. Phys. Lett.* **82**, 526 (2003).
- 48 M. RÜETSCHI, P. GRÜTTER, J. FÜNFSCHILLING and H. J. GÜNTHERODT, *Science* **265**, 512 (1994).
- 49 J. H. KIM, M. YONEYA and H. YOKOYAMA, *Nature* **420**, 159 (2002).
- 50 G. DERUE, S. COPPÉE, S. GABRIELE, M. SURIN, V. GESKIN, F. MONTEVERDE, P. LECLÈRE, R. LAZZARONI and P. DAMMAN, *J. Am. Chem. Soc.* **127**, 8018 (2005).

- 51 M. MURGIA, P. MEI, F. BISCARINI, C. TALIANI, Italian Patent Application MI2001A002075 (October 2001).
- 52 M. CAVALLINI, F. BISCARINI, S. LEÓN, F. ZERBETTO, G. BOTTARI and D. A. LEIGH, *Science* **299**, 531 (2003).
- 53 (a) J. F. MOULIN, J. C. KENGNE, R. KSHIRSAGAR, M. CAVALLINI, F. BISCARINI, S. LEÓN, F. ZERBETTO, G. BOTTARI and D. A. LEIGH, *J. Am. Chem. Soc.* (2005), **128**, 526 (2006); (b) C. P. COLLIER, E. W. WONG, M. BELOHRADSKÝ, F. M. RAYMO, J. F. STODDART, P. J. KUEKES, R. S. WILLIAMS and J. R. HEATH, *Science* **285**, 391 (1999).
- 54 (a) F. G. GATTI, D. A. LEIGH, S. A. NEPOGODIEV, A. M. Z. SLAWIN, S. J. TEAT and J. K. Y. WONG, *J. Am. Chem. Soc.* **123**, 5983 (2001); (b) J. BERNA, D. A. LEIGH, M. LUBOMSKA, S. M. MENDOZA, E. M. PEREZ, P. RUDOLF, G. TEOBALDI and F. ZERBETTO, *Nature Materials* **4**, 704 (2005).
- 55 F. BISCARINI, M. CAVALLINI, R. KSHIRSAGAR, D. A. LEIGH, S. LEÓN and F. ZERBETTO, in communication (2006).
- 56 R. K. SMITH, P. A. LEWIS and P. S. WEISS, *Prog. Surf. Sci.* **75**, 1 (2004).
- 57 S. KRÄMER, R. Y. FUIERER and C. B. GORMAN, *Chem. Rev.* **103**, 4367 (2003).
- 58 H. A. BIEBUYCK, N. B. LARSEN, E. DELMARCHE and B. MICHEL, *IBM J. Res. Dev. Opt. Lithogr.* **41**, 159 (1997).
- 59 U. KLEINEBERG, A. BRECHLING, M. SUNDERMANN and U. HEINZMANN, *Adv. Funct. Mater.* **11**, 208 (2001).
- 60 (a) R. R. FUIERER, R. L. CARROLL, D. L. FELDHEIM and C. B. GORMAN, *Adv. Mater.* **14**, 154 (2002); (b) C. B. GORMAN, R. L. CARROLL, Y. F. HE, F. TIAN and R. FUIERER, *Langmuir* **16**, 6312 (2000).
- 61 J. CHEN, M. A. REED, C. L. ASPLUND, A. M. CASSELL, M. L. MYRICK, A. M. RAWLETT, J. M. TOUR and P. G. VAN PATTEN, *Appl. Phys. Lett.* **75**, 624 (1999).
- 62 M. BRINKMANN, S. GRAFF and F. BISCARINI, *Phys. Rev. B* **66**, 1 654 301 (2002).
- 63 R. GARCIA, R. V. MARTINEZ and J. MARTINEZ, *Chem. Soc. Rev.* **35**, 29 (2006).
- 64 J. A. DAGATA, J. SCHNEIR, H. H. HARARY, C. J. EVANS, M. T. POSTEK and J. BENNET, *J. Appl. Phys. Lett.* **56**, 2001 (1990).
- 65 E. S. SNOW, P. M. CAMPBELL, F. A. BUOT, D. PARK, C. R. MARRIAN and R. MAGNO, *Appl. Phys. Lett.* **72**, 3071 (1998).
- 66 K. MATSUMOTO, Y. GOTOH, T. MAEDA, J. A. DAGATA and J. S. HARRIS, *Appl. Phys. Lett.* **76**, 239 (2000).
- 67 V. BOUCHIAT, M. FAUCHER, C. THIRION, W. WERNSDORFER, T. FOURNIER and B. PANNETIER, *Appl. Phys. Lett.* **79**, 123 (2001).
- 68 F. S. CHIEN, Y. C. CHOU, T. T. CHEN, W. F. HSIEH, T. S. CHAO and S. J. Gwo, *Appl. Phys.* **89**, 2465 (2001).
- 69 R. GARCIA, M. TELLO, J. F. MOULIN and F. BISCARINI, *Nano Lett.* **4**, 1115 (2004).
- 70 E. B. COOPER, S. R. MANALIS, H. FANG, H. DAI, K. MATSUMOTO, S. C. MINNE, T. HUNT and C. F. QUATE, *Appl. Phys. Lett.* **75**, 3566 (1999).
- 71 K. MATSUMOTO, M. ISHII and K. SEGAWA, *J. Vac. Sci. Technol. B* **14**, 1331 (1996).
- 72 P. M. CAMPBELL, E. S. SNOW and P. J. McMARR, *Appl. Phys. Lett.* **66**, 1388 (1995).
- 73 J. A. DAGATA, J. SCHNEIR, H. H. HARARY, C. J. EVANS, M. T. POSTEK and J. BENNET, *Appl. Phys. Lett.* **56**, 2001 (1990).
- 74 C. T. SALLING and M. G. LAGALLY, *Science* **265**, 502 (1994).
- 75 A. BOISEN, K. BIRKELUND, O. HANSEN and F. GREY, *J. Vac. Sci. Technol. B* **16**, 2977 (1998).
- 76 G. ABADAL, A. BOISEN, Z. J. DAVIS, O. HANSEN and F. GREY, *Appl. Phys. Lett.* **74**, 3206 (1999).
- 77 D. WANG, L. TSAU and K. L. WANG, *Appl. Phys. Lett.* **65**, 1415 (1994).
- 78 R. GARCIA, M. CALLEJA, F. PEREZ-MURANO, *Appl. Phys. Lett.* **72**, 2295 (1998).
- 79 R. GARCIA, M. CALLEJA and H. ROHRER, *J. Appl. Phys.* **86**, 1898 (1999).
- 80 J. A. DAGATA, T. INOUE and H.

- YOKOYAMA, *Appl. Phys. Lett.* **73**, 271 (1998).
- 81 J. A. DAGATA, T. INOUE, J. ITOH, K. MATSUMOTO and H. YOKOYAMA, *J. Appl. Phys.* **84**, 6891 (1998).
- 82 B. LEGRAND, D. STIÉVENARD, *Appl. Phys. Lett.* **76**, 1018 (2000).
- 83 E. B. COOPER, S. R. MANALIS, H. FANG, H. DAI, K. MATSUMOTO, S. C. MINNE, T. HUNT and C. F. QUATE, *Appl. Phys. Lett.* **75**, 3566 (1999).
- 84 Y. OKADA, Y. LUCHI, M. KAWABE and J. S. HARRIS, *J. Appl. Phys.* **88**, 1136 (2000).
- 85 E. DUBOIS and J. L. BUBENDORFF, *J. Appl. Phys.* **87**, 8148 (2000).
- 86 J. SHIRAKASHI, K. MATSUMOTO, N. MIURA and M. KONAGAI, *Jpn. J. Appl. Phys.* **36**, L1257 (1997).
- 87 E. SNOW, P. M. CABELL and F. K. PERKINS, *Proc. IEEE*, **85**, 601 (1997).
- 88 M. TELLO and R. GARCÍA, *Appl. Phys. Lett.* **79**, 424 (2001).
- 89 M. TELLO, F. GARCÍA and R. GARCÍA, *J. Appl. Phys.* **92**, 4075 (2002).
- 90 A. HIRAI and K. H. ITOH, *Phys. E* **23**, 248 (2004).
- 91 H. Z. SONG, T. OHSHIMA, Y. OKADA, K. AKAHANE, T. MIYAZAWA, M. KAWABE and N. YOKO, *Proc. 26th Int. Conf. Phys. Semiconductors*, Institute of Physics Conference, Vol. 171, 2003, p. 32.
- 92 S. GWO, *J. Phys. Chem. Sol.* **62**, 1673 (2001).
- 93 J. C. GARNO, Y. YANG, N. A. AMRO, S. CRUCHON-DUPEYRAT, S. CHEN and G. LIU, *Nano Lett.* **3**, 389 (2003).
- 94 F. DINELLI, M. MURGIA, M. CAVALLINI, P. LEVY, F. BISCARINI and D. M. DE LEEUW, *Phys. Rev. Lett.* **92**, 116802 (2004).
- 95 V. DEDIU, M. MURGIA, F. C. MATACOTTA, C. TALIANI and S. BARBANERA, *Solid State Commun.* **122**, 181 (2002).
- 96 S. E. SHAHEEN, C. J. BRABEC, N. S. SARICIFTCI, F. PADINGER, T. FROMHERZ and J. C. HUMMELEN, *Appl. Phys. Lett.* **78**, 841 (2001).
- 97 H. SUGIMURA, T. HANJI, K. HAYASHI and O. TAKAI, *Adv. Mater.* **14**, 524 (2002).
- 98 H. SUGIMURA, O. TAKAI and N. NAKAGIRI, *J. Electroanal. Chem.* **473**, 230 (1999).
- 99 J. W. ZHENG, Z. H. ZHU, H. F. CHEN and Z. F. LIU, *Langmuir* **16**, 4409 (2000).
- 100 Q. LI, J. W. ZHENG and Z. F. LIU, *Langmuir* **19**, 166 (2003).
- 101 A. ULMAN, *An Introduction to Ultrathin Organic Films from Langmuir-Blodgett to Self-Assembly*, Academic Press, New York, 1991, p. 278.
- 102 F. SCHREIBER, *Prog. Surf. Sci.* **65**, 151 (2000).
- 103 L. H. DUBOIS and R. G. NUZZO, *Annu. Rev. Phys. Chem.* **43**, 437 (1992).
- 104 G. E. POIRIER, *Chem. Rev.* **97**, 1117 (1997).
- 105 H. SUGIMURA and N. NAKAGIRI, *J. Am. Chem. Soc.* **119**, 9226 (1997).
- 106 H. SUGIMURA and N. NAKAGIRI, *J. Vac. Sci. Technol. A* **14**, 1223 (1996).
- 107 H. SUGIMURA and N. NAKAGIRI, *Langmuir* **11**, 3623 (1995).
- 108 J. TAMAYO and R. GARCÍA, *Langmuir* **12**, 4430 (1996).
- 109 R. MAOZ, S. R. COHEN and J. SAGIV, *Adv. Mater.* **11**, 55 (1999).
- 110 S. HOEPPENER, R. MAOZ, S. R. COHEN, L. F. CHI, H. FUCHS and J. SAGIV, *Adv. Mater.* **14**, 1036 (2002).
- 111 R. MAOZ, E. FRYDMAN, S. R. COHEN and J. SAGIV, *Adv. Mater.* **12**, 725 (2000).
- 112 D. V. VEZENOV, A. V. ZHUK, G. M. WHITESIDES and C. M. LIEBER, *J. Am. Chem. Soc.* **124**, 10578 (2002).
- 113 R. MAOZ, E. FRYDMAN, S. R. COHEN and J. SAGIV, *Adv. Mater.* **12**, 424 (2000).
- 114 G. SCHMID, *Chem. Rev.* **92**, 1709 (1992).
- 115 U. SIMON, G. SCHON and G. SCHMID, *Angew. Chem. Int. Ed. Engl.* **32**, 250 (1993).
- 116 G. SCHMID, W. MEYER-ZAIKA, R. PUGIN, T. SAWITOWSKI, J. P. MAJORAL, A. M. CAMINADE and C. O. TURRIN, *Chem. Eur. J.* **6**, 1693 (2000).
- 117 A. BAPTISTE, A. GIBAUD, J. F. BARDEAU, K. WEN, R. MAOZ and J. SAGIV, *Langmuir* **18**, 3916 (2002).
- 118 R. MAOZ, J. SAGIV, D. DEGENHARDT,

- H. MOHWALD and P. QUINT, *Supramol. Sci.* **2**, 9 (1995).
- 119 S. LIU, R. MAOZ, G. SHMID and J. SAGIV, *Nano Lett.* **2**, 1055 (2002).
- 120 W. T. MÜLLER, D. L. KLEIN, T. LEE, J. CLARKE, P. L. MCEUEN and P. G. SCHULTZ, *Science* **268**, 272 (1995).
- 121 M. PÉTER, X.-M. LI, J. HUSKENS, D. N. REINHOUDT, *J. Am. Chem. Soc.* **126**, 11 684 (2004).
- 122 L. BLASDEL, S. BANERJEE and S. S. WONG, *Langmuir* **18**, 5055 (2002).
- 123 J. WANG, J. R. KENSETH, V. W. JONES, J. B. D. GREEN, M. T. MCDERMOTT and M. D. PORTER, *J. Am. Chem. Soc.* **119**, 12 796 (1997).
- 124 C. BLACKLEDGE, D. A. EGBRETSON and J. D. McDONALD, *Langmuir* **16**, 8317 (2000).
- 125 X. M. LI, J. HUSKENS and D. N. REINHOUDT, *J. Mater Chem.* **14**, 2954 (2004).
- 126 J. HUSKENS, X. M. LI, M. PÉTER and D. N. REINHOUDT, *Proc. Nanotech 2004*, NSTI, Boston, 2004, Vol. 1, p. 447.
- 127 S. XU and G. Y. LIU, *Langmuir* **13**, 127 (1997).
- 128 C. E. D. CHIDSEY, G. Y. LIU, P. ROWNTREE and G. SCOLES, *J. Chem. Phys.* **91**, 4421 (1989).
- 129 X. D. XIAO, G. Y. LIU, D. H. CHARYCH and M. SALMERON, *Langmuir* **11**, 1600 (1995).
- 130 R. MAOZ, R. YAM, G. BERKOVIC and J. SAGIV, *Organic Thin Films and Surfaces: Directions for the Nineties*, Thin Films 20, Academic Press, Boston, 1995, p 41.
- 131 G. Y. LIU, S. XU, Y. L. QIAN, *Acc. Chem. Res.* **33**, 457 (2000).
- 132 S. XU, P. E. LAIBINIS and G. Y. LIU, *J. Am. Chem. Soc.* **120**, 9356 (1998).
- 133 S. XU, S. MILLER, P. E. LAIBINIS and G. Y. LIU, *Langmuir* **15**, 7244 (1999).
- 134 M. Z. LIU and G. Y. LIU, *Langmuir* **21**, 1972 (2005).
- 135 D. J. ZHOU, X. Z. WANG and L. BIRCH, *Langmuir* **19**, 10557 (2003).
- 136 M. A. CASE, G. L. MCLENDON, Y. HU, T. K. VANDERLICK and G. SCOLES, *Nano Lett.* **3**, 425 (2003).
- 137 Y. HU, A. DAS, M. H. HECHT and G. SCOLES, *Langmuir* **21**, 9103 (2005).
- 138 N. SEVERIN, J. BARNER, A. A. KALACHEV and J. P. RABE, *Nano Lett.* **4**, 577 (2004).
- 139 J. BARNER, F. MALLWITZ, L. SHU, A. D. SCHLÜTER and J. P. RABE, *Angew. Chem. Int. Ed.* **42**, 1932 (2003).

6 Dip-Pen Nanolithography

*Seunghun Hong, Ray Eby, Sung Myung, Byung Yang Lee,
Saleem G. Rao, and Joonkyung Jang*

6.1 Introduction

6.1.1 History of Writing

Pen writing is one of the oldest methods of creating patterns on solid surfaces. One of the oldest pieces of writing on papyrus known to us today is the Egyptian “Prisse Papyrus,” which dates back to 2000 BC. The Romans used reed pens to write documents on paper [1]. Then the quill pen appeared in about 700 AD, and it became a main writing tool until 1800 AD. Quill pens are made of birds’ feathers. After the development of advanced metallurgy during the Industrial Revolution, feathers were replaced by metallic nibs.

One important event in the history of pens may be the invention of fountain pens. Working fountain pens were first invented by Lewis Edson Waterman in 1884 [2]. Before then, one had to dip the pen into an inkwell frequently to write long documents. Waterman attached a small inkwell as a part of the pen and modified the shape of the nib to achieve stable ink flow.

Modern pen writing has been automated by the development of electronics and mechanics. Current ink jet printers, with the help of microelectromechanical system (MEMS) technology, can now deposit a picoliter of liquid ink with $\sim 20 \mu\text{m}$ spatial resolution. However, modern automated pens still share remarkable similarities with their predecessors: liquid ink and capillary flow. For all conventional pen writing, solid ink materials are first mixed with solvent to prepare liquid ink, then during the writing process the liquid ink is deposited onto a surface via capillary flow or a small driving pressure on it. When the writing has been done, the solvent molecules are vaporized, leaving only solid ink patterns on the surface.

6.1.2

The Age of Microfabrication

One key technology in modern microelectronics is the microfabrication process for solid-state materials. Figure 6.1 shows the basic steps of the microfabrication technique. In this process, solid surfaces are first coated with a polymer resist layer, and then a specific region on the resist layer is exposed to the UV light (in the case of photolithography) through a photographic mask, or to the nanoscale elec-

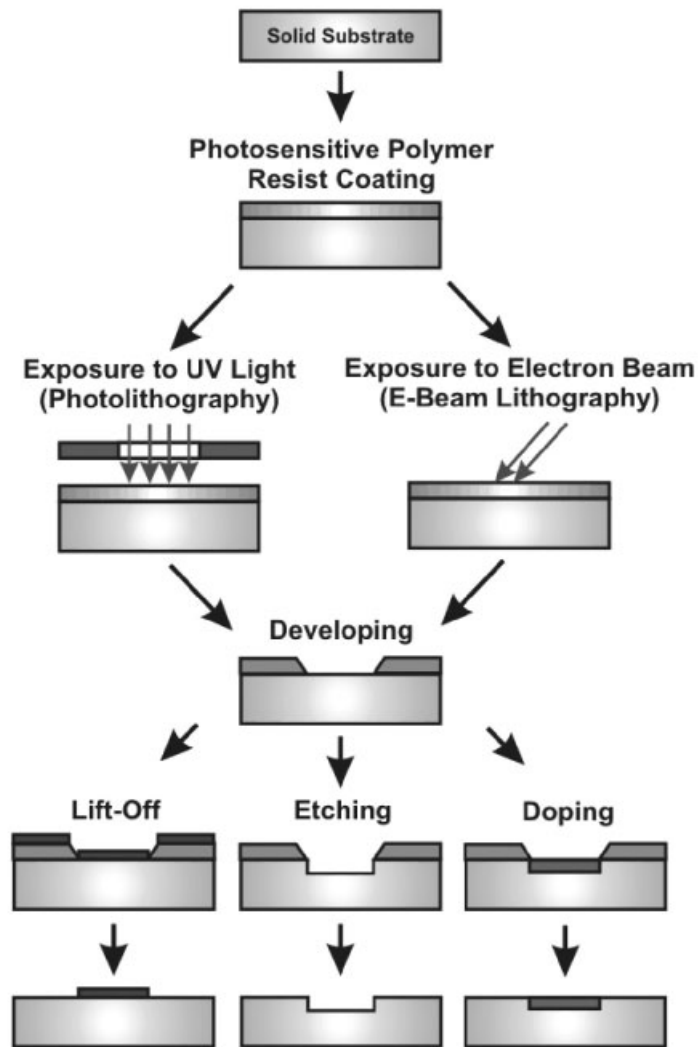


Fig. 6.1 The basic steps of photolithography and e-beam lithography.

tron beam (in the case of e-beam lithography). The exposure to light or an e-beam breaks (or strengthens) the molecular bonding in the polymer resist layer. The exposed (or unexposed) resist layer is removed by immersing the substrate in certain solvents, and the polymer resist patterns are left on the specific area of the substrate. The polymer resist pattern can be used as a resist for subsequent etching or other processing steps. By repeating these processes, many complicated microelectronic components can be created on a single substrate. It should be noted that photolithography is a fast parallel patterning method where a large surface area is exposed simultaneously through a photographic mask. On the other hand, since the exposure in e-beam lithography method is usually done by a single electron beam with a nanoscale diameter, it takes longer to pattern a large number of circuits with the e-beam lithography method than with photolithography.

Due to its high throughput, photolithography has been a workhorse technique in the modern semiconductor industry. During the last four decades, the semiconductor industry has been working extensively on improving the resolution of the photolithography method so that more components can be integrated in a single chip. This size reduction and higher degree of integration are crucial in improving the performance and power efficiency of the integrated circuits, which can reduce the manufacturing cost effectively. Currently, microelectronic chips with a feature size as small as 65 nm are commercially available.

The resolution of photolithography is subject to the limitation set by optical diffraction according to the Rayleigh equation, Eq. (1) [3], where λ is the wavelength of light used, NA is the numerical aperture of the lens system, and k_1 is a constant that depends on the photoresist.

$$R = k_1 \lambda / NA \quad (1)$$

It is usually believed that the resolution of photolithography is approximately $\lambda/2$. Extensive efforts have been made to use shorter-wavelength light to improve the resolution. One problem in using shorter-wavelength light is a lack of transparent optics. In other words, since extreme UV light is absorbed by most materials, it is increasingly difficult to build a lens. Recent photolithographic exposure systems using 13.5 nm wavelength light utilizes reflection optics to focus the light. Currently, it is expected that one can reduce the size of electronic circuits to 20 nm using conventional photolithographic technology.

Unlike the photolithographic method, which requires a photomask with fixed-shape patterns, e-beam lithography allows us to “write” patterns directly onto the surface using an electron beam, and it is extremely easy to modify the shapes of patterns. Such flexibility can be very important during the development of new devices when one has constantly to modify their design. Even though semiconductor device manufacture is dominated by the photolithographic method, a series of “writing” tools (e.g., e-beam lithography, focused ion beam, laser CVD systems) have also been utilized extensively for various purposes, such as rapid prototyping, photomask repair, and flat panel display repair.

6.1.3

New Building Blocks in the Era of Nanotechnology

Recently, the dramatic development of nanotechnology and biological science has provided us with new nanoscale building blocks (e.g., nanoparticles, carbon nanotubes, nanowires, and protein motors) for a generation of new functional devices. These include biological sensors [4–8] to detect harmful viruses, and protein motor-based nanomechanical systems [9]. These new generation devices can be termed “hybrid devices” because they are composed of organic materials as well as solid-state nanostructures. Such hybrid devices are expected to flourish during next few decades because there is a huge demand for new functional devices, especially for medical and biological applications. One significant difference between hybrid devices and conventional solid-state electronics is the mode of fabrication. Since, with hybrid devices, most of the molecular functional units are first synthesized under solution or vapor conditions, additional nanometer-scale assembly steps are required to fabricate such structures. In contrast, the functional components (e.g., transistors, resistors) of conventional solid-state devices are fabricated directly by modifying the solid substrate. Conventional microfabrication techniques such as photolithography cannot be used for fabricating molecule-based structures because of the complex chemical reactivity of most of the molecular units.

Various new methods have been proposed for patterning these new materials for hybrid device structures. A promising method for soft materials is dip-pen nanolithography (DPN) where a nanoscale atomic force microscope tip is utilized as a pen to deposit general organic molecules directly onto solid substrates without any complicated processing steps. Significantly, since DPN does not utilize any resist layers or harsh processing conditions, it can be utilized for virtually any molecular species. In the following sections, we will provide an overview of the DPN method.

6.2

Basics of Dip-Pen Nanolithography

6.2.1

Basic Concepts

The dip-pen nanolithography (DPN) process is a new direct-deposition technique that was first developed in Mirkin’s laboratory at Northwestern University in 1998 [10–14]. It utilizes an atomic force microscope (AFM) tip as a nanoscale pen, molecular substances as ink, and solid substrates as paper. Figure 6.2A shows the basic mechanism of DPN as well as approximate dimensions of typical pen and ink molecules. When the molecule-coated tip is in contact with the substrate, molecules diffuse down onto the substrate, chemically anchor to the surface, and form well-ordered self-assembled monolayer (SAM) patterns. Under ambient conditions,

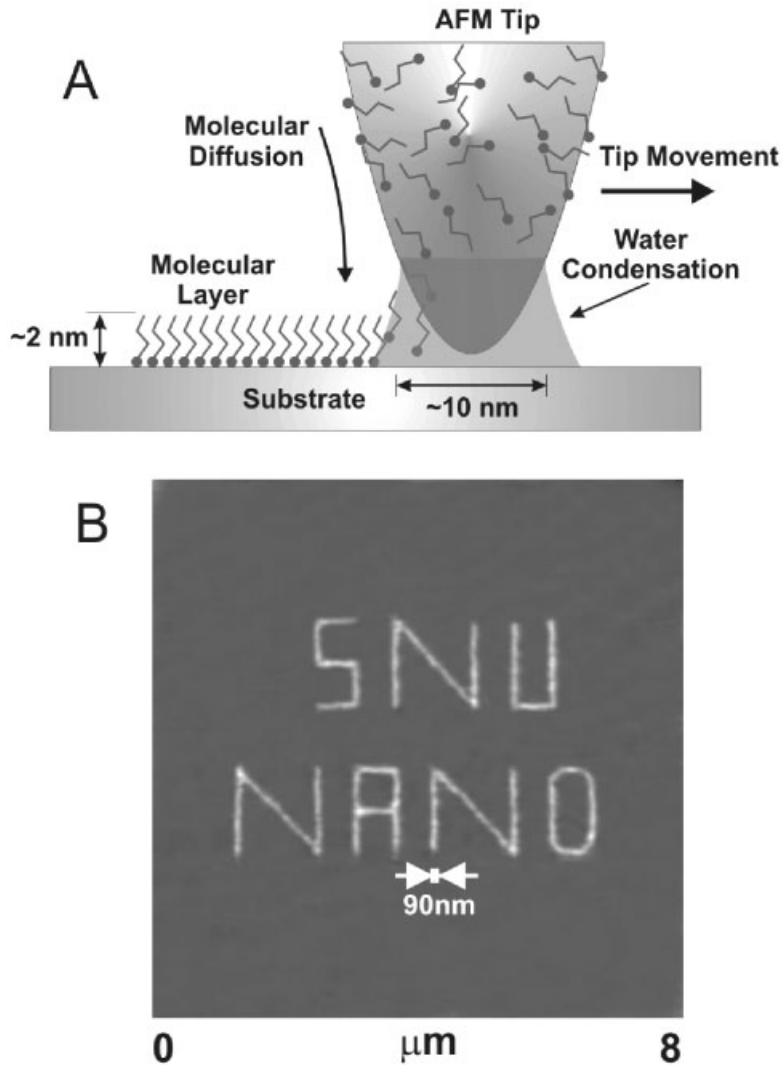


Fig. 6.2 (A) Schematic diagram depicting dip-pen nanolithography. (Adapted from ref. 11, Piner et al., *Science* **1999**, 283, 661 with permission from the American Association for the Advancement of Science, 2005.) (B)

Nanoscale letters written by dip-pen nanolithography. The letters are written with 16-mercaptohexadecanoic acid on an amorphous Au surface.

water condenses at the AFM tip/substrate junction and affects the molecular diffusion. Like macroscale quill pens, the molecular ink coating on the tip surface works as an ink reservoir. A number of variables, including relative humidity, temperature, and the tip speed, can be adjusted to control the ink transport rate, feature size, and line width.

Figure 6.2B shows sample patterns generated by DPN. With the help of automated lithography software, one can print out patterns directly from a personal computer onto solid substrates similarly to the way that ink-jet printers print graphics on paper.

Several important characteristics of DPN are summarized below.

One aspect of practical importance is a stable ink deposition rate. When the DPN process is stabilized, the deposition rate of molecules from the tip to the substrate remains almost constant. The stable writing speed can be attributed to a small contact point between the AFM tip and the substrate; a relatively small amount of molecular inks is deposited onto the surface compared with that on the AFM tip. It is for the same reason that macroscale quill pens and fountain pens have a stable ink deposition rate.

Secondly, DPN relies on molecular diffusion for writing, and it usually does not require external forces. With the same environmental conditions, the amount of molecules deposited depends simply on the contact time between the tip and the substrate. However, additional forces such as electric field can be utilized to achieve a better control of the process.

Thirdly, since DPN is based on diffusion of individual molecules, its behavior depends on several environmental conditions, including temperature and humidity. For example, the temperature change can change the diffusion constant of molecules on the surface. The change in humidity should alter the amount of water condensation at the tip/substrate junction as well as that on the substrate surface, and it will change the behavior of diffusing molecules.

6.2.2

Ink and Pen

DPN has been utilized to deposit various organic molecular species. Most commonly used organic molecules form self-assembled monolayers (SAMs) on substrates (Fig. 6.3A). These molecules comprise three different parts: (a) a chemisorbing group, (b) an end group, and (c) a spacer (the inert part). When these molecules are deposited onto an appropriate substrate, they anchor chemically to the substrate and form a well-ordered crystalline monolayer film with a thickness ranging usually from 1 to 10 nm. Molecules that form SAMs on various substrates are listed in Table 6.1. Specific bonding groups can be chosen, depending on the substrate. By depositing these molecules, one can completely change the chemical properties of the surface to that of the end groups. Various end groups can be used, depending on the specifics of the applications. For example, one can even use specific sequence DNA or proteins as end groups.

The best characterized systems of SAMs are alkanethiols $R(\text{CH}_2)_n\text{SH}$ adsorbed on a gold surface (Fig. 6.3B). When these molecules are deposited via DPN, they also form high-quality crystalline SAMs like those resulting from bulk solution immersion or vapor deposition methods. For example, when 1-octadecanethiol molecules are deposited onto the atomically flat Au(111) surface via DPN, the molecular patterns show hexagonal crystalline structures (Fig. 6.3C).

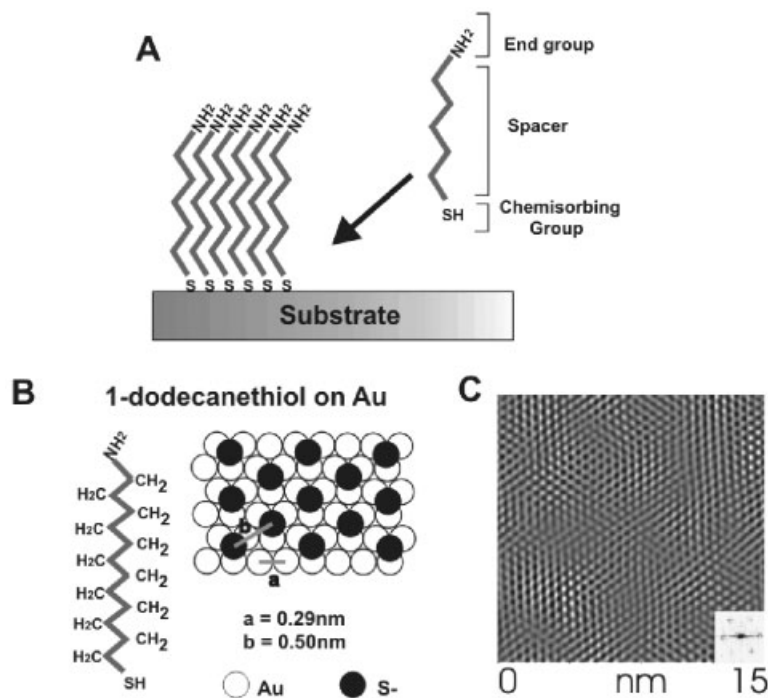


Fig. 6.3 (A) Self-assembled monolayer molecules. (B) An alkanethiol on Au(111). (C) Lattice resolved lateral force image of a 1-octadecanethiol self-assembled monolayer deposited onto Au(111) by DPN. The image has been filtered with a fast Fourier filter, and

the FFT of the raw data is shown in the lower right insert. (Adapted from ref. 11, Piner et al., *Science* **1999**, 283, 661, with permission from the American Association for the Advancement of Science, 2005.)

Even though a self-assembled monolayer with chemical surface bonding helps to make DPN writing reliable, the covalent surface bonding of molecules to the substrate is not a necessary condition for DPN writing. There are several reports of molecules being utilized without covalent bonding to the surface. Usually, it is possible to deposit molecules via DPN if the molecules have a large diffusion constant and some affinity for the substrate. Various molecular species that have been used in the DPN process are listed in Table 6.2.

Various AFM tips have been utilized as a pen in the DPN process. The most common materials for AFM tips are Si_3N_4 and Si. Si_3N_4 tips usually are pyramidal in shape, while Si tips are conical [49]. The heights of AFM tips are usually about 3–10 μm . The diameter of the end of the tip can be as small as ~ 10 nm. The sharpness of the tip is one of the major factors determining the resolution of the DPN process. Utilizing commercial silicon nitride AFM tips, Hong et al. demonstrated patterning of molecular nanostructures, size ~ 10 nm, via DPN [14]. Further improvement of the resolution can be expected if special tips are used. Possi-

Table 6.1 Self-assembled monolayer molecules on different substrates. (Adapted from ref. 44, Xia et al., *Angew. Chem. Int. Ed.* **1998**, 37, 550 (1998) with permission from Wiley-VCH Verlag GmbH, 2005.)

Substrate	Molecular species	Molecular examples	References
Au	RSH, ArSH	C ₁₂ H ₂₅ SH, C ₆ H ₅ SH, 4-PySH	15–17
	RSSR' (disulfides)	(C ₂₂ H ₄₅) ₂ S ₂ , (C ₁₉ H ₃₉) ₂ S ₂ , [CH ₃ (CH ₂) ₁₅ S] ₂	26, 27
	RSR' (sulfides)	[CH ₃ (CH ₂) ₉] ₂ S, CH ₃ (CH ₂) ₁₁ S(CH ₂) ₁₀ CO ₂ H	28, 29
	RSO ₂ H	C ₆ H ₅ SO ₂ H	30
	R ₃ P	(C ₆ H ₁₁) ₃ P	31
Ag	RSH, ArSH	C ₁₈ H ₃₇ SH, C ₆ H ₅ SH	18, 19
Cu	RSH, ArSH	C ₆ F ₅ SH, C ₁₀ H ₂₁ SH, C ₈ H ₁₇ SH	20–22
GaAs	RSH, ArSH	C ₁₈ H ₃₇ SH	23
InP	RSH, ArSH	C ₁₈ H ₃₇ SH, C ₆ H ₁₃ SH	24, 25
Pt	RNC	(C ₅ H ₆)Fe(C ₅ H ₅)(CH ₂) ₁₂ NC	32
SiO ₂ , glass	RSiCl ₃ , RSi(OR') ₃	C ₁₀ SiCl ₃ , C ₁₂ SiCl ₃ , C ₁₈ SiCl ₃ , CH ₂ =CHCH ₂ SiCl ₃ , C ₁₂ H ₂₅ SiCl ₃	33–35
Si/SiH	(RCOO) ₂	[CH ₃ (CH ₂) ₁₀ COO] ₂ , [CH ₃ (CH ₂) ₁₆ COO] ₂	36
	RCH=CH ₂	CH ₃ (CH ₂) ₁₅ CH=CH ₂ , CH ₃ (CH ₂) ₈ CH=CH ₂	37
Si/SiCl	RLi, RMgX	C ₄ H ₉ Li, C ₁₈ H ₃₇ Li, C ₄ H ₉ MgX, C ₁₂ H ₂₅ MgX (X = Br, Cl)	38
Metal oxides	RCOOH	C ₁₅ H ₃₁ COOH, H ₂ C=CH(CH ₂) ₁₉ COOH, CH ₃ (CH ₂) _m OC ₁₀ H ₆ COOH (m = 9, 15–19)	39, 40
	RCONHOH	CH ₃ (CH ₂) ₁₆ CONHOH, HO(CH ₂) ₁₅ CONHOH	41
ZrO ₂	RPO ₃ H ₂	Zr(O ₃ PCH ₂ CH ₂ COOH) ₂	42
RPO ₃ H ₂	In ₂ O ₃ /SnO ₂ (ITO)	(C ₅ H ₆)Fe(C ₅ H ₅)(CH ₂) ₆ PO ₃ H ₂	43

ble higher-resolution tips are carbon nanotube tips [50] and electrodeposited carbon tips [51].

Since the DPN method utilizes a molecule-coated AFM tip to deposit organic molecules, ink loading on the tip surface is critical for reliable DPN writing. For this, the surface chemistry of AFM tips should be considered. When the AFM tip is coated from the solution of molecular ink, the amount of ink loaded is determined by the adhesion properties of the solvent molecules. Even though “clean” Si₃N₄ and Si surfaces are hydrophilic, the tip surfaces become hydrophobic after a

Table 6.2 Organic molecular inks tested via DPN.

Molecular ink	Substrate	Bonding	Examples	References
Alkanethiols	Au	RS–Au	CH ₃ (CH ₂) ₁₇ SH, HS(CH ₂) ₁₅ COOH	10–14
Thiol-modified DNA	Au	RS–Au	5′-HS(CH ₂) ₆ -CAC·GAC·GTT· GTA·AAA·CGA·CGG·CCA·G-3′	45b
Thiol-modified proteins	Au	RS–Au	thiol-modified collagen	57
DNA	SiO ₂	covalent bond	5′-HS(CH ₂) ₁₈ -CAC·AAA·ACG· GGG·GCG·G-3′	56
Inorganic precursor	Si, SiO ₂	Si–O–metal bonding	SnCl ₄ and P-23, AlCl ₃ and P-123	46
Dye molecules	glass	van der Waals	rhodamine 6G (R6G)	47
Protein	glass	chemical bond	ysaxonin-1 on silane-modified surfaces	47
Polymer	glass	hydrogen bond or electrostatic interaction	PAA and PAM PAA, PAH, and SPS	47
Metal	Si, Ge	electric-field induced chemical reactions	H ₂ PtCl ₆	62
Water	mica	capillary force	H ₂ O	48
Conducting polymer	SiO ₂	electrostatic interaction	trimethoxysilylpropyldiethyle netriamine (DETA)	60
Silane	SiO _x , GaAs	covalent bond	hexamethyldisilazane	84
Large nanostructures	SiO _x	adhesion of solvent to substrate	colloidal particles	85, 86

couple of days of exposure to air, due to the hydrocarbon contamination. Since various biomolecules can be dissolved only in polar solvents such as water, surface treatment is necessary to remove the hydrocarbon contamination for a reliable tip coating with biomolecules.

6.2.3

DPN Writing Procedure

Solution or vapor coating methods can be utilized to coat the tip with organic molecular species.

In the solution coating method, the solution of the desired molecular species is first prepared with appropriate solvents. For example, a 1 mM solution of 16-mercaptohexadecanoic acid in acetonitrile has been prepared in order to make molecular ink. The AFM tip is dipped into the solution for a short time period (e.g., ~30 s), and excess molecular ink is blown dry with clean nitrogen gas. This process leaves a thin, solid molecular coating on the AFM tip [10–14].

The vapor coating method can be used to coat molecules with a high vapor pressure. In this method, the AFM tip and molecules are placed together in a small, closed reaction vessel and the vessel is heated to vaporize the molecular species. When the vessel is cooled, the vaporized molecules are adsorbed onto the AFM tip surface and a thin molecular layer is formed. In the case of 1-octadecanethiol (ODT), 200 mg ODT and AFM tips are placed in a small closed tin can (~15 mL) and the tin can is heated to 60 °C for 20 min. When the tin can is cooled to room temperature, the vaporized molecules are adsorbed on the AFM tip surface and result in a thin molecular coating.

Even though both coating methods lead to a *solid* molecular coating on the AFM tip, the properties of the coatings on the AFM tip by the two different methods may be quite different. A vapor-coated molecular coating is usually pure and contains less impurity. In the solution coating method, the molecular coating on the AFM tip contains a significant number of solvent molecules for a period as long as a couple of hours. During that time, the solvent molecules significantly enhance the diffusion of organic molecules, and thus they enhance the DPN writing speed. For example, 16-mercaptohexadecanoic acid (MHA) molecules coated from 1 mM acetonitrile solution will contain a significant amount of solvent and will have a high writing speed for a couple of hours. Also, the residual solvent molecules may alter the behavior of DPN writing under different conditions of temperature and humidity.

After tip coating, DPN writing can be accomplished simply by putting the AFM tip in direct contact with the substrate. A smaller contact force is preferred to avoid any accidental damage on the substrate due to the contact force. In the common DPN process, the AFM tip is operated in a contact mode with a contact force of ~1 nN and the tip moves along the substrate to direct the deposition of molecular species onto the desired region. However, some researchers have demonstrated DPN writing in a tapping mode, in which the AFM tip oscillates and gently taps the substrate. As a result, the AFM tip periodically makes contact with the substrate only in a short time period. In this case, the deposition rate depends on the AFM set point because the effective contact time changes, depending on the set point. The advantage of tapping mode writing is that the interaction between the AFM tip and the substrate is much weaker than that in a contact mode. DPN writ-

ing in noncontact mode may be more suitable for extremely soft nanostructures such as weakly-bound proteins [52].

The patterned surface can be imaged and tested with the molecule-coated AFM tip (though there is a little deposition of molecules while patterns are imaged with a coated AFM tip). Since the molecular coating on the AFM tip is very thin, one can still image surface patterns with the molecule-coated AFM tip. A most common method for imaging thin organic molecular patterns is lateral force microscopy (LFM) in a contact mode or phase imaging in a noncontact mode. Lateral force microscopy measures the tip bending due to the frictional force, whereas phase imaging measures the phase shift of the tip oscillation caused by the attractive force between the AFM tip and the molecular patterns. Since the frictional force also originates from the attractive force, both techniques are utilizing the attractive force map to characterize the molecular patterns. In the air, the attractive force is usually determined by capillary force due to the water meniscus at the tip/substrate junction. The capillary force is larger than any other attractive forces by an order of magnitude at least. Since the magnitude of the capillary force depends on the hydrophobicity of the tip and the surface, LFM or phase images under ambient conditions simply measure the hydrophobicity of the molecular patterns.

In the DPN process, complicated patterns can be generated by combination of two basic patterns: a) dots and b) lines. A dot pattern can be generated by holding the molecule-coated AFM tip at a fixed position on the substrate so that molecules diffuse out in a radial direction to form a circular “dot” pattern (Fig. 6.4A). The size of the dot pattern is determined by the contact time between the AFM tip and the substrate. Line patterns can be generated by moving the AFM tip with a constant speed while it is in contact with the substrate. Here, the line width is determined by the moving speed of the AFM tip.

For practical lithography applications, one should be able to predict the final shapes of the molecular patterns obtained by the DPN process. It is especially crucial to predict precisely the sizes of the two basic patterns, “dots” and “lines”. If deposited molecules form SAMs with a uniform density, the total number of deposited molecules is proportional to the area of the molecular patterns. Making the assumption of “constant deposition rate” which has been experimentally proven in many cases, a simple empirical equation (Eq. (2), where C is the deposition rate) can be applied to characterize the DPN-generated patterns.

$$\text{area} = C \times (\text{contact time}) \quad (2)$$

From a practical point of view, this equation implies that if the deposition constant C is measured once, one can predict the pattern size precisely for a known contact time. For example, for dot patterns, $\text{area} = \pi R^2 = Ct$ (assuming the surface density of the pattern is 1 per unit area), which results in Eq. (3) for the radius.

$$R = \sqrt{Ct/\pi} \quad (3)$$

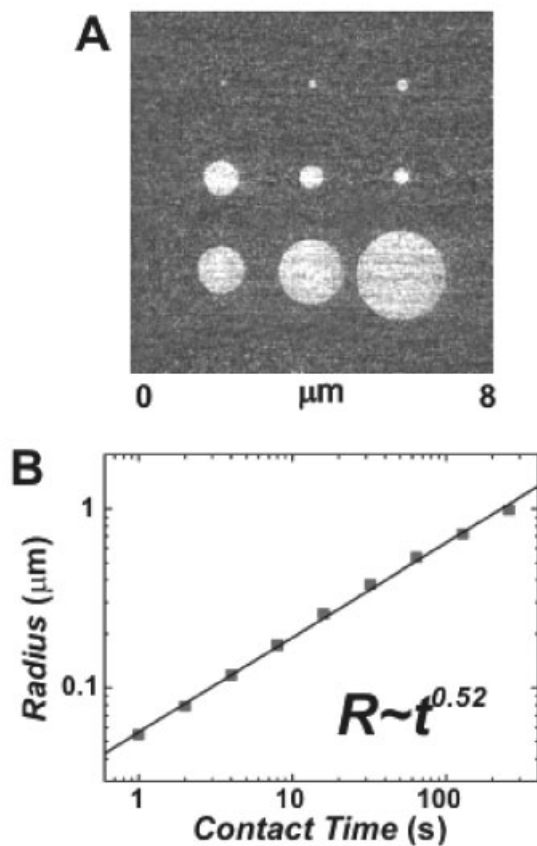


Fig. 6.4 (A) Typical DPN-generated “dot” patterns. Each dot is generated by holding the AFM tip coated with 16-mercaptohexadecanoic acid at a fixed point on the Au substrate. If the deposition rate is constant, R scales with $t^{0.5}$. (B) Variation of R with t showing a constant deposition rate of the DPN writing. (Adapted from ref. 53, Manandhar et al., *Physical Review Letters* **2003**, 90, 115 505 with permission from the American Physical Society, 2005.)

For line patterns $A = WL = Ct$, where W and L are the width and the length of the line, respectively, so Eq. (4) applies.

$$W = C/(L/t) = C/\text{speed} \quad (4)$$

C can be measured easily by a simple test experiment before the actual DPN patterning. Once C is measured, one can generate “dot” and “line” patterns of the desired size by controlling the contact time and tip sweeping speed. Eventually, one can get more complicated patterns with a high precision.

In the scanning probe-based lithography processes which rely on a contact force or electric current as a means of writing, it is very difficult to predict precisely the

shape and size of the final patterns. However, in the DPN process, once one finds out the diffusion constant C by a simple test experiment, one can control the pattern size precisely for the rest of the experiments. This predictability is one of the most critical advantages of the DPN process as a practical lithographic method.

6.3

Lithographic Capability of Dip-Pen Nanolithography

6.3.1

Resolution

Hong et al. demonstrated ~ 10 nm resolution of DPN writing [10]. The ultimate resolution of DPN should depend on various parameters such as the tip diameter, substrate roughness, and the properties of molecules. Figure 6.5 shows example patterns of 16-mercaptohexadecanoic acid (MHA) on Au(111), which can be achieved routinely by DPN under ambient conditions without any special preparation. It should be noted that, considering the lattice structures of SAMs, a single 15 nm diameter dot is composed of less than 5000 molecules. Since DPN utilizes

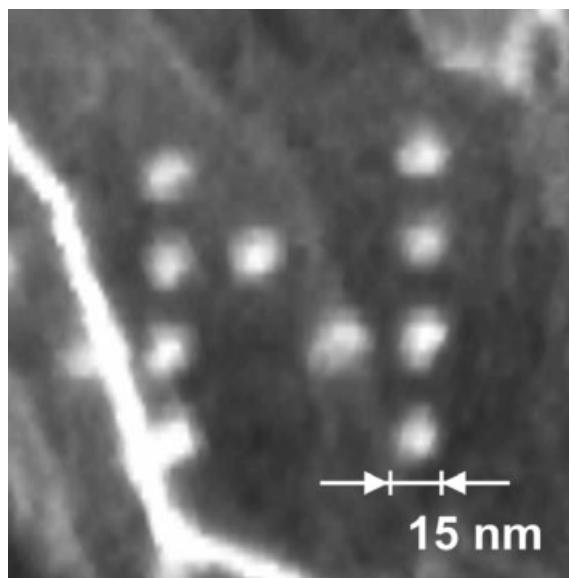


Fig. 6.5 Lateral force microscope image of 15 nm dot patterns on atomically flat Au(111). Each dot is composed of 16-mercaptohexadecanoic acid molecules. The bright line on the lower left-hand corner

represents the step edge of the Au(111) surface. (Adapted from ref. 10, Hong et al., *Science* **1999**, 286, 523 with permission from the American Association for the Advancement of Science, 2005.)

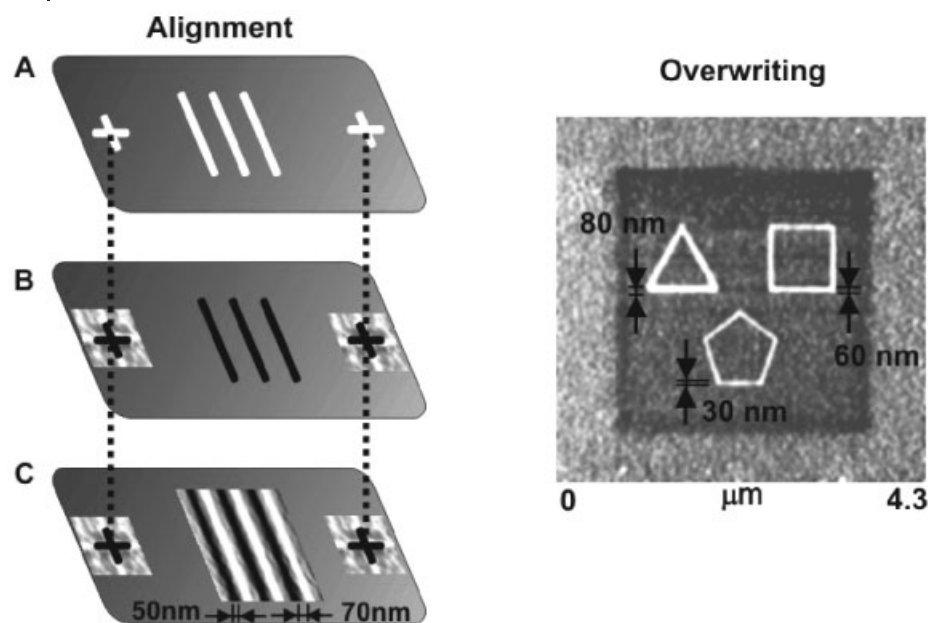


Fig. 6.6 Left: the method for generating aligned soft nanostructures. Right: SAMs in the shapes of polygons drawn by DPN with 16-mercaptohexadecanoic acid on an Au surface. An ODT SAM has been overwritten

around the polygons. (Adapted from ref. 10, Hong et al., *Science* **1999**, 286, 523 with permission from the American Association for the Advancement of Science, 2005.)

an AFM tip as a patterning tool, its resolution is not limited by the wavelength of light. Sharper tips can be used to achieve a better resolution. The current resolution of DPN writing could be improved if special tips such as carbon nanotube tips were used.

Moreover, DPN has several major advantages over traditional nanolithographic techniques: ultrahigh registration and multiple-ink patterning [10]. Because DPN allows imaging of nanostructures with the same tool that is used to form them, it can be used to generate and align nanostructures with pre-existing patterns on the substrate with ultrahigh registration (Fig. 6.6). With the help of the dip-pen nanolithography software, one can generate multicomponent patterns using alignment marks, a strategy analogous to that used to register e-beam lithography patterns. A distinct advantage of this approach over e-beam methods is that it utilizes the scanning probe for generating and locating the alignment marks. This is very important because it is less destructive than e-beam methodology for finding these marks (i.e., it is compatible with soft materials), and it is an inherently higher-resolution imaging technique than optical or e-beam methods.

6.3.2

Overcoming Speed Limits via Multiple-Pen Writing

One major limitation of serial writing processes is their patterning speeds. Since one has to generate complicated patterns with a *single* pen, this usually takes much longer than in parallel patterning methods such as photolithography. One strategy to overcome this limitation is writing with *multiple* pens simultaneously. In most other scanning probe lithography methods, the writing speed depends on the contact force or applied electric field between the AFM tip and the substrate. Since these parameters depend on the surface conditions, complicated feedback circuits are required to precisely maintain identical contact forces or electric fields on each tip. In this case, to achieve an identical pattern size, one has to build a separate feedback circuit for each AFM tip, which dramatically increases the instrumentation cost.

Since DPN writing is based on a thermal diffusion process, the deposition rate of molecular ink does not depend on the variation of the contact forces. In the case of DPN with multiple pens, even with different contact forces on each AFM tip, each tip should generate the same patterns. Figure 6.7 depicts the multiple-pen writing strategy schematically. In this scheme, the laser feedback is applied to the AFM tip with a greatest separation from the surface to ensure that all other AFM tips are in

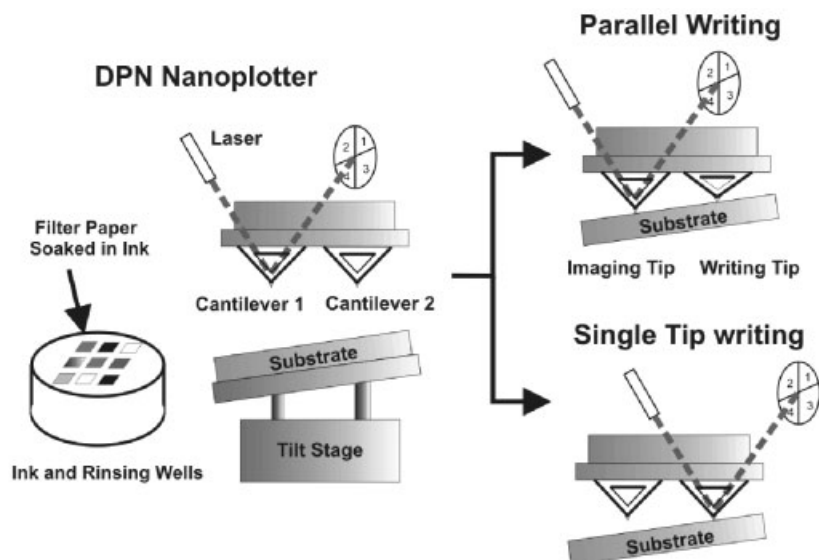


Fig. 6.7 Multiple dip-pen writing utilizing a single-force feedback system. (Adapted from ref. 12, Hong et al., *Science* **2000**, 288, 1808 with permission from the American Association for the Advancement of Science, 2005.)

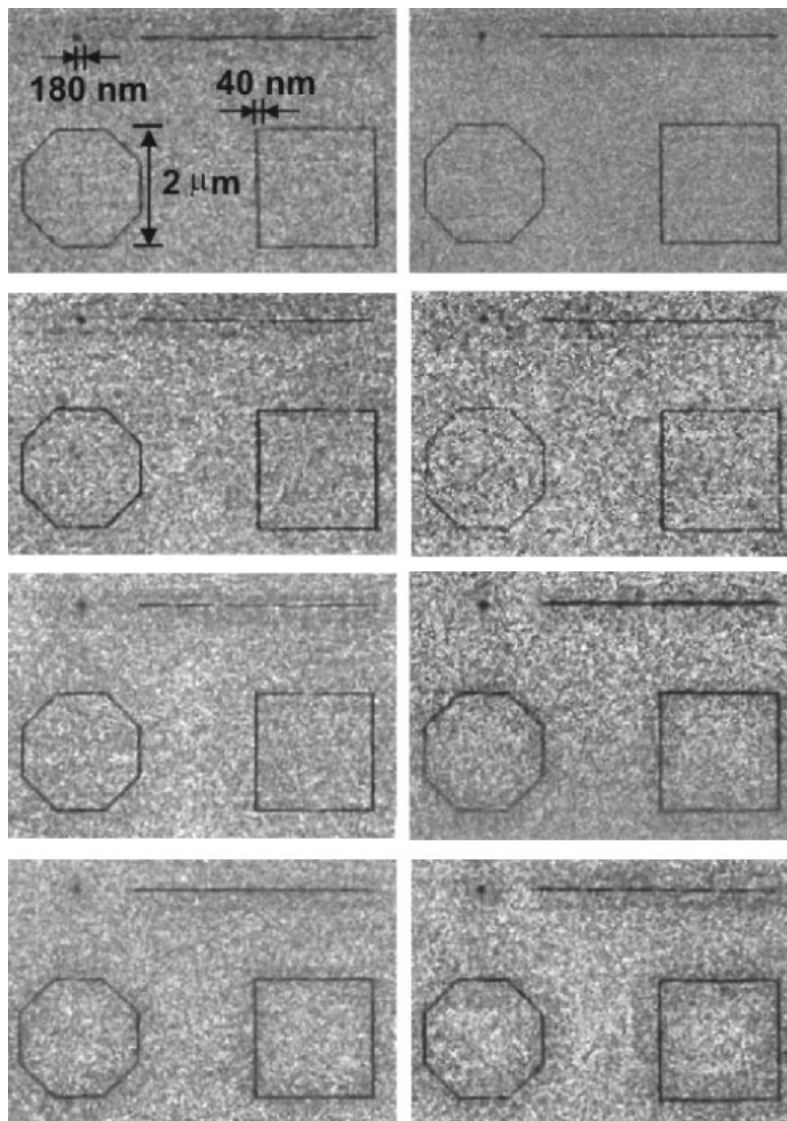


Fig. 6.8 Lateral force microscope images of eight identical patterns generated with one imaging tip and eight writing tips coated with 1-octadecanethiol molecules. (Adapted from

ref. 12, Hong et al., *Science* **2000**, 288, 1808 with permission from the American Association for the Advancement of Science, 2005.)

contact with the substrate. Hong et al. demonstrated that DPN writing with eight pens and a single feedback gives identical nanoscale patterns (Fig. 6.8) [12]. The maximum force variation possible on the contact point depends on the mechanical strength of the SAMs and the substrates. Under ambient conditions, one can apply

up to ~ 100 nN contact force on alkanethiol SAMs without significant structural damage [54]. Extensive efforts are currently being made to increase the density of tips. Zhang et al. demonstrated high-density 32-pen parallel writing [55]. IBM developed a “Millipede” system for different purposes. Here, multiple AFM tips are used to record information on polymer surfaces.

6.3.3

Patterning Extreme Materials: Biomaterials and Conducting Polymers

DPN allows one to directly deposit general biological molecules onto solid surfaces with a nanoscale resolution, which can be important for various future applications such as ultrahigh-density gene chips or nanoscale biosensors.

Additional consideration is usually required for DPN patterning of biomolecules. First, most biomolecules are relatively big compared with other self-assembled monolayer molecules. As a result, the interaction between AFM tips and biomolecules can be very large. Contact-mode writing with a small contact force or tapping-mode writing is often necessary for a stable DPN patterning of large biomolecules [10]. Secondly, most biomolecules prefer water as the solvent, so the AFM tip needs to be treated to make it hydrophilic. Finally, some biological molecules lose their functionality and are destroyed when dried. These sensitive molecules could be patterned via a surface-templated assembly process instead of a direct deposition method. In this method, the surface is first coated with specific functional groups and the assembly of biomolecules is directed via a specific assembly.

Wilson et al. demonstrated direct patterning of thiol-modified collagen molecules, ~ 100 nm in size, on an Au surface [57]. In this experiment, thiol groups bond to the Au surface and form stable structures. However, Wilson et al. also observed that the contact-mode writing is not suitable for patterning large biomolecules because the direct contact of the AFM tip with the molecules can destroy the biomolecular structures on the surface. Tapping-mode patterning is first applied to generate the organic molecular patterns on the surface. In the tapping mode, the AFM tip gently taps the surface, which can minimize the interaction between the AFM tip and the surface of nanostructures. It allows one to create stable biomolecular structures with less damage. By this method, Wilson et al. created collagen patterns with 30 nm line width [57].

Demers et al. demonstrated the direct deposition of thiol-modified DNA molecules (Fig. 6.9) [58]. To enhance the ink loading on the AFM tip, the surface of the AFM tip was first modified by 3'-aminopropyltrimethoxysilane, which promotes reliable adhesion of the DNA ink to the tip surface. Demers et al. also demonstrated the direct deposition of DNA onto an SiO₂ surface. Before the DPN writing, the surface of a thermally oxidized Si wafer was activated with 3'-mercaptopropyltrimethoxysilane (MPTMS). Then, DNA molecules with acrylamide groups were deposited via DPN, and formed stable nanostructures on the surface. The final patterns were characterized by nanoparticle assembly and optical methods.

Conducting polymers are of great interest these days, due to their possible appli-

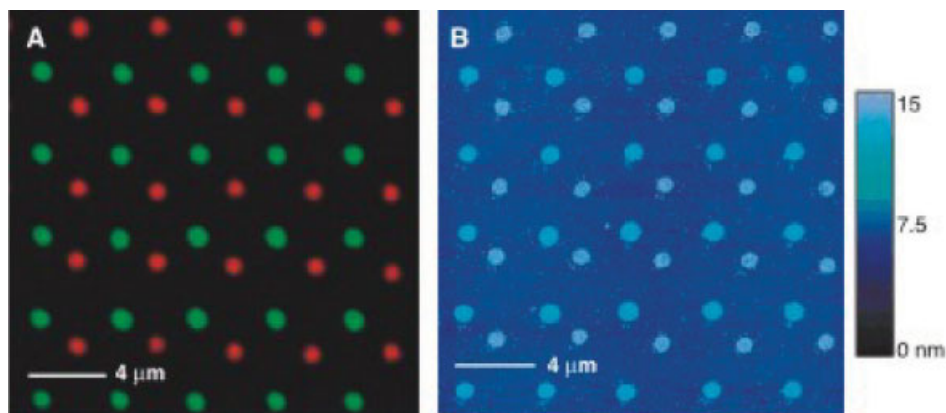


Fig. 6.9 Direct patterning of multiple-DNA inks by DPN. (A) Combined red–green epifluorescence image of two different fluorophore-labeled sequences (Oregon Green 488-X and Texas Red-X) simultaneously hybridized to a two-sequence array deposited on a SiO₂ substrate by DPN. (B) Tapping

mode AFM image of 5 and 13 nm diameter gold nanoparticles assembled on the same pattern after dehybridization of the fluorophore-labeled DNA. (Adapted from ref. 58, Demers et al., *Science* **2002**, 296, 1836 with permission from the American Association for the Advancement of Science, 2005.)

cations in organic display and flexible electronic circuits. They form well-ordered crystalline structures on insulating surfaces such as SiO₂. However, conducting polymers usually do not have strong chemical bonds to the substrate. Since their electronic properties are determined by the crystalline structures, any chemical modification can change their electronic structures significantly.

Lim et al. utilized electrostatic interaction between conducting polymers and substrates to create polymer nanostructures on the surface (Fig. 6.10) [59]. In their experiment, self-doped sulfonated polyaniline (SPAN) and doped polypyrrole (PPY) conducting polymers dissolved in water are used for writing. SPAN and PPY have negatively or positively charged backbones, respectively. The SiO₂ surface is positively charged by coating the surface with trimethoxysilylpropyldiethylenetriamine (DETA) and negatively by piranha solution. Negatively charged SPAN can be deposited only onto the positively charged DETA-coated surface, while positively charged PPY molecules can assemble on the surface cleaned with piranha solution. This experiment shows that it is possible to generate stable nanostructures utilizing electrostatic interactions. The constant deposition rate is also confirmed in the conducting-polymer writing process.

6.3.4

Unconventional DPN

The major driving force of the conventional DPN patterning is the diffusion process of organic molecules. However, one can apply additional forces to provide a

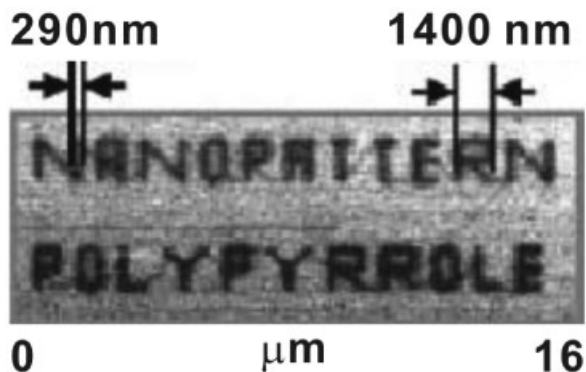


Fig. 6.10 Lateral force microscope image of PPY nanopatterns generated by DPN (Adapted from Fig. 2 in ref. 59, Lim et al., *Advanced Materials* **2002**, *14*, 1474 with permission from Wiley-VCH Verlag GmbH, 2005.)

better control of the deposition process. Also, it is possible to deposit molecules without covalent bonds to the substrate.

Liu et al. used an electric current to induce electrochemical reactions during the DPN writing process (Fig. 6.11). In electrochemical DPN, precursor molecules are utilized to create metallic structures on a solid surface. For example, Liu et al. coated the AFM tip surface with H_2PtCl_6 and applied the current-inducing chemical reaction [61] in Eq. (5).

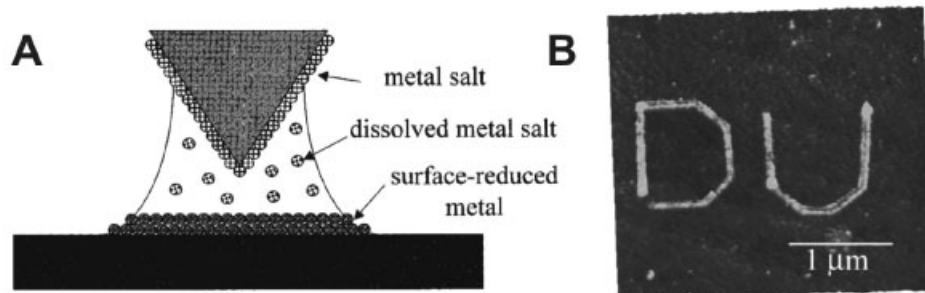


Fig. 6.11 (A) Schematic diagram depicting the DPN process driven by an electrochemical process. (B) Tapping-mode image of Au lines generated by electrochemical DPN. (Adapted from ref. 60, Maynor et al., *Langmuir* **2001**, *17*, 2575 with permission from the American Chemical Society, 2005.)

Here, the water meniscus between the AFM tip and the surface works as a small reaction vessel. The writing leaves Pt nanostructures on the silicon surface. Liu et al. demonstrated successfully the deposition of Au, Ge, Ag, Cu, and Pd with this strategy [60, 61]. These results demonstrate that DPN can be exploited to generate metallic nanostructures on solid surfaces. Metallic nanostructures are of particular interest in the semiconductor industry because they allow one to modify electronic circuits at nanometer-scale resolution without any complicated processing steps.

In most DPN processes, molecules are deposited directly onto a bare surface. If more molecules are deposited on top of another molecular layer, depending on their bonding energies and detailed kinetics an exchange reaction may occur. The exchange can be enhanced by a strong contact force during the DPN writing. Liu et al. coated the AFM tip with molecules and wrote patterns on top of other molecular layers (Fig. 6.12) [62]. The strong contact force induced the exchange reaction and the molecules from the AFM tip could replace the molecular layer on the surface.

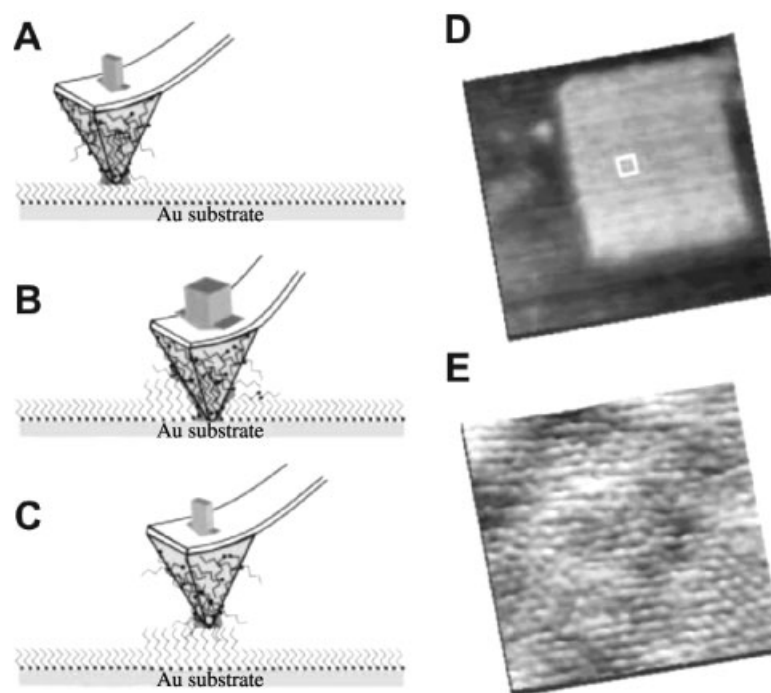


Fig. 6.12 (A–C) DPN combined with the nanografting method. (D) $170 \text{ nm} \times 160 \text{ nm}$ topographic image of $\text{C}_{10}\text{S}/\text{Au}$ SAM containing a $100 \text{ nm} \times 120 \text{ nm}$ rectangular area of $\text{CF}_{12}\text{C}_2\text{S}/\text{Au}$ SAM. (E) High-resolution 10

$\text{nm} \times 10 \text{ nm}$ image of $\text{CF}_{12}\text{C}_2\text{S}/\text{Au}$ SAM as indicated in Fig. 6.14(D). (Adapted from ref. 62c, N. A. Amro et al., *Langmuir* **2000**, *16*, 3006 with permission from the American Chemical Society, 2005.)

6.3.5

New Pens and Hardware

Development of DPN was originally based on atomic force microscopy which was optimized for high-resolution imaging. Since then, there have been extensive efforts to develop new hardware optimized for dip-pen nanolithography.

A DPN stamp tip fabricated by coating the conventional AFM tip with a thin polydimethylsiloxane (PDMS) layer has been reported (Fig. 6.13A). Since the PDMS layer can absorb a large amount of molecular ink, the stamp tip shows improved ink loading properties. Zhang et al. reported a pen made of polymer (Fig. 6.13B). Since they are made entirely of polymers, such pens can be fabricated easily. Sheehan et al. reported an AFM tip equipped with a heater (Fig. 6.13C), using which enables the DPN writing to be turned on and off. Bullen et al.

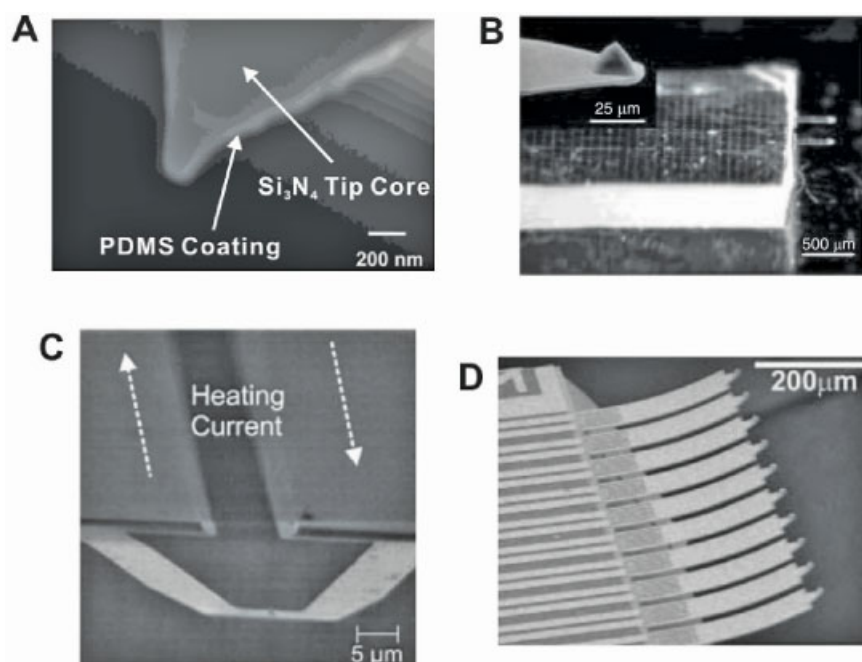


Fig. 6.13 New pens used for DPN. (A) AFM tip with a PDMS coating. (Adapted from ref. 63, Zhang et al. *Nano Letters* **2004**, *4*, 1649 with permission from the American Chemical Society, 2005.) (B) Pen made from polymers. (Adapted from ref. 64, Wang et al., *Langmuir* **2003**, *19*, 8951 with permission from the American Chemical Society, 2005.) (C) Pen with a heater, (Adapted from ref. 65, Sheehan

et al., *Applied Physics Letters* **2004**, *85*, 1589 with permission from the American Physical Society, 2005.) (D) Multiple pens which can be actuated individually by a thermal actuation mechanism. (Adapted from ref. 66, Bullen et al., *Applied Physics Letters* **2004**, *84*, 789 with permission from the American Physical Society, 2005.)

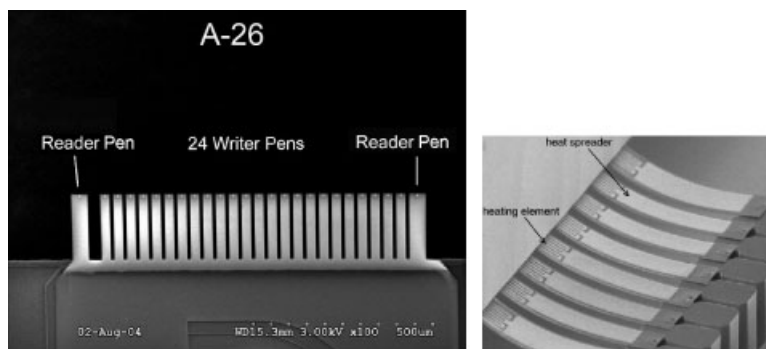


Fig. 6.14 Left: SEM image of a passive multi-pen array of 26 DPN pens. (Courtesy of NanoInk, Inc.) Right: SEM image of an Active^{hskip.75}™ Pen array dipping into a matching inkwell array.

developed an array of pens which can be actuated individually via a thermal actuation mechanism (Fig. 6.13D).

An integrated DPN system comprising a complete set of hardware, software, and consumables has been developed by NanoInk, Inc. The system allows one to perform entire DPN processing steps. For example, the software platform takes advantage of the alignment capability of the DPN process, and it allows one to generate multiple-level molecular patterns easily. Figure 6.14 shows both passive and ActiveTM Pen arrays. The passive arrays can cover an area of up to $1000\ \mu\text{m} \times 90\ \mu\text{m}$ before having to realign with the sample stage. The throughput is n times faster for n -pens, relative to patterning with a single AFM pen. The Active arrays have one fundamental difference from those described in Chang Liu's work: namely, they move down into contact with the surface when activated, in contrast to earlier designs. While it is challenging from a fabrication standpoint, this design allows for pens to be in the "off" state, or even fail, and therefore not be writing on the surface when they should not. The Active Pens combined with the integrated DPN patterning system made truly possible the "nanoplotter" for general organic molecular patterning.

6.4 Other Applications

6.4.1 Etching Resist Patterning

One can utilize the SAM patterns via DPN to fabricate solid nanostructures (Fig. 6.15A). In this process, the monolayer patterns are used as an etching resist layer. Weinberger et al. demonstrated etching of Au using 1-octadecanethiol as an etch-

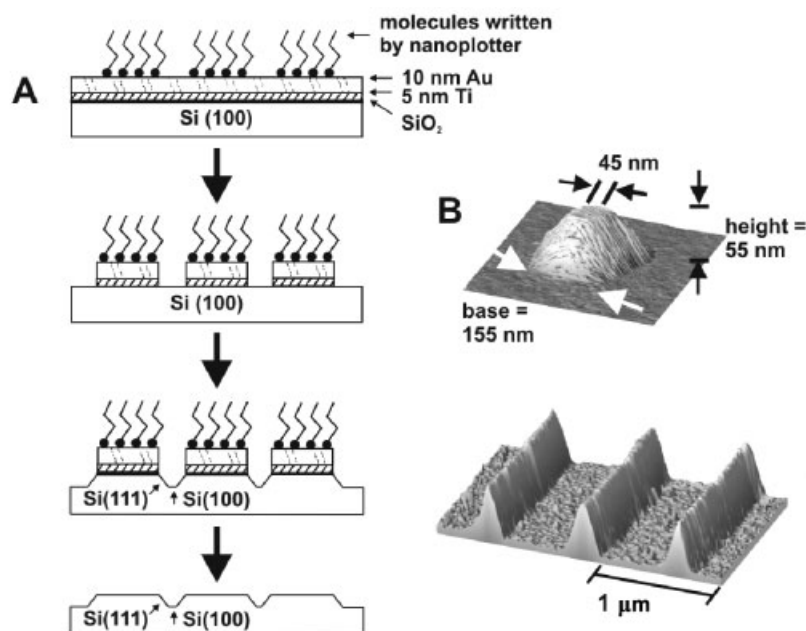


Fig. 6.15 Solid nanostructure fabrication using DPN. (Adapted from ref. 13, Weinberger et al., *Advanced Materials* **2000**, *12*, 1601 with permission from Wiley-VCH Verlag GmbH, 2005.)

ing resist layer [13]. Then, the etched Au patterns are used as an etching resist for the silicon etching process (Fig. 6.15B).

Significantly, since the thickness of the usual SAM is ~ 2 nm, it can be an ideal etching resist layer. Also, the resolution of DPN is not limited by optical wavelength. One disadvantage for practical applications might be its slow speed because DPN is a serial process. Liu et al. demonstrated fabrication of multiple solid nanostructures via a multiple-pen writing strategy [55]. Considering recent active work on multiple-pen systems such as Millipede from IBM, further improvement of its speed can be expected. Table 6.3 shows possible SAM resist layers with corresponding etchants.

6.4.2

Nanoassembly

Nature uses molecular recognition between complex macromolecules to form sophisticated meso- and macroscopic architectures. Proteins, DNA, and other biomolecular structures have all been programmed to form specific structures based upon relatively simple precursor molecules such as nucleotides or peptides. Recently, significant efforts have been directed to constructing functional materials utilizing the molecular recognition mechanism.

Table 6.3 Possible combinations of SAMs and etchants.
(Adapted from ref. 44, Xia et al., *Angew. Chem. Int. Ed.* **1998**,
37, 550 with permission from Wiley-VCH Verlag GmbH, 2005).

Surface	SAM	Etchant	Molecular examples	References
Au	thiol	KCN/O ₂	HS(CH ₂) ₁₅ SH, HS(CH ₂) ₁₈ SH	13, 67–69
Ag	thiol	KCN/O ₂	CH ₃ (CH ₂) ₁₅ SH	70, 73
Cu	thiol	FeCl ₃ /HCl	CH ₃ (CH ₂) ₁₅ SH	68, 71
GaAs	thiol	HCl/HNO ₃	CH ₃ (CH ₂) ₁₅ SH	68, 74
Al	RPO ₃ ²⁻	HCl/HNO ₃	C ₁₈ PO(OH) ₂	72
Si/SiO ₂	RSiO _{3/2}	HF/NH ₄ F	HSC ₁₅ H ₃₀ COOH	75
Glass	RSiO _{3/2}	HF/NH ₄ F	HSC ₁₅ H ₃₀ COOH	75

In the example shown in Fig. 6.16, dot patterns composed of 16-mercaptohexadecanoic acid (MHA) are first generated by DPN. The MHA molecules bond to the Au surface with thiol groups and expose carboxylic acid groups on the SAM surface. After patterning MHA by DPN, the remaining surface area

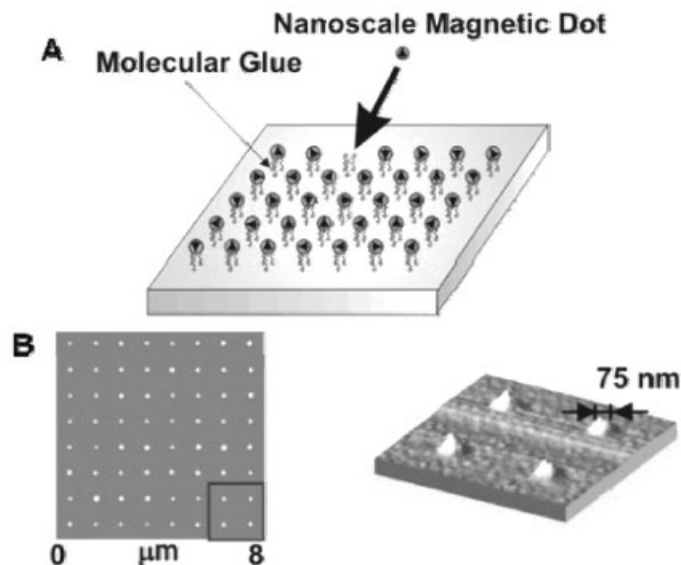


Fig. 6.16 (A) Surface-templated assembly process for nanoparticles. (B) An array of iron oxide dots prepared by a surface-templated assembly process. (Adapted from ref. 76, Liu et al., *Advanced Materials* **2002**, *14*, 231 with permission from Wiley-VCH Verlag GmbH, 2005.)

should be passivated with 1-octadecanethiol, which generates SAM terminated with methyl ($-\text{CH}_3$) groups. Then the sample is placed in the solution containing iron oxide nanoparticles. The Fe_3O_4 magnetic nanoparticles have a specific affinity for the carboxylic groups. Figure 6.16B shows magnetic nanoparticle patterns assembled on the SAM surface terminated with carboxylic acid groups ($-\text{COOH}$).

Various interactions can be used to assemble nanostructures specifically on a desired surface area. These include covalent bonding, electrostatic interactions, and biomolecular interactions. Biomolecular interaction is especially intriguing because of its variety and specificity. Unlike most other molecular recognition mechanisms where possible choices are limited (e.g., thiol to Au, carboxylic acid to aluminum, etc.), biomolecular recognition provides a virtually infinite number of combinations. For example, Demers et al. demonstrated a surface functionalization with single strand DNA (ssDNA) molecules [58]. When the functionalized substrate is immersed in the solution of DNA-functionalized nanoparticles, only nanoparticles with a specific complementary sequence of ssDNAs can assemble on the desired surface area. Suppose one uses ssDNA with n base pairs. Since each base pair of ssDNA can have four different sequences (A, T, G, or C), 4^n different combinations are possible.

In addition to simple dot structures, Hong et al. applied the surface-templated assembly process to assemble carbon nanotubes with precise locations and orientations (Fig. 6.17) [77]. In this case the solid surface is first functionalized by two dif-

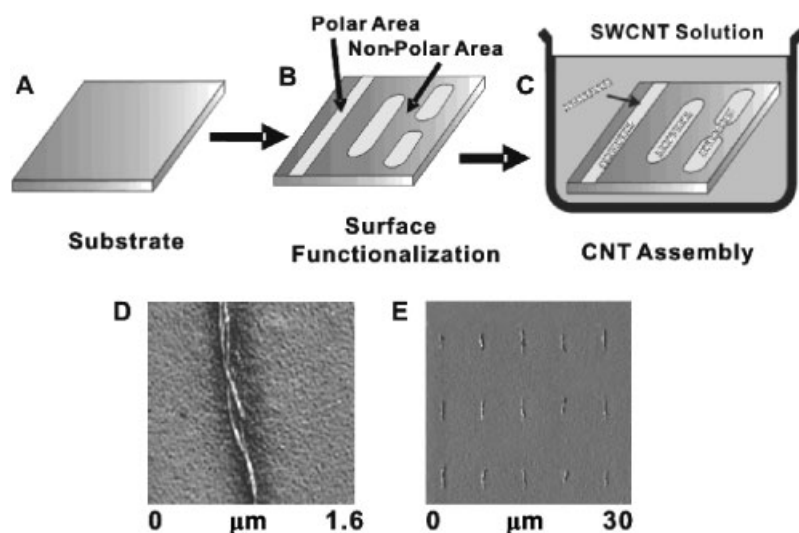


Fig. 6.17 (A–C) The surface-templated assembly process of carbon nanotubes. SWCNT, single-wall carbon nanotube. (D) Carbon nanotubes assembled on nanoscale molecular patterns. (E) Individual carbon

nanotube arrays assembled on polar molecular patterns. (Adapted from ref. 77, Rao et al., *Nature* **2003**, 425, 36 with permission from Nature Publishing Co., 2005.)

ferent SAMs with polar and non-polar end groups, respectively. When the substrate is placed in a carbon nanotube suspension, carbon nanotubes are attracted to the surface molecular patterns and align along the patterns. Using this process, Hong et al. demonstrated assembly of millions of carbon nanotube arrays. This process may enable carbon nanotube-based electronics in the future.

6.5 Nanoscale Statistical Physics Inspired by DPN

DPN also inspired, in addition to practical applications, the advancement of many scientific areas such as nanoscale statistical physics.

6.5.1 DPN Theory

The DPN process can be understood as four steps (Fig. 6.18): 1) molecular transport from the tip to the surface, 2) lateral diffusion of molecules on the surface, 3) molecular bonding to the substrate, and 4) reorganization of molecular species on the bare substrates. In many previous experimental results, DPN writing was demonstrated to have an almost constant deposition rate, which is mainly because the

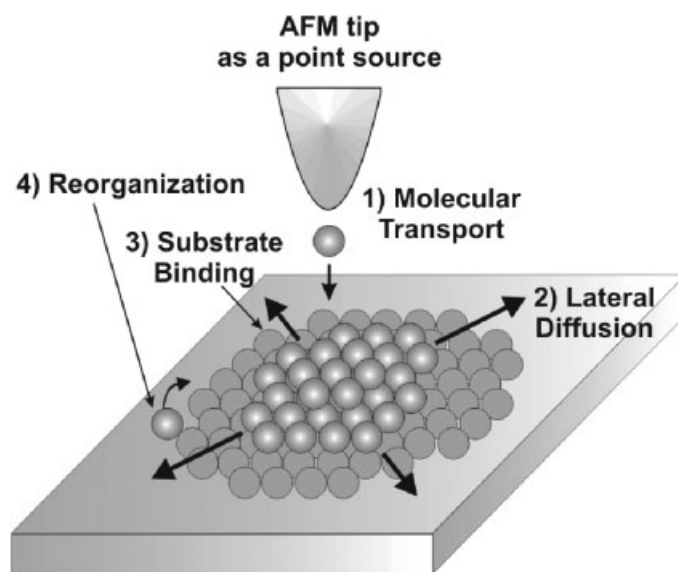


Fig. 6.18 DPN process with strong surface bonding. (Adapted from ref. 53, Manandhar et al., *Physical Review Letters* **2003**, *90*, 115 505 with permission from the American Physical Society, 2005.)

number of molecules deposited is much smaller than the number of organic molecules on the AFM tip. It should also be noted that the reorganization process occurs only if the molecular bonding to the substrate is very weak.

Jang et al. presented a theoretical model for the DPN writing in the case of a constant deposition rate and strong molecular bonding to the surface [78]. The basic assumptions are:

- the deposition rate remains constant throughout the process;
- whenever the molecules hit the bare surfaces, they bond irreversibly to the surface without any reorganization process;
- molecules can diffuse via a random walk only on the area covered by other molecules.

For a tip fixed in position, the ink diffusion is isotropic, giving (filled) circles on the surfaces. Assuming cylindrical symmetry of diffusion and treating the position of an ink molecule as a continuous variable r , a simple analytic theory for the circle growth can be derived by using a diffusion equation [Eq. (6)], where C is the number density of molecules at distance r and time t . D is the molecular diffusion constant.

$$\frac{\partial C}{\partial t} = \frac{1}{r} \frac{\partial}{\partial r} \left(rD \frac{\partial C}{\partial r} \right) \quad (6)$$

In this picture, molecules cannot move on the bare surface but can diffuse in the region already covered by other molecules. The boundary of a circle with radius $R(t)$ varies in time, and mathematically this is a moving boundary problem. Its solution is detailed in ref. 78. The number densities inside and outside the boundary are given by Eqs. (7) and (8), where λ^2 satisfies the equation, $e^{-\lambda^2} = \frac{4D}{(n/\pi\rho)} \lambda^2$, n is the molecular deposition rate, ρ is the monolayer surface density, and Ei is the exponential integral function.

$$C(r, t) = \rho - \frac{n}{4\pi D} \left[Ei\left(\frac{-r^2}{4Dt}\right) - Ei(-\lambda^2) \right] \quad (7)$$

$$C(r, t) = 0 \quad (8)$$

Even though Jang et al. successfully explained the pattern formation on the substrate [78], the theory simply assumes a constant deposition rate and does not provide any explanation for the deposition step. Several researchers presented different models.

Sheehan adopted a different assumption to describe the DPN process, based on the diffusion model [79]. Instead of a constant deposition rate, the density of molecules below the contact point is assumed to be identical to that on the AFM tip and remains constant throughout the DPN process. This assumption provides a

solution different from that of Jang et al. The analytical approximation is stated in Eq. (9), where γ is Euler's gamma ($\cong 0.577$), and a is the area of the contact point. However, this solution provides a rapidly decreasing flux (deposition rate), which is inconsistent with some of the experimental results that indicate a constant or increasing flux (Fig. 6.4).

$$C(r, t) = C_0 \frac{Ei(r^2/4Dt)}{\ln(4Dt/a^2 e^{2\gamma})} \quad (9)$$

Considering the complicated geometry of the tip–surface junction and possible water condensation in the case of experiments in air, the constant density assumption may be too greatly simplified to explain the deposition process in the DPN. This contradiction implies that it is necessary to consider more complicated aspects of tip–substrate junctions, such as the water meniscus, to provide a proper description of the DPN process.

Week et al. presented a model taking into account the water meniscus at the junction between the AFM tip and the substrate [80]. Here, the deposition of organic molecules is explained by their dissolution kinetics in the water meniscus at the tip/substrate junction. In the model, the total number of molecules N transferred to the substrate is given by the integral of the transfer rate dN/dT over the total tip–surface contact time τ . This theory gives Eq. (10) for the radius of the “dot” pattern R , where τ represents the contact time, and β_+ and β_- are molecular flux coefficients from and to the tip, respectively.

$$R^2 = A \left[\beta_+ \tau - \pi a^2 \beta_- \int_0^\tau C_0(r) dt \right] \quad (10)$$

The results show a transition to the diffusive regime with a slow diffusion rate after a long time. In the model, the density of the molecules on the substrate below the AFM tip depends on the dissolution kinetics of thiol molecules and surface diffusion.

6.5.2

Nanoscale Water Condensation

The above theories successfully described several aspects of DPN using strongly bonding molecular species. However, they could not explain a broad variety of experimental results using various molecular species. One example is the change in deposition rate under different humidity conditions. Experiments show quite different humidity dependence of the deposition rate depending on the molecular species. This implies that water condensation plays a significant role in the DPN process. The above theories, due to their phenomenological nature, take the deposition rate as given, and thus cannot predict how it depends on humidity. What happens is that, under ambient conditions, water condenses on solid surfaces and then a water meniscus forms at the contact point between the AFM tip and the

substrate. The water meniscus formed at the contact should affect the deposition rate directly.

It is reasonable to believe that a water meniscus between the tip and the substrate triggers the downward flow of molecules from the tip in DPN. The meniscus serves as a transport channel for the molecules. The water meniscus has not been observed directly, however, and the ultimate resolution, exact mechanism, and thermodynamic dependence of DPN are not currently known. The resolution of DPN might depend crucially on the width of the water meniscus. The macroscopic Kelvin equation [82] has commonly been adopted to predict the shape and size of this nanoscale water meniscus. However, for nanoscale problems, this macroscopic approach is questionable because of finite-size effects that give rise to large fluctuations in the size and shape of the meniscus. Jang et al. [81] used Monte Carlo simulations to investigate the nanoscale water condensation (Fig. 6.19). The meniscus width is found to be sensitive to the hydrophobicity of the tip, the tip–substrate distance, and the humidity [83]. Unlike the assumptions of the Kelvin equation, nanometer-wide menisci show relatively large fluctuations in their widths. As a result, there is a minimum width for a stable meniscus, which is found to be about 2 nm. This width might set the limit of the ultimate resolution possible in DPN.

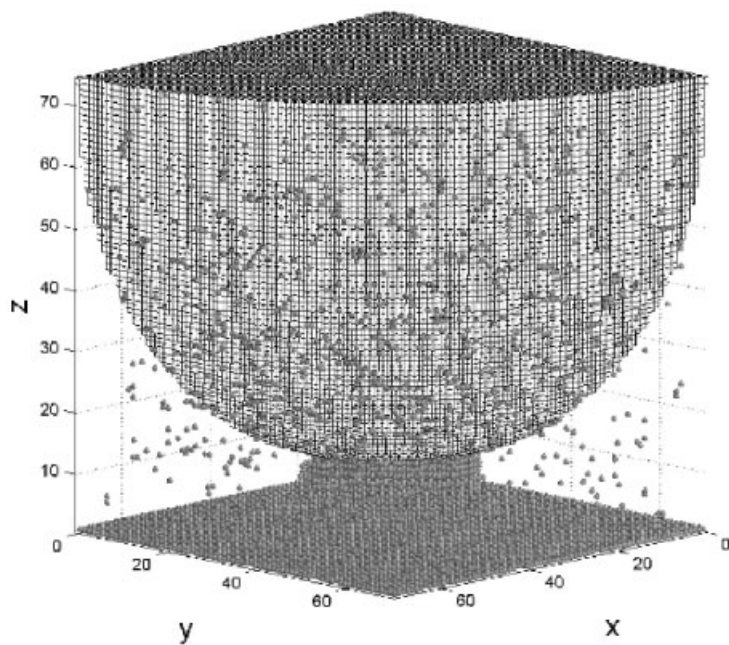


Fig. 6.19 Snapshot of a liquid meniscus condensed between a spherical AFM tip and a flat surface. (Adapted from ref. 81, Jang et al., *Physical Review Letters* **2004**, 92, 085504 with permission from the American Physical Society, 2005.)

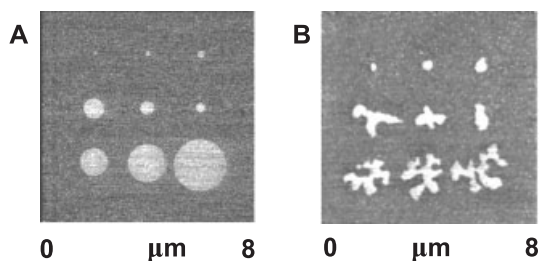


Fig. 6.20 (A) Circular dot patterns generated by DPN using MHA molecules on Au. (B) Fractal-like dot patterns of DDA molecules on mica. (Adapted from ref. 53, Manandhar et al., *Physical Review Letters* **2003**, *90*, 115 505 with permission from the American Physical Society, 2005.)

6.5.3

Anomalous Surface Diffusion

If the deposited molecules bond strongly to the bare surface, they always form circular dot patterns (Fig. 6.20A). In contrast, in the case of weak surface bonding the deposited molecules can reorganize on the surface and form fractal-like patterns. When 1-dodecylamine (DDA) is deposited onto mica surfaces, molecules form noncircular patterns. Even though it is not clear whether the patterns are indeed fractal, a scaling analysis shows they have a fractal dimension of 1.5, which is significantly smaller than the fractal dimension of normal 2D patterns (Fig. 6.20B).

Fractal-like pattern formation is also very common in thin-film growth such as in metal evaporation onto solid substrates. For the case of bulk thin films, fractal growth has been explained by the diffusion-limited aggregation (DLA) model, according to which molecules are deposited all over the surface area and individual molecules approach the nucleation site via a random walk. Once a molecule hits the nucleation cluster, it sticks to the cluster. In this case, the diffusing molecules are more likely to be captured by the extended arm, resulting in a fractal growth. Contrarily, molecules in DPN process are deposited at the center of the nucleation site, which still results in fractal-like patterns. This new phenomenon has been observed only after the invention of dip-pen nanolithography. The exact reason of this anomalous pattern formation has not been fully understood yet.

6.6

Conclusions

DPN is a newly developed general molecular nanopatterning method. Since DPN can deposit organic molecules directly onto solid substrates without any resist layers, it can be utilized in virtually any chemical or biological molecular patterning. Importantly, its extremely high resolution of ~ 10 nm and alignment capability

for multiple-level patterns makes DPN an ideal tool for nanopatterning organic molecular species on solid substrates.

The development of the DPN method could be a historic event that opens up the door to a generation of new functional devices. Since one can now combine chemical or biological molecules with conventional solid-state devices, it is possible to envision new hybrid devices. These include nanoscale biological sensors to detect a single biomolecular unit [4–8], molecular electronic devices, and nanomechanical systems driven by biological motors [9]. As predicted by many pioneering researchers, it is now the dawn of a new age in which people are beginning to understand and manipulate individual molecular functionality. It is the time when mankind is first touching the secret of life at the molecular level. For the next few decades, new functional devices assembled by the DPN method could flourish and eventually change the face of everyday human life.

Acknowledgements

This work is supported by the Korean Research Foundation (KRF-2004-042-C00063). SH also acknowledges the National Research Laboratory Program of the Korean Ministry of Science and Technology for financial support. JJ gratefully acknowledges the funding from Pusan National University Grant – 2003.

References

- 1 D. GEYER, *Collecting Writing Instruments*, Schiffer Publishing, Atglen, PA, USA, 1990.
- 2 J. BOURQUE, The Waterman Pen, *American Heritage* 1992, 43, 30.
- 3 S. OKAZAKI, *J. Vac. Sci. Technol. B* 1991, 9, 2829.
- 4 T. A. TATON, C. A. MIRKIN, and R. L. LETSINGER, *Science* 2000, 289, 1757.
- 5 Y. CUI, Q. WEI, H. PARK, and C. M. LIEBER, *Science* 2001, 293, 1289.
- 6 a) G. S. WILSON and Y. HU, *Chem. Rev.* 2000, 100, 2693. b) L. C. CLARK JR., on *Biosensors: Fundamentals and Applications*, Oxford University Press, New York, 1987.
- 7 a) M. M. MILLER, P. E. SHEEHAN, R. L. EDELSTEIN, C. R. TAMANAH, L. ZHONG, S. BOUNNAK, L. J. WHITMAN, and R. J. COLTON, *J. Magn. Magn. Mater.* 2001, 225, 138. b) R. G. RUDNITSKY, E. M. CHOW, and T. W. KENNY, *Sensors and Actuators A – Physical* 2000, 83, 256.
- 8 a) J. FRITZ, M. K. BALLER, H. P. LANG, H. ROTHUIZEN, P. VETTIGER, E. MEYER, H. J. GÜNTHERODT, Ch. GERBER, and J. K. GIMZEWSKI, *Science* 2000, 288, 316.
- 9 a) J. R. SELLERS and B. KACHAR, *Science* 1990, 249, 406. b) R. K. SOONG, G. D. BACHAND, H. P. NEVES, A. G. OLKHOVETS, H. G. CRAIGHEAD, and C. D. MONTEMAGNO, *Science* 2000, 290, 1555.
- 10 S. HONG, J. ZHU, and C. A. MIRKIN, *Science* 1999, 286, 523.
- 11 R. PINER, J. ZHU, F. XU, S. HONG, and C. A. MIRKIN, *Science* 1999, 283, 661.
- 12 S. HONG and C. A. MIRKIN, *Science* 2000, 288, 1808.
- 13 D. A. WEINBERGER, S. HONG, C. A. MIRKIN, B. W. WESSELS, and T. B. HIGGINS, *Adv. Mater.* 2000, 12, 1600.
- 14 S. HONG, J. ZHU, and C. A. MIRKIN, *Langmuir* 1999, 10, 7897.
- 15 E. DELAMARCHE, B. MICHEL, H. KANG,

- and Ch. GERBER, *Langmuir* **1994**, *10*, 4103.
- 16 T. SAWAGUCHI, S. YOSHIMOTO, F. MIZUTANI, and I. TANIGUCHI, *Electrochim. Acta* **2000**, *45*, 2861.
- 17 H. ZHANG, H.-X. HE, J. WANG, and Z.-F. LIU, *Langmuir* **2000**, *16*, 4554.
- 18 P. FENTER, P. EISENBERGER, J. LI, N. CAMILLONE, S. BERNASEK, G. SCOLES, T. A. RAMANARAYANAN, and K. S. LIANG, *Langmuir* **1991**, *7*, 2013.
- 19 M. H. SCHOENFISCH and J. E. PEMBERTON, *J. Am. Chem. Soc.* **1998**, *120*, 4502.
- 20 T. VONDRAK, C. J. CRAMER, and X. Y. ZHU, *J. Phys. Chem. B* **1998**, *103*, 8915.
- 21 P. E. LAIBINIS, G. M. WHITESIDES, D. L. ALLARA, Y. T. TAO, A. N. PARIKH, and R. G. NUZZO, *J. Am. Chem. Soc.* **1991**, *113*, 7152.
- 22 H. RIELEY and G. K. KENDALL, *Langmuir* **1999**, *15*, 8867.
- 23 J. F. DORSTEN, J. E. MASLAR, and P. W. BOHN, *Appl. Phys. Lett.* **1995**, *66*, 1755.
- 24 Y. GU, Z. LIN, R. A. BUTERA, V. S. SMENTKOWSKI, and D. H. WALDECK, *Langmuir* **1995**, *11*, 1849.
- 25 D. ZERULLA, D. MAYER, K. H. HALLMEIER, and T. CHASSÉ, *Chem. Phys. Lett.* **1999**, *311*, 8.
- 26 H. A. BIEBUYCK, C. D. BAIN, and G. M. WHITESIDES, *Langmuir* **1994**, *10*, 1825.
- 27 R. G. NUZZO and D. L. ALLARA, *J. Am. Chem. Soc.* **1983**, *105*, 4481.
- 28 E. B. TROUGHTON, C. D. BAIN, G. M. WHITESIDES, R. G. NUZZO, D. L. ALLARA, and M. D. PORTER, *Langmuir* **1988**, *4*, 365.
- 29 E. KATZ, N. ITZHAK, and I. WILLNER, *J. Electroanal. Chem.* **1992**, *336*, 357.
- 30 J. E. CHADWICK, D. C. MYLES, and R. L. GARRELL, *J. Am. Chem. Soc.* **1993**, *115*, 10364.
- 31 K. UVDAL, D. C. MYLES, and R. L. GARRELL, *Langmuir* **1995**, *11*, 1252.
- 32 J. J. HICKMAN, P. E. LAIBINIS, D. I. AUERBACH, C. ZOU, T. J. GARDNER, G. M. WHITESIDES, and M. S. WRIGHTON, *Langmuir* **1992**, *8*, 357.
- 33 J. B. BRZOSKA, I. B. AZOUZ, and F. RONDELEZ, *Langmuir* **1994**, *10*, 4367.
- 34 M. J. WIRTH, R. W. P. FAIRBANK, and H. O. FATUNMBI, *Science* **1997**, *275*, 44.
- 35 A. N. PARIKH, D. L. ALLARA, I. B. AZOUZ, and F. RONDELEZ, *J. Phys. Chem.* **1994**, *98*, 7577.
- 36 M. R. LINFORD and C. E. D. CHIDSEY, *J. Am. Chem. Soc.* **1993**, *115*, 12631.
- 37 M. R. LINFORD, P. FENTER, P. M. EISENBERGER, and C. E. D. CHIDSEY, *J. Am. Chem. Soc.* **1995**, *117*, 3145.
- 38 A. BANSAL, X. LI, I. LAUERMANN, N. S. LEWIS, S. I. YI, and W. H. WEINBERG, *J. Am. Chem. Soc.* **1996**, *118*, 7225.
- 39 D. L. ALLARA and R. G. NUZZO, *Langmuir* **1985**, *1*, 52.
- 40 P. E. LAIBINIS, J. J. HICKINAN, M. S. WRIGHTON, and G. M. WHITESIDES, *Science* **1989**, *245*, 845.
- 41 J. P. FOLKERS, C. B. GORMAN, P. E. LAIBINIS, S. BUCHHOLZ, G. M. WHITESIDES, and R. G. NUZZO, *Langmuir* **1995**, *11*, 813.
- 42 M. E. THOMPSON, *Chem. Mater.* **1994**, *6*, 1168.
- 43 T. J. GARDNER, C. D. FRISBIE, and M. S. WRIGHTON, *J. Am. Chem. Soc.* **1995**, *117*, 6927.
- 44 Y. XIA and G. M. WHITESIDES, *Angew. Chem. Int. Ed.* **1998**, *37*, 550.
- 45 a) M. J. TARLOV, D. R. F. BURGESS JR., and G. FILLEN, *J. Am. Chem. Soc.* **1993**, *115*, 5305. b) T. M. HERNE and M. J. TARLOV, *J. Am. Chem. Soc.* **1997**, *119*, 8916; c) H. TAKIGUCHI, K. SATO, T. ISHIDA, K. ABE, K. YASE, and K. TAMADA, *Langmuir* **2000**, *16*, 1703.
- 46 M. SU, X. LIU, S.-Y. LI, V. P. DRAVID, and C. A. MIRKIN, *J. Am. Chem. Soc.* **2002**, *124*, 1560.
- 47 A. NOY, A. E. MILLER, J. E. KLARE, B. L. WEEKS, B. W. WOODS, and J. J. DEYOREO, *Nano Lett.* **2002**, *2*, 109.
- 48 R. PINER and C. A. MIRKIN, *Langmuir* **1997**, *13*, 6864.
- 49 G. WURTZ, R. BACHELOT, and P. ROYER, *Rev. Sci. Instrum.* **1998**, *69*, 1735.
- 50 a) S. S. WONG, E. JOSELEVICH, A. T. WOOLLEY, C. L. CHEUNG, and C. M. LIEBER, *Nature* **1998**, *394*, 52. b) S. S. WONG, J. D. HARPER, P. T. LANSBURY, and C. M. LIEBER, *J. Am. Chem. Soc.* **1998**, *120*, 603.
- 51 a) C. BUSTAMANTE, D. A. ERIE, and D.

- KELLER, *Curr. Opin. Struc. Biol.* **1994**, 4, 750. b) C. BUSTAMANTE and D. KELLER, *Phys. Today* **1998**, 48, 32.
- 52 A. A. BASKI, to be published in *Advanced Semiconductor and Organic Nano-Techniques*, edited H. MORKOC, Academic Press, San Diego, CA **2003**, Part 3, p. 1.
- 53 P. MANANDHAR, J. JANG, G. SCHATZ, M. RATNER, and S. HONG, *Phys. Rev. Lett.* **2003**, 90, 115 505.
- 54 C. B. GORMAN, Y. HE, and R. L. CARROLL, *Langmuir* **2001**, 17, 5324.
- 55 M. ZHANG, D. BULLEN, S.-W. CHUNG, S. HONG, K. S. RYU, Z. FAN, C. A. MIRKIN, and C. LIU, *Nanotechnology* **2002**, 13, 212.
- 56 R. LENIGK, M. CARLES, N. Y. IP, and N. J. SUCHER, *Langmuir* **2001**, 17, 2497.
- 57 D. L. WILSON, R. MARTIN, S. HONG, M. CRONIN-GLOMB, C. A. MIRKIN, and D. L. KAPLAN, *Proc. Natl. Acad. Sci. USA* **2001**, 98, 13 660.
- 58 L. M. DEMERS, D. S. GINGER, S.-J. PARK, Z. LI, S.-W. CHUNG, C. A. MIRKIN, *Science* **2002**, 296, 1836.
- 59 J.-H. LIM and C. A. MIRKIN, *Adv. Mater.* **2002**, 14, 1474.
- 60 B. W. MAYNOR, Y. LI, and J. LIU, *Langmuir* **2001**, 17, 2575.
- 61 Y. LI, B. W. MAYNOR, and J. LIU, *J. Am. Chem. Soc.* **2001**, 123, 2105.
- 62 a) S. XU and G. Y. LIU, *Langmuir* **1997**, 13, 127. b) K. WADU-MESTHRIGE, S. XU, and G. Y. LIU, *Langmuir* **1999**, 15, 8580. c) N. A. AMRO, S. XU, and G. Y. LIU, *Langmuir* **2000**, 16, 3006.
- 63 H. ZHANG, R. ELGHANIAN, N. A. AMRO, S. DISAWAL, and R. EBY, *Nano Lett.* **2004**, 4, 1649.
- 64 X. WANG, K. S. RYU, D. A. BULLEN, J. ZOU, H. ZHANG, C. A. MIRKIN, and C. LIU, *Langmuir* **2003**, 19, 8951.
- 65 P. E. SHEEHAN, L. J. WHITMAN, W. P. KING, and B. A. NELSON, *Appl. Phys. Lett.* **2004**, 85, 1589.
- 66 DAVID BULLEN, SUNG-WOOK CHUNG, XUEFENG WANG, JUN ZOU, CHAD A. MIRKIN, and CHANG LIU, *Appl. Phys. Lett.* **2004**, 84, 789.
- 67 A. KUMAR and G. M. WHITESIDES, *Appl. Phys. Lett.* **1993**, 63, 2002.
- 68 a) J. L. WILBUR, A. KUMAR, E. KIM, and G. M. WHITESIDES, *Adv. Mater.* **1994**, 6, 600. b) A. KUMAR, N. L. ABBOTT, E. KIM, H. A. BIEBUYCK, and G. M. WHITESIDES, *Accounts. Chem. Res.* **1995**, 28, 219. c) G. M. WHITESIDES and C. B. GORMAN, in *Handbook of Surface Imaging and Visualization*, edited A. T. HUBBARD, CRC Press, Boca Raton, FL **1995**, p. 713. d) J. L. WILBUR, A. KUMAR, H. A. BIEBUYCK, E. KIM, and G. M. WHITESIDES, *Nanotechnology* **1996**, 7, 452. e) Y. XIA, X.-M. ZHAO, and G. M. WHITESIDES, *Microelectron. Eng.* **1996**, 32, 255. f) H. A. BIEBUYCK, N. B. LARSEN, E. DELAMARCHE, and B. MICHEL, *IBM J. Res. Dev.* **1997**, 41, 159.
- 69 A. KUMAR, H. BIEBUYCK, and G. M. WHITESIDES, *Langmuir* **1994**, 10, 1498.
- 70 a) Y. XIA, E. KIM, and G. M. WHITESIDES, *J. Electrochem. Soc.* **1996**, 143, 1070. b) X. M. YANG, A. A. TRYK, K. HASIMOTO, and A. FUJISHIMA, *Appl. Phys. Lett.* **1996**, 69, 4020.
- 71 T. P. MOFFAT and H. YANG, *J. Electrochem. Soc.* **1995**, 142, L220.
- 72 L. B. GOETTING, T. DENG, and G. M. WHITESIDES, *Langmuir* **1999**, 15, 1182.
- 73 Y. XIA, X.-M. ZHAO, E. KIM, and G. M. WHITESIDES, *Chem. Mater.* **1995**, 7, 2332.
- 74 M. LERCEL, R. C. TIBERIO, P. F. CHAPMAN, H. G. CRAIGHEAD, C. W. SHEEN, A. N. PARIKH, and D. L. ALLARA, *J. Vac. Sci. Technol. B* **1993**, 11, 2823.
- 75 W. T. HUCK, L. YAN, A. STROOCK, R. HAAG, and G. M. WHITESIDES, *Langmuir* **1999**, 15, 6862.
- 76 X. LIU, L. FU, S. HONG, V. P. DRAVID, and C. A. MIRKIN, *Adv. Mater.* **2002**, 14, 231.
- 77 S. G. RAO, L. HUANG, W. SETYAWAN, S. HONG, *Nature* **2003**, 425, 36.
- 78 J. JANG, S. HONG, G. C. SCHATZ, and M. A. RATNER, *J. Chem. Phys.* **2001**, 115, 2721.
- 79 P. E. SHEEHAN and L. J. WHITMAN, *Phys. Rev. Lett.* **2002**, 88, 156 104.
- 80 B. L. WEEKS, A. NOY, A. E. MILLER, and J. J. DE YOREO, *Phys. Rev. Lett.* **2002**, 88, 255 505.

- 81 J. JANG, G. C. SCHATZ, and M. A. RATNER, *Phys. Rev. Lett.* **2004**, 92, 085504.
- 82 L. R. FISHER and J. N. ISRAELACHVILI, *J. Colloid. Interface Sci.* **1981**, 80, 528.
- 83 J. JANG, G. C. SCHATZ, and M. A. RATNER, *J. Chem. Phys.* **2002**, 116, 3875.
- 84 A. IVANISEVIC and C. A. MIRKIN, *J. Am. Chem. Soc.* **2001**, 123, 7887.
- 85 M. B. ALI, T. ONDARCUHU, M. BRUST, and C. JOACHIM, *Langmuir* **2002**, 18, 872.
- 86 J. C. GARNO, Y. YANG, N. A. AMRO, S. CRUNCHON-DUPEYRAT, S. CHEN, and G. LIU, *Nano Lett.* **2003**, 3, 389.

Mechanical Properties

7 Scanning Probe Microscopy of Complex Polymer Systems: Beyond Imaging their Morphology

*Philippe Leclère, Pascal Viville, Mélanie Jeusette, Jean-Pierre Aimé,
and Roberto Lazzaroni*

7.1 Introduction

The development of nanoscience involves a large effort to study and understand nanometer-scale physical phenomena. Methods using local force probes naturally provide important contributions to these studies. In particular, dynamic force techniques, i.e., using an oscillating probe, are well adapted to soft samples such as polymer materials or biological systems. The first demonstration of their potential was the elucidation of the phase-separated microstructure in thin films of block copolymers with tapping mode atomic force microscopy (TM-AFM) [1–7].

In dynamic modes, two types of operation are possible: either the oscillation amplitude is fixed and the measured signal is the resonance frequency (this is called the noncontact resonant force mode [8]), or the oscillation frequency is fixed and the variations of the amplitude and phase are recorded. This mode is commonly named tapping mode (it is also known as intermittent contact mode [9]) and is the one that is considered in this review. Tapping mode images can be of two different types: in the first, the image corresponds to the changes in the piezoactuator height that are necessary to maintain a fixed oscillation amplitude, through a feedback loop (the height image); in the second, the image contains the changes in the oscillator phase delay relative to the excitation signal (the phase image). The phase measurement in many cases yields images reflecting tiny variations of the local properties of the sample surface. On that basis, it is possible to extract useful information from tapping mode phase images of soft samples, especially for samples showing small-scale compositional heterogeneity, for instance blends of hard and soft materials [5, 10].

Despite the success of TM-AFM for microstructural characterization, important questions remain about the physical origin of the image contrast [11–15]. The height images are generally considered to display topographic information, but it must be kept in mind that the local mechanical properties of the sample (i.e., the possibility that the tip penetrates the surface slightly) may also contribute to the contrast in the height image. For the phase image, in the dominant repulsive re-

gime the phase shifts are related to the local mechanical properties. It is worth to mentioning that, in order to keep the oscillating behavior of the tip well defined, the perturbation to the oscillator due to the contact with the surface is chosen to be small; in other words, the reduction of the free amplitude (the set point) is only a few percent. This method has two advantages: from an experimental point of view this allows easy identification of hard and soft domains: the strongly phase-shifted parts of the image corresponding to hard domains. From a theoretical point of view, it allows the use of simple approximations providing analytical solutions that help to interpret the experimental data [5, 13–15].

This chapter is organized as follows: we first present the major morphological features observed with TM-AFM in a series of polymer systems of growing complexity: polymer blends, block copolymers, and hyperbranched polymers. We then summarize the models that describe the behavior of the oscillating tip interacting with the surface and we present a straightforward method, based on the analysis of approach–retract curves, which provides unambiguous quantitative measurement of the local mechanical response and/or topographic contribution(s). We illustrate our approach with different polymer systems that present pure topographic contrast, pure mechanical contrast, or a mixture of the two contributions.

We briefly discuss results, showing how a simple analysis of the sample mechanical response is able to provide information on the vertical location of nano-objects inside a polymer network.

7.2

Microscopic Morphologies of Multicomponent Polymer Systems

As mentioned above, the discrimination between the mechanical and topographic responses in AFM images of viscoelastic materials (such as polymers) has become a critical issue. We address this issue by characterizing designed model polymer systems containing two (or more) chemically distinct components. The most straightforward and simple system is a binary polymer blend (i.e., a mixture of two components A and B). In most cases, polymer blends exhibit a phase separation at length scales that can be easily addressed by AFM (within the range between 100 nm and a few microns) [16]. As the mechanical and chemical properties of polymer blends are determined largely by their phase behavior, the understanding of phase separation processes and the corresponding evolution in morphology is of prime importance and these have been widely studied [16–19]. Let us recall here that phase separation in polymer blends is due to simple thermodynamic considerations: (a) the low entropy of mixing associated with the long molecular structures of polymers; and (b) the fact that the enthalpy of mixing is unfavorable when the chemical nature of the two components is different and there is no specific interaction between them. In the molten state, binary polymer blends exhibit phase-separated domains that depend on the composition of the mixture and the temperature. Most polymer blends exhibit lower critical solution temperatures (LCSTs), meaning that the two polymers become more miscible as the temperature is low-

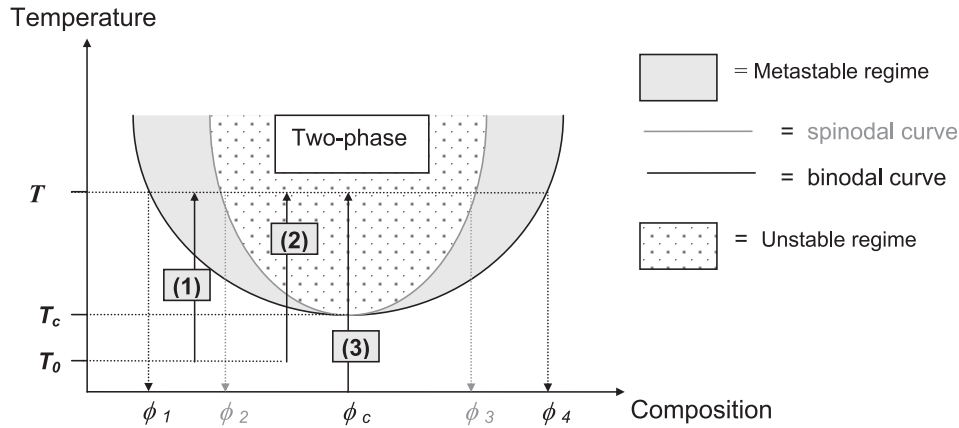


Fig. 7.1 Phase diagram of polymer blends as a function of composition and temperature. While the binodal separates the one-phase region from the metastable regime, the spinodal curve separates the metastable from the unstable regime within the two-phase region. The binodal and spinodal curves meet at the critical point.

ered (Fig. 7.1). The solid line is called the binodal curve and the dashed line is the spinodal curve. These two lines define regions where the kinetics of phase separation are different [16–19].

In contrast, thin films of binary polymer blends prepared from a solution can, in certain conditions, show a homogenous morphology corresponding to mixing of the two components at the molecular level. This particular case can be reached, for instance, when the blend is trapped in an out-of-equilibrium state, due to the very quick evaporation of the solvent. Starting from this situation, controlled phase separation can then be induced by thermal annealing above the LCST curve (Fig. 7.1). The phase separation process can take place following two regimes. In the so-called “nucleation and growth” process, a transition (1) from T_0 to T leads to the formation of small phase-separated domains with composition ϕ_1 and ϕ_4 , which can then gradually grow in size. This “nucleation and growth” process occurs only if the transition takes place in the metastable region of the phase diagram. In contrast, the case of a spinodal demixing, for instance transition (2) from T_0 to T , leads to the quick and spontaneous development of a co-continuous binary morphology. The difference in concentration $\delta\phi$ between the phase-separated domains tends to the limit compositions ϕ_2 and ϕ_3 . In the particular case where the initial composition of the blend is ϕ_c , i.e., the concentration at the critical point (T_c, ϕ_c), the transition (3) always leads to the instability area of the phase diagram, meaning that the phase separation takes place in the spinodal regime. In both cases (spinodal and binodal), the domains that are generated in the early stages of the phase separation can later grow in size by coalescence [16–19].

In this review, we have chosen to describe a particular polymer blend based on poly(methyl methacrylate) (PMMA) and poly(ϵ -caprolactone) (PCL) which sponta-

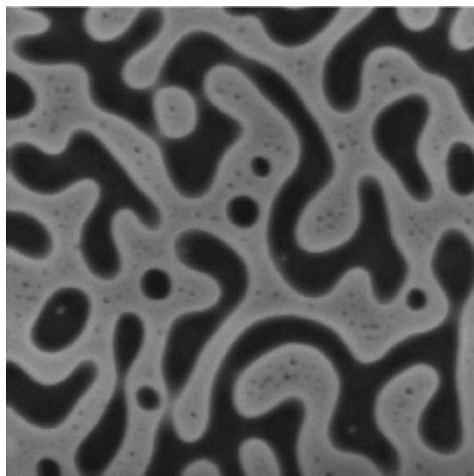


Fig. 7.2 TM-AFM height image ($8.0 \times 8.0 \mu\text{m}^2$) of a 75:25 PMMA–PCL co-continuous polymer blend film. PMMA appears brighter than PCL. The vertical gray scale is 80 nm.

neously phase-separates in well-defined domains when prepared as thin films from solution. The main interest of this system lies in the fact that both components are biocompatible and that PCL is also biodegradable, making these materials very interesting for biomedical applications. In certain conditions (solvent, composition, deposition conditions, etc.), PMMA/PCL naturally phase-separates, producing domains rich in semicrystalline PCL (dark areas) embedded in an amorphous matrix rich in PMMA (bright areas), and leading to the coexistence at the surface of both rigid, partly crystalline regions and softer amorphous regions (Fig. 7.2). The AFM characterization of these heterogeneous systems deserves special attention because both topographic and mechanical aspects are present in the images.

An alternative approach to polymer blends is the elaboration of copolymers for which different macromolecular sequences, with controlled degrees of polymerization, are covalently bonded to yield block architectures such as AB diblock, ABA or ABC triblock, or $(AB)_n$ multiblock types [20, 21]. More recently, star-block architectures having a central point with three or more arms, each of which is a block copolymer usually of the AB type, have been attracting intense interest. Similarly to the polymer blends, the different sequences within the copolymer chains phase-separate, but the fact that they are covalently bonded imposes a constraint on the phase separation process. Therefore a classical phase diagram, such as that shown in Fig. 7.1, cannot be used to describe the process. Instead, phase separation in block copolymers is described by the term “order–disorder transition” (ODT) (Fig. 7.3). At sufficiently high temperatures or when they are sufficiently diluted in a good solvent, the blocks can intermix freely generating the “disordered” structure shown on the right in Fig. 7.3. However, in most conditions, the blocks spontane-

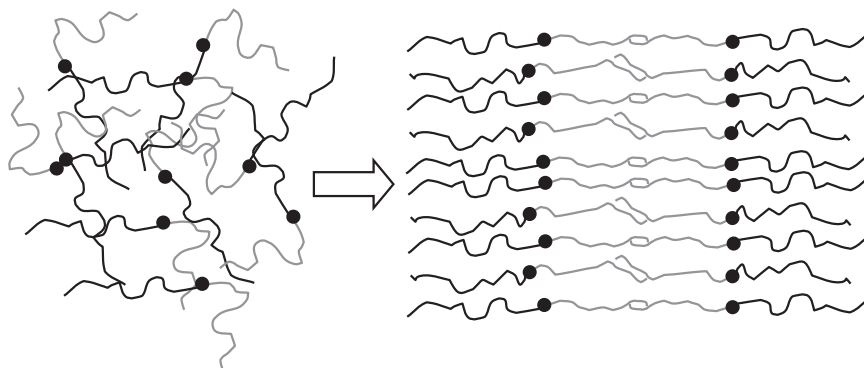


Fig. 7.3 Schematic representation of the order–disorder transition (ODT) in block copolymers.

ously self-assemble into a diversity of mesophases corresponding to pure distinct nanodomains composed of the different blocks (shown at the top of Fig. 7.4a). The size and the shape of those domains are governed mainly by the relative block lengths. Figure 7.4 shows the typical phase diagram [22] and the known equilibrium mesophases (spheres, cylinders, lamellae, and gyroids) observed for amorphous diblock copolymers, where the different blocks self-assemble into distinct domains. In this phase diagram, f_A is the volume fraction of block A, χ is the Flory interaction parameter, and N is the degree of polymerization.

Because of the constraint imposed by the covalent bonding between the blocks and the typical molecular weight values of the blocks (between 5000 and 100 000), phase separation in block copolymers occurs at a length scale that is much smaller than for polymer blends. Along the same lines, the very well-defined periodicity of the phase-separated domains makes these materials very interesting model systems for AFM measurements, in particular for quantitative investigations.

Among the various block copolymer architectures described in the literature, the most commonly studied system consists in linear diblock or triblock copolymers combining thermoplastic and elastomeric sequences. These materials, known as “thermoplastic elastomers,” exhibit synergic properties that fill the gap between pure rigid materials and soft elastomers and are therefore a valuable alternative to polymer blends [23]. Below the glass transition temperature (T_g) of the thermoplastic component, the thermoplastic microdomains are rigid and act as physical crosslinks for the elastomeric matrix, so that the material behaves as a vulcanized rubber. Above the T_g of the thermoplastic microdomains, the copolymer flows and the material can be processed by traditional techniques. Because these materials exhibit a regular, periodic array of domains with different local mechanical properties, they constitute ideal model systems for the present study. Over the past few years, we have characterized thin films of symmetric all-acrylate triblock systems [1, 4, 6, 24]. The central block of these copolymers consists of a low- T_g poly(alkyl

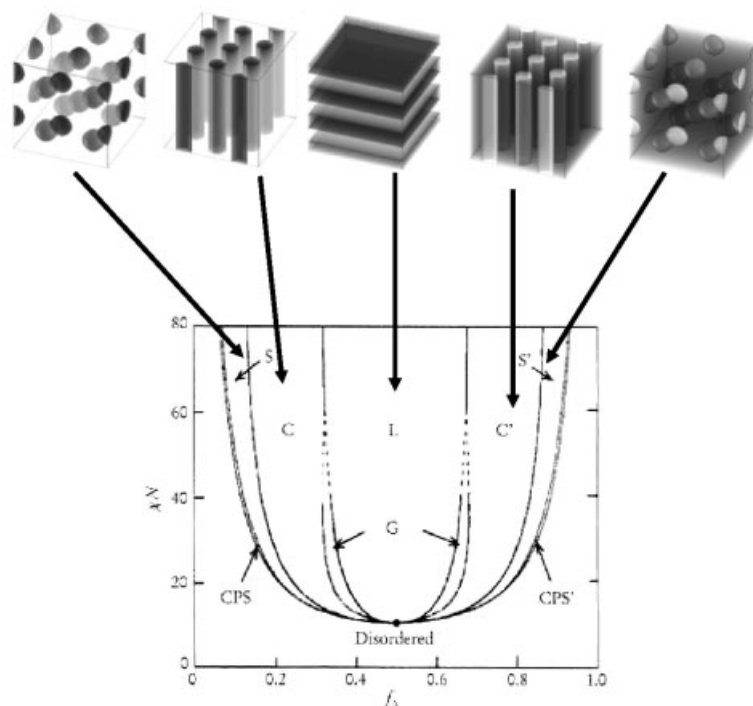
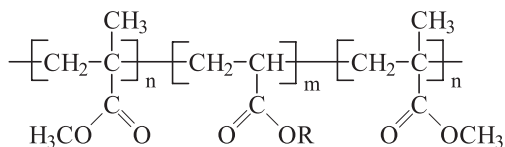


Fig. 7.4 Phase diagram of diblock copolymers illustrating the different morphologies (S = spheres, C = cylinders, G = gyroids, L = lamellae). (Adapted from ref. 22.)

acrylate) rubbery sequence (see Scheme 7.1), which is the major component of the copolymer. The outer two blocks are identical thermoplastic sequences of poly(methyl methacrylate), PMMA. The PMMA homopolymer has a T_g well above room temperature ($T_g = 110\text{ }^\circ\text{C}$).

When prepared from solutions in a good solvent of the constitutive sequences, films of copolymers like those shown in Scheme 7.1 exhibit nanophase separation between pure rubbery and glassy domains. Selecting the appropriate proportion of PMMA in the copolymer allows a highly regular lamellar morphology to be obtained (Fig. 7.5).



Scheme 7.1 Chemical structure of the triblock copolymers (R = alkyl).

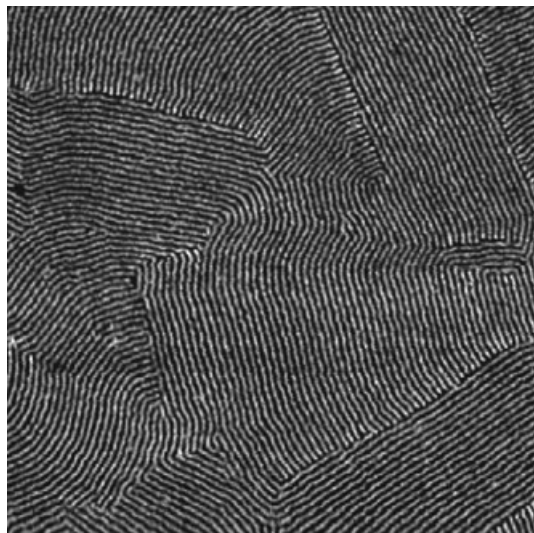


Fig. 7.5 TM-AFM phase image ($2.0 \times 2.0 \mu\text{m}^2$) of a film of PMMA-*b*-poly(butyl acrylate)-*b*-PMMA block copolymer annealed at 140°C , illustrating the lamellar morphology. The lamellar period is 27 nm.

When dissolved in a solvent that is selective for only one constituent, block copolymers tend to self-assemble into micelles or vesicles (micelles are filled objects while vesicles are hollow objects). This process originates from the minimization of the interactions between the solvent and the insoluble segment(s) of the copolymer. The micelles are characterized by a core-shell structure in which the insoluble block forms the core and the soluble chains form the diffuse corona. Such organized structures have made diblock copolymers of great importance in nanotechnology applications; micellar systems are indeed used in many industrial and pharmaceutical preparations as dispersants, stabilizers, wetting agents, etc. As an illustration, we show, in Fig. 7.6(a), the morphology that is typically obtained when linear poly(styrene)₂₉₀-*b*-poly(isoprene)₁₁₀ (PS₂₉₀-*b*-PI₁₁₀) (volume fraction $\Phi_{\text{PS}} = 0.78$) diblock copolymer molecules spontaneously self-assemble into unimodal spherical micelles in the presence of heptane, a selective solvent for the PI blocks. In this case, the PI blocks can fully extend into the solvent to stabilize the PS core, yielding 40 nm-wide spherical micelles. The aggregation of linear molecules in these micelles is a process that is independent of the solution concentration [25, 26].

Recently, we have shown that chain cyclization is a key parameter that strongly affects the micellar aggregation of PS₂₉₀-*b*-PI₁₁₀ diblock copolymers in heptane: both the size and the shape of the micelles evolve when the concentration is increased, starting from small individual “sunflower-like” micelles at low concentra-

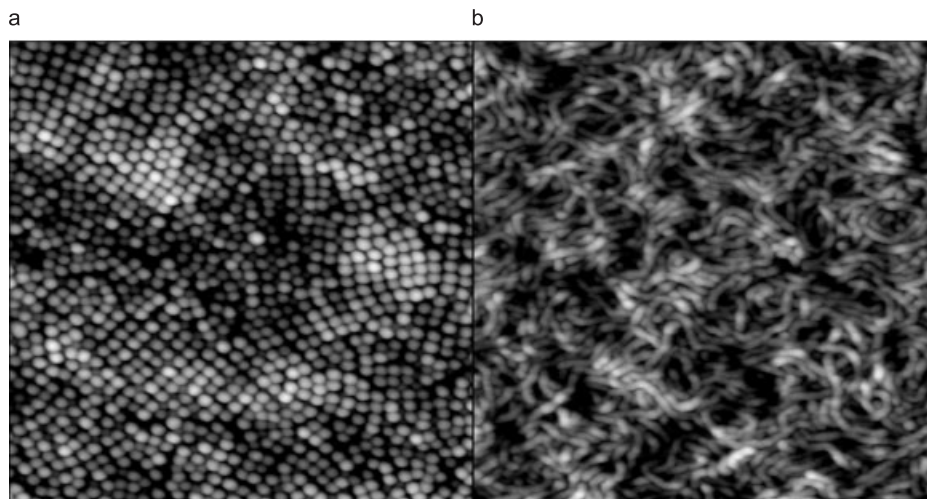


Fig. 7.6 TM-AFM topography images ($1.5 \times 1.5 \mu\text{m}^2$) of micelles of $\text{PS}_{290}\text{-}b\text{-PI}_{110}$ copolymers obtained from 3 mg mL^{-1} solutions in heptane: micellar aggregation of (a) the linear and (b) the cyclic form.

tions, to giant worm-like micelles at higher concentrations (Fig. 7.6b, below). The “sunflower” micelles are formed in the case of the cyclic copolymer because the short PI corona loops back into the large PS core. The giant worm-like micelles result from the unidirectional self-assembly of “sunflower-like” elementary micelles [25, 26].

As a step further in the design of complex polymer architectures, the preparation of unique macromolecular objects with topologically organized elementary building blocks (for instance, highly specific branched and hyperbranched polymers with dendritic, dendronized, star- and comb-like architectures) is being pursued intensively [27–29]. Thanks to well-controlled multistep synthetic approaches, different degrees of molecular architecture complexity can be generated and various molecular assemblies can be prepared. AFM analysis not only provides information on the nanoscale organization of these branched copolymer molecules in thin solid films but also allows determination of their molecular characteristics such as the geometrical parameters (contour length, width, and height), the molar mass distribution, and chain conformation [30–32].

In Fig. 7.7, we show some of the typical morphologies that can be obtained for those complex polymer systems. Comb-like polymer chains, shown in Fig. 7.7(a), adopt a worm-like cylindrical brush conformation instead of a statistical coil because of the steric hindrance due to the lateral segments. Depending on the density of branches, the stiffness of the chain is modified; in a situation where the branch density becomes very high, the steric repulsion between the side chains

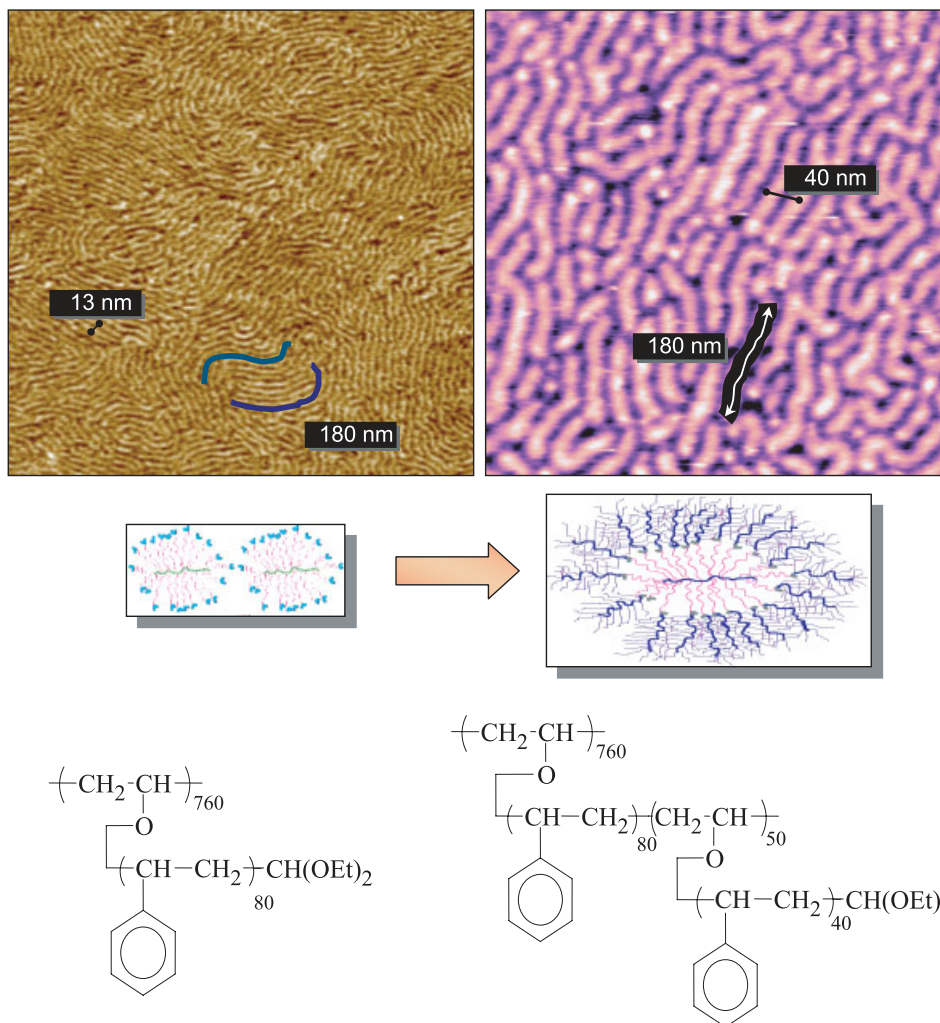


Fig. 7.7 Top: TM-AFM images ($750 \times 750 \text{ nm}^2$) of the surface organization of the (760/80) comb-like (left, phase image, z scale is 15°) and (760/80/50/40) arborescent (right, height image, z scale is 10 nm) copolymer molecules. Bottom: schematic representations of the two molecular architectures.

leads to such stiffening of the backbone that the persistence length becomes comparable with the contour length of the molecule.

Important information also revealed by the AFM imaging is the relationship between the geometrical parameters of the molecules and their architecture. As an example, Fig. 7.7 shows the large increase in width of the molecules when their

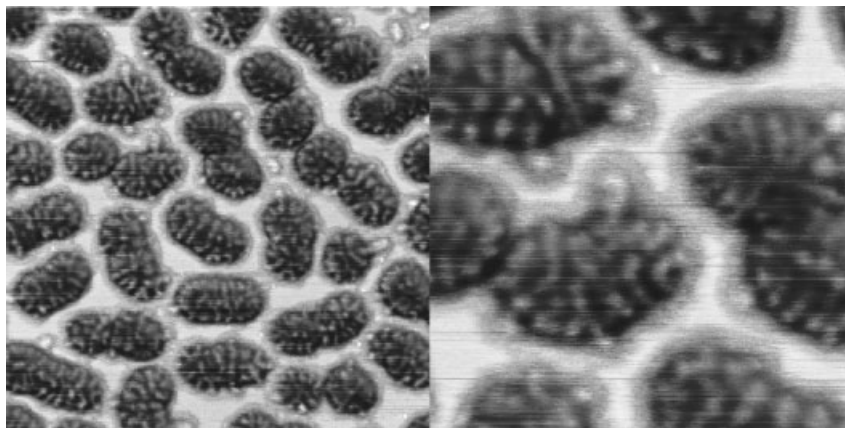


Fig. 7.8 TM-AFM images of single amphipathic core-shell dendrigraft molecules composed of PCEVE₂₀₀-g-(PS₅₀-b-(PCEVE₅₀-g-(PS₅₀-b-PsiVE₉₀-b-PGVE₁₂))) deposited on mica from a 0.01 wt.% THF solution. Left: 800 × 800 nm² phase image. Right: 300 × 300 nm² phase image. These images highlight the internal molecular structure.

structural complexity is modified from a comb-like compound made of a backbone of chloroethyl vinyl ether (CEVE) units bearing poly(styrene) (PS) grafted chains to a first-generation arborescent (PCEVE-g-(PS-b-(PCEVE-g-PS))) copolymer. This large increase in molecule thickness is explained by the fact that, in the arborescent system, each lateral segment of the molecule consists of a “comb-like” structure, bound to a common backbone. The higher steric hindrance of these longer and bulkier side chains causes the average thickness of the molecules to increase from 13 ± 0.7 nm for an (800/80) comb-like copolymer up to 40 ± 1.1 nm for an (800/80/50/40) arborescent copolymer, consistently with the evolution of the corresponding molecular masses.

Along the same lines, it is also possible to synthesize hyperbranched macromolecules constituted of distinct amphipathic subdomains. The internal morphological organization of single nano-objects into discrete subdomains with different properties may give rise to important developments in the nanotechnology area. In Fig. 7.8, we show the morphology of such amphipathic core-shell dendrigrafts composed of PCEVE₂₀₀-g-(PS₅₀-b-(PCEVE₅₀-g-(PS₅₀-b-PsiVE₉₀-b-PGVE₁₂))) whose peripheral functionalities are diblock copolymers made of 2-((*tert*-butyldimethylsilyl)-oxy)ethyl vinyl ether (SiVE) sequences and galactose-substituted vinyl ether (GVE) sequences. These macromolecules exhibit an internal structure that corresponds to phase segregation between the PS blocks and the PVE blocks. The dimensions and organization of these subdomains are likely to be governed by the reduced mobility of the external diblock branches of the dendrigrafts, which are attached at one end to the central backbone and therefore can interdigitate and aggregate only with the neighboring branches.

These amphipathic core-shell dendrigrafts with hard/soft, polar/nonpolar, or

hydrophilic/hydrophobic subdomains can be considered as the first practical examples of this class of molecules; in addition, they are very good model systems to help understand the contribution of the mechanical and topographic response in the AFM images.

7.3

Methodology

7.3.1

Intermittent Contact versus Noncontact Atomic Force Microscopy

Dynamic modes were first conceived to minimize the contact between the tip apex and the surface, while keeping the ability to measure weak variations of the force. Thus, images can be recorded with only a very brief intermittent contact over a cycle of oscillation or even with no contact at all. As a result, if not totally removed, the shear forces are significantly reduced. The development of dynamic modes can be seen as a breakthrough in scanning probe microscopy as their ability to probe minute forces has opened avenues in imaging soft materials reproducibly and routinely, reaching atomic resolution in ultrahigh-vacuum conditions.

Two modes of operation can be considered for measuring changes of the oscillating behavior when the tip interacts with a surface:

- In the amplitude modulation (AM) mode [9, 33], often called the “tapping” mode, the tip–cantilever system is excited at a fixed drive frequency and a fixed amplitude. As microscopes using this mode are commercially available and measurements do not require particularly stringent constraints, the AM mode is the one most commonly used. Its first major success was its ability to image polymers without inducing severe damage, in contrast to what happens in contact mode [1–3]. As a result, many AM studies are dedicated to very soft samples such as biological systems and polymers [2, 15, 34]. Consequently, the approach described in this methodology section can be applied to the AFM imaging of polymers, DNA, and proteins. However, while the AM mode provides a convenient and easy way to image soft materials, quantitative analysis of the experimental data is still not easy. Because the tip–cantilever oscillator can exhibit a nonlinear behavior when brought into the proximity of the surface, the interpretation of the variations of the oscillation amplitude and the phase at a fixed drive frequency and fixed drive excitation is far from being straightforward [35, 36]. In particular, changes in the oscillation amplitude can be the result of either a conservative or a dissipative interaction. Also, a decrease of the phase can be due to either an attractive or a repulsive interaction. Therefore, only simultaneous recording of the amplitude and the phase variations together with appropriate models can help reach a proper interpretation of the data.
- The second mode uses the frequency modulation (FM) technique; it is often called the noncontact resonant mode [8]. The FM mode was first used under

ultrahigh-vacuum experimental conditions to image semiconductor surfaces. The basic idea is to use a negative resonant frequency shift at constant oscillation amplitude as the error signal to control the distance between the tip and the surface. When this is done, the interaction between the tip and the surface remains attractive so that the tip never touches the surface. The key experimental achievement was to show that the FM mode was able to obtain images with contrast on the atomic scale [37]. The experimental parameters that depend on the interaction between the tip and the surface are the resonance frequency variation and the damping signal extracted from the energy per cycle supplied to keep the oscillation amplitude constant. Contrary to AM, in which the oscillation amplitude is kept constant, the physical origin of the changes for the oscillating properties at the resonance frequency is straightforwardly attributed. The frequency shift is related only to conservative interactions, and the additional damping signal is governed only by the dissipative interaction. However, the high sensitivity of the FM mode sets severe conditions on the quality of the sample (nearly flat surfaces at the image scale with little contamination), as compared with AM mode. The interpretation of the data can then be simplified *a priori*, as illustrated in ref. [38], where the tip-sample force is extracted from the frequency and damping signals recorded during FM approach-and-retract curves.

7.3.2

Modeling the Oscillating Behavior

As an introduction to this section, we first discuss the modeling of the oscillator to interpret FM experimental data, then we move on to variations of the oscillation amplitude and phase as recorded in tapping mode experiments.

7.3.2.1 Conservative Interaction

Any variation of the resonant frequency shift from the basis of the harmonic oscillator theory corresponds to either a change in the mass of the oscillator or a change in an effective spring constant. For an AFM oscillator, a mass transfer is not expected; therefore an effective spring constant taking into account the variation of the interaction force is responsible for the frequency shift. A general expression to describe the resonant frequency shift is Eq. (1), where ν_0 is the resonant frequency in the absence of any interaction, $k_{\text{int}}^{\text{eff}}$ is an effective spring constant describing the change in the interaction between the tip and the surface over a cycle; ν and k_c are the resonant frequency and cantilever spring constant, respectively.

$$\Delta\nu = \nu_0 \left(\sqrt{1 + \frac{k_{\text{int}}^{\text{eff}}}{k_c}} - 1 \right) \quad (1)$$

The high sensitivity of commercially available electronics allows easy measurements of weak effective spring constants. For example, with a cantilever spring constant $k_c = 10 \text{ N m}^{-1}$, an effective spring constant as small as $k_{\text{int}}^{\text{eff}} 10^{-4} \text{ N m}^{-1}$ can be recorded readily with commercially available frequency demodulators [39].

From the experiments, one would like to deduce the laws of interaction from the variations of the oscillation behavior. There have been numerous studies aimed at relating the frequency shifts to the attractive tip–sample interaction that considered a power-law dependence for the attractive interaction such as Eq. (2).

$$F_{\text{int}}(D - x(t)) = -\frac{C}{(D - x(t))^n} \quad (2)$$

The resonance frequency shift was first derived using the Hamilton–Jacobi formalism; the frequency shift is then given by Eq. (3), where $I_1(n) = \int_{-\infty}^{\infty} \frac{1}{(1 + y^2)^n} dy$ gives tabulated values (see, e.g., ref. 36). Δ is the shortest distance between the tip and the surface, A_0 is the resonance amplitude, and C is a constant related to the strength of the attractive interaction [40].

$$\Delta\nu(\Delta, k, A_0, C, n) \cong -\frac{1}{\sqrt{2\pi}} \frac{v_0}{kA_0^{3/2}} \frac{C}{\Delta^{n-1/2}} I_1(n) \quad (3)$$

A more general development based on the principle of least action was then proposed; it gives similar results. This method includes the influence of the quality factor, so it is not restricted to the analysis of the resonant frequency shifts [41].

Only a few analyses have been dedicated to the study of the tip–sample interaction when the tip penetrates the material. This is by far the most difficult case to solve. It is mostly related to experimental situations in which significant indentation occurs, and thus to studies performed on soft materials. In that case, the balance between the repulsive and the attractive interaction needs to be evaluated. Due to the complexity of the problem, phenomenological approaches, including contact mechanics, are often used [36, 42]. In particular when contact mechanics is used, a singularity between the attractive and the repulsive interactions appears; it can only be removed with an approximate expression and the introduction of a characteristic length as a contact distance. In addition, in contact mechanics a nonlinear relationship links the elastic repulsive force and the indentation depth so that analytical expressions cannot be obtained [42–43].

7.3.2.2 Dissipative Interaction

In addition to the conservative forces acting during the tip sample interaction, one must also consider dissipative interactions, which give rise to additional energy losses during each oscillation period. Dissipation manifests itself as a hysteresis of the force versus displacement curve. Dissipation mechanisms may involve electrical losses, time delays, such as those that happen in viscoelastic materials [13, 15, 44], or mechanical instabilities due to adhesion [24, 45].

The discrimination between the contributions of viscous processes and mechanical instabilities to the energy loss might sometimes be difficult to achieve. However, several features are specific to each mechanism. Energy loss due to viscous

effects exhibits an oscillation amplitude dependence and, when soft materials are involved, an indentation depth dependence. For adhesion hysteresis without any viscous effect, an instability criterion governs the energy loss [45]. Consequently, the additional dissipated energy must be a constant [39, 45]. Since the present review deals with soft polymer samples, we focus mostly on additional damping due to a viscous behavior. The total damping coefficient is expressed in Eq. (4) [11], where $\gamma_0 = \frac{k_c}{\omega_0 Q}$ is the damping coefficient of the AFM oscillator in the absence of interaction between the tip and the surface.

$$\gamma_{tot} = \gamma_0 + \gamma_{int} \quad (4)$$

Typically, in vacuum, $\gamma_0 = 2 \times 10^{-9} \text{ N s m}^{-1}$ with $k_c = 20 \text{ N m}^{-1}$, $\omega_0/2\pi = 175 \text{ kHz}$ and $Q = 20000$. For an oscillation amplitude $A = 10 \text{ nm}$, the corresponding dissipated energy per period without interaction is:

$$\langle E_{diss}^0 \rangle = \frac{k_c \pi A^2}{Q} \approx \pi 10^{-19} \text{ J}$$

In air, $Q = 500$ and the dissipated energy becomes $\langle E_{diss}^0 \rangle = \frac{k_c \pi A^2}{Q} \approx 10^{-17} \text{ J}$. The measured damping signal, measured upon interaction, is given by Eq. (5)

$$Damp = Damp_0 \left(1 + \frac{\gamma_{int}}{\gamma_0} \right) \quad (5)$$

Writing $\frac{\gamma_{int}}{\gamma_0} = \frac{\langle E_{diss}^{int} \rangle_T}{\langle E_{diss}^0 \rangle_T}$, the additional damping coefficient γ_{int} can be converted into the dissipated power. Thus in ambient conditions, one can measure a damping increase of about 10^{-19} J , while in vacuum at room temperature it can be as low as $k_B T$.

In order to extract the main features when tip indentation takes place, one can borrow approaches usually employed to interpret rheological experiments. We shall consider a simple shear experiment, in which the viscoelastic material is squeezed between two flat plates. The lower plate is set idle and a lateral oscillatory motion is imposed on the upper plate. The indentation of the tip inside the polymer is assimilated into the motion of the upper plate. To determine the constitutive equation for the problem, we describe the viscoelastic material with a simple Maxwell model [15, 46]. The corresponding mechanical element is made of a spring and a dashpot in series. The constitutive equation is Eq. (6), where σ is the stress in the mechanical element and $\dot{\gamma}$ the shear rate. τ_s is the relaxation time, and η the zero-frequency viscosity.

$$\sigma(t) + \tau_s \dot{\sigma}(t) = -\eta \dot{\gamma}(t) \quad (6)$$

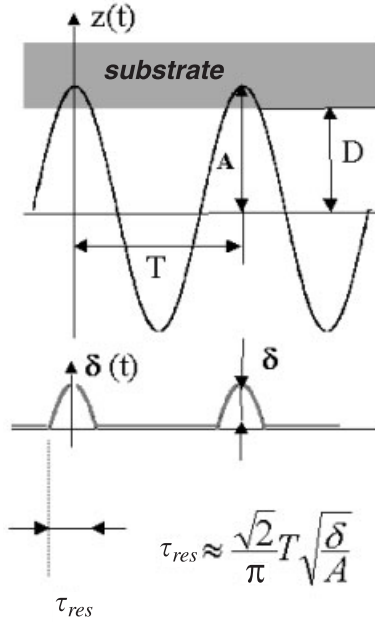


Fig. 7.9 The indentation δ at fixed amplitude A .

The basic assumptions are that the sample displacement in intermittent contact is imposed by the tip and that the material is incompressible. Contrary to usual rheological experiments, the imposed displacement when the tip is inside the polymer is not simply given by the oscillation of the tip. The displacement is imposed by pulses and the time dependence of the indentation depth is given by Eq. (7); $\delta(t) = 0$ elsewhere.

$$\delta(t) = A \cos(\omega t) - D \quad \text{for } t \leq |\tau_{res}/2| \quad (7)$$

D is the distance between the surface and the tip at rest, with $A > D$; τ_{res} , the residence time of the tip in the sample, is the fraction of the oscillation period T such that $A \cos(\omega t) > D$ giving $A \cos(\omega \tau_{res}/2) = D$ or $\tau_{res} = 2/\omega \arccos(D/A) \approx \pi/T(2\delta/A)^{1/2}$ for $\delta \ll A$ (see Fig. 7.9).

The Fourier components of the even function $\delta(t) = \sum_{n=0}^{\infty} \delta_n \cos(n\omega t)$ are given by Eq. (8)

$$\delta_n = \frac{A}{\pi} \left\{ \frac{\sin\left[(n-1)\frac{\omega\tau_{res}}{2}\right]}{n-1} + \frac{\sin\left[(n+1)\frac{\omega\tau_{res}}{2}\right]}{n+1} \right\} - \frac{2D}{\pi} \frac{\sin\left(n\frac{\omega\tau_{res}}{2}\right)}{n} \quad (8)$$

This expression is not very convenient to use. The coefficients vanish rapidly with increasing n , with a sharpening of their distribution when τ_{res} increases. Fol-

lowing an approach similar to that given in reference [44], we define a maximum harmonic number $n_0 = T/\tau_{res}$ such that the coefficients δ_n are set as $2\delta\tau_{res}/T$ for $n \leq n_0$ and $\delta_n = 0$ for $n > n_0$. This simplified assumption leads to tractable expressions for the damping coefficient.

To calculate the stress and the dissipated energy, we use the Boltzmann superposition principle relating the stress to the history of the strain [47], to obtain Eq. (9), where $G(t) = \eta/\tau_s \exp(-t/\tau_s)$ is the material relaxation modulus.

$$\sigma(t) = - \int_{-\infty}^t G(t-t') \dot{\gamma}(t') dt' \quad (9)$$

For the sake of simplicity, we neglect the tensorial aspects and consider a simple shear strain. An estimation of the shear rate $\dot{\gamma}$ can be obtained assuming a no slip condition at the surface of the tip and a displacement vanishing inside the material over a distance similar to the radius of contact ϕ from the surface. Hence we set $\gamma \sim \delta/\phi$ and $\dot{\gamma} \sim \dot{\delta}/\phi$, where ϕ is the tip contact diameter. This nanorheological experiment gives a large γ of about 1 and, since the residence time is typically on the order of 1 μ s, the shear rate is also very large ($\dot{\gamma} \sim 10^6 \text{ s}^{-1}$).

To calculate the stress $\sigma(t)$ [Eq. (9)], we use the approximate Fourier coefficient of the displacement δ_n with the variable transformation $s = t - t'$:

$$\dot{\gamma}(t') = -\frac{1}{\phi} \sum_{n=1}^{\infty} n\omega\delta_n \sin(n\omega(t-s)) \cong -\langle\delta_n\rangle \frac{1}{\phi} \sum_{n=1}^{n_0} n\omega \sin(n\omega(t-s))$$

and the corresponding stress generated by the tip motion [Eq. (10)], using the well-known relationships [Eqs. (11)] between the real and imaginary parts of the complex viscosity and modulus [47].

$$\sigma(t) = 2 \frac{\tau_{res}}{T} \frac{\delta}{\phi} \sum_{n=1}^{n_0} \left\{ \left[\int_0^{\infty} G(s) n\omega \sin(n\omega s) ds \right] \cos(n\omega t) - \left[\int_0^{\infty} G(s) n\omega \sin(n\omega s) ds \right] \sin(n\omega t) \right\} \quad (10)$$

$$\eta'(\omega) = \int_0^{\infty} G(s) \cos(\omega s) ds = \frac{G''(\omega)}{\omega}, \quad \eta''(\omega) = \int_0^{\infty} G(s) \sin(\omega s) ds = \frac{G'(\omega)}{\omega} \quad (11)$$

Equation (10) can be rewritten as Eq. (12).

$$\sigma(t) = 2 \frac{\tau_{res}}{T} \frac{\delta}{\phi} \sum_{n=1}^{n_0} \{ n\omega \eta''(n\omega) \cos(n\omega t) - n\omega \eta'(n\omega) \sin(n\omega t) \} \quad (12)$$

The corresponding energy loss per period is given by Eq. (13), where S is the surface contact between the tip and the sample.

$$E_T^{diss} = S \int_0^T \sigma(t) \dot{\delta} dt \quad (13)$$

Using the approximate sample speed $\dot{\delta}(t) = 2\delta \frac{\tau_{res}}{T} \sum_{n=0}^{n_0} \cos(n\omega t)$ and Eq. (12), we obtain Eq. (14) after a straightforward calculation.

$$E_T^{diss} \cong \frac{S}{\phi} \left[2\delta \frac{\tau_{res}}{T} \right]^2 \frac{T}{2} \sum_{n=1}^{n_0} (n\omega)^2 \eta'(n\omega) \quad (14)$$

With the real part of the Maxwell model complex viscosity $\eta'(\omega) = \frac{\eta_s}{1 + (\omega\tau_s)^2}$ we are led to Eq. (15).

$$E_T^{diss} \cong 4\pi \frac{S}{\phi} \left[\delta \frac{\tau_{res}}{T} \right]^2 \sum_{n=1}^{n_0} n^2 \omega \frac{\eta_s}{1 + (\tau_s n \omega)^2} \quad (15)$$

Finally, the measured damping coefficient γ_{int} is deduced from the relationship $E_T^{diss} = \pi \gamma_{int} \omega_0 A^2$. In Eq. (15), the major difficulty is to evaluate the geometrical parameters S and ϕ , where ϕ is the contact diameter between the tip and the sample: ϕ and the area S must be expressed as a function of the indentation depth δ . The relationship between the indentation depth and the geometrical parameter driving the shear displacement inside the polymer is not known. Unfortunately, in AFM all the geometrical aspects of the contact between the tip and the sample are not well defined; therefore, as an example, we only consider a conical tip shape. For a conical tip $\phi = 2\delta \tan \beta$ and $S = \pi \frac{\tan \beta}{\cos \beta} \delta^2$, where β is the cone half-angle. Then this simple geometrical consideration gives Eq. (16) for the damping coefficient γ_{int} .

$$\gamma_{int} = \frac{4}{\pi} \frac{\delta^4}{A^3} \sum_{n=1}^{n_0} n^2 \eta'(n\omega) \quad (16)$$

From this expression, two asymptotic forms of γ_{int} for fast ($\tau_s n_0 \omega \ll 1$) and slow ($\tau_s \omega \gg 1$) relaxation times of the sample can be obtained:

- For $\tau_s n_0 \omega \ll 1$ $\eta'(n\omega) \cong \eta$ for all n , so therefore Eq. (17) holds.

$$\gamma_{int}^f \cong \frac{4\pi^2 \delta^3}{\pi \omega_0 A^2} \left[\frac{\tau_{res}}{T} \right]^2 \eta_s \omega \sum_{n=1}^{n_0} n^2 \cong \frac{4\pi^2 \delta^3}{\pi \omega_0 A^2} \left[\frac{\tau_{res}}{T} \right]^2 \eta_s \omega \frac{n_0^3}{3} = \frac{\sqrt{2}}{3} \pi^2 \eta_s \frac{\delta^{5/2}}{A^{3/2}} \quad (17)$$

The $A^{-3/2}$ power-law dependence is characteristic of relaxation processes with time constants much smaller than the residence time τ_{res} .

- For $\tau_s \omega \gg 1$ then $\eta'(n\omega) \cong \frac{\eta_s}{(\tau_s n \omega)^2}$ for all n , and Eq. (18) applies.

$$\gamma_{\text{int}}^s \cong \frac{4\pi^2 \delta^3}{\pi \omega_0 A^2} \left[\frac{\tau_{\text{res}}}{T} \right]^2 \frac{\eta_s}{\tau_s^2 \omega} \sum_{n=1}^{n_0} 1 = 2\sqrt{2} \frac{\eta_s}{(\tau_s \omega)^2} \frac{\delta^{7/2}}{A^{5/2}} \quad (18)$$

For large relaxation times τ_s , the damping follows a $(\tau_s \omega)^{-2}$ power law; thus relaxation processes with too long a τ_s do not contribute to dissipation. At fixed indentation δ , the oscillation amplitude dependence $A^{-5/2}$ corresponds to the characteristic asymptotic behavior for relaxation times much longer than the oscillation period T .

These two asymptotic behaviors, namely $A^{-3/2}$ for short τ_s and $A^{-5/2}$ for long τ_s , provide a way to address the relaxation times of the sample and possibly the type of molecular motion induced by the tip [41, 44]. For relaxation times longer than the residence time but shorter than the oscillation period, the power-law dependence on the oscillation amplitude must be intermediate between $-3/2$ and $-5/2$. In that situation, the exponent α of the amplitude power-law dependence $A^{-\alpha}$ for the damping coefficient can be calculated numerically with Eq. (19), where the exact δ_n are now used.

$$\gamma_{\text{int}} = \frac{S}{\pi \omega_0 A^\alpha} \frac{T}{2} \sum_{n=1}^{\infty} (n\omega)^2 \delta_n^2 \eta'(n\omega) \quad (19)$$

The damping coefficient γ_{int} is calculated as a function of the oscillation amplitude A for a given indentation δ and relaxation time τ_s , with a range of τ_s large enough to overlap the two asymptotic regimes. The $\gamma_{\text{int}}(A)$ curves are fitted to a power law $A^{-\alpha}$ for each τ_s , giving a curve $\alpha(\tau_s)$ reported in Fig. 7.10.

7.3.2.3 Stationary States and Transient States: Error and Phase Signal

The immediate success of the AM-AFM mode was that commercially available microscopes were able to image soft polymer surfaces without inducing severe damage on the sample [9]. Thus, the first goal of reducing shear forces was achieved successfully. However, using the AM mode is certainly not the easiest way to understand the nonlinear behavior of the AFM oscillator near the surface. The intrinsic difficulty is that measurements at a fixed drive frequency and fixed drive excitation cannot provide a complete picture of the changes in the resonance curve, which makes the understanding of the changes in the oscillating properties difficult [33, 35, 41–43, 48].

For experimentalists, the main drawback of the AM mode is the time constant related to the quality factor. Between each experimental measurement that involves a variation of the oscillation amplitude, one needs to wait a few $\tau = Q/\omega$ to work again with the stationary state. This bandwidth effect was at the origin of the development of the FM mode [8]. When images are taken with some transient states,

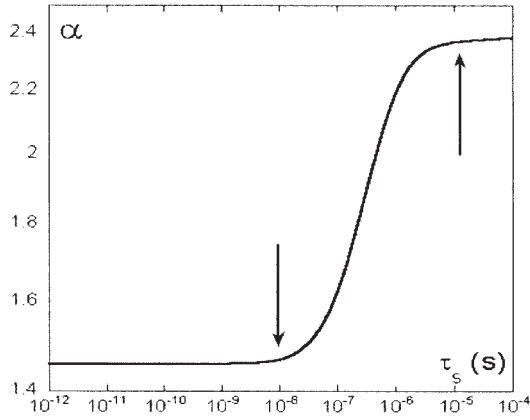


Fig. 7.10 Variation of the amplitude exponent [see Eqs. (16)–(18)] as a function of the sample relaxation time. Note that for very short and long times, the exact numerical results are close to those derived with analytical expressions [Eqs. (17) and (18)].

the feedback control may not work properly and the error signal may modify the phase image significantly [49]. A simple way to illustrate this effect is to perform a first-order expansion on the phase measurement. From the expression of the damping coefficient [Eq. (4)], the phase is described by Eq. (20), where ω_r and A_r are the frequency and oscillation amplitude at the resonance, and γ_0 is the damping coefficient when the tip does not interact with the surface.

$$\sin(\phi) = -\frac{\omega}{\omega_r} \frac{A}{A_r} \left(1 + \frac{\gamma_{\text{int}}}{\gamma_0}\right) \quad (20)$$

Writing ϕ_0 and A_0 for the phase and oscillation amplitude of the oscillator far from the surface, we obtain Eq. (21).

$$\sin(\phi_0) = -\frac{\omega}{\omega_r} \frac{A}{A_r} \quad (21)$$

Then writing $\phi = \bar{\phi} + \Delta\phi$, with $\Delta\phi \ll 1$, gives Eq. (22), where ΔA is the change in the amplitude related to the transient state.

$$\begin{aligned} \sin(\bar{\phi}) \cos(\Delta\phi) + \sin(\Delta\phi) \cos(\bar{\phi}) &\approx \sin(\bar{\phi}) + (\Delta\phi) \cos(\bar{\phi}) \\ \sin(\bar{\phi}) \left[1 + \frac{(\Delta\phi) \cos(\bar{\phi})}{\sin(\bar{\phi})}\right] &\approx -\frac{\omega}{\omega_r} \frac{A + \Delta A}{A_r} \left(1 + \frac{\gamma_{\text{int}}}{\gamma_0}\right) \end{aligned} \quad (22)$$

For the sake of simplicity, working at $\phi_0 = -\frac{\pi}{4} \approx \bar{\phi}$ and using Eq. (21) with no damping for the oscillation amplitude A , Eq. (22) is rewritten, to the first order, as Eqs. (23).

$$\begin{aligned} (\Delta\phi) \frac{\omega}{\omega_r} \frac{A}{A_r} &\approx -\frac{\omega}{\omega_r} \left(\frac{\Delta A}{A_r} + \frac{A}{A_r} \frac{\gamma_{\text{int}}}{\gamma_0} \right) \\ \Delta\phi &\approx -\frac{\Delta A}{A} + \frac{\gamma_{\text{int}}}{\gamma_0} \end{aligned} \quad (23)$$

Therefore, when the feedback control is not properly achieved, as happens when the raster scan velocity is too high, the phase images may mostly contain the relative error signal $\Delta A/A$. When viscoelastic materials are investigated, it might become a very complex and intricate problem that can be partly solved by investigating the sample properties with approach–retract curves.

7.3.2.4 Influence of the Quality Factor upon the Sensitivity

Besides the consideration of the transient time, the use of a high quality factor and the variation of the amplitude as the error signal can be very useful when very soft samples are studied [14, 42]. It can be demonstrated and shown experimentally that a high quality factor in the AM mode can significantly enhance the sensitivity.

To simplify the demonstration, we first study an harmonic oscillator. We set the reduced coordinates $u = \omega/\omega_0$, $a = A/A_0$, $d = D/A_0$. With D the distance between the cantilever at rest and the surface, Eqs. (24) and (25) are obtained.

$$a(u) = \frac{1}{\sqrt{Q^2(1-u^2)^2 + u^2}} \quad (24)$$

$$\phi(u) = \arctan\left(\frac{u}{Q(u^2-1)}\right) \quad (25)$$

Within a linear approximation, a force gradient leads to the frequency shift given by Eq. (26).

$$u_F' = u \pm \Delta u_F \approx \left[u \pm \frac{\nabla F(d)}{2k} \right] \quad (26)$$

When the shift of the resonance frequency is weak, the corresponding change in the oscillation amplitude can be evaluated by Eq. (27), for which the slope is expressed by Eq. (28).

$$\Delta a_F \cong \frac{da}{du} \Delta u_F \quad (27)$$

$$\frac{da}{du} = -\frac{u[2Q^2(u^2-1)+1]}{[Q^2(u^2-1)^2+u^2]^{3/2}} \quad (28)$$

Equation (28) becomes easier to use when the drive frequency u is set at $-\pi/4$ or $3\pi/4$, these two values being close to the maximum of the oscillator sensitivity. At these locations on the resonance curve, one has $Q(u-1) = 1$, and with $Q \gg 1$ Eq. (28) becomes Eq. (29).

$$\frac{da}{du} \approx Q \quad (29)$$

Therefore, when the amplitude is varied for a suitable value of the drive frequency, the sensitivity is proportional to the quality factor. For soft materials this result is of primary importance as it indicates that, with a quality factor high enough, one can image without inducing any indentation into the sample.

Using the crude approximation of a linear elastic response of the surface, one gets relationship (30) between the tip–surface distance and the oscillation amplitude [41], where κ_e is the reduced contact stiffness $\kappa_e = k_e/k$ (k being the cantilever spring constant and k_e the contact stiffness), and with $A > D$ and $A - D = \delta_e$, the indentation depth into the sample.

$$D = A \left[1 - \frac{3\pi}{4\sqrt{2}} \frac{Q(u^2 - 1) + \sqrt{\frac{A_0^2}{A^2} - 1}}{Q\kappa_e} \right]^{2/3} \quad (30)$$

However, even at the resonance frequency ($u = 1$), Eq. (30) remains obscure, and does not help much to understand the main features for intermittent contact situations. Investigating the evolution of the slope as a function of the indentation depth is more appropriate. For the static mode, the slope of the deflection is given by Eq. (31).

$$p(\delta_L) = \frac{1}{1 + \frac{k}{k_e}} \quad (31)$$

For the dynamic mode the slope of the variation of the oscillation amplitude $p(A) = \delta A / \delta D$ is calculated from Eq. (30), as in Eq. (32), where $b(A)$ is a complex function of the amplitude, which is almost constant over a large domain of amplitude variation [41].

$$p(A) = \frac{1}{1 + b(A) \left(\frac{k}{Qk_e} \right)^{2/3}} \quad (32)$$

The main result is that, compared with the static mode, the ratio between the cantilever stiffness and the contact stiffness involves the Q prefactor in the dynamic mode. Therefore the quality factor can significantly enhance the influence of the repulsive interaction, leading to an apparent, much larger, contact stiffness.

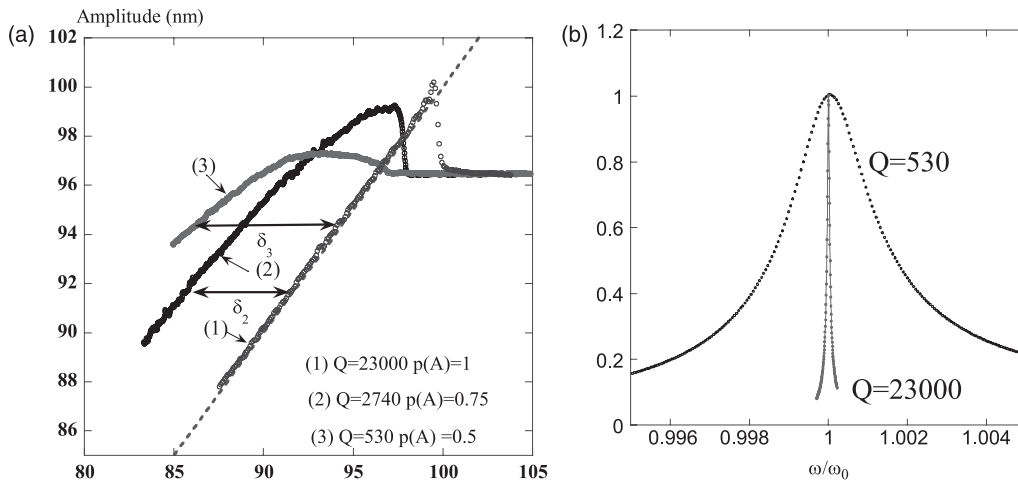


Fig. 7.11 (a) Variation of the amplitude oscillation in AM-AFM on a poly(isoprene) melt. At atmospheric pressure $Q = 530$; at $p = 10$ mbar (7.5 Torr), $Q = 2740$; at $p = 2 \times 10^{-7}$ Torr, $Q = 23\,000$. The broken line is the location of the surface. Arrows show a

maximum in the indentation depth of $\delta_3 = 8$ nm and $\delta_2 = 6$ nm for $Q = 530$ and $Q = 2740$, respectively. (b) Resonance curves at atmospheric pressure and 2×10^{-7} Torr. (Courtesy from *Eur. Phys. Lett.* [14].)

As an example we extract some results from ref. 14 obtained on a polymer melt poly(isoprene) (see Fig. 7.11). The quality factor was varied by changing the vacuum conditions down to 10^{-7} Torr. At such a pressure, the quality factor is $Q = 23\,000$ and the polymer can appear as hard as silica [14]. The slope $p(A)$ is equal to 1, similarly to the case of an infinitely hard surface.

7.3.2.5 Approach–Retract Curve (ARC) Analysis

Usually two tapping mode images are recorded simultaneously. Recording the vertical displacements of the piezo actuator necessary to maintain the oscillator amplitude at a fixed amplitude (the “set-point” rms value) gives the height image. The phase images are formed by the oscillator phase values for those sample–tip positions. All the sections extracted from the images are recorded “as is” without any filter or image treatment. For display purposes, the height images shown are flattened.

Height and phase images of the area of interest (typically a few hundred nanometers) are recorded at 90° scanning direction (see below), at a given set point and fixed frequency. The important point here is to test the repulsive regime, which can be distinguished by a phase delay value always above -90° . Then approach–retract curves are recorded for the same drive amplitude and frequency on a line along the Y axis (usually the image central line) every 5 nm.

When approach–retract curves are being recorded, the sample is moved up and

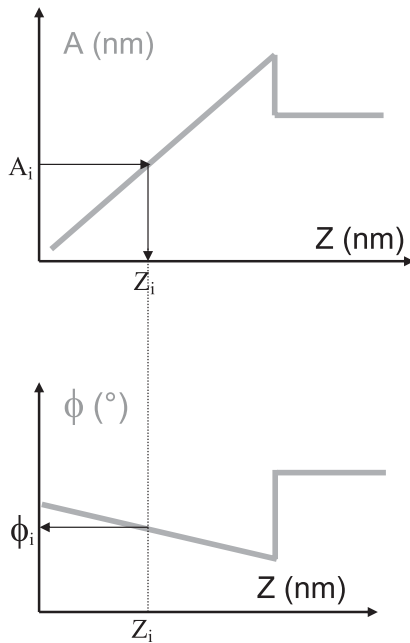


Fig. 7.12 Sketches of the approach part of the approach–retract curves when performed at a frequency slightly below resonance: amplitude A and phase ϕ variations versus vertical displacement Z . To analyze the curves, the amplitude A_i , the corresponding piezoactuator vertical location Z_i , and the corresponding phase ϕ_i are recorded at the set-point value.

down (in the Z direction) at a fixed X, Y location on the surface (see Fig. 7.12). The amplitude and phase are recorded as a function of the vertical displacement of the piezoactuator holding the sample. Typical experimental conditions are 0.5 Hz for the vertical movement frequency and 20 nm for the vertical extension. The experiments are performed at an oscillator frequency slightly below its resonance, as this makes the sample surface location for the approach–retract curves easier. Modeling of the nonlinear behavior of the oscillating cantilever in an attractive field has shown that, at a frequency slightly below resonance, the amplitude and phase exhibit a bifurcation from one state to another (when attractive interaction becomes dominant). This bifurcation happens very close to the surface (typically at 1 nm or less) [39, 42]. The distance at which the oscillator bifurcates from the free amplitude to a higher one (hereafter called D_{bif}) is connected to the strength of the attractive interaction.

To measure and correct the possible drift of the sample holder, height and phase images are then recorded again at the same sample location and under the same amplitude conditions after the series of approach–retract curves has been recorded.

For the image reconstruction, the approach–retract curves are recorded, then analyzed as indicated in Fig. 7.12. The first step is to adjust the distance D_{bif} at which

the oscillator bifurcates, to the same vertical position value for all the approach–retract curves. Such an adjustment assumes a similar tip–sample attractive interaction for all domains, as discussed below. The D_{bif} adjustment makes it possible to extract selectively the mechanical part that participates in the contrast between the different domains; therefore it provides a quantitative measurement of the mechanical contribution. In other words, setting the D_{bif} at an identical vertical distance for all the approach–retract curves is a way to remove the contribution of the topography.

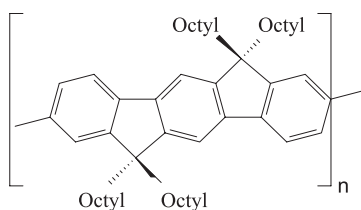
From the amplitude curve, one then checks the vertical position Z_i corresponding to the image fixed amplitude A_i (the set point). Then, from the phase curve, one obtains the corresponding phase, denoted ϕ_i . This operation is repeated for all the Y positions: Z_i and ϕ_i values are thus recorded for all Y positions for which the approach–retract curves are measured. One thus obtains plots of the piezoactuator heights (Z_i) and phases (ϕ_i) versus Y sample locations, which are then compared with the corresponding sections of the tapping mode height and phase images.

7.4 Combined Analysis of Height and Phase Images

Starting from a system in which the contrast observed in the height images is purely topographic (thin films of an indenofluorene homopolymer), we then describe systems where the contrast reflects the difference in mechanical response (indentation) of the different microscopic domains (block copolymers used as thermoplastic elastomers). In that case, it is found that there is no topographic contribution to the phase and height contrast. Finally, we show the example of a polymer blend in which the height images contain information on both the topographic profile and the difference in mechanical response.

7.4.1 Pure Topographic Contribution

We first applied this technique to thin films of a conjugated semiconducting polymer (poly(indenofluorene); see Scheme 7.2). Figure 7.13 illustrates the typical mor-



Scheme 7.2 Chemical structure of poly(indenofluorene) ($n = 20\text{--}22$).

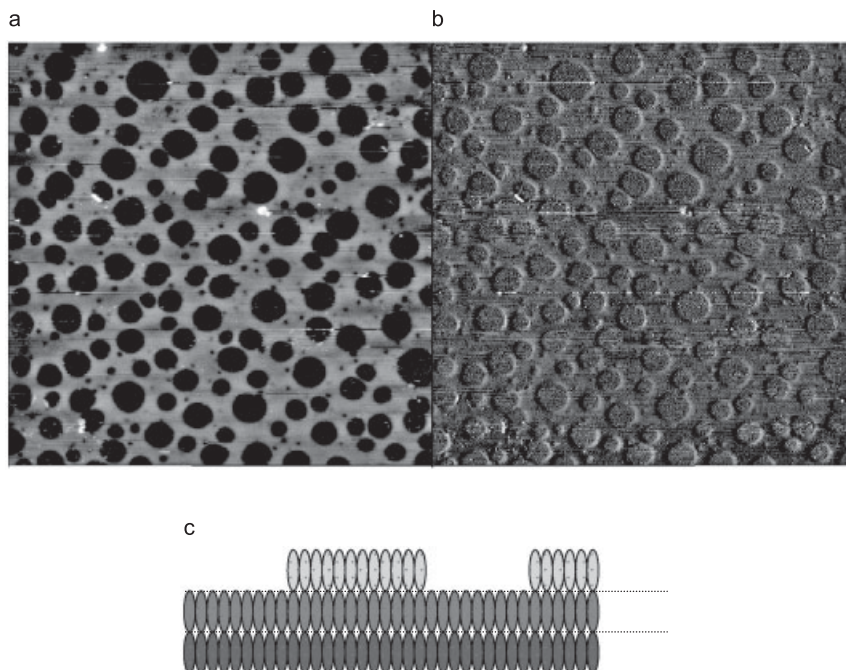


Fig. 7.13 (a) Tapping mode AFM height image ($30.0 \times 30.0 \mu\text{m}^2$) of a thin deposit of poly(indenofluorene). The vertical scale is 100 nm. (b) Corresponding phase image. The vertical scale is 1.0° . (c) Proposed model for the molecular organization within the film.

phology observed by AFM after annealing. The analysis of the height image shows a difference of 18 nm between the upper (brighter) layer and the lower (darker) layer. In the phase image (vertical gray scale 1.0°), there is no significant contrast between the two layers and only the contours of the cavities are visible. This contrast is mainly due to the discontinuity of the topographic features and is enhanced in the error signal. This is consistent with the description of the influence of the error signal at the domain edges (*vide infra*).

The length of extended poly(indenofluorene) chains with 20 units is estimated to be around 18.5 nm. This strongly suggests that the layers are made of molecules standing up perpendicularly to the substrate, as depicted in Fig. 7.13(c). The fact that the phase contrast between the different layers is very low means that the tip is probing the same material, or at least material with the same mechanical properties. For this sample, approach–retract curves are strictly identical, whatever the location on the sample. This implies that the contrast observed on the height image is purely topographic.

7.4.2

Pure Mechanical Contribution

In this section, we illustrate the concepts described above by applying the methodology to a combination of polymer materials for which the response to the oscillating tip is markedly different. This behavior is typically observed in block copolymers used as thermoplastic elastomers or pressure sensitive adhesives. In triblock systems, the central block of these copolymers consists of a rubbery sequence (i.e., the glass transition temperature (T_g) is lower than room temperature), which is the major component of the copolymer. The outer two blocks are thermoplastics (i.e., T_g is well above room temperature). Because the components are incompatible, the material phase-separates on the microscopic scale, into pure rubbery and glassy domains. Below the T_g of the thermoplastic component, the thermoplastic microdomains are rigid and act as physical crosslinks for the elastomeric matrix, so that the material behaves as a vulcanized rubber.

As an example we show the results reported in ref. 5. Figure 7.14(a, b) represents the area chosen for the image reconstruction, with lamellae oriented nearly perpendicular to the scan direction and a clearly marked contrast between the domains both in height and phase images. Approach–retract curves recorded on the two spots indicated in Fig. 7.14(b) are shown in Fig. 7.15 giving the amplitude (Fig. 7.15a) and phase variations (Fig. 7.15b).

The oscillator responses are clearly different for the two areas. The signature of the glassy domain is represented by gray curves, whereas the elastomeric domain corresponds to the black curves. The different behaviors can be attributed to different interactions between the tip and the elastomeric and glassy domains. The

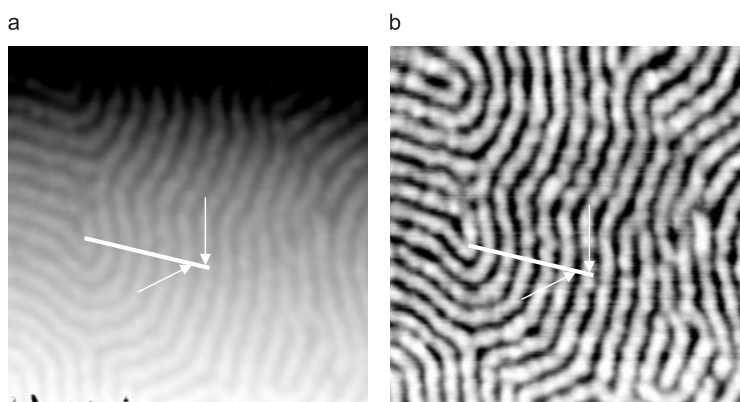


Fig. 7.14 (a) Height image (500×500 nm; the gray scale is 10 nm). The bright areas correspond to the upper parts and the dark areas to the lower parts of the image. (b) Phase image (the gray scale is 5°). The two white arrows indicate the two locations corresponding to two different domains, where

the approach–retract curves shown in Fig. 7.15 are recorded. The white line corresponds to the section used for the comparison with the section built from the approach–retract curves. (Reprinted with permission from Ref. 5. Copyright 2000 American Chemical Society.)

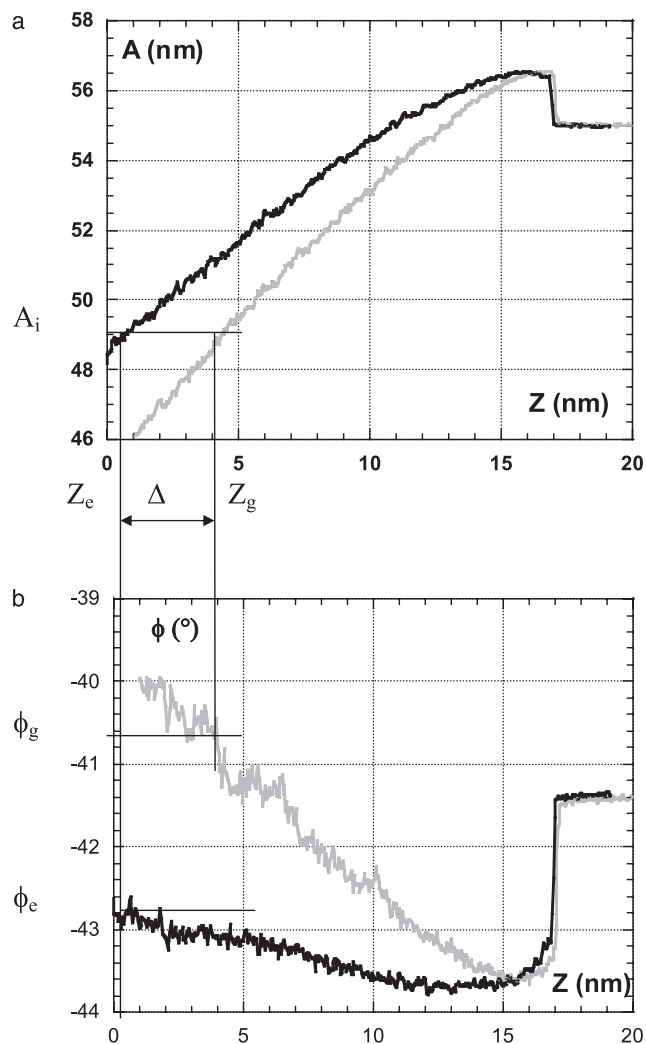


Fig. 7.15 Experimental approach curves recorded on the two locations shown in Fig. 7.14a, b. The gray curves (corresponding to the bright areas in Fig. 7.14a, b) correspond to the harder, glassy domain, and the black ones (dark areas of Fig. 7.14a, b) to the softer, elastomeric domain. (a) Amplitude A variation with the piezoactuator vertical Z position during the approach. (b) Phase ϕ variation with the piezoactuator vertical Z position during the approach. Both amplitude and phase variations

are different for the two domains due to different local interactions with the tip resulting in a mechanical contrast. The fixed image amplitude of 49 nm corresponds to a vertical piezoactuator movement between the two domains of $\Delta Z = Z_g - Z_e \approx 3.2$ nm, which implies a phase difference of about $\Delta\phi = \phi_g - \phi_e \approx 2.0^\circ$ for those two particular X , Y locations on the sample. (Reprinted with permission from Ref. 5. Copyright 2000 American Chemical Society.)

harder domain (glassy) response has a greater slope than the softer one. Without any topographic considerations, the amplitude variations on the two domains show that the piezoactuator has to bring the sample closer to the tip for the elastomeric domain than for the glassy one. Consequently, the net result will be an apparently greater height for the glassy domains. For example, with the experimental conditions chosen here, i.e., a working amplitude of 49 nm (the set-point value) for a free amplitude $A_f = 55$ nm, the sample holder has to move upward by an additional amount of $\Delta = 3.2$ nm (see Fig. 7.15a) when intermittent contact situations occur on the elastomeric domain, compared with the intermittent contact situation on the glassy domain. Due to the dominant repulsive regime, the recorded difference is only related to the difference in the slopes of the curves, and thus in turn to changes of the local mechanical properties. This difference corresponds to the change in the indentation depth.

The differences in piezoactuator heights on the glassy and elastomeric domains also imply differences in the phase values of about 2.0° , as shown in Fig. 7.15(b), with a larger phase shift for the elastomeric domain. All the approach–retract curves are analyzed following the same procedure, giving a section plot of the piezoactuator heights and oscillator phases.

The next step is to compare the height and phase image sections with sections built from the approach–retract curve data. As mentioned in Section 7.3, piezoactuator drift may affect the reconstructed section. For instance, in the example shown here, the images taken before and after the recording of the approach–retract curves do show a piezoactuator drift of 55 nm in the X direction (toward the bottom of the page) and 16 nm in the Y direction (to the right, horizontally). For the reconstructed sections, a continuous drift with time along this particular direction is considered. Different sections are chosen on the image, from the starting point of the approach–retract experiments toward the direction of the drift, by also considering the ceramic displacement imposed. They are then compared with the section reconstructed from the approach–retract curve analysis; the image section with the best correspondence is chosen, as represented by the line on Fig. 7.14.

The resulting image sections are displayed in Fig. 7.16(a) (height) and 7.16(b) (phase), together with the data from the approach–retract curve analysis. The correspondence between the two sets of data (height or phase images and approach–retract analysis) appears to be very good. This agreement means that for the copolymers studied, the contrast in the height image is related to different oscillator responses on the glassy and elastomeric domains, with no discernible, topographic contribution to the contrast. Therefore, the contrast is mostly due to changes in the local mechanical properties of the sample.

A block copolymer exhibiting a highly regular lamellar microphase separation between glassy and elastomeric domains can be considered as a model example. The “approach–retract curve” method applied to the system discussed here indicates a dominant contribution of the mechanical properties to the contrast in the height image. It is therefore possible to evaluate experimentally the mechanical and topographic contributions to tapping mode height images. To achieve such an

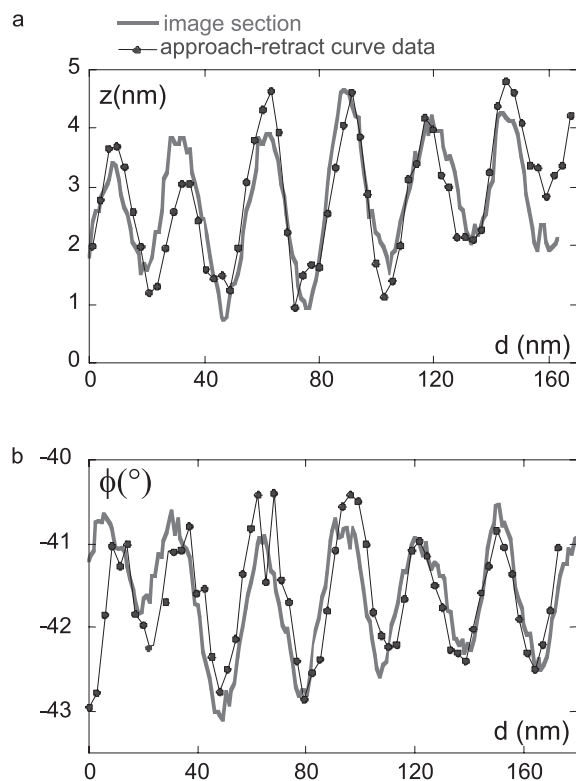


Fig. 7.16 (a) Comparison between the height data. (b) Comparison between the phase data. The approach–retract curves have been recorded along the line shown on Fig. 7.14. (Courtesy of ACS [5].)

estimate, a number of experimental conditions are required. The oscillator must scan the sample adiabatically. Growth of nanoprotuberances has to be prevented and the change in the strength of the attractive interaction between the two types of domains must be minimized [50]. The last two points can be achieved easily by choosing a suitable oscillation amplitude such that the oscillator works in the dominant repulsive regime.

7.4.3

Mixed Contributions

The contrast in the height images obtained on a large number of polymer systems, such as polymer blends, originates from mixed contributions of tip indentation and true topography. As an example, we describe here the results obtained on a blend made of PMMA and poly(ϵ -caprolactone) (PCL). Figure 7.17(a) shows a

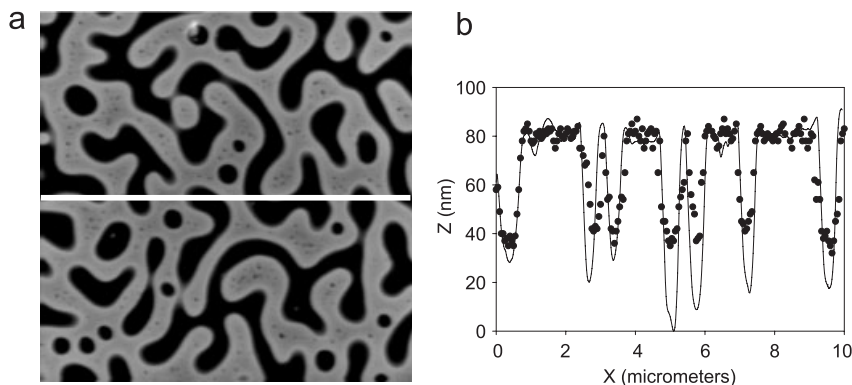


Fig. 7.17 (a) TM-AFM height image ($10.0 \times 10.0 \mu\text{m}^2$) of a PMMA–PCL co-continuous polymer blend (75:25). The vertical scale is 80 nm. (b) Image section and its

reconstruction from approach–retract curve analysis. The solid line corresponds to the image section and the black dots are the reconstructed data.

height image of a 75:25 wt.% PMMA/PCL system. From the section analysis (Fig. 7.17b) and the bearing analysis of the topographic image, it appears that the dark areas, corresponding to the softer component (i.e., the PCL-rich domains), are located approximately 60 nm below the bright (mechanically harder) PMMA-rich domains.

Approach–retract curves recorded on different domains on the polymer blend surface are markedly different: the slope of the amplitude/distance curve is 0.75 for the harder, glassy domains while it is smaller (0.60) on the softer domains, meaning that, for the same set point, there is larger tip indentation in the softer domains. Using the same procedure as described for the block copolymers, we measure a difference of about 15 nm between the lowest points in the image section and the corresponding reconstruction (Fig. 7.17b). Therefore, from these data (160 points), it appears that, in this case, an indentation of about 15 nm in the PCL softer domains has to be considered to fit the experimental data. Note that, at room temperature, PCL is largely above its glass temperature transition ($T_g = -60 \text{ }^\circ\text{C}$). Therefore, the 60 nm height difference recorded in the height images corresponds to a 15 nm indentation into PCL domains that are actually 45 nm below the level of the PMMA domains. This height difference probably originates from the process of film formation from the solution of the two polymers in a common solvent. The topographic modulation can be explained by a different rate of solvent evaporation during the film drying process for the two phases [51].

In this work, we have deliberately not reported the effect of the imaging parameters such as the set-point value. This domain is well described in the literature [10, 35, 52–56]. The complex dependence of TM-AFM images on these imaging parameters gives rise to the notion that the results may be subject to various uncontrolled artifacts and raises the question of whether and how reproducible imaging conditions can be established. Typical problems occurring when TM-AFM is

applied to soft materials (such as polymers) concern the quantitative reproducibility of height and phase images, the distinction between real surface topography and indentation, and even the frequently occurring contrast inversion of height and phase images [3, 57–59]. Krausch and coworkers have investigated in detail the processes involved when soft polymers are imaged in TM-AFM and they conclude also that with a simple procedure that the changes in height and phase contrast could be attributed to the crossover between the attractive and repulsive regimes.

7.5

Concluding Remarks

In this chapter, we have described a simple and straightforward method (based on the analysis of approach–retract curves) to: (a) give a quantitative estimation of the topographic and the mechanical contribution to height and phase images; (b) assign the various components in images of heterogeneous polymer materials. This technique has been used successfully for distinguishing pure topographic or pure mechanical contrast, as well as for systems with a mixing of the two contributions to the AFM images.

Acknowledgements

The authors are grateful to R. Jérôme and colleagues (CERM, University of Liège, Belgium) and P. Roose and F. Simal (Cytec, Belgium) for providing the block copolymers. Dendrigraft and hyperbranched polymers were prepared by M. Schapacher and A. Deffieux in LCPO – University of Bordeaux (France). Conjugated polymers were kindly provided by A. Grimsdale and K. Müllen (MPI-P, Mainz, Germany). Research in Mons is partly supported by the Belgian Science Policy Program “Pôle d’Attraction Interuniversitaire en Chimie Supramoléculaire et Catalyse Supramoléculaire” (PAI 5/3), the European Commission and the Government of the Région Wallonne (Phasing Out Program). Ph.L. is “Chercheur qualifié du FNRS” (Belgium).

References

- 1 LECLÈRE, Ph.; LAZZARONI, R.; BRÉDAS, J. L.; YU, J. M.; DUBOIS, Ph.; JÉRÔME, R. *Langmuir* **1996**, *12*, 4317.
- 2 STOCKER, W.; BECKMANN, J.; STADLER, R.; RABE, J. P. *Macromolecules* **1996**, *29*, 7502.
- 3 MAGONOV, S. N.; ELINGS, V.; WANGBO, M. H. *Surf. Sci.* **1997**, *389*, 201.
- 4 LECLÈRE, Ph.; MOINEAU, G.; MINET, M.; DUBOIS, Ph.; JÉRÔME, R.; BRÉDAS, J. L.; LAZZARONI R. *Langmuir* **1999**, *15*, 3915.
- 5 KOPP-MARSAUDON, S.; LECLÈRE, Ph.; DUBOURG, F.; LAZZARONI, R.; AIMÉ, J. P. *Langmuir* **2000**, *16*, 8432.
- 6 RASMONT, A.; LECLÈRE, Ph.; DONEUX,

- C.; LAMBIN, G.; TONG, J. D.; JÉRÔME, R.; BRÉDAS, J. L.; LAZZARONI, R. *Colloids and Surfaces B: Biointerfaces* **2000**, *19*, 381.
- 7 KONRAD, M.; KNOLL, A.; KRAUSCH, G.; MAGERLE, R. *Macromolecules* **2000**, *33*, 5518.
- 8 ALBRECHT, T. R.; GRÜTTER, P.; HORNE, D.; RUGARD, D. *J. Appl. Phys.* **1991**, *69*, 668.
- 9 ZHONG, Q.; INNISS, D.; KJOLLER, K.; ELINGS, V. B. *Surf. Sci.* **1993**, *290*, L688.
- 10 KNOLL, A.; MAGERLE, R.; KRAUSCH, G. *Macromolecules* **2001**, *34*, 4159.
- 11 CLEVELAND, J. P.; ANCZYKOWSKI, B.; SCHMID, A. E.; ELINGS, V. B. *Appl. Phys. Lett.* **1998**, *72*, 2613.
- 12 GARCIA, R.; SAN PAULO, A. *Phys. Rev. B* **1999**, *60*, 4961.
- 13 DUBOURG, F.; AIMÉ, J. P.; MARSAUDON, S.; BOISGARD, R.; LECLÈRE, Ph. *Eur. Phys. J. E* **2001**, *6*, 49.
- 14 DUBOURG, F.; AIMÉ, J. P.; COUTURIER, G.; SALARDENNE, J. *Eur. Phys. Lett.* **2003**, *62*, 671.
- 15 DUBOURG, F.; AIMÉ, J. P.; MARSAUDON, S.; COUTURIER, G.; BOISGARD, R. *J. Phys.: Cond. Matter* **2003**, *15*, 6167.
- 16 VIVILLE, P.; BISCARINI, F.; BRÉDAS, J. L.; LAZZARONI, R. *J. Phys. Chem. B* **2001**, *105*, 7455.
- 17 BATES, F. S. *Science* **1991**, *251*, 898.
- 18 ERMI, B. D.; KARIM, A.; DOUGLAS, J. F. *J. Appl. Polym. Sci.* **1998**, *36*, 191.
- 19 ERMI, B. D.; NISATO, G.; DOUGLAS, J. F.; ROGERS, J. A.; KARIM, A. **1998**, *81*, 3900.
- 20 MORTON, M. In *Thermoplastic Elastomers*; LEGGE, N. R.; HOLDEN, G.; SCHROEDER, H. E. Eds.; Hanser: Munich, **1987**, p. 67.
- 21 HOLDEN, G.; LEGGE, N. R. In *Thermoplastic Elastomers – A Comprehensive Review*; HOLDEN, G.; LEGGE, N. R.; SCHROEDER, H. E., Eds.; Hanser: Munich, **1987**; Chap. 3.
- 22 BATES, F. S.; FREDRIKSSON, G. H. *Annu. Rev. Phys. Chem.* **1990**, *41*, 525.
- 23 For more information concerning thermoplastic elastomers, see *Thermoplastic Elastomers*, 2nd edn., HOLDEN, G.; LEGGE, N. R.; QUIRK, R.; SCHROEDER, H. E., Eds. Hanser: Munich, **1996**.
- 24 (a) TONG, J. D.; LECLÈRE, Ph.; RASMONT, A.; BRÉDAS, J. L.; LAZZARONI, R.; JÉRÔME, R. *Macromolecular Chemistry and Physics* **2000**, *201*, 1250; (b) TONG, J. D.; MOINEAU, G.; LECLÈRE, Ph.; BRÉDAS, J. L.; LAZZARONI, R.; JÉRÔME, R. *Macromolecules* **2000**, *33*, 470.
- 25 BORSALI, R.; MINATTI, E.; PUTEAUX, J. L.; SCHAPPACHER, M.; DEFFIEUX, A.; VIVILLE, P.; LAZZARONI, R.; NARAYANAN, T. *Langmuir* **2003**, *19*, 6.
- 26 MINATTI, E.; VIVILLE, P.; BORSALI, R.; SCHAPPACHER, M.; DEFFIEUX, A.; LAZZARONI, R. *Macromolecules* **2003**, *36*, 4125.
- 27 DEFFIEUX, A.; SCHAPPACHER, M. *Macromolecules* **2000**, *33*, 7371.
- 28 SCHAPPACHER, M.; DEFFIEUX, A.; PUTTEAUX, J. L.; VIVILLE, P.; LAZZARONI, R. *Macromolecules* **2003**, *36*, 5776.
- 29 VIVILLE, P.; LECLÈRE, Ph.; DEFFIEUX, A.; SCHAPPACHER, M.; BERNARD, J.; BORSALI, R.; BRÉDAS, J. L.; LAZZARONI, R. *Polymer* **2004**, *45*, 1833.
- 30 SHEIKO, S. S.; DA SILVA, M.; SHIRVANIANTS, D. G.; LARUE, I.; PROKHOROVA, S. A.; BEERS, K.; MATYJASZEWSKI, K. *J. Am. Chem. Soc.* **2003**, *125*, 6725.
- 31 QIN, S.; MATYJASZEWSKI, K.; XU, H.; SHEIKO, S. S. *Macromolecules* **2003**, *36*, 605.
- 32 BOYCE, J. R.; SHIRVANIANTS, D.; SHEIKO, S. S.; IVANOV, D. A.; QIN, S. H.; BÖRNER, H. G.; MATYJASZEWSKI, K. *Langmuir* **2004**, *20*, 6005.
- 33 GLEYZES, P.; KUO, K.; BOCCARA, A. C. *Appl. Phys. Lett.* **1991**, *58*, 2989.
- 34 NONY, L.; BOISGARD, R.; AIMÉ, J. P. *Biomacromolecules* **2001**, *2*, 827.
- 35 (a) ANCZYKOWSKI, B.; KRÜGER, D. and FUCHS, H. *Phys. Rev. B* **1996**, *53*, 15485; (b) TAMAYO, J.; GARCIA, R. *Appl. Phys. Lett.* **1997**, *71*, 2394; (c) BOISGARD, R.; MICHEL, D.; AIMÉ, J. P. *Surf. Sci.* **1998**, *401*, 199.
- 36 GARCIA, R.; PEREZ, R. *Surf. Sci. Rep.* **2002**, *47*, 197.
- 37 (a) SUGAWARA, Y.; OHTA, M.; UYAMA,

- H.; MORIAT, S. *Science*, **1995**, *270*, 1646; (b) GIESSIBL, F. J. *Science* **1995**, *267*, 68.
- 38 (a) LANTZ, M. A.; HUG, H. J.; VAN SCHENDEL, P. J. A.; HOFFMANN, R.; MARTIN, S.; BARATOFF, A.; ABDURIXIT, A.; GÜNTHERODT, H. J. and GERBER, Ch. *Phys. Rev. Lett.* **2000**, *84*, 2642; (b) HÖLSCHER, H.; SCHWARZ, A.; ALLERS, W.; SCHWARZ, U. D.; WIESENDANGER, R. *Phys. Rev. B* **2000**, *61*, 12678.
- 39 DIETZEL, D.; FAUCHER, M.; IAIA, A.; AIMÉ, J. P.; MARSAUDON, S.; BONNOT, A. M.; BOUCHIAT, V.; COUTURIER, G. *Nanotechnology* **2004**, *16*, S73–S78.
- 40 GIESSIBL, F. J. *Phys. Rev. B* **1997**, *56*, 16010.
- 41 BOISGARD, R.; MICHEL, D.; AIMÉ, J. P. *Surf. Sci.* **1998**, *401*, 199; AIMÉ, J. P.; BOISGARD, R.; NONY, L.; COUTURIER, G. *Phys. Rev. Lett.* **1999**, *82*, 3388.
- 42 (a) WANG, L. *Surf. Sci.* **1999**, *429*, 178; (b) NONY, L.; BOISGARD, R.; AIMÉ, J. P. *J. Chem. Phys.* **1999**, *111*, 1615.
- 43 WANG, L. *Appl. Phys. Lett.* **1998**, *73*, 3781.
- 44 BOISGARD, R.; AIMÉ, J. P. *Surf. Sci.* **2002**, *511*, 171.
- 45 SCHIRMEISEN, A.; CROSS, G.; STALDER, A.; GRÜTTER, P.; DÜRIG, U. *New J. Phys.* **2000**, *2*, 29.
- 46 DUBOURG, F. Ph.D. Thesis (University of Bordeaux, France).
- 47 FERRY, J. D. *Viscoelastic Properties of Polymers*, 3rd edn.; Wiley: New York, **1980**.
- 48 SAN PAULO, A.; GARCIA, R. *Phys. Rev. B* **2001**, *64*, 1934.
- 49 STARK, M.; MÖLLER, C.; MÜLLER, D. J.; GUCKENBERGER, R. *Biophys. J.* **2001**, *80*, 3009.
- 50 AIMÉ, J. P.; MICHEL, D.; BOISGARD, R. and NONY, L. *Phys. Rev. B* **1999**, *59*, 2407.
- 51 WALHEIM, S.; BÖLTAU, M.; MLYNEK, J.; KRAUSCH, G.; STEINER, U. *Macromolecules*, **1999**, *30*, 4995.
- 52 BURNHAM, N. A. *Appl. Phys. Lett.* **1993**, *63*, 114.
- 53 BURNHAM, N. A.; BEHREND, O. P.; OUVELEY, F.; GREMAUD, G.; GALLO, P. J.; GOURDON, D.; DUPAS, E.; KULIK, A. J.; POLLOCK, H. M.; BRIGGS, G. A. D. *Nanotechnology* **1997**, *8*, 67.
- 54 GOTSMAN, B.; KRÜGER, D.; FUCHS, H. *Europhys. Lett.* **1997**, *39*, 153.
- 55 (a) BRANDSCH, R.; BAR, G.; WHANGBO, M.-H. *Langmuir* **1997**, *13*, 6349; (b) BAR, G.; BRANDSCH, R. *Langmuir* **1998**, *14*, 7343.
- 56 BERQUAND, A.; MAZERAN, P. E.; LAVAL, J. M. *Surf. Sci.* **2003**, *523*, 125.
- 57 PICKERING, J. P.; VANCISO, G. J. *Polym. Bull.* **1998**, *40*, 549.
- 58 SPATZ, J. P.; SHEIKO, S. S.; MÖLLER, M.; WINKLER, R. G.; REINEKER, P.; MARTI, O. *Langmuir* **1997**, *13*, 4699.
- 59 (a) KÜLHE, A.; SORENSEN, A. H.; BOHR, J. J. *Appl. Phys.* **1997**, *81*, 6562; (b) KÜLHE, A.; SORENSEN, A. H.; ZANDBERGEN, J. B.; BOHR, J. *Appl. Phys. A* **1998**, *66*, S329.

8 Pulsed Force Mode SFM

Alexander Gigler and Othmar Marti

8.1 Introduction

With the miniaturization of technological components, the ratio of surface area to the enclosed volume is increasing. Therefore, properties of surface features are becoming more and more interesting to scientists. Meanwhile lateral dimensions of several micrometers and surface roughnesses of some tens of nanometers are common. Through the invention of scanning probe microscopy (SPM) techniques, these dimensions became accessible. However, not only the topography of the samples can be investigated, but also their very local mechanical behavior. This possibility has driven scientists in every nanotech laboratory to develop a broad range of operating modes for SPM systems. A variety of forces is involved in the interaction of the tip and the surface, such as elasto-mechanical forces, adhesion, electrochemical forces in the presence of electrolytes, and hydrodynamic forces such as the liquid neck between the tip apex and the sample in ambient conditions. It is necessary to distinguish between these effects to understand the interaction and to separate artifacts from real data. This chapter explores the capabilities of pulsed force mode (PFM) data acquisition to get an almost complete characterization of tip-sample interactions, and thus of sample materials.

8.2 Modes of SPM Operation

Based on the original ideas of SPM (Binnig and Rohrer, 1982; Hansma and Tersoff, 1987), an atomic force microscope (AFM) has been conceived (Binnig et al., 1986). The reviews by Colton et al. (1998), Sarid (1991), and VanLandingham et al. (2000) give a general overview.

Generally speaking, an AFM utilizes some kind of micro-fabricated stylus to probe the surface of a sample locally (Fig. 8.1A). An analogous example in an everyday setting is the needle of a record player that follows the topographical features representing the audio information. To the first order, the deflection z of the

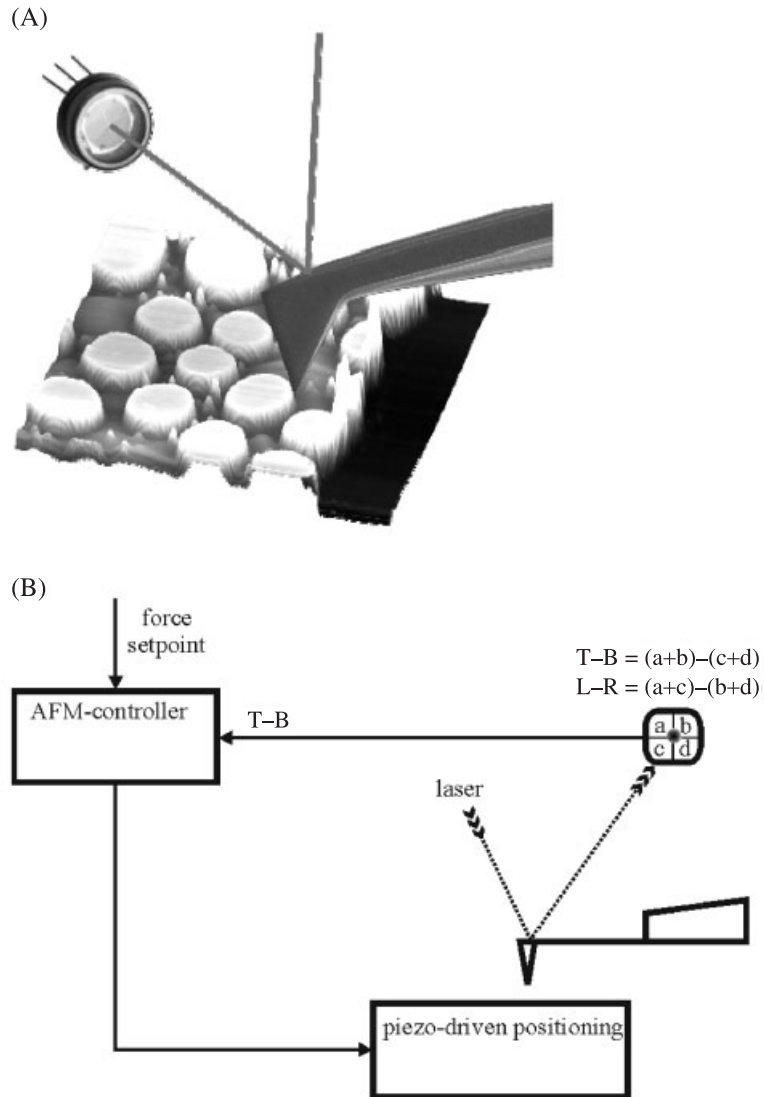


Fig. 8.1 The detection system of an AFM. (A) An SEM image of a cantilever scanning a polymer blend. The surface was scratched to reveal the silicon substrate below. This area was used as reference material. Also shown: the four-segment photo-diode used in the

optical lever detection system. (B) Schematic of the detection principle. A feedback loop controls the positioning of the sample relative to the tip. It ensures permanent contact with the sample at a given pre-set force.

Table 8.1 Typical geometrical dimensions of AFM cantilevers.

Length [μm]	Width [μm]	Thickness [μm]	Tip height [μm]	Stiffness [N m^{-1}] @ frequency [kHz]
225 ± 5	48 ± 5	1.0 ± 0.5	12 ± 2	0.2 @ 25
225 ± 5	48 ± 5	3.0 ± 0.5	12 ± 2	2.8 @ 75
160 ± 5	50 ± 5	4.6 ± 0.5	11 ± 2	42.0 @ 300

stylus when a force F is applied at one end of it can be assumed to follow a linear force law [Eq. (1)] (see Cleveland et al., 1993; Hutter and Bechhoefer, 1993a,b; Burnham et al., 2000, for more details).

$$F = -kz \quad \text{with} \quad \frac{1}{k} = \frac{1}{k_{\text{lever}}} + \frac{1}{k_{\text{sample}}} \quad (1)$$

In the discussion below we will assume that a beam of rectangular shape (a cantilever) has a tip at the end. Typical sizes are given in Table 8.1. In the literature we find a broad variety of modes for static and dynamic operation of an AFM (Marti et al., 1988, 1990; Martin et al., 1988; Bietsch et al., 2000; Cappella and Dietler, 1999; Colchero, 1993; Krottil et al., 2000a; Miyatani et al., 1997; Rosa-Zeiser et al., 1997; Spizig, 2002; Weilandt, 1996; de Pablo, 1998).

8.2.1

Static Modes

8.2.1.1 Constant Height Mode

To scan across the surface, the tip has to be kept in contact with the sample. The easiest method is to hold the base of the cantilever at a given height above the surface and to move the sample laterally. This is known as constant height mode. As it crosses elevated surface features, the deflection of the stylus will increase. This corresponds to a higher force. One of the most widespread methods of detecting the deflection of the cantilever, and thus to measure forces, is the optical lever technique as described by Meyer (Meyer and Amer, 1988a,b, 1990) or Alexander et al. (1989). A focused laser beam is directed toward the back of the stylus – or cantilever – and the beam is then reflected to the center of a position-sensitive detector (PSD). In a detector with four quadrants; the difference in current from the upper and lower or the left- and right-hand sides can be used to determine the position of the laser spot on the detector. As the deflection is dependent on the bending of the probe, the differential signals give a direct measure of the forces acting

on the contact (Fig. 8.1B). The difference between the top and bottom components ($T - B$) is proportional to the normal deflection, while a left minus right signal ($L - R$) corresponds to a torsional bending of the probe due to frictional forces arising when the sample is moved perpendicular to the cantilever.

8.2.1.2 Constant Deflection Mode

As the deflection is not controlled while a sample surface is being scanned at a preset height, elevated features are subject to higher forces. These forces may be great enough to destroy or deform the sample. Keeping the deflection constant resolves that problem. A control-electronics is used to minimize the force error signal, i.e., the deviation of the detected deflection from a given setpoint (desired deflection) by repositioning of the probe. This is known as a constant deflection or constant force mode. It offers one of the simplest ways to characterize a sample. The lateral forces induced by the relative motion of the tip and sample make it possible to classify the composition of the local material.

8.2.2

Dynamic Modes

In dynamic operation, things are not quite that easy. Sustaining a constant average force or a constant peak force is necessary to scan across the surface. There are resonant and nonresonant modes which provide different degrees of insight into sample behavior, but, at the same time, minimize specific problems. Resonant modes of operation are noncontact, tapping, and self-excitation modes, while nonresonant modes are pulsed force mode (PFM) or, using a similar strategy, jumping mode (JM).

Noncontact mode allows scanning and imaging of very delicate samples in the attractive regime of the surface potential. It provides a good insight into short-range attractive forces, but does not allow acquisition of direct information on the material below the tip, due to the lack of immediate contact. Applying larger excitation amplitudes, one is operating in the so-called intermittent contact mode, which implies that the tip periodically comes into contact with the sample surface (Luna et al., 1998). Coming to the repulsive regime of the interaction potential of the sample, we reach the tapping mode. Here the tip impacts the surface once during each of its oscillation. The observables in this mode are the amplitude of the cantilever oscillation and the phase shift compared to the excitation of the cantilever (Winkler et al., 1996; Cleveland et al., 1998). Both observables are analyzed by a lock-in amplifier. Since the cantilever is moved through the repulsive as well as the attractive regime during every oscillation period, amplitude and phase are affected by both regimes. Thus the tip-sample interaction affects those quantities in a non-trivial way, which, except in special cases, is not invertible. In tapping mode the average amplitude of the cantilever oscillation is measured, so there is no control of the force applied to the sample. Far below resonance, however, direct control of the peak force is possible, e.g., in PFM or JM.

8.2.2.1 Resonant Modes

To understand the advantages of PFM we will first summarize the resonant modes of operation. Due to the movement within the surface potential of the sample (e.g., Lennard-Jones), the oscillator will be damped depending on the properties of the materials close to the tip. This causes a shift in frequency as well as in phase. To compensate for one of these effects, the probe is repositioned.

The operating frequency is determined by the eigenfrequencies of the rectangular cantilever according to Eq. (2), E being Young's modulus, d the thickness, b the width, L the length, A the cross-section, and ρ the mass density of the cantilever-beam. (see Budó, 1969 for details).

$$\nu_n = \frac{(\alpha_n L)^2}{2\pi L^2} \sqrt{\frac{Ed^3b}{12\rho A}} \quad (2)$$

The characteristic equation of a cantilever beam is $\cos(\alpha_n L) \cosh(\alpha_n L) + 1 = 0$. The coefficients for the resonance frequencies are

$$\alpha_0 L = 1.875, \alpha_1 L = 4.694, \alpha_2 L = 7.855, \dots \alpha_n L \approx (2n - 1) \frac{\pi}{2} \quad \forall n \geq 4$$

Thus, the frequency of the fundamental mode is given by Eq. (3).

$$\nu_0 = \frac{(1.875)^2}{2\pi L^2} \sqrt{\frac{Ed^3b}{12\rho A}} \quad (3)$$

There are two different ways to drive the cantilever close to its resonance. By the first method, in tapping mode, the cantilever is driven by an external oscillator at a frequency chosen reasonably close to its eigenfrequency. The eigenfrequency of the system is lowered and the amplitude drops when the oscillation is damped by the tip-sample interaction. However, the cantilever beam is still driven at the preset external frequency. The energy transferred to the cantilever in each period thus varies with position. This is the mechanism on which the tapping mode is based. The second way to achieve resonant excitation alleviates this problem. In the so-called self-excited oscillation mode, the measured deflection of the cantilever (due to thermal excitation or drive) is phase-shifted by 90° , amplified, and finally fed back to the drive unit, thereby pumping energy into this oscillation of the cantilever. Driving always happens at the actual eigenfrequency of the system. This method is self-adjusting, i.e., once started, the cantilever will oscillate at its eigenfrequency only. In both cases, however, we can determine the surface potential by exploring the shift in frequency. With the force being the first derivative of the potential, a modulated cantilever will always measure the second derivative of the interaction potential for small modulation amplitudes [Eq. (4)].

$$\frac{\partial^2 E_{pot}}{\partial z^2} = -\frac{\partial F}{\partial z} = -\frac{F_{mod}}{z_{mod}} \quad (4)$$

8.2.2.2 Force Modulation Mode

As stated before, there is also a category of dynamic AFM modes which does not operate at the eigenfrequency of the cantilever. When scanning in contact with the surface, we can apply an additional oscillation to the position of the base of the cantilever. The force on the contact is thus modulated. This force modulation mode is very similar to a classical method in material science, i.e., dynamic mechanical analysis (DMA). As in DMA, $\frac{\partial F}{\partial z}$ is measured for a range of frequencies.

We obtain a quantity directly related to the elastic properties of the sample. This kind of “nanoscale DMA” with an AFM has been reported successful by Balooch et al. (2004). As the AFM is operated in permanent direct contact with the sample, it therefore gives rise to wear of the surface.

8.2.2.3 Nanoindentations

The nanoindentation regime is reached when the peak forces exceed a sample- and tip-dependent level (Boschung et al., 1994; Drechsler et al., 1998; VanLandingham et al., 1999, 2000; Bogetti et al., 1999). The resulting permanent deformation is a means of examining the plasticity at the nanoscale. Experiments in this direction have been carried out by Hinz et al. (2004), for example, who investigated the temperature dependence of the indentation formation process in thin polymer films (35 nm PMMA). They were able to measure the sample compliance below and above the glass temperature. However, in most AFM experiments destruction of the surface is an unwanted side effect of intermittent or full-contact AFM.

8.3

Pulsed Force Mode

Various properties, measured simultaneously at the same point of the sample, facilitate the characterization of the behavior of the sample material. An overview of the theoretical description of the tip-sample contact will be given in Section 8.4. To keep the measurement process as nondestructive as possible, the tip must be in contact for only the shortest time possible. This can be achieved in pulsed force mode (PFM) (Rosa-Zeiser, 1997; Rosa-Zeiser et al., 1997; Luginbühl et al., 2001; Krottil et al., 2000b; Spizig, 2002) or jumping mode (JM). Here, the tip follows a predefined approach and retract trajectory. Such a controlled positioning is not possible in a resonant mode of operation as discussed above. Even though in PFM, as well as in JM, most of the tip’s lateral scanning movement is out of contact, the shear forces acting between the tip and the sample cannot be fully neglected. An elaborate study of the jumping mode was conducted by Moreno-Herrero et al. (2000). On the other hand, a controlled lateral excitation with simultaneous PFM operation can also be utilized to learn about further frictional properties of the sample surface. An example of CODYMode operation (Krottil et al., 2000b) is described in Section 8.6.9 and Section 8.3.3.

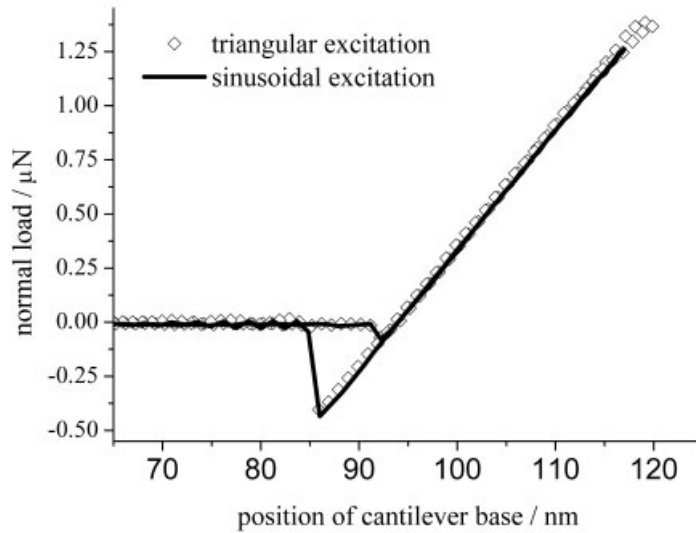


Fig. 8.2 Force versus distance curve as acquired by AFM. The measured force is plotted versus the position of the base of the cantilever. As it comes closer to the surface, the tip snaps into contact with the surface. On further approach, the cantilever is forced to bend backward depending on the elastic, viscoelastic, and plastic behavior of the sample

material. A certain maximum force is reached, then the base is retracted causing relaxation of the cantilever. On the retrace, a material-dependent negative force has to be exceeded to pull off the tip from the surface. All forces have to be measured relative to the “free” position of the cantilever at the point furthest to the left.

At low speeds and triangular modulation the approach–retraction cycle described above is known as the force–distance curve (FDC), as seen in Fig. 8.2. In the literature FDCs are well examined by many sources (Bulychev et al., 1975, 1976; Mizes et al., 1991; Pharr et al., 1992; Boehnke et al., 1999; Prokhorenko et al., 2004). The pull-off force, i.e., the peak attractive force on retraction, provides an easy way to measure local adhesion.

By applying a triangular modulation to the base of the cantilever, the tip is brought periodically into contact with the sample surface. Local adhesion, elastic, viscoelastic, and plastic properties of the sample can be derived from the measured forces and positions. However, the range of accessible deformation rates is quite limited. In FDCs only repeat-rates of a few hertz are used, since the bandwidth of the excitation electronics in general is not sufficiently wide for a triangular signal. Fourier decomposition of a triangular wave shows that several higher harmonics have to be taken into account in order to synthesize a real triangular wave. Hence, the low-pass behavior of amplifiers and other components affects the shape of the transmitted curve and thus the cantilever positioning. For sinusoidal drive

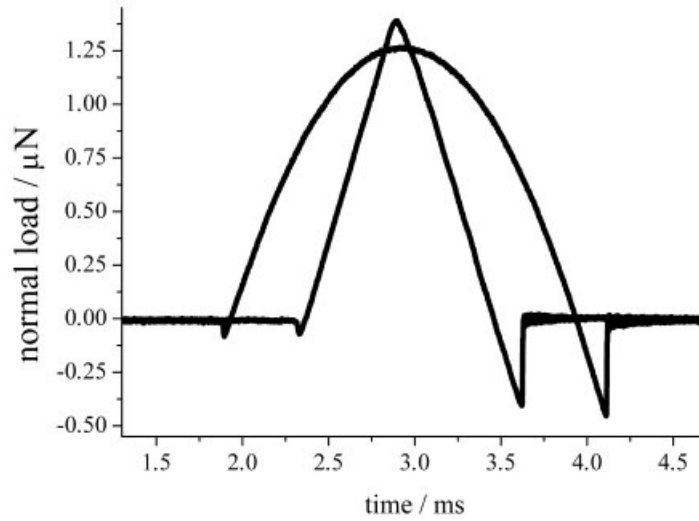


Fig. 8.3 Development of the force within the time domain. The response of the system upon modulation with a triangular and a sinusoidal trajectory are shown. The snap-in, maximum force, repulsive regime, pull-off force, and baseline can be identified on the curve. However, in order to sustain the steep turns, the triangular wave is bandwidth-limited

to a certain maximum velocity (or repetition rate). By coordinate transformation (assigning the trajectory of the base of the cantilever to the horizontal axis of the force plot), the modulation-specific curve shape is removed from the curve shape. What is remaining is the classical FDC plot (Fig. 8.2).

signals this dispersion does not occur. Therefore, a purely sinusoidal modulation will not suffer from this bandwidth limitation. Nevertheless phase shifts between the drive signal and the cantilever movement are present. In addition, sinusoidal drive eliminates the excitation of spurious resonances in the AFM. A setup designed for minimal disturbance of the drive signals is the pulsed force mode. The equivalence between this mode and FDCs can be shown by simple transformations. Examples of FDCs and force curves acquired using PFM are shown in Fig. 8.3. Both curves were measured with the same AFM setup at the same frequency of 100 Hz. It is obvious that at the turning point of the triangular drive, either the triangular wave shape is not transmitted correctly to the cantilever, or the cantilever is excited at its resonance, or both. Yet it is clear that for repeat rates of more than 100 Hz of a triangular modulation higher harmonics from the wave shape couple to the cantilever. The interpretation of the results becomes very intricate. If the mechanical processes could be modeled analytically, it would be possible to simulate FDCs at those high repeat rates. However, PFM offers a compromise, since it can be operated in a frequency range from 50 to 20 kHz, which has

been verified experimentally. It has the advantage that the content of higher harmonics is negligible in the spectrum of the waveform, avoiding possible problems.

Given that each material has its own characteristic temporal response as shown in Fig. 8.3, one might conclude that the type of the excitation function could affect the results. The coordinate transformation $x(t) = A_0 \sin(\omega t + \theta)$ removes the trajectory from the signal. The resulting data turn out to be the equivalent to those obtained by triangular excitation. This can be seen in the sinusoidal trace in Fig. 8.2.

8.3.1

Technical Implementation of Pulsed Force Mode

The setup of a pulsed force mode is fairly straightforward. What is needed is the possibility of modulating the tip-sample distance in order to rupture the point of contact before a new approach curve is acquired. Actually, the contact time should be kept as short as possible to avoid sample destruction during the lateral scanning movement. This z -modulation is usually conducted by a separate piezo within the cantilever holder. Sampling and recording of the measurement data is another demanding task. On the one hand, data acquisition has to be sophisticated enough to allow reduction of the amount of data to a reasonable scale; on the other hand, the data should only be compressed to a predetermined margin of error.

In the analog implementation of the measurement system, this is accomplished by peak-pickers and sample-and-hold circuitry, while with the new digital version it is possible to capture and store the entire data of an experiment. The digitization is therefore very demanding, and has been set up as a dedicated transfer-and-storage connection. The I/O system, for example, has to be constantly able to handle about 10 MB s^{-1} for a 1 kHz experiment. For a typical experimental run with a scan rate of about one line per second, this adds up to a file size of several gigabytes. In any case, the data also have to be processed. Here, the analog setup has a clear advantage over the digital version, since only the most important points and features of the interaction are investigated in this case. On the other hand, all the information contained in the remaining force curve is neglected. To record these data as well means that a more powerful CPU has to process the streaming data. This is done by a field-programmable gate array (FPGA), which mimics the analog behavior by operating simple algorithms such as peak-picking and sample and hold in real time, while being able to analyze the data more thoroughly in an off-line data evaluation.

Another advantage of the digital implementation is that a synthesized curve can be used as a modulation signal. Thus, the curve shape is interpolated between 5000 support points. Triangular and sinusoidal curves as well as (for example) trapezoidal excitations can be realized, and material responses to changing excitations can be investigated. By simply switching to one or the other modulation function inside the software, this can even be done at exactly the same position of the sample, allowing direct comparison of the results. With the analog setup this has not been possible without major modification.

8.3.2

Analogies and Differences between PFM, JM, and Force–Volume Mode

To complete our overviews of measurement modes, we refer to the jumping mode (JM) as proposed by de Pablo et al. (1998). In this mode, the tip is positioned at a certain discrete scanning position before running a single FDC. Since this is done for every point of the scan, mapping of material parameters is possible, too. Both PFM and JM are imaging techniques, and thus three-dimensional in the sense that, because the applied maximum force is kept constant, the tip is following the topography under a predetermined stress. This 3D image can then be correlated with the material properties deduced from the indentation measurements and is therefore adding a fourth dimension – the material properties – to the topographical measurements. These measurement modes are usually referred to as “force–volume modes”.

8.3.3

Extending PFM to CODYMode for Full Mechanical Characterization of Samples

While, in general, the lateral motion of the cantilever should be conducted off-contact to avoid the destruction of soft sample features, lateral forces acting between the scanning tip and the surface can also be exploited to study the frictional properties at the nanoscale. Friction force microscopy (FFM) is one of the possible scanning modes accessing these frictional properties – but with the shortcoming of permanent contact with the surface. In FFM the tip scans across the surface and the lateral force signal is evaluated for friction information by subtracting the forward and backward line scan. A calibration procedure has been described by Varenberg et al. (2003). Thus, the method results in a map of friction parameters correlated with topographical features. However, piezo creep and drifts in the measurement result in an offset between the forward and backward traces, which causes problems in the data evaluation. A better method is to oscillate or shake the sample relative to the scanning tip and to use the torsional amplitude of the cantilever as a measure for the frictional behavior. Anyhow, in this mode, the tip is still in permanent contact with the surface, with the problem of destruction at hand. Thus, it is reasonable to combine the pulsed force mode with this dynamic FFM method, resulting in the so called combined dynamic mode (CODYMode) as described by Krottil et al. (2000b). In this mode the sample is shaken permanently at a small amplitude and a high frequency, resulting in relative tip–sample velocities in the order of centimeters or even meters per second. While the tip is in repulsive contact with the sample, the cantilever experiences the lateral forces causing torsion of the beam, while – at a different frequency – being modulated to measure the elastic and viscoelastic material properties as well as adhesion (described in other sections). The correlation of mechanical features and frictional behavior at the nanoscale can be investigated by this technique, perhaps leading to a conclusive theory of friction processes at this length scale.

8.4

Theoretical Description of Contact Mechanics

To understand the nature of the forces and signals in PFM, we need to give an abridged description of contact mechanics.

8.4.1

Hertzian Modeling

The contact mechanics of rigid bodies has first been described by H. Hertz (Hertz, 1882). Assuming two perfectly elastic spheres made of an isotropic material (R_m , E_m , ν_m , being radius, Young's modulus, and Poisson's ratio of each sphere of index m respectively), whose centers are being pushed towards each other (Fig. 8.4) by a load P and neglecting adhesion forces, he was able to calculate the analytical solution to the problem.

Assuming that the spheres are only deformed inside the area of contact, one can calculate the geometric changes. Two spheres of radius R_1 and R_2 are given by

$$R_1^2 = r^2 + (R_1 - z_1(r))^2$$

$$R_2^2 = r^2 + (R_2 - z_2(r))^2$$

z_1 and z_2 being the distances from the x -axis.

For small distances r from the main axis z , $z_1(r)$ and $z_2(r)$ can be written as

$$z_1(r) = \frac{r}{2} \frac{1}{R_1}$$

$$z_2(r) = \frac{r}{2} \frac{1}{R_2}$$

The sum equals the distance of two opposing points of the spheres (M, N). Thus, pushing together the two spheres by a distance δ leads to a change in distance along each sphere's boarder line. The deformation of both spheres along the x -axis then is:

$$\begin{aligned} \Delta(r) &= \delta_1 + \delta_2 - (z_1 + z_2) \\ &= \delta - \frac{r^2}{2} \left(\frac{1}{R_1} + \frac{1}{R_2} \right) \\ &= \delta - \frac{r^2}{2} \frac{1}{R} \end{aligned} \tag{5}$$

Per definition R is the effective radius:

$$\frac{1}{R} = \frac{1}{R_1} + \frac{1}{R_2}$$

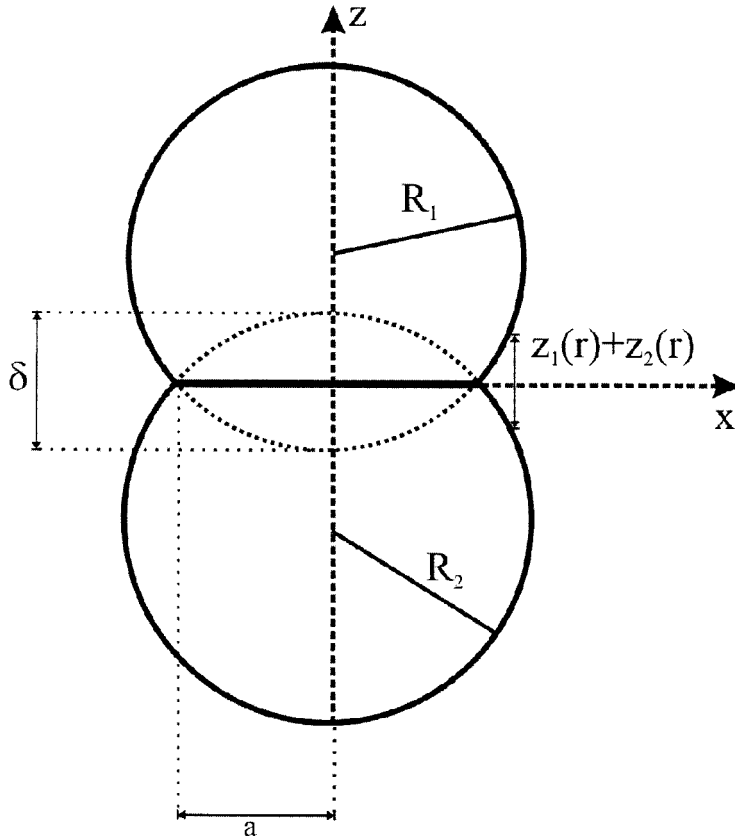


Fig. 8.4 The situation of the impact of two fully elastic spheres of radius R_1 and R_2 as used for the derivation of the Hertzian contact model. At a given force, the centers of the spheres will be closer by a distance δ , resulting in a deformed contact area of radius a . Before

the impact two points on the spheres at the same distance r from the z -axis have been separated by $z_1(r) + z_2(r)$. The displacement δ moves sphere 1 by δ_1 and sphere 2 by δ_2 , while the distance between the points only changes by $\delta_1 + \delta_2 - (z_1(r) + z_2(r))$.

On the other hand, this deformation also has to be the result of an elastic deformation by pushing the spheres together. The pressure distribution for this problem is

$$p(r) = p_0 \sqrt{1 - \frac{r^2}{a^2}}$$

r being the actual position within the area $A = \pi a^2$ of radius a and p_0 being the maximum pressure in the center of this area (Fig. 8.5A). Within the loaded circle, the local displacement of sphere with the index m along the z -axis is given by.

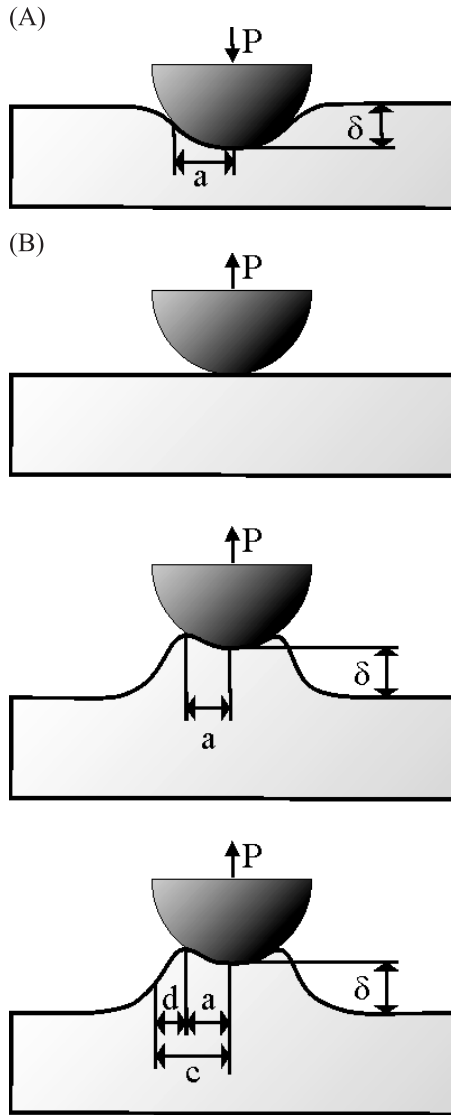


Fig. 8.5 (A) Indentation of a sphere into an elastic half-space (valid for all contact models). (B) The basic difference between DMT, JKR, and Maugis, namely the definition of the area that is involved in adhesive forces. In the DMT model (upper image) it is only an annular zone around the Hertzian contact area which causes

adhesion. The JKR model (middle) assumes that only the contact area contributes to the adhesive force, but the surface is compliant enough to adhere to the tip even beyond point zero. Both models are special cases of the more general Maugis model (bottom).

$$u_{z_m}(r) = \frac{1 - \nu_m^2}{E_m} \frac{\pi}{4} \frac{p_0}{a} (2a^2 - r^2) \quad r \leq a$$

as described by Maugis (2000) and Johnson (1996). Thus, the total deformation is – again – the sum of these displacements and has to equal $\Delta(r)$ as calculated above:

$$\Delta(r) = \left(\frac{1 - \nu_1^2}{E_1} + \frac{1 - \nu_2^2}{E_2} \right) \frac{\pi}{4} \frac{p_0}{a} (2a^2 - r^2) \quad (6)$$

The total load P loading this area can be calculated as the integral of the pressure distribution over the entire area and comes out as

$$P = p_0 \frac{2}{3} a^2$$

Comparison of the coefficients of the two equations for $\Delta(r)$ gives

$$\begin{aligned} \delta &= \left(\frac{1 - \nu_1^2}{E_1} + \frac{1 - \nu_2^2}{E_2} \right) p_0 \frac{\pi^2 a}{2} \\ \frac{r^2}{2R} &= \left(\frac{1 - \nu_1^2}{E_1} + \frac{1 - \nu_2^2}{E_2} \right) p_0 \frac{\pi^2}{4a} r^2 \\ \Leftrightarrow \frac{1}{R} &= \left(\frac{1 - \nu_1^2}{E_1} + \frac{1 - \nu_2^2}{E_2} \right) p_0 \frac{\pi^2}{2a} \end{aligned} \quad (7)$$

It is easy to see that by multiplying of the above equations for δ and $\frac{1}{R}$, the contact radius is

$$a = \sqrt{R\delta}$$

Defining an effective modulus K as

$$\frac{1}{K} = \frac{3}{4} \left(\frac{1 - \nu_1^2}{E_1} + \frac{1 - \nu_2^2}{E_2} \right)$$

and using $P = p_0 \frac{2}{3} a^2$, this contact radius can also be written as

$$a = \left(\frac{PR}{K} \right)^{1/3} . \quad (8)$$

Also, by solving for P , the dependency of the force on the deformation of the spheres is

$$P = K \sqrt{R\delta^3} \quad (9)$$

Given this load, the deformation can also be written as

$$\delta = \left(\frac{P^2}{K^2 R} \right)^{1/3} \quad (10)$$

In the following we will use the effective radius R and the effective modulus K in the description of contact mechanics:

$$\begin{aligned} \frac{1}{R} &= \frac{1}{R_1} + \frac{1}{R_2} \\ \frac{1}{K} &= \frac{3}{4} \left(\frac{1 - \nu_1^2}{E_1} + \frac{1 - \nu_2^2}{E_2} \right) \end{aligned} \quad (11)$$

It is obvious that for a sphere of infinite radius R_2 , the effective radius equals R_1 . This describes a fully elastic sphere indenting into a fully elastic half-space. Furthermore, if one sphere is incompressible, e.g. meaning E_1 tends to infinity, only the other one will be deformed.

8.4.2

Sneddon's Extensions to the Hertzian Model

Based on the calculations performed by Hertz in 1882, Sneddon (1965) went on to extend the theoretical description to nonspherical, but also axisymmetric, indenters. Later, many groups (Bulychev et al., 1975, 1976; Shorshorov et al., 1981; King, 1987; Oliver and Pharr, 1992; Pharr et al., 1992; Lankarani and Nikraves, 1994; Carpick et al., 1999) extended the theories to virtually every sufficiently smooth indenter shape with rotational symmetry. A brief summary will be given below.

The basic assumption for the calculations is that, for a purely elastic material, the stiffness S (or the change in force upon a given change in indentation) will be directly proportional to the root of the contact area of indenter and surface at this position [Eq. (12)].

$$S = \frac{dP}{d\delta} \propto \sqrt{A} \quad (12)$$

For some of the most important boundaries of indenters, we will now show the consequences.

One of the easiest shapes for an indenter is a cylinder that confers a "flat-punch." In this case, the radius of the indenter is constant for all depths: $r(\delta) \equiv R \forall \delta$. Clearly, the area of the punch is thus a constant, too: $A \equiv \pi R^2$. This implies $S \propto \text{constant}$, which results in a linear dependence of the force $P = \int S d\delta \propto \delta$.

A spherical indenter with a boundary line of $r(\delta) = \sqrt{R^2 - (R - \delta)^2} \approx \sqrt{2R\delta}$ implies a stiffness $S \propto \sqrt{\pi 2R\delta}$, which means that the force will be $P = \int S d\delta \propto \delta^{3/2}$, which exactly reproduces the Hertzian behavior. Due to the approximation of the

contact radius, this description is correct only for indentation depths that are small compared with the radius of the sphere ($\delta = R/3$ already results in an error of 10%). Using a parabolic curve to describe the surface of the indenter, we find $r(\delta) = \sqrt{\delta}$, $S \propto \sqrt{\delta}$ and, hence, the force $P \propto \delta^{3/2}$, which is exactly the same as the result of a sphere for small indentations (near its apex, a sphere can be approximated as a paraboloid).

Carrying out the same calculation for a cone which has a straight line as its boundary results in a radius $r(\delta) = \delta$ and a stiffness $S \propto \delta$. This leads to the force law $P = \int S d\delta \propto \delta^2$.

For a curve of the arbitrary shape $r(\delta) = \delta^{1/\alpha}$, the stiffness will be proportional to $\delta^{1/\alpha}$ as well, while the force on the contact will increase as $P = \int S d\delta \propto \delta^{1+1/\alpha}$. This last equation with all its simplicity has the power to explain measured indentation data. One often finds exponents greater than 2 which cannot be explained by standard indenter shapes. However, if the indenter were formulated as a root function, it would even allow for an exponent of 3. The only problem of this formulation is that one of the basic assumptions was to have a smooth surface, in order to avoid singularities in the pressure distribution at point zero. Thus, this theory would be applicable only at large indentations. The small indentation depths could be modeled with an indenter made of a small spherical part attached to the root shape. Thus, this would be a clever way to circumvent the problem of the singularity, while having an exponent greater than 2. Anyway, this correction has been neglected throughout the published literature for the conical indenter, too. Only the shapes of indentation curves at the initial contact are affected by this problem. From the analytical point of view, one simply has to be aware that basic assumptions are violated at this point.

Recently, there have been several attempts to give a more general description of an indenter by Borodich et al. (2003, 2004) or for more specialized, more realistic shapes, e.g., a Vickers indenter which is a pyramidal tip, by Franco et al. (2004).

8.4.3

Models Incorporating Adhesion

One of the shortcomings of the Hertzian model, and thus the Sneddon extensions, is that adhesion is not part of the model. A more complete approach was chosen by Maugis (1992, 2000) based on an earlier theory of Dugdale (1960). Their theory contains an adjustment parameter for the systematic inclusion of adhesion effects [Eq. (13)].

$$\lambda = 2\sigma_0 \left(\frac{\pi \varpi K^2}{R} \right)^{-1/3} \quad (13)$$

It is assumed that the region in which adhesive forces are acting is larger than the contact area derived in the Hertzian model; $m = c/a$ being the parameter determining the actual region of influence of adhesion (Fig. 8.5B).

Equations (14) and (15) describe the depth of indentation δ and the load P , σ_0 being the surface stress at the edge of the contact.

$$\delta = \frac{a^2}{R} - \frac{8a\sigma_0\sqrt{m^2 - 1}}{3K} \quad (14)$$

$$P = \frac{a^3 K}{R} - 2a^2 \sigma_0 \left(\sqrt{m^2 - 1} + \frac{m^2}{\tan(\sqrt{m^2 - 1})} \right) \quad (15)$$

There are two limiting cases where the Maugis–Dugdale model (MD) is reduced to much simpler theories, the Johnson–Kendall–Roberts model (JKR) (Johnson et al., 1971; Johnson and Greenwood, 1997) and the Derjaguin–Muller–Toporov model (DMT) (Derjaguin et al., 1975; Muller et al., 1980). JKR holds for the special case when adhesive forces are acting in only the region of immediate contact, while DMT describes the situation when these forces are acting along only the circumference of the contact. In addition, JKR assumes that the sample is compliant enough to adjust to the detaching sphere, while DMT claims that the surface will not deform on detachment.

To derive the JKR model, one has to assume that the maximum indentation force leads to the same radius of contact as the Hertzian model ($a^3 = PR/K$), while at the same time, at zero load, the sphere is still in contact with the surface. For this situation the radius of contact a_0 and the depth of indentation d_0 are given by Eqs. (16) and (17), where ϖ is Dupr e’s work of adhesion to separate two solids reversibly and isothermally.

$$a_0 = \left(\frac{6\pi\varpi R^2}{K} \right)^{1/3} \quad (16)$$

$$\delta_0 = \frac{a_0^2}{3R} \quad (17)$$

Generally, the radius of contact is given by Eq. (18).

$$a^3 = \frac{PR}{K} \left[1 + \frac{3\pi\varpi R}{P} + \sqrt{2 \frac{3\pi\varpi R}{P} + \left(\frac{3\pi\varpi R}{P} \right)^2} \right] \quad (18)$$

It is obvious that for the nonadhesive case ($\varpi = 0$) this equals the Hertzian contact. Pulling indenter and surface further apart, one reaches an unstable position where the indenter finally detaches. The force at which this occurs is F_{adh} [Eq. (19)] with a contact radius of a [Eq. (20)].

$$F_{adh} = -\frac{3}{2}\pi\varpi R \quad (19)$$

$$a = \left(\frac{3}{2} \frac{\pi\varpi R^2}{K} \right)^{1/3} \quad \text{or} \quad a = 0.63a_0 \quad (20)$$

The “indentation depth” δ of this position is obtained from Eq. (21).

$$\delta = -\frac{a^2}{3R} = -\left(\frac{\pi^2 \varpi^2 R}{12K^2}\right)^{1/3} \quad (21)$$

In the DMT model describing an adhesive contact of an elastic sphere with an elastic surface, it is assumed that adhesive forces originate from a ring-shaped zone around the contact radius and that the surface does not deform due to adhesion. The deformation profile is therefore identical with the one derived in the Hertzian model. The contact radius is given by Eq. (22), where the nonadhesive case yields the Hertzian contact again.

$$a^3 = \frac{PR}{K} + \frac{2\pi\varpi R^2}{K} \quad (22)$$

The depth of indentation is given by Eq. (23).

$$\delta = \frac{a^2}{R} = \left(\frac{P}{K\sqrt{R}} + \frac{2\pi\varpi\sqrt{R}}{K}\right)^{2/3} \quad (23)$$

Under zero load the contact radius at an indentation of $\delta_0 = a_0^2/R$ is given by Eq. (24).

$$a_0^3 = \frac{2\pi\varpi R^2}{K} \quad (24)$$

The pull-off force is $F_{adh} = -2\pi\varpi R$ at depth $\delta = 0$ and $a = 0$. The behavior of a DMT-like indenter is simply that of a Hertzian sphere, but offset by the adhesive force. By introducing normalization parameters, we can compare the theoretical descriptions more easily:

- reduced contact area $A = \frac{a}{\left(\frac{\pi\varpi R^2}{K}\right)^{1/3}}$
- reduced force on the contact $\bar{P} = \frac{P}{\pi\varpi R}$
- reduced indentation depth $\Delta = \frac{\delta}{\left(\frac{\pi^2 \varpi^2 R}{12K^2}\right)^{1/3}}$
- degree of adhesion according to Maugis $\lambda = \frac{\delta}{\left(\frac{\pi\varpi K^2}{R}\right)^{1/3}}$.

Thus, the equations describing the contacts are simplified to the versions listed in Table 8.2. The reduced force curves versus indentation depth are shown in Fig. 8.6 for comparison.

Table 8.2 Simplified equations for contact mechanics of two spheres.

Model	Reduced load and indentation depth
Hertzian	$\bar{P} = A^3$ $\Delta = A^2$
DMT	$\bar{P} = A^3 - 2$ $\Delta = A^2$
JKR	$\bar{P} = A^3 - A\sqrt{6A}$ $\Delta = A^2 - \frac{2}{3}\sqrt{6A}$
MD	$\bar{P}_{adh} = A^3 - \lambda A^2(\sqrt{m^2 - 1} + m^2 \tan^{-1} \sqrt{m^2 - 1})$ $\Delta = A^2 - \frac{4}{3}A\lambda\sqrt{m^2 - 1}$

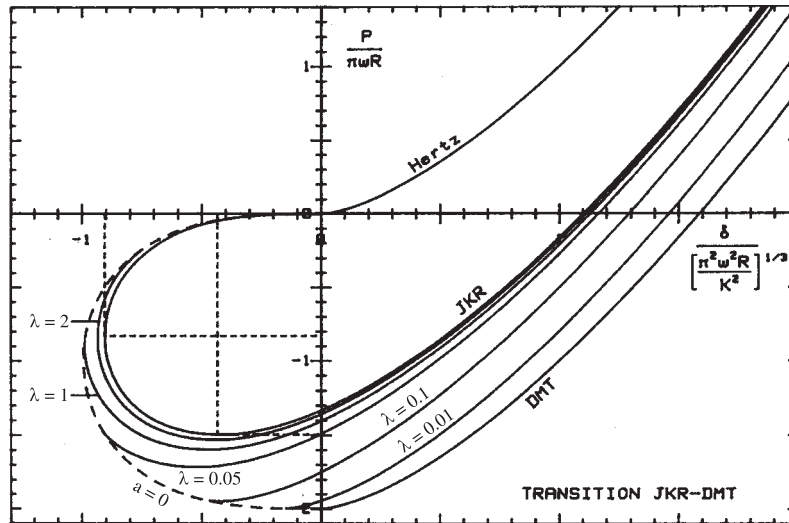


Fig. 8.6 With normalized parameters, all the models describing contact mechanics can be plotted in one graph. Clearly, the DMT curve differs from the Hertzian curve only by a constant offset, while the JKR plot has a steeper increase. However, JKR and Maugis–Dugdale are the only theories describing

negative indentation depths which explain the pull-off behavior of very compliant materials, thus giving an explanation for the hysteresis in detachment processes. (Taken from Maugis (2000) with kind permission from Springer.)

8.5

AFM Measurements Using Pulsed Force Mode

The AFM is an instrument whereby an indenter can be moved toward and away from the sample surface with sub-nanometer precision. Furthermore, it is possible to measure forces with a precision down to 10^{-11} N. Although the measured indentation curves, either in the FDC or the PFM mode, can be understood in terms of the models discussed in the Section 8.4, effects of viscosity and plasticity are difficult to handle. The next sections are devoted to a thorough description of the data acquisition and analysis processes in PFM.

8.5.1

Force Curves

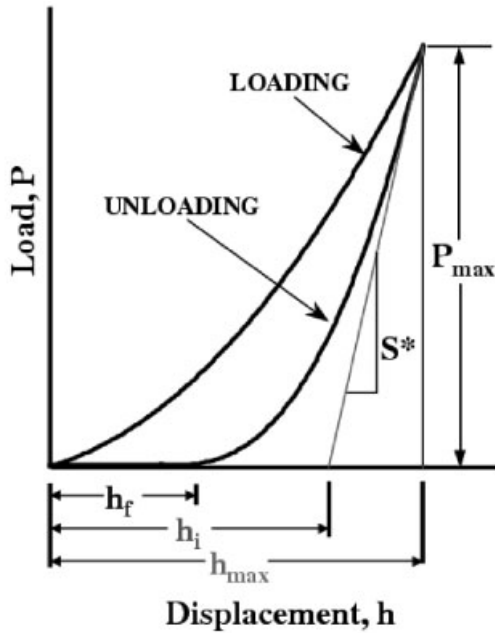
At large tip-sample separations the cantilever is influenced only by long-range forces. These forces include electrostatic interactions due to localized charges or potential variations, magnetic interactions if a specially treated cantilever is in use, or van der Waals forces. However, at large distances all possible forces vary slowly with the tip-sample separation. This is especially true if magnetic forces and electrostatic forces are absent. Being out of contact, the position of the cantilever is smeared out by thermal oscillations (remember: there is an energy of $3k_B T/2$ in every degree of freedom). Thus, the average force measured far away from the surface serves as the baseline of the force curve. From now on we will use this baseline force as the zero reference for all measured curves. Closer to the surface, local effects become increasingly important. In the case of a charged sample, the bending of the baseline while approaching the surface makes it possible to measure the electrostatic interaction. The tip moves in an effective potential consisting of the highly nonharmonic interaction potential between the tip and the sample and the harmonic potential of the cantilevered oscillator. This effective potential has multiple local minima at smaller separations. Therefore we expect instability points and hysteresis. The first contact will be established when the thermal oscillation of the cantilever is bringing the tip close enough to the surface to snap in. In the repulsive regime, the models described above can be used for modeling. For purely elastic samples the theories of Hertz, JKR, DMT, and MD seem to be appropriate. During the indentation, the sample is deformed by the tip of the cantilever. The mechanical work is partially stored as elastic potential energy and partially dissipated in viscoelastic processes and in plastic deformation. Whereas during the approach the material is pushed away, the sample pushes the tip back on release. The area under the force-distance curve therefore corresponds to the energy dissipated in one cycle (hysteresis). The ratio of the dissipated energy to the total energy involved is a measure of the dissipative properties of the material.

The detachment behavior can be observed at the snap-off. Depending on sample compliance and the mutual adhesive interaction forces between the sample and the tip (in most cases SiO groups), either the tip can detach as soon as the surface

is back in the relaxed state, or it can even pull on the surface, resulting in a negative indentation. Except for the Hertzian model, which excludes adhesion, this process is described by all models. However, the physical origin of the adhesive behavior can be manifold. Only the sum of all the interactions can be measured by the AFM. Wetting of the tip by the sample material is one of the effects, but van der Waals forces, electrostatic forces, or even hydrodynamic forces such as the formation of a liquid neck between the tip-apex and the sample in ambient conditions can also be involved (Tabor, 1977; Werf et al., 1994; Stifter et al., 1998, 2000). To avoid the influence of the last of these, it is possible to conduct measurements in a liquid environment such as water or a buffer solution. The latter is especially suitable for the investigation of biological samples, which has drawn considerable attention recently. Another possibility is to chemically functionalize the tip surface in order to achieve a hydrophobic behavior, e.g., by silanization. The sudden jolt on the cantilever upon snap-off excites the eigenfrequency of the cantilever. The damping of this oscillation depends on dissipative processes within the cantilever (usually quantified by a quality factor Q) and external processes such as hydrodynamic damping in liquids. The frequency of this relaxation oscillation is usually lower than the eigenfrequency of the free cantilever. This frequency shift can be induced by the higher external damping close to the sample, or (hard to measure with large cantilevers) by material transferred from the sample to the tip.

In 1992 Oliver and Pharr (Oliver and Pharr, 1992; Pharr et al., 1992) described the evaluation of force curves on materials showing elastic and plastic deformation, in order to give a guideline on how to evaluate force curves leaving permanent deformation marks on the surface (Fig. 8.7). Their strategy was to assume that the material, once deformed by the application of high forces, pushes back due to its elastic properties alone. That is to say, the retraction path of a force curve is affected only by the elastic recovery of the sample. The offset between the zero position of the force curves upon approach and retraction is assigned to a remanent depth, i.e., the depth of the permanent deformation of the sample.

Note that we have not made any assumptions about the trajectory of the tip of the cantilever, so far. The description is valid for a linear as well as a sinusoidal movement. What is the difference between PFM operation and running FDCs? If one is interested in learning about material parameters for quasi-static strains and stresses, FDCs are the tool of choice. However, if the material parameters are to be mapped to the surface or if the rate dependence of the behavior under stresses and strains is to be investigated, much higher repetition rates are necessary. This is where the PFM, with its repetition rates from 50 to 20 kHz, comes in handy. At low rates it is acceptable to use triangular waves to drive the cantilever position. However, at higher rates the filter characteristics of amplifiers and piezo-ceramics cause different amplifications and phase shifts for the harmonics of the triangular drive, thus inducing distortion (remember: the higher harmonics in a triangular wave are necessary for the instantaneous change of slope at the turning points). Furthermore, mechanical resonances in the AFM might be excited by the triangular wave.



h_{\max} = maximum displacement
 h_f = final depth
 h_i = intercept displacement

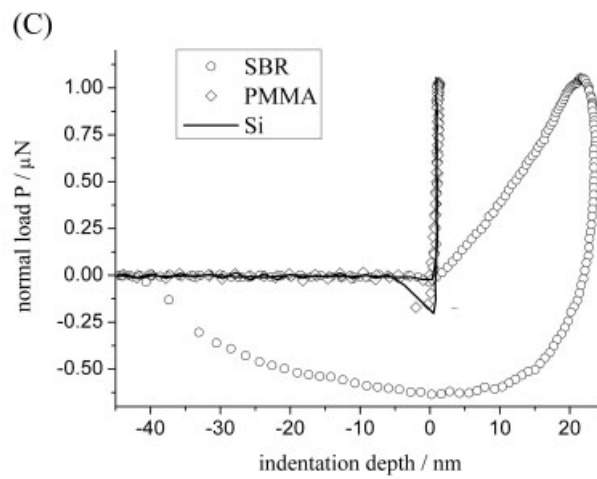
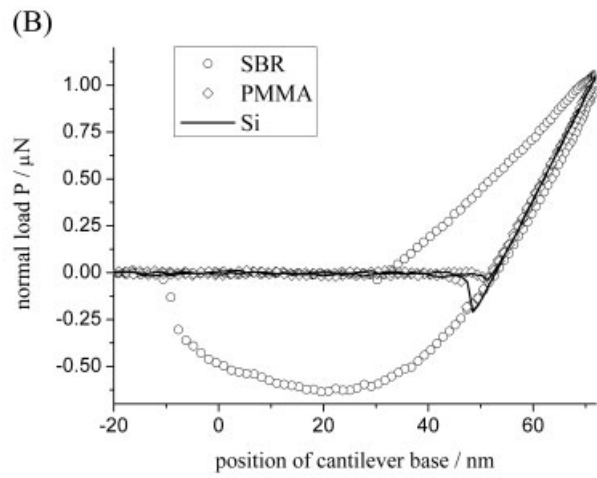
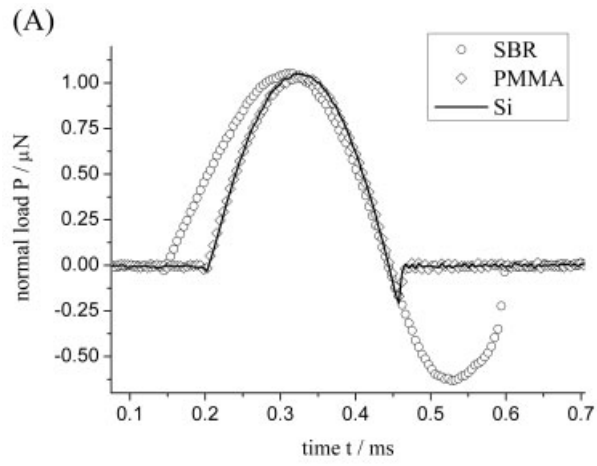
Fig. 8.7 The very common method for evaluation of FDCs, developed by Oliver and Pharr (Oliver and Pharr, 1992; Pharr et al., 1992) and based on the assumption that the first part of the retrace (unloading) of the cantilever will show purely elastic behavior, since the plastic deformation has to be caused on the indentation trace (loading). For purely

elastic and plastic materials the analysis is in good agreement with the permanent deformations caused in nanoindentations (Hinz et al., 2004). Viscoelastic effects are not included in their description. (Taken from Oliver and Pharr (1992) with kind permission from the Materials Research Society.)

8.5.2

Data Evaluation

Evaluation of FDCs or of curves acquired by PFM has to be carried out carefully. As a reference material some sort of hard sample with well-known elastic properties is used for calibration measurements. In our case we use a silicon surface as reference, since silicon is one of the best known hard materials. When in contact, the movement of the cantilever base will be converted directly and almost without losses into deflection of the cantilever. Therefore there is a one-to-one relationship between the movement of the base of the cantilever and the deflection. This means the slope of the calibration force curve can be used to assess the sensitivity of the



measurement system. Thus, deflection can always be converted into a force acting on the tip. The calibration signal accounts for both, the cantilever bending and the (very small) deformation of the tip–sample contact. The trajectory of the tip, or in other words the position of the tip on top of the sample surface, is the sum of the change in position due to cantilever bending and the actual indentation into the material. Therefore, the reference slope always has to be subtracted from the position imposed on the base of the cantilever by modulating the z -positioning piezo. After subtraction, we know the real position of the tip in the material of the surface. The force versus indentation plots can be created and evaluated according to the theories for data evaluation described above. It is obvious from our example that the softer the material, the deeper the indentation will be at the same load. For the same indentation depth, soft cantilevers require a much larger deflection than stiff cantilevers. Therefore, the errors after the subtraction of the reference curve are much larger for soft cantilevers. As a guideline one should use cantilevers which are as stiff as possible.

The measurements shown in Fig. 8.8 were carried out on three different samples: silicon, poly(methyl methacrylate) (PMMA) and styrene–butadiene rubber (SBR). The macroscopic material properties can be found in Table 8.3. The experimental settings for our measurements were: modulation amplitude 145 nm; modulation frequency 1.0 kHz; maximum normal load 1.1 μN . The experiment was conducted in ambient conditions with a cantilever of 55 N m^{-1} force constant at a fundamental frequency of 328 kHz.

The temporal response of the sample materials is shown in Fig. 8.8 A as acquired by the PFM. Following the calibration and evaluation strategy explained above, the force vs. time curves can be converted into classical FDCs as seen in Fig. 8.8 B. Using the sample substrate (silicon) as an on-line reference (made visible by scratching the spin-coated surface in advance), data can be analyzed from the force vs. indentation plots (Fig. 8.8 C).

In our example, silicon shows a small indentation which stops right after the point of contact, while PMMA allows some deformation, and SBR seems not to resist the indentation much. The behavior of silicon is not surprising, since this hard material follows the Hertzian description quite perfectly. Since the scale of the indentation (4 nm) is small compared with the radius of the tip (approx. 50 nm, estimated from SEM imagery), a Hertzian model is justified. It reveals an almost perfect elastic behavior for indentation and retraction. The width of the hysteresis loop

Fig. 8.8 Stepwise analysis of PFM curves. Three materials were probed in this typical measurement: SBR, PMMA, and silicon. From the temporal response (A), the known trajectory of the base of the cantilever can be removed (B), although there is no significant difference visible between the sample materials. Silicon is taken as the reference material. The slope of the calibration curve is subtracted from all other data in order to rescale the horizontal axis. Finally (C), all three materials are plotted versus the indentation depth (the real physical quantity). The areas now correspond to the work applied to the sample. The theories of continuum mechanics can be used to analyze the data, revealing the Young's moduli or surface energies of the sample materials.

Table 8.3 Characteristics of the sample materials as used for the measurements shown in Figs. 8.8 and 8.9.

	SBR	PMMA	Silicon wafer
Radius of gyration	14 nm	7 nm	–
Glass temperature	–20 °C	118 °C	–
Molecular weight	390 kg mol ⁻¹	100 kg mol ⁻¹	
Specialty	not crosslinked 30% S + 70% BR statistically arranged	–	cleaned by sonication: 15 min toluene 15 min ethanol 15 min toluene
Young's modulus (bulk, static)	50–150 MPa	3.3 GPa	60–150 GPa
Expected behavior	rubber-elastic pronounced relaxation	elastic glassy	hard marginal deformation
Polymer structure			–

is below the noise level. PMMA also behaves elastically, but with a much flatter slope than silicon. However, since we are applying quite high forces to the sample it is astonishing that no deformation occurs. This is in contrast to FDC measurements (Hinz et al., 2004), where residual indentations were observed. The main difference between those FDC measurements and our PFM data is the interaction time (or the frequency range) between the tip and the sample. It is known from classical DMA measurements (Ferry, 1980) that polymers respond quite differently to stimuli at different frequencies. The theoretical side of DMA is covered by Christensen (1982). One can infer from those DMA measurements that PMMA at the PFM interaction times (10–100 μ s) is an almost perfectly elastic material, whereas at interaction times of 1 s (FDC) viscoelastic processes are important. On SBR, on the other hand, we find a huge area under the force trace which means that large amounts of energy are dissipated by the material either by plasticity or viscoelasticity. However, since we are not able to observe surface destruction on the SBR areas, we conclude that the dissipative behavior has to be attributed to viscoelasticity alone. Otherwise the surface would have to show remanent plastic deformations. The timescale at which this relaxation happens has to be above 50 μ s, since the sample does not push back quickly enough for a fully elastic behavior to be ob-

served in the PFM curves. The timescale also has to be clearly below 1 ms, since the surface is restored within a single cycle. Another effect of time-dependent elasticity can be seen at the position where the maximum force is reached. While silicon and PMMA also reach their maximum indentation depth at this point, the tip creeps to deeper indentations on SBR afterward. This is because of the delayed deformation of viscous materials under strain. In Fig. 8.9(A), the indentation depths at which F_{\max} is reached are compared for all three sample components. This is what can be measured directly from the curves in Fig. 8.8(C). The post-flow, or creep, can be seen in Fig. 8.9(B).

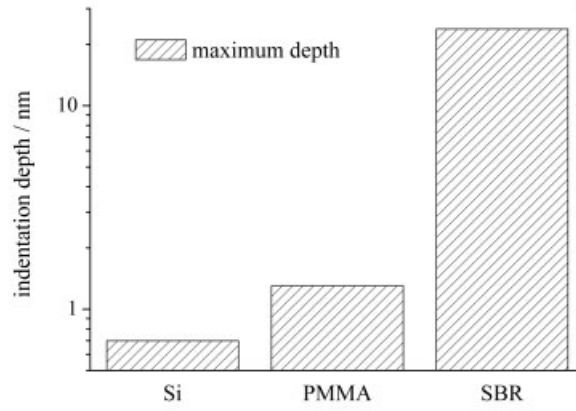
The adhesive properties of the materials are also highly interesting and comply with intuition. Silicon and PMMA demand about the same pull-off force to detach the tip from the surface, while SBR shows greater affinity for the silicon of the cantilever tip. Due to its large compliance, it is even possible to deform the surface outward, resulting in a negative detachment position. Thus, it is the stickiest of the three materials. At edge positions one has to be aware that topographical features have an influence on the contact area and thus on the adhesive behavior. As Stifter et al. (1998, 2000) showed in a series of papers, the changes in adhesion in SPM measurements is caused mainly by the topographic shape of the samples. In turn, their model makes it possible to determine the tip shape parameters when the shape of the sample is known, e.g., a step on an HOPG surface or a step on a calibration grating.

As stated before, the area under a force curve corresponds directly to work involved in the motion. First, let us look at the energy deposited in the material during indentation. During the trace (approaching the surface) elastic, plastic, and viscoelastic forces are acting on the tip. In other words, work has to be done in order to push the tip into the sample. The elastic parts will be recovered on the release, while the plastic deformation will remain as a permanent deformation and the viscoelastic part heats the sample. The position at which the force equals zero again on this retrace gives an estimate of the depth of the permanent indentation. This is only valid, however, if the recovery rate of the material is higher than the retraction rate of the tip. In Fig. 8.9(B), the energy deposited in the material during the trace part, the hysteresis of a single cycle, and the energy required for detachment from the surface are shown. For silicon no hysteresis is observed, and there is only a minuscule amount for PMMA. For SBR the hysteresis is about 10 times greater. A similar result is found for detachment. Silicon and PMMA do not differ too much (PMMA being a little less adhesive than silicon), while SBR firmly sticks to the tip until the contact ruptures.

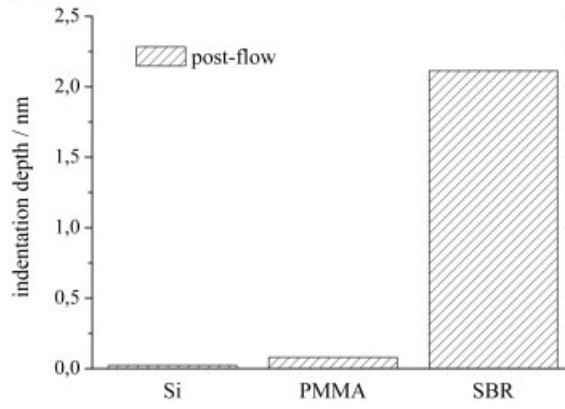
8.6 Applications of Pulsed Force Mode

Experiments utilizing PFM have been conducted in many laboratories and have also been reported in various papers. Among these, there are measurements on polymer blends; thin films a few nanometers thick; nanostructured, magnetic,

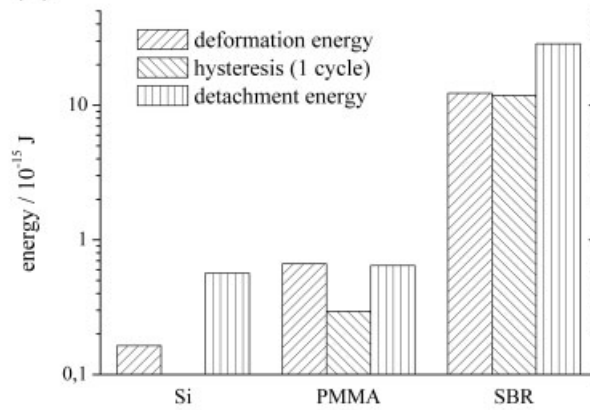
(A)



(B)



(C)



electrostatically charged surfaces; or even biological samples. In the next sections we will comment on some typical applications.

8.6.1

Examination of Dewetting Polymer Blends

One of the most recent reports was published by Stenert et al. (2004), who applied PFM to a dewetting polymer system composed of PMMA and PnBA. PFM was used to unveil differences in compliance of the materials as well as to minimize the lateral straining of the material by the relative movement of the tip and sample while in contact. On the materials side, their results revealed the influence of the addition of poly(methyl methacrylate)-*block*-polystyrene (PMMA-*b*-PS) and PS-*b*-poly(*n*-butyl acrylate) (PS-*b*-PnBA) diblock copolymers on the structure and the mechanical properties of PMMA/PnBA polymer blends.

8.6.2

Excimer Laser Ablation of PMMA and Adhesion Measurements by PFM

A study of the incubation states of UV-laser irradiated polymer samples using an AFM operated in PFM was recently presented by Hopp et al. (2004b). Illuminating the targets (Fig. 8.10A) with a certain number of laser pulses (193 nm, 20 ns, 1 Hz) at fluences of 5.8 to 8.9 mJ cm⁻², they observed changes in pull-off forces on PMMA (Fig. 8.10C). However, below 100 pulses the topography did not change remarkably, while above this threshold significant alterations were observed (Fig. 8.10B). Their conclusion is that the decomposition of PMMA dramatically lowers the surface energy and thus the adhesion of the surface.

8.6.3

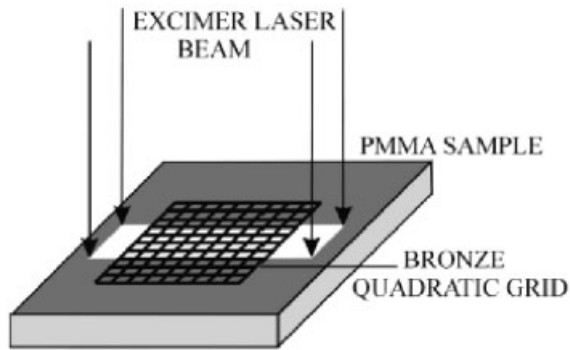
Temperature-Dependent PFM Investigations of Crystalline PTFE

Crystalline structures of thin layers of PTFE have also been studied recently. Kresz and coworkers (Kresz et al., 2004; Hopp et al., 2004a) wanted to find out whether annealing changes the adhesive properties of their pulsed-laser deposited samples. It turned out that due to annealing at 320 °C the effective surface reached a maxi-

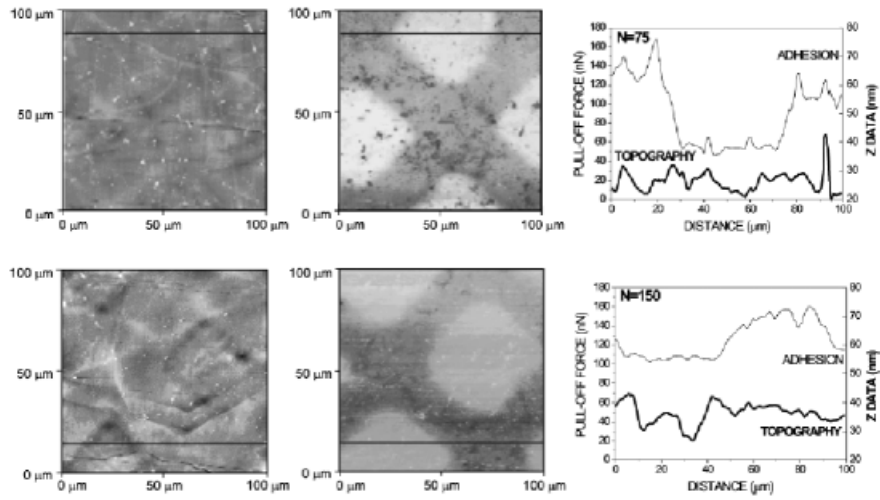
←

Fig. 8.9 Local behavior of the materials derived from the PFM curves in Fig. 8.8. (A) The depth at which the pre-set maximum force was reached. (B) From the curve describing SBR, one can clearly measure a post-flow (creep) distance, i.e., the difference between the position of maximum force and the maximum indentation depth. (C) Characteristic energies involved in the indentation process. Deformation energy: the energy that is deposited in the sample on the loading path. Hysteresis energy: during unloading, the surface recovers and energy is set free, except for the amount lost in the hysteresis of the material. In case of SBR, the ratio of energy lost in one cycle is above 90% while for the other materials it is close to zero. Detachment energy: this reveals that SBR is the stickiest of the three materials.

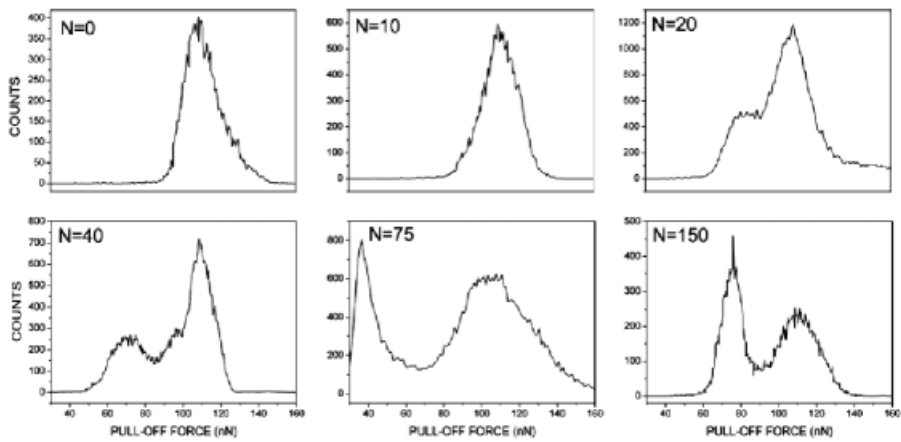
(A)



(B)



(C)



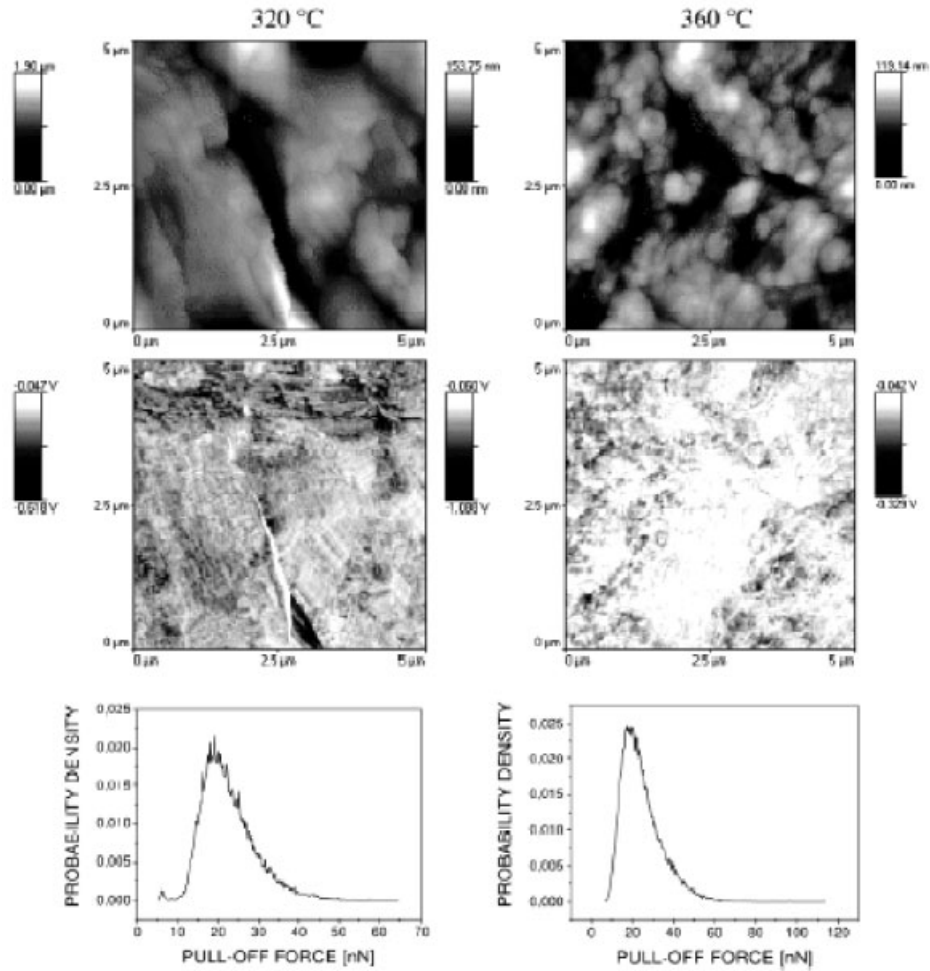


Fig. 8.11 PFM images of thin layers of PTFE post-annealed at different temperatures. Top row: topography; middle row: adhesion; bottom row: histogram of the adhesion maps. (Taken from Kresz et al. (2004) with kind permission from Elsevier.)

Fig. 8.10 (A) Schematic of the experiment by Hopp et al. for lateral structuring of a PMMA film. (B) After 75 pulses, the sample morphology (left-hand column) was not modified, whereas at 150 pulses changes are obvious. Adhesion (center) is already influenced at very low numbers of pulses. The

line traces (right) indicated in the images confirm the modifications. (C) Histogram analysis also confirms the modifications. With an increasing number of pulses, areas of low adhesion grow. (Taken from Hopp et al. (2004b) with kind permission from the American Institute of Physics.)

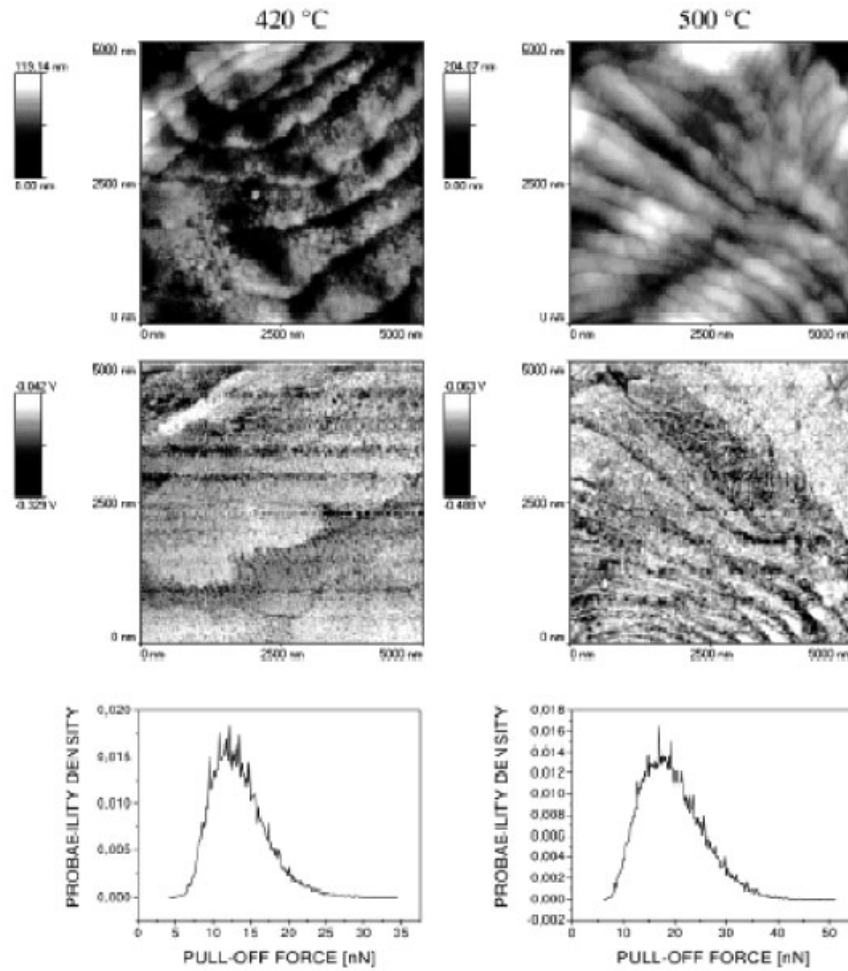


Fig. 8.11 (continued)

imum value, while it was reduced to a constant value for annealing in a range of 360–500 °C (Fig. 8.11). For a special cool-down procedure they achieved ring-like structures on their PTFE samples, which revealed a significant increase in adhesion compared with regular pulsed-laser deposited Teflon.

8.6.4

Conducting PFM of Lithographically Structured Circuitry

Since the STM can test topographical and electronic properties only on fully conductive surfaces, it is not applicable to electronic circuitry separated by insulators

approaching the nanoscale. However, AFM techniques usually cannot gain information on the electronic behavior of materials. Thus, by using PFM combined with a conducting tip, as Bietsch and coworkers did (Bietsch, 2000; Bietsch et al., 2000), one can probe conducting and nonconducting surfaces, while at the same time minimizing the lateral strain of the sample. Topography and stiffness (Fig. 8.12A,B respectively), which make a differentiation of the materials possible, are merged with the information of the conductance of the sample at the point of contact (Fig. 8.12C). The particles that can be seen isolated on the left half of the stiffness map do not contribute to the conductance map. In this method, the surface electronics was hard-wired to a potential, while the tip was used as voltage probe. The advantage of the method is the merging of traditional AFM fields with those of STM.

8.6.5

Investigation of Very Thin Layers of Poly(vinyl alcohol) in PFM

For many technical applications, the understanding of the mechanical behavior of very thin layers of polymers is important. A sample system on which this was demonstrated recently in an impressive manner was poly(vinyl alcohol) on a mica surface. The topography image shows that the layer has a thickness of only 9 nm (Fig. 8.13A). Beyond the beautiful structures that formed after evaporation of the water which acted as solvent, Spizig (2002) was able to distinguish between the surface materials with respect to stiffness and adhesion (Fig. 8.13B,C respectively).

8.6.6

PFM in Liquids with Chemically Modified Tips

For medical and biological AFM samples it is very important to control the adhesive properties of the surfaces in use. Cells, for example, stick only to specially treated coverslips. The tip of the cantilever can serve as a model for such an investigation. It can be chemically modified, e.g., by CH_3 or NH_2 groups, in order to model a silicon surface which is functionalized, while the opposing sample surface is sparsely covered by the other material (e.g. the cells). When the surface is being scanned, there will be situations where the functionalized tip faces silicon and situations where the contact is on the tested substance. This kind of experiment was conducted by Schneider et al. (2002), who examined polyethyleneimine in an aqueous solution using PFM.

8.6.7

Electric Double Layer – PFM in Liquids

From the middle of the 1990s, several publications exist on the successful application of PFM to the measurement of electronic double layers (EDLs) in liquid

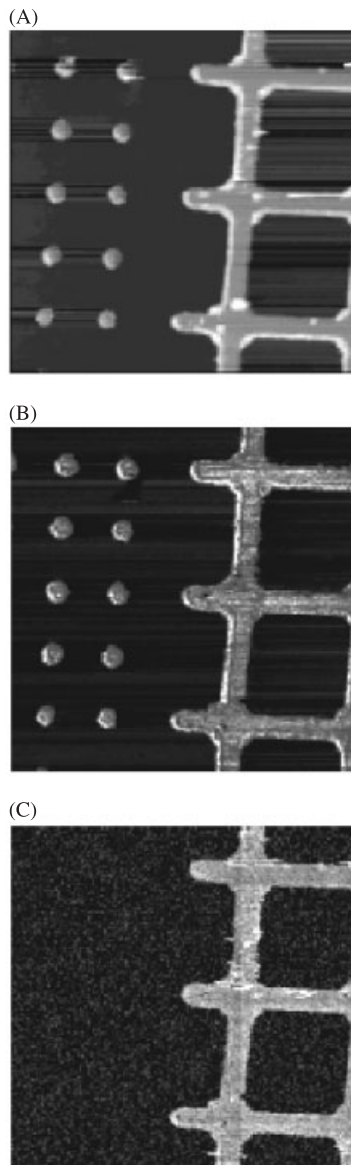


Fig. 8.12 With a conducting tip and a special setup, conducting PFM is possible. It provides simultaneous information on topography (A; z-scale: 0–90 nm), adhesion (B; brighter areas: stronger adhesion), and current (C; current: 0–100 nA). The material contrast of gold

structures 50 nm thick on an SiO_2 surface is clearly reflected in the adhesion map. The conducting mesh appears bright in the current image, as opposed to the insulating dots. (Taken from Bietsch, 2000) with kind permission from A. Bietsch and WITec GmbH.)

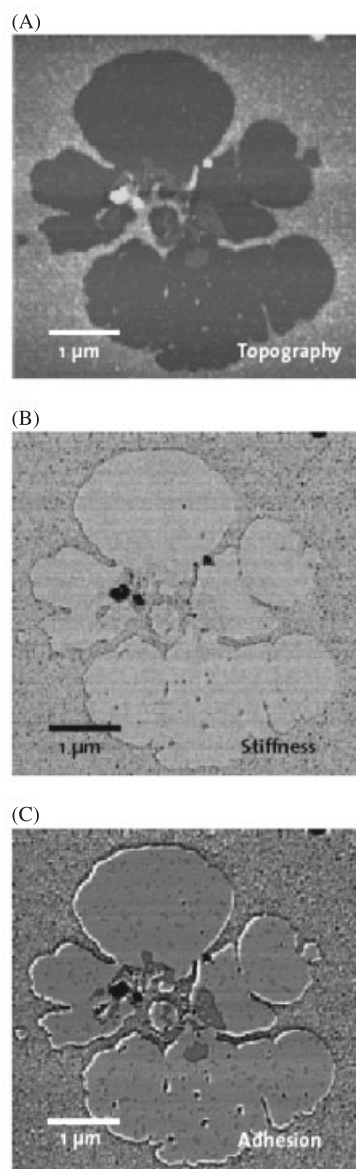


Fig. 8.13 The properties of poly(vinyl alcohol) on mica observed by PFM (Spizig, 2002). (A) Topography: three different phases with layer thicknesses up to 9 nm can be distinguished. (B) Local stiffness in the different phases: due to the thin-layer structures, only low forces

could be applied, to ensure that substrate properties were not measured (brighter colors represent higher stiffness values). (C) Adhesion map of the sample. (Taken from Spizig (2002) with kind permission from P. Spizig and WITec GmbH.)

(Stifter, 1996; Weilandt, 1996; Miyatani et al., 1997, 1998; Rosa-Zeiser et al., 1997). Liquid/solid interfaces tend to be charged due to the ionization or dissociation of surface groups. The different chemical potentials are adjusted by a charged double layer, the EDL. The strength of the EDL relates to the work function of the surface. Both the tip and the sample interfaces with the liquid are covered by an EDL, albeit of different strengths. With the approach of two EDLs, in this case the Si_3N_4 AFM tip and the quartz surface, forces arise which pull down the cantilever. Thus, by measuring the deflection of the cantilever shortly before the snap-in of the tip, the EDL force can be determined (Fig. 8.14A). Oscilloscope traces of such a measurement in Fig. 8.14(B,C) show attractive forces on the cantilever for EDLs of different signs, and repulsion of the cantilever for EDLs of the same sign. The interaction is described by the Derjaguin–Landau–Verwey–Overbeek (DLVO) theory. It has been found that, even up to 1 kHz, this method with PFM can be used to measure the effect of the EDL (Fig. 8.14D).

8.6.8

Measuring Biological Samples in Liquids

PFM and JM are very promising candidates for imaging biological samples in liquids. Tapping mode, however, is not very useful in this environment, since the resonant behavior of the cantilever changes to rather chaotic motion, making scanning impossible. Thus, subresonant modes, such as PFM and JM, can be used, because very slow motion through the liquid is possible. Fluid dynamics will also cause a damping effect, but this can be compensated for in data evaluation. See, for example, Moreno-Herrero et al. (2003, 2004) and de Pablo et al. (2003) for more detail.

8.6.9

Combined Mechanical Measurements – CODYMode

The basic PFM is not able to measure lateral forces. When the sample is modulated laterally while a PFM measurement is being made, a torsional motion is induced in the cantilever during the contact time. The cantilever torsion is detected during the repulsive contact time by a lock-in technique (Fig. 8.15A). This setup was developed by Krottil (Krottil et al., 2000b,c; Krottil, 2000d) and is known as CODYMode (Krottil et al., 2000a). It is capable of discerning between materials from their frictional or lateral force properties on the nanoscale. The sample system in this case was a polymer mixture of P β BMA and P2VP (see Krottil (2000d) for details) dewetting on an oxide surface. The structures revealed clear contrasts in adhesion, stiffness, and friction (Fig. 8.15B). At high lateral modulation frequencies and at low lateral amplitudes, the experiment resembles a high-speed DMA experiment.

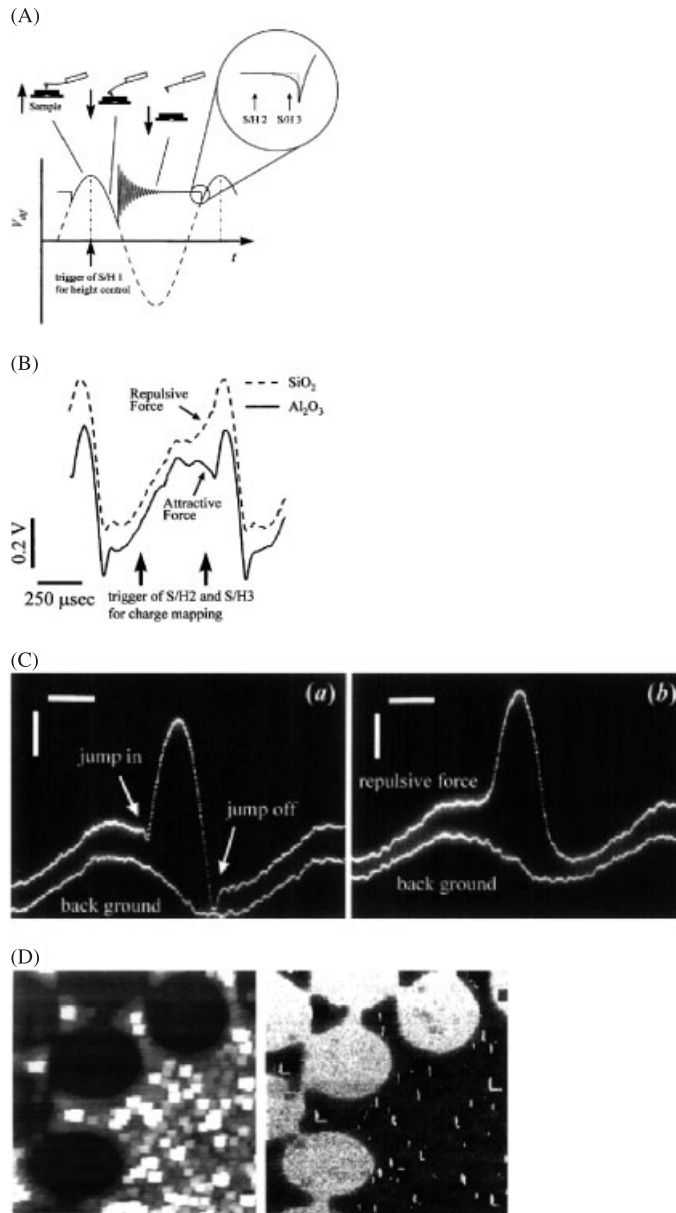
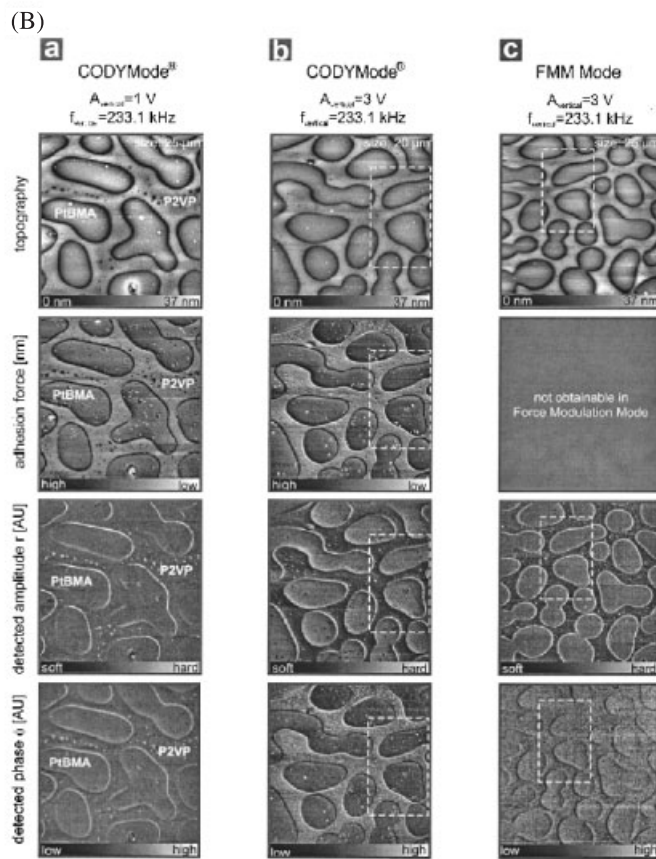
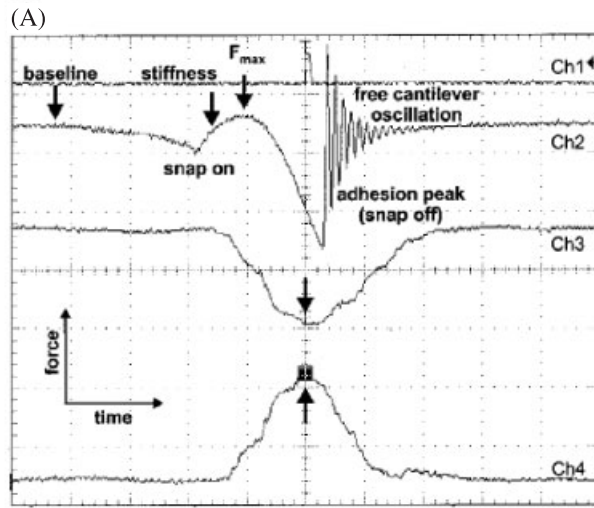


Fig. 8.14 (A) Schematic of PFM for measurement of EDL forces. The difference between the baseline and a point shortly before snap-in has to be measured (S/H 2, S/H 3: sample and hold 2 and 3 in the image). (B) The result of an EDL measurement: depending on the charges on the surface, repulsion or attraction occurs. (C) Oscillo-

scope traces showing that the snap-off behavior also is influenced by the EDLs. (D) A structured surface (Al_2O_3 on SiO_2) was scanned in this mode and allowed mapping of the EDL forces. (Taken from Miyatani et al. (1997, 1998) with kind permission from the American Institute of Physics.)



8.7 Conclusions

PFM has become one of the indispensable tools for surface characterization. Due to the intermittent nature of the tip–sample contact a broad variety of sample surfaces, both delicate and robust, can be imaged. The PFM is a tool bridging the gap between FDC measurements and tapping mode. As in FDC measurements, detailed information is available on the different phases of the tip–sample interaction. As in tapping mode, samples can be characterized very efficiently with many data points. Large maps of material properties can be obtained. To understand the measured interaction curves and to relate their features to materials, a much more detailed theoretical framework is needed. Unlike FDCs, we cannot assume a quasi-static situation. Unlike in tapping mode, it is not possible to condense the entire interaction into two observables.

We have outlined relevant theories to understand the elastic response of samples. Much less is known about the time-dependent viscoelastic and plastic response. Only a close collaboration between theorists and experimentalists will be able to resolve issues pending in data interpretation. A reliable model of viscoelastic and plastic interactions between the tip and the sample would unleash the full power of PFM.

We have reviewed examples of experiments in PFM. It has been shown that soft materials are well suited to be imaged with this method. Hydrophobic and hydrophilic surfaces show a large contrast in the adhesion image. Materials with different compliances will give excellent stiffness maps. It has been shown that PFM can be used in liquids, and that it measures medium-range forces such as EDL forces. Finally we have shown that friction measurements can be combined with lateral force measurements. Lateral forces include friction forces, but are much more general. They also exist as shear forces or viscous drag forces. The latter are measured in DMA. Hence the CODYMode is an interesting candidate for high-speed DMA.

Since PFM integrates well into existing AFM systems and with the advent of the high data volume recording “digital pulsed force mode” tool, it will become even more important for materials-related sciences.

← **Fig. 8.15** CODYMode makes it possible to combine the measurement of mechanical properties as known from PFM with the measurement of lateral forces. Using a lock-in technique, the torsion of the cantilever during contact is analyzed. (A) A typical measurement: the channels shown correspond to: Ch1, trigger signal; Ch2, PFM force curve; Ch3, real part, and Ch4, imaginary part of the $L - R$ signal. (B) CODYMode scans of a polymer sample, showing results for all its physical properties in comparison with force modulation mode. (Taken from Krottil et al. (2000b) with kind permission from the American Institute of Physics.)

Acknowledgements

The authors first thank their colleagues at the Department of Experimental Physics at the University of Ulm. M. Asbach and D. Told helped with the sample preparation and H. Schimming with the electronics. We gratefully acknowledge discussions with M. Pietralla, G.-I. Asbach, B. Heise, and S. Hild. For cooperation and discussion the authors thank WITec GmbH, and in particular W. Ibach, D. Sanchen, P. Spizig, G. Volswinkler, and A. Jauß.

This work was supported by the German Science Foundation (SFB-239 and SFB-569) and the DAAD Projektbezogener Personenaustausch mit der Republik Ungarn. A. Gigler is specially indebted to the Landesstiftung Baden-Württemberg (Kompetenznetz: Funktionelle Nanostrukturen) for financial support.

References

1. Tapping Mode is a trademark of Veeco Instruments, www.veeco.com
 2. PFM and CODYMode are trademarks of WITec GmbH, www.witec.de
- ALEXANDER, S., HELLEMANS, L., MARTI, O., SCHNEIR, J., ELINGS, V., HANSMA, P. K., LONGMIRE, M., GURLEY, J. (1989), An atomic-resolution atomic-force microscope implemented using an optical lever, *J. Appl. Phys.*, Vol. 65, pp. 164–167.
- BALOOCH, G., MARSHALL, G. W., MARSHALL, S. J., WARREN, O. L., ASIF, S. A. S., BALOOCH, M. (2004), Evaluation of a new modulus mapping technique to investigate microstructural features of human teeth, *Biomechanics*, Vol. 37(8), pp. 1223–1232.
- BIETSCH, A. (2000), High-resolution microcontact printing and characterization of nanowires by conducting atomic force microscopy. Thesis, University of Ulm, Germany.
- BIETSCH, A., SCHNEIDER, M. A., WELLAND, M. E., MICHEL, B. (2000), Electrical testing of gold nanostructures by conducting atomic force microscopy, *J. Vac. Sci. Technol. B*, Vol. 18, pp. 1160–1170.
- BINNIG, G., ROHRER, H. (1982), Scanning tunneling microscopy, *Helvetica Physica Acta*, Vol. 55, pp. 726–735.
- BINNIG, G., QUATE, C. F., GERBER, Ch. (1986), Atomic force microscope, *Phys. Rev. Lett.*, Vol. 56, pp. 930–933.
- BOEHNKE, U.-C., BRODOWSKY, H. M., GROOTHUES, H., KREMER, F. (1999), Investigations of the force–distance behaviour in polar liquids, *J. Phys. Chem. B.*, Vol. 103(32), pp. 6741–6745.
- BOGETTI, T. A., WANG, T., VANLANDINGHAM, M. R., EDULJEE, R. F., GILLESPIE, J. W. JR. (1999), Characterization of nanoscale property variations in polymer composite systems: Part 2 – finite element modeling, *Composites Part A*, Vol. 30, pp. 85–94.
- BORODICH, F. M., KEER, L. M., KORACH, C. S. (2003), Analytical study of fundamental nanoindentation test relations for indenters of non-ideal shapes, *Nanotechnology*, Vol. 14, pp. 803–808.
- BORODICH, F. M., KEER, L. M. (2004), Evaluation of elastic modulus of materials by adhesive (no-slip) nano-indentation, *Proc.: Mathematical, Physical and Engineering Sciences*, Vol. 460(2042), pp. 507–514.
- BOSCHUNG, E., HEUBERGER, M., DIETLER, G. (1994), Energy dissipation during nanoscale indentation of polymers with an atomic force microscope, *Appl. Phys. Lett.*, Vol. 64(26), pp. 3566–3568.
- BUDÓ, A. (1969), *Theoretische Mechanik*, 5th edn., VEB Deutscher Verlag der Wissenschaften, Berlin.
- BULYCHEV, S. I., ALEKHIN, V. P., SHORSHOROV, M. Kh., TERNOVSKII, A. P., SHNYREV, G. D. (1975), Determining Young's modulus from the indenter penetration diagram, *Industrial Lab.*, Vol. 41, pp. 1409–1412.
- BULYCHEV, S. I., ALEKHIN, V. P., SHORSHOROV, M. Kh., TERNOVSKII, A. P.

- (1976), Mechanical properties of materials studied from kinetic diagrams of load versus depth of impression during microimpression, *Strength Mater.*, Vol. 8, pp. 1084–1089.
- BURNHAM, N. A., BAKER, S. P., POLLOCK, H. M. (2000), Model for mechanical properties nanoprobess, *J. Mater. Res.*, Vol. 15(9), pp. 2006–2014.
- CAPPELLA, B., DIETLER, G. (1999), Force–distance curves by atomic force microscopy, *Surf. Sci. Reports*, Vol. 34, pp. 1–104.
- CARPICK, R. W., OGLETTREE, D. F., SALMERON, M. (1999), A general equation for fitting contact area and friction vs. load measurements, *Colloid Interface Sci.*, Vol. 211, pp. 395–400.
- CHRISTENSEN, R. M. (1982), *Theory of viscoelasticity*, Academic Press Inc., London.
- CLEVELAND, J. P., MANNE, S., BOCEK, D., HANSMA, P. K. (1993), A nondestructive method for determining the spring constant of cantilevers for scanning force microscopy, *Rev. Sci. Instrum.*, Vol. 64, pp. 403–405.
- CLEVELAND, J. P., ANCYKOWSKI, B., SCHMID, A. E., ELINGS, V. B. (1998), Energy dissipation in tapping-mode atomic force microscopy, *Appl. Phys. Lett.*, Vol. 72, pp. 2613–2615.
- COLCHERO, J. (1993), *Reibungskraft-mikroskopie*. Thesis, University of Konstanz, Germany.
- COLTON, R. J., ENGEL, A., FROMMER, J. E., GAUB, H. E., GEWIRTH, A., GUCKENBERGER, R., HECKL, W. M., PARKINSON, B., RABE, J., (1998), *Procedures in Scanning Probe Microscopies*. Wiley & Sons Inc., New York.
- DE PABLO, P. J., COLCHERO, J., GÓMEZ-HERRERO, J., BARÓ, A. M. (1998), Jumping mode scanning force microscopy, *Appl. Phys. Lett.* Vol. 73, pp. 3300–3302.
- DE PABLO, P. J., SCHAAP, I. A. T., MACKINTOSH, F. C., SCHMIDT, C. F. (2003), Deformation and collapse of microtubules on the nanometer scale, *Phys. Rev. Lett.*, Vol. 91(9), pp. 098101-1–4.
- DERJAGUIN, B. V., MULLER, V. M., TOPOROV, Yu. P. (1975), Effect of contact deformations on the adhesion of particles, *J. Colloid Interface Sci.*, Vol. 53, pp. 314–325.
- DRECHSLER, D., KARBACH, A., FUCHS, H. (1998), Nanoindentation on polycarbonate/polymethyl methacrylate blends, *Applied Physics A*, Vol. 66, pp. S825–S829.
- DUGDALE, D. S. (1960), *J. Mech. Phys. Solids*, Vol. 8, pp. 100–104.
- FERRY, J. D. (1980), *Viscoelastic Properties of Polymers*, Wiley, New York.
- FRANCO JR., A. R., PINTAÚDE, G., SINATORA, A., PINEDO, C. E. (2004), The use of a Vickers indenter in depth sensing indentation for measuring elastic modulus and Vickers hardness, *Mater. Res.*, Vol. 7(3), pp. 483–491.
- HANSMA, P. K., TERSOFF, J. (1987), Scanning tunneling microscopy, *J. Appl. Phys.*, Vol. 61, pp. R1–R23.
- HERTZ, H. (1882), Über die Berührung fester elastischer Körper, *J. Reine Angew. Mathematik*, Vol. 92, pp. 156–171.
- HINZ, M., KLEINER, A., HILD, S., MARTI, O., DÜRIG, U., GOTSMANN, B., DRECHSLER, U., ALBRECHT, T. R., VETTIGER, P. (2004), Temperature dependent nano indentation of thin polymer films with the scanning force microscope, *Europ. Polym. J.*, Vol. 40(5), pp. 957–964.
- HOPP, B., KRESZ, N., KOKAVECZ, J., SMAUSZ, T., SCHIEFERDECKER, H., DORING, A., MARTI, O., BOR, Z. (2004a), Adhesive and morphological characteristics of surface chemically modified polytetrafluoroethylene films, *Applied Surf. Sci.*, Vol. 221(1–4), pp. 437–443.
- HOPP, B., SMAUSZ, T., KOKAVECZ, J., KRESZ, N., BOR, Z., HILD, S., MARTI, O. (2004b), Investigation of incubation in ArF excimer laser irradiated poly(methyl-methacrylate) using pulsed force mode atomic force microscopy, *Appl. Phys.*, Vol. 96(10), pp. 5548–5551.
- HUTTER, J. L., BECHHOEFER, J. (1993a), Calibration of atomic-force microscope tips, *Rev. Sci. Instrum.*, Vol. 64(7), pp. 1868–1873.
- HUTTER, J. L., BECHHOEFER, J. (1993b), Erratum: Calibration of atomic-force microscope tips [Rev. Sci. Instrum., Vol. 64(7), p. 1868, 1993], *Rev. Sci. Instrum.*, Vol. 64(11), p. 3342.
- JOHNSON, K. L. (1996), *Contact Mechanics*, Cambridge University Press.
- JOHNSON, K. L., KENDALL, K., ROBERTS, A. D. (1971), Surface energy and the contact of elastic solids, *Proc. R. Soc. Lond. A*, Vol. 324, pp. 301–313.
- JOHNSON, K. L., GREENWOOD, J. A. (1997), An adhesion map for the contact of elastic

- spheres, *J. Colloid Interface Sci.*, Vol. 192, pp. 326–333.
- KING, R. B. (1987), Elastic analysis of some punch problems for a layered medium, *Int. J. Solids Structures*, Vol. 23(12), pp. 1657–1664.
- KRESZ, N., KOKAVECZ, J., SMAUSZ, T., HOPP, B., CSETE, M., HILD, S., MARTI, O. (2004), Investigation of pulsed laser deposited crystalline PTFE thin layer with pulsed force mode AFM, *Thin Solid Films*, Vol. 453–454, pp. 239–244.
- KROTTIL, H.-U. (2000d), CODYMode Scanning Force Microscopy: The Concurrent Measurement of Adhesion, Friction and Viscoelasticity, Shaker Verlag, Aachen.
- KROTTIL, H.-U., STIFTER, T., MARTI, O. (2000a), Verfahren und Vorrichtung zur gleichzeitigen Bestimmung der Adhäsion, der Reibung und weiterer Materialeigenschaften einer Probenoberfläche, Patent No. DE: PCT/DE00/00003, Europa 2000.
- KROTTIL, H.-U., STIFTER, T., MARTI, O. (2000b), Concurrent measurement of adhesive and elastic surface properties with a new modulation technique for scanning force microscopy, *Rev. Sci. Instrum.*, Vol. 71, pp. 2765–2771.
- KROTTIL, H.-U., STIFTER, T., MARTI, O. (2000c), Combined dynamic adhesion and friction measurement with the scanning force microscope, *Appl. Phys. Lett.*, Vol. 77, pp. 3857–3859.
- LANGARANI, H. M., NIKRAVESH, P. E. (1994), Continuous contact force models for impact in multibody systems, *Nonlinear Dynamics*, Vol. 5, pp. 193–207.
- LUGINBÜHL, R., GARRISON, M. D., CHRISTOS, J., OVERNEY, R. M., WEISS, L., SCHIEFER-DECKER, H., HILD, S. (2001), Chemical and Contact Mechanical Characterization of Thin Plasma Deposited Hexafluoropropylene Films, *ACS Symposium 787 Fluorinated Surfaces, Coatings and Films*.
- LUNA, M., COLCHERO, J., BARÓ, A. M. (1988), Intermittent contact scanning force microscopy: The role of the liquid necks, *Appl. Phys. Lett.*, Vol. 72(26), pp. 3461–3463.
- MARTI, O., GOULD, S., HANSMA, P. K. (1988), Atomic resolution atomic force microscopy of graphite and the “native oxide” on silicon, *J. Vac. Sci. Technol. A*, Vol. 6, pp. 287–290.
- MARTI, O., COLCHERO, J., MLYNEK, J. (1990), Combined scanning force and friction microscopy of mica, *Nanotechnology*, Vol. 1, pp. 141–144.
- MARTIN, Y., ABRAHAM, D. W., WICKRAMASINGHE, H. K. (1988), High-resolution capacitance measurement and potentiometry by force microscopy, *Appl. Phys. Lett.*, Vol. 52, pp. 1103–1105.
- MAUGIS, D. (1992), Adhesion of spheres: The JKR–DMT transition using a Dugdale model, *J. Colloid Interface Sci.*, Vol. 150, pp. 243–2469.
- MAUGIS, D. (2000), Contact, Adhesion, and Rupture of Elastic Solids, Springer, Berlin.
- MEYER, G., AMER, N. M. (1988a), Novel optical approach to atomic force microscopy, *Appl. Phys. Lett.*, Vol. 53, pp. 1045–1047.
- MEYER, G., AMER, N. M. (1988b), Erratum: Novel optical approach to atomic force microscopy [*Appl. Phys. Lett.*, Vol. 53, p. 1045, 1988], *Appl. Phys. Lett.*, Vol. 53, pp. 2400–2402.
- MEYER, G., AMER, N. M. (1990), Simultaneous measurement of lateral and normal forces with an optical-beam-deflection atomic force microscope, *Appl. Phys. Lett.*, Vol. 57, pp. 2089–2091.
- MIYATANI, T., HORII, M., ROSA, A., FUJIIHIRA, M., MARTI, O. (1997), Mapping of electrical double-layer force between tip and sample surfaces in water by pulsed-force-mode atomic force microscopy, *Appl. Phys. Lett.*, Vol. 71(18), pp. 2632–2634.
- MIYATANI, T., OKAMOTO, S., ROSA, A., MARTI, O., FUJIIHIRA, M. (1998), Surface charge mapping of solid surfaces in water by pulsed-force-mode atomic force microscopy, *Appl. Phys. A*, Vol. 66, pp. 349–352.
- MIZES, H. A., LOH, K.-G., MILLER, R. J. D., AHUJA, S. K., GRABOWSKI, E. F. (1991), Submicron probe of polymer adhesion with atomic force microscopy: dependence on topography and material inhomogeneities, *Appl. Phys. Lett.*, Vol. 59, pp. 2901–2903.
- MORENO-HERRERO, F., DE PABLO, P. J., COLCHERO, J., GÓMEZ HERRERO, J., BARÓ, A. (2000), The role of shear forces in scanning force microscopy: a comparison between the jumping mode and tapping mode, *Surf. Sci.*, Vol. 453, pp. 152–158.
- MORENO-HERRERO, F., COLCHERO, J., BARÓ, A. M. (2003), DNA height in scanning force microscopy, *Ultramicroscopy*, Vol. 96(2), pp. 167–174.
- MORENO-HERRERO, F., COLCHERO, J., GÓMEZ HERRERO, J., BARÓ, A. M. (2004), Atomic

- force microscopy contact, tapping, and jumping modes for imaging biological samples in liquids, *Phys. Rev. E*, Vol. 69(3), pp. 031915-1-9.
- MULLER, V. M., YUSHENKO, V. S., DERJAGUIN, B. V. (1980), On the influence of molecular forces on the deformation of an elastic sphere and its sticking to a rigid plane, *J. Colloid Interface Sci.*, Vol. 77, pp. 91-101.
- OLIVER, W. C., PHARR, G. M. (1992), A new improved technique for determining hardness and elastic modulus using load and displacement sensing indentation experiments, *Mater. Res.*, Vol. 7(6), pp. 1564-1582.
- PHARR, G. M., OLIVER, W. C., BROTZEN, F. R. (1992), On the generality of the relationship among contact stiffness, contact area, and elastic modulus during indentation, *Mater. Res.*, Vol. 7(3), pp. 613-617.
- PROKHORENKO, P., RUDNITSKY, V., KREN, A. (2004), Impact indentation testing of rubbers and plastics, *Review of Quantitative Nondestructive Evaluation*, Vol. 23, pp. 1135-1139.
- ROSA-ZEISER, A., WEILANDT, E., HILD, S., MARTI, O. (1997), The simultaneous measurement of elastic, electrostatic and adhesive properties by scanning force microscopy: pulsed-force mode operation, *Meas. Sci. Technol.*, Vol. 8, pp. 1333-1338.
- ROSA-ZEISER, A. (1997), *Der Pulsed Force Mode als kraftmikroskopische Untersuchungsmethode für unterschiedlich gefüllten Naturkautschuk bei linearer Deformation*, Shaker Verlag, Aachen. Thesis, University of Ulm, Germany.
- SARID, D. (1991), *Scanning Force Microscopy*, Oxford University Press, New York.
- SCHNEIDER, M., ZHU, M., PAPASTAVROU, G., AKARI, S., MÖHWALD, H. (2002), Chemical pulsed-force microscopy of single polyethyleneimine molecules in aqueous solution, *Langmuir*, Vol. 18(3), pp. 602-606.
- SHORSHOROV, M. Kh., BULYCHEV, S. I., ALEKLIN, V. P. (1981), Work of plastic and elastic deformation during indenter indentation, *Sov. Phys.-Doklady*, Vol. 26, pp. 769-770.
- SNEDDON, I. N. (1965), The relation between load and penetration in the axisymmetric Boussinesq problem for a punch of arbitrary profile, *Int. J. Eng. Sci.*, Vol. 3, pp. 47-57.
- SPIZIG, P. M. (2002), *Dynamische Rasterkraftmikroskopie*. Thesis, University of Ulm, Germany.
- STENERT, M., DÖRING, A., BANDERMANN, F. (2004), Poly(methyl methacrylate)-*block*-polystyrene and polystyrene-*block*-poly(*n*-butyl acrylate) as compatibilizers in PMMA/PnBA blends, *e-Polymers*, Vol. 15, pp. 1-16.
- STIFTER, T. (1996), *Kraftwechselwirkung im Rasterkraftmikroskop bei elektrochemischer Potentialkontrolle*. Thesis, University of Ulm, Germany.
- STIFTER, T., WEILANDT, E., MARTI, O., HILD, S. (1998), Influence of the topography on adhesion measured by SFM, *Appl. Phys. A*, Vol. 66, pp. 597-605.
- STIFTER, T., MARTI, O., BHUSHAN, B. (2000), Theoretical investigation of the distance dependence of capillary and van der Waals forces in SFM, *Phys. Rev. B*, Vol. 62(20), pp. 13 667-13 673.
- TABOR, D. (1977), Surface forces and surface interactions, *J. Colloid Interface Sci.*, Vol. 58, pp. 2-13.
- VANLANDINGHAM, M. R., DAGASTINE, R. R., EDULJEE, R. F., MCCULLOUGH, R. L., GILLESPIE, J. W. JR. (1999), Characterization of nanoscale property variations in polymer composite systems: Part 1 - Experimental results, *Composites Part A*, Vol. 30, pp. 75-83.
- VANLANDINGHAM, M. R., VILLARRUBIA, J. S., GUTHRIE, W. F., MEYERS, G. F. (2000), Nanoindentation of polymers: an overview, *Recent Advances in Scanning Probe Microscopy*, Proc. 220th American Chemical Society National Meeting, Vol. 44.
- VARENBERG, M., ETSION, I., HALPERIN, G. (2003), An improved wedge calibration method for lateral force in atomic force microscopy, *Rev. Sci. Instr.*, Vol. 74(7), pp. 3362-3367.
- WEILANDT, E. (1996), *Kräfte an Graphitoberflächen unter elektrochemischer Potentialkontrolle*. Thesis, University of Ulm, Germany.
- WERF, K. O., VAN DER PUTMAN, C. A. J., GROOTH, B. G., DE GREVE, J. (1994), Adhesion force imaging in air and liquid by adhesion mode atomic force microscopy, *Appl. Phys. Lett.*, Vol. 65, pp. 1195-1197.
- WINKLER, R. G., SPATZ, J. P., SHEIKO, S., MÖLLER, M., REINEKER, P., MARTI, O. (1996), Imaging material properties by resonant tapping-force microscopy: A model investigation, *Phys. Rev. B*, Vol. 54, pp. 8908-8912.

9 Force Spectroscopy

Phil Williams

9.1 Introduction

Measuring the strength of a molecular attachment with the atomic force microscope has been a growing pastime of researchers for the past ten years. Pioneering experiments published in 1994 by Lee et al. [1] and Moy et al. [2, 3] measuring the interaction between biotin, a small ligand (vitamin H), and a receptor (streptavidin) spawned a highly interesting field of research. Many other interactions were sooner or later measured, including interactions between complementary DNA oligonucleotides (1994) [4] and between antibodies and their antigens (1996) [5], intramolecular forces within polymers (1997) [6], and forces within folded proteins (1997) [7]. At first sight it seemed obvious that the force measured in these experiments was directly related to the affinity of the interaction (indeed, this is probably why the high-affinity streptavidin–biotin interaction, with a k_D of 10^{-15} M, was chosen as the model system). However, similarities in force with biotin analogues of different affinity indicated that this was not entirely true [2]. In an attempt to understand the molecular origins of the force, experiments were undertaken on site-directed mutants, and in 1995 Chilkoti et al. suggested that the strength of the interaction was generally related to the enthalpic activation barrier to ligand dissociation [8]. To probe the atomistic origins of the forces measured, molecular dynamics calculations were attempted and in 1996 Grubmuller et al. published the results of one such study of the streptavidin–biotin interaction [9]. This pioneering work has led to a valuable tool to study the dissociation of complexes and the unfolding of proteins under force. The year 1997 heralded a significant leap in the understanding of what the measured force actually meant with, Evans and Ritchie's publication of the theory of dynamic force spectroscopy (DFS) [10]. Until then several assumptions had been made as to what made an interaction “strong,” including the ideas that strength was related to affinity, and that the measured force was the mechanical energy gradient of the interaction potential. Blind to this (a lesson to a young researcher in reading the literature before submitting a manuscript!) we were studying the streptavidin–biotin interaction using the atomic force microscope (AFM) with different retract velocities of the cantilever. From our

own molecular dynamics simulations we knew that molecular motion was important and were attempting to measure the motion of the receptor by pulling the ligand out at different velocities. We believed that we should see a change in the force behavior with speed, and if we pulled quickly enough, could catch and measure friction due the streptavidin hindering the motion of the ligand. For some reason we had a logarithmic dependence of the measured force with the retract velocity. Our submission for publication of these naively driven experiments in 1998 coincided with that of the first dynamic force spectroscopy study by Evans [11]. The theory of DFS not only explained previously anomalous results and our velocity dependence [12], but also paved the way to new experiments, new simulation methodologies, and new insight to Nature's capacity to manipulate energy potentials and engineer molecular systems for a diversity of function. Here I will attempt to cover the basics of the force measurement experiment and the theory behind DFS, describe methods and the use of computer simulation, and review some studies of receptor–ligand interactions and protein unfolding. Little of this work is my own, and I am indebted to friends and colleagues for their pioneering studies and inspiration.

9.2 Basic Experiments

The basic force experiment is relatively simple. Two surfaces are functionalized with molecules that interact; a flat substrate and the probe. These are then brought into contact and withdrawn, and any adhesion is measured (Fig. 9.1). Providing that adequate controls have been used, this adhesion is attributed to the interaction between the molecules. This sounds simple. The “devil is in the detail,” however. Functionalization of the surfaces to present the molecules in their natural form is not trivial. Experiments with single molecules require meticulous sample preparation to inspire some confidence that what is measured is related to the molecule under study, and not a contaminant or artifact of the system. Ideally, surfaces should be characterized at each stage of their preparation, and we, for example, routinely deploy microscopy, SIMS, XPS, and FTIR [12–18]. The surfaces should also undergo passivation to remove “nonspecific” forces, i.e., those not due to the molecules of interest, and this is commonly achieved using albumin, short polymers, or hydrophilically terminated alkanes. A successful study of a molecular system stems from studying single interactions. The functional molecules have to be diluted across the surfaces to restrict the formation of multiple interactions on contact. A particular problem with the AFM is how to touch the surfaces lightly together; this is necessary to further restrict the formation of multiple interactions and inhibit sample deformation and degradation, as it is difficult to achieve contact forces of less than 100 pN. There are several instrumental problems that have to be overcome, the most pressing being the accurate calibration of the spring constant of the AFM cantilever. Finally, as discussed below, the single-molecule interactions are driven by random thermal fluctuations, and behave differently each time they

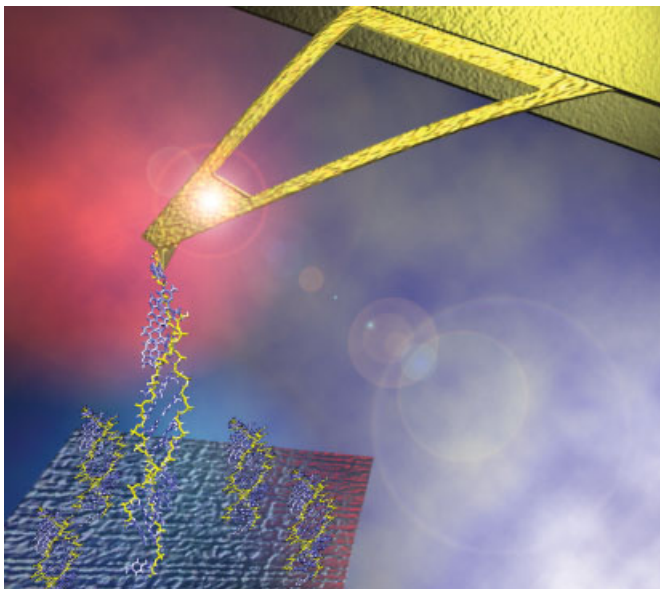


Fig. 9.1 Schematic representation of an AFM “pulling” DNA.

are measured. Thus, one has to measure the interaction many times, requiring many samples, tips, strong coffees, and days of experimentation.

9.3 Theory

It is important to consider the physics of the molecular interaction in order to understand the force experiment. Many researchers, me included, began by thinking that the AFM measures the strength of the interaction by pulling on the molecule and seeing how much force is required to break the intermolecular bond. Indeed, one still reads about bond strength quoted in piconewtons, or hears questions as to what force a particular bond breaks. A better foundation from which to understand the measurements stems from a consideration of diffusion, ignoring (for the most part) classical mechanics, and convincing oneself that the AFM does not “pull” anything.

A molecular interaction is held together by the free-energy penalty on separation. Biochemists describe interactions in terms of affinity, related to the difference in free energy between the partners when bound together and when separated at infinite distance. Affinity describes an equilibrium state and tells nothing about the rate of bond formation and separation, only their ratio. An interaction that takes 1 s to form and 1 min to dissociate has the same affinity as one that takes 1 min

to form and 1 h to dissociate. It is possible, therefore, to have two ligands to the same receptor that exhibit the same affinity but have vastly different interaction times. If, for the above example, the receptor were part of a complex pathway that takes several seconds to effect, the more slowly unbinding ligand would instigate a response whereas the faster one would not, even though their affinities to the receptor were the same. A better description of the interaction is formed by consideration of the rates of association and dissociation, i.e., the kinetics.

Biology takes place in warm, salty water. The rate at which small objects move in such an environment was studied in the early 19th century by Brown. In the early 20th century accurate theories were propounded that described this Brownian motion (two independent researchers, Einstein and Smoluchowski, published papers on Brownian motion, both in 1905) showing that the motion was thermally driven diffusion. In the 1940s, Kramers showed that chemical reactions in such condensed systems are governed by the same diffusive processes. Molecular pairs associate and dissociate through diffusion. Kramers showed that the rate of thermally driven escape from a binding potential over an activation energy barrier E_{ts} can be written as Eq. (1), where ζ is the frictional coefficient of movement (viscous damping) and ω is the curvature (stiffness) of the potential at the (c) bound and (ts) transition state.

$$v_{off} = \left(\frac{(\omega_c \omega_{ts})^{1/2}}{2\pi\zeta} \right) \exp\left(-\frac{E_{ts}}{k_B T} \right) \quad (1)$$

An alternative view, described by Evans, is to replace the description of the landscape through the curvature terms by confinement and transition-state widths [10]. For instance, with a harmonic approximation for the local shape, the curvature of the bound state ω_c , measured in $k_B T \text{ nm}^{-2}$, can be represented by the width of the potential l_c at $1 k_B T$ above the minimum, as $(2/\omega_c)^{1/2}$. Equation (1) can be expressed as Eq. (2), where D is the diffusion coefficient (equal to $k_B T/\zeta$) and l_c and l_{ts} are the “widths” of the bound and unbonding transition state respectively.

$$v_{off} = \frac{D}{l_c l_{ts}} \exp\left(-\frac{E_{ts}}{k_B T} \right) \quad (2)$$

This representation is useful, as for molecular interactions limits can be placed on the magnitudes of these lengths. The diffusion constant can also be estimated (see Section 9.8).

Equation (2) describes the dissociation rate of the molecular complex. The rate is governed by the size of the free-energy barrier to dissociation and the temperature. (Temperature has several effects on the rate. Both the numerator and the denominator in the exponential change through entropic effects and heat capacity and the change in thermal energy $k_B T$; the prefactor changes too, as diffusion is also thermally driven.) Application of a force to the system places a bias on the energy land-

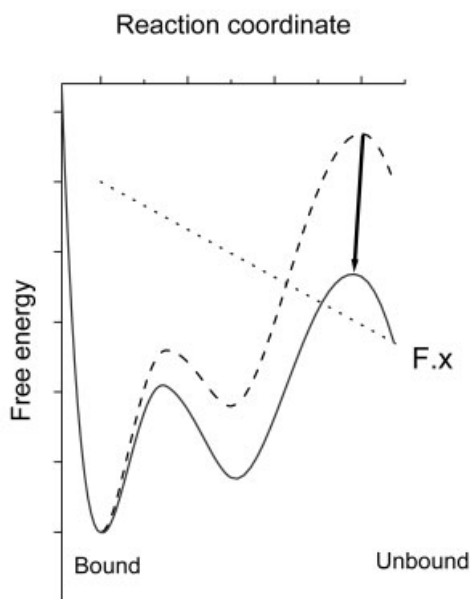


Fig. 9.2 The “energy landscape” of an interaction is the free energy (with one degree of freedom removed) of the system along a reaction coordinate. Force acting along the reaction coordinate has the effect of tilting the landscape in the direction in which force is applied. The magnitude of the activation

energy required to surmount the barrier is reduced, and the displacement of the transition state may move, depending on the shape of the potential. All energies are reduced under a persistent force F depending on the displacement from the bound state x .

scape in the direction in which force is applied. If the force is applied so that some component lies along the direction of the transition state, the magnitude of the free-energy barrier to dissociation is reduced by an amount equal to the product of the force applied and the projected displacement of the transition state along the direction of the force. A force of 4 pN applied to a transition state 1 nm away will lower the activation energy required for dissociation by $1 k_B T$ (since thermal energy is 4.11 pN nm), thereby increasing the dissociation rate almost three-fold. Force acts as a catalyst and causes an exponential increase in the rate of unbinding. As shown in Fig. 9.2, depending on the shape of the landscape, force can cause a slight shift in the position, as well as the height, of the transition state. For deep (height-to-width) harmonic wells the shift is small and the overwhelming effect on kinetics is the exponentiation through the reduction in activation energy required [10] (it is possible, in theory at least, to measure this small change in the transition-state location under force and to deduce a more detailed picture of the curvature of the energy landscape, but to date this has not been achieved).

The effect of a constant force on the system can be expressed as Eq. (3), where f is the force, x_{ts} is the displacement of the transition state from the bound state

along the direction of force, and $g(\cdot)$ describes the effect of force on x_{ts} , which from here we will ignore, and assume $g(\cdot)$ to be unity.

$$v_{\text{off}}(f) = g\left(\frac{fx_{\text{ts}}}{k_{\text{B}}T}\right) \left(\frac{D}{l_{\text{c}}l_{\text{ts}}}\right) \exp\left(-\frac{(E_{\text{ts}} - fx_{\text{ts}})}{k_{\text{B}}T}\right) \quad (3)$$

Force has the effect of increasing dissociation. As can be seen, the measurable exponential effect of force on the dissociation rate, termed the force scale $f_{\beta} = k_{\text{B}}T/x_{\text{ts}}$, is a measure of the transition-state displacement x_{ts} .

All we need to do is measure the lifetime of the interaction under different forces, then we find x_{ts} and can extrapolate a lifetime under no force. This sounds simple. However, there are a few things we have not yet considered. Firstly, dissociation is thermally driven and is a diffusion process. It is therefore stochastic and the dissociation rate above describes the decay of bound states in time. We need, therefore, to measure the dissociation times for many single interactions under these different forces. There is no single value of force at which a bond breaks. Secondly, to do the above experiment we have to apply a known force to the system and measure the lifetime of the bond. Under very low forces the bond may last for many hours. Under high forces the bond may break within a few microseconds. Thus we need force stability and temporal resolution (and researcher patience!) across many orders of time, which are all difficult to achieve. Thirdly, the force should be applied instantaneously and for high forces this is again difficult to achieve. Whilst such “constant force” experiments are now being undertaken [19, 20] the usual method of measurement is to apply a ramp of force.

9.4 The Ramp-of-Force Experiment

The normal force experiment comprises bringing two functionalized surfaces together, compressing the surfaces to a fixed (and often with AFM, too high!) force, and then loading the bond by withdrawal of the AFM cantilever at a fixed velocity. The molecular bond formed on contact of the surfaces experiences a ramp of force. It is important here to consider briefly the timescales over which the force is ramped (the loading rate, r_{f}) and the bond breaks. We will consider a typical AFM cantilever of stiffness 100 pN nm^{-1} being retracted at $10\,000 \text{ nm s}^{-1}$ (AFM levers are usually softer than this – the molecular tethers are much softer than this – and such high speeds are troublesome through hydrodynamic effects). The loading rate is $1\,000\,000 \text{ pN s}^{-1}$. Thermal energy is 4 pN nm , and it takes $4 \text{ }\mu\text{s}$ to apply $1 k_{\text{B}}T$ of energy to a bond that is 1 nm in length. The molecular system is diffusing considerably faster than this (diffusion constant of a protein movement in a membrane is around $10^{-8} \text{ cm}^2 \text{ s}^{-1}$; with $l_{\text{c}}l_{\text{ts}}$ of the order 0.1 nm^2 the kinetic prefactor is of order 0.01 ns^{-1}). Thus, even in this extreme example of ultra-fast AFM loading, the force can be considered static on the timescale of the bond even though it is

ramped experimentally. The ramp-of-force experiment can be considered a collection of many experiments over a continuous range of constant force.

Since dissociation is stochastic, we must consider an ensemble or population of bonds. For a simple two-state system (bonded or not) the population of bonded states can be followed in time through a simple rate equation [Eq. (4)].

$$\frac{dS}{dt} = -v_{\text{off}}(t)S(t) + v_{\text{on}}(t)[1 - S(t)] \quad (4)$$

Here $S(t)$ is the population of bonded states at time t , $v_{\text{off}}(t)$ is the rate of unbonding at this time and $v_{\text{on}}(t)$ is the rate of bonding. With a ramp of force we can interconvert between time and force, so the rate equation can be expressed as Eq. (5), where $r_f = df/dt$ is the loading rate.

$$\frac{dS}{df} = \frac{1}{r_f} \{-v_{\text{off}}(f)S(f) + v_{\text{on}}(f)[1 - S(f)]\} \quad (5)$$

For the same reason that force can cause an exponential increase in dissociation, it also causes a concomitant exponential decrease in the rate of association. Therefore, for simplicity, we can safely ignore rebonding. Certainly for experiments with systems immobilized with soft tethers at the point of unbonding the free-energy minimum is so far from the bound state that rebonding can never occur [21]. The simple rate equation can be integrated to reveal the probability of remaining bonded for a ramp of force, as in Eq. (6).

$$S(f) = \exp\left(-\int_0^f (v_{\text{off}}(g)/r_f) dg\right) \quad (6)$$

In the experiment, the probability that an unbonding event will be measured at a given force is the product of the unbonding probability at the force [Eq. (2)] and the probability that the system remains bonded up to this force [Eq. (6)]. This product [Eq. (7)] describes the force distribution, the probability of measuring a rupture force.

$$p(f) = \left(\frac{1}{r_f} v_{\text{off}} \exp\left(\frac{f}{f_\beta}\right)\right) \exp\left(\frac{1}{r_f} \left(f_\beta v_{\text{off}} - f_\beta v_{\text{off}} \exp\left(\frac{f}{f_\beta}\right)\right)\right) \quad (7)$$

To emphasize, this is a distribution. There is no single value of force at which a molecular complex will break. Sometimes a bond can withstand a high force. Sometimes the same bond will break before any measurable force has been applied. As an example, Fig. 9.3 shows the results of measuring the force at which a strand of double helical RNA dissociates when stressed by the AFM [40] at a loading rate of $r_f = 10\,000$ pN s⁻¹. In the hundred or so tests of bond strength, a different rupture force was obtained each time, ranging from 20 pN to over 80 pN. The histogram of these forces, using a 10 pN bin, is shown (left).

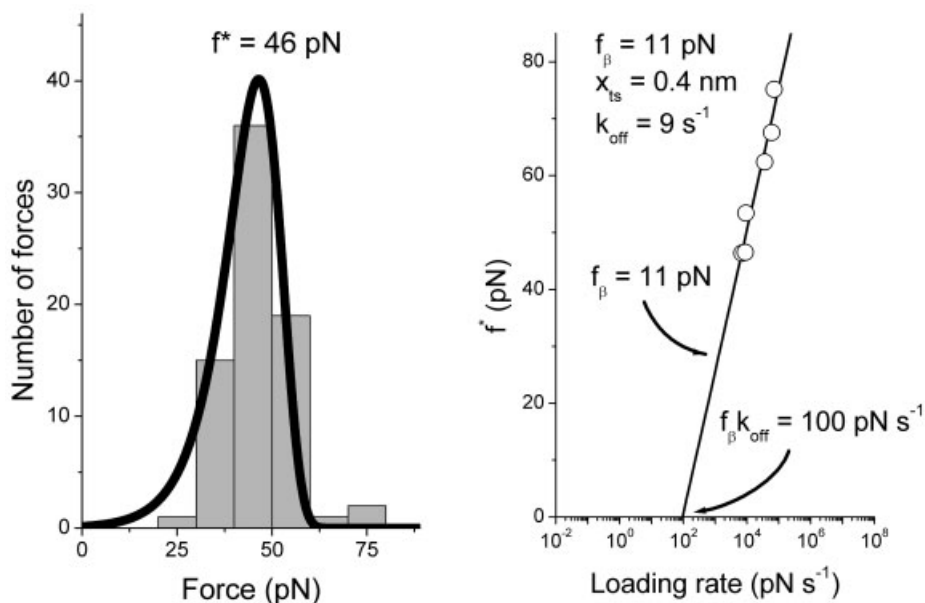


Fig. 9.3 Measurements and dynamic force spectrum for the dissociation of a strand of double helical RNA. Left: over 100 forces were measured at a loading rate of $10\,000\text{ pN s}^{-1}$. The distribution of measured forces, here binned in 10 pN groups, has a mode at 46 pN . Right: plotting f^* against the loading rate used is the dynamic force spectrum. For this simple system, a single linear region is observed with a force scale (slope) of 11 pN .

This single slope indicates a barrier at $k_B T/f_\beta = 0.4\text{ nm}$. The intercept of $f_\beta k_{\text{off}} = 100\text{ pN s}^{-1}$ reveals the transition rate over this barrier of 9 s^{-1} . Using these values of f_β and k_{off} , the full force distribution can be predicted. This is overlaid as the solid line on the measured forces histogram. A deviation between the force distributions measured and predicted warrants further investigation.

All of the kinetics is contained within this distribution. For systems with large energy barriers and hence slow dissociation rates, large forces, on average, are required. The position of the distribution relates to the dissociation rate. For systems with large barrier displacements (low force scales) the kinetics are more influenced by force, with the probability of rupture increasing rapidly and the probability of survival decreasing rapidly with force. The shape of the distribution reflects the force scale (see Appendix). However, experimental error will also influence the distribution. The system can be described by the most probable rupture force f^* (where $p(f)$ is a maximum) as a function of loading rate. In the example shown in Fig. 9.3, f^* is 46 pN .

The position of this maximum in $p(f)$ can be found by differentiation. For this simple case, where r_f is a constant, we get Eq. (8).

$$f^* = f_\beta [\ln(r_f) - \ln(f_\beta v_o)] \quad (8)$$

This equation describes the essential features of dynamic force spectroscopy. The force (related to the time) at which a system ruptures is measured under a variety of loading rates (related to the force at rupture) and from this both the force scale (and hence x_{ts}) (in the example $f_{\beta} = 11$ pN, $x_{ts} = 0.4$ nm) and extrapolated dissociation rate (above $f_{\beta}k_{off} = 100$ pN s⁻¹; therefore $k_{off} = 9$ s⁻¹) are measured. Of course it is only valid for a constant- r_f , no-rebonding, two-state system and where the rate at which the transition energy is lowered by force ($x_{ts}r_f/k_B T$) is very much less than the prefactor ($D/k_c l_{ts}$). This very-simple expression [8], derived with the few assumptions, describes and matches well many experimental measurements, as indicated in Fig. 9.3. It is only when the loading becomes nonlinear, as is the case with many AFM measurements, that more complicated analyses are necessary.

9.5

Multiple Transition States

The simple analysis above described the unbonding of a two-state system, where a single transition state dominates kinetics. Of course, the complex intermolecular bonding of large macromolecular system can lead to the creation of complex energy landscapes with multiple transition states and corresponding intermediate energy minima. In force measurements, where energy barriers are suppressed by an amount proportional to their displacement along the projection of force, outer and originally larger distal barriers can soon be suppressed below smaller inner barriers, which for higher forces become dominant. Where multiple transition states exist, multiple kinetics display as a staircase of unbonding exponentials.

9.6

Multiple Bonds

Multiple bonds can often be treated as a single “compound bond” of multiple transition states [22]. The landscape formed by these transition states depends on the bond cooperativity and architecture. The simplest case is when the multiple bonds form a complex that ruptures cooperatively. Here, cooperativity is defined in terms of time: a correlation in the order at which the component bonds fail.

An example of multiple bonds forming a system that fails cooperatively under force is that of short oligonucleotide double helices [14]. For double strands up to 30 base-pairs in length, the duplex behaves as a single bond in which all break instantaneously under axial (5' to 5') loading. When axially loaded, there is a gain in length on breakage of each base-pair, and as the system behaves cooperatively, with all bonds breaking together, there is one transition state. The distance to this transition state and its magnitude are related to the number of base-pairs in the duplex. This was very elegantly demonstrated by Strunz et al. [23], who showed that

increasing duplex length caused a decrease in the force scale (linear increase in x_{ts}) and an exponential decrease in the force-free dissociation rate k_{off} .

Unambiguous examples of cooperative failure of bonds loaded in parallel, where the force is shared over the connections but again the bonds fail together, are more difficult to find. In the case of parallel loading, each bond will contribute to the magnitude of the transition-state energy, causing an exponential decrease in the dissociation rate, but the distance to the transition state, and hence the force scale, remain that of the single bond. Noncooperative failure of bonds loaded in series and parallel has been demonstrated, though. In serial loading, each bond in the chain experiences the same force, as was the case for the cooperative duplex above, but here each bond behaves independently. So, for N bonds in series, there are N points of failure. The effect of having multiple bonds in series is therefore to increase the failure rate (k_{off}) of the system. For instance, we showed that the dynamic force spectrum of two iminobiotin–streptavidin bonds loaded in series was shifted in k_{off} by a factor of 2 compared with one bond [24].

Series loading is also present in the protein unfolding experiments where tandem repeats of the protein under investigation are stressed. When pulling on a chain of 12 proteins, for instance, one is 12 times more likely to measure an unfolding event than when stressing just one. This makes a full and proper analysis of these data a lengthy procedure, since each event has to be considered separately. One has to know how many domains are in the chain that is being stressed between the tip and the surface for each test, and this is often far from obvious from the data.

Instances of bonds loaded in parallel are more difficult to find as one can never be certain that the nanoscale contact permits equal sharing of the force, but systems showing the behavior of parallel-loaded bonds have been seen. For example, recently we have revisited the force-induced melting of RNA duplexes using a biomembrane force probe, and we obtained data that could be explained by loading of two strands at once. Also, experiments on antibody systems with multiple-epitopes show behavior that can be explained similarly, although in all cases it is problematic to differentiate between these data and those from many randomly loaded connections.

9.7 Distributions

Since unbonding is a stochastic process, the event must be measured many times to produce an accurate picture of the dissociation kinetics. It is insufficient to measure the average force at unbonding since the average of Eq. (7) is undetermined (for a two-state system the average force at rupture is approximately 0.6 times the force scale higher than the modal force [22]). Measuring the average force $\langle f \rangle$ and modal force f^* at a fixed rate r_f gives a further indication of the force scale according to Eq. (9)

$$f_{\beta} \approx \frac{f^* - \langle f \rangle}{\gamma_E} \quad (9)$$

and the force-free bond lifetime as in Eq. (10), where γ_E is Euler's constant, 0.5772 ...

$$\frac{1}{k_{\text{off}}} \approx \left(\frac{f^* - \langle f \rangle}{\gamma_E r_f} \right) \exp \left(\frac{f^* \gamma_E}{f^* - \langle f \rangle} \right) \quad (10)$$

Instrumental noise, measuring of the occasional multiple interaction, and so on, can all affect the mean value of the distribution. Equation (8), on which dynamic force spectroscopy is based, describes the behavior of the modal force and not the mean, and this modal value must be found from the experimental data. Whilst binning and producing a histogram is often used (as in Fig. 9.3), the method suffers from problems with sampling, a finite bin size, and hence force resolution. A useful method that is now being employed is to reconstruct the probability distribution by assuming each measurement made has been drawn from a Gaussian distribution, the width of which is related to the force resolution and noise of the instrument. These Gaussians, one for each force measurement, are summed and the peak of its total distribution is found as the mode. We use this method to find the mode only, as this reconstructed distribution hides the statistics by giving no indication of the number of data points measured. A standard histogram is constructed, using bin sizes equal to the Gaussian width chosen and offset so that the largest bin surrounds the modal value. This method of analysis is also useful in determining the error in the data, and a Bootstrap Monte Carlo method is used to determine the error in the modal value. It should be remembered that the error in the modal force is not the width of the distribution of forces measured, or their standard deviation. Unbonding is probabilistic. The spread in force is related to the thermal force scale f_{β} (see below). The error in the data indicates how well the most probable unbonding force can be determined, and is similar to the standard error of the mean [23]. Finally, having extracted the force scale(s) and off rate(s) from the dynamic force spectrum, the match between the predicted force distributions [Eq. (7)] and the measured histogram produced above is an important and vital check on the data (see, for example, Patel et al. [24] and Fig. 9.3).

9.8 Simulations

Being capable of revealing the presence and location of multiple transition states along a reaction coordinate, dynamic force spectroscopy provides a unique insight into the energetics of an interaction. Molecular simulation is a useful adjunct to provide atomistic insight.

Molecular dynamics (MD) is an obvious method by which to simulate the force experiment. MD is a process in which Newton's equations of motion for atoms

under empirical forces are solved in time. The forces are calculated as a sum of terms (the force field) derived to represent covalent bonding, valency, steric interactions, and coulombic terms. Additional terms can be added, for instance terms based on molecular surface area to represent implicit solvent, giving rise to a number of force fields, each with their pros and cons. The greatest limitation of MD is the difficulty in integrating the equations of motion. To maintain stability, the time step over which the motions can be followed has to be considerably shorter than the highest vibrational period in the system. Therefore, integration time steps of 1 or 2 fs have to be used. Since the kinetic prefactor, the timescale over which thermally driven events commence, can be of the order of $1 \mu\text{s}^{-1}$, accurate simulations of the experiment are problematic. Even if multiple microsecond simulations could be performed routinely – and with the ever-increasing power of computer hardware this is becoming a reality – the empirical force fields and simulation methods have not been parameterized or characterized over such extended times.

The pioneering study of Grubmuller and coworkers, published in 1996, involved the MD simulation of the removal of biotin from streptavidin [9]. For the loading rates used in the simulations a range of unbonding forces were found that scaled linearly with the retract velocity. Here, however, forces were measured as the maximum mechanical force experienced on the ligand, related to the maximum slope of the energy potential. As we have seen, the experiment does not measure this force (again, nothing is “pulled”, as such) but it does measure the time taken for the ligand to jump over the transition state. As highlighted by Evans, force-scaling linearly with speed suggests that such MD simulations can be used to measure the friction coefficient [10]. In the case of the biotin–streptavidin simulations a value of $\zeta \approx 2 \times 10^{-8} \text{ pN s nm}^{-1}$ was found, indicating a diffusion constant of $\zeta/k_{\text{B}}T = 2 \times 10^8 \text{ nm}^2 \text{ s}^{-1}$. The nanometer-sized bonding pocket with $l_{\text{c}}l_{\text{ts}}$ of the order of 0.1 nm^2 suggests a kinetic prefactor of order 1 ns^{-1} . Thus, for this interaction, many nanoseconds of simulated time are required to remain within the thermally active regime. Our recent MD calculations (A.B. Patel, PhD Thesis, University of Nottingham) reveal this slow, multiple nanosecond period of fluctuation in the biotin position (Fig. 9.4).

Whilst it is extremely difficult to perform accurate simulations within the thermal regime of the experiment, such simulations offer insight into the dissociation process. Certainly for systems like the streptavidin–biotin interaction, there is really only one path across which the biotin can traverse to dissociate. In the experiment, the biotin diffuses along this path; in the simulation it is pulled, but along the same path. Presumably the interactions that the ligand breaks and makes on its travels will be similar to both experiment and simulation. The variation in number and strength of the interaction seen in the simulations of different ligands or receptors can be used, therefore, to predict an ordering of the forces measured experimentally. For example, crude simulations predicted an ordering and relative ratio of interaction energies for biotin, desthiobiotin and iminobiotin unbonding from streptavidin of 1:0.7:0.5 respectively, which was in qualitative agreement with the forces measured [25]. In the situations where there is considerable confor-

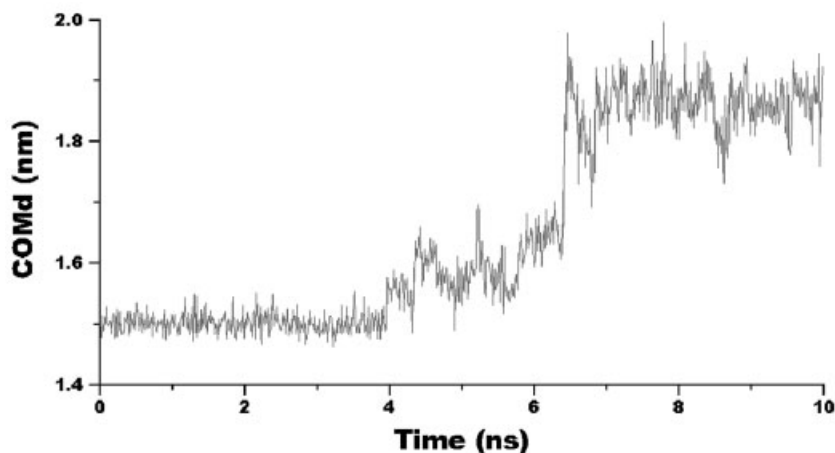


Fig. 9.4 Molecular dynamics simulations of a receptor/ligand complex reveal the timescale of diffusive processes in the nanosecond regime. Here, biotin is seen to hop along the bonding pocket in multi-nanosecond steps.

mational flexibility and multiple potential paths for dissociation, the simulations and experiments diverge and there is little reason to believe that the dissociation path seen will be similar. An example is that of the force-induced dissociation of small oligonucleotide double helices. DFS studies show cooperativity in melting (the time for strand dissociation scales exponentially with length, indicating that all base-pair interactions contribute to the dissociation energy barrier, and the displacement of the transition state increases linearly with strand length) that is not seen in simulations (my colleague, Charlie Laughton, and coworkers showed that the difficulty in sampling conformational space in such simulations, again related to the time available, is a severely limiting factor [26]).

MD simulations are been used more often to predict, interpret, and direct force-directed protein unfolding experiments. Inspired by Rief's unfolding studies of titin [7], Schulten and colleagues developed the method of steered molecular dynamics (SMD) to pull on the N- and C-termini of proteins [27]. There are two general methods for SMD, the constant-velocity (cv) and constant-force (cf) protocols. cvSMD applies a harmonic constraint to a specified atom, and fixes another in space. The constraint, akin to a spring such as an AFM lever, is moved away from the fixed atom at a constant velocity. Due to the limitations of simulation time, both high spring constants and high retract velocities are required to see an event in the time available. The first SMD studies of the unfolding of titin, for instance, used spring constants of 4 N m^{-1} and retract velocities of 50 and 100 m s^{-1} , giving loading rates of 2×10^{11} and $4 \times 10^{11} \text{ N s}^{-1}$. In contrast to the extreme experimental case above, where the loading rate of 10^6 pN s^{-1} drops the 1 nm barrier by $1 k_B T$ every $4 \mu\text{s}$, it takes just 20 ps for the lower of these two rates to reduce the bar-

rier by $1 k_B T$. As here $x_u r_f / k_B T > D / l_c l_{ts}$, the simulations are out of the thermally active regime and force is no longer static on the molecular timescale. However, despite these limitations, features were noted in the simulations, such as the formation of an unfolding intermediate with the detachment of a strand, that were later confirmed in experiments by Fernandez and colleagues [28]. The fact that there is some correlation between the experiment and simulation, at least in terms on the initial unfolding pathway under force, suggests that for this protein, which has a mechanical and structural role, Nature has evolved its energy landscape to focus a deeply channeled and solitary forced unfolding pathway. I doubt we will be so fortunate for proteins that have no mechanical role [29].

cfSMD is a similar method in which a constant force is applied to a specified atom and another fixed one. As the ramp-of-force experiment is essentially one of constant force (see above), this method is arguably closer to that experiment than cvSMD. In cfSMD studies, the time taken to traverse the landscape is recorded. Unfortunately, the time taken for something to occur is not known nor can it be predicted, so cfSMD simulations have to be run and refined without any certainty of how long they will take. With cvSMD simulations the time required to traverse a certain distance is known.

Having obtained a trajectory from a simulation, and convinced oneself that the pathway seen matches the experiment, one can use the energies extracted to predict the dynamic force behavior (with the proviso that calculated energies are inaccurate, since entropy is poorly determined). For example, the simulations of a 12-base-pair DNA helix mentioned above [26] suggested a free-energy barrier to strand melting of around $40 k_B T$ situated at 1.3 nm. Reasonable values for the prefactor suggest that $40 k_B T$ is a considerable overestimation (a fast 1 ns^{-1} prefactor gives the dodecamer's duplex lifetime of several years) but nevertheless this lifetime and force scale $f_\beta = 4.11/1.3 = 3.2 \text{ pN}$ can be used to predict a dynamic force spectrum using Eq. (8) (Fig. 9.5).

An alternative method for predicting the force spectrum from simulated data is to perform a Monte Carlo simulation using the energy landscape predicted from the MD (or other) calculation. For example, taking an energy landscape measured from an adiabatic mapping study of the dissociation of biotin from streptavidin [30], we were able to predict the dynamic force spectrum that would be seen for such a system [31]. Whilst this Monte Carlo method provided little that could not be obtained from the rate equations and expressions for force given above, it did confirm these expressions. Critically, linear regimes in the predicted DFS plot corresponded to the presence of energy barriers on the profile, and the width of the predicted force distributions remained constant across each barrier probed.

9.8.1

An Example: The Streptavidin–Biotin Interaction

The ligand–receptor interaction most widely studied by force spectroscopy is that of streptavidin and biotin. Using a biomembrane force probe, Merkel et al. revealed a dynamic force spectrum of the streptavidin/biotin interaction with two regimes

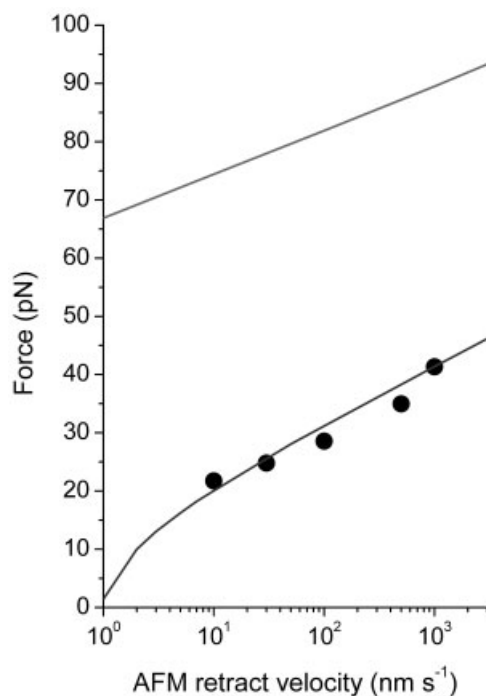


Fig. 9.5 The atomic force microscope has been used to study the dynamic force spectra of DNA duplex dissociation (force-induced melting). Strunz et al. measured the force spectrum for dissociation of a 10 mer (solid circles), which showed a force scale of 4 pN [23]. Molecular modeling studies of strand dissociation show good agreement in

transition-state location but are incapable of accurately measuring the energies upper line prediction of 12 mer dissociation using data from ref. 26). The lower line is the force spectrum fitted to the experimental data using a force scale indicated by the molecular modeling studies [23] (3.8 pN for a 10 mer) with a dissociation rate of 0.05 s^{-1} .

of force (Fig. 9.6, solid circles) [11]. The low-force regime to 85 pN, with a force scale of 8 pN, indicated a transition state 0.5 nm along the unbonding coordinate, and the high-force regime above 85 pN indicated a state at 0.12 nm ($f_{\beta} = 34 \text{ pN}$). Our 1998 AFM experiments also revealed this 0.12 nm state (Fig. 9.6, diamonds) [12], but at the time we were unable to achieve sufficiently low loading rates to measure forces below 85 pN and probe the second barrier. Recently, however, using soft AFM levers we have been able to measure the transition between these two regimes of force and reveal both transition states with the AFM (Fig. 9.6, triangles). The inability of the AFM compared with the biomembrane force probe (BFP) is, however, clearly evident in Fig. 9.5 (see also Williams et al. [32]). Other AFM studies have revealed this outer state; those shown in Fig. 9.6 as hexagons are the results of a study by Lo et al. [33].

Using all of the data presented in Fig. 9.5 we reveal a more detailed picture of the interaction. Two energy barriers are probed, located at 0.1 nm ($f_{\beta 1} = 44 \text{ pN}$)

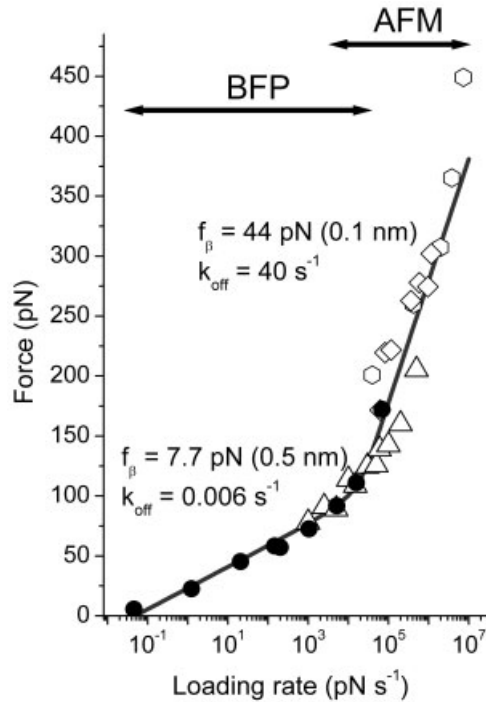


Fig. 9.6 Dynamic force spectra of the streptavidin–biotin interaction taken using the biomembrane force probe (solid circles) [11] and the atomic force microscope (diamonds [12], triangles and hexagons [33]). The limitation of the AFM to studying low force

and slow dissociation kinetics is clearly evident. In combination, the data reveal two transition states at 44 and 7.7 pN with transition rates of 40 and 0.006 s⁻¹, respectively.

and 0.5 nm ($f_{\beta 2} = 7.7$ pN). The rates of transition over these are $k_{\text{off}1} = 40$ s⁻¹ and $k_{\text{off}2} = 0.006$ s⁻¹ respectively. If we assume a constant prefactor for the kinetics over these two barriers, the ratio of unbonding rates provides an estimation of the difference in free energy of the two transition states, as $-\log(k_{\text{off}2}/k_{\text{off}1}) \sim 9 k_B T$ (~ 5 kcal mol⁻¹). The value of the prefactor is required to estimate the magnitude of the energy barriers relative to the bound state; assuming it to be 10⁹ s⁻¹ (as discussed above), the two rates equate to free-energy barrier heights of 17 and 26 $k_B T$ (10 and 15 kcal mol⁻¹). The lifetime of the biotin–streptavidin interaction is, on average, longer than 1/0.006 s, indicating that there must be at least one higher energy barrier more not probed in the force experiments. To not be seen suggests that this barrier is beyond 0.5 nm and suppressed by 6 pN of force (the lowest measured by the BFP) below that of the barrier at 0.5 nm. We can reasonably assume that there is not a barrier further away than the entrance to the bonding pocket, which is known to be around 1.3 nm in length. At 6 pN of force, the 0.5 nm barrier has been suppressed by $(6 \times 0.5/4.11 =)$ 0.7 $k_B T$ and the outer, hidden barrier by

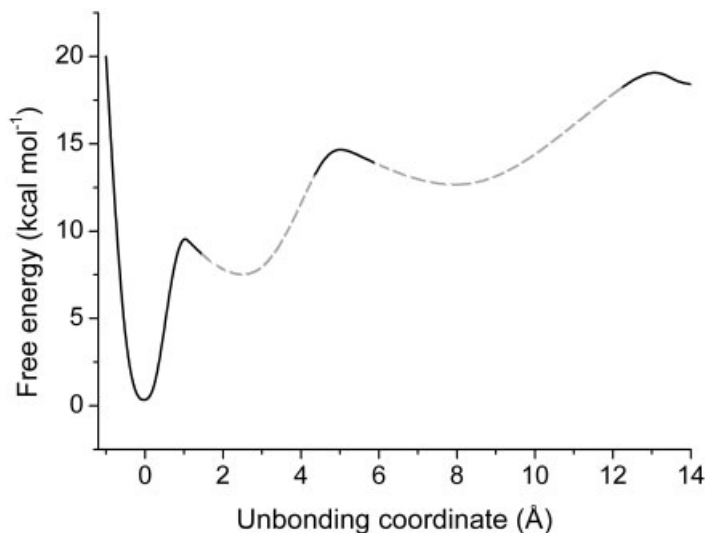


Fig. 9.7 The dynamic force spectrum showed in Fig. 9.5, in combination with solution kinetic data, reveal a picture of the dissociation energy landscape of the streptavidin–biotin system.

$1.9 k_B T$. To remain hidden in the force spectrum, therefore, the outer barrier cannot be more than $1.2 k_B T$ higher than that at 0.5 nm , which we have speculated is around $26 k_B T$. The free energy of unbonding of biotin to streptavidin is approximately $28 k_B T$, or $16.5 \text{ kcal mol}^{-1}$ (of course, this value depends on our assumption of the kinetic prefactor, and will change by only $1.4 \text{ kcal mol}^{-1}$ with change in the prefactor by an each order of magnitude). The bonding free energy has been measured as $-18.3 \text{ kcal mol}^{-1}$. Together, the data indicate that the prefactor is between 10^9 and 10^{10} s^{-1} , and that there is an interaction energy landscape that has little or no energy barrier to entry of the ligand (Fig. 9.7).

SMD simulations of the interaction reveal regions of hiatus in the movement of biotin out of the pocket, situated at 0.12 and 0.5 nm from the bound state. The match in experimental and simulated barrier locations permits some confident speculation as to the origins of the transition states; the breakage of certain hydrogen bonds, the formation of new ones, and the disruption of hydrophobic packing.

9.9 The Future

DFS is, I believe (although I'm biased), a remarkable experimental methodology capable of revealing hitherto hidden details of the energy landscape of molecular

interactions. There are many technological developments required to permit the wholesale study of systems in a biological context. Streptavidin–biotin was chosen as the model system due to the high mutual affinity of the constituents [1–3, 8, 9, 11, 12, 18, 24, 25, 30, 31, 34–36]. We have seen that this interaction has many transition states and energy barriers along the dissociation pathway. Unfortunately, these inner barriers hide more distal barriers, and stop the AFM from probing them. Even the BFP has been unable to probe the full unbonding landscape of this “model” system. DFS has been used to study many interesting ligand–receptor systems, including antibodies with their antigens [5, 15–17, 37, 38], substrates and cofactors bonding to enzymes [39], and force used to study the mechanical properties of biopolymers [4, 6, 14, 23, 40–52]. DFS has been particularly successful when applied to the study of biological systems that have a mechanical role; unfolding of structural proteins (e.g., titin [7, 27, 28, 32, 53–67], fibronectin [68–72]), motile-cell surface receptors (e.g., selectins [73, 74]), adhesion interactions (e.g., cadherins [75]), cellular cytoskeleton (e.g., spectrin [46]), and suchlike. Here, simulations have proved capable of, and invaluable for, interpreting the events of dissociation.

In the future, we will see new technologies and methodologies capable of measuring interactions that are under lower forces, and hence less perturbed. Some exciting developments are being made in the use of oscillating forces to probe fluctuations in structure and decouple conservative and dissipative energies of the interaction, and in active force control for constant force measurements. Major developments in simulation are required, and some are afoot. Whilst Moore’s law is providing an order-of-magnitude increase in simulation time every three or four years or so, significant developments in simulation strategy are enabling simulations to span microseconds of time on today’s computer clusters. The combination of hardware and software developments will produce bonding and unbonding trajectories over biological timescales in full atomistic detail.

References

- 1 LEE, G. U., KIDWELL, D. A., COLTON, R. J. Sensing discrete streptavidin biotin interactions with atomic-force microscopy. *Langmuir* 10, 354–357 (1994).
- 2 MOY, V. T., FLORIN, E. L., GAUB, H. E. Intermolecular forces and energies between ligands and receptors. *Science* 266, 257–259 (1994).
- 3 FLORIN, E. L., MOY, V. T., GAUB, H. E. Adhesion forces between individual ligand–receptor pairs. *Science* 264, 415–417 (1994).
- 4 LEE, G. U., CHRISSEY, L. A., COLTON, R. J. Direct measurement of the forces between complementary strands of DNA. *Science* 266, 771–773 (1994).
- 5 HINTERDORFER, P., BAUMGARTNER, W., GRUBER, H. J., SCHILCHER, K., SCHINDLER, H. Detection and localization of individual antibody–antigen recognition events by atomic force microscopy. *Proceedings of the National Academy of Sciences of the United States of America* 93, 3477–3481 (1996).
- 6 RIEF, M., OESTERHELT, F., HEYMANN, B., GAUB, H. E. Single molecule force spectroscopy on polysaccharides by atomic force microscopy. *Science* 275, 1295–1297 (1997).

- 7 RIEF, M., GAUTEL, M., OESTERHEIT, F., FERNANDEZ, J. M., GAUB, H. E. Reversible unfolding of individual titin immunoglobulin domains by AFM. *Science* 276, 1109–1112 (1997).
- 8 CHILKOTI, A., BOLAND, T., RATNER, B. D., STAYTON, P. S. The relationship between ligand-binding thermodynamics and protein–ligand interaction forces measured by atomic force microscopy. *Biophysical Journal* 69, 2125–2130 (1995).
- 9 GRUBMULLER, H., HEYMANN, B., TAVAN, P. Ligand binding: molecular mechanics calculation of the streptavidin biotin rupture force. *Science* 271, 997–999 (1996).
- 10 EVANS, E., RITCHIE, K. Dynamic strength of molecular adhesion bonds. *Biophysical Journal* 72, 1541–1555 (1997).
- 11 MERKEL, R., NASSOY, P., LEUNG, A., RITCHIE, K., EVANS, E. Energy landscapes of receptor–ligand bonds explored with dynamic force spectroscopy. *Nature* 397, 50–53 (1999).
- 12 WILLIAMS, P. M., MOORE, A., STEVENS, M. M., ALLEN, S., DAVIES, M. C., ROBERTS, C. J., TENDLER, S. J. B. On the dynamic behaviour of the forced dissociation of ligand–receptor pairs. *Journal of the Chemical Society – Perkin Transactions 2*, 5–8 (2000).
- 13 WILDE, L. M., ALLEN, S., DAVIES, M. C., TENDLER, S. J. B., WILLIAMS, P. M., ROBERTS, C. J. Bifunctional atomic force microscopy probes for molecular screening applications. *Analytica Chimica Acta* 479, 77–85 (2003).
- 14 POPE, L. H., DAVIES, M. C., LAUGHTON, C. A., ROBERTS, C. J., TENDLER, S. J. B., WILLIAMS, P. M. Force-induced melting of a short DNA double helix. *European Biophysics Journal with Biophysics Letters* 30, 53–62 (2001).
- 15 ALLEN, S., CHEN, X., DAVIES, J., DAVIES, M. C., DAWKES, A. C., EDWARDS, J. C., ROBERTS, C. J., TENDLER, S. J. B., WILLIAMS, P. M. The influence of epitope availability on atomic-force microscope studies of antigen–antibody interactions. *Biochemical Journal* 341, 173–178 (1999).
- 16 ALLEN, S., CHEN, X., DAVIES, J., DAVIES, M. C., DAWKES, A. C., EDWARDS, J. C., ROBERTS, C. J., TENDLER, S. J. B., WILLIAMS, P. M. The application of force microscopy to immunodiagnostic systems imaging and biomolecular adhesion measurements. *Applied Physics A – Materials Science & Processing* 66, S255–S261 (1998).
- 17 ALLEN, S., CHEN, X. Y., DAVIES, J., DAVIES, M. C., DAWKES, A. C., EDWARDS, J. C., ROBERTS, C. J., SEFTON, J., TENDLER, S. J. B., WILLIAMS, P. M. Detection of antigen–antibody binding events with the atomic force microscope. *Biochemistry* 36, 7457–7463 (1997).
- 18 ALLEN, S., DAVIES, J., DAWKES, A. C., DAVIES, M. C., EDWARDS, J. C., PARKER, M. C., ROBERTS, C. J., SEFTON, J., TENDLER, S. J. B., WILLIAMS, P. M. In situ observation of streptavidin–biotin binding on an immunoassay well surface using an atomic force microscope. *Febs Letters* 390, 161–164 (1996).
- 19 SCHLIERF, M., LI, H. B., FERNANDEZ, J. M. The unfolding kinetics of ubiquitin captured with single-molecule force–clamp techniques. *Proceedings of the National Academy of Sciences of the United States of America* 101, 7299–7304 (2004).
- 20 FERNANDEZ, J. M., LI, H. B. Force–clamp spectroscopy monitors the folding trajectory of a single protein. *Science* 303, 1674–1678 (2004).
- 21 EVANS, E., RITCHIE, K. Strength of a weak bond connecting flexible polymer chains. *Biophysical Journal* 76, 2439–2447 (1999).
- 22 WILLIAMS, P. M. Analytical descriptions of dynamic force spectroscopy: Behaviour of multiple connections. *Analytica Chimica Acta* 479, 107–115 (2003).
- 23 STRUNZ, T., OROSZLAN, K., SCHAFFER, R., GUNTHERODT, H. J. Dynamic force spectroscopy of single DNA molecules. *Proceedings of the National Academy of Sciences of the United States of America* 96, 11277–11282 (1999).
- 24 PATEL, A. B., ALLEN, S., DAVIES, M. C.,

- ROBERTS, C. J., TENDLER, S. J. B., WILLIAMS, P. M. Influence of architecture on the kinetic stability of molecular assemblies. *Journal of the American Chemical Society* 126, 1318–1319 (2004).
- 25 MOORE, A., WILLIAMS, P. M., DAVIES, M. C., JACKSON, D. E., ROBERTS, C. J., TENDLER, S. J. B. Analyzing the origins of receptor–ligand adhesion forces measured by the scanning force microscope. *Journal of the Chemical Society – Perkin Transactions 2*, 419–423 (1999).
- 26 HARRIS, S. A., SANDS, Z. A., LAUGHTON, C. A. Molecular dynamics simulations of duplex stretching reveal the importance of entropy in determining the biomechanical properties of DNA. *Biochemical Journal* 88, 1684–1691 (2005).
- 27 LU, H., ISRALEWITZ, B., KRAMMER, A., VOGEL, V., SCHULTEN, K. Unfolding of titin immunoglobulin domains by steered molecular dynamics simulation. *Biophysical Journal* 75, 662–671 (1998).
- 28 MARSZALEK, P. E., LU, H., LI, H. B., CARRION-VAZQUEZ, M., OBERHAUSER, A. F., SCHULTEN, K., FERNANDEZ, J. M. Mechanical unfolding intermediates in titin modules. *Nature* 402, 100–103 (1999).
- 29 BEST, R. B., LI, B., STEWARD, A., DAGGETT, V., CLARKE, J. Can non-mechanical proteins withstand force? Stretching barnase by atomic force microscopy and molecular dynamics simulation. *Biophysical Journal* 81, 2344–2356 (2001).
- 30 MOORE, A., WILLIAMS, P. M., DAVIES, M. C., JACKSON, D. E., ROBERTS, C. J., TENDLER, S. J. B. Enthalpic approach to the analysis of the scanning force ligand rupture experiment. *Journal of the Chemical Society – Perkin Transactions 2*, 253–258 (1998).
- 31 GALLIGAN, E., ROBERTS, C. J., DAVIES, M. C., TENDLER, S. J. B., WILLIAMS, P. M. Simulating the dynamic strength of molecular interactions. *Journal of Chemical Physics* 114, 3208–3214 (2001).
- 32 WILLIAMS, P. M., FOWLER, S. B., BEST, R. B., TOCA-HERRERA, J. L., SCOTT, K. A., STEWARD, A., CLARKE, J. Hidden complexity in the mechanical properties of titin. *Nature* 422, 446–449 (2003).
- 33 LO, Y. S., ZHU, Y. J., BEEBE, T. P. Loading-rate dependence of individual ligand–receptor forces studied by atomic force microscopy. *Langmuir* 17, 3741–3748 (2001).
- 34 STAYTON, P. S., FREITAG, S., KLUMB, L. A., CHILKOTI, A., CHU, V., PENZOTTI, J. E., TO, R., HYRE, D., LE TRONG, I., LYBRAND, T. P., STENKAMP, R. E. Streptavidin–biotin binding energetics. *Biomolecular Engineering* 16, 39–44 (1999).
- 35 IZRAILEV, S., STEPANIANTS, S., BALSERA, M., OONO, Y., SCHULTEN, K. Molecular dynamics study of unbinding of the avidin–biotin complex. *Biophysical Journal* 72, 1568–1581 (1997).
- 36 CHILKOTI, A., STAYTON, P. S. Molecular origins of the slow streptavidin–biotin dissociation kinetics. *Journal of the American Chemical Society* 117, 10 622–10 628 (1995).
- 37 RAAB, A., HAN, W. H., BADT, D., SMITH-GILL, S. J., LINDSAY, S. M., SCHINDLER, H., HINTERDORFER, P. Antibody recognition imaging by force microscopy. *Nature Biotechnology* 17, 902–905 (1999).
- 38 HEYMANN, B., GRUBMULLER, H. AN02/DNP–hapten unbinding forces studied by molecular dynamics atomic force microscopy simulations. *Chemical Physics Letters* 303, 1–9 (1999).
- 39 RIGBY-SINGLETON, S. M., ALLEN, S., DAVIES, M. C., ROBERTS, C. J., TENDLER, S. J. B., WILLIAMS, P. M. Direct measurement of drug–enzyme interactions by atomic force microscopy; dihydrofolate reductase and methotrexate. *Journal of the Chemical Society – Perkin Transactions 2*, 1722–1727 (2002).
- 40 GREEN, N. H., WILLIAMS, P. M., WAHAB, O., DAVIES, M. C., ROBERTS, C. J., TENDLER, S. J. B., ALLEN, S. Single-molecule investigations of RNA dissociation. *Biophysical Journal* 86, 3811–3821 (2004).

- 41 KRAUTBAUER, R., RIEF, M., GAUB, H. E. Unzipping DNA oligomers. *Nano Letters* 3, 493–496 (2003).
- 42 MARSZALEK, P. E., LI, H. B., OBERHAUSER, A. F., FERNANDEZ, J. M. Chair–boat transitions in single polysaccharide molecules observed with force–ramp AFM. *Proceedings of the National Academy of Sciences of the United States of America* 99, 4278–4283 (2002).
- 43 KRAUTBAUER, R., POPE, L. H., SCHRADER, T. E., ALLEN, S., GAUB, H. E. Discriminating small molecule DNA binding modes by single molecule force spectroscopy. *Febs Letters* 510, 154–158 (2002).
- 44 KRAUTBAUER, R., FISCHERLANDER, S., ALLEN, S., GAUB, H. E. Mechanical fingerprints of DNA drug complexes. *Single Molecules* 3, 97–103 (2002).
- 45 CLAUSEN-SCHAUMANN, H., RIEF, M., TOLKSDORF, C., GAUB, H. E. Mechanical stability of single DNA molecules. *Biophysical Journal* 78, 1997–2007 (2000).
- 46 RIEF, M., PASCUAL, J., SARASTE, M., GAUB, H. E. Single molecule force spectroscopy of spectrin repeats: low unfolding forces in helix bundles. *Journal of Molecular Biology* 286, 553–561 (1999).
- 47 RIEF, M., CLAUSEN-SCHAUMANN, H., GAUB, H. E. Sequence-dependent mechanics of single DNA molecules. *Nature Structural Biology* 6, 346–349 (1999).
- 48 LI, H. B., RIEF, M., OESTERHELT, F., GAUB, H. E., ZHANG, X., SHEN, J. C. Single-molecule force spectroscopy on polysaccharides by AFM – nanomechanical fingerprint of alpha-(1,4)-linked polysaccharides. *Chemical Physics Letters* 305, 197–201 (1999).
- 49 LI, H., RIEF, M., OESTERHELT, F., GAUB, H. E. Force spectroscopy on single xanthan molecules. *Applied Physics A – Materials Science, Processing* 68, 407–410 (1999).
- 50 HEYMAN, B., GRUBMULLER, H. “Chair–boat” transitions and side groups affect the stiffness of polysaccharides. *Chemical Physics Letters* 305, 202–208 (1999).
- 51 HEYMAN, B., GRUBMULLER, H. Elastic properties of poly(ethylene-glycol) studied by molecular dynamics stretching simulations. *Chemical Physics Letters* 307, 425–432 (1999).
- 52 LI, H. B., RIEF, M., OESTERHELT, F., GAUB, H. E. Single-molecule force spectroscopy on Xanthan by AFM. *Advanced Materials* 10, 316–319 (1998).
- 53 ROUNSEVELL, R. W. S., STEWARD, A., CLARKE, J. Biophysical investigations of engineered polyproteins: implications for force data. *Biophysical Journal* 88, 2022–2029 (2005).
- 54 LI, H. B., FERNANDEZ, J. M. Mechanical design of the first proximal Ig domain of human cardiac titin revealed by single molecule force spectroscopy. *Journal of Molecular Biology* 334, 75–86 (2003).
- 55 BEST, R. B., FOWLER, S. B., HERRERA, J. L. T., STEWARD, A., PACI, E., CLARKE, J. Mechanical unfolding of a titin Ig domain: structure of transition state revealed by combining atomic force microscopy, protein engineering and molecular dynamics simulations. *Journal of Molecular Biology* 330, 867–877 (2003).
- 56 BEST, R. B., BROCKWELL, D. J., TOCA-HERRERA, J. L., BLAKE, A. W., SMITH, D. A., RADFORD, S. E., CLARKE, J. Force mode atomic force microscopy as a tool for protein folding studies. *Analytica Chimica Acta* 479, 87–105 (2003).
- 57 LI, H. B., LINKE, W. A., OBERHAUSER, A. F., CARRION-VAZQUEZ, M., KERKVILLET, J. G., LU, H., MARSZALEK, P. E., FERNANDEZ, J. M. Reverse engineering of the giant muscle protein titin. *Nature* 418, 998–1002 (2002).
- 58 GAO, M., WILMANN, M., SCHULTEN, K. Steered molecular dynamics studies of titin I1 domain unfolding. *Biophysical Journal* 83, 3435–3445 (2002).
- 59 FOWLER, S. B., BEST, R. B., HERRERA, J. L. T., RUTHERFORD, T. J., STEWARD, A., PACI, E., KARPLUS, M., CLARKE, J. Mechanical unfolding of a titin Ig domain: structure of unfolding

- intermediate revealed by combining AFM, molecular dynamics simulations, NMR and protein engineering. *Journal of Molecular Biology* 322, 841–849 (2002).
- 60 BEST, R. B., FOWLER, S. B., TOCA-HERRERA, J. L., CLARKE, J. A simple method for probing the mechanical unfolding pathway of proteins in detail. *Proceedings of the National Academy of Sciences of the United States of America* 99, 12 143–12 148 (2002).
- 61 OBERHAUSER, A. F., HANSMA, P. K., CARRION-VAZQUEZ, M., FERNANDEZ, J. M. Stepwise unfolding of titin under force–clamp atomic force microscopy. *Proceedings of the National Academy of Sciences of the United States of America* 98, 468–472 (2001).
- 62 LU, H., SCHULTEN, K. The key event in force-induced unfolding of titin's immunoglobulin domains. *Biophysical Journal* 79, 51–65 (2000).
- 63 LI, H. B., OBERHAUSER, A. F., FOWLER, S. B., CLARKE, J., FERNANDEZ, J. M. Atomic force microscopy reveals the mechanical design of a modular protein. *Proceedings of the National Academy of Sciences of the United States of America* 97, 6527–6531 (2000).
- 64 LI, H. B., CARRION-VAZQUEZ, M., OBERHAUSER, A. F., MARSZALEK, P. E., FERNANDEZ, J. M. Point mutations alter the mechanical stability of immunoglobulin modules. *Nature Structural Biology* 7, 1117–1120 (2000).
- 65 OBERHAUSER, A. F., MARSZALEK, P. E., CARRION-VAZQUEZ, M., FERNANDEZ, J. M. Single protein misfolding events captured by atomic force microscopy. *Nature Structural Biology* 6, 1025–1028 (1999).
- 66 LU, H., SCHULTEN, K. Steered molecular dynamics simulations of force-induced protein domain unfolding. *Proteins–Structure Function and Genetics* 35, 453–463 (1999).
- 67 CARRION-VAZQUEZ, M., OBERHAUSER, A. F., FOWLER, S. B., MARSZALEK, P. E., BROEDEL, S. E., CLARKE, J., FERNANDEZ, J. M. Mechanical and chemical unfolding of a single protein: a comparison. *Proceedings of the National Academy of Sciences of the United States of America* 96, 3694–3699 (1999).
- 68 LI, L. W., HUANG, H. H. L., BADILLA, C. L., FERNANDEZ, J. M. Mechanical unfolding intermediates observed by single-molecule force spectroscopy in a fibronectin type III module. *Journal of Molecular Biology* 345, 817–826 (2005).
- 69 ROUNSEVELL, R. W. S., CLARKE, J. FnIII domains: Predicting mechanical stability. *Structure* 12, 4–5 (2004).
- 70 CRAIG, D., GAO, M., SCHULTEN, K., VOGEL, V. Steered molecular dynamics simulations of the extracellular matrix protein fibronectin. *Molecular Biology of the Cell* 13, 1137 (2002).
- 71 CRAIG, D., KRAMMER, A., SCHULTEN, K., VOGEL, V. Comparison of the early stages of forced unfolding for fibronectin type III modules. *Proceedings of the National Academy of Sciences of the United States of America* 98, 5590–5595 (2001).
- 72 RIEF, M., GAUTEL, M., SCHEMMEL, A., GAUB, H. E. The mechanical stability of immunoglobulin and fibronectin III domains in the muscle protein titin measured by atomic force microscopy. *Biophysical Journal* 75, 3008–3014 (1998).
- 73 EVANS, E., LEUNG, A., HEINRICH, V., ZHU, C. Mechanical switching and coupling between two dissociation pathways in a P-selectin adhesion bond. *Proceedings of the National Academy of Sciences of the United States of America* 101, 11 281–11 286 (2004).
- 74 EVANS, E., LEUNG, A., HAMMER, D., SIMON, S. Chemically distinct transition states govern rapid dissociation of single L-selectin bonds under force. *Proceedings of the National Academy of Sciences of the United States of America* 98, 3784–3789 (2001).
- 75 BAUMGARTNER, W., HINTERDORFER, P., NESS, W., RAAB, A., VESTWEBER, D., SCHINDLER, H., DRENCKHAHN, D. Cadherin interaction probed by atomic force microscopy. *Proceedings of the National Academy of Sciences of the United States of America* 97, 4005–4010 (2000).

Appendix

As highlighted discussed in 9.4, for any given transition state the shape of force distribution is invariant to the loading rate.

We will start with the generic expression for the dissociation probability for a single bond, where the energy barrier does not shift under force.

$$p(f) = \frac{1}{r_f} v_0 \exp\left(\frac{f}{f_\beta}\right) \exp\left[\frac{v_0 f_\beta}{r_f} \left(1 - \exp\left(\frac{f}{f_\beta}\right)\right)\right]$$

This is the generic expression for $p(f)$ for the simple, single barrier. The shape of the distribution can be described by the curvature at the top, where $p(f)$ is maximal (i.e., $dp(f)/df = 0$). The curvature is the second derivative of $p(f)$, ($d^2p(f)/df^2$), and the (Gaussian) width of the distribution is the curvature divided by $-p(f)$.

To differentiate $p(f)$ longhand, we expand it to

$$p(f) = \frac{v_0}{r_f} \exp\left(\frac{v_0 f_\beta}{r_f}\right) \exp\left(\frac{f}{f_\beta}\right) \exp\left[-\frac{v_0 f_\beta}{r_f} \exp\left(\frac{f}{f_\beta}\right)\right]$$

We can now differentiate by parts ($u dv/dx + v du/dx$, etc.). This requires the first derivative of the second exponential, which is

$$\frac{\partial \exp\left[-\frac{v_0 f_\beta}{r_f} \exp\left(\frac{f}{f_\beta}\right)\right]}{\partial f} = \exp\left[-\frac{v_0 f_\beta}{r_f} \exp\left(\frac{f}{f_\beta}\right)\right] \left(-\frac{v_0}{r_f} \exp\left(\frac{f}{f_\beta}\right)\right)$$

and so

$$\begin{aligned} \frac{\partial p(f)}{\partial f} &= \left\{ \frac{v_0}{r_f} \exp\left(\frac{v_0 f_\beta}{r_f}\right) \right\} \exp\left(\frac{f}{f_\beta}\right) \exp\left[-\frac{v_0 f_\beta}{r_f} \exp\left(\frac{f}{f_\beta}\right)\right] \left(-\frac{v_0}{r_f} \exp\left(\frac{f}{f_\beta}\right)\right) \\ &\quad + \exp\left[-\frac{v_0 f_\beta}{r_f} \exp\left(\frac{f}{f_\beta}\right)\right] \left\{ \frac{v_0}{r_f} \frac{1}{f_\beta} \exp\left(\frac{v_0 f_\beta}{r_f}\right) \right\} \exp\left(\frac{f}{f_\beta}\right) \\ \frac{\partial p(f)}{\partial f} &= \frac{v_0}{r_f} \exp\left(\frac{v_0 f_\beta}{r_f}\right) \exp\left(\frac{f}{f_\beta}\right) \exp\left[-\frac{v_0 f_\beta}{r_f} \exp\left(\frac{f}{f_\beta}\right)\right] \left(\frac{1}{f_\beta} - \frac{v_0}{r_f} \exp\left(\frac{f}{f_\beta}\right)\right) \end{aligned}$$

We could simplify this, but for fun we will leave it alone. We need to differentiate again, first part first, second part next. For the first part we'll put all the f -terms to the end as

$$\left\{ \frac{v_0}{r_f} \exp\left(\frac{v_0 f_\beta}{r_f}\right) \right\} \exp\left[-\frac{v_0 f_\beta}{r_f} \exp\left(\frac{f}{f_\beta}\right)\right] \exp\left(\frac{f}{f_\beta}\right) \left(-\frac{v_0}{r_f} \exp\left(\frac{f}{f_\beta}\right)\right)$$

The first derivative of this is

$$\begin{aligned} & \left\{ \frac{v_0}{r_f} \exp\left(\frac{v_0 f_\beta}{r_f}\right) \right\} \exp\left[-\frac{v_0 f_\beta}{r_f} \exp\left(\frac{f}{f_\beta}\right)\right] \exp\left(\frac{f}{f_\beta}\right) \left(-\frac{v_0}{r_f} \frac{1}{f_\beta} \exp\left(\frac{f}{f_\beta}\right)\right) \\ & + \left\{ \frac{v_0}{r_f} \exp\left(\frac{v_0 f_\beta}{r_f}\right) \right\} \exp\left[-\frac{v_0 f_\beta}{r_f} \exp\left(\frac{f}{f_\beta}\right)\right] \frac{1}{f_\beta} \exp\left(\frac{f}{f_\beta}\right) \left(-\frac{v_0}{r_f} \exp\left(\frac{f}{f_\beta}\right)\right) \\ & + \left\{ \frac{v_0}{r_f} \exp\left(\frac{v_0 f_\beta}{r_f}\right) \right\} \exp\left[-\frac{v_0 f_\beta}{r_f} \exp\left(\frac{f}{f_\beta}\right)\right] \\ & \times \left(-\frac{v_0}{r_f} \exp\left(\frac{f}{f_\beta}\right)\right) \exp\left(\frac{f}{f_\beta}\right) \left(-\frac{v_0}{r_f} \exp\left(\frac{f}{f_\beta}\right)\right) \end{aligned}$$

We now rearrange the second part, f -terms to the end

$$\frac{v_0}{r_f} \frac{1}{f_\beta} \exp\left(\frac{v_0 f_\beta}{r_f}\right) \exp\left[-\frac{v_0 f_\beta}{r_f} \exp\left(\frac{f}{f_\beta}\right)\right] \exp\left(\frac{f}{f_\beta}\right)$$

and take the first derivative to give

$$\begin{aligned} & \frac{v_0}{r_f} \frac{1}{f_\beta} \exp\left(\frac{v_0 f_\beta}{r_f}\right) \exp\left[-\frac{v_0 f_\beta}{r_f} \exp\left(\frac{f}{f_\beta}\right)\right] \frac{1}{f_\beta} \exp\left(\frac{f}{f_\beta}\right) \\ & + \frac{v_0}{r_f} \frac{1}{f_\beta} \exp\left(\frac{v_0 f_\beta}{r_f}\right) \exp\left[-\frac{v_0 f_\beta}{r_f} \exp\left(\frac{f}{f_\beta}\right)\right] \left(-\frac{v_0}{r_f} \exp\left(\frac{f}{f_\beta}\right)\right) \exp\left(\frac{f}{f_\beta}\right) \end{aligned}$$

So the full second derivative of $p(f)$ is:

$$\begin{aligned} \frac{\partial^2 p(f)}{\partial f^2} &= \left\{ \frac{v_0}{r_f} \exp\left(\frac{v_0 f_\beta}{r_f}\right) \right\} \exp\left[-\frac{v_0 f_\beta}{r_f} \exp\left(\frac{f}{f_\beta}\right)\right] \exp\left(\frac{f}{f_\beta}\right) \left(-\frac{v_0}{r_f} \frac{1}{f_\beta} \exp\left(\frac{f}{f_\beta}\right)\right) \\ & + \left\{ \frac{v_0}{r_f} \exp\left(\frac{v_0 f_\beta}{r_f}\right) \right\} \exp\left[-\frac{v_0 f_\beta}{r_f} \exp\left(\frac{f}{f_\beta}\right)\right] \frac{1}{f_\beta} \exp\left(\frac{f}{f_\beta}\right) \left(-\frac{v_0}{r_f} \exp\left(\frac{f}{f_\beta}\right)\right) \\ & + \left\{ \frac{v_0}{r_f} \exp\left(\frac{v_0 f_\beta}{r_f}\right) \right\} \exp\left[-\frac{v_0 f_\beta}{r_f} \exp\left(\frac{f}{f_\beta}\right)\right] \\ & \times \left(-\frac{v_0}{r_f} \exp\left(\frac{f}{f_\beta}\right)\right) \exp\left(\frac{f}{f_\beta}\right) \left(-\frac{v_0}{r_f} \exp\left(\frac{f}{f_\beta}\right)\right) \\ & + \frac{v_0}{r_f} \frac{1}{f_\beta} \exp\left(\frac{v_0 f_\beta}{r_f}\right) \exp\left[-\frac{v_0 f_\beta}{r_f} \exp\left(\frac{f}{f_\beta}\right)\right] \frac{1}{f_\beta} \exp\left(\frac{f}{f_\beta}\right) \\ & + \frac{v_0}{r_f} \frac{1}{f_\beta} \exp\left(\frac{v_0 f_\beta}{r_f}\right) \exp\left[-\frac{v_0 f_\beta}{r_f} \exp\left(\frac{f}{f_\beta}\right)\right] \left(-\frac{v_0}{r_f} \exp\left(\frac{f}{f_\beta}\right)\right) \exp\left(\frac{f}{f_\beta}\right) \end{aligned}$$

Some rearrangement gives

$$\begin{aligned} \frac{\partial^2 p(f)}{\partial f^2} &= \frac{v_0}{r_f} \exp\left(\frac{v_0 f_\beta}{r_f}\right) \exp\left[-\frac{v_0 f_\beta}{r_f} \exp\left(\frac{f}{f_\beta}\right)\right] \exp\left(\frac{f}{f_\beta}\right) \\ &\left\{ -\frac{v_0}{r_f} \frac{1}{f_\beta} \exp\left(\frac{f}{f_\beta}\right) + \frac{1}{f_\beta} \left(-\frac{v_0}{r_f} \exp\left(\frac{f}{f_\beta}\right)\right) + \left(-\frac{v_0}{r_f} \exp\left(\frac{f}{f_\beta}\right)\right) \right. \\ &\quad \left. \times \left(-\frac{v_0}{r_f} \exp\left(\frac{f}{f_\beta}\right)\right) + \frac{1}{f_\beta} \frac{1}{f_\beta} + \frac{1}{f_\beta} \left(-\frac{v_0}{r_f} \exp\left(\frac{f}{f_\beta}\right)\right) \right\} \end{aligned}$$

Dividing by $p(f)$ gives

$$\begin{aligned} &\left\{ -\frac{v_0}{r_f} \frac{1}{f_\beta} \exp\left(\frac{f}{f_\beta}\right) + \frac{1}{f_\beta} \left(-\frac{v_0}{r_f} \exp\left(\frac{f}{f_\beta}\right)\right) + \left(-\frac{v_0}{r_f} \exp\left(\frac{f}{f_\beta}\right)\right) \right. \\ &\quad \left. \times \left(-\frac{v_0}{r_f} \exp\left(\frac{f}{f_\beta}\right)\right) + \frac{1}{f_\beta} \frac{1}{f_\beta} + \frac{1}{f_\beta} \left(-\frac{v_0}{r_f} \exp\left(\frac{f}{f_\beta}\right)\right) \right\} \end{aligned}$$

The force where the distribution is maximum is of course known, as

$$f^* = f_\beta \ln\left(\frac{r_f}{f_\beta v_0}\right)$$

and so

$$v_0 \exp\left(\frac{f^*}{f_\beta}\right) = \frac{r_f}{f_\beta}$$

First, let us simplify the first derivative to

$$\frac{\partial p(f)}{\partial f} = \left\{ \frac{v_0}{r_f} \exp\left(\frac{v_0 f_\beta}{r_f}\right) \exp\left(\frac{f}{f_\beta}\right) \exp\left[-\frac{v_0 f_\beta}{r_f} \exp\left(\frac{f}{f_\beta}\right)\right] \right\} \left\{ \frac{1}{f_\beta} - \frac{v_0}{r_f} \exp\left(\frac{f}{f_\beta}\right) \right\}$$

And at f^*

$$v_0 \exp\left(\frac{f^*}{f_\beta}\right) = \frac{r_f}{f_\beta}$$

Therefore

$$-\frac{1}{p(f)} \frac{\partial^2 p(f)}{\partial f^2} = -\left\{ -\frac{1}{f_\beta^2} - \frac{1}{f_\beta^2} + \frac{1}{f_\beta^2} + \frac{1}{f_\beta^2} - \frac{1}{f_\beta^2} \right\} = \frac{1}{f_\beta^2}$$

Bond Strength and Tracking Chemical Reactions

10

Chemical Force Microscopy: Nanometer-Scale Surface Analysis with Chemical Sensitivity

Holger Schönherr and G. Julius Vancso

10.1

Introduction: Mapping of Surface Composition by AFM Approaches

The invention of scanning tunneling microscopy (STM) [1] and atomic force microscopy (AFM) [2] in the 1980s had an enormous impact on science and technology. Soon after its invention, the scanning probe microscopy (SPM) family rapidly found widespread application in vastly different disciplines. Currently, SPM technology is widely recognized as one of the prime driving forces and workhorses of cutting-edge materials science, nanoscience, and nanotechnology [3, 4]. These local proximal probe techniques possess the unique advantage of providing at the same time molecular-scale analysis [5] *and* manipulation capabilities [6, 7]. SPM techniques, and in particular AFM, are hence considered key enabling technologies for these areas, including nanobiotechnology and advanced materials science [8].

The combination of extremely high-resolution real-space imaging capabilities with various contrast mechanisms in SPM allowed researchers to garner previously unavailable information down to submolecular and atomic detail. As will be introduced and reviewed in this chapter, the functionalization of AFM probe tips by self-assembled monolayers (SAMs) introduced a new dimension – i.e., chemistry – to atomic force microscopy (Fig. 10.1).

Following, for instance, the report by Overney and coworkers, who showed that domains of different chemical composition in Langmuir–Blodgett (LB) layers can be differentiated owing to different frictional forces measured by AFM [9], countless studies have been published in which compositional mapping was achieved by means of AFM. In addition to mapping lateral (friction) forces, the force modulation mode [10] or intermittent contact mode phase imaging [11] are frequently applied to obtain such information. In most cases, the surface compositional mapping relies on variations in mechanical properties and energy dissipation of the sample surface [12, 13]; hence the information is only very distantly related to chemical composition.

Chemical imaging with high lateral resolution ($<1\ \mu\text{m}$) can be performed with only very few techniques. Recent progress in time-of-flight secondary-ion mass spectrometry (ToF-SIMS) using cluster-ion guns has pushed the resolution in

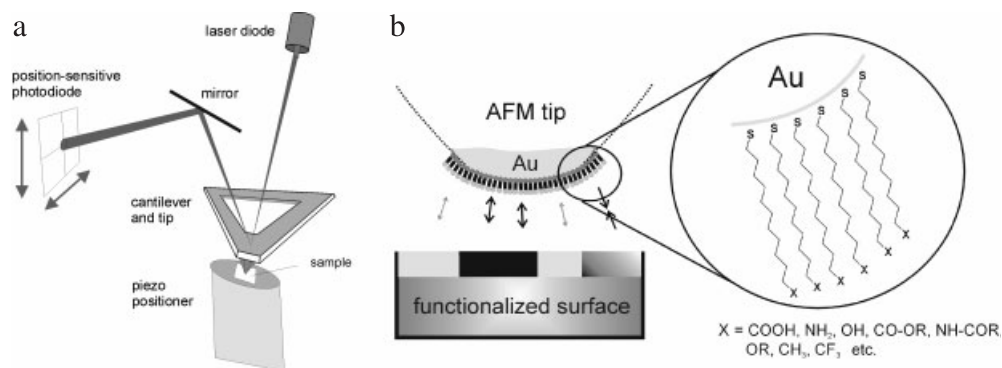


Fig. 10.1 (a) Schematic diagram of an AFM. (b) Schematic drawing of an alkanethiol monolayer-modified gold-coated AFM tip used for CFM and interactions between exposed functional groups on the contacting surfaces (right: chemically modified AFM tip and functionalized surface, with different functionalities and interactions indicated by different gray scales and arrows, respectively). For details on the self-assembled monolayer-based tip functionalization, see text. (Adapted with permission from ref. 35.)

semi-quantitative analysis of surface chemistry down to the 100 nm range [14]. However, this technique requires vacuum-compatible samples. Soft condensed matter, in particular organic and biologically relevant material, is also only in exceptional cases amenable to element-specific TEM due to beam damage and incompatibility with vacuum [15]. *In-situ* imaging, e.g., under physiological conditions, is virtually impossible. Hence imaging with chemical sensitivity has been largely unachievable in many important areas.

The recent advances in nanoscale chemistry (nanopatterning via soft lithographic [16, 17], scanning probe lithographic [6, 7, 18], and other approaches; synthesis of nanometer-scale polymers [19]; self-assembled supramolecular aggregates [20]; and single-molecule approaches [21], for instance) clearly require and would benefit from an advanced, chemically sensitive surface characterization technique that operates at these length scales. In nanoscience and nanotechnology, in particular, where nanoscale objects and molecules are addressed in a one-to-one relationship and where one relies on nanometer-scale structural and functional control, the combination of chemically sensitive mapping with topographic imaging seems highly desirable. Until recently, however, there were few, if any, solutions available apart from STM imaging, which is limited to studies on conductive substrates.

The development of chemical force microscopy (CFM) has begun to close this apparent gap. (CFM is typically used as a synonym for “AFM using defined surface chemistry on AFM probe tips in order to assess and quantify differences in surface chemical composition (using friction or adhesion differences related to interactions between functional groups or atoms exposed on both tip and sample surface as contrast).”) The extension of pioneering work carried out, e.g., in Lieber’s group

[22, 23], led to the development of chemically sensitive imaging on the nanometer scale by CFM [24–28] and enabled, among other achievements, the delivery of reactants in preselected positions, the fabrication of patterns on length scales between 100 μm and tens of nanometers, and the formation and rupture of host-guest complexes and chemical bonds [29]. In the context of a rapidly accelerating development in nanoscience and nano(bio)technology, the use of state-of-the-art AFM approaches using chemically modified probe tips (Fig. 10.1) has become a very important methodology in many areas [30–34].

Central to the CFM approach is the chemical modification of AFM probe tips (Fig. 10.1b) [22]. By control of the surface chemistry of the tip as well as the imaging medium, the intermolecular interactions between the functional groups exposed on the tip and on the sample surface can be systematically varied and controlled. These spatially different interactions can be detected in normal or lateral force measurements, thus providing access to variations in, e.g., surface chemistry averaged over the tip-sample contact area.

In this chapter, we further address the viability of imaging with chemical sensitivity, as well as the pitfalls, limitations, and difficulties. In addition, we discuss selected recent examples that demonstrate the usefulness, the unique character, and the added value of the CFM approach for technologically relevant applications. Single-molecule force spectroscopy will only be mentioned very briefly (for a complementary overview on “Force spectroscopy to explore supramolecular interactions,” see Chapter 11). This chapter is not intended to be encyclopedic; the choice of the examples discussed reflects our preferences and scientific taste. We regret if we have left out (by accident or by choice) articles from the literature which the corresponding authors would miss, and we offer our apologies to those who consider these omissions as negligence on our part.

10.2

Chemical Force Microscopy: Basics

The functionalization of force microscopy tips, which has been known about for years, can be employed in order to control tip-sample interactions. (Untreated clean silicon (oxy)nitride or silicon tips can be considered as one particular tip functionality. Due to the variations in the composition (e.g., the oxygen content may vary) however, chemically modified tips can be prepared much more reproducibly.) The first studies on chemically modified tips aimed at optimized imaging conditions, e.g., on rough surfaces [36]. In addition, the modification of tips with micron-sized spherical particles, such as silica particles, is well known. This approach allowed Ducker and coworkers to probe the interaction between individual colloidal particles and various surfaces [37]. As briefly mentioned in Section 10.1, CFM is an AFM-based technique aimed at the determination and mapping of the distribution of chemically distinct functional groups on surfaces [22, 23, 33, 34]. The technique relies on control of the interactions between tip and the sample surface, which is achieved through controlled chemical modification/

functionalization of AFM probe tips. The exposed functional groups, together with the imaging medium, determine the type and the range of forces that act between the tip and the surface [38]. In order to appreciate the vast potential and to realize the limitations of CFM, a discussion of tip-surface modification approaches (Section 10.2.1), as well as interaction forces (Section 10.2.2) and rudimentary CFM experiments (Section 10.2.3) is required.

10.2.1

Surface Modification Procedures for Tip Modification

The requirements for the tip-surface modification are stringent in order to achieve stable, robust, and reproducible tip functionalities. We will briefly discuss three monolayer-based approaches, as well as functionalized carbon nanotube (CNT)-modified tips as chemical probes. Common to the former approaches is the spontaneous formation of highly ordered monomolecular layers that expose, at their interface with the contacting medium, terminal functional groups in the ω -position of long alkane chains (Fig. 10.1b).

10.2.1.1 Thiol-Based Self-Assembled Monolayers (SAMs) on Gold

The most established and widespread approach relies on the SAM formation of thiols, or disulfides, on gold [39]. Thereby the composition and properties of molecularly thin, covalently immobilized coatings can be controlled down to the molecular level [40–42]. The drawback of an additional metal coating on the AFM probe tip (Ti or Cr primer plus Au), which leads to increased overall tip radii and a granular tip morphology, is counterbalanced by the broad range of functional groups that can be introduced in a simple one-step modification without interfering with the assembly process. With the exception of sulfur- and some phosphorous-containing functional groups and isonitriles, essentially all organic functional groups can be introduced [39–42]. Functional groups that are reactive toward thiols can be introduced via the corresponding disulfides [43] (Fig. 10.2) or as protected thiols [44]. Co-adsorption of different thiols provides access to a wide

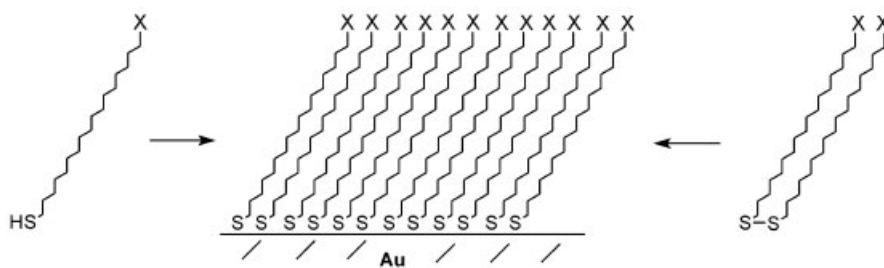


Fig. 10.2 Schematic drawing of self-assembly of *n*-alkanethiols and disulfides on gold. The functional group X in the ω position determines to a large extent the surface properties of the SAM.

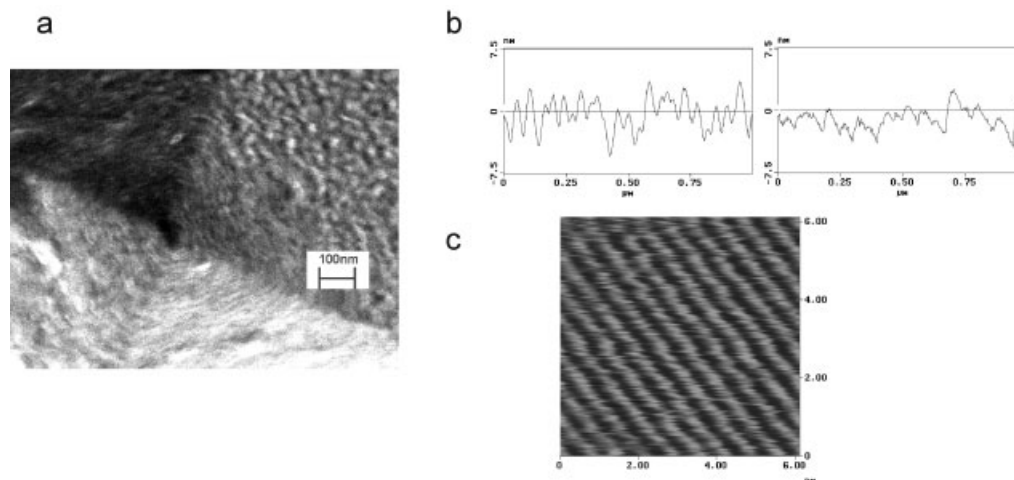


Fig. 10.3 (a) High-resolution SEM image of a gold/SAM-coated AFM tip. (b) Cross-sections of AFM height images made on SrTiO₃ crystal [53] with an AFM tip before (left) and after gold coating (right). (c) Contact mode height image of oriented PTFE crystalline facet. (Adapted with permission from ref. 35.)

variety of surface compositions, and hence surface and interfacial free energies. However, the fractional surface coverages often differ from the ratios of the concentrations of the corresponding thiols in solution [45].

Another successful approach is the use of asymmetrically substituted disulfides. It is generally assumed that self-assembly of alkanethiols and the corresponding disulfides on Au(111) leads to the formation of virtually identical SAMs (Fig. 10.2). There is ample experimental evidence that this assumption is fulfilled [46–48]. Scanning tunneling microscopy (STM) results provided direct evidence for the proposed scenario shown in Fig. 10.2 [49]. Both chains of an alkyl hydroxyalkyl disulfide were shown to assemble in neighboring positions [50]. Thus, the ratio of exposed functional groups on the surface is 1:1, and in absence of lateral mobility the mixture is homogeneous down to a molecular level [51].

It is important to note that the granular gold coating (Fig. 10.3a) obtained by evaporation in high vacuum is the same as for metal coatings obtained in the same evaporation run on flat glass, silicon, or other substrates (see below). Such substrates are commonly used for SAM formation and characterization [52]. In addition to standard characterization data by contact angle measurements, ellipsometry, or surface plasmon resonance measurements, X-ray photoelectron spectroscopy (XPS) and grazing-angle reflection Fourier transform infrared spectroscopy, AFM studies provided direct evidence for negligible differences in local order in SAMs on granular gold (see below).

The granular texture of the gold leads to a sometimes *a-priori* ill-defined tip radius. Using appropriate imaging standards, the tip radius can be determined

conveniently. The morphology of the gold coating can be visualized using a high-resolution scanning electron microscopy (SEM). In Fig. 10.3a a top view of a SAM-coated AFM tip is shown. The gold grains with a typical diameter of 30–70 nm are clearly visible.

In fact, significantly enlarged tip radii and significantly reduced tip radii (in the case of individual grains at the very apex) have both been observed. Considering the different requirements for imaging of very flat and rough samples, as well as the choice of the imaging mode (topography imaging, friction force imaging or pull-off force mapping; see Section 10.2.2), it is clear that a gold-coated tip is less suitable for imaging rough samples. This is exemplified in the cross-sectional plots recorded on a standard SrTiO₃ specimen for tip sharpness assessment [53, 54] (Fig. 10.3b) and an oriented PTFE specimen (Fig. 10.3c). The contour of the SrTiO₃ imaging standard can no longer be followed accurately after Au evaporation. By contrast, on the molecularly smooth PTFE sample, gold-coated tips can be used to obtain molecular-resolution images of uniaxially oriented PTFE despite the increased radius, as shown in this high-resolution AFM image.

The most important requirements for successful tip functionalization, i.e., the high quality and order of the monolayers on the tips themselves, is probably fulfilled with the thiol–gold system. It is of course very difficult or almost impossible to characterize the monolayer exactly at the apex of an AFM tip by independent techniques, owing to its size of only several nanometers squared. Therefore it is important to choose a SAM system which is generally applicable for the introduction of a large variety of functional groups and, at the same time, allows one to obtain high-quality layers very reproducibly.

10.2.1.2 SAMs on Hydroxylated Silicon and Si₃N₄

An alternative to SAM formation on Au-coated tips is the direct functionalization of hydroxyl groups present on oxidized silicon, or silicon nitride, tips using trichlorosilane or triethoxysilane chemistry [55–58]. These reactive silane derivatives form chemically stable SAMs via robust Si–O–Si bridges as a consequence of condensation reactions. Especially for the highly reactive trichlorosilanes, the reaction conditions have been reported to be difficult to control. Aggregation of the silanes, instead of the desired crosslinking in the layers, has been observed. However, if the preparation conditions are well controlled, high-quality SAMs can be prepared (Fig. 10.4a).

The disadvantage of the silane-based approaches compared with the thiol–gold system is the limited number of compatible functional groups for attachment in ω -positions. While triethoxysilanes are compatible with terminal amino groups, for other standard functional groups, such as OH or COOH, protection/deprotection chemistry must be performed, which gives rise to additional complications. Similarly to the thiol systems, binary solutions give rise to mixed SAMs with intermediate properties [59].

More recently, the covalent coupling of ω -vinyl compounds on H-terminated silicon has been reported also as a means of modifying AFM probes [60–62]. The different possible ways to induce this coupling reaction, which yields very stable Si–C

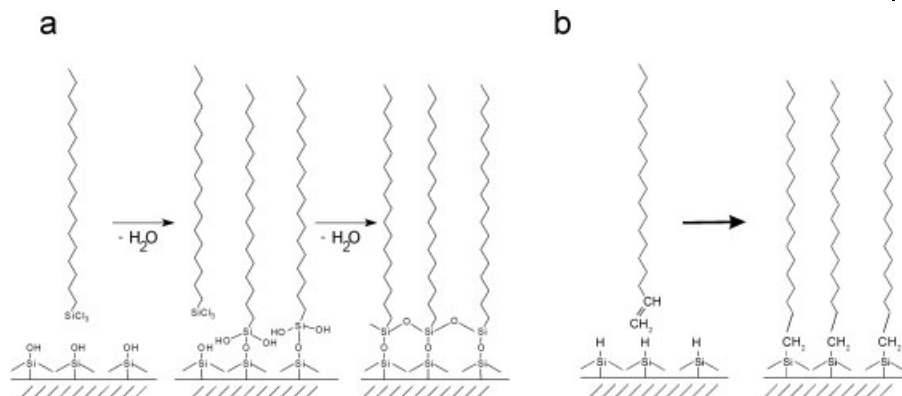


Fig. 10.4 (a) Schematic drawing of the idealized condensation reaction of trichlorosilanes on oxidized silicon, which leads to an internally crosslinked SAM. (b) Attachment of terminal vinyl compounds to H-terminated silicon.

covalent bonds, involve photochemical, thermal, and catalytic routes, as reviewed recently [63]. Again, the variety of compatible functional groups is limited in comparison with the thiol–gold system. Amine terminal functional groups have been prepared successfully [64]. Via hydrolysis and activation of, for instance, terminal ester groups, various functionalities, such as acids, alcohols, or amides, are accessible.

10.2.1.3 Modified Carbon Nanotube Probes

The use of carbon-nanotube modified tips, which were also chemically modified, pushed the resolution limit to the extreme [65–67]. There are various methods of obtaining CNT-modified tips: among the most prominent are gluing of multiwall or single-wall CNTs to AFM tips, and catalytic growth of tubes at the AFM tip or on cantilevers. Figure 10.5 shows a schematic of a CNT-modified probe tip and its chemical derivatization. As the number of interacting functional groups is very small, adhesive forces are minimal. Owing to the buckling properties of CNTs, friction force mapping to obtain chemical contrast is usually not possible. To circumvent these problems, tapping mode AFM phase imaging has been proposed for compositional mapping [67, 68].

10.2.2

Force Measurements and Mapping in CFM

The chemical contrast necessary for imaging is achieved by exploiting the spatial (or temporal) variations of tip–sample forces in quantitative measurements. These forces between the tip and selected areas on the surface of interest can be detected in the surface-normal direction (pull-off forces) and/or in the tangential (lateral) di-

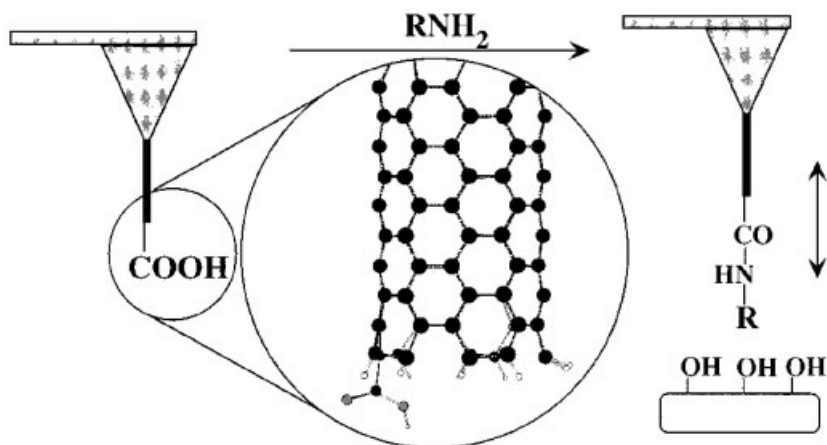


Fig. 10.5 Schematic of a CNT-functionalized AFM probe tip which has been chemically derivatized, and of a functional CNT tip interacting with a hydroxylated surface. (Reprinted in part with permission from ref. 67. Copyright 1998, American Chemical Society.)

rection (friction forces). Depending on the interaction forces, the tip–sample contact area can be very small. Consequently, CFM mapping of the lateral distribution of functional groups can be performed down to the sub-50 nm level, and in some cases down to molecular length scales. The discussion of examples and applications of CFM mandates a closer look at some underlying rudimentary principles.

10.2.2.1 Normal Forces

In general, contact mode AFM can also be used to measure both repulsive and attractive forces between a sample and a surface with high accuracy (force–displacement measurements). Examples include electrostatic forces, electrostatic double-layer forces, hydrogen bonding, van der Waals interactions, and magnetic forces [38]. The resolution limit for an optical detection system and typical commercially available cantilever spring constants has been estimated to be in the order of 10^{-11} N [69]. Depending on the detection system, the force constant, the stiffness, and the resonance frequency of the cantilever, even smaller forces can be measured [70].

In a force–displacement measurements experiment, the sample is moved up and down (in and out of contact with the tip) at a fixed position (x , y). In Fig. 10.6(a) the corresponding movements of piezo (sample) and cantilever deflection are depicted schematically. The resulting force–distance plot (force–displacement curve) is shown in Fig. 10.6(b). The interpretation of force curves has been discussed in detail, e.g., by Burnham et al. [71] and by Cappella and Dietler [72].

To avoid the contribution of capillary forces in adhesion (and also friction) measurements, CFM experiments are most often carried out in an appropriate imaging

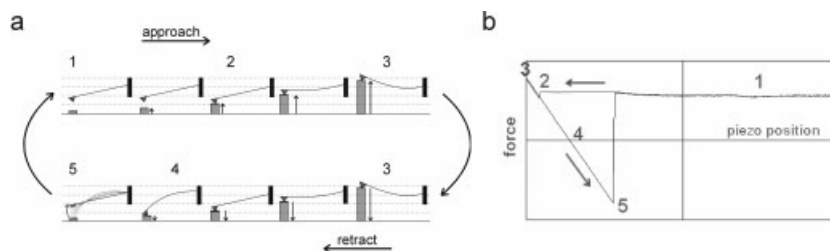


Fig. 10.6 (a) Measurement of force–distance curves (schematic representation). (b) Schematic force–distance plot (reproduced with permission from ref. 35). The sample approaches the tip (1, top); at some distance the gradient of the force overcomes the cantilever spring constant and the tip jumps into contact (2); further movement upward causes a deflection of the cantilever (3); during retraction the tip adheres to the substrate (4), and snaps off when the spring constant overcomes the force gradient (5, bottom). The adhesion between the tip and the sample is characterized by the so-called pull-off or pull-out force (snap off) [72]. A quantitative determination of forces requires a thorough calibration of the cantilever spring constant [74–77].

liquid using a liquid cell [73, 78]. In addition to the elimination of capillary forces, the choice of the solvent may be a means of controlling tip–sample interactions and of enhancing a specific contrast [79].

The pull-off force data can be evaluated, e.g., based on contact mechanics models, including those developed by Johnson–Kendall–Roberts (JKR) or by Derjaguin, Muller, and Toporov (DMT) (see also ref. 23). Unlike Hertz theory, these theories take adhesion explicitly into account [80, 81]. The JKR theory of *continuum* contact mechanics was shown to yield a reasonable description of CFM data [23]. Other authors have applied the DMT theory to related problems, with more success [82]. Recent atomistic molecular dynamics simulations show some discrepancies; however, the JKR model, of all the models tested, provides the best overall agreement with the simulations [83]. For the interactions between a sphere with radius R and a planar surface, a general equation relating contact area A and load L can be derived [Eq. (1), where K denotes the reduced modulus and W_{12} denotes the work of adhesion].

$$A^{3/2} = \pi^{3/2} R / K \{ L + 3\pi R W_{12} + [6\pi R W_{12} L + (3\pi R W_{12})^2]^{1/2} \} \quad (1)$$

The work of adhesion W_{12} can be expressed as a function of the surface free energies of the tip (γ_1), the sample γ_2 , and the corresponding interfacial free energy γ_{12} [Eq. (2)].

$$W_{12} = \gamma_1 + \gamma_2 - \gamma_{12} \quad (2)$$

For the contact area at pull-off one obtains Eq. (3), whereas the DMT theory affords Eq. (4).

$$F_{\text{pull-off}} = -\frac{3}{2}\pi RW_{12} \quad (3)$$

$$F_{\text{pull-off}} = -2\pi RW_{12} \quad (4)$$

Thus, the different surface free energies γ_i can, in principle, be determined experimentally, based on AFM pull-off force measurements. These equations form the basis for CFM and allow one to discriminate between different materials.

Interactions of chemically defined AFM tips with apolar surfaces via van der Waals forces can be described quantitatively. For rigid bodies, surface forces originating from van der Waals interactions can be calculated from the nonretarded Hamaker constant (A_{total}), which can be split into two terms that account for the dipole–dipole and the dipole-induced dipole contributions ($A_{v=0}$) on the one hand, and the dispersion (London) contributions on the other hand ($A_{v>0}$). The Hamaker constant can be calculated based on the Lifshitz theory [84, 85] of van der Waals forces. According to Israelachvili [86], for a system in which two macroscopic phases (1, 2) interact across a third phase, these contributions can be obtained from the corresponding static dielectric constants ($\epsilon_1, \epsilon_2, \epsilon_3$) and optical refractive indices (n_1, n_2, n_3) as shown in Eq. (5), where ν_e denotes the electronic absorption frequency.

$$A_{\text{total}} = A_{v=0} + A_{v>0} \approx \frac{3}{4}kT \left(\frac{\epsilon_1 - \epsilon_3}{\epsilon_1 + \epsilon_3} \right) \left(\frac{\epsilon_2 - \epsilon_3}{\epsilon_2 + \epsilon_3} \right) + \frac{3h\nu_e}{8\sqrt{2}} \\ \times \frac{(n_1^2 - n_3^2)(n_2^2 - n_3^2)}{(n_1^2 + n_3^2)^{1/2}(n_2^2 + n_3^2)^{1/2} \{ (n_1^2 + n_3^2)^{1/2} + (n_2^2 + n_3^2)^{1/2} \}} \quad (5)$$

If the dielectric constants of the tip, the sample, and the medium match closely, the first term is suppressed and the dispersion forces play the dominant role in determining the tip–sample adhesion [79].

Laterally resolved imaging of pull-off forces in contact mode AFM is a viable strategy toward chemical imaging. In this approach [87–90], force–displacement curves are recorded for each pixel and the pull-off force, as a measure for adhesion, is evaluated for each pixel. Particularly for adhesion mapping, the use of chemically functionalized AFM probe tips [22] has been shown to be a suitable approach to map chemical composition and functional group distributions down to the sub-50 nm scale [91]. For an example of chemical imaging using laterally resolved pull-off forces, see ref. 92. Here a phase-separated Langmuir–Blodgett (LB) film was investigated. The differences in pull-off force were shown to agree favorably with the differences in surface energies among the two types of domains.

The slow data acquisition rates of force curve mapping have been overcome in the so-called “pulsed force mode” AFM technique [93]. In this mode, the sample is modulated sinusoidally (~ 1 kHz) during a conventional contact mode AFM scan with an amplitude, which is large enough to overcome the adhesive interactions. Instead of recording the complete f–d curve, only four characteristic data points are captured to allow one to determine pull-off force and sample stiffness.

While the approach has the advantage of significantly increased rates of data acquisition, under certain circumstances important details of the f - d curves, such as multiple pull-off events or the signature of double-layer repulsion, may be not recorded or may be overlooked.

10.2.2.2 Lateral Forces

In addition to adhesion measurements, measurements of friction forces (or lateral forces) [54] by AFM can be used to differentiate among materials [94, 95].

An early description of (macroscopic) friction, Amontons' law, describes the relationship between friction force F_{friction} and applied load L for rough surfaces (multiasperity contact), according to Eq. (6), where μ represents the friction coefficient.

$$F_{\text{friction}} = \mu L \quad (6)$$

This equation has been modified to account for the adhesion that is observed at zero load [Eq. (7), with constants α and $F(0)$ which are related to the chemical composition of the interface] [96].

$$F_{\text{friction}} = \alpha L + F(0) \quad (7)$$

For a single asperity contact the friction force F_{friction} is proportional to contact area A ; τ denotes the interfacial shear strength [97].

$$F_{\text{friction}} = \tau A \quad (8)$$

The contact area A can be calculated, e.g., according to the JKR theory [Eq. (1)]. Experimental data (high-vacuum AFM measurements on mica) could be fitted well using this approach [98]. However, it should be noted that friction forces have been shown to be proportional to the adhesion hysteresis, as discussed by Israelachvili [38].

10.2.2.3 Intermittent Contact Mode Phase Imaging

Tapping mode phase imaging with modified tips was employed recently in liquid to distinguish differences in adhesion [68]. Under certain conditions, the phase signal in intermittent contact mode can be sensitive to attractive forces. Contrast of materials on the basis of adhesive interactions has been demonstrated for different phases in polymer blends [99], as well as SAMs on gold [100]. The phase signal, however, can also contain information about the stiffness of the tip-sample contact.

Using intermittent contact mode phase imaging, Wong and coworkers showed that chemically distinct domains in SAMs can be imaged successfully with chemically modified CNTs [67]. Adhesive interactions between a benzylamine-modified CNT and patterned SAM surfaces led to a pronounced phase lag, which was used to identify the CH_3 region in a matrix of COOH .

10.2.3

AFM Using Chemically Modified Tips

The stability of the SAMs, as well as the gold coating on the modified tips, is an important issue. Only intact and unchanged sensor coatings allow one to perform reproducible measurements. Some rudimentary aspects are treated briefly in Section 10.2.3.1.

10.2.3.1 Stability of SAMs and Modified Tips

The pressure between the tip and the sample surface can reach values of several tens to a hundred megapascals (MPa) [101]. During pull-off force measurements the SAM–gold assembly at the tip apex must withstand small repulsive *normal* forces, and during friction measurements *lateral* shear forces. These forces can be adjusted by the operator. If the modified AFM tips are used in a scanning imaging mode, e.g., in friction mode, the adjustment of the feedback loop is crucial to avoid high forces. However, despite an optimized feedback loop, steps and other topographical features can result in high peak forces and concomitant damage or loss of the functional layer. Work by Salmeron and coworkers has shown that SAMs are stable under pressures up to 2.4 GPa, above which thiol molecules are reversibly displaced [101].

In addition, the lattice structure of a large variety of SAMs was imaged on sputtered gold on mica or glass [102, 103]. Images with lattice resolution were obtained on a variety of SAMs with normal forces between 0.1 and ~125 nN without any evidence for monolayer damage (Fig. 10.7, right) as seen in lower-resolution AFM images of the scanned areas (Fig. 10.7, left).

It can be concluded that SAMs on sputtered gold can withstand the pressure and the lateral forces of a scanning AFM tip. In addition, the lattice structure of the SAMs was the same on atomically flat Au(111) and sputtered gold, which implies that the curvature of the gold grains of 20–50 nm grain size has a negligible influence on the SAM structure [102].

The stability of the tip in time in liquid media is another important aspect, because CFM experiments are carried out in liquid media to avoid capillary forces. Well-known limitations are the susceptibility of sulfur-based SAMs toward oxidation by oxygen in the presence of UV light [104–107] or toward oxidation by ozone [108]. On the timescale of minutes to hours, exchange reaction may take place in aggressive media, such as dichloromethane or toluene [109]. Likewise, trichlorosilane- or triethoxysilane-based SAMs may suffer from hydrolytic cleavage at extreme pH values.

However, for the media that are used mostly, such as ethanol or water, tip coatings were found to be stable. For instance, pull-off forces measured for the combination of octadecanethiol tip versus octadecanethiol, SAMs in aqueous NaOH were stable for more than 60 min [110]. In addition, force titration and single-molecule force spectroscopy experiments (see below), which are typically recorded over timescales of hours, have in many cases shown reproducible data for hours [30].

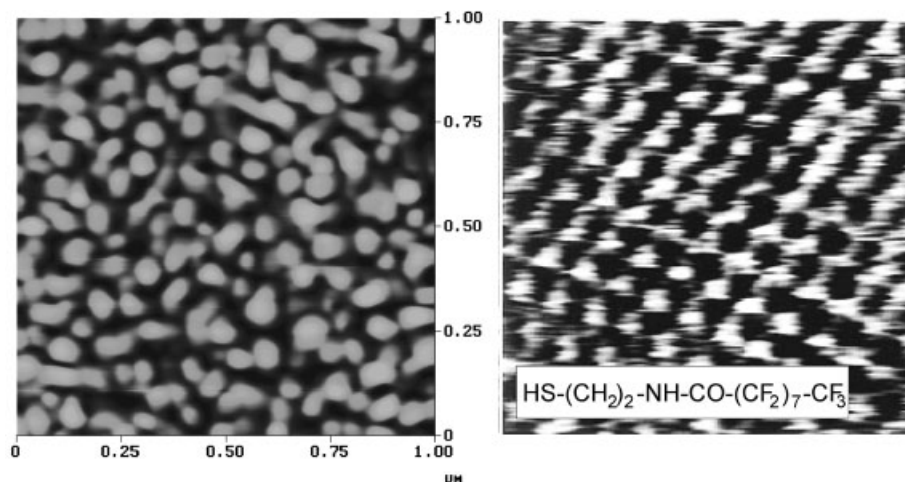


Fig. 10.7 AFM images of sputtered gold on mica (left, z-scale 25 nm) and a SAM of a fluorinated thiol on the same substrate (right, image size 6.0 nm \times 6.0 nm). (Reprinted (in parts) with permission from ref. 102. Copyright 1997, American Chemical Society.)

10.2.3.2 Imaging with Optimized Forces

Chemically modified AFM tips were applied to optimize the imaging conditions on rough surfaces by controlling the tip-sample van der Waals forces [36], and to enhance contrast in imaging of single polyethyleneimine polymers adsorbed on negatively charged latex spheres [111] as well as in low normal force imaging by reducing capillary forces [112].

An example of the reduction in imaging forces for AFM measurements in air is shown in Fig. 10.8(a). Here the packing of polyethylene chains was visualized with a CF_3 -terminated chemically modified AFM tip [113]. The average distance (4.8 Å) corresponds to the lattice parameter b of the orthorhombic unit cell of PE ($b = 4.946 \text{ \AA}$) [114]. The quality of the resolution of the image is comparable with images taken with unmodified tips. Hence, although the tip used is modified (concomitantly with an increase in tip radius), it is still possible to image with subnanometer lattice resolution. The reduction in pull-off force and hence the reduction in imaging forces is evident from the f - d curves shown in Fig. 10.8(b) and 8(c). The pull-off forces measured with CF_3 and other hydrophobic tips on the PE sample in air showed a significant decrease compared with untreated or hydrophilic (COOH) tips. This decrease in pull-off force can be interpreted as a result of the reduction of capillary forces [115].

10.2.3.3 Distinguishing Different Functional Groups on Surfaces by CFM

As mentioned above, CFM relies on the detection of distinct interactions between the functionalized AFM tips and functional groups exposed at sample surfaces in a

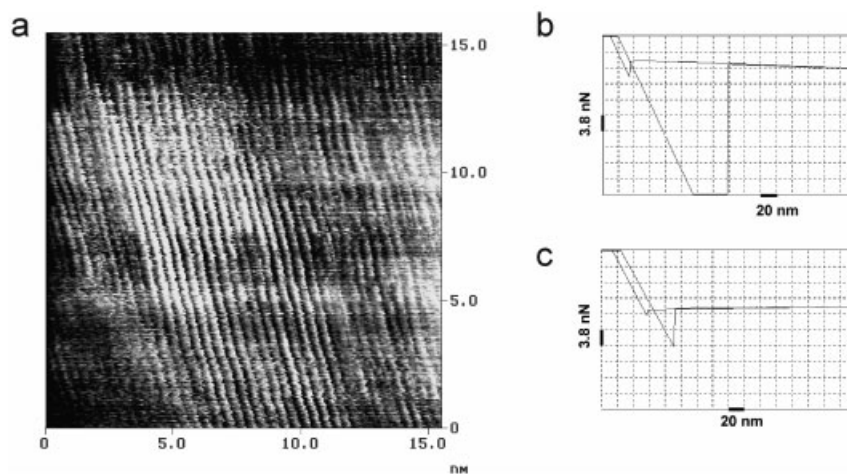


Fig. 10.8 (a) High-resolution AFM friction image of the (bc) facet on microtomed surfaces of uniaxially oriented high-density PE obtained with a CF_3 -modified AFM tip in air. Force–distance plots of an unmodified (b) and a CF_3 -terminated tip (c) measured on high-density PE in air. (Reprinted (in parts) with permission from ref. 113. Copyright 1997, American Chemical Society.)

suitable medium (see the schematic in Fig. 10.1). In the first proof-of-concept experiments, the force experienced by chemically modified tips on well-defined model surfaces composed of SAMs on gold, which exposed different functional groups at the surface, was shown by the Lieber group to indeed depend on the nature of the interacting functional groups. These observations were consistently made in both pull-off force and friction measurements [22, 23].

Mutual interactions between carboxylic acid (COOH) groups in ethanol were found to be stronger than the interactions of methyl (CH_3) groups with each other. The combination COOH/CH_3 yielded the smallest interaction (Fig. 10.9a). As shown in Fig. 10.9(b), the pull-off forces show a broad distribution around a mean value; hence a thorough statistical analysis is required. The different interacting pairs can also be differentiated on the basis of the friction coefficients (Fig. 10.9c).

This strategy was demonstrated for a number of surfaces and liquid environments (including variable pH values), and also AFM imaging modes [116, 117]. For instance, the linear relationship of the pull-off force measured on various surface-treated polymers as a function of the cosine of the static water contact angle (which is proportional to the surface free energy difference $\gamma_{\text{SV}} - \gamma_{\text{SL}}$, with $s = \text{solid}$, $v = \text{vapor}$, $l = \text{liquid}$) shows that the measured data are not restricted to SAM systems and that adhesion forces on the one hand, and surface energy differences on the other hand, are directly related [118].

On patterned SAM samples, prepared (e.g.) by UV lithography or microcontact printing, the areas of different chemical composition can be visualized (Fig. 10.10) [23].

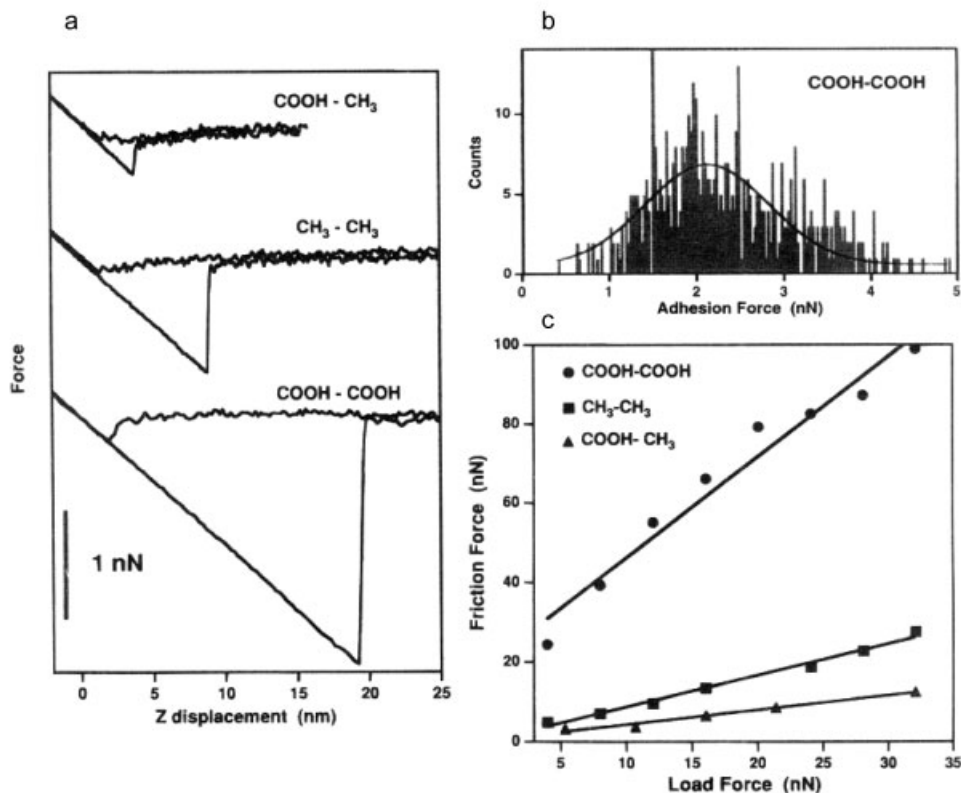


Fig. 10.9 (a) Representative force–distance curves recorded for COOH/CH₃, CH₃/CH₃, and COOH/COOH tip/sample functionalizations (60 nm tip radius). All data were obtained in neat ethanol. (Reprinted with permission from ref 116. Copyright 1995, American Chemical Society.) (b) Histogram showing the number of times that a given adhesion force was observed in repetitive measurements using COOH-terminated samples and tips. The histogram represents

approximately 400 tip–sample contacts for one functionalized tip in ethanol. (Reprinted (in parts) with permission from ref 116. Copyright 1995, American Chemical Society.) (c) Summary of the friction force vs. applied load data recorded for functionalized samples and tips terminating with COOH/CH₃, CH₃/CH₃, and COOH/COOH in EtOH. (Reprinted with permission from ref 116. Copyright 1995, American Chemical Society.)

JKR theory provides an expression for the tip–sample area at pull-off and hence allows one to estimate the number of effectively interacting molecular pairs. Depending on the tip radius and the value chosen for the modulus of the gold, the number may range from 10 to >100 molecules.

10.2.3.4 Artifacts and Experimental Difficulties

The application of CFM can be complicated in some cases by the presence of artifacts and experimental difficulties. These result in uncertainties in the interpreta-

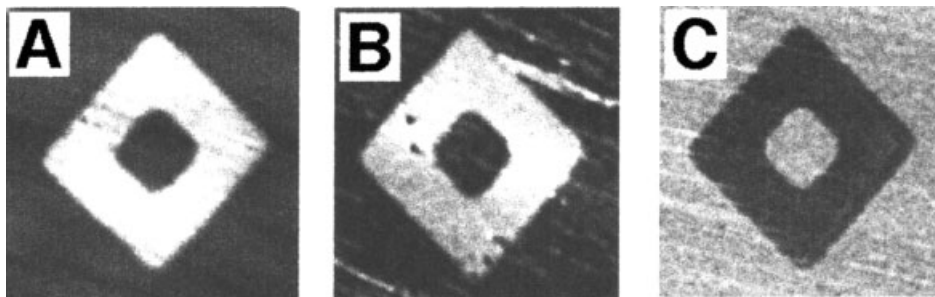


Fig. 10.10 Force microscopy images of a CH_3 -terminated square in a COOH square surrounded by a CH_3 SAM pattern prepared by microcontact printing. The images are recorded in ethanol and represent: (A) a friction map recorded with a tip modified with a COOH -terminated SAM; (B) a phase lag map acquired with a tip modified with a CH_3 -

terminated SAM; (C) a phase lag map acquired with a tip terminating in COOH groups. Light areas in (A) indicate higher friction; dark regions in (B) and (C) indicate greater phase lag. Image sizes are $20\ \mu\text{m} \times 20\ \mu\text{m}$. (Reprinted with permission from ref. 23. Copyright 1997, Annual Reviews Inc.)

tion of the acquired data. Apart from technical difficulties related to the precise calibration of the relevant cantilever spring constants [54], one may need to consider the effect of tip and/or sample roughness on the measured forces [119–121] and the possible coupling of topography to the friction images, as well as the difficulties of relating the conveniently attainable friction forces with the surface chemical composition in some oriented or conformationally disordered systems.

Some of the measurements discussed in Section 10.2.3.3 were performed on sputtered or evaporated gold, which possesses a granular morphology (having an rms roughness of a few nanometers). However, realistic samples, such as polymers, can easily possess rms roughness values of several tens of nanometers. Based on simple geometric considerations one can expect a distribution of contact areas which should broaden with increasing roughness.

In Fig. 10.11 a height and a corresponding force–volume image are shown which were recorded with a CH_3 -terminated tip on a thin poly(vinyl alcohol) (PVA) fiber [122] deposited on an octadecanethiol SAM on a granular gold surface. The influence of the tip–sample contact area is clearly recognized. The occurrence of areas of high and low adhesive forces, which are oriented parallel to the fiber axis, can be attributed to an increased and decreased effective contact area between the side of the tip as compared with the tip apex. As the fiber shape is not known *a priori*, no definite conclusions about the chemical identity can be obtained. Similarly, the pull-off forces are smallest on top of the gold grains (see insets), where the contact area is minimized, while the highest forces are measured between the grains. The differences in contact area on this chemically *homogeneous* surface give rise to artifacts in CFM. This effect has also been discussed in ref. 123.

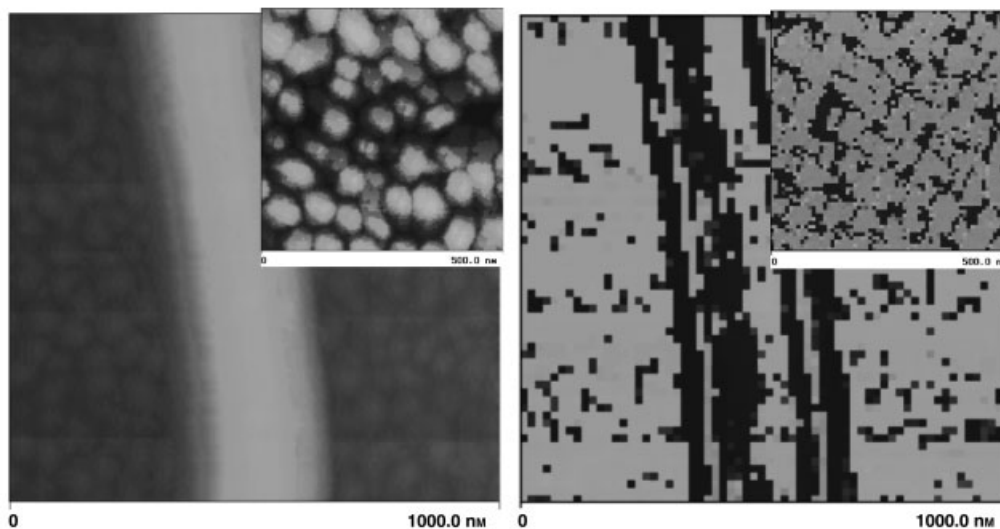


Fig. 10.11 Height (left) and pull-off force images (right) of electrospun PVA fiber on a SAM of octadecanethiol (insets: high-resolution height and pull-off force images of the underlying gold substrate). The gray scale denotes: bright (low forces) to dark (high forces), -4 nN to -30 nN. (Reproduced with permission from ref. 35.)

Another illustrative example is the case of chemically oxidized low-density polyethylene (LDPE). For this material the oxidation leads to a pronounced increase in surface free energy (assessed by contact angle measurements) and also roughness. The effect of reduced tip-sample contact area, however, overruled possible effects of increased adhesive interactions in any medium tested [124]. These observations indicate that force data must be interpreted carefully. In particular, attention must be paid to avoid coupling of the topography to the force images.

There are abundant reports in the literature which show that there may not be a simple relationship between friction and pull-off forces for chemically identical surface systems, such as well-defined monolayers terminated by identical functional groups [125, 126]. In these cases contributions of different modes of energy dissipation are thought to affect the tribological behavior. For example, AFM friction experiments using (unmodified) silicon nitride tips performed on (a) silane-based SAMs on mica and (b) organosulfur-based SAMs on Au(111) [125, 126] show this pronounced effect (Fig. 10.12).

The silane layers (Fig. 10.12a) show increasing friction forces with decreasing chain length. This increase in friction forces is attributed to the increased disorder which is concomitant with decreasing chain length. It has been reasoned that disorder favors an increase in the number and type of low-energy modes that are available for excitation and energy dissipation [126].

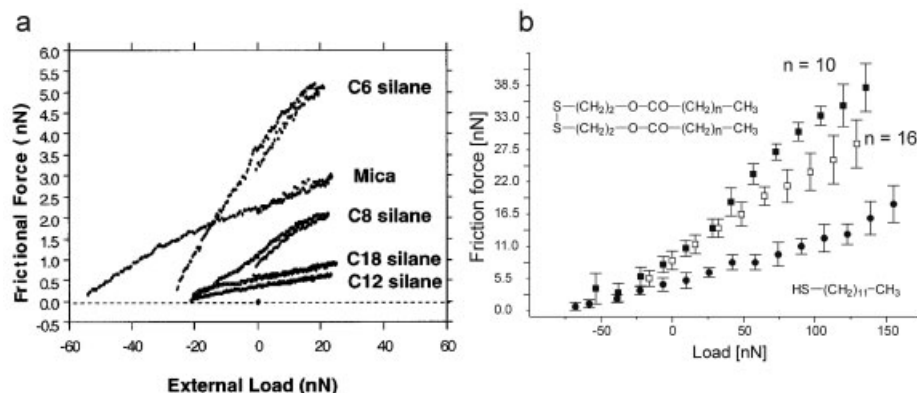


Fig. 10.12 (a) Friction vs. load curves obtained for C₁₈, C₁₂, C₈, and C₆ alkylsilane monolayers on mica and a Si₃N₄ tip. A curve for mica is also shown as a reference. (Reprinted with permission from ref. 126.

Copyright 1997 American Chemical Society); (b) Friction force vs. load plot for hydrocarbon thiol and disulfides. (Reprinted with permission from ref. 125. Copyright 1999, Elsevier.)

The contact angles measured with water on the organosulfur-based SAMs were reported to be slightly lower for the short-chain or disordered disulfide systems (Fig. 10.12b), respectively, but in terms of surface chemical composition there are no significant differences [127]. The observed frictional differences are the result of the difference in phase states of the SAM (liquid-like versus solid-like), which is coupled to differences in the modes available for energy dissipation. These results show that identical functional groups exposed at the surface may give rise to different friction forces and coefficients in CFM, and that the definition of the conformational order of SAMs used in CFM on tips may be a critical factor for the acquired tribological data.

Friction forces on oriented samples may also depend on the relative angle between the directions of scan and orientation. The phenomenon of friction anisotropy has been observed for a variety of different samples, including highly oriented pyrolytic graphite [128], lipid bilayers [129], lamellar polymer crystals [130], and uniaxially oriented polymers [113, 131]. The friction anisotropy in these samples is due to the differences in azimuthal orientation of structurally equivalent domains or features, but certainly *not* differences in surface chemical composition. The domains can consist of crystal lattices with different tilt angles of molecules [132], or different polymer lamellar crystal fold planes (Fig. 10.13). None of these observations of friction differences is at all related to differences in surface energy or chemical composition in the context of CFM.

The example of lamellar PE crystals demonstrates that the interpretation of friction images may require detailed knowledge about the specimens, and that this can be a shortcoming of friction mode CFM on oriented samples.

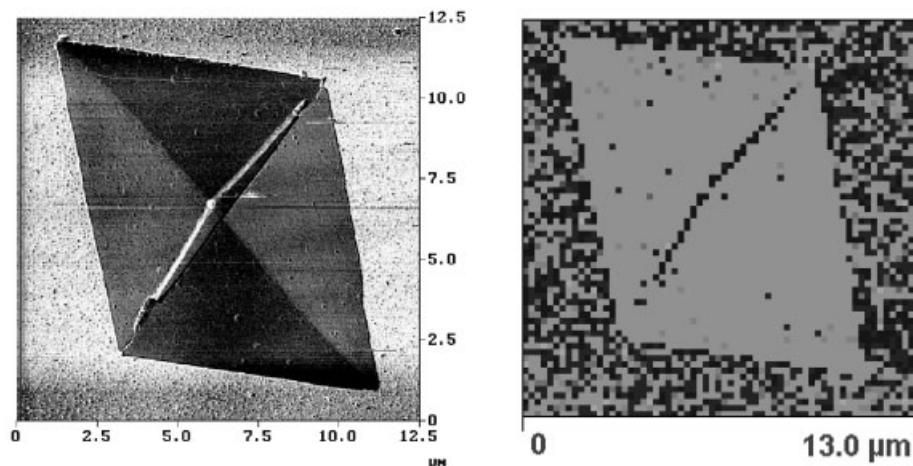


Fig. 10.13 Left: friction force image of a solution-grown PE lamellar crystal obtained in air. Right: pull-off force image of the same lamellar PE crystal. Bright tones correspond to low pull-off forces (-50 nN), dark tones to high forces (-80 nN). The friction and pull-off forces of PE in air have lower values than mica. (Reproduced with permission from ref. 133. Copyright 1999, American Chemical Society.)

10.3 Applications of CFM

As discussed above, tip-sample forces are the basis for chemically sensitive imaging by CFM. Thus, in addition to the control of these forces by means of functionalized tips and by appropriate choice of the imaging medium, the measurement and understanding of the factors that contribute to the interactions are central elements of the CFM strategy. Following a discussion of some corresponding fundamental aspects, key applications of CFM will be highlighted.

10.3.1 Surface Characterization by CFM

Surface characterization by CFM may comprise the quantitative determination of relevant surface physicochemical parameters, including the determination of local surface chemical composition.

10.3.1.1 Tip-Sample Forces and Interfacial Free Energies

The usefulness of pull-off force and friction force measurements for distinguishing between differently terminated SAMs has been discussed above. In addition, the determination of pull-off forces can be used in conjunction with a measurement of the tip radius and the application of Eqs. (2) and (3) to deduce free energies of surfaces, which are difficult (or even impossible) to assess by other methods. In particular, CFM is applicable to high free energy surfaces which are readily wetted

by liquids. For instance, the surface free energy of COOH SAMs in contact with EtOH was determined as $\gamma_{\text{COOH}} = 4.5 \text{ mJ m}^{-2}$. The interfacial free-energy $\gamma_{\text{CH}_3\text{-COOH}}$ was found to be 5.8 mJ m^{-2} [116].

The role of the imaging medium was considered by Sinniah et al. [134], who discussed the effect of solvent exclusion on the adhesive forces between the cantilever tip and the surface in CFM. The effect was found to be most pronounced in water, while media such as ethanol and hexadecane showed smaller contributions of solvent exclusion. For ethanol the authors suggested contributions also from solvent-mediated tip-sample interactions. These considerations are important for understanding and predicting contrast in CFM force imaging, as will be further discussed in Section 10.3.2.

Support for the contribution of the solvent comes from temperature-dependent CFM studies reported by Noy and coworkers [135]. In these experiments clear evidence for entropic contributions were observed, which have been attributed to the solvent. As shown in Fig. 10.14, the pull-off forces between a COOH-terminated tip

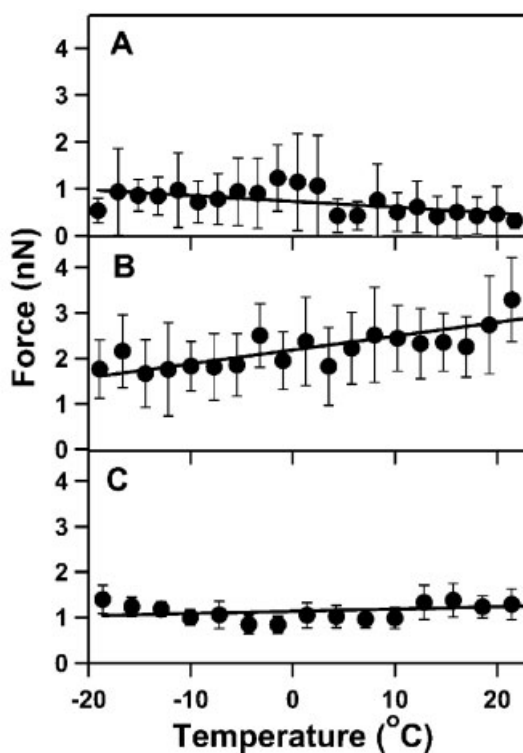


Fig. 10.14 Plots of measured adhesion force as a function of temperature for COOH-terminated tip and sample, in (A) hexane; (B) ethanol; (C) ethanol-hexane mixture (1:1).

Each data point corresponds to an average of 40 individual force vs. distance curves. (Reprinted with permission from ref. 135. Copyright 2003, American Chemical Society.)

and a sample show different dependences in different media. The increase in the pull-off forces with temperature observed in ethanol is attributed to the presence of an entropic barrier originating from the ordering of the ethanol molecules at the solution/substrate interface.

For a rationalization of image contrast in CFM, it is necessary to understand the contributions of different interactions. In the case of apolar polymers, pull-off force results showed excellent agreement with calculations based on the Lifshitz theory of van der Waals interactions (see Section 10.2.2.1). Using an appropriate imaging medium (i.e., perfluorodecalin), the dispersive van der Waals forces could be amplified, which allowed Feldman et al. to differentiate apolar polymers with, e.g., gold-coated or silicon oxide-coated AFM probe tips (Fig. 10.15) [79].

For polar polymers, the same authors reported a reasonable correlation with water contact angles [79]. Similar observations were made for a range of surface-treated polyolefins (Fig. 10.16) [91].

More recently, Vezenov et al. investigated the adhesion between epoxy resins and functionalized tips by CFM, and in particular the role of H-bonding in this process [136]. The chemical character of both the tip functionality and the resin, and additionally the type of liquid, influenced the pull-off forces. In alcohol–water mixtures a direct correlation between surface free energy and adhesion forces was observed. The authors show that the trends in the magnitude of the pull-off forces for chemically heterogeneous systems measured by CFM can be rationalized quantitatively by the surface tension of components approach. However, they noted an effect of inelastic deformations of the polymer, which contributed to the measured pull-off forces.

Different chemical compositions may also occur as a consequence of exposure of different crystallographic facets in crystalline materials. For instance, CFM in intermittent contact mode was used to differentiate different crystallographic planes in measurements with SAM-modified probes in various relative humidities [137]. Using hydrophobic methyl-terminated and hydrophilic carboxylic-acid derivatized AFM tips, the (001) and (100) surfaces of individual aspirin crystals could be distinguished in amplitude–phase, distance (a–p,d) measurements. The authors concluded that the observed differences in the a–p,d measurements were due to distinct variations in the surface chemistry of the crystal planes.

A similar differentiation of crystal facets was reported for single crystals of cholesterol monohydrate [138]. CFM pull-off force experiments showed that the cholesterol monohydrate plate face is terminated with 3-hydroxyl groups (002) in aqueous environments. When the imaging medium is changed to anhydrous ethylene glycol solution, the surface becomes terminated predominantly with alkyl groups (001).

On the basis of the brief discussion above, it becomes clear that technologically relevant questions regarding surface homogeneity at sub-50 nm length scales [23, 91] and dispersion of phases in multiphase systems, as well as the localization of additives [139], can be addressed by CFM.

The highly localized character of CFM has been quantified in the early work of Lieber and coworkers based on the application of JKR theory [23]. Other work sug-

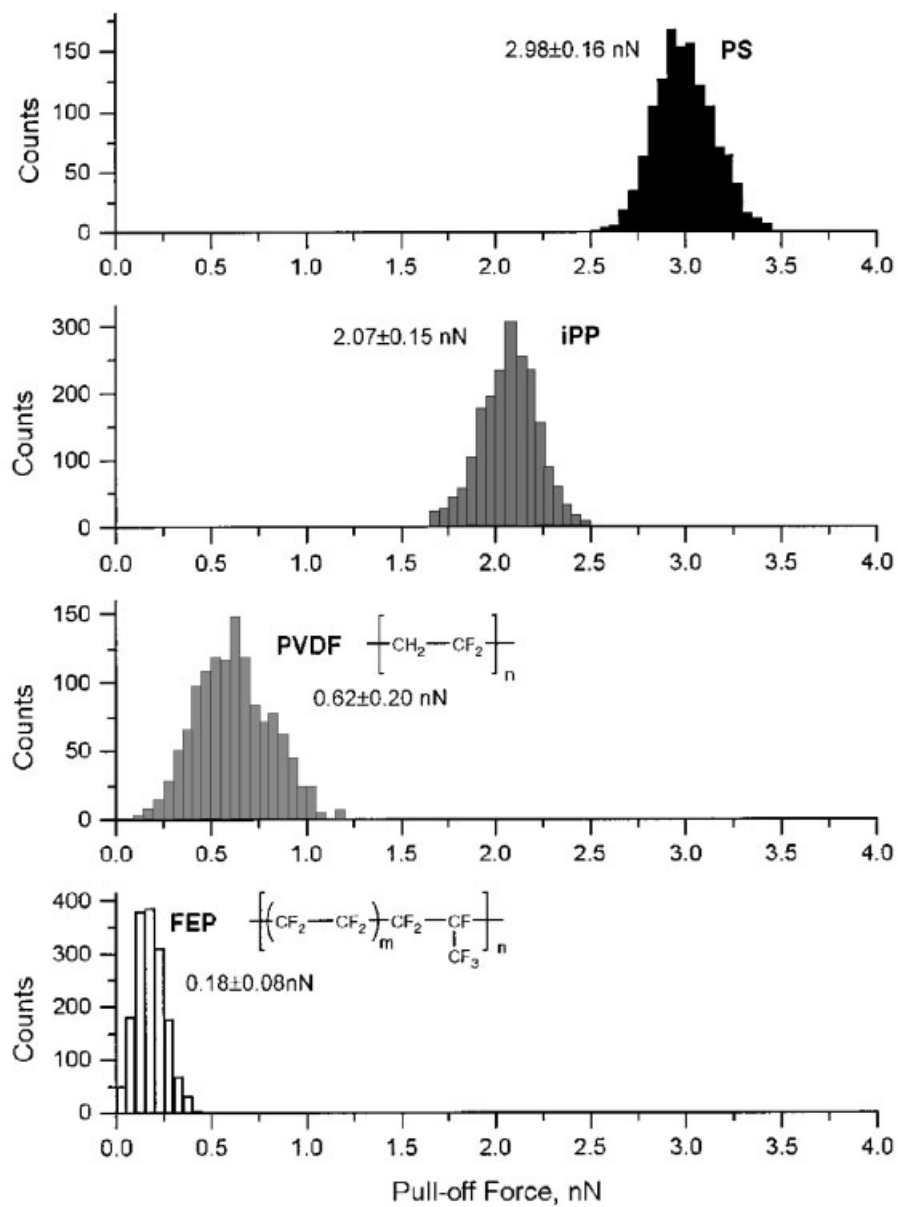


Fig. 10.15 Pull-off force histograms recorded with a SiO_x probe on polystyrene (PS), isotactic polypropylene (iPP), poly(vinyl difluoride) (PVDF), and poly(tetrafluoroethylene-co-hexafluoropropylene) (FEP), respectively, in perfluorodecalin. (Reprinted with permission from ref. 79. Copyright 1998, American Chemical Society.)

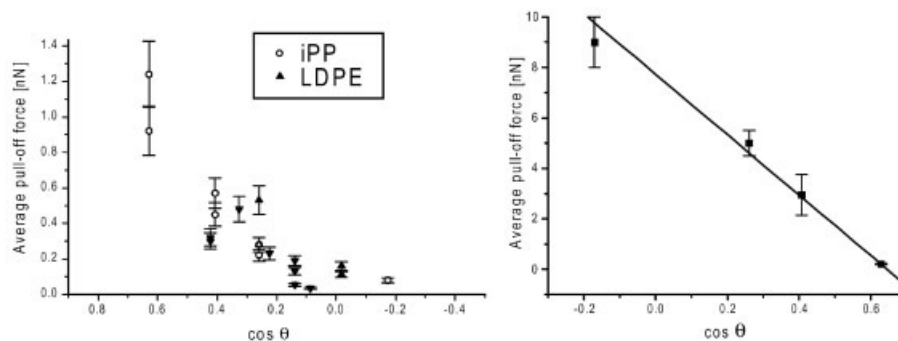


Fig. 10.16 Average pull-off forces measured with COOH-terminated tips on modified polyolefin surfaces (iPP, isotactic polypropylene; LDPE, low-density polyethylene) in ethanol (left) and with OH-terminated tips on oxyfluorinated iPP in water (pH 3.8, right) as a function of $\cos \theta$ (θ = contact angle measured with water). (Reprinted in part/adapted with permission from ref. 91. Copyright 2000, American Chemical Society.)

gested that the number of effectively interacting molecular pairs can be obtained from a statistical analysis and the assumption that the number of molecular contacts and the pull-off force are proportional [140]. More recently, pull-off forces in CFM were modeled by Skulason and Frisbie using a modified JKR model that accounts, via a modified work of adhesion, for the formation of discrete numbers of chemical bonds (n_{bonds}) between the tip and the surface [141]. According to these authors the pull-off force scales as $(n_{\text{bonds}})^{1/2}$, in contrast to previous assumptions which stated a linear scaling [140]. The proposed model can explain the periodic peak progressions observed in pull-off force histograms [141].

While the interactions discussed so far are not specific in the sense of molecular recognition, an abundance of examples have been reported in the literature where specific interactions were determined by CFM approaches. One of the spectacular results is the chiral recognition reported by McKendry et al. [142]. These authors studied the pull-off forces between AFM tips and surfaces functionalized with different enantiomers of mandelic acid. Using CFM adhesion force and the frictional force measurements these authors showed that different combinations of enantiomers on the surface and tip lead to consistently different pull-off force values. The histograms (Fig. 10.17) show that the interactions between *R* and *S* forms are much stronger than *R*–*R* and *S*–*S* interactions. Data acquired with a racemic tip show intermediate adhesion force values. This behavior was attributed to different adhesion forces between transient diastereomeric complexes formed between the chiral molecule on the tip and either the *R*- or the *S*-mandelic acid on the surface.

A very closely related field is the so-called single-molecule force spectroscopy [30–32]. Here AFM tips are functionalized, e.g., with ligand molecules. Specific interactions with surface-immobilized receptors are measured. The first examples include relatively large molecules, often with biological relevance, such as DNA [143], cell adhesion molecules [144], or biotin–streptavidin [145]. The determination of

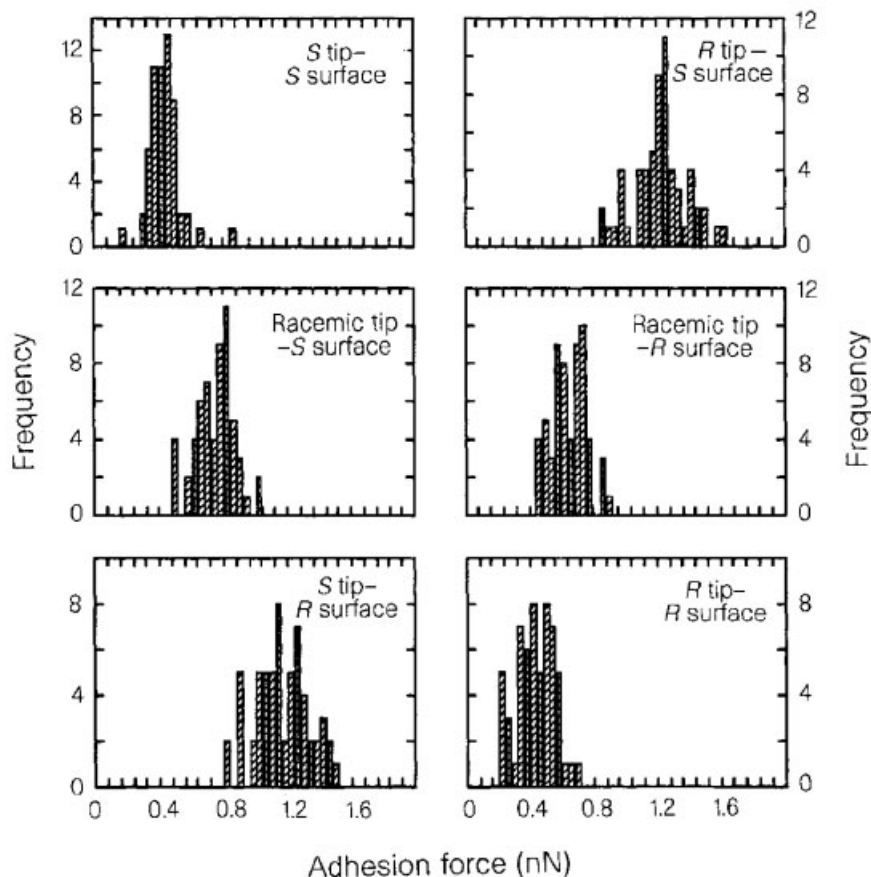


Fig. 10.17 Histograms of the pull-off forces for different combinations of *R* and *S* enantiomers of mandelic acid. To minimize variations in data caused by use of different tips, measurements (60 *f*-*d* curves per

combination) were made using a single tip on each of the six chiral surfaces. (Reproduced with permission from ref. 142. Copyright 1998, Nature Macmillan Publishers Ltd.)

single nucleobase-pair mismatches has been reported [146]. More recently this method was also extended to measure individual supramolecular host-guest interactions (see also Chapter 11) [29, 147-149].

10.3.1.2 Acid-Base Titrations

An important application of CFM is the determination of the ionization states of surfaces. Via pH dependent force or friction measurements, various authors have attempted to determine surface pK_a values, as well as to localize ionizable groups in heterogeneous systems [117, 150].

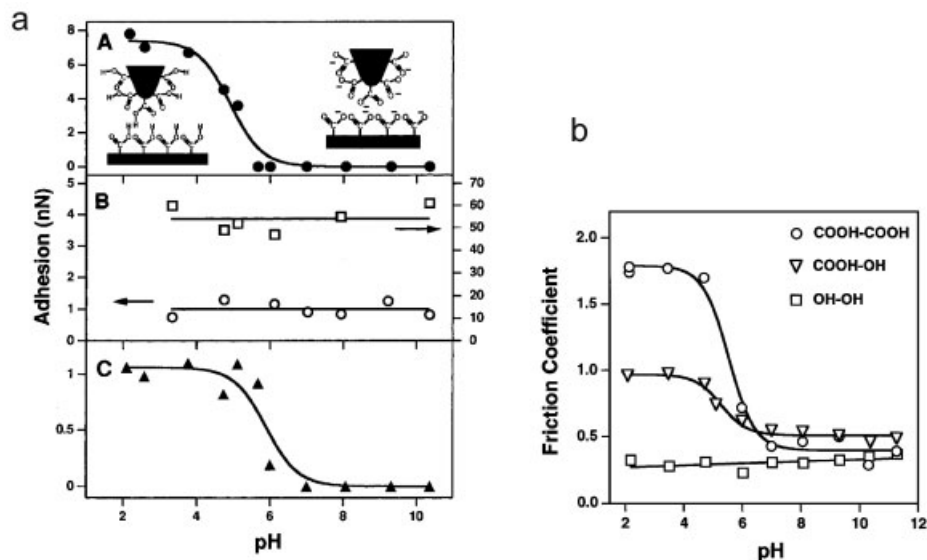


Fig. 10.18 (a) Adhesion force titration curves recorded in buffered solutions. Adhesion force vs. pH for: (A) COOH/COOH; (B) CH₃/CH₃ (filled squares); OH/OH (filled circles); (C) COOH/OH contacts. The diagrams of the tip and sample show the interfacial chemistry of the surface functionality schematically; they do

not portray the hydrocarbon chain or true tip-sample contact area accurately. (b) Friction coefficient vs. pH for COOH-COOH, COOH-OH, and OH-OH contacts. (Reprinted with permission from ref. 117. Copyright 1997, American Chemical Society.)

As shown in Fig. 10.18, pull-off force or friction measurements of SAMs with various end groups are sensitive to the state of ionization [117]. Since the corresponding data recorded on hydroxyl-terminated SAMs do not show any dependence on pH, the titration behavior can be attributed to different degrees of protonation of the carboxylic acid groups. For applications it is imperative to utilize a tip functionality, such as OH, that does not show any pH-dependent forces in the pH range investigated.

The general features of the force titration measurements have been confirmed by various groups [150, 151]. However, the effect of ionic strength has been addressed only more recently. Smith and coworkers reported a very strong dependence of the chemical force titration behavior of carboxylic and phosphonic acid functionalized tips and substrates on the electrolyte concentration [152]. At higher ionic strengths, sigmoidal curves similar to those shown in Fig. 10.18(a) were observed, while at lower ionic strengths there was a clear maximum in the force versus pH data (Fig. 10.19). This maximum in the low electrolyte concentration force titrations was attributed to the formation of strong hydrogen bonds between neutral and ionized species on the CFM tip and the substrate. For high ionic

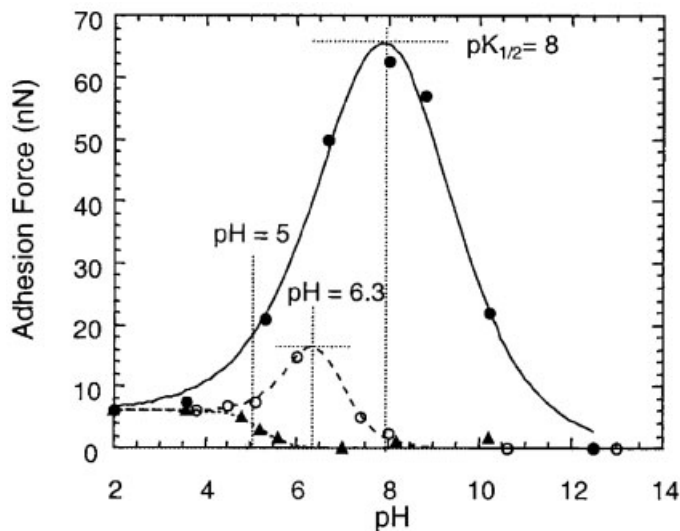


Fig. 10.19 Chemical force titration curves for tip and substrate, both modified with 11-mercaptoundecanoic acid SAMs acquired at three electrolyte concentrations: low (10^{-7} M, solid circles), intermediate (10^{-4} M, open

circles), and high (10^{-1} M, solid triangles). The curves have been added only as a guide to the eye. (Reprinted with permission from ref. 152. Copyright 2000, American Chemical Society.)

strengths the formation of an electric double layer prevents formation of the H-bonds. Smith et al. also noted that the determination of the pK_a can only be achieved under low-salt conditions.

10.3.1.3 Following Surface Chemical Reactions in SAMs

The measurements of pull-off forces for various pH values are in fact CFM measurements that aim at following interfacial chemical reactions. Owing to the sensitivity of pull-off forces in CFM to surface chemical composition, this method can also be used to probe surface chemical reactions *ex situ* (in principle with high lateral resolution), or even *in situ*.

An early example published in the literature is the gas-phase reaction of surface-immobilized hydroxyalkanethiols with isocyanates. Werts and coworkers showed that this surface chemical reaction can be followed *ex situ* [153]. Based on the assumption that the free energies of the CFM probe/sample surface interface and of the sample surface are only influenced by the change in the end groups during the reaction, and that the energies are directly proportional to the fraction of CH_3 and OH groups, conversions were calculated from the measured pull-off forces using JKR theory. In principle, CFM can complement other surface analytical techniques in order to assess the extent of surface reactions. However, instrumental drift in the intrinsically slow *in-situ* force mapping during wet chemical reactions on

surfaces (a 64×64 pixel² map is typically acquired in several minutes) prevented the application of CFM for *in-situ* studies of reactions with high resolution.

Using a slight modification of the CFM approach it is possible to circumvent these problems. In the “inverted CFM” approach [110], the reactants to be studied are immobilized on a gold-coated AFM tip. To follow the kinetics of the reaction of the functional groups exposed in the SAM on the tip, the variation of pull-off forces between the tip coated with the reactant and an inert surface is monitored as a function of time *in situ* in the reaction medium. As the surface characteristics of the inert substrate do *not* vary as a function of position, the pull-off force values contain compositional information only about those reactant groups on the tip that reside inside the tip–sample contact area [154]. This approach can provide quantitative information about the rate and mechanisms of surface reactions in SAMs down to a level of 10–100 molecules based on pull-off force data, as shown in Fig. 10.20 [155].

10.3.2

Compositional Mapping of Heterogeneous Surfaces

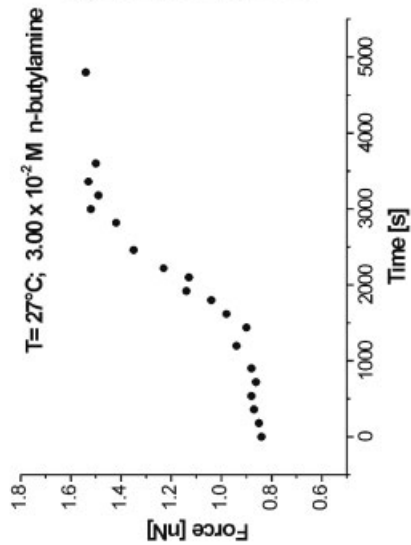
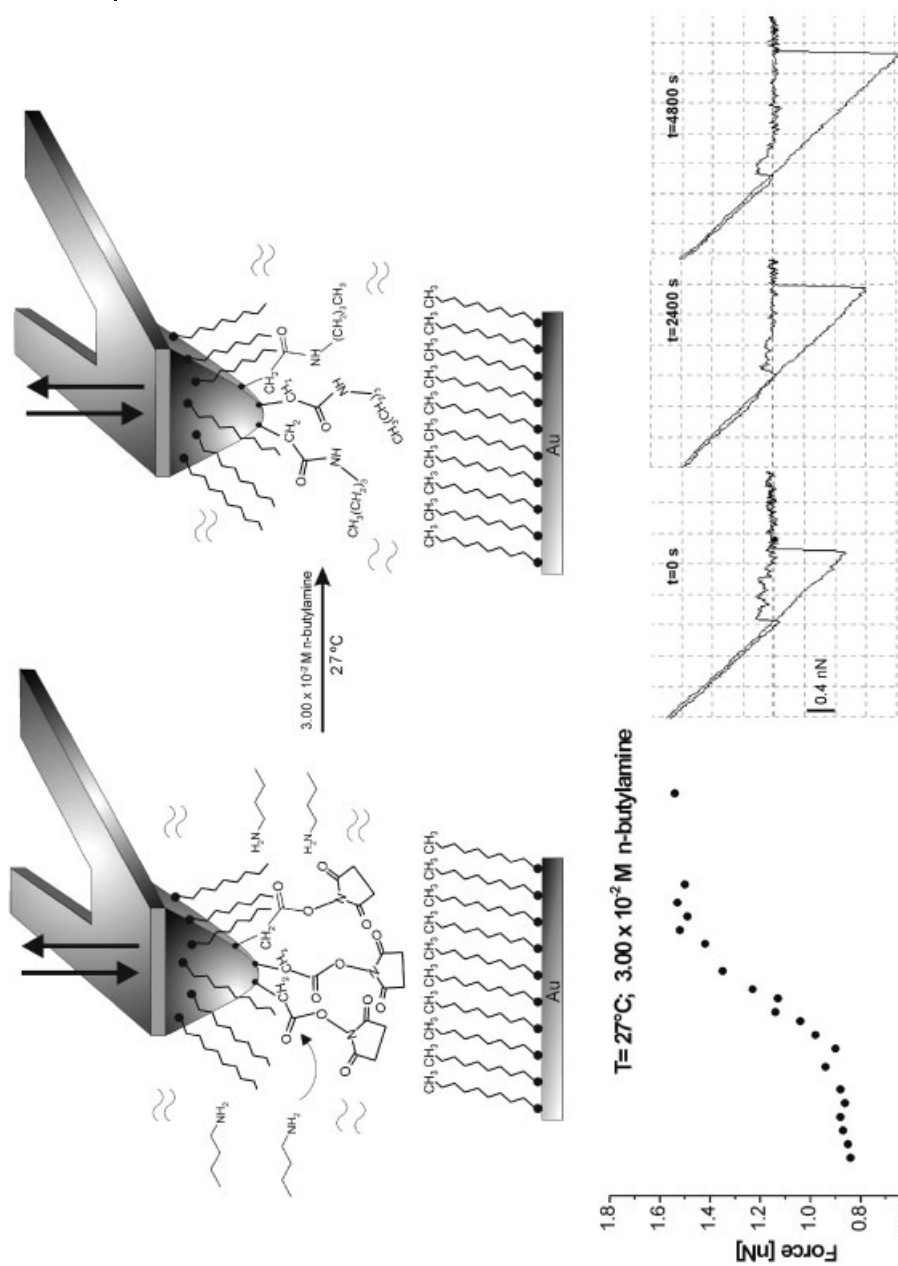
The laterally resolved mapping of chemical compositions on organic and polymeric surfaces down to the nanometer size regime remains a challenge. Recent progress in CFM has demonstrated that this previously unattainable regime can in principle be analyzed. However, it must be noted that friction measurements which are devoid of quantitative information on local surface chemical composition are frequently reported in the literature. This shortcoming originates from instrumental problems and lack of proper calibration and quantification.

10.3.2.1 Micro- and Nanometer-Scale Patterned SAMs

Patterned SAMs have been excellent model systems for validating the CFM approach, as shown in the original work of Lieber and coworkers [22]. In Fig. 10.10 data taken in tapping mode, as well as friction mode CFM, on micron-scale patterned SAMs have been shown. Considering the very limited tip–sample contact area, it is clear that a resolution down to the nanometer size regime is in principle feasible.

The mapping of patterned monolayers prepared by microcontact printing, lithography, and other approaches is amply described in the literature. This work on highly defined model systems helped to establish CFM as a surface analytical technique with chemical sensitivity [22–24, 33, 34, 116, 117, 156, 157]. In addition, new insight into patterned thin-layer systems has been obtained [158].

Recent work by Brewer and Leggett indicated that binary SAMs on gold may show phase separation [159]. The pull-off force distributions of single-component systems can be fitted to symmetric Gaussian distributions, irrespective of the nature of the terminal group on either the tip or the SAM. By contrast, the distributions of mixed binary SAMs were asymmetric and could not be fitted with a Gaussian distribution. The authors attribute this finding to the presence of phase separation.



10.3.2.2 Heterogeneous and Multiphase Systems

In this section we will discuss several representative examples in which heterogeneous systems with typical length scales of microns down to single molecules have been analyzed successfully by CFM.

The previously discussed selective amplification of dispersive van der Waals interactions in the work of Feldman et al. has also been exploited by these authors to image a phase-separated blend of polystyrene (PS) and poly(methyl methacrylate) (PMMA) with chemical contrast [79]. For this purpose gold-coated and silicon oxide-coated tips were used in perfluorodecalin as imaging medium. The gold-coated tip experienced higher friction forces on the PS than on the PMMA. Interestingly, the silicon oxide-terminated tip shows an inverted contrast, consistently with the theory (Fig. 10.21). This exemplifies the way in which the above-mentioned Lifshitz theory can be applied successfully to predict the chemical contrast for various apolar polymers imaged by different tips. It should be noted, however, that the optical constants of the materials in question must be known or must be determined independently in order for Eq. (5) to become applicable.

Sinniah et al. also reported on the successful discrimination of different components of polymer blends [134]. Their work was based on the differences in solvent exclusion effects among polyamide-rich regions from poly(ethylene glycol)-rich regions in a blocky segmented copolymer in water. The combination of hydrophobic methoxy-terminated tips and more hydrophobic polyamide-rich domains led to pronounced solvent exclusion and hence the corresponding friction forces exceeded those measured on the PEG-rich domains. Using amide-terminated tips, the contrast was significantly reduced, which implies imaging with predictable contrast.

Chemically heterogeneous polymer samples with smaller structures were investigated by Werts et al., who reported on successful chemically sensitive imaging of a microphase-separated block copolymer (PS–poly(vinylpyridine) (PVP) heteroarm star copolymer) [160]. The resolution of the CFM data is consequently better than ~ 30 nm. Using carboxylic-acid functionalized tips, the friction contrast was pronounced, while methyl-terminated tips yielded no contrast between the

← **Fig. 10.20** Top: schematic drawing of “inverted” CFM (iCFM) for the reaction between *N*-hydroxysuccinimide (NHS) esters and *n*-butylamine in an aqueous medium. In iCFM the pull-off forces between an AFM tip covered with a SAM of the *N*-hydroxysuccinimidyl-terminated disulfide NHS–C10 and an inert octadecanethiol SAM are measured *in situ* during the conversion of the reactive groups attached to the tip. The interaction between the tip and the inert surface varies systematically with the extent of the reaction and hence allows one to investigate the reaction kinetics quantitatively. (Reprinted with permission from ref. 155. Copyright 2004, Elsevier.) Bottom: variation of pull-off forces as function of reaction time during aminolysis of NHS–C10 determined by iCFM. Each data point corresponds to the mean pull-off value of 200 individual pull-off events. Representative force–displacement curves are shown as insets ($F \propto$ extent of reaction). (Reprinted with permission from ref. 154. Copyright, 2004 Elsevier.)

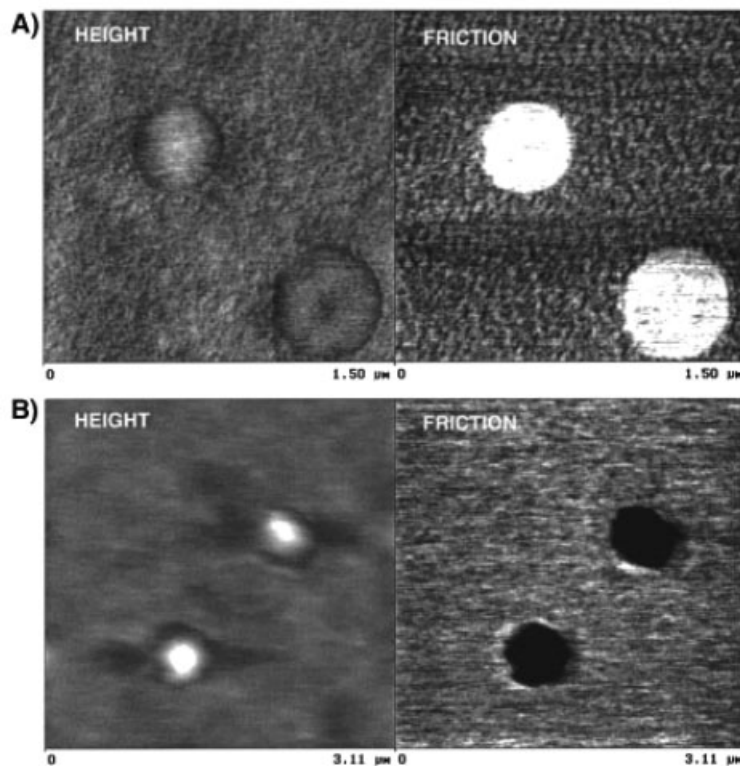


Fig. 10.21 Height (AFM) and friction (LFM) images of a spin-cast polystyrene/poly(methyl methacrylate) polymer blend [PS/PMMA (1:10 w/w)], obtained with (A) gold-coated and (B) SiO_x tips under perfluorodecalin. (Reprinted with permission from ref. 79. Copyright 1998, American Chemical Society.)

microphase-separated domains. This observation was attributed to the strong interactions between the carboxylic acid groups on the tip and the pendant pyridine groups of the 2-PVP block.

Heterogeneous, particulate-filled elastomer samples, as well as various industrially applied rubbers, have been investigated by Trifonova and coworkers [161]. While the silica and carbon black filler particles were also detected in intermittent contact AFM phase images, the mapping of pull-off forces using derivatized tips showed that CFM can be used to differentiate and distinguish filler particles and elastomeric matrix. Since filler particle surface properties and distributions are directly coupled to mechanical properties of the elastomers, CFM can provide important insights on the nanometer scale.

Duwez et al. showed that additives on the surface of polypropylene can be detected and mapped by CFM [162]. Modified AFM tips with methyl and hydroxyl terminal functional groups were used to first characterize the adhesive interaction

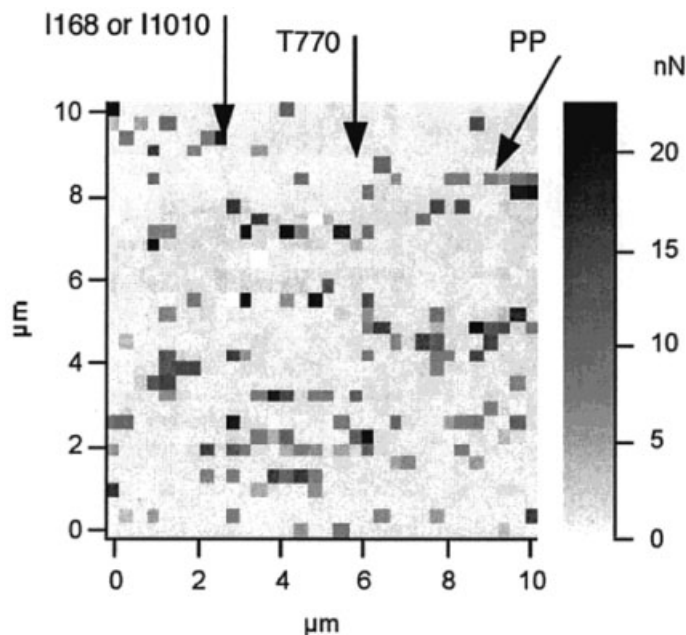


Fig. 10.22 Adhesion map obtained on stabilized polypropylene (0.05 wt.% of Irganox 1010, 0.1 wt.% of Irgafos 168, and 0.5 wt.% of Tinuvin 770) with a CH_3 -terminated tip in water. Dark shading indicates high adhesion (10–20 nN), and bright shading indicates low adhesion (1–2 nN). (Reprinted with permission from ref. 162. Copyright 2001, American Chemical Society).

on different known additives in water and in a nitrogen atmosphere (Fig. 10.22). Thereby a characteristic fingerprint was obtained for each additive. Finally, it could be shown on the basis of pull-off force measurements that a UV stabilizer covers the polymer surface.

Single, surface-adsorbed, positively charged, high molar mass polyethyleneimine (PEI) molecules were investigated by Schneider et al. using tips modified with amino- and methyl-terminated groups. The molecules were shown to adsorb as individual molecules with a measured diameter between 30 and 60 nm. In pulsed force CFM scans, enhanced chemical sensitivity was observed. While methyl-terminated tips showed high adhesive forces on the molecules (Fig. 10.23, left), the amino-terminated probes showed low adhesion at pH 6, where partial protonation of the tip can be expected (Fig. 10.23, right) [163]. Hence the imaging with chemical sensitivity was demonstrated for single large macromolecules.

10.3.2.3 Surface-Treated Polymers

Oxyfluorinated isotactic polypropylene (iPP) films [164], plasma-polymerized allylamine (PPAA) [165], and plasma-modified iPP [166] were investigated by CFM measurements using OH-terminated tips in an aqueous medium at variable pH

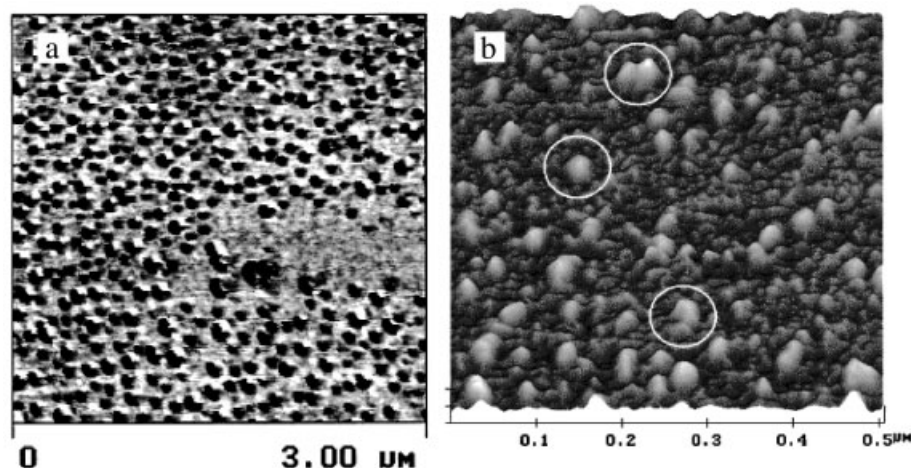


Fig. 10.23 (a) *In-situ* pulsed force adhesion image of single PEI molecules on mica with a CH_3 -modified tip using scanning force microscopy at pH 2. (b) *In-situ* pulsed force image of randomly arranged single PEI molecules on a mica surface using a NH_2 -modified tip by scanning force microscopy at pH 6. (Reprinted (in parts) with permission from ref. 163. Copyright 2002, American Chemical Society.)

[91]. Oxyfluorination introduces carbonyl groups, α -fluorocarboxylic acids, peroxides, hydroxyl groups, ether groups, and acid fluoride groups that hydrolyze slowly in contact with atmospheric moisture to form carboxylic acids. The plasma-modified iPP and the PPAA possess ionizable COOH and NH_2 groups, respectively. By means of pH-dependent pull-off force measurements the contribution of the ionizable functional groups can be separated from the rest. In these studies, hydroxy-terminated (OH) tips were used as these do not show any pH dependence in force measurements [117], while the interaction between these hydrophilic tips and various surfaces is relatively weak in aqueous environment [134]. By measuring pull-off forces as a function of pH, a corresponding “force titration” curve and a “force $\text{p}K_a$ ” value can be obtained. As displayed in Fig. 10.24, the pull-off forces on the different films show a clear dependence on the pH of the solution, while the untreated iPP film (Fig. 10.24c) does not show any dependence.

The force images acquired on oxyfluorinated iPP at pH 6.8 often showed significant local variations in pull-off force (Fig. 10.25) [91]. At pH 8.0 the interaction was exclusively repulsive. The observation of patches where high forces are measured at pH close to the “ $\text{p}K_a$ ”, and the observation of homogeneous repulsion at $\text{pH} > \text{“p}K_a\text{”}$ indicate that the local functional group distribution cannot be homogeneous.

Arrows indicate small areas of high pull-off force measured at pH 6.8, which were interpreted as areas where the carboxylic acid groups are protonated to a significant extent. The diameter of these areas is ~ 30 nm. For higher pH values

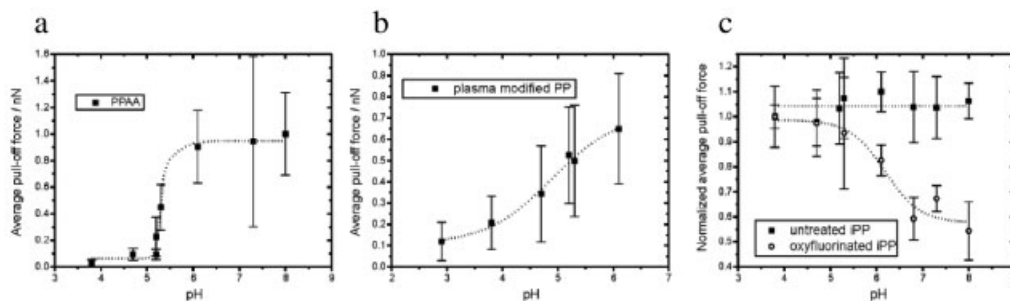


Fig. 10.24 Force titration data acquired with hydroxy-terminated tips for representative samples of the three model surfaces studied. For (a) PPAA and (b) ammonia plasma-modified PP the average pull-off forces are shown; (c) for the untreated and oxyfluorinated iPP the values were normalized to the values

found for pH 3.8 (errors bars correspond to the standard deviation of the mean determined from the pull-off force distribution histograms). The dotted lines have been added to guide the eye. (Reprinted with permission from ref. 166. Copyright 1997, Royal Chemical Society.)

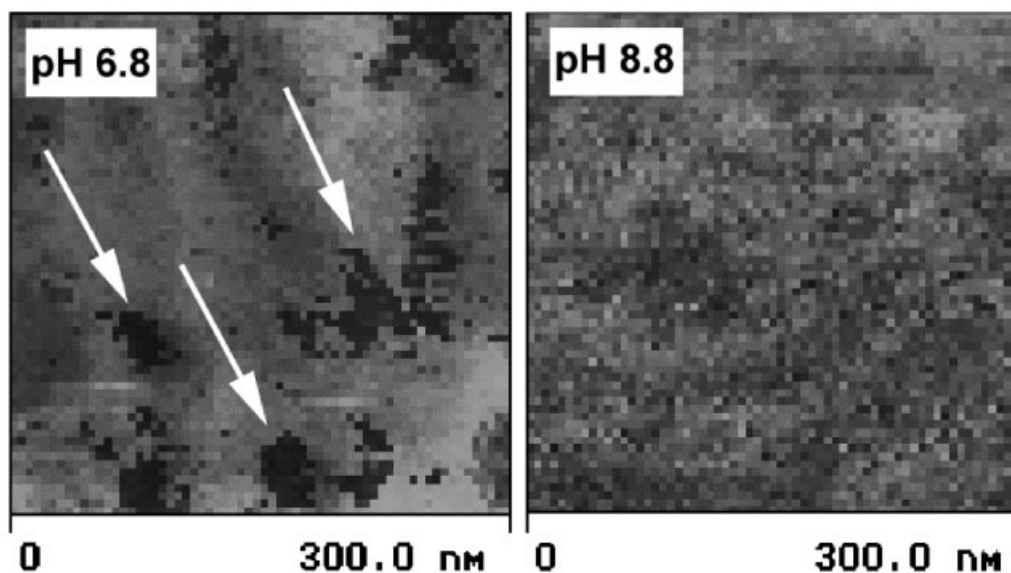


Fig. 10.25 Force–volume images of oxyfluorinated iPP ($\gamma = 39.6 \text{ mN m}^{-1}$) at pH 6.8 (left) and pH 8.8 (right). Dark color indicates high adhesion ($\approx 0.3 \text{ nN}$ for pH 6.8, $\approx 0 \text{ nN}$ for pH 8.8); bright color indicates low adhesion (0 nN for pH 6.8 and pH 8.8). The arrows indicate areas of high pull-off forces,

which were attributed to domains with the most hydrophobic character, i.e., a lower density of polar COOH and OH functional groups introduced by the oxyfluorination. (Reprinted (in parts) with permission from ref. 91. Copyright 2000, American Chemical Society.)

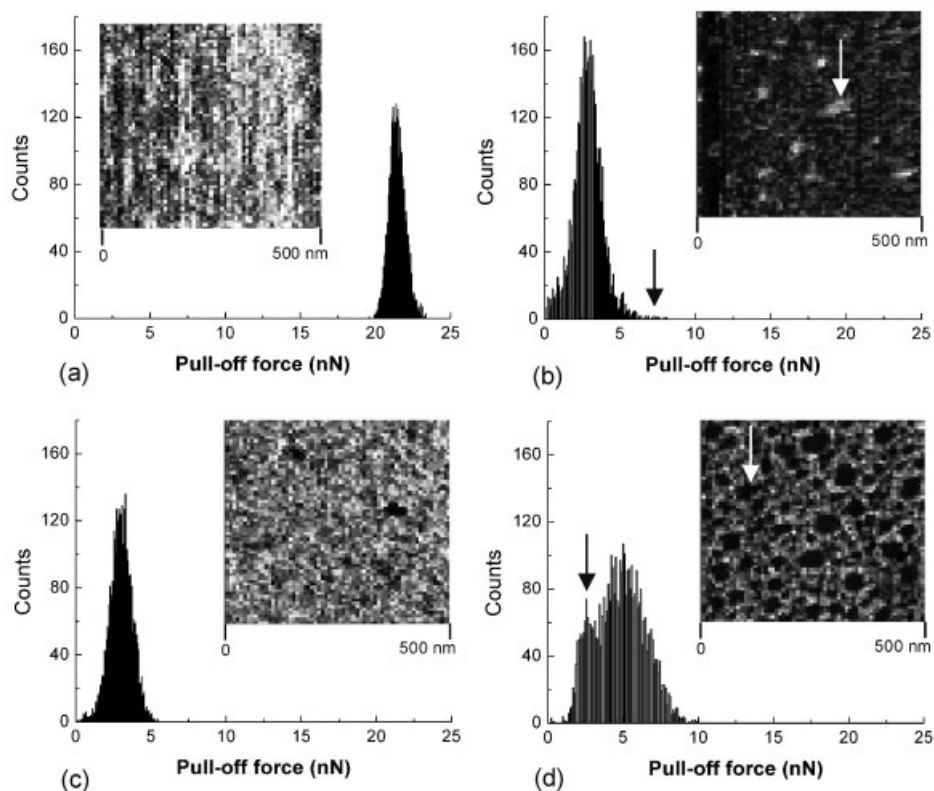


Fig. 10.26 Representative histograms of the pull-off forces and corresponding adhesion (pull-off force) images of: (a) unexposed PDMS, and oxidized PDMS (b) 0.1, (c) 8, and (d) 40 days after exposure for 60 min to UV/

ozone. In the adhesion images, the gray scales are individually scaled from dark (low pull-off) to bright (high pull-off). (Reprinted with permission from ref. 167. Copyright 2004, American Chemical Society.)

(pH > 8.0) only repulsion is detected. The areas in which attractive interactions are measured at pH 6.8 contain carboxylic acid groups with a higher “ pK_a ” than the regions, where repulsion is observed. This can be attributed tentatively to a difference in local hydrophobicity. The most hydrophobic local environments will be the areas where the deprotonation of carboxylic acid groups is least favored. Thus, these areas will be more protonated at pH 6.8 than the more hydrophilic areas.

Hillborg and coworkers investigated the surface hydrophobicity of UV/ozone-treated poly(dimethylsiloxane) (PDMS) as a function of storage/recovery time using CFM [167]. The CFM data (pull-off force images and the corresponding histograms/force distributions) showed that laterally homogeneously oxidized surfaces are obtained for exposure times of less than 30 min. These surfaces are characterized by an increased modulus and by a high segmental mobility of PDMS. The subsequent “hydrophobic recovery” is accompanied by a gradual increase in

pull-off forces and a decrease in normalized modulus. The corresponding values were found to approach the values of unexposed PDMS after 8–50 days. Longer exposure times (60 min) led to the formation of a hydrophilic silica-like surface layer. Under these conditions a gradual surface reconstruction within the silica-like layer occurred with time after exposure, where a hydrophilic SiO_x-enriched phase formed <100 nm-sized domains, surrounded by a more hydrophobic matrix with a lower normalized modulus (Fig. 10.26).

These data show that CFM can provide important insights into surface properties and their transient behavior, including compositional surface heterogeneity, at sub-100 nm length scales in relevant areas for surface and nanoscience/nanotechnology applications (e.g., soft lithography and microfluidics).

10.4 Outlook

More than ten years after the first reports on chemical force microscopy, AFM-based approaches for high-resolution lateral mapping of surface chemical compositions have been significantly improved and a large body of literature is now available. The attention has been focused on refining chemical modification procedures of CFM probe tips and on a more fundamental understanding of tip–sample interactions. Furthermore, the improvement of lateral and force resolution, and, quite importantly, the application of the methodology to tackle previously unanswered or inaccessible questions and problems were addressed. It is fair to say that “chemical imaging” at this point remains indirect, as it is inherently mediated by tip–sample interactions and adhesive (or frictional) forces. Thus, CFM cannot compare in terms of quality (features) with the physicochemical data that provide atomic number contrast, as obtained in energy-dispersive X-ray analysis (EDX), spectroscopic traces of specific chromophores in various local spectroscopies (fluorescence or Raman nearfield scanning optical microscopy, NSOM), or direct structural information via characteristic molecular fragments in ToF-SIMS.

However, the combination of high (in some cases much higher than any alternative technique) lateral resolution topographic imaging with indirect, but highly localized, chemical information (in some cases down to the single-molecule level), and with the possibilities of acquiring data in liquid media under physiological *in-vitro* conditions, places CFM in a unique position for surface analysis in many areas. Applications in the area of surface-treated, aged, or filled polymers, as well as in the area of well-defined single crystals of biologically relevant or chemically heterogeneous materials, underline the viability and importance of this methodology. Hence we expect that CFM will contribute increasingly to the solution of problems in applications ranging from heterogeneous multiphase systems, through surface versus bulk behavior, surface blooming of additives, and aging, to *in-situ* studies of surface reactions. Finally, the recent developments aimed at unraveling interactions in host–guest (supramolecular) chemistry at the level of individual molecules rely on CFM approaches; the combination of quantitative force

measurements with nanometer-scale localization [168] promises exciting breakthroughs in the near future. The impact on advanced materials science and surface characterization, as well as on nano(bio)science and nano(bio)technology, will be substantial and will provide truly new insight and capabilities, in particular in the analysis of nanometer-scale patterns and arrays. The development of absolute surface chemical analysis by CFM has still a long way to go, but exciting times are ahead of us for sure.

Acknowledgements

The authors acknowledge all colleagues, current and previous collaborators, co-workers, and students for sharing their ideas, as well as for enlightening and stimulating discussions. The MESA⁺ Institute for Nanotechnology of the University of Twente and the Council for Chemical Sciences of the Netherlands Organization for Scientific Research (CW-NWO) are acknowledged for financial support.

References

- 1 G. BINNIG, H. ROHRER, C. GERBER, E. WEIBEL, *Appl. Phys. Lett.* **1982**, *40*, 178.
- 2 G. BINNIG, C. F. QUATE, C. GERBER, *Phys. Rev. Lett.* **1986**, *56*, 930.
- 3 *Dekker Encyclopedia of Nanoscience and Nanotechnology*, J. A. SCHWARZ, C. I. CONTESCU, K. PUTYERA (eds.), Vols. 1–5, Marcel Dekker, New York, **2004**.
- 4 F. J. GIESSIBL, *Rev. Mod. Phys.* **2003**, *75*, 949.
- 5 J. YANG, *Cell Biochem. Biophys.* **2004**, *41*, 435.
- 6 S. KRÄMER, R. R. FUJERER, C. B. GORMAN, *Chem. Rev.* **2003**, *103*, 4367.
- 7 D. WOUTERS, U. S. SCHUBERT, *Angew. Chem. Int. Ed.* **2004**, *43*, 2480.
- 8 R. J. COLTON, A. ENGEL, J. E. FROMMER, H. E. GAUB, A. A. GEWIRTH, R. GUCKENBERGER, J. RABE, W. M. HECKL, B. PARKINSON, *Procedures in Scanning Probe Microscopies*, Wiley, New York, **1998**.
- 9 R. M. OVERNEY, E. MEYER, J. FROMMER, D. BRODBECK, R. LÜTHI, L. HOWALD, H.-J. GÜNTHERODT, M. FUJIHIRA, H. TAKANO, Y. GOTOH, *Nature* **1992**, *359*, 133.
- 10 L.-F. CHI, M. ANDERS, H. FUCHS, R. R. JOHNSTON, H. RINGSDORF, *Science* **1993**, *259*, 213.
- 11 S. N. MAGONOV, V. ELINGS, M.-H. WHANGBO, *Surf. Sci.* **1997**, *375*, L385.
- 12 R. GARCIA, R. PEREZ, *Surf. Sci. Rep.* **2002**, *47*, 197.
- 13 M. MUNZ, B. CAPPELLA, H. STURM, M. GEUSS, E. SCHULZ, *Adv. Polym. Sci.* **2003**, *164*, 87.
- 14 D. E. WEIBEL, N. LOCKYER, J. C. VICKERMAN, *Appl. Surf. Sci.* **2004**, *231–232*, 146.
- 15 A. DUCHESNE, G. LIESER, G. WEGNER, *Coll. Polym. Sci.* **1994**, *272*, 1329.
- 16 Y. N. XIA, G. M. WHITESIDES, *Annu. Rev. Mater. Sci.* **1998**, *28*, 153.
- 17 H. W. LI, W. T. S. HUCK, *Curr. Opin. Solid State Mater. Sci.* **2002**, *6*, 3.
- 18 G. Y. LIU, S. XU, Y. L. QIAN, *Acc. Chem. Res.* **2000**, *33*, 457.
- 19 S. S. SHEIKO, M. MÖLLER, *Chem. Rev.* **2001**, *101*, 4099.
- 20 H. SCHÖNHERR, M. CREGO-CALAMA, G. J. VANCOSO, D. N. REINHOUDT, in: *Dekker Encyclopedia of Nanoscience and Nanotechnology*, J. A. SCHWARZ, C. I.

- CONTESCU, K. PUTYERA (eds.), Marcel Dekker, New York, 2004, p. 155.
- 21 J. K. GIMZEWSKI, C. JOACHIM, *Science* **1999**, 283, 1683.
 - 22 C. D. FRISBIE, L. F. ROZSNYAI, A. NOY, M. S. WRIGHTON, C. M. LIEBER, *Science* **1994**, 265, 2071.
 - 23 A. NOY, D. V. VEZENOV, C. M. LIEBER, *Annu. Rev. Mater. Sci.* **1997**, 27, 381.
 - 24 R. C. THOMAS, P. TANGYUNYONG, T. A. MICHALSKE, R. M. CROOKS, *J. Phys. Chem.* **1994**, 98, 4493.
 - 25 J. B. D. GREEN, M. T. McDERMOTT, M. D. PORTER, L. M. SIPERKO, *J. Phys. Chem.* **1995**, 99, 10960.
 - 26 R. C. THOMAS, J. E. HOUSTON, R. M. CROOKS, T. KIM, T. A. MICHALSKE, *J. Am. Chem. Soc.* **1995**, 117, 3830.
 - 27 S. AKARI, D. HORN, H. KELLER, W. SCHREPP, *Adv. Mater.* **1995**, 7, 549.
 - 28 E. W. VAN DER VEGTE, G. HADZIOANNOU, *Langmuir* **1997**, 13, 4357.
 - 29 H. SCHÖNHERR, M. W. J. BEULEN, J. BÜGLER, J. HUSKENS, F. C. J. M. VAN VEGGEL, D. N. REINHOUDT, G. J. VANC SO, *J. Am. Chem. Soc.* **2000**, 122, 4963.
 - 30 T. HUGEL, M. SEITZ, *Macromol. Rapid Commun.* **2001**, 22, 989.
 - 31 A. JANSHOFF, M. NEITZERT, Y. OBERDÖRFER, H. FUCHS, *Angew. Chem. Int. Ed.* **2000**, 39, 3212.
 - 32 W. ZHANG, X. ZHANG, *Prog. Polym. Sci.* **2003**, 28, 1271.
 - 33 H. TAKANO, J. R. KENSETH, S. S. WONG, J. C. O'BRIEN, M. D. PORTER, *Chem. Rev.* **1999**, 99, 2845.
 - 34 G. J. VANC SO, H. HILLBORG, H. SCHÖNHERR, *Adv. Polym. Sci.* **2005**, 182, 55.
 - 35 H. SCHÖNHERR, Ph.D. thesis, University of Twente, The Netherlands, 1999.
 - 36 R. L. ALLEY, K. KOMVOPOULOS, R. T. HOWE, *J. Appl. Phys.* **1994**, 76, 5731.
 - 37 W. A. DUCKER, T. J. SENDEN, R. M. PASHLEY, *Nature* **1991**, 353, 239.
 - 38 J. N. ISRAELACHVILI, *Intermolecular and Surface Forces*, 2nd edn., Academic Press, London, 1991.
 - 39 L. H. DUBOIS, R. G. NUZZO, *Annu. Rev. Phys. Chem.* **1992**, 43, 437.
 - 40 A. ULMAN, *An Introduction to Ultrathin Organic Films: From Langmuir-Blodgett to Self-Assembly*, Academic Press, New York, 1991.
 - 41 A. ULMAN, *Chem. Rev.* **1996**, 96, 1533.
 - 42 F. SCHREIBER, *Progr. Surf. Sci.* **2000**, 65, 151.
 - 43 R. G. NUZZO, D. L. ALLARA, *J. Am. Chem. Soc.* **1983**, 105, 4481.
 - 44 J. M. TOUR, L. JONES, D. L. PEARSON, J. J. S. LAMBA, T. P. BURG IN, G. M. WHITESIDES, D. L. ALLARA, A. N. PARIKH, S. V. ATRE, *J. Am. Chem. Soc.* **1995**, 117, 9529.
 - 45 P. E. LAIBINIS, R. G. NUZZO, G. M. WHITESIDES, *J. Phys. Chem.* **1992**, 96, 5097.
 - 46 H. A. BIEBUYCK, C. D. BAIN, G. M. WHITESIDES, *Langmuir* **1994**, 10, 1825.
 - 47 T. T. WOOSTER, P. R. GAMM, W. E. GEIGER, A. M. OLIVER, A. J. BLACK, D. C. CRAIG, M. N. PADDON-ROW, *Langmuir* **1996**, 12, 6616.
 - 48 X. Y. TANG, T. W. SCHNEIDER, J. W. WALKER, D. A. BUTTRY, *Langmuir* **1996**, 12, 5921.
 - 49 T. TAKAMI, E. DELAMARCHE, B. MICHEL, C. GERBER, H. WOLF, H. RINGSDORF, *Langmuir* **1995**, 11, 3876.
 - 50 C. D. BAIN, H. A. BIEBUYCK, G. M. WHITESIDES, *Langmuir* **1989**, 5, 723.
 - 51 C. D. BAIN, G. M. WHITESIDES, *Science* **1988**, 240, 62.
 - 52 P. GUPTA, A. ULMAN, S. FANFAN, A. KORNI AKOV, K. LOOS, *J. Am. Chem. Soc.* **2005**, 127, 4.
 - 53 S. S. SHEIKO, M. MÖLLER, E. M. C. M. REUVEKAMP, H. W. ZANDBERGEN, *Phys. Rev. Part B* **1993**, 48, 5675.
 - 54 R. W. CARPICK, M. SALMERON, *Chem. Rev.* **1997**, 97, 1163.
 - 55 J. SAGIV, *J. Am. Chem. Soc.* **1980**, 102, 92.
 - 56 R. MAOZ, J. SAGIV, *J. Coll. Interface Sci.* **1984**, 100, 465.
 - 57 T. ITO, M. NAMBA, P. BUHLMANN, Y. UMEZAWA, *Langmuir* **1997**, 13, 4323.
 - 58 J. E. HEADRICK, C. L. BERRIE, *Langmuir* **2004**, 20, 4124.
 - 59 J. Y. M. YANG, C. W. FRANK, in: *Organic Thin Films*, C. W. FRANK (ed.), ACS Symposium Series, Vol. 695, American Chemical Society, New York, 1998, p. 67.

- 60 M. R. LINFORD, C. E. D. CHIDSEY, *J. Am. Chem. Soc.* **1993**, *115*, 12 631.
- 61 M. R. LINFORD, P. FENTER, P. M. EISENBERGER, C. E. D. CHIDSEY, *J. Am. Chem. Soc.* **1995**, *117*, 3145.
- 62 A. B. SIEVAL, V. VLEEMING, H. ZUILHOF, E. J. R. SUDHOLTER, *Langmuir* **1999**, *15*, 8288.
- 63 J. M. BURIK, *Chem. Rev.* **2002**, *102*, 1271.
- 64 A. B. SIEVAL, R. LINKE, G. HEIJ, G. MEIJER, H. ZUILHOF, E. J. R. SUDHOLTER, *Langmuir* **2001**, *17*, 7554.
- 65 H. DAI, J. H. HAFNER, A. G. RINZLER, D. T. COLBERT, R. E. SMALLEY, *Nature* **1996**, *384*, 147.
- 66 S. S. WONG, E. JOSELEVICH, A. T. WOOLLEY, C. L. CHEUNG, C. M. LIEBER, *Nature* **1998**, *394*, 52.
- 67 S. S. WONG, A. T. WOOLLEY, E. JOSELEVICH, C. L. CHEUNG, C. M. LIEBER, *J. Am. Chem. Soc.* **1998**, *120*, 8557.
- 68 A. NOY, C. H. SANDERS, D. V. VEZENOV, S. S. WONG, C. M. LIEBER, *Langmuir* **1998**, *14*, 1508.
- 69 C. A. J. PUTMAN, B. D. DE GROOTH, N. F. VAN HULST, J. GREVE, *J. Appl. Phys.* **1992**, *72*, 6.
- 70 M. B. VIANI, T. E. SCHAFFER, G. T. PALOCCI, L. I. PIETRASANTA, B. L. SMITH, J. B. THOMPSON, M. RICHTER, M. RIEF, H. E. GAUB, K. W. PLAXCO, A. N. CLELAND, H. G. HANSMA, P. K. HANSMA, *Rev. Sci. Instrum.* **1999**, *70*, 4300.
- 71 N. A. BURNHAM, R. J. COLTON, H. M. POLLOCK, *Nanotechnology* **1993**, *4*, 64.
- 72 B. CAPPELLA, G. DIETLER, *Surf. Sci. Rep.* **1999**, *34*, 1.
- 73 A. L. WEISENHORN, P. MAIVALD, H.-J. BUTT, P. K. HANSMA, *Phys. Rev. B* **1992**, *45*, 11 226.
- 74 J. P. CLEVEL, S. MANNE, D. BOCEK, P. K. HANSMA, *Rev. Sci. Instr.* **1993**, *64*, 403.
- 75 J. L. HUTTER, J. BECHHOEFER, *Rev. Sci. Instr.* **1993**, *64*, 1868.
- 76 J. E. SADER, I. LARSON, P. MULVANEY, L. R. WHITE, *Rev. Sci. Instr.* **1995**, *66*, 3789.
- 77 M. TORTONESE, M. KIRK, *Proc. SPIE* **1997**, *3009*, 53.
- 78 J. L. HUTTER, J. BECHHOEFER, *J. Vac. Sci. Technol.* **1994**, *12*, 2251.
- 79 K. FELDMAN, T. TERVOORT, P. SMITH, N. D. SPENCER, *Langmuir* **1998**, *14*, 372.
- 80 K. L. JOHNSON, K. KENDALL, A. D. ROBERTS, *Proc. R. Soc. London A* **1971**, *324*, 301.
- 81 B. V. DERJAGUIN, V. K. MÜLLER, Y. P. TOPOROV, *J. Coll. Interf. Sci.* **1975**, *53*, 314.
- 82 J. DRELICH, G. W. TORMOEN, E. R. BEACH, *J. Coll. Interf. Sci.* **2004**, *280*, 484.
- 83 D. L. PATRICK, J. F. FLANAGAN, P. KOHL, R. M. LYNDEN-BELL, *J. Am. Chem. Soc.* **2003**, *125*, 6762.
- 84 E. M. LIFSHITZ, *Soviet Phys. JETP (Engl. Transl.)* **1956**, *2*, 73.
- 85 J. N. ISRAELACHVILI, D. TABOR, *Prog. Surf. Membr. Sci.* **1973**, *7*, 1.
- 86 J. N. ISRAELACHVILI, *Intermolecular Surface Forces*, 2nd edn., Academic Press, London, **1991**, Chapter 11.
- 87 S. A. JOYCE, J. E. HOUSTON, T. A. MICHALSKE, *Appl. Phys. Lett.* **1992**, *60*, 1175.
- 88 K. O. VAN DER WERF, C. A. J. PUTMAN, B. G. DE GROOTH, J. GREVE, *Appl. Phys. Lett.* **1994**, *65*, 1195.
- 89 D. R. BASELT, J. D. BALDESCHWIELER, *J. Appl. Phys.* **1994**, *76*, 33.
- 90 H. A. MIZES, K.-G. LOH, R. J. D. MILLER, S. K. AHUJA, E. F. GRABOWSKI, *Appl. Phys. Lett.* **1991**, *59*, 2901.
- 91 H. SCHÖNHERR, Z. HRUSKA, G. J. VANCISO, *Macromolecules* **2000**, *33*, 4532.
- 92 C. E. H. BERGER, K. O. VAN DER WERF, R. P. H. KOOYMAN, B. G. DE GROOTH, J. GREVE, *Langmuir* **1995**, *11*, 4188.
- 93 H. U. KROTH, T. STIFTER, H. WASCHIPKY, K. WEISHAUP, S. HILD, O. MARTI, *Surf. Interf. Anal.* **1999**, *27*, 336.
- 94 *Fundamentals of Friction*, I. L. SINGER, H. M. POLLOCK (eds.), Kluwer, The Netherlands, **1992**.
- 95 E. MEYER, R. M. OVERNEY, K. DRANSFELD, T. GYALOG, *Nanoscience: Friction and Rheology on the Nanometer Scale*, World Scientific, Singapore, **1998**.
- 96 B. J. BRISCOE, D. C. B. EVANS, *Proc. R. Soc., Ser. A* **1982**, *380*, 389.

- 97 F. P. BOWDEN, D. TABOR, *Friction Lubrication of Solids, Part II*, Oxford University Press, 1964.
- 98 R. W. CARPICK, N. AGRAÏT, D. F. OGLETREE, M. SALMERON, *Langmuir* **1996**, *12*, 3334.
- 99 G. BAR, Y. THOMANN, R. BRANDSCH, H. J. CANTOW, M. H. WHANGBO, *Langmuir* **1997**, *13*, 3807.
- 100 G. BAR, S. RUBIN, A. N. PARIKH, B. I. SWANSON, T. A. ZAWODZINSKI, M. H. WHANGBO, *Langmuir* **1997**, *13*, 373.
- 101 G.-Y. LIU, M. SALMERON, *Langmuir* **1994**, *10*, 367.
- 102 H. SCHÖNHERR, G. J. VANCOSO, *Langmuir* **1997**, *13*, 3769.
- 103 H.-J. BUTT, K. SEIFERT, E. BAMBERG, *J. Phys. Chem.* **1993**, *97*, 7316.
- 104 J. HUANG, J. C. HEMMINGER, *J. Am. Chem. Soc.* **1993**, *115*, 3342.
- 105 M. LEWIS, M. TARLOV, K. CARRON, *J. Am. Chem. Soc.* **1995**, *117*, 9574.
- 106 M. J. TARLOV, D. R. F. BURGESS JR., G. GILLEN, *J. Am. Chem. Soc.* **1993**, *115*, 5305.
- 107 J. HUANG, D. A. DAHLGREN, J. C. HEMMINGER, *Langmuir* **1994**, *10*, 626.
- 108 M. H. SCHOENFISCH, J. E. PEMBERTON, *J. Am. Chem. Soc.* **1998**, *120*, 4502.
- 109 J. B. SCHLENOFF, M. LI, H. LY, *J. Am. Chem. Soc.* **1995**, *117*, 12528.
- 110 H. SCHÖNHERR, V. CHECHIK, C. J. M. STIRLING, G. J. VANCOSO, *J. Am. Chem. Soc.* **2000**, *122*, 3679.
- 111 S. AKARI, W. SCHREPP, D. HORN, *Langmuir* **1996**, *12*, 857.
- 112 R. D. PINER, C. A. MIRKIN, *Langmuir* **1997**, *13*, 6864.
- 113 H. SCHÖNHERR, G. J. VANCOSO, *Macromolecules* **1997**, *30*, 6391.
- 114 B. WUNDERLICH, *Macromolecular Physics*, Vol. 1, Academic Press, New York 1973, p. 97.
- 115 M. BINGGELI, C. M. MATE, *Appl. Phys. Lett.* **1994**, *65*, 415.
- 116 A. NOY, C. D. FRISBIE, L. F. ROZSNYAI, M. S. WRIGHTON, C. M. LIEBER, *J. Am. Chem. Soc.* **1995**, *117*, 7943.
- 117 D. V. VEZENOV, A. NOY, L. F. ROZSNYAI, C. M. LIEBER, *J. Am. Chem. Soc.* **1997**, *119*, 2006.
- 118 H. SCHÖNHERR, G. J. VANCOSO, *Polym. Prepr.* **1998**, *39(2)*, 1177.
- 119 Y. I. RABINOVICH, J. J. ADLER, A. ATA, R. K. SINGH, B. M. MOUDGIL, *J. Coll. Interf. Sci.* **2000**, *232*, 10.
- 120 Y. I. RABINOVICH, J. J. ADLER, A. ATA, R. K. SINGH, B. M. MOUDGIL, *J. Coll. Interf. Sci.* **2000**, *232*, 17.
- 121 E. R. BEACH, G. W. TORMOEN, J. DRELICH, R. HAN, *J. Coll. Interf. Sci.* **2002**, *247*, 84.
- 122 R. JAEGER, M. M. BERGSHOEF, C. MARTÍN I BATLLE, H. SCHÖNHERR, G. J. VANCOSO, *Macromol. Symp.* **1998**, *127*, 141.
- 123 R. MCKENDRY, M.-E. THEOCLITOU, C. ABELL, T. RAYMENT, *Langmuir* **1998**, *14*, 2846.
- 124 H. SCHÖNHERR, G. J. VANCOSO, *J. Polym. Sci. B, Polym. Phys.* **1998**, *36*, 2483.
- 125 H. SCHÖNHERR, G. J. VANCOSO, *Mater. Sci. Eng. C* **1999**, *8-9*, 243.
- 126 A. LIO, D. H. CHARYCH, M. SALMERON, *J. Phys. Chem. B* **1997**, *101*, 3800.
- 127 H. SCHÖNHERR, H. RINGSDORF, *Langmuir* **1996**, *12*, 3891.
- 128 C. M. MATE, G. M. MCCCELL, R. ERISSON, S. CHIANG, *Phys. Rev. Lett.* **1987**, *59*, 1942.
- 129 R. M. OVERNEY, H. TAKANO, M. FUJIIHIRA, W. PAULUS, H. RINGSDORF, *Phys. Rev. Lett.* **1994**, *72*, 3546.
- 130 R. NISMAN, P. SMITH, G. J. VANCOSO, *Langmuir* **1994**, *10*, 1667.
- 131 G. J. VANCOSO, S. FÖRSTER, H. LEIST, *Macromolecules* **1996**, *29*, 2158.
- 132 M. LILEY, D. GOURDON, D. STAMOU, U. MESETH, T. M. FISCHER, C. LAUTZ, H. STAHLBERG, H. VOGEL, N. A. BURNHAM, C. DUSCHL, *Science* **1998**, *280*, 273.
- 133 G. J. VANCOSO, H. SCHÖNHERR, in: *Microstructure and Microtribology of Polymer Surfaces*, V. V. TSUKRUK, K. J. WAHL (eds.), ACS Symposium Series, Vol. 741, American Chemical Society, New York, **1999**, p. 317.
- 134 S. K. SINNIH, A. B. STEEL, C. J. MILLER, J. E. REUTTROBEY, *J. Am. Chem. Soc.* **1996**, *118*, 8925.
- 135 A. NOY, S. ZEPEDA, C. A. ORME, Y. YEH, J. J. DE YOREO, *J. Am. Chem. Soc.* **2003**, *125*, 1356.
- 136 D. V. VEZENOV, A. V. ZHUK, G. M.

- WHITESIDES, C. M. LIEBER, *J. Am. Chem. Soc.* **2002**, *124*, 10578.
- 137 A. DANESH, M. C. DAVIES, S. J. HINDER, C. J. ROBERTS, S. J. B. TENDLER, P. M. WILLIAMS, M. J. WILKINS, *Anal. Chem.* **2000**, *72*, 3419.
- 138 R. S. ABENDAN, J. A. SWIFT, *Langmuir* **2002**, *18*, 4847.
- 139 A. S. DUWEZ, B. NYSTEN, *Langmuir* **2001**, *17*, 8287.
- 140 T. HAN, J. M. WILLIAMS, T. P. BEEBE JR., *Anal. Chim. Acta* **1995**, *307*, 365.
- 141 H. SKULASON, C. D. FRISBIE, *Anal. Chem.* **2002**, *74*, 3096.
- 142 R. MCKENDRY, M. E. THEOCLITOU, T. RAYMENT, C. ABBELL, *Nature* **1998**, *391*, 566.
- 143 G. U. LEE, L. A. CHRISEY, R. J. COLTON, *Science* **1994**, *266*, 771.
- 144 U. DAMMER, O. POPESCU, P. WAGNER, D. ANSELMETTI, H.-J. GÜNTHERODT, G. N. MISEVIC, *Science* **1995**, *267*, 1173.
- 145 E.-L. FLORIN, V. T. MOY, H. E. GAUB, *Science* **1994**, *264*, 415.
- 146 O. LIUBASHEVSKI, F. PATOLSKY, I. WILLNER, *Langmuir* **2001**, *17*, 5134.
- 147 S. ZAPOTOCZNY, T. AULETTA, M. R. DE JONG, H. SCHÖNHERR, J. HUSKENS, F. C. J. M. VAN VEGGEL, D. N. REINHOUDT, G. J. VANC SO, *Langmuir* **2002**, *18*, 6988.
- 148 T. AULETTA, M. R. DE JONG, A. MULDER, F. C. J. M. VAN VEGGEL, J. HUSKENS, D. N. REINHOUDT, S. ZOU, S. ZAPOTOCZNY, H. SCHÖNHERR, G. J. VANC SO, K. KUIPERS, *J. Am. Chem. Soc.* **2004**, *126*, 1577.
- 149 S. ZOU, H. SCHÖNHERR, G. J. VANC SO, *Angew. Chem. Int. Ed.* **2005**, *44*, 956.
- 150 E. W. VAN DER VEGTE, G. HADZIIOANNOU, *J. Phys. Chem.* **1997**, *101*, 9563.
- 151 H. X. HE, W. HUANG, H. ZHANG, Q. G. LI, S. F. Y. LI, Z. F. LIU, *Langmuir* **2000**, *16*, 517.
- 152 D. A. SMITH, M. L. WALLWORK, J. ZHANG, J. KIRKHAM, C. ROBINSON, A. MARSH, M. WONG, *J. Phys. Chem. B* **2000**, *104*, 8862.
- 153 M. P. L. WERTS, E. W. VAN DER VEGTE, G. HADZIIOANNOU, *Langmuir* **1997**, *13*, 4939.
- 154 B. DORDI, J. P. PICKERING, H. SCHÖNHERR, G. J. VANC SO, *Eur. Polym. J.* **2004**, *40*, 939.
- 155 B. DORDI, J. P. PICKERING, H. SCHÖNHERR, G. J. VANC SO, *Surf. Sci.* **2004**, *570*, 57.
- 156 M. FUJIIHARA, M. FURUGORI, U. AKIBA, Y. TANI, *Ultramicroscopy* **2001**, *86*, 75.
- 157 M. FUJIIHARA, Y. TANI, M. FURUGORI, U. AKIBA, Y. OKABE, *Ultramicroscopy* **2001**, *86*, 63.
- 158 A. T. A. JENKINS, N. BODEN, R. J. BUSHBY, S. D. EVANS, P. F. KNOWLES, R. E. MILES, S. D. OGIER, H. SCHÖNHERR, G. J. VANC SO, *J. Am. Chem. Soc.* **1999**, *121*, 5274.
- 159 N. J. BREWER, G. J. LEGGETT, *Langmuir* **2004**, *20*, 4109.
- 160 M. P. L. WERTS, E. W. VAN DER VEGTE, V. GRAYER, E. ESSELINK, C. TSITSILIANIS, G. HADZIIOANNOU, *Adv. Mater.* **1998**, *10*, 452.
- 161 D. TRIFONOVA, H. SCHÖNHERR, L. VAN DER DOES, P. J. P. JANSSEN, J. W. M. NOORDERMEER, G. J. VANC SO, *Rubber Chem. Technol.* **1999**, *72*, 862.
- 162 A. S. DUWEZ, C. POLEUNIS, P. BERTRAND, B. NYSTEN, *Langmuir* **2001**, *17*, 6351.
- 163 M. SCHNEIDER, M. ZHU, G. PAPASTAVROU, S. AKARI, H. MÖHWALD, *Langmuir* **2002**, *18*, 602.
- 164 H. SCHÖNHERR, Z. HRUSKA, G. J. VANC SO, *Macromolecules* **1998**, *31*, 3679.
- 165 H. SCHÖNHERR, M. T. VAN OS, R. FÖRCH, R. B. TIMMONS, W. KNOLL, G. J. VANC SO, *Chem. Mater.* **2000**, *12*, 3689.
- 166 H. SCHÖNHERR, M. T. VAN OS, Z. HRUSKA, J. KURDI, R. FÖRCH, F. AREFI-KHONSARI, W. KNOLL, G. J. VANC SO, *J. Chem. Soc., Chem. Com.* **2000**, 1303.
- 167 H. HILLBORG, N. TOMCZAK, A. OLÀH, H. SCHÖNHERR, G. J. VANC SO, *Langmuir* **2004**, *20*, 785.
- 168 C. STROH, H. WANG, R. BASH, B. ASHCROFT, J. NELSON, H. GRUBER, D. LOHR, S. M. LINDSAY, P. HINTERDORFER, *Proc. Nat. Acad. Sci. USA* **2004**, *101*, 12503.

11

Atomic Force Microscopy-Based Single-Molecule Force Spectroscopy of Synthetic Supramolecular Dimers and Polymers

Shan Zou, Holger Schönherr, and G. Julius Vancso

11.1 Introduction

Controlled formation and breaking of covalent bonds have ruled molecular chemistry for more than a century. Over the last few decades studies involving noncovalent interactions have gained significant momentum in attempts to complement the brilliant achievements of covalent chemistry and to prepare well-defined structures with molecules that associate in spontaneous self-assembly processes, which are governed by supramolecular interactions. The building blocks are products of covalent chemistry; the well-defined aggregates are, however, creations based on noncovalent, supramolecular interactions. The corresponding forces are relatively weak, they may be highly directional, they depend on temperature, deformation rate and molecular environment, and they enable spontaneous or directed assembly of complex, reversible molecular architectures. Formation and rupture of these bonds depend on their potential energy landscapes. The strength of these forces has traditionally been assessed by ensemble thermodynamics approaches using thermodynamic potentials (enthalpy, free energy). However, with the swiftly growing interest in molecular nanotechnologies there is increasing need for knowledge regarding molecular stability and bond strengths from the single-molecule perspective, i.e., without ensemble averaging. In this contribution we summarize some recent achievements obtained in our laboratories, and by others, regarding the determination of single-molecule supramolecular interaction forces for different types of complex interactions, focusing on artificial (as opposed to natural) systems. The tool we focus upon for single-molecule force measurements is atomic force microscopy (AFM) [1, 2]. Since AFM is not the only tool that allows one to measure the strength of relatively weak supramolecular forces, other approaches will also be mentioned briefly.

AFM has experienced an enormous growth and development concerning the sophistication and user-friendliness of related instrumentation, as well as the range of applications. Initially AFM had been considered as an alternative tool for surface imaging, applicable down to nanometer length scales. However, AFM's potential to characterize and investigate physical properties of surfaces (friction, modulus,

hardness, etc.) and to study dynamic processes occurring at surfaces versus time in various media has been quickly recognized. In addition, the development of controlled chemical functionalization approaches of the probe tip has opened a new dimension, i.e., chemistry, in research on molecular length scales using AFM (see also Chapter 10) [3–5]. The combination of all these applications with *in-situ* investigations of surface physicochemical processes, and with environmentally controlled studies, as well as nanoscale lithography, have made AFM a versatile, enabling platform in nanoscience and nanotechnology [6].

Breaking of single-molecule “adhesive bonds” has already been the subject of early AFM studies. Hansma and coworkers have reported for the first time discrete jumps, interpreted as breaking single-molecule bonds, in force–distance curves measured between silicon nitride tips and glass surfaces [7]. The authors constructed rupture force distribution curves using the values of the force jumps measured. Characteristic maxima at integer multiples of a principal rupture force of approximately 1×10^{-11} N were observed. Hansma et al. concluded that the most likely explanation for the discrete, quantized rupture events can be given by assuming that breaking of individual H-bonds and their multiples in ordered hydration layers between tip and substrate occurred, which were responsible for the local maximum values in the distributions.

Tip functionalization approaches have allowed one to directly study interaction forces acting between selected pairs of molecules. For this purpose one of the interacting partners is attached to the tip and the other to the “sample” (or substrate) surface. The tip is then positioned so that contact with the sampled surface between the molecular pairs of interest is established. AFM is used in this configuration as a sensitive force measurement device. By pulling the interacting molecules apart, force–distance curves (corresponding to a molecular-scale equivalent of a stress–strain test) are detected. At failure and rupture of contacts the strength of individual supramolecular chemical bonds can be directly probed. Such force–stretching relationships of molecular linkages binding the tip and probed surface together can nowadays be probed as a function of pulling speed, temperature, and solvent environment, and the weakest bonds in the molecular architectures linking tip and substrate can be broken. Corresponding molecular stress–strain and rupture experiments, termed force spectroscopy, are gaining momentum in the determination of bond strengths expressed in force, and in studies of the actual behavior of individual molecules (as opposed to measurements of ensemble averages). For example, in an early study, Gaub and coworkers attached avidin at high dilution to AFM tip surfaces, and measured force spectra after forming receptor–ligand complexes of biotin (coupled to agarose) immobilized at the probed substrate [8]. The authors ensured that only a restricted number of ligand–receptor bonds could form and observed rupture forces, which were integer multiples of a minimum force (160 ± 20 pN). This minimum force was interpreted as the unbinding force of individual ligand–receptor molecular pairs. Parallel with this work, in an independent study, forces acting between complementary strands of DNA have been determined. DNA oligonucleotides were covalently attached to the AFM tip and to a substrate and the molecular link was brought to rupture [9].

Rupture forces measured between 20-base strands fell into three distinct groups of forces, which nested at 1.52, 1.11, and 0.83 nN, respectively. These forces were associated by the authors with breaking of the interchain interactions between a single pair of molecules involving 20, 16, and 12 base-pairs, respectively.

Subsequent theoretical [10] and experimental research [11] involving systematic biomembrane force probe investigations (in aqueous media) proved that early AFM measurements represent only a single point in a continuous spectrum of bond strengths. Rupture forces may depend strongly on the experimental loading rates that the bond experiences [11]. These studies emphasized theoretical predictions that the values of rupture forces will depend logarithmically on the rate at which the load is applied, depending on the lifetime of the supramolecular bond in comparison with the duration of a single, experimentally realized rupture event. This milestone study established the physical foundations of quantitative single-molecule force spectroscopy [12–16].

In addition to strengths of supramolecular interactions in biomacromolecules, rupture of single covalent bonds has also been investigated [17]. By using different surface chemistries for the attachment, it was found that the silicon–carbon bond ruptured at 2.0 ± 0.3 nN, whereas the sulfur–gold system showed rupture forces of 1.4 ± 0.3 nN at force-loading rates of 10 nN s^{-1} . These latter forces have been more recently attributed to the rupture of gold–gold atomic contacts [18]. Based on these early results, and on a swift development in single-molecule force spectroscopy, an alternative approach to describe the strength of chemical bonds using forces is emerging. This approach complements the usual thermodynamic analyses, which discuss bond strengths in terms of ensemble averages and molar quantities.

There are many instances in biochemistry, supramolecular chemistry, and nanotechnology when knowledge of the strength of individual chemical bonds, i.e., the knowledge of how much force individual bonds can sustain, is of fundamental importance. Examples cover a broad range from drug design, where determining the binding of a drug molecule with its receptor is of prime importance for drug efficiency, via molecular diagnostics and molecular sensors, to reversible bond rupture in hydrogen-bond mediated macromolecular networks in the bulk [19–21], all the way up to supramolecular polymers (in the bulk, as well as in solution) [22–24]. Regarding the last example, if bond strengths were known on the single-molecule level as a function of deformation (loading) rate, a quantitative understanding and explanation of the unique bulk physical properties resting on first principles approaches could also be established, e.g., regarding the nonlinear mechanical behavior of supramolecular polymers at high deformation rates. Furthermore, in molecular nanofabrication by force, molecules should be grabbed, moved, and deposited one by one in a directly controlled fashion, using a device which bridges the length scales between macroscopic and nanometer dimensions (such as AFM). The development of corresponding bottom-up molecular fabrication processes renders knowledge of bond strengths and their dependence on temperature and unbinding rates indispensable.

Beyond relevance for nanotechnology, single-molecule force experiments unveil

mechanical characteristics of isolated molecules, as opposed to measuring the macroscopic response of their bulk. Molecules have become directly observable (via force measurements) and can be visualized on nanometer length scales using AFM. One is now in a position to develop molecular theories which connect observations on the length scale level of individual molecules with bulk experiments and bulk thermodynamics, such as rate constants, reaction free energies, and eventually chemical affinity. Molecular-level data on stress–strain behavior and deformation of single (macro)molecules allow one to develop molecular-scale theories for materials science which explain bulk behavior (e.g., viscoelasticity). Fine details of potential energy landscapes of complex (bio)macromolecules which have not been accessible earlier, including intermediate states in complex biological macromolecules, can now be researched directly. The current focus in this area is primarily on biomolecules and biomacromolecules. We believe, however, that the underlying behavior must first be thoroughly understood and described for relatively simple, well-defined, primarily synthetic, supramolecular systems, which exhibit simple potential energy landscapes (e.g., one barrier). This refers to both thermodynamic quasi-equilibrium (no loading-rate dependence for single-molecule force spectra), as well as non-equilibrium situations (with considerable loading-rate dependence) before tackling more complex supramolecular structures with multiple-bond schemes. In this review, using a few selected articles from the literature as well as our own previously published work, we summarize the current state-of-the-art regarding the development of single-molecule force spectroscopy applied to synthetic, supramolecular dimers and polymers. Biological molecules (or macromolecules) are thus not treated in this contribution.

We begin this chapter with a short summary of supramolecular interactions in Section 11.2. The principles of single-molecule force spectroscopy (SMFS) regarding the theoretical foundations, as well as AFM-based experimental details, are then introduced in Section 11.3. Special attention is given to the loading-rate dependence of supramolecular rupture forces. This loading-rate dependence introduces a new variable, i.e., time, into bond stability considerations. As the first group of examples (Section 11.4.1), we discuss single-molecule behavior of inclusion complexes, with a focus on small apolar molecules which bind into β -cyclodextrin (β -CD) cavities in aqueous environments as well as other inclusion complexes. Section 11.4.2 on H-bonding interactions follows. Metal-containing supramolecular bonds are discussed in Section 11.4.3. The review will be complemented by a description of charge-transfer interactions (Section 11.4.4), and in Section 11.5 a conclusion together with an outlook sketching possible future opportunities and recent trends.

11.2 Supramolecular Interactions

Noncovalent interactions govern molecular recognition and the structure of many biomolecules [25], as well as artificial supramolecular assemblies [26–30]. Hence

their measurement is important for an understanding of the underlying physics. The corresponding interatomic and intermolecular interactions can be directly or indirectly assessed, for instance, in AFM force–displacement curves recorded between AFM tips and sample surfaces functionalized with the corresponding host and guest moieties [31–33]. Depending on the nature of the exposed (organic) functional groups and the medium, the tip–sample forces may comprise, among others, electrostatic forces (Coulomb forces), dipolar interactions, and van der Waals forces, as well as the more specific and directional forces of H-bonding, metal–ligand interactions (coordinative bonds), and π stacking interactions. The latter directional forces are most important in the context of molecular recognition and supramolecular organization, and consequently in the context of single-molecule force spectroscopy of supramolecular dimers and polymers. In addition to these specific forces, dispersive van der Waals interactions, solvent effects, and entropic contributions (hydrophobic effects) can be relevant [34–37]. It should also be noted that these interactions typically do not act independently. Multiple interactions may give rise to allosteric and cooperativity effects (multivalency).

11.2.1

Hydrogen Bonds

Apart from the obvious importance in nature (biology), e.g., for protein secondary structures such as the alpha-helix, and for DNA base-pairing [38], H-bonds are of central importance in supramolecular chemistry [39]. In conjunction with scaffolds that provide the necessary pre-organization, H-bonds combine directionality, strength, and some degree of specificity. H-bonds occur between H-bond donors (D), which are characterized by a hydrogen atom bound covalently to a substantially electronegative heteroatom (e.g., nitrogen or oxygen), and acceptors (A) that possess a lone pair of outer-shell electrons, respectively. It is widely accepted that H-bonds are primarily electrostatic in nature [34, 35, 40]. Depending on the heteroatoms, individual H-bonds are characterized by an energy of binding of ~ -10 to -40 kJ mol⁻¹. Rigid scaffolds and the use of multiple H-bonds provide means to increase the level of directionality; thus thermodynamically stable self-assembled structures can be formed (typical energies up to ~ 120 kJ mol⁻¹). An illustrative example is the melamine–isocyanuric lattice [41–43] shown in Fig. 11.1A. By exploiting the pre-organization of a melamine-derivatized calix[4]arene scaffold, double rosette assemblies **1a**₃•(DEB)₆ or **1b**₃•(DEB)₆ are formed in the presence of two equivalents of 5,5-diethylbarbiturate (DEB) (or isocyanuric acid) (Fig. 11.1B) [44].

In addition to the number of primary interactions (i.e., the number of H-bonds formed), the strength of multiple H-bonding arrays is also determined by (electrostatic) secondary interactions (Fig. 11.2). In this case, the secondary interactions add $+2.9$ kJ mol⁻¹, or -2.9 kJ mol⁻¹, for each repulsive and attractive secondary interaction, respectively, to the strength of -8 kJ mol⁻¹ of each primary interaction [46–48]. While these values have been confirmed in a number of cases, there are notable exceptions. In the case of a high level of pre-organization, significantly higher complexation constants have been observed (see also below). Additional fac-

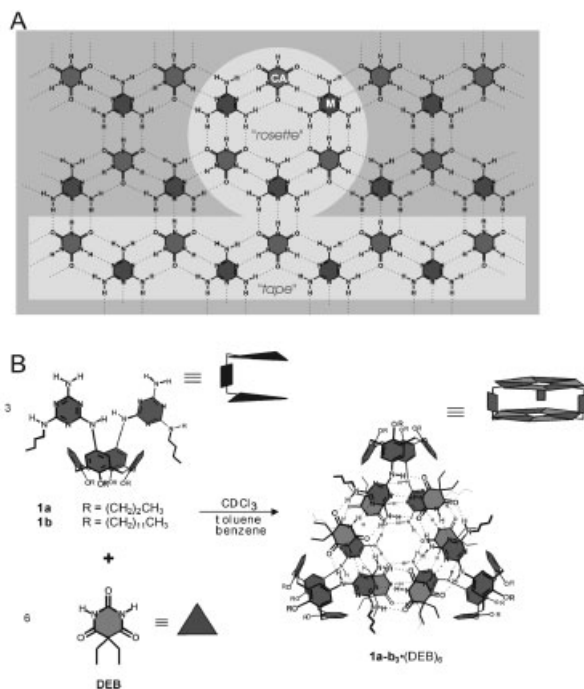


Fig. 11.1 (A) 2D infinite melamine–isocyanuric acid lattice. (B) Formation of discrete double rosette assemblies **1a₃•(DEB)₆** and **1b₃•(DEB)₆**. (Figures reproduced with permission from ref. 45. Copyright 2004, Marcel Dekker Inc.)

tors which can be used to modulate the strength of H-bonded arrays have been reviewed recently [49]. Obviously, the complex stability is also influenced to a large extent by the solvent, as well as by temperature. Illustrative examples of the relationship between complex stability and different hydrogen-bonding motifs are shown in Fig. 11.2A.

The corresponding association properties of motifs with multiple H-bonding have been exploited in association polymers, as well as in reversible, or “supramolecular”, polymers. Stadler and coworkers described divalent self-complementary H-bonding dimers of 4-(3,5-dioxo-1,2,4-triazolin-4-yl)benzoic acid (U4A) in U4A-derivatized side chain polymers, such as polybutadiene [19]. In neat materials, the self-complementary H-bonded dimers afforded intermolecular junction points in supramolecular network structures which exhibited unusual thermoreversible elastomeric properties (Fig. 11.2B).

Extending the number of H-bonds [22, 26], Lehn et al. realized the formation of more stable supramolecular polymers by using bifunctional molecules with complementary triple hydrogen-bonding functionalities (Fig. 11.2C) [50, 51]. This liquid-crystalline material consists of supramolecular polymer chains.

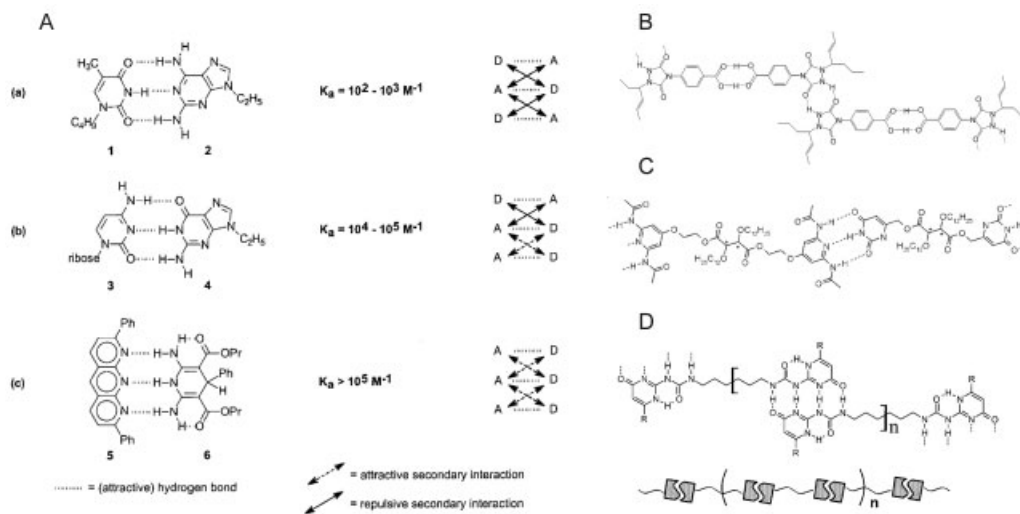


Fig. 11.2 (A) Stability of dimeric complexes with different triple hydrogen-bonding motifs. (B) H-bonding interactions between different polybutadiene chains derivatized with 4-(3,5-dioxo-1,2,4-triazolin-4-yl)benzoic acid. (Reproduced with permission from ref. 19. Copyright 1991, Hühthig & Wepf.) (C) Linear

supramolecular polymer reported by Lehn and coworkers. (D) Polymeric assembly of a bifunctional ureidopyrimidinone derivative reported by Meijer et al. (Figures in A, C, and D reproduced with permission from ref. 24. Copyright 2001, American Chemical Society.)

Meijer, Sijbesma, and coworkers extended the successful strategy further in an attempt to synthesize self-complementary molecules which interact so strongly with each other that supramolecular polymer chains with appreciable molar mass are formed also in solution. In self-complementary quadruple H-bonding DDAA arrays, realized for instance in the 2-ureido-4[1*H*]-pyrimidinone (UPy) motif employed for the fabrication of supramolecular polymers (Fig. 11.2D) [24, 52], favorable secondary interactions lead to an increase in complexation constant of three to four orders of magnitude compared with a DADA arrangement of donors and acceptors.

11.2.2

Coordinative Bonds

The second class of important noncovalent interactions that will be discussed briefly is based on metal–ligand interactions. Coordinative bonds, which are based on dative bonds formed between outer-shell electrons of organic ligands and unoccupied outer-shell orbitals of (transition) metal centers, can reach magnitudes of bond energy up to several hundred kilojoules per mole. The fundamental bond formation processes can be understood on the basis of crystal field, valence bond or molecular orbital theories and constitute, owing to their importance in inorganic

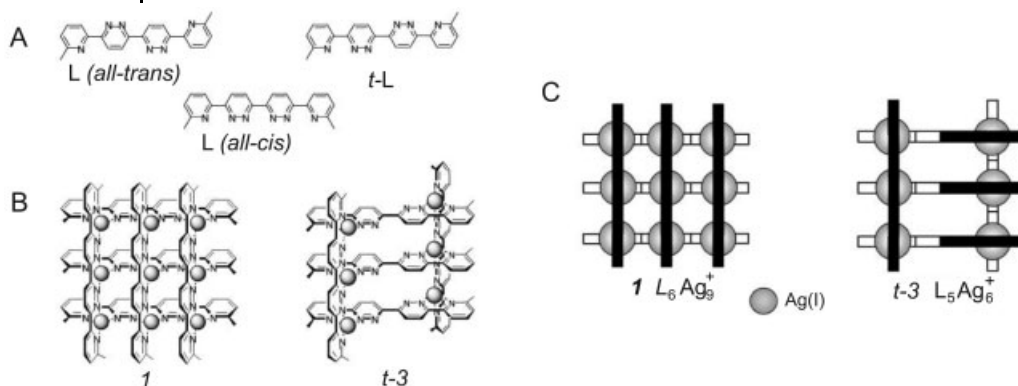


Fig. 11.3 (A) Definition of the form of the different ligands L used by Lehn and coworkers. (B) Structures of the grid complexes 1 and t-3. (C) Schematic representations of the grid complexes; the

white bars denote the parts of the ligands behind the silver cations, and the black bars represent those in front. (Reproduced with permission from ref. 55. Copyright 2002, Wiley-VCH.)

complex chemistry, a very mature subject [53]. The rich chemistry of (transition) metal centers and various classes of ligands, including crown ethers [28], provide a virtually unlimited range of possible supramolecular architectures and may impart functionality to these complexes [22, 26–28, 36, 37, 42, 43, 54, 55]. The coordination geometry of the metal center, as well as the functionality of the ligands, dictates the geometry of the supramolecular complexes formed (Fig. 11.3) [54]. Thus, individual complexes, linear chains, networks, defined grids, etc., can be formed.

These structures possess strength that is tunable via the size and nature of the metal center and the chemical nature of the ligands. Furthermore, the metal centers are addressable by, e.g., light or redox stimuli [56].

11.2.3

π -Electron Stacking

A last important class of supramolecular forces, which also has a counterpart in natural systems [25, 57, 58], is based on the mutual interaction of aromatic π -electron systems and those of π systems with cations [59] or C–H residues. For π -electron interactions, three different geometries can be distinguished: The edge–face geometry, which can be considered a CH– π interaction (Fig. 11.4Aa), the offset stacked orientation (Fig. 11.4Ab), and finally the face-to-face stacked orientation (Fig. 11.4Ac). The magnitudes of energies associated with the edge–face and offset stacked geometry interactions are typically several kilojoules per mole [60]. While these forces alone are too weak to be of general use for obtaining stable supramolecular architectures, π -stacking interactions of aromatic ring systems have been shown to be very useful to further stabilization of H-bonds (Fig. 11.4B) [61].

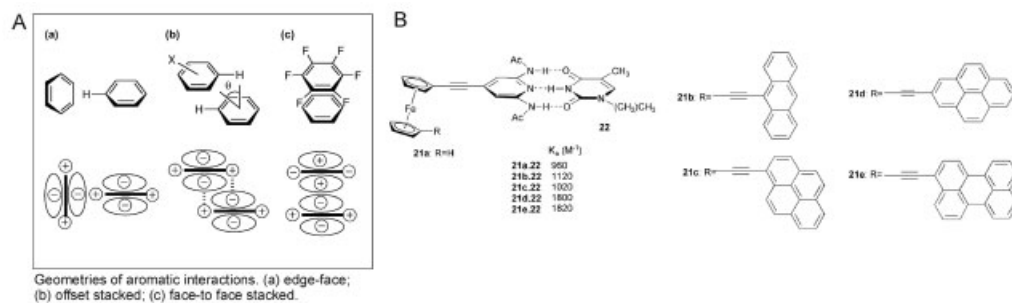


Fig. 11.4 (A) Three different geometries of aromatic π stacking. (Reproduced with permission from ref. 25. Copyright 2002, Elsevier Science.) (B) Stabilization of hydrogen bonds using π -stacking interactions. (Reproduced with permission from ref. 49. Copyright 2002, Royal Chemical Society.)

11.3

AFM-Based Single-Molecule Force Spectroscopy (SMFS)

In this section we first focus on experimental aspects of SMFS measurements. Emphasis is laid on AFM-related approaches, but we begin with a brief account of experiments used to measure forces on the single-molecule level.

11.3.1

SMFS Experiments

With the development of precise instrumentation, many elegant force-sensing techniques, differing in the range of force and measurement timescale, have become available. Clausen-Schaumann et al. [62] summarized and compared the most important experimental tools for single-molecule studies, which comprise magnetic beads [63], optical tweezers [64], glass microneedles [65], the biomembrane force probe (BFP) [66], the force clamp [67, 68], and AFM [1, 2] (cf. Table 1 in ref. [62]). With the accessible force window, the whole range from entropic forces at several piconewtons to the rupture of covalent bonds at a few nanonewtons can be investigated. Also, by combining the methods, a dynamic range from $\sim 10 \mu\text{s}$ to more than 1 s can be achieved.

Among all the force spectroscopy techniques, AFM-based SMFS has proven to be the most versatile platform for the investigation of *individual* supramolecular complexes in a wide range of media and for direct determination of unbinding forces of single, weak, supramolecular bonds [62, 69]. The principle of SMFS experiments has been thoroughly described in reviews [12, 16, 69] and other papers [62, 70–75]. In brief, macromolecular spacer chains (biomacromolecules, polymers) functionalized with a guest moiety are immobilized on a solid substrate, e.g., by the end-grafting method, to ensure probing of the individual recognition

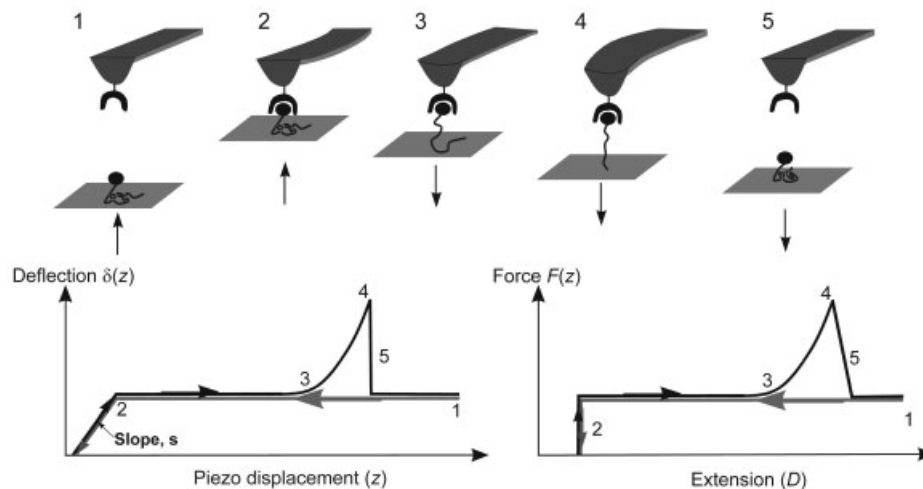


Fig. 11.5 Schematic illustration of the single-molecule force–distance measurements on surface-attached single-polymer chains. The conversion of the recorded signal (left: cantilever deflection–piezo displacement) into elastic profiles of a single-polymer chain (right: force–extension) is shown.

sites (Fig. 11.5). The tip, derivatized with a receptor moiety, is then brought into contact with the sample substrate (which is mounted on the piezo tube) by the movement of the piezo. During this process the cantilever does not bend if there are no long-range interactions, as shown in Fig. 11.5, 1. While the tip is in contact with the sample (Fig. 11.5, 2), the cantilever bends against the substrate and a repulsive signal is recorded. Upon separation of the tip and the sample (see Fig. 11.5, 3), the tip and substrate remain linked due to the specific recognition (or other intermolecular forces) between the interacting pair of molecules, and the polymeric spacer starts to be stretched (Fig. 11.5, 4), resulting in the bending of the cantilever toward the substrate. When the polymer spacer is stretched further, the weakest link along the system ruptures (or the segment of the macromolecule detaches from the substrate and/or from the tip). The cantilever then jumps back to its relaxed state rapidly, causing a sudden drop on the recorded deflection (force) trace. This drop in force is attributed to the rupture of the specific (supramolecular) bonds between the pairs of molecules that get separated (e.g., ligand–receptor, host–guest and other supramolecular complexes). The “stretching” region (from 3 to 4 in Fig. 11.5) describes the elasticity of the macromolecular spacer.

It should be noted that the cantilever deflection ($\delta(z)$ nm) and piezo displacement ($z(t)$ nm; t denotes time) data are recorded and have to be transformed into force–extension curves, as shown schematically in Fig. 11.5. In order to convert this information, the slope s of the part in the curve reflecting the bending of the cantilever upon contacting and indenting the substrate surface is first determined. During the stretching experiments, the real distance between the AFM tip and the surface (extension, $D(t)$) is obtained from $D(t) = z(t) - \delta(z)/s$. The force $F(z)$

is calculated by using Hooke's law for a linear elastic spring (cantilever) as $F(z) = k_c \delta(z)$; k_c is the spring constant of the cantilever, obtained by various calibration techniques, e.g., from the thermal oscillation spectrum of the cantilever [76–78]. The rupture force of a single complex (e.g., a ligand–receptor pair) is determined from statistical analyses of the pull-off forces of many recorded force curves. If the elastic parameters of the polymeric spacer are known, single-molecule interactions can be verified directly.

In SMFS experiments, the loading rate can be determined directly from the slope of the force–extension curve near the rupture point. For instance, the force values for the last n data points (just before the rupture point) are easily measured on the force–extension curve. From the piezo ramp rate the corresponding time for each data point can be calculated. Thus, the force (in piconewtons) of these n data points can be plotted against time (in seconds). A linear least-squares fit of these data points affords the loading rate in piconewtons per second.

11.3.2

Rupture Forces of Molecular Bonds

Specific noncovalent forces between (macro)molecules may lead to molecular recognition according to the lock and key principle. Similar criteria can be used to label interactions for artificial supramolecular dimers, etc., for which a favorable approach geometry exists that maximizes attractive interaction forces. These directional forces are superimposed on the ever-present nonspecific attraction/repulsion related to London dispersion interactions and other nonspecific electrostatic forces, which are not specific for the given bonding (“docking”) geometry. The distance dependences of these forces are different, so the various contributions can be separated, e.g., by using spacer strategies [79–82]. For describing the strength of the supramolecular interactions, e.g., receptor–ligand bonds, Evans et al. [10, 11, 66, 83] developed a theoretical basis which constitutes the foundation for experimental dynamic force spectroscopy. In the model, the strength of weak noncovalent bonds is described by applying Kramers' theory [84] of transition states, used in reaction kinetics in liquids under the influence of externally applied forces. The predicted dependences of unbinding force on the loading rate applied to the receptor–ligand bond reveal details of the molecular dynamics of the recognition process and energy landscapes [11, 15].

11.3.2.1 Rupture of Single Bonds

The binding energy E_B , given by the free-energy difference between the bound and the free states, is the common thermodynamic, ensemble-level parameter to describe the strength of a chemical bond. E_B determines the ratio of bound complexes [AB] to the product of free reactants [A] [B] at equilibrium in solution. At thermodynamic equilibrium, the number of complexes that form per unit time, $k_{\text{on}}[A][B]$, equals the number of complexes that dissociate per unit time, $k_{\text{off}}[AB]$. The kinetic rate constants, on-rate k_{on} and off-rate k_{off} , are related to the equilibrium dissociation constant K_D through $K_D = k_{\text{off}}/k_{\text{on}}$ [85, 86].

The underlying physics of the molecular pulling and rupture event of, e.g., host–

guest complexes, as mentioned later, has been developed based on transition-state theories of Kramers and Bell [84, 87]. The models we discuss briefly assume that the dynamics in the stretched molecule have a diffusive character [10, 66, 88]. Thus, the system undergoes Brownian motion on the free-energy hypersurface. Under the applied force the binding units will be pulled along a favored pathway, which coincides with the reaction coordinate. The Evans model will be discussed first.

The average lifetime of a reversible ligand–receptor bond, $t_{\text{off}}(0)$, is given by $t_{\text{off}}(0) = 1/k_{\text{off}}$. Therefore, ligands will dissociate from receptors without any force being applied to the bond at times greater than $t_{\text{off}}(0)$. When a force is applied to a bound complex, a deformation of the interaction energy landscape occurs corresponding to the addition of the potential related to the external force, and the activation energy barrier is lowered, as shown in Fig. 11.6A. Thus, the input of thermal energy by forces acting in this time regime has reduced the bond lifetime. The lifetime $t_{\text{off}}(f)$ of a bond loaded with a constant force f is given by Eq. (1), where x_{β} is interpreted as the distance of the energy barrier E_b from the energy minimum along the direction of the applied force; t_D is the diffusive relaxation time of the bound complex.

$$t_{\text{off}}(f) = t_D \exp[(E_b - x_{\beta}f)/k_B T] \quad (1)$$

This should be compared with the lifetime at zero force, $t_{\text{off}}(0)$, for a single sharp energy barrier [Eq. (2)].

$$t_{\text{off}}(f) = t_{\text{off}}(0) \exp(-x_{\beta}f/k_B T) \quad (2)$$

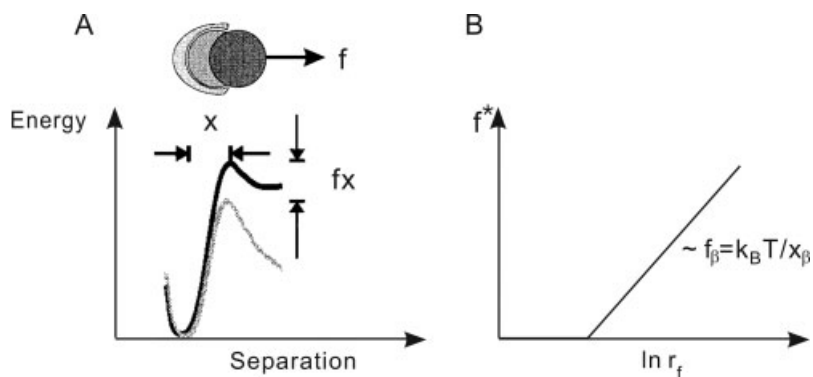


Fig. 11.6 (A) Dissociation over a single sharp energy barrier. The barrier is decreased by the applied constant force f , a characteristic length scale x is interpreted as the distance of the energy barrier from the energy minimum along the projection of the force. (Figure reproduced with permission from ref. 89. Copyright 2000, Biophysical Society.) (B) Dynamic strength

spectra for unbinding over the conceptual energy barrier in (A). The most likely detachment force f^* vs. $\ln(\text{loading rate})$ (r_f) can be plotted as a straight line with a slope $f_{\beta} = k_B T/x_{\beta}$ set by the projected location of the barrier x_{β} along the direction of the force. (Reproduced with permission from ref. 85. Copyright 1998, Royal Chemical Society.)

In far-from-equilibrium situations, the two binding partners are further separated after dissociation has occurred. Therefore, rebinding and back-reactions are negligible. During force determination in AFM measurements (or by other techniques, such as the BFP), an effective force increase or loading rate r_f can be deduced from $r_f = df/dt$. Using $t_{\text{off}}(f) = k_{\text{off}}^{-1}(f)$ relates the kinetic off-rate at a given force f , $k_{\text{off}}(f)$ to the off-rate at zero force, $k_{\text{off}}(0)$ by Eq. (3).

$$k_{\text{off}}(f) = k_{\text{off}}(0) \exp(x_\beta f / k_B T) \quad (3)$$

In the case of a single sharp energy barrier the most probable force for rupture f^* can be written as a function of loading rate r_f (Fig. 11.6B), as in Eq. (4), which introduces the thermal force $f_\beta = k_B T / x_\beta$, and a thermal scale for loading rate $r_f^0 = f_\beta / t_{\text{off}}(0)$.

$$f^* = f_\beta \ln(r_f / r_f^0) \quad (4)$$

The unbinding force (f^*) scales linearly with the logarithm of the loading rate. For a single barrier, this would give rise to a simple, linear dependence of the force versus $\log(\text{loading rate})$, as shown in Fig. 11.6B.

In cases where more barriers are involved along the escape pathway, the curve will follow a sequence of linear regimes, each of which marks a particular barrier. Hence, the transition from one regime to the other is associated with a sudden change of slope determined by the characteristic barrier length scale [11, 15, 85].

11.3.2.2 Crossover from Near-Equilibrium to Far-from-Equilibrium Unbinding and Effect of Soft Polymer Linkages on Strengths

As shown in Fig. 11.6A, the energy landscape of the bond is tilted when an external force is applied, which increases the opportunity of the bond to rebind after a rupture. In AFM experiments, a transient capture well occurs (which enables the rebinding) when pulling on the bond, due to the presence of the linkage (the spacer + cantilever), as illustrated in Fig. 11.7A. Only if the linkage is very soft, or the applied force becomes large enough to drop the energy level of the capture well below the bound state, does the energy landscape approach the far-from-equilibrium condition. Thus the crossover [15] from near-equilibrium to far-from-equilibrium situations can be defined as the point when the forward rate of the barrier pathway exceeds the backward rate, i.e., $k_{\rightarrow} > k_{\leftarrow}$. Here, the ratio of rebinding-to-unbinding rates will diminish, as it is proportional to $\exp(-f^2 / 2\kappa_s)$, (the dimensionless linkage stiffness $\kappa_s = \kappa_s x_\beta^2 / k_B T$, and force $f = f / f_\beta$). In order to achieve complete unbinding (far-from-equilibrium), the force must rise above the approximate value in Eq. (5), where the equilibrium constant K_{eq} equals $t_{\text{off}} / t_{\text{on}}$.

$$f_{\otimes} \sim [2\kappa_s k_B T \ln(K_{\text{eq}})]^{1/2} \quad (5)$$

The influence of linkage stiffness κ_s on both crossover force f_{\otimes} and rupture loading rate r_f is shown in Fig. 11.7B. The experimental results showed that the stiffer the linkage, the larger the most probable rupture force at low loading rates.

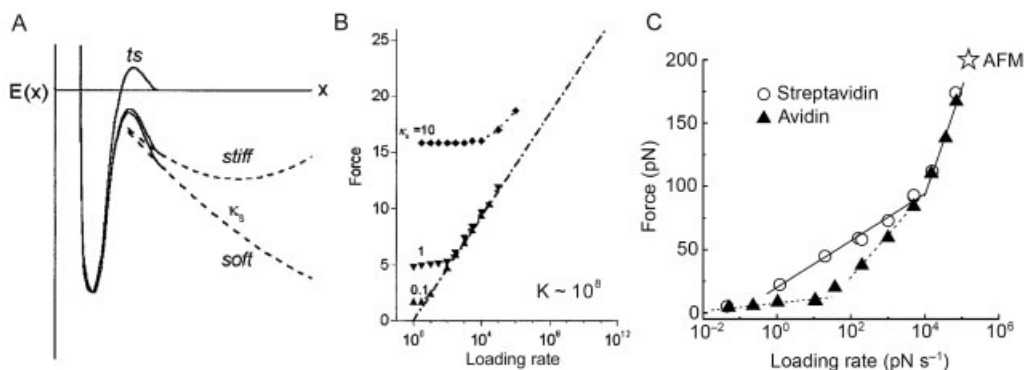


Fig. 11.7 (A) Conceptual energy landscapes for a simple bond pulled by a soft and a stiff spring, respectively. (B) Dynamic spectra of most frequent rupture force produced at low loading rates by rebinding as a function of probe linkage stiffness. Equilibrium constant $K = t_{\text{off}}/t_{\text{on}}$. (Figures reproduced with

permission from ref. 15. Copyright 2001, *Annual Reviews*.) (C) Force–loading rate plot determined for the interaction between biotin and streptavidin by Evans et al. using the BFP method in aqueous medium. (Reproduced with permission from ref. 11. Copyright 1999, Macmillan Magazines.)

For multiple energy barriers a linear relationship is predicted consisting of linear sections between the dissociation force and the logarithm of the loading rate, with each section corresponding to a given barrier in the potential energy landscape passed in the direction of applied force under its load. A prominent example is the forced unbinding of the biotin–streptavidin complex (Fig. 11.7C). The polymer linkers used in single-molecule experiments help to hold back the rebinding events. At low speed (i.e., in near-equilibrium situations), however, the bond strength can be altered by polymer linkages.

The recent Hummer–Szabo model [88] differs from the Evans model in allowing for the position of the rate-limiting barrier to fluctuate under load. This model, however, has more parameters, and has not been tested (to our knowledge) on single, synthetic, one-barrier, supramolecular systems. The additional parameters that one can fit include the effective spring constant (cantilever and spacer) and the effective diffusion coefficient.

11.3.2.3 Rupture of Multiple Bonds

Force spectra for multiple bonds can provide useful insights into the nature of hidden interactions in a molecular assembly. However, the effect of cooperativity in multiple-bond detachment is complicated and thus difficult to measure. Here, we consider only the case of bonds in parallel (Fig. 11.8A) (i.e., the force is spread evenly across entire bonds), and the case of bonds in series (Fig. 11.8B) (i.e., the force is applied equally to each bond). In any states, such a system behaves like a “macro-single bond” with a barrier given by the sum of the individual barrier energies [90].

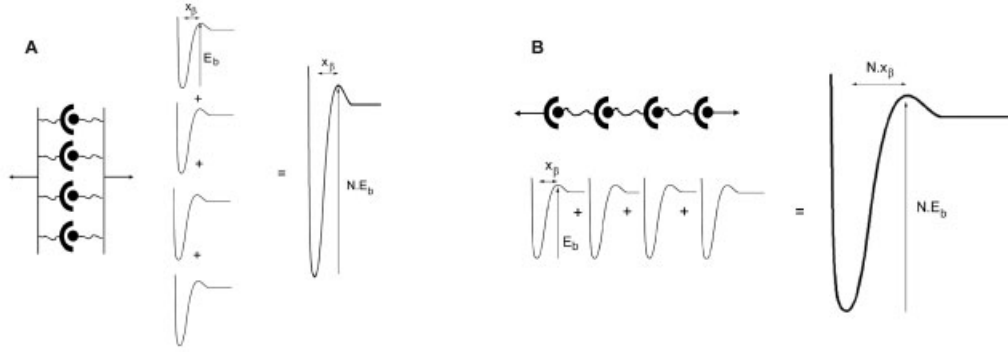


Fig. 11.8 A system of identical attachments that fail cooperatively when loaded (A) in parallel or (B) in series can be considered as a single bond with a barrier scale N times that of the single bond. (Figures adapted from ref. 90. Copyright 2002, EPD Science Springer-Verlag.)

For a simple ideal bond, the lifetime is set by the exponential magnitude of the energy barrier with a diffusive relaxation time [Eq. (1)]. With N identical bonds, cooperative unbinding leads to a large increase in the timescale for dissociation, according to Eq. (6).

$$t_{\text{off}}(N) \approx N t_{\text{off}} \exp[(N-1)E_b/k_B T] \quad (6)$$

For identical cooperative bonds in parallel (Fig. 11.8A), the location of the transition state x_β and the thermal force scale f_β remain those for the single bond. Hence, for bonds in parallel that are broken far from equilibrium, the force can be estimated from Eq. (7), which implies that the force needed to break a parallel bond attachment is essentially a factor of N larger than for a single bond under the same rate of loading.

$$f^* \approx f_\beta [\ln(r_f) + \ln(N) + (N-1)E_b/k_B T] \quad (7)$$

For identical bonds in series (Fig. 11.8B), each bond contributes an increase in length along the direction of force, i.e., $x_\beta = N x_{\beta}$, and the thermal force scale is lowered N -fold, i.e., f_β/N . Hence, for N bonds in series, far from equilibrium, the force can be approximated as in Eq. (8):

$$f^* \approx f_\beta/N [\ln(r_f) + 2 \ln(N) + (N-1)E_b/k_B T] \quad (8)$$

Here, each bond experiences the same force and any rupture event leads to the rupture of the attachment. Thus in far-from-equilibrium situations, the rate of rupture events is N times faster than the rate for one bond, which weakens the attach-

ment slightly compared with that of a single bond at a given loading rate [Eq. (9)], where r_f is the dimensionless loading rate.

$$f^* = f_{\beta}[\ln(r_f) - \ln(N)] \quad (9)$$

11.4

SMFS of Synthetic Supramolecular Dimers and Polymers

11.4.1

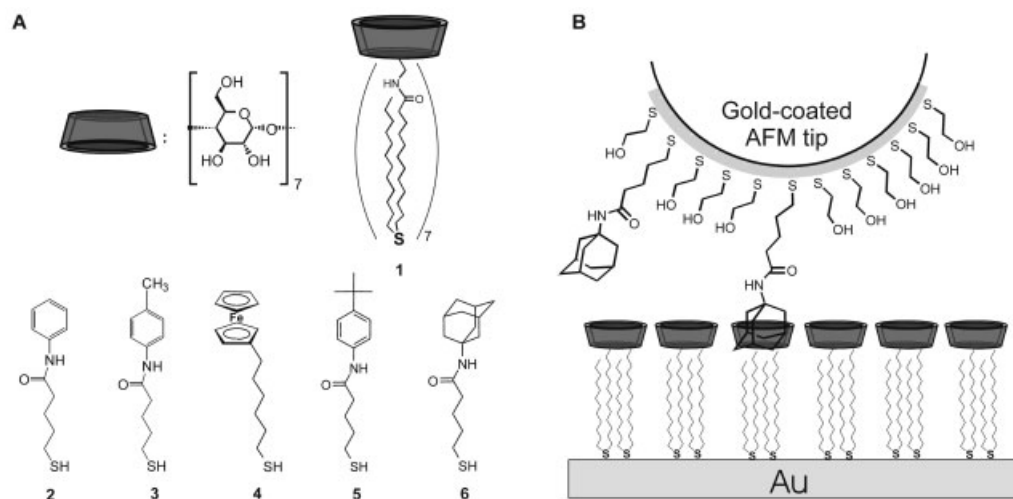
Host–Guest Interactions in Inclusion Complexes

Inclusion complexes can be defined as supramolecular complexes in which one component (the host, or receptor) forms a cavity in which molecular entities of a second species (the guest, or ligand) can nestle. There is no covalent bonding between the guest and the host, and binding forces (attraction) are due to supramolecular interactions. β -Cyclodextrin (β -CD) is a widely researched host, which is built up from seven glucose units forming a cyclic ring with the shape of a truncated cylinder [91]. The central section of the molecule encompasses a cavity which can accommodate nonpolar, lipophilic guest molecules of suitable size (like ferrocene) in aqueous solutions. Molecular similarity plays an essential role in determining the binding strength of ligand–receptor complexes. The strength of the interaction depends on the complementarities of the shape and volume of the species (or, in other words, on their surface potential).

11.4.1.1 β -CD-Based Inclusion Complexes

The complexation behavior of various moieties shown in Scheme 11.1A, immobilized in mixed self-assembled monolayers (SAMs) with 2-hydroxyethanethiol (C2OH) on an AFM tip with heptathioether β -CD SAMs in aqueous media have been studied by AFM-based force spectroscopy, as shown in Scheme 11.1B [92–94].

This supramolecular host–guest (HG) system is characterized by fast complexation/decomplexation kinetics; thus the guest moieties have the possibility of decomplexing and rebinding spontaneously many times during the recording of an AFM force–distance curve, as long as the tip stays in close proximity to the β -CD SAM. In consecutive experiments performed on the same system, sawtooth-like unloading force curves were obtained, which showed characteristic force jumps (see also Fig. 11.11A). Statistical analyses of the pull-off data for the ferrocene– β -CD system showed a periodic distribution of forces. The maxima were found to correspond to integer multiples of a fundamental force quantum [93]. In accordance with the long timescale of the AFM pull-off experiments (timescale $\sim 1000 \mu\text{s}$) relative to decomplexation–recomplexation dynamics, this force quantum ($55 \pm 10 \text{ pN}$) was found to be independent of the loading rate, which was varied over three orders of magnitude (Fig. 11.9) [92, 93]. This observation indicated that the system is indeed probed under quasi-equilibrium conditions.



Scheme 11.1 (A) Chemical structure of β -CD adsorbate **1** and guest molecules **2–6** for immobilization on AFM tips. (B) Schematic drawing of single-molecule force spectroscopy of **6** immobilized in a hydroxyl-terminated SAM on a gold-coated AFM tip and SAM of **1** on Au(111) (five of the seven alkylsulfide substituents on the β -CD have been omitted for clarity). (Reproduced with permission from ref. 95.)

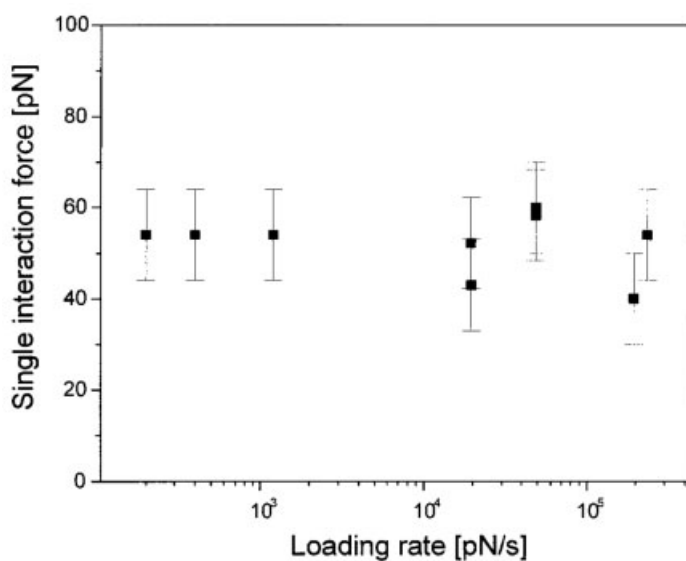


Fig. 11.9 Loading rate dependence of the single host–guest complex rupture force for the interaction between β -CD and ferrocene in an aqueous medium. (Reproduced with permission from ref. 93. Copyright 2000, American Chemical Society.)

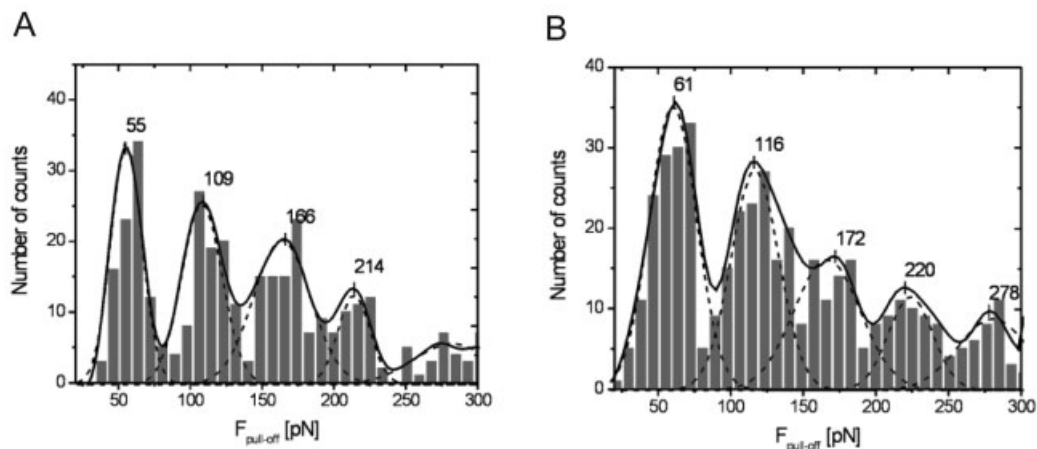


Fig. 11.10 Histograms of pull-off forces for the systems containing (A) guest 4 (0.2%)–C2OH; (B) guest 16-ferrocenylhexadecanethiol (0.2%)–C2OH. The solid lines represent the fast Fourier transform (FFT)-smoothed

histograms as a guide for the eye; Gaussian curves fitted to the histograms are drawn as broken lines. (Reproduced with permission from ref. 92. Copyright 2002, American Chemical Society.)

The force quantum was also found to be independent of the number of available guests [94] and the length of the spacer [92] between the guest and the surface, as shown in Fig. 11.10. The quasi-thermodynamic equilibrium conditions reported in this early work imply that there is a correlation between unbinding forces and equilibrium complexation constants for closely related guest– β -CD systems (Scheme 11.1, above).

To test this notion, the magnitude of single supramolecular host–guest complex rupture forces of the apolar guests, studied previously by surface plasmon resonance on surfaces and isothermal calorimetry in solution [96, 97], on highly ordered β -CD SAMs was determined by single-molecule force spectroscopy in aqueous media.

Specific interactions between the β -CD host monolayers and guest 6 (Scheme 11.1) immobilized in mixed SAMs of C2OH on AFM tips were detected in aqueous medium in force–displacement (f – d) curves, as shown in Fig. 11.11. The f – d curves obtained using tips with 1% and higher surface coverage of guest molecules showed multiple pull-off events upon retraction of the sample from the tip (Fig. 11.11A). These multiple pull-off events were absent when tips without any guests or “receptor” SAMs without β -CD units were utilized. When an aqueous solution of the binding guest 1-anilinonaphthalene-8-sulfonic acid (1,8-ANS, $K = 2.6 \times 10^4 \text{ M}^{-1}$ [93], $c \sim 0.1 \text{ mM}$) was injected into the liquid cell, the number of multiple pull-off events decreased markedly. This effect can be attributed to the partial blocking of the β -CD cavities due to the binding of 1,8-ANS to the β -CD host sites (competition of 1,8-ANS with 6). After the 1,8-ANS had been washed away with

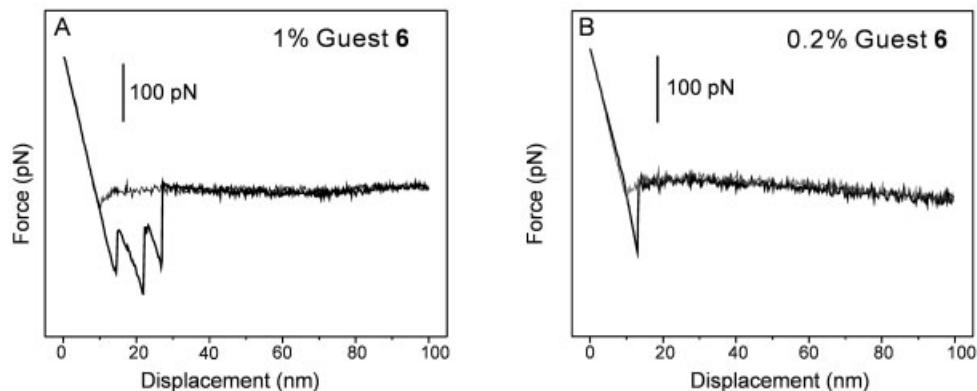


Fig. 11.11 Force–displacement curves for the interaction of (A) 1% adamantane **6**, and (B) 0.2% adamantane **6**, with β -CD SAMs **1** on Au(111) measured in MilliQ water (nominal loading rate $\sim 20 \text{ nN s}^{-1}$, temperature = 301 K). (Reproduced with permission from ref. 95.)

water, the multiple pull-offs were observed again. For the cases of guests **3** and **5**, which possess lower association constants with monolayer **1**, the number of pull-off events was reduced more drastically, as reported previously [92, 93]. These observations are in agreement with a reversible blocking of a large proportion of the available cavities in the monolayer of **1** by the external guest.

Dilution of the guest molecules in the C2OH SAMs to 0.2% led to a significant reduction in the number of pull-off events (f - d curves with pull-off events were less than 20% of the tip–sample contacts). For very sharp tips, single pull-off events were observed in more than 70% of the successful pull-off events (Fig. 11.11B).

The force histogram analyses of the rupture events observed for the interactions between β -CD and **6** for two different coverage values on the tip are summarized in Fig. 11.12. The presence of multiple peaks in the rupture force histograms is observed for higher coverage of the guest on the tip. The local maxima occur at 100 pN and 197 pN, respectively, determined from fast Fourier transform (FFT) smoothed force histograms. The peaks are attributed to the rupture of one and two independent adamantane– β -CD complexes, respectively. Based on three independent data sets, the mean value of the force quantum of $102 \pm 15 \text{ pN}$ was determined for the single adamantane– β -CD complex rupture force.

The multimodal distribution of rupture forces is contrasted by the f - d data measured between AFM tips functionalized with pure C2OH SAMs and β -CD SAMs, which can be described by a single broad distribution of forces centered at $\sim 300 \text{ pN}$.

For lower coverage values of **6**, the distribution of the observed single pull-off events showed a single broad maximum at around 105 pN (Fig. 11.12B). This value

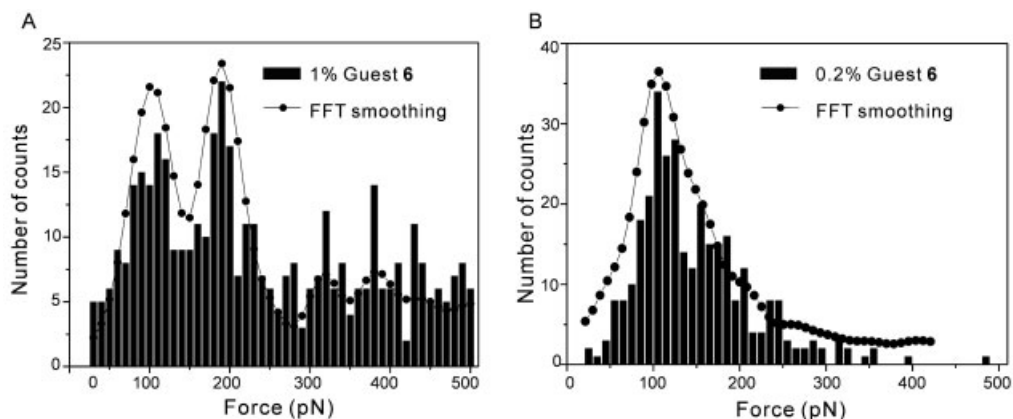


Fig. 11.12 Statistical analyses of pull-off events of observed for (A) multiple and (B) single pull-off events between monolayers 1 and guest 6. The lines correspond to the FFT-smoothened data. (Reproduced with permission from ref. 95.)

is in good agreement with the first local force maximum observed at high degrees of coverage of adamantane on the tips (Fig. 11.12A) and hence is attributed to the rupture force of a single HG complex. The width of the peak, however, suggests that there is a significant contribution of a higher force component, most likely the rupture of two independent adamantane- β -CD complexes (~ 200 pN).

Multiple pull-off events were observed reproducibly in the case of high (1%) coverage of guest molecules on AFM tips, and predominantly single pull-off events in the case of low (0.2%) coverage of molecules on the tip. Thus, the number of resolved pull-off events and hence interacting β -CD and guest moieties 6 qualitatively scales with the composition of the SAM on the functionalized AFM tips. In the case of low guest coverage on the tip, the predominant peak in the histogram is consistent with the detection of single unbinding events. These observations support the interpretation that the individually resolved pull-off events can indeed be attributed to specific host-guest complex rupture events.

In agreement with previous reports [92, 93, 98], the quantized force was unaffected by the (nominal) loading rate (using linkages with the same stiffness), which was varied over several orders of magnitude in the range of 10^3 – 10^5 pN s $^{-1}$, for tips covered with mixed SAMs of C2OH containing 1% of 6. Thus, the rupture forces were probed by force spectroscopy under conditions of quasi-thermodynamic equilibrium.

SMFS measurements of the weakly binding guests 2 and 3 were carried out on SAMs of 1. Force-displacement curves for these adsorbates (concn. 2%) also showed the characteristic multiple pull-off events (no data shown). All pull-off forces determined from individually resolved events were plotted in histograms. FFT smoothing of the force histograms for tips functionalized with 2 and 3 affords

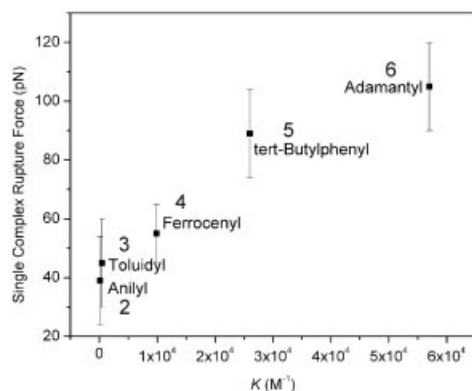


Fig. 11.13 Correlation of individual unbinding forces and complexation constants K . (Reproduced with permission from ref. 95.)

periodic distributions of forces, regardless of the bin size, with force quanta of 39 ± 15 and 45 ± 15 pN, respectively. Similarly to the previously discussed HG pair [92, 93], these force quanta are attributed to the rupture force of individual supramolecular β -CD–guest complexes. The forces are significantly lower than those determined for the more strongly binding guests. Using the primary force “quantum” as the single host–guest rupture force for the different guests, a correlation could be established for this type of specific bonding geometry between the single-complex rupture force and the bulk complexation constant (Fig. 11.13).

The observed loading rate independence of the single-complex rupture forces suggests that the rupture is probed under quasi-thermodynamic conditions. In order to derive a relation between ΔG° and the HG complex rupture force $F_{\text{pull-off}}$ for an individual host–guest pair, a model [99] based on a Lennard-Jones potential (LJP) [100, 101] has been developed by Huskens et al. [94]. From the model, which does not require the use of adjustable parameters, it is possible to calculate the dependence of the probability of pull-off $p_{\text{pull-off}}$, and the dependence of the pull-off force on the Gibbs free energy. This dependence can be compared with the experimental data obtained previously, including the data reported above. According to this model, the pull-off force was found to be a function of $(-\Delta G^\circ)^{1/2}$. The order of magnitude, as well as the increasing trend, of the rupture forces observed with increasing $-\Delta G^\circ$ agrees well with the predictions of the model [94].

11.4.1.2 Inclusion Complexes of Resorc[4]arene CavitanDs

Very recently, Eckel et al. [82] reported on a single-molecule force spectroscopy study aiming at the determination of the unbinding forces in inclusion complexes of individual ammonium and substituted ammonium cations with resorc[4]arene-based cavitanDs. In these host–guest complexes the binding of the cations is facili-

tated by ion–dipole interactions, as well as contributions originating from hydrogen bonds and cation– π interactions between the positively charged cation and the aromatic rings of the cavitand. The strength of interactions is governed by the cation size and leads to specificity of the recognition process. In the experiments the cations were covalently attached to the AFM tip via a flexible poly(ethylene glycol) (PEG) spacer. As discussed by Hinterdorfer and coworkers [79] and shown by others [80, 81, 102, 103], such a spacer provides a means to suppress non-specific interactions and to identify individual host–guest complex rupture events.

SMFS data acquired with PEG-cation modified tips on diluted SAMs of the 2,8,14,20-tetra-[10-(decylthio)decyl] cavitand in ethanol showed the characteristic stretching of the PEG spacer followed by a single-step unbinding (Fig. 11.14A). The analysis of the unbinding forces and probabilities for differently substituted ammonium ions indicated the specific and selective nature of these host–guest interactions. The unbinding forces displayed a pronounced loading rate dependence (Fig. 11.14B), from which the authors calculated bond lifetimes of $\tau = 1.01$ s and $\tau = 53.5$ s for the ammonium residue and the trimethyl ammonium residue, respectively.

11.4.1.3 Inclusion Complexes of Crown Ethers

Kado and Kimura reported on an AFM investigation of the complexation behavior of 18-crown-6 with ammonium ions in ethanol [104]. As briefly mentioned in Sec-

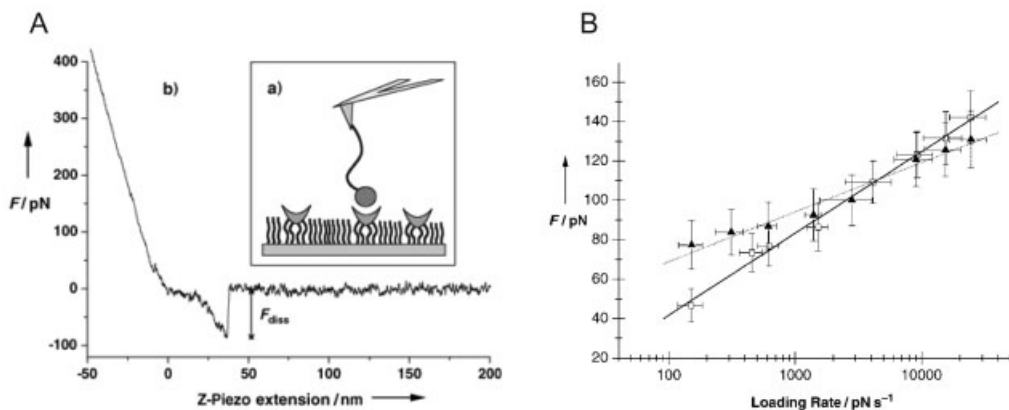


Fig. 11.14 (A) Force spectroscopy: (a) schematic setup. The cavitand is immobilized together with bis(decyl) sulfide in a 1:40 mixture on a gold substrate. The (tetraorganyl)ammonium residue (shaded circle) is attached to an Si_3N_4 AFM tip by a flexible polymer linker. (b) Typical force–distance curve (only the retractive trace is shown). The stretching of the PEG linker over a certain distance before bond rupture (tip

detachment and relaxation of the cantilever) indicates an unbinding event. (B) Unbinding forces, plotted logarithmically against the corresponding loading rates, for the binding of the ammonium (squares) and trimethylammonium (triangles) residues to the resorcin[4]arene cavitand. (Figures reproduced with permission from ref. 82. Copyright 2005, Wiley-VCH.)

tion 11.2.2, crown ethers, such as the 18-crown-6 described, belong to the well-known class of artificial macrocyclic compounds that complex alkali metal and ammonium ions. In Kado and Kimura's experiments, the interaction forces between gold-coated AFM tips and mica surfaces modified with 6-mercaptohexyloxymethyl-18-crown-6 and 3-(aminopropyl)triethoxysilane (APTES), respectively, were measured. Typical force–displacement curves are shown in Fig. 11.15. Single, as well as multiple, pull-off events were observed. Upon addition of $\text{CF}_3\text{SO}_3\text{K}$ to the ethanol, the magnitude of the pull-off force decreased markedly.

Control experiments carried out with octadecylsilane layers on mica, as well as the blocking experiments with solution-borne potassium ions mentioned above suggested that the observed forces are indeed specific crown–ammonium ion interactions. The pull-off forces were also reported to depend on the pH, when measurements were carried out in aqueous solution. Statistical analysis of the force data by an autocorrelation method and a Poisson method indicated that the magnitude of the rupture force of individual 18-crown-6–ammonium ion complexes is approximately 60 pN in ethanol.

In an extension of this work, Kimura and coworkers studied the interaction of dibenzo crown ethers adsorbed on HOPG with ammonium-ion modified probe tips in ethanol [105]. In this case also, specific interactions were observed, as evidenced by the agreement of force data recorded with different cations and ion se-

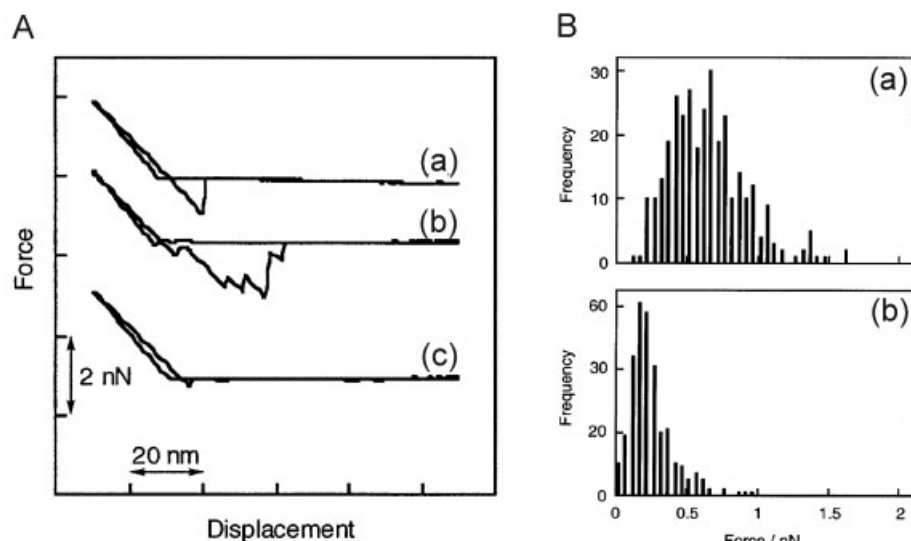


Fig. 11.15 (A) Force curves observed on APTES/mica substrate using 18-crown-6/tip: (a) a typical force curve; (b) a less typical force curve showing multiple pull-off events observed in ethanol; (c) a force curve showing a smaller adhesion force due to blocking in an ethanol solution containing 10 mmol dm^{-3} $\text{CF}_3\text{SO}_3\text{K}$. (B) Histograms for adhesion forces

obtained from each set of repetitive force measurements in ethanol using APTES/mica substrate and 18-crown-6/tip, (a) in the absence of and (b) in the presence of potassium ions. The histograms were drawn at a force interval of 50 pN. (Reproduced with permission from ref. 104. Copyright 2003, American Chemical Society.)

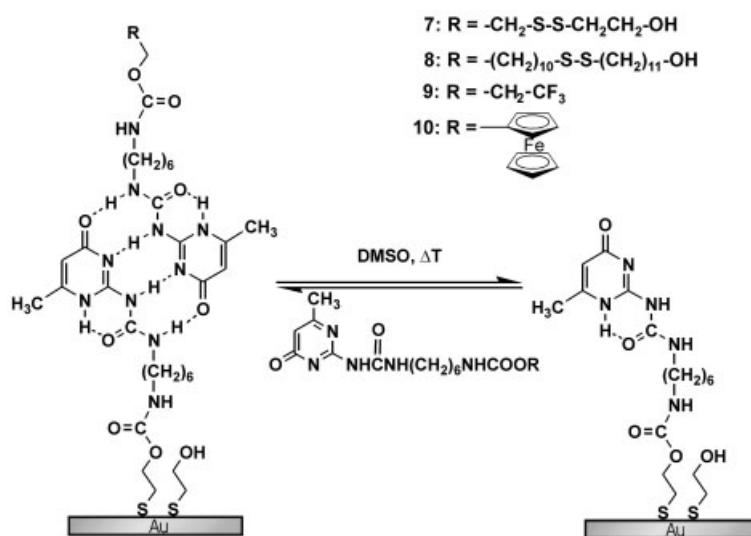
lectivity known from solution studies. These data suggest that simple physical adsorption of the target molecules onto substrates provides a method of studying specific interactions between host and guest molecules by means of AFM-based force spectroscopy.

11.4.2

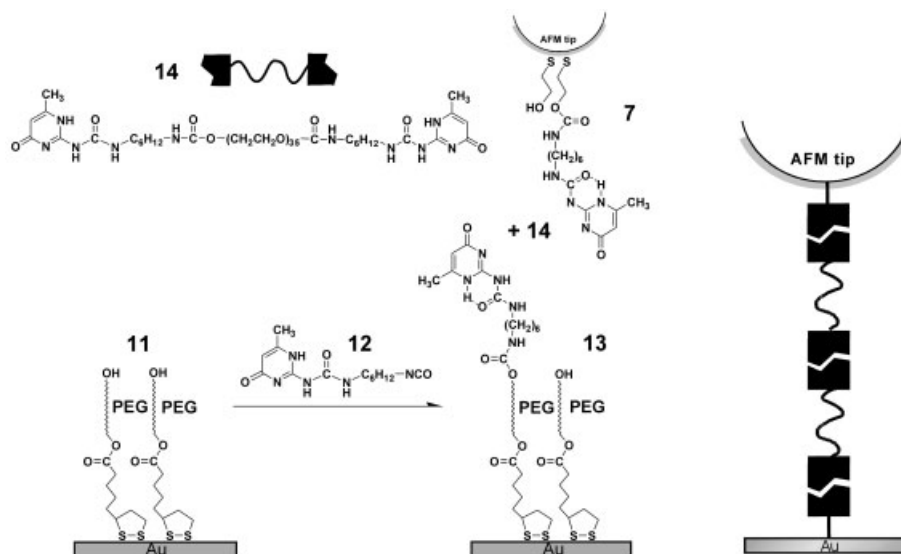
Host–Guest Interactions via H-bonds: Quadruple H-bonded UPy Complexes

As outlined in Section 11.2.1, supramolecular chemistry utilizes multiple, reversible, cooperative hydrogen-bonding interactions to fabricate self-organized structures with a very rich structural hierarchy [36, 37]. The corresponding intermolecular interactions (forces) [34] govern the interplay of order and mobility [106], as well as the properties *and* functionality (recognition, reaction, transport, regulation, etc.) in such systems [30, 49, 106].

Vancso and coworkers [81] have undertaken systematic single-force spectroscopy studies that targeted such artificial, supramolecular H-bonded species. The work is based on a versatile substrate-immobilized molecular platform [107] for the controlled immobilization or growth of complex supramolecular architectures. This platform is derived from the self-complementary quadruple hydrogen-bonded UPy motif, previously introduced by Meijer, Sijbesma, and coworkers [24, 52]. Scheme 11.2 shows the molecular recognition of surface-bound self-complementary UPy



Scheme 11.2 The complex formation of 2-ureido-4[1*H*]-pyrimidinone moieties at Au surfaces through quadruple hydrogen bonds can be conveniently controlled via solvent or temperature. (Reproduced with permission from ref. 107. Copyright 2003, American Chemical Society.)



Scheme 11.3 Molarly thin layers of ω -hydroxy-terminated PEG are obtained by self-assembly of disulfide **11** from chloroform solution onto Au(111) surfaces, followed by reaction with isocyanate **12** to form a layer exposing UPy moieties **13**. Supramolecular polymers, which are formed by self-complementary association of the telechelic

PEG derivative **14** in hexadecane solution, can be probed by AFM (right-hand scheme) utilizing gold-coated AFM tips functionalized with a SAM of the asymmetrically substituted UPy disulfide **7** in hexadecane. (Reproduced with permission from ref. 81. Copyright 2005, Wiley-VCH.)

moieties with external UPy guests, as studied in SAMs on Au by exploiting the dependence of the dimerization constant on solvent and temperature [107].

This platform is the basis for addressing both the individual interactions of dimeric UPy complexes, and the study of individual supramolecular polymer chains. As illustrated in Scheme 11.3, such experiments involve the probing of a dynamic “macromolecule” that is composed of reversibly aggregated self-complementary building blocks.

The systematic investigation of single-chain mechanical properties of supramolecular UPy polymers was based on the measurement of the *individual* molecular interactions present in these supramolecular polymers. For this purpose, monolayer architecture **13**, comprising surface-immobilized ω -hydroxy PEG chains, was prepared on Au(111) by coupling UPy isocyanate **12** with the hydroxy functionalities of a layer of **11** (Scheme 11.3) [81]. Similarly to **7**, this architecture ensures that the UPy units are available for complexation in a solution-like environment, as indicated by differential pulse voltammetry experiments with ferrocenyl-labeled UPy derivative **10**. Layers of **13** thus expose chemically accessible UPy units tethered via PEG spacers to gold surfaces. Since the mechanical properties of these

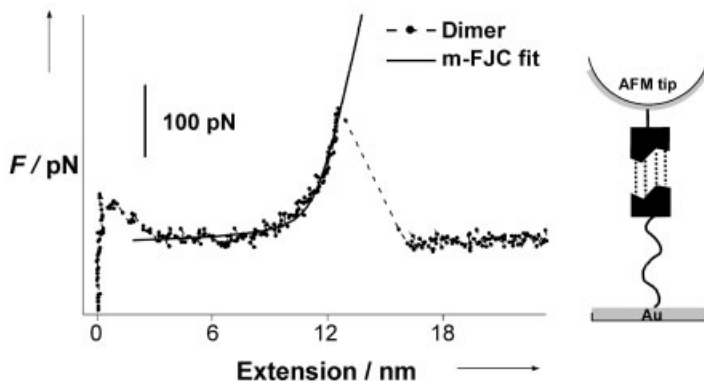


Fig. 11.16 Force–extension curve measured between a gold-coated AFM tip functionalized with a SAM of UPy disulfide **7** and an Au(111) sample functionalized with a layer of **13** in hexadecane. The fit of the data to the m-FJC model is shown as a solid line. (Reproduced with permission from ref. 81. Copyright 2005, Wiley-VCH.)

spacers are known [108, 109], the stretching of *single* macromolecules in SMFS measurements can be identified and verified.

F–d curves measured in hexadecane (HD) between **13** immobilized on Au(111) and AFM tips functionalized with **7** showed the typical stretching of the PEG spacer followed by a sharply defined bond rupture event (Fig. 11.16). The force–extension curves were fitted to the modified freely jointed chain (m-FJC) model [Eq. (10)]. Based on the good agreement of the fitted elasticity parameters (Kuhn length 0.65 ± 0.08 nm; segment elasticity 6.2 ± 0.6 nN nm⁻¹) with literature data [108, 109] and of the contour length with the theoretical contour length of the linker utilized (12 ± 3 nm), the stretching of an individual PEG segment of **13** was ascertained.

$$x(F) = \left[\coth\left(\frac{FI_K}{k_B T}\right) - \frac{k_B T}{FI_K} \right] \left[L_{\text{contour}} + \frac{n}{K_{\text{segment}}} F \right] \quad (10)$$

In this equation, x is the extension of the polymer chain; F is the applied force; I_K (Kuhn length) is the length of the statistically independent segment; n is the number of segments, which equals L_{contour}/I_K ; K_{segment} is the segment elasticity, which characterizes the deformability of the segment; k_B is the Boltzmann constant; and T is the temperature.

These fit parameters agree well with, and thus confirm, the successful stretching of *single* PEG chains. The observed extensions agree favorably with the contour length of the linker (approximately 12 ± 3 nm; PEG chain is 9.5 ± 1.0 nm). Since *single* PEG chains are stretched, the rupture forces of a single UPy–UPy complex can be determined directly as 180 ± 21 pN in HD ($T = 301$ K, loading rate 35 nN s⁻¹).

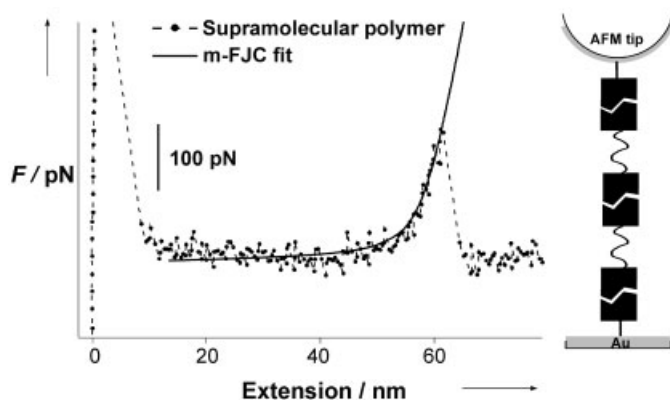


Fig. 11.17 Force–extension curve measured between a gold-coated AFM tip and an Au(111) sample, both functionalized with layers of **7** in the presence of the bifunctional bis-UPy derivative **14** in hexadecane. The fit of the data to the m-FJC model is shown as a solid line. (Reproduced with permission from ref. 81. Copyright 2005, Wiley-VCH.)

To probe single-chain mechanical properties of UPy-based supramolecular *polymers*, AFM measurements were carried out with tips and substrates both modified with the short-chain UPy disulfide **7** in the presence of bis-UPy **14** in HD (10^{-3} mM). Owing to the high complexation constant of $\geq 10^9$ m^{-1} and a complex lifetime in excess of 1 s [110, 111], bis-UPy will form supramolecular polymers with an effective degree of polymerization of ~ 40 in solution [81]. Figure 11.17 shows a typical force–extension curve measured under these experimental conditions.

A significant restoring force was observed only for extensions > 50 nm. The elasticity parameters are, to within experimental error, equal to the data measured for a single PEG chain (Kuhn length 0.68 ± 0.08 nm; segment elasticity 7.6 ± 2.5 nN nm^{-1}), thus indicating that in this experiment also a *single* PEG “chain” was stretched. The significantly greater stretching length (\gg contour length of a single PEG segment) indicates that supramolecular polymers were indeed stretched, which appears to be reasonable considering the lifetimes of UPy complexes in HD. By contrast, *f–d* curves recorded in 15% DMSO in isopropanol showed a markedly different stretching length distribution. In this case, only very short chains were stretched, comparably to the situation observed for the dimer experiment in HD. A very similar reduction in stretching length was observed in blocking experiments with a trifluoromethyl-functionalized UPy derivative **9** [81].

The mean value of the rupture forces observed for the supramolecular polymers in HD (172 ± 23 pN) is equal, to within the error, to the rupture force of the dimeric complex. These data suggest, however, that the rupture forces decrease slightly with increasing lengths of the stretched supramolecular polymer chains. This observation is in full agreement with the theory developed by Evans and co-workers [10, 66, 90] who predict a decreasing magnitude of the single-complex

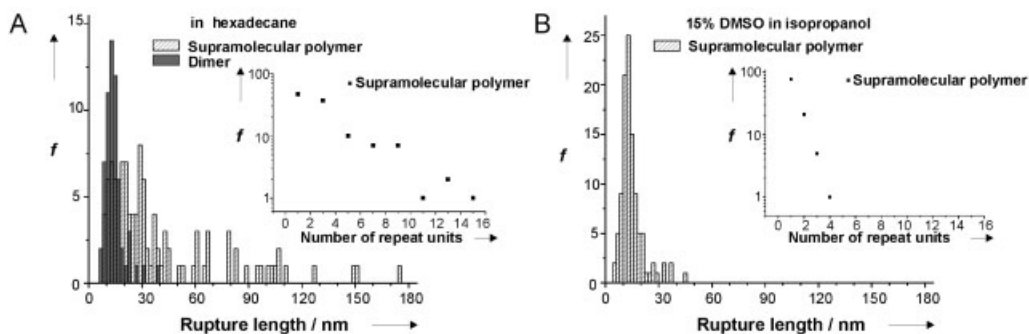


Fig. 11.18 (A) Histogram of extension lengths observed for the experiment probing the dimeric interactions and the supramolecular polymers in hexadecane (inset: number of extension events (f) vs. number of repeat units in stretched supramolecular polymers calculated on the basis of the length of one repeat unit). (B) Histogram of extension lengths observed for the experiment probing the supramolecular polymers in 15% DMSO in isopropanol (inset: number of extension events vs. number of repeat units). (Reproduced with permission from ref. 81. Copyright 2005, Wiley-VCH.)

rupture force with increasing spacer length and increasing number of consecutive bonds along one molecule [compare Section 11.3.2.3, Eq. (8)] [90].

Stretching lengths of more than 150 nm were detected in HD (Fig. 11.18A, left), which corresponds to a “degree of polymerization” of up to 15, assuming a “monomer length” of 12 nm. The probability of stretching a supramolecular polymer chain that bridges the gap between substrate and tip appears to be an exponential function of the chain length (inset in Fig. 11.18A). In the presence of DMSO the hydrogen bonds are disrupted [52, 112, 113] and consequently the stretching and rupture of long supramolecular polymers is not observed (Fig. 11.18B).

These AFM data show that supramolecular polymers can indeed be investigated at the single-molecule level. In PEG-based telechelic bis-UPy materials, the individual reversible linking sites along a supramolecular polymer chain, i.e., the complexes based on self-complementary recognition of 2-ureido-4[1*H*]-pyrimidinone, act as independent bonds in series. Since the material properties, including viscosity, composition, or chain length, are functions of various external parameters and stimuli, which can be investigated *in situ*, highly useful information for the design and construction of nanometer-scale devices and stimuli-responsive systems will now become directly accessible from SMFS experiments.

The same quadruple H-bonding UPy motif used in supramolecular polymers was explored by Guan and coworkers as a means to design biomimetic modular macromolecules with improved mechanical properties [114]. The characteristic unfolding pattern of globular proteins, such as titin [115] and those found in abalone shells [116], and the relationship between the unfolding behavior and desirable mechanical properties (high strength, toughness, and elasticity), inspired the syn-

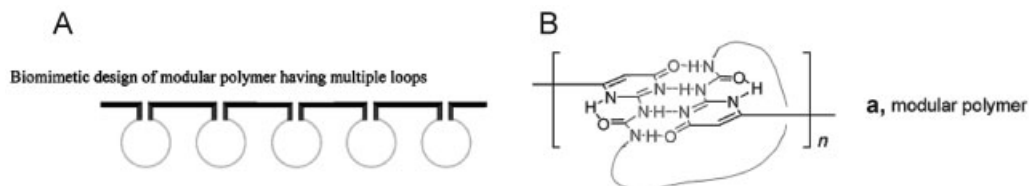


Fig. 11.19 (A) Design of a modular polymer containing multiple loops held by secondary forces. (B) Schematic of the molecular structure of a modular UPy polymer **a** (the loop stands for the PTMG linker). (Reproduced with permission from ref. 114. Copyright 2004, American Chemical Society.)

thesis of poly(tetramethylene glycol) (PTMG)-based polymers incorporating UPy groups (Fig. 11.19). These substituents provide a pathway to multiple internal loops via intramolecular H-bonding.

AFM-based SMFS studies were conducted on gold samples, which were coated with the modular polymer by physisorption [114]. The sequential unfolding of loops in the modular polymer chain was observed in force–displacement measurements conducted in toluene as a characteristic sawtooth pattern. These sawtooth-shaped force–extension curves reflect a constant force sustained over the entire extension, which makes the polymer strong, along with a large area under the force–extension curve, making it tough as well. Recently, the general strategy has been extended to double closed loop topologies utilizing peptidomimetic β -sheets [117].

The unbinding events of the UPy-based modular polymers showed consistently two peak forces of ~ 100 pN and another at ~ 200 pN (at piezo retraction velocities of $0.06\text{--}0.35 \mu\text{m s}^{-1}$). The authors attributed these different unbinding forces to rupture of isolated UPy complexes in different UPy dimer topologies formed along the polymer chains. These values are in a similar range of magnitudes to the rupture forces of UPy dimers that we reported [81], which were found to be 180 ± 21 pN in HD ($T = 301$ K, loading rate 35 nN/s). However, since the loading rates and solvent media (toluene versus hexadecane) were different for the two experiments and since the serial character of the rupture of the modular polymer can be expected to influence these values, these force data cannot be directly compared.

The UPy-based modular polymers can be considered as protein mimics; however, they are different from the reversible supramolecular polymers discussed in Section 11.2.1. These latter polymers consist of low molar mass building blocks that form the polymer chains by reversible self-association. A recent report by Craig and coworkers [118] discussed a related system. Self-assembled bridges between AFM tips and substrate surfaces, based on oligonucleotide-containing monomers, were detected in SMFS measurements in aqueous media [118]. The assembly was found to be reversible and was inhibited by a competitive, nonpoly-

merizing oligonucleotide. The authors interpreted the observation that the rupture forces of these assemblies were independent of polymer bridge length as an indication that the bridging moieties are composed of independent bonds switched in series.

11.4.3

Metal-Mediated Coordination Interactions

11.4.3.1 Interactions Between Histidine and Nickel Nitrilotriacetate

Unbinding forces between individual histidine residue (His) tags and individual Ni nitrilotriacetate (nta) chelating groups in single-molecule experiments were measured by Samori and coworkers [80]. These coordinative interactions are of paramount importance for isolation and purification of recombinant proteins via Ni-nta-functionalized chromatography matrices, as well as for biosensor surfaces. Typically a sequence of six consecutive His tags is attached to the primary sequence of recombinant proteins.

For AFM-based SMFS experiments an α,ω -cysteine, His_{*n*}-terminated peptide (HCys-(Gly)₆-(His)_{*n*}-OH, *n* = 2, 6) was immobilized on gold-coated AFM tips (Fig. 11.20A). Force–distance curves were recorded on commercially available Ni-nta-functionalized sensor surfaces (the attachment to the carboxymethylated dextran sensor layer comprises a C₁₈ spacer). As shown in Fig. 11.20B, the force–extension curves displayed a characteristic elastic response followed by a sharply defined unbinding (rupture) event. The elastic response was attributed to stretching of the carboxymethylated dextran matrix, whereas the pull-off event was interpreted as unbinding of the His–Ni–nta complex (~300 pN for *n* = 2).

The specificity of the binding was confirmed by using the Fe^{III}–nta as binding partner, which led to a higher magnitude of the rupture forces, and by performing the experiments in the absence of nickel ions. The latter experiments showed negligible pull-off forces (Fig. 11.20C). The authors also showed evidence for stretching of individual dextran chains by normalizing the force–extension data.

For the His₆-terminated protein, the magnitude of complex rupture forces was increased markedly (~500 pN). This observation indicates that both His₂ and His₆ tags can form complexes with markedly different stabilities and with different “energy landscapes” along their force-driven dissociation pathway. The detailed analysis of the data revealed also that the probability that the encounters between a 6 × His tag and a Ni–nta group develop a stable bond is much higher than that for a 2 × His tag.

11.4.3.2 Metallo-Supramolecular Ruthenium(II) Complexes

A widely studied linkage in metallo-supramolecular chemistry comprises terpyridine units, which form stable metal complexes, e.g., with Ru²⁺ ions. A metal complexing polymer incorporating terpyridine units connected via PEG linkages has been studied by Schubert, Gaub and coworkers using SMFS [102]. An asymmetrically substituted PEG was attached to a substrate and to an AFM tip via standard coupling chemistry. The other terminating group was a terpyridine ligand for both

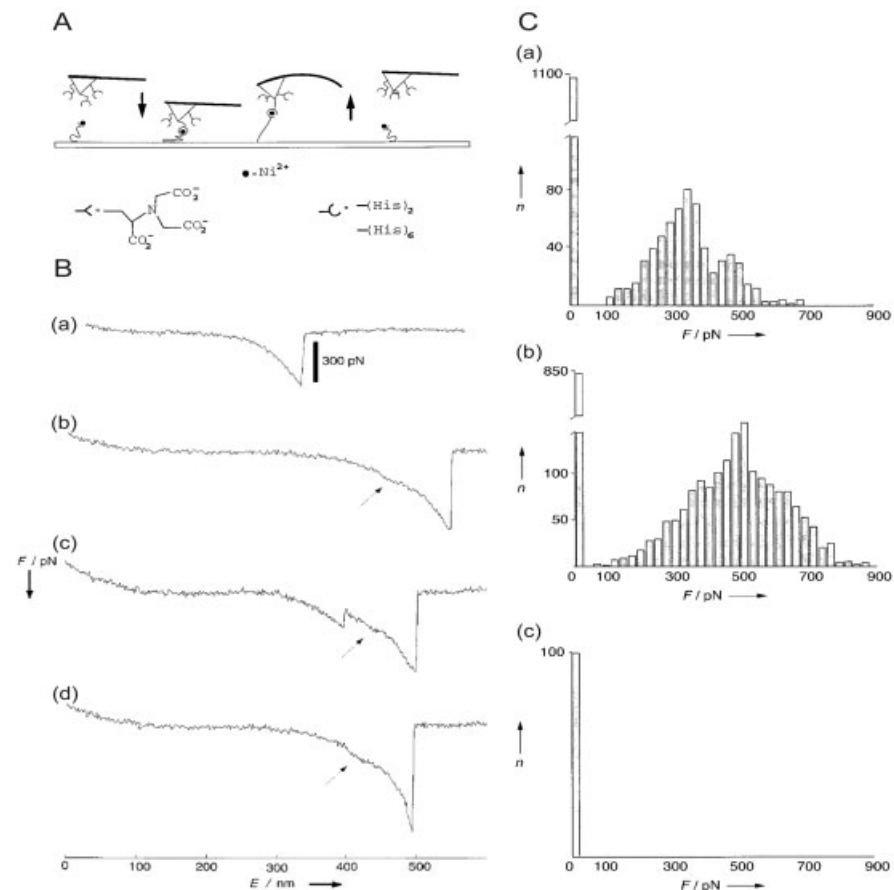


Fig. 11.20 (A) Sketch of the approach, binding, stretching, and unbinding of a His-tagged peptide covalently bound to an AFM tip in an approach and retraction cycle. (B) Characteristic shape of the force (F) vs. extension (E) unbinding traces associated with the rupture of the coordination bond between His tags and (a–c) nickel(II)–nta; (d) iron(III)–nta. Single rupture events (a, b, d) and sequential two-bond ruptures at about 280 and 600 pN (c) are shown. When a conformational transition of the carboxymethylated dextran

chain also took place, it was revealed by the plateau at about 300 pN, which is marked by arrows in b–d. (C) Histogram of the distribution (n , number of events) of all the unbinding forces (F) recorded with the Ni–nta-functionalized substrate and (a) the 2 \times His tag and (b) the 6 \times His tag. No binding event was recorded when the substrate was depleted of nickel(II) ions (c). (Reproduced with permission from ref. 80. Copyright 2000, Wiley-VCH.)

tip and surface. The rupture force of individual bis(terpyridine)–ruthenium(II) complexes was determined to be 95 pN at a force loading rate of 1 nN s^{−1} (Fig. 11.21). Simultaneous rupturing of multiple parallel metallo-supramolecular bonds was also observed.

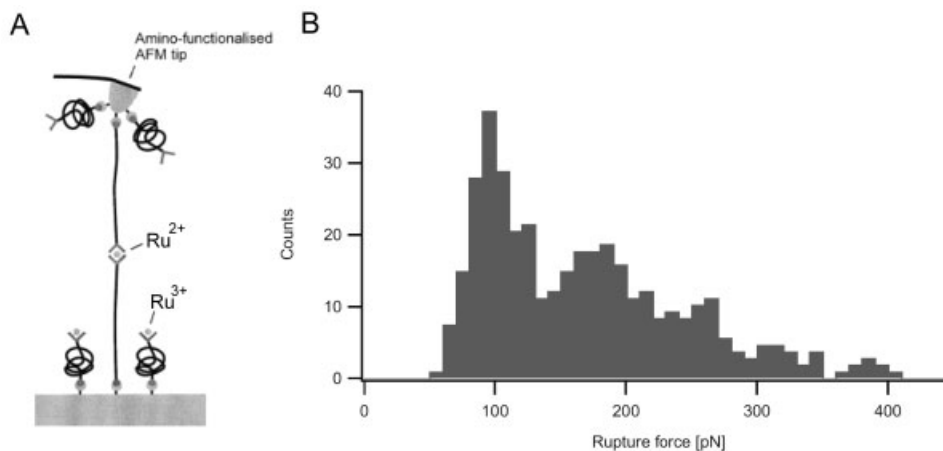


Fig. 11.21 (A) Schematic illustration of a substrate coated with terpyridine–ruthenium(III) mono-complexes, and the tip with free terpyridine units. The bis-complexes can only be formed between the free terpyridines at the tip and the mono-complexes bound to the substrate. Ruthenium(III) is reduced to ruthenium(II) during this process (solvent, DMSO). (B) Histogram of the bond rupture forces of the polymer–ruthenium(II) complexes at pulling velocity 118 nm s^{-1} . (Reproduced with permission from ref. 102. Copyright 2003, Wiley-VCH.)

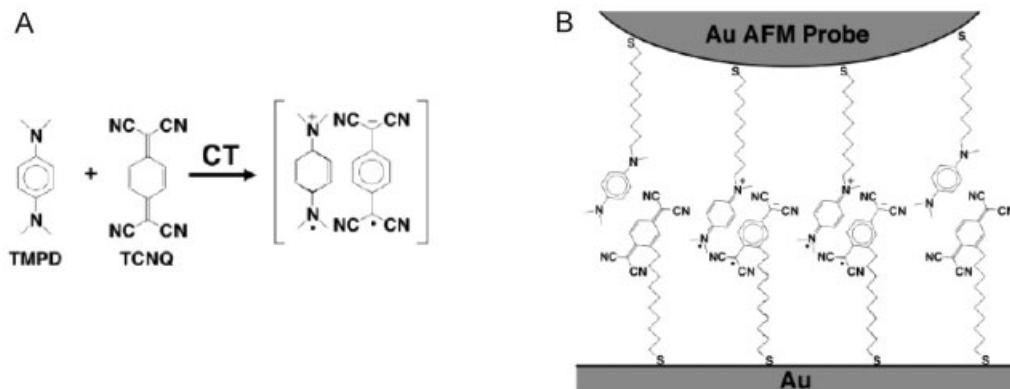
11.4.4

Charge-Transfer Complexes

Due to their fascinating electronic properties, charge-transfer (CT) complexes, which organize in so-called “quasi-one-dimensional crystals,” have attracted great interest since the late 1970s. Although the technological expectations have not been fulfilled, research efforts in materials chemistry and solid-state physics aiming at this class of materials resulted in knowledge which serves as part of the foundation of the modern science of organic, advanced, molecular materials with electrical, optoelectronic, and photovoltaic functions [119].

The unique properties of electroactive charge-transfer complexes depend on the spatial organization of the donor and acceptor molecules, and on their relative orientation. Stacking and intermolecular π – π interactions are, for example, crucial for the conducting properties of these organic materials. Alternative stacking, herringbone structures, dimers and higher “mers”, etc., may form, depending on the stoichiometry and molecular structure. Early work in electroactive charge-transfer complexes used tetracyanoquinodimethane (TCNQ) as the electron acceptor and tetramethylphenylenediamine (TMPD) as the electron donor (for the formation of a charge-transfer complex, see Scheme 11.4) [120].

TMPD-functionalized alkanethiols and TCNQ-terminated, symmetric disulfides have been immobilized on Au, forming self-assembled monolayers [121].



Scheme 11.4 (A) Formation of a CT complex between TMPD and TCNQ. (B) Schematic representation of CT complex formation between tip and substrate. (Figures reproduced with permission from ref. 122. Copyright 2002, American Chemical Society.)

These films, which allow one to tune the electronic structure of metal/organic interfaces, were used to study charge-transfer chemistry and interactions in interfacial adhesion measurements by AFM (Scheme 11.4B). Direct detection of single-bond forces by observing the rupture of individual charge-transfer complexes in a CHCl_3 solvent environment was reported [122, 123].

The pull-off forces exhibited periodic histograms with a “quantum” of 70 pN. This was interpreted as the rupture force between individual TMPD–TCNQ donor–acceptor complexes. From the molecular rupture force, bond dissociation energies were estimated; the results obtained were in reasonable agreement with ensemble-average thermodynamic data. Interestingly, the mean pull-off forces obtained were more than an order of magnitude greater than the forces for TMPD–TMPD and TCNQ–TCNQ contacts, indicating the specific nature of the TMPD–TCNQ charge-transfer complex rupture force. This work demonstrates a possible general strategy to study specific charge-transfer interactions for donor–acceptor complexes.

11.5 Conclusions and Outlook

Single-molecule force spectroscopy (SMFS) is a swiftly developing analytical approach that allows one to study the mechanical properties of individual (macro)-molecules and single supramolecular and covalent bonds under dynamic loading conditions. Force–extension diagrams captured by SMFS yield direct information, as a function of applied extension, on axial stretching, stress under torsional load,

and rupture (bond) strength values. Time-dependent force spectra are helpful to elucidate the parameters of the free-energy hypersurface along the force-driven reaction coordinate.

AFM has been used increasingly as a method of choice in SMFS due to its simplicity, the broad range of accessible forces, its great force sensitivity, applicability in different media and at different temperatures, and the possibilities of easy attachment of the molecules of interest to AFM tips and substrates probed. In this review we have described a selection of examples to illustrate the use of AFM-based SMFS applied to synthetic supramolecular complexes, including dimers and polymers. We began with an overview of supramolecular interactions and continued with a short technical description of AFM-based SMFS. Special attention was paid to an overview of the theories describing the loading rate dependence of the most probable rupture forces (thermodynamic quasi-equilibrium and non-equilibrium) and the interrelationship between the loading rate dependence and the corresponding potential energy landscape. In the main part of the chapter we gave an account of loading-rate dependent and/or independent rupture forces for inclusion ligand–receptor guest–host systems, complexes linked via H-bonds, quadruple H-bonded supramolecular dimers and polymers, metal-mediated coordinative bonds, and charge-transfer complexes.

The formation and dissociation of specific, supramolecular bonds play a crucial role in the function of biological systems. Thus, it is not surprising that early work in SMFS focused on biological macromolecules, their elastic properties, and their binding strength. The decisive role that the dynamic loading conditions and spacer stiffness represent in bond rupture forces was pointed out at an early stage. These theoretical results enabled the performance of quantitative and comparative single-molecule studies. Intensive research efforts on biological systems shed further light, from the molecular perspective, on enzyme reactions, protein unfolding (and to a lesser extent folding), details of the energy landscape of complex supramolecular architectures, solvent bridges and their role in the stabilization of molecular superstructures, the structure-stabilizing role of H-bonds, etc. Current theoretical models (Bell–Evans, Hummer–Szabo) of loading-rate dependence are based on the Kramers transition state theory, assuming Brownian dynamics. It is assumed that the favored pathway of the unbinding reaction coordinate falls in the direction of the applied force. This implies that other dynamic processes are fast compared with the experimental unbinding along the dissociation pathway. Although thermodynamic parameters of the potential energy landscape and the corresponding prominent energy barriers can be determined for the cases which fulfill the assumptions of the theories, establishment of detailed libraries of corresponding thermodynamic data is still only at its beginning. We expect that the dynamic force–strain analysis experiments (in different environments, i.e., of temperature, solvent, gases, etc.) and theoretical models will be further refined, and the measurements will become more precise and accurate. To us it appeared that in the course of this research one should consider going back to the foundations of simple supramolecular interactions measured on well-defined and well-understood molecules, and begin to establish quantitative relationships for their dissociation

using SMFS approaches. In many of these systems the distance dependence of the interactions is known, and the specific interactions can be separated from the non-specific ones, e.g., by using flexible spacers inserted between the molecular species of interest and the tip (or substrate, or both). Although in these systems the potential energy landscapes are fairly simple, their dynamic behavior in quasi-thermodynamic equilibrium, and transitions to non-equilibrium, constitute a virtually unexplored area of research. With the fast development in single-molecule science we anticipate that the strength of supramolecular interactions will be described also in terms of rupture forces of single bonds, which will complement ensemble-average thermodynamic approaches regarding bond strength and bond stability. It must be emphasized that for such bond rupture force libraries, loading dynamics, spacer stiffness and loading history must also be specified. As SMFS experiments are usually performed on molecules in confinement (e.g., attached to surfaces), physical effects of this confinement must also be considered as compared with the bulk behavior for which bond stability data may be known. Links between ensemble-averaged conventional thermodynamic descriptions and single-molecular behavior will eventually be established. Molecular-level dynamic force spectra can furthermore constitute the basis of first-principles descriptions of the physics of molecular materials. For example, we believe that knowledge of the stability and rupture of quadruply H-bonded complementary blocks under different dynamic loading conditions and in different environments will eventually allow one to establish a full and quantitative description of the melt rheology and peculiar ensemble mechanical properties of H-bonded supramolecular polymers and elastomeric networks.

Molecular biologists will further benefit from the developments in AFM-SMFS. A broad range of problems related to biomolecular architecture, and biological processes observed *in situ*, will be quantitatively accessible. The structure, properties, and function of biological molecules in natural habitats and under artificial conditions can be tackled at the single-molecule level. In combination with ensemble-average approaches and other single-molecule techniques, single-molecule force spectroscopy will undoubtedly help toward better understanding of the (bio)chemistry and physics of life. These achievements foreseen in the nanosciences will serve to realize developments in nanotechnology for applications in bottom-up, controlled, force-based nanofabrication approaches (using force), and in the design and construction of functional structures including optical, electronic, and sensing molecular devices.

Acknowledgments

The authors are indebted to the MESA⁺ Institute for Nanotechnology of the University of Twente and the Netherlands Foundation for Chemical Research (NWO-CW) for financial support. Professors David N. Reinhoudt and Jurriaan Huskens are thanked for the long-standing collaborations and for the many most useful and inspiring scientific discussions.

References

- 1 G. BINNIG, C. F. QUATE, C. GERBER, *Phys. Rev. Lett.* **1986**, *56*, 930–933.
- 2 R. J. COLTON, A. ENGEL, J. E. FROMMER, H. GAUB, A. GEWIRTH, R. GUCKENBERGER, W. HECKL, B. PARKINSON, J. RABE, *Procedures in Scanning Probe Microscopies*, Wiley, New York, **1998**.
- 3 C. D. FRISBIE, L. F. ROZSNYAI, A. NOY, M. S. WRIGHTON, C. M. LIEBER, *Science* **1994**, *265*, 2071–2074.
- 4 A. NOY, C. D. FRISBIE, L. F. ROZSNYAI, M. S. WRIGHTON, C. M. LIEBER, *J. Am. Chem. Soc.* **1995**, *117*, 7943–7951.
- 5 A. NOY, D. V. VEZENOV, C. M. LIEBER, *Annu. Rev. Mater. Sci.* **1997**, *27*, 381–421.
- 6 P. SAMORI, *J. Mater. Chem.* **2004**, *14*, 1353–1366.
- 7 J. H. HOH, J. P. CLEVELAND, C. B. PRATER, J. P. REVEL, P. K. HANSMA, *J. Am. Chem. Soc.* **1992**, *114*, 4917–4918.
- 8 E. L. FLORIN, V. T. MOY, H. E. GAUB, *Science* **1994**, *264*, 415–417.
- 9 G. U. LEE, L. A. CHRISSEY, R. J. COLTON, *Science* **1994**, *266*, 771–773.
- 10 E. EVANS, K. RITCHIE, *Biophys. J.* **1997**, *72*, 1541–1555.
- 11 R. MERKEL, P. NASSOY, A. LEUNG, K. RITCHIE, E. EVANS, *Nature* **1999**, *397*, 50–53.
- 12 A. JANSHOFF, M. NEITZERT, Y. OBERDORFER, H. FUCHS, *Angew. Chem. Int. Ed.* **2000**, *39*, 3213–3237.
- 13 J. ZLATANOVA, S. M. LINDSAY, S. H. LEUBA, *Prog. Biophys. Mol. Biol.* **2000**, *74*, 37–61.
- 14 R. MERKEL, *Phys. Rev. Rev. Sect. Phys. Lett.* **2001**, *346*, 344–385.
- 15 E. EVANS, *Annu. Rev. Biophys. Biomol. Struct.* **2001**, *30*, 105–128.
- 16 T. HUGEL, M. SEITZ, *Macromol. Rapid Commun.* **2001**, *22*, 989–1016.
- 17 M. GRANDBOIS, M. BEYER, M. RIEF, H. CLAUSEN-SCHAUMANN, H. E. GAUB, *Science* **1999**, *283*, 1727–1730.
- 18 D. KRUGER, H. FUCHS, R. ROUSSEAU, D. MARX, M. PARRINELLO, *Phys. Rev. Lett.* **2002**, *89*.
- 19 C. HILGER, R. STADLER, *Macromol. Chem. Phys.* **1991**, *192*, 805–817.
- 20 M. MULLER, A. DARDIN, U. SEIDEL, V. BALSAMO, B. IVAN, H. W. SPIESS, R. STADLER, *Macromolecules* **1996**, *29*, 2577–2583.
- 21 L. D. FREITAS, M. M. JACOBI, G. GONCALVES, R. STADLER, *Macromolecules* **1998**, *31*, 3379–3382.
- 22 J. M. LEHN, *Angew. Chem. Int. Ed. Engl.* **1990**, *29*, 1304–1319.
- 23 S. BOILEAU, L. BOUTEILLER, F. LAUPRETRE, F. LORTIE, *New J. Chem.* **2000**, *24*, 845–848.
- 24 L. BRUNSVELD, B. J. B. FOLMER, E. W. MEIJER, R. P. SIJBESMA, *Chem. Rev.* **2001**, *101*, 4071–4097.
- 25 M. L. WATERS, *Curr. Opin. Chem. Biol.* **2002**, *6*, 736–741.
- 26 J. M. LEHN, *Angew. Chem. Int. Ed. Engl.* **1988**, *27*, 89–112.
- 27 D. J. CRAM, *Angew. Chem. Int. Ed. Engl.* **1988**, *27*, 1009–1020.
- 28 C. J. PEDERSEN, *Angew. Chem. Int. Ed. Engl.* **1988**, *27*, 1021–1027.
- 29 G. M. WHITESIDES, E. E. SIMANEK, J. P. MATHIAS, C. T. SETO, D. N. CHIN, M. MAMMEN, D. M. GORDON, *Acc. Chem. Res.* **1995**, *28*, 37–44.
- 30 D. N. REINHOUDT, M. CREGO-CALAMA, *Science* **2002**, *295*, 2403–2407.
- 31 A. L. WEISENHORN, P. MAIVALD, H. J. BUTT, P. K. HANSMA, *Phys. Rev. B* **1992**, *45*, 11 226–11 232.
- 32 B. CAPPELLA, G. DIETLER, *Surf. Sci. Reports* **1999**, *34*, 1–104.
- 33 G. J. VANCISO, H. HILLBORG, H. SCHÖNHERR, *Adv. Polym. Sci.* **2005**, *182*, 55–129.
- 34 J. N. ISRAELACHVILI, *Intermolecular and Surface Forces: With Applications to Colloidal and Biological Systems*, 2nd edn., Academic Press, New York, **1991**.
- 35 S. SCHEINER, *Molecular Interactions: From van der Waals to Strongly Bound Complexes*, Chichester: John Wiley & Sons, **1997**.
- 36 J. M. LEHN, *Supramolecular Chemistry: Concepts and Perspectives*, John Wiley & Sons, New York, **1995**.
- 37 D. N. REINHOUDT, *Supramolecular Materials and Technologies*, John Wiley & Sons, New York, **1999**.

- 38 G. A. JEFFERY, W. SAENGER, *Hydrogen Bonding in Biological Structures*, Springer-Verlag, Berlin, 1991.
- 39 L. J. PRINS, D. N. REINHOUDT, P. TIMMERMAN, *Angew. Chem. Int. Ed.* **2001**, *40*, 2383–2426.
- 40 G. A. JEFFERY, *An Introduction to Hydrogen Bonding*, Oxford University Press, New York, 1997.
- 41 J. M. LEHN, M. MASCAL, A. DECIAN, J. FISCHER, *J. Chem. Soc. Chem. Commun.* **1990**, 479–481.
- 42 C. T. SETO, G. M. WHITESIDES, *J. Am. Chem. Soc.* **1990**, *112*, 6409–6411.
- 43 J. A. ZERKOWSKI, C. T. SETO, D. A. WIERDA, G. M. WHITESIDES, *J. Am. Chem. Soc.* **1990**, *112*, 9025–9026.
- 44 R. H. VREEKAMP, J. P. M. VAN DUYNHOVEN, M. HUBERT, W. VERBOOM, D. N. REINHOUDT, *Angew. Chem. Int. Ed. Engl.* **1996**, *35*, 1215–1218.
- 45 H. SCHÖNHERR, M. CREGO-CALAMA, G. J. VANCOSO, D. N. REINHOUDT, *Dekker Encyclopedia of Nanoscience and Nanotechnology*, Marcel Dekker, New York, 2004.
- 46 W. L. JORGENSEN, J. PRANATA, *J. Am. Chem. Soc.* **1990**, *112*, 2008–2010.
- 47 J. PRANATA, S. G. WIERSCHKE, W. L. JORGENSEN, *J. Am. Chem. Soc.* **1991**, *113*, 2810–2819.
- 48 J. SARTORIUS, H. J. SCHNEIDER, *Chem. Eur. J.* **1996**, *2*, 1446–1452.
- 49 G. COOKE, V. M. ROTELLO, *Chem. Soc. Rev.* **2002**, *31*, 275–286.
- 50 C. FOUQUEY, J.-M. LEHN, A.-M. LEVELUT, *Adv. Mater.* **1990**, *2*, 254–257.
- 51 M. KOTERA, J. M. LEHN, J. P. VIGNERON, *J. Chem. Soc. Chem. Commun.* **1994**, 197–199.
- 52 R. P. SIJBESMA, F. H. BEIJER, L. BRUNSVELD, B. J. B. FOLMER, J. HIRSCHBERG, R. F. M. LANGE, J. K. L. LOWE, E. W. MEIJER, *Science* **1997**, *278*, 1601–1604.
- 53 G. WILKINSON, R. D. GILLARD, J. A. MCCLEVERTY, *Comprehensive Coordination Chemistry: The Synthesis, Reactions, Properties and Applications of Coordination Compounds*, Pergamon Press, Oxford, 1987.
- 54 M. RUBEN, J. ROJO, F. J. ROMERO-SALGUERO, L. H. UPPADINE, J. M. LEHN, *Angew. Chem. Int. Ed.* **2004**, *43*, 3644–3662.
- 55 A. MARQUIS, J. P. KINTZINGER, R. GRAFF, P. N. W. BAXTER, J. M. LEHN, *Angew. Chem. Int. Ed.* **2002**, *41*, 2760–2764.
- 56 H. HOFMEIER, U. S. SCHUBERT, *Chem. Soc. Rev.* **2004**, *33*, 373–399.
- 57 D. D. BOEHR, A. R. FARLEY, G. D. WRIGHT, J. R. COX, *Chem. Biol.* **2002**, *9*, 1209–1217.
- 58 E. GAZIT, *FASEB J.* **2002**, *16*, 77–83.
- 59 L. K. TSOU, C. D. TATKO, M. L. WATERS, *J. Am. Chem. Soc.* **2002**, *124*, 14917–14921.
- 60 For the benzene–perfluorobenzene interaction, which can be considered as an example of the aromatic π – π interaction in the face-to-face stacked orientation, an energy of -15.5 kJ mol⁻¹ has been calculated (J. WEST, S. MECOZZI, D. A. DOUGHERTY, *J. Phys. Org. Chem.* **1997**, *10*, 347–350).
- 61 M. INOUE, Y. HYODO, H. NAKAZUMI, *J. Org. Chem.* **1999**, *64*, 2704–2710.
- 62 H. CLAUSEN-SCHAUMANN, M. SEITZ, R. KRAUTBAUER, H. E. GAUB, *Curr. Opin. Chem. Biol.* **2000**, *4*, 524–530.
- 63 S. B. SMITH, L. FINZI, C. BUSTAMANTE, *Science* **1992**, *258*, 1122–1126.
- 64 A. ASHKIN, K. SCHUTZE, J. M. DZIEDZIC, U. EUTENEUER, M. SCHLIWA, *Nature* **1990**, *348*, 346–348.
- 65 A. KISHINO, T. YANAGIDA, *Nature* **1988**, *334*, 74–76.
- 66 E. EVANS, K. RITCHIE, R. MERKEL, *Biophys. J.* **1995**, *68*, 2580–2587.
- 67 M. SCHLIERF, H. B. LI, J. M. FERNANDEZ, *P. Natl. Acad. Sci. USA* **2004**, *101*, 7299–7304.
- 68 J. M. FERNANDEZ, H. B. LI, *Science* **2004**, *303*, 1674–1678.
- 69 W. ZHANG, X. ZHANG, *Prog. Polym. Sci.* **2003**, *28*, 1271–1295.
- 70 P. E. MARSZALEK, A. F. OBERHAUSER, Y. P. PANG, J. M. FERNANDEZ, *Nature* **1998**, *396*, 661–664.
- 71 M. LUDWIG, M. RIEF, L. SCHMIDT, H. LI, F. OESTERHELT, M. GAUTEL, H. E. GAUB, *Appl. Phys. A* **1999**, *68*, 173–176.
- 72 C. ORTIZ, G. HADZIIOANNOU, *Macromolecules* **1999**, *32*, 780–787.
- 73 J. E. BEMIS, B. B. AKHREMITCHEV,

- G. C. WALKER, *Langmuir* **1999**, *15*, 2799–2805.
- 74 S. ZOU, W. K. ZHANG, X. ZHANG, B. Z. JIANG, *Langmuir* **2001**, *17*, 4799–4808.
- 75 C. WANG, W. Q. SHI, W. K. ZHANG, X. ZHANG, Y. KATSUMOTO, Y. OZAKI, *Nano Lett.* **2002**, *2*, 1169–1172.
- 76 J. L. HUTTER, J. BECHHOEFER, *Rev. Sci. Instrum.* **1993**, *64*, 1868–1873.
- 77 H. J. BUTT, M. JASCHKE, *Nanotechnology* **1995**, *6*, 1–7.
- 78 J. E. SADER, I. LARSON, P. MULVANEY, L. R. WHITE, *Rev. Sci. Instrum.* **1995**, *66*, 3789–3798.
- 79 P. HINTERDORFER, F. KIENBERGER, A. RAAB, H. J. GRUBER, W. BAUMGARTNER, G. KADA, C. RIENER, S. WIELERT-BADT, C. BORKEN, H. SCHINDLER, *Single Mol.* **2000**, *1*, 99–103.
- 80 M. CONTI, G. FALINI, B. SAMORI, *Angew. Chem. Int. Ed.* **2000**, *39*, 215–218.
- 81 S. ZOU, H. SCHÖNHERR, G. J. VANCOSO, *Angew. Chem. Int. Ed.* **2005**, *44*, 956–959.
- 82 R. ECKEL, R. ROS, B. DECKER, J. MATTAY, D. ANSELMETTI, *Angew. Chem. Int. Ed.* **2005**, *44*, 484–488.
- 83 E. EVANS, K. RITCHIE, *Biophys. J.* **1999**, *76*, 2439–2447.
- 84 H. A. KRAMERS, *Physica* **1940**, *7*, 284–304.
- 85 E. EVANS, *Farad. Discuss.* **1998**, *111*, 1–16.
- 86 T. STRUNZ, K. OROSLAN, R. SCHAFFER, H. J. GUNTHERODT, *P. Natl. Acad. Sci. USA* **1999**, *96*, 11 277–11 282.
- 87 G. I. BELL, *Science* **1978**, *200*, 618–627.
- 88 G. HUMMER, A. SZABO, *Biophys. J.* **2003**, *85*, 5–15.
- 89 T. STRUNZ, K. OROSLAN, I. SCHUMAKOVITCH, H. J. GUNTHERODT, M. HEGNER, *Biophys. J.* **2000**, *79*, 1206–1212.
- 90 E. EVANS, P. WILLIAMS, in *Physics of Bio-Molecules and Cells*, EDP Science Springer-Verlag, **2002**, p. 145.
- 91 G. WENZ, *Angew. Chem. Int. Ed. Engl.* **1994**, *33*, 803–822.
- 92 S. ZAPOTOCZNY, T. AULETTA, M. R. DE JONG, H. SCHÖNHERR, J. HUSKENS, F. C. J. M. VAN VEGGEL, D. N. REINHOUDT, G. J. VANCOSO, *Langmuir* **2002**, *18*, 6988–6994.
- 93 H. SCHÖNHERR, M. W. J. BEULEN, J. BÜGLER, J. HUSKENS, F. C. J. M. VAN VEGGEL, D. N. REINHOUDT, G. J. VANCOSO, *J. Am. Chem. Soc.* **2000**, *122*, 4963–4967.
- 94 T. AULETTA, M. R. DE JONG, A. MULDER, F. C. J. M. VAN VEGGEL, J. HUSKENS, D. N. REINHOUDT, S. ZOU, S. ZAPOTOCZNY, H. SCHÖNHERR, G. J. VANCOSO, L. KUIPERS, *J. Am. Chem. Soc.* **2004**, *126*, 1577–1584.
- 95 S. ZOU, Ph.D. Thesis, University of Twente, Enschede, **2005**.
- 96 J. HUSKENS, A. MULDER, T. AULETTA, C. A. NIJHUIS, M. J. W. LUDDEN, D. N. REINHOUDT, *J. Am. Chem. Soc.* **2004**, *126*, 6784–6797.
- 97 A. MULDER, T. AULETTA, A. SARTORI, S. DEL CIOTTO, A. CASNATI, R. UNGARO, J. HUSKENS, D. N. REINHOUDT, *J. Am. Chem. Soc.* **2004**, *126*, 6627–6636.
- 98 S. ZOU, S. ZAPOTOCZNY, M. R. DE JONG, T. AULETTA, H. SCHÖNHERR, J. HUSKENS, F. C. J. M. VAN VEGGEL, D. N. REINHOUDT, G. J. VANCOSO, *Polym. Mater. Sci. Eng.* **2003**, *88*, 453–454.
- 99 Expanding on the approach proposed by Hansma and coworkers [100] for measuring interaction potentials, WILLEMSSEN et al. [101] demonstrated that the total potential can be derived from the probability distribution of the tip position by monitoring the Brownian movement of an AFM tip in a potential well. The total potential consists of the sum of the harmonic cantilever potential and the tip–surface interaction potential.
- 100 J. P. CLEVELAND, T. E. SCHAEFFER, P. K. HANSMA, *Phys. Rev. B* **1995**, *52*, R8692–R8695.
- 101 O. H. WILLEMSSEN, L. KUIPERS, K. O. VAN DER WERF, B. G. DE GROOTH, J. GREVE, *Langmuir* **2000**, *16*, 4339–4347.
- 102 M. KUDERA, C. ESCHBAUMER, H. E. GAUB, U. S. SCHUBERT, *Adv. Funct. Mater.* **2003**, *13*, 615–620.
- 103 C. FRIEDSAM, A. K. WEHLE, F. KUHNER, H. E. GAUB, *J. Phys. Cond. Matt.* **2003**, *15*, S1709–S1723.

- 104 S. KADO, K. KIMURA, *J. Am. Chem. Soc.* **2003**, *125*, 4560–4564.
- 105 S. KADO, K. YAMADA, K. KIMURA, *Langmuir* **2004**, *20*, 3259–3263.
- 106 H. RINGSDORF, B. SCHLARB, J. VENZMER, *Angew. Chem. Int. Ed. Engl.* **1988**, *27*, 113–158.
- 107 S. ZOU, Z. H. ZHANG, R. FORCH, W. KNOLL, H. SCHÖNHERR, G. J. VANCOSO, *Langmuir* **2003**, *19*, 8618–8621.
- 108 F. OESTERHELT, M. RIEF, H. E. GAUB, *New J. Phys.* **1999**, *1*, 6.1–6.11.
- 109 F. KIENBERGER, V. P. PASTUSHENKO, G. KADA, H. J. GRUBER, C. RIENER, H. SCHINDLER, P. HINTERDORFER, *Single Mol.* **2000**, *1*, 123–128.
- 110 A. T. TEN CATE, R. P. SIJBESMA, *Macromol. Rapid Commun.* **2002**, *23*, 1094–1112.
- 111 S. H. M. SONTJENS, R. P. SIJBESMA, M. H. P. VAN GENDEREN, E. W. MEIJER, *J. Am. Chem. Soc.* **2000**, *122*, 7487–7493.
- 112 F. H. BEIJER, R. P. SIJBESMA, H. KOOIJMAN, A. L. SPEK, E. W. MEIJER, *J. Am. Chem. Soc.* **1998**, *120*, 6761–6769.
- 113 F. H. BEIJER, H. KOOIJMAN, A. L. SPEK, R. P. SIJBESMA, E. W. MEIJER, *Angew. Chem. Int. Ed.* **1998**, *37*, 75–78.
- 114 Z. B. GUAN, J. T. ROLAND, J. Z. BAI, S. X. MA, T. M. MCINTIRE, M. NGUYEN, *J. Am. Chem. Soc.* **2004**, *126*, 2058–2065.
- 115 M. RIEF, M. GAUTEL, F. OESTERHELT, J. M. FERNANDEZ, H. E. GAUB, *Science* **1997**, *276*, 1109–1112.
- 116 A. M. BELCHER, X. H. WU, R. J. CHRISTENSEN, P. K. HANSMA, G. D. STUCKY, D. E. MORSE, *Nature* **1996**, *381*, 56–58.
- 117 J. T. ROLAND, Z. B. GUAN, *J. Am. Chem. Soc.* **2004**, *126*, 14 328–14 329.
- 118 F. R. KERSEY, G. LEE, P. MARSZALEK, S. L. CRAIG, *J. Am. Chem. Soc.* **2004**, *126*, 3038–3039.
- 119 E. M. CONWELL, *Highly Conducting Quasi-One-Dimensional Organic Crystals*, Academic Press, Boston, **1988**.
- 120 A. K. BANDYOPADHYAY, S. CHATTERJEE, S. V. SUBRAMANYAM, B. R. BULKA, *J. Phys. C: Solid State Phys.* **1980**, *13*, L803–L807.
- 121 H. SKULASON, C. D. FRISBIE, *Langmuir* **1998**, *14*, 5834–5840.
- 122 H. SKULASON, C. D. FRISBIE, *J. Am. Chem. Soc.* **2002**, *124*, 15 125–15 133.
- 123 H. SKULASON, C. D. FRISBIE, *Anal. Chem.* **2002**, *74*, 3096–3104.

Electrical Properties of Nanoscale Objects

12 Electrical Measurements with SFM-Based Techniques

Pedro. J. de Pablo, Cristina Gómez Navarro and Julio Gómez-Herrero



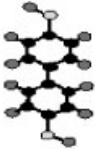


12.1 Introduction

Since the invention of the transistor [1] and the integrated circuit [2], miniaturization of electronic components has been a main goal in research for the last 55 years. Moreover, in 1965 Gordon Moore, cofounder of Intel, observed that the number of transistors per square inch on integrated circuits had doubled every year since the integrated circuit was invented [3]. Moore predicted that this trend would continue for the foreseeable future. However, in subsequent years, the pace slowed down and nowadays the density of electronics components per unit area is doubled every 18 months. Some experts are pointing out that current microfabrication techniques are faced with several problems for further growth in packaging density, such as heat dissipation and, mainly, quantum effects [4]. In order to overcome these problems, many groups around the world are tackling the task of using molecules to perform molecular electronics.

Molecular electronics is the event horizon for circuit miniaturization. As the dimensions of electronic components are shrunk to the molecular level, important quantum mechanical effects arise [5]. Under these circumstances, electronic transport no longer obeys Ohm's law and the electrons propagate through extended orbitals showing similar scattering effects to those observed in electromagnetic waves traveling along an optic fiber. As in any new discipline of human knowledge, molecular electronics has to overcome a number of difficult problems which require the combined efforts of theory and experiments. On one hand, electrical transport through single molecules is not well understood; questions as basic as what is the dissipation and the resistance of a molecule-based circuit have to be addressed. On the other hand, experiments at single-molecule level must be performed in a sufficiently reliable way.

Table 12.1 sets out some of the difficulties involved for the experimental setup required to carry out experiments on this topic. It shows a collection of the molecular systems which are possible candidates for applications in molecular electronics. They are classified by considering several features. A remarkable one is

Table 12.1 Classification of several nanometric systems for electrical transport according to composition, geometry, dimensions, etc.

	Metallic break-junctions	Carbon nanotube	Organic molecule	Quantum wire	DNA
					
Composition	Au, Cu, Ag ...	C	C, H, O ...	AsGa/AlGaAs, Au,	C, H, O, N, P ...
Geometry	?	tubular	chemically defined	planar 2D	double helix
Width	atomic	1–40 nm	1 nm	several nm	2 nm
Length	<5 nm	1–5 μm	<10 nm	tens of nanometers	several μm
Electrical connections	easy	problematic	problematic	easy	problematic
Production	mechanical contact	arch discharge, CVD	reaction tube	highly specialized lithographic techniques	reaction tube
Large-scale production	difficult	easy	easy	difficult	easy
Transport mechanism	ballistic	?	?	ballistic	?

that the systems with ballistic transport [5] and easy electrical contacts, i.e., metallic break junctions and quantum wires, which could be really interesting for molecular electronics, are very difficult to produce on an industrial scale. However, they have been used with great success for basic research. In contrast, the systems which are easy to produce in multi-gram quantities, such as carbon nanotubes, DNA, or organic molecules, do not show well-controlled electronic transport properties and are not easy to connect with macroscopic electrodes. It is evident that the most interesting systems to use in molecular electronics are those which are easy to produce on an industrial scale. If we pay attention to the geometry of the systems, we can classify them as “long” and “short” systems in Table 12.1. Break

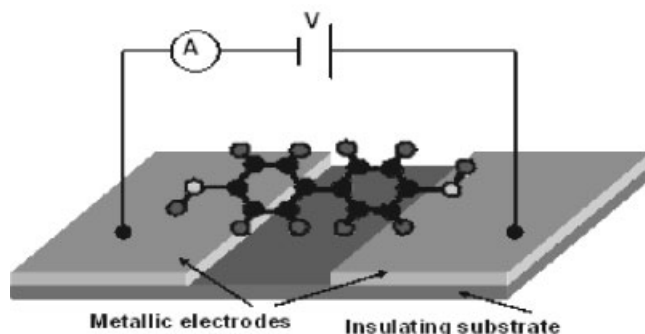


Fig. 12.1 Ideal electrical transport experiment on a nanometric system: a single molecule between two electrodes where a voltage V is applied while the current is measured.

junctions [6], molecules, and quantum wires [7] can be considered as short systems, since their length is generally less than 10 times their width. Most organic molecules can be also classified as short molecules (SMs). Accordingly, we consider carbon nanotubes and DNA to be long systems since their typical length is well above 10 times their width. Consequently we call them molecular wires (MWs). In both cases electrical contacts are necessary to explore their electrical properties by using techniques which are adequate for their nanometric dimensions.

The typical approach is to hook the SM or MW between several (generally two) macroscopic contacts with a voltage between them in order to pass a current (Fig. 12.1). These kinds of contacts are made by lithographic techniques and have revealed much about the transport properties of these systems [8]. However, with these setups it is quite difficult to focus the experiment at the single-molecule level (in the SM case), and moreover some of the basic features of the system such as the molecule conductivity along its length (in the MW case) are hard to explore.

It may seem that scanning tunneling microscopy (STM) [9] could make these measurements. In STM a sharp metallic tip is made to approach a conducting surface until a tunneling current I appears [10]. Considering a one-dimensional tunneling junction, this current is found to depend on the distance z between the tip and the sample and the local work function ϕ of the sample [Eq. (1)].

$$I \propto e^{-\sqrt{\phi}z} \quad (1)$$

Then, without establishing any mechanical contact between tip and sample, it is possible to map the topographies of the surface because of the strong dependence on z . The dependence on ϕ tells us that we are obtaining a mixture of the topography and the electronic properties of the sample. Moreover, in the case of single molecules, STM allows us to obtain their density of states, which is related to, but

not the same as, the conductance. For example, STM can be used to determine the electronic structure of C_{60} molecules adsorbed as monolayer or submonolayer states [11]; but STM cannot be used trivially to study the conductance of a molecule between two electrodes, which is the basic characterization for any MW. In this respect, scanning force microscopy (SFM) is more suitable than STM for performing electrical transport measurements. Herein we will focus on the electrical measurements of molecules, by both contacting the tip with a single molecule and performing electrical noncontact measurements.

12.2 SFM Tips

The reason why AFM is so useful for measuring the electrical transport of molecules lies in the nanometric size of the tip. Normally, its final diameter is between 10 and 50 nm, which is smaller than the length of a typical MW. This makes it possible to use the tip as a mobile electrode, which can be positioned anywhere along the length of the molecule. As we will see, for some special conductive configurations AFM tips can be used to measure the conductance of short molecules as well.

In order to be able to use the tip as an electrode we need it to be conductive. Usually the tips are made of silicon and silicon nitride, which are good insulators. In order to fabricate conducting tips the common strategy is to cover them with gold, which has very low resistivity and is a noble metal. The problem is that the adhesion between the gold and the tip is very poor, and the tip is very prone to wear out while scanning. One solution is to cover the tip, first with a thin layer of reactive metal such as titanium, chromium, or cobalt, and then with gold.

In more detail, the metallization process consists of two steps: first a 60 nm thick layer of titanium is evaporated, either thermally or by sputtering, onto the tips while they are spinning below the metal source. Second, without breaking the vacuum, a layer of gold 50 nm thick is deposited on the spinning tips. In order to cover the tip pyramid faces (Fig. 12.2a) as much as possible, the tip is rotated during evaporation. This fact is not trivial because the faces of the tip pyramid are very steep, and they do not get covered unless the evaporation is perpendicular to their surfaces. Another critical point is to avoid the increment of temperature of the cantilevers as much as possible, because they bend and then it is difficult to focus the laser of the microscope. This can be done by using a very low covering rate, or by placing the tips far enough from the metal source. In Fig. 12.2b the apex of the tip is shown covered with gold: grains as small as 20 nm can be seen easily.

Even with all these precautions tip metallization is not the final solution because, if the tip crashes, the gold can be worn out from the apex as in Fig. 12.2(c), where the real tip shows through again from the gold layer covering it. Real all-metal tips would be a much better solution, but to the best of our knowledge these tips are not commercially available.

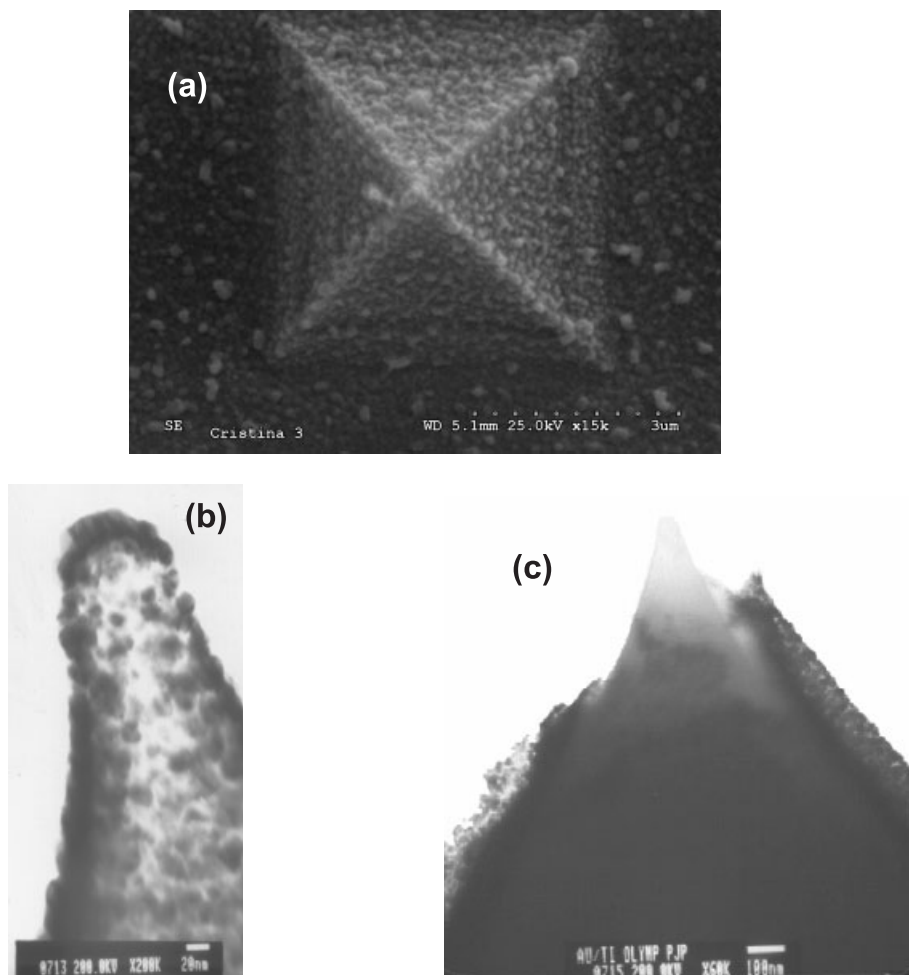


Fig. 12.2 SFM tip metallization. (a) The pyramid of a metallized SFM tip completely covered with gold on all the faces. (b) The apex of the tip, showing final gold grains of size 20 nm. (c) A used tip, where the metallization has gone at the tip apex alone, although it remains on the rest of the surface.

12.3 Setups for Short Molecules

Given the difference in geometry between SM and MW, it seems logical to design different SFM-based setups for each of them. SMs usually self-assemble on the surface, forming 2D monolayers [12]. The electrical properties of this geometry have been probed in different ways.

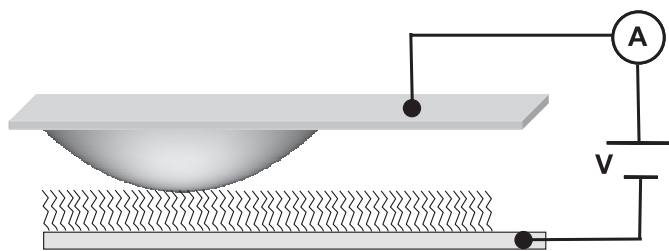


Fig. 12.3 Typical SFM configuration for measuring electrical transport of short molecules (SMs) in monolayers. The metallized tip is one electrode, the gold surface being the other. Compare with Fig. 12.1.

Figure 12.3 is a sketch of the setup used to probe the electrical properties of alkanethiol monolayers [13]. In this kind of experiment one electrode is the Au-coated tip and the other is the gold substrate, probing the vertical electrical properties. The experiment is performed as follows: first an area of the sample with the alkanethiol monolayer is selected; then the tip is brought into contact with the monolayer at a selected spot, the applied force being controlled via a force–distance curve (FZ); afterward a ramp of voltage is applied to the tip, while registering the current flowing from the gold to the tip, through the molecules just below the tip (IV). When the experiment is performed at low voltages (Fig. 12.4a), an almost linear IV is obtained. An obvious and interesting result is that the conductivity of the electrical contact between the tip and the molecules increases with the applied force.

Reference [14] analyzes this issue in light of the increment of contact area between tip and sample. Considering a Hertzian deformation [15] of the surface, the contact radius a depends upon the applied force F as $a^3 \propto F$. If, as a first approximation, we assume that the electrical current is proportional to the contact area, the resistance R of the contact depends upon the applied force F as $R \propto F^{-2/3}$. The dependence of the contact resistance upon the loading force (Fig. 12.4b) can be fitted to $R \propto F^\alpha$, where α changes with the interval of applied forces (see inset, Fig. 12.4b). For low forces α has a value very close to $-\frac{2}{3}$. When the force is above 60 nN, α is -7.5 , getting far away from $-\frac{2}{3}$. A possible reason for that is the deformation of the monolayer by the tip, thus changing the electrical properties at molecular level. In relation to this last experiment there is an important question that should be considered: following ref. 13; while increasing the loading force, can we expect discrete increments of the current as soon as a new molecule is contributing to the contact? To address this issue several points should be taken into account: the resolution of the experiment, the number of molecules in contact with the tip at a certain loading force, and the lateral electrical contact between the molecules of the monolayer.

Following 16, we can describe the current using the Landauer formula for the

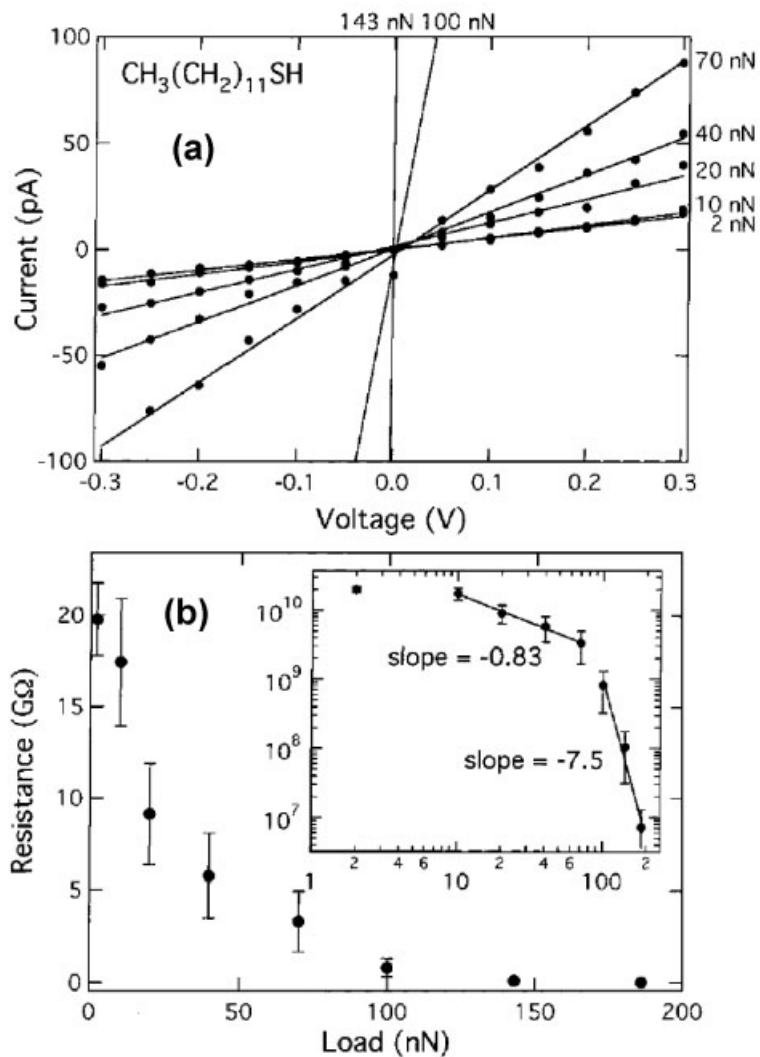


Fig. 12.4 (a) IV characteristics of a $\text{CH}_3(\text{CH}_2)_{11}\text{SH}$ SAM as a function of applied load on the conducting tip. Traces were acquired with one tip. Solid lines are linear fits. Resistance was taken to be the reciprocal of the slope of each straight-line fit in (a). Inset is a log-log plot showing two power-law scaling regimes. Adapted from ref. 14. (b) Junction resistance vs. applied load.

linear conductance, G , of the electrode–molecule–electrode junction as in Eq. (2), where e is the electronic charge and h is Planck’s constant [5].

$$G = \frac{2e^2}{h} T \quad (2)$$

Here T is a function that reflects the efficiency of electron transmission from one contact to the other. Three components contribute to this transmission function [Eq. (3), where T_{tip} and T_{subs} reflect the charge transmission through the electrodes and T_{mol} reflects the transport through the molecule).

$$T = T_{tip} \cdot T_{subs} \cdot T_{mol} \quad (3)$$

If the product $T_{subs} \cdot T_{mol}$ is low compared with T_{mol} because there are weak electrical contacts, the current becomes reduced in the junction. This is a typical result when the molecules are physisorbed on the electrodes. If coherent, nonresonant tunneling through molecules is approximated as tunneling through a rectangular barrier, we have Eq. (4), where l is the width of the barrier (height of the monolayer), and β is the tunneling decay parameter in units of $(\text{length})^{-1}$ given for symmetric coupling by Eq. (5).

$$T_{mol} = \exp(-\beta \cdot l) \quad (4)$$

$$\beta = 2 \frac{\sqrt{2m^*(\phi - (eV/2))}}{\hbar^2} \quad (5)$$

Here \hbar is the reduced Planck's constant, ϕ is the barrier height for tunneling through the LUMO or HOMO levels, m^* the effective electron mass and V the applied bias voltage. In ref. 13 β is derived from monolayers with different numbers of carbon atoms in the alkanethiol chain, thus changing the height of the monolayer and, consequently, the l parameter (see Fig. 12.5). The latter also shows the

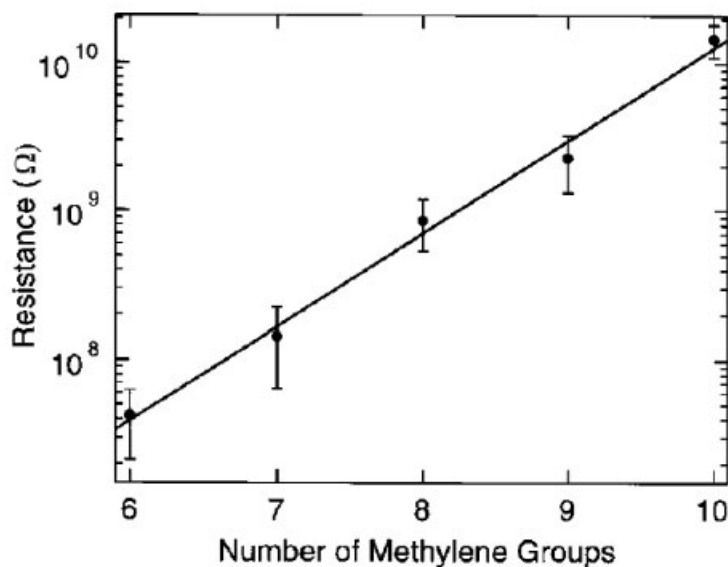


Fig. 12.5 Resistance vs. number of carbon atoms in the alkane chains. Adapted from ref. 13.

sensitivity of the electrical transport of the monolayer to the molecule architecture [14]. As alternative geometry, the tip can be covered with the same SAM and bi-layer experiments can be performed [14]. In ref. 16 there is a comparison of the electrical properties of tens of organic molecules using SFM.

In the experiments discussed above, the alkanethiol monolayer is chemisorbed on the gold surface using an S group as linker. In principle, this ensures the electrical contact of the molecule to the gold. However, there is no chemical link between the tip and the molecules. This could explain, for example, why the resistance of organic molecules depends strongly on the loading force of the tip. Another point emphasized in ref. 14 is that the resistance of the contact depends on the nature and size of the tip. For example, in Fig. 12.5 the resistance for molecules with six methylene groups is about $40\text{ M}\Omega$, while in Fig. 2 of ref. 14 a resistance of $10\text{ M}\Omega$ is obtained for the same molecular chain.

These issues hide the real electronic properties of organic molecules. In order to avoid this, a new experimental setup was designed [17]. The philosophy is sketched in the inset of Fig. 12.6(a): the monolayer of organic molecules is chemically attached to the gold substrate and, on the upper side, to gold nanoparticles. In this new approximation, the molecule is chemically hooked by two electrodes. Then the SFM gold-covered tip is brought into contact on those gold nanoparticles to perform IV curves. Five different IV curves are found (Fig. 12.6a), all being a multiple integer of a fundamental one. This would correspond to the linking of one to five octanethiol molecules to the gold particle, each carrying the same current. Analysis of FZ curves together with current-distance (IZ) curves (Fig. 12.6b) from experiments performed on gold particles shows that the mechanical contact and the electrical contact are clearly simultaneous. Moreover, the current reaches a constant value which does not depend on the applied force. However, when the

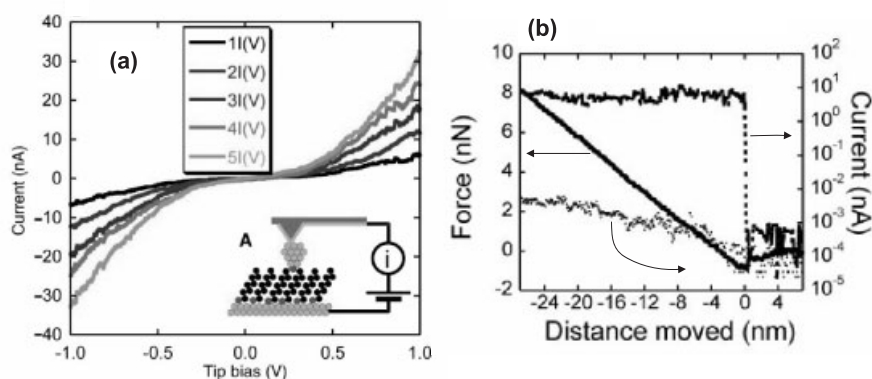


Fig. 12.6 Electrical transport single-molecule experiments on SM monolayers. (a) Five IV curves representative of distinct families, and which are integer multiples of the fundamental curve $1I(V)$. Inset: schematic of the experi-

ment. (b) Current and force measured as the tip approaches the surface. Dashed line: tip approaching a gold particle of the monolayer; dotted line: tip approaching the monolayer itself. Adapted from ref. 17.

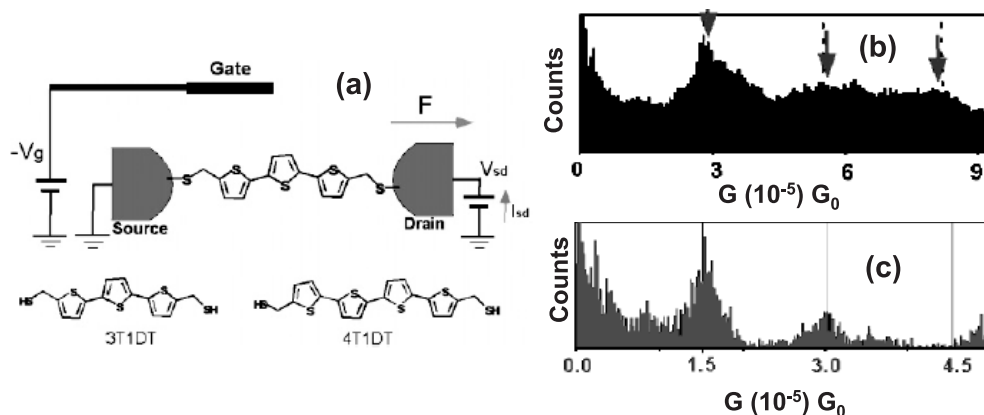


Fig. 12.7 Electrical transport single-molecule experiments on SM in solution. (a) Schematic of the setup, where the right-hand electrode is the SFM tip. (b) Conductance histogram for a

4T1DT molecule. (c) Simultaneously acquired histogram of forces: every conductance peak corresponds to a force peak. Adapted from ref. 20.

same experiment is performed on the naked monolayer, the resistance is much higher and the current obtained does depend on the loading force (dotted line in Fig. 12.6b). The data are interpreted as current flowing through a fixed number of molecules connected to the gold particle. This explains why the current does not depend on the loading force.

There are other approximations for contact SM which combine SFM with the electrochemical STM break junction method [18]. This method measures the conductivity of molecules in solution [19] by pulling the tip from the gold surface and engaging a few molecules between the tip and the gold surface (Fig. 12.7a). For example, in ref. 20 (Fig. 12.7b), the changes in conductivity are correlated with changes in force, characterizing the electromechanical properties of SMs.

12.4 Experiments with Molecular Wires (MWs)

During recent years SFM has been used to probe the electrical properties of several MWs, mainly carbon nanotubes [21], DNA, and occasionally polymeric formations such as V_2O_5 nanofibers and coordination polymers. A “molecular wire” can be defined as a molecule whose length is more than 10 times its width, with the ability to transport electrical current with a reasonably low resistance. Thus we consider experiments where the total resistance ranges between tens of kilohms and a few megaohms. The one-dimensional geometry of MW allows the adsorption of molecules on insulating surfaces. The experiments are performed using a fixed electrode and the metallized AFM tip as a second mobile electrode (see the sketch

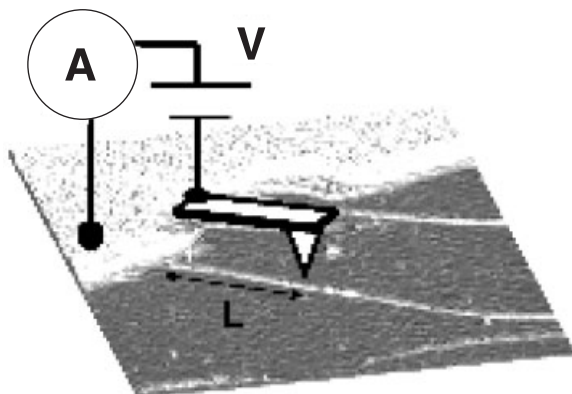


Fig. 12.8 Typical experimental configuration for electrical transport experiments on molecular wires (MWs). The molecule (in this case an SWNT) is half-covered with a macroscopic electrode, and the tip acts like a mobile electrode along the uncovered length of the molecule. The tip establishes contact with the molecule at a certain length L from the electrode, applying voltages (V) and measuring currents (A).

in Fig. 12.8). Although this is the typical experimental configuration, as stated in ref. 22, we discuss many other possibilities where the abilities of SFM can be exploited beyond mere contact with the molecule.

12.4.1

Contact Experiments on Long Molecules

We define a contact experiment as one in which the tip establishes mechanical and electrical contact with the molecule, measuring the current flowing through it. The sample preparation, once the molecules are adsorbed on an isolating surface (commonly SiO_2), involves the evaporation of several macroscopic gold electrodes (Fig. 12.9a) [23] using a variety of shadow-masking techniques. The result is a random distribution of molecules, in which some of them are partially covered by the metal used in the evaporation, commonly Au (Fig. 12.9b).

Usually the molecule is probed electrically along the uncovered length using a fixed voltage between the tip and the sample [22]. If the molecules are well attached to the surface and the SFM can be used in contact mode, a current map can be obtained simultaneously with the topography. This is the case when measuring multi-walled carbon nanotubes (MWNTs). For example, in ref. 22 it is possible to know the intrinsic resistance of the nanotube. The total measured resistance R_t can be expressed as Eq. (6), where R_{MW} is the intrinsic resistance of the MW; R_{CT} is the contact resistance of the tip with the MW; and R_{CE} is the contact resistance of the MW with the macroscopic electrode.

$$R_t = R_{MW} + R_{CT} + R_{CE} \quad (6)$$

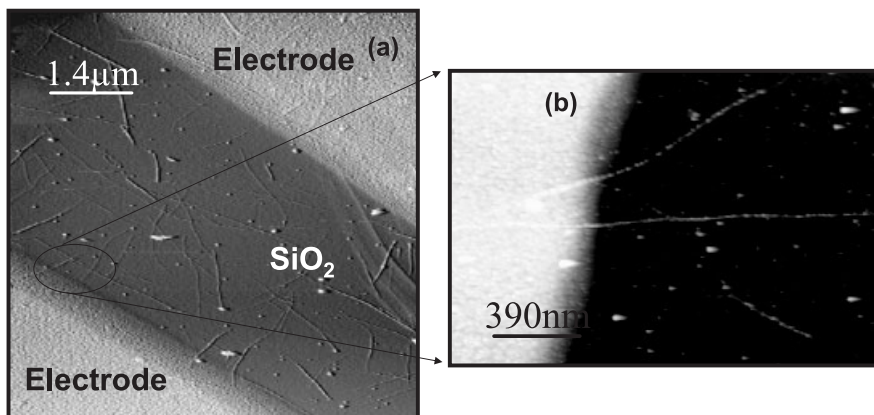


Fig. 12.9 Sample fabrication for MW electrical transport experiments. (a) Two gold electrodes are evaporated on an insulating surface covered with a serendipitous distribution of molecules. (b) Some of these molecules are electrically contacted by the electrode, leaving an uncovered length for doing the experiments, as in Fig. 12.7.

However, the high lateral forces involved in the contact mode modify molecules like single-walled carbon nanotubes (SWNTs) and DNA. In these cases, it is not possible to use the contact mode, and noncontact dynamic force microscopy (NCDFM) [24] becomes mandatory. When using SFM in NCDFM it is very difficult to obtain current maps, owing to the lack of mechanical and electrical contact with the sample. Therefore, a different strategy has to be applied in order to get electrical information about the molecules.

12.4.1.1 Contact Experiments in Single-Walled Carbon Nanotubes

Once we are scanning in NCDFM, the simplest strategy is to locate a spot of a selected carbon nanotube and record an FZ curve while applying a voltage. One important advantage of this experimental setup is that it makes it possible to measure the current flowing through the molecule as a function of the tip load. In Fig. 12.10(a) the variation of the current between the tip and a carbon nanotube as the tip approaches the surface is shown. The most outstanding detail is that the mechanical contact and the electrical contact are simultaneous [25] (z piezo displacement = 32 nm), as in ref. 17. Afterward the current remains stable until the tip releases the molecule in the backward cycle. The voltage applied between the tip and the sample is 100 mV, resulting in a resistance of 100 k Ω . The question of whether there is simultaneous electrical and mechanical contact is not so straightforward. In Fig. 12.10(b) the same kind of experiment is presented, but now on gold. It is clear that while the mechanical contact takes place at a z piezo displacement of 16 nm, the electrical contact comes later at 20 nm. Afterward the current grows until the preamplifier is saturated at 30 μ A. Moreover, in Fig. 12.10(c) we reproduce Fig. 3 of ref. 26. The upper graph is an FZ curve for a me-

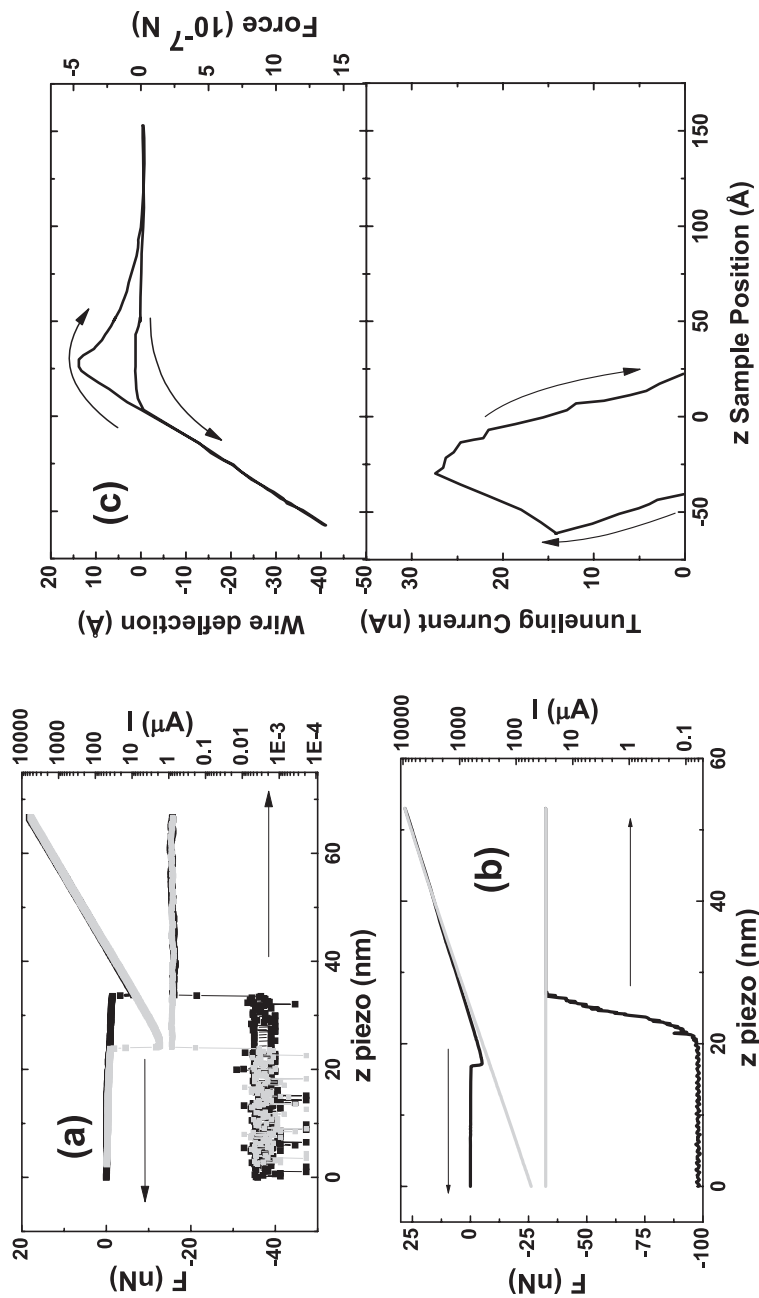


Fig. 12.10 Current vs. applied force for different systems. All the plots show current and force vs. z piezo displacement. (a) When the experiment is performed on an SWNT, mechanical and electrical contacts are simultaneous. However, the same experiment on a gold surface (b) shows the electrical contact well after the mechanical one. The approaching cycle is represented by black curves and the retracting one by the gray ones. Adapted from ref. 25. (c) Same experiment on HOPG, showing the same delay of the current (lower graph) as of the loading force (upper graph). Adapted from ref. 26.

tallic wire on highly oriented pyrolytic graphite (HOPG). The lower curve represents the variation of the current flowing through the tip. Once more, the electrical contact (z piezo = 50 Å) comes well after the mechanical contact is established (z sample position = 0 Å).

Let us consider now the forces needed to establish contact in each case, that is, 12 nN (adhesion force) for the carbon nanotube, more than 30 nN for the gold and more than 1 μN for the case of graphite. It is clear that the lowest force is for the carbon nanotube. For many purposes SWNTs can essentially be considered as wrapped graphene planes [27]. Thus, their surface chemical properties might be similar to those of HOPG. In particular, both surfaces are inert and hydrophobic. Thus similar IZ curves might be expected. Accordingly the main difference between the experiments presented above is not due to the chemistry or to the material, but to the geometry of the system. When the experiments are performed in the ambient atmosphere, a molecular thin layer of water and/or contamination is present between the tip and the sample [28]. When the tip approaches the sample, this layer has to be penetrated in order to establish electrical contact. A pressure has to be applied to achieve this. In the case of HOPG, the interaction between interatomic layers is fairly small, and thus any loading force induces surface deformation, increasing the contact area between the tip and the sample and thereby reducing the applied pressure [29]. In the case of SWNTs, the contact area is determined by the nanotube radius, being much smaller than the tip radius, which in our experiments is about 30 nm. Therefore for a given loading force the tip–nanotube pressure is much greater than the corresponding one on a flat surface such as HOPG or gold. Thus the electrical contact is produced at much smaller forces in the nanotube case. A nanotube may be visualized as an extremely sharp knife (<1 nm edge) cutting through the contamination layer [25]. This intuitive idea can be developed further by calculating the pressure of the tip–sample contact under the different experimental conditions. Using Hertz theory [15], and taking into account the adhesion force that is also acting on the tip–sample system, the contact radius a is given by Eq. (7), where F_{adh} is the adhesion force, F is the external loading force, $1/R_{tip} + 1/R_{sample}$ is the effective radius of curvature R^* , and $1/E^* = (1 - \sigma_{tip})/E_{tip} + (1 - \sigma_{sample})/E_{sample}$ is the effective Young's modulus with E_{tip} and E_{sample} the Young's modulus of the tip and the sample, respectively.

$$a^3(F) = \frac{3}{4} \frac{R^*(F + F_{adh})}{E^*} \quad (7)$$

σ_{sample} and σ_{tip} are the corresponding Poisson ratios. The pressure within the contact is given by Eq. (8), where ρ is the distance from the center of the contact.

$$P(\rho) = \frac{3F}{2\pi a^2} \sqrt{1 - \frac{\rho}{a}} \quad (8)$$

For the nanotube–tip system one obtains a contact radius of 0.25 nm and a maximum pressure of 75 GPa, while for the two flat surfaces one finds values of 6 nm

and 0.6 GPa in the case of the HOPG surface, and 2.5 nm and 4 GPa in the case of the gold electrode [25]. Therefore the pressure, which is believed to be the important parameter involved in the formation of an electrical contact on the carbon nanotube, can be two orders of magnitude greater within the nanotube–tip system than in the systems with flat surfaces.

In the previous experiment a constant voltage was applied to the nanotube, which provides limited information on the electrical transport properties of SWNTs. This can be improved by performing IVs at different spots on the carbon nanotube [30]. Once an SWNT is selected, it is feasible to measure IV curves at different positions along it by using the tip as a mobile electrode as follows: the scanning motion is stopped on top of the selected carbon nanotube, and the AFM tip is made to approach it until mechanical and electrical contact is established. Then a ramp of voltage is applied between the tip and the nanotube, registering simultaneously the current (IV). This is a major advantage with respect to other experimental setups where IV curves can only be acquired on one SWNT and for a unique SWNT length. In Fig. 12.11(a) six IVs taken on the nanotube at different lengths from the gold electrode are shown. With good control of the process the IVs can be repeated with small variations in the IV characteristics, so that any uncontrolled damage on the nanotube can be disregarded. IVs performed on metallic SWNTs show a linear regime around 0 V and then a clear saturation of the conductance at high voltages (Fig. 12.11a, inset) that, according to ref. 31, is attributed to electron–phonon interaction. The total resistance R of a contact measurement is a combination of three different contributions R_e , R_t , $R_i(L)$, where R_e and R_t are the contact resistances of the nanotube with the gold electrode and with the SFM tip, respectively, and $R_i(L)$ is the intrinsic resistance of the nanotube that depends on its length L and the density of defects along the nanotube. The resistance R_e with the gold electrode may vary from one nanotube to another but is constant for a given nanotube. In any case, neither of those two factors depends on the distance L to the gold electrode. It should be noticed that, at least for the case of arc-discharge SWNTs [30], with low intrinsic resistance are rather exceptional. A large percentage of experimental measurements reveal that the resistance is far from being constant for nanotubes longer than 1 μm . For a metallic SWNT the resistance value $R(L)$ (see Fig. 12.11b), using the linear part of each IV curve, is close to 0 V. Every IV curve is taken at a different distance to the electrode L . The data can be fitted to a good approximation by Eq. (9), where $R_c = R_e + R_t$ is the contact resistance, R_0 is the quantum resistance $h/2e^2$ (the factor $\frac{1}{2}$ accounts for the two conductance channels of a metallic SWNT), and ℓ is a characteristic length of the system that is identified with the electron mean free path. From the fit in Fig. 12.11(b), for this nanotube the contact resistance is found to be $R_c \cong 54 \text{ k}\Omega$ and $\ell \cong 305 \text{ nm}$.

$$R(L) = R_c + \frac{1}{2}R_0 \exp(L/\ell) \quad (9)$$

The relevant point here is that the resistance versus length plots are nonlinear and

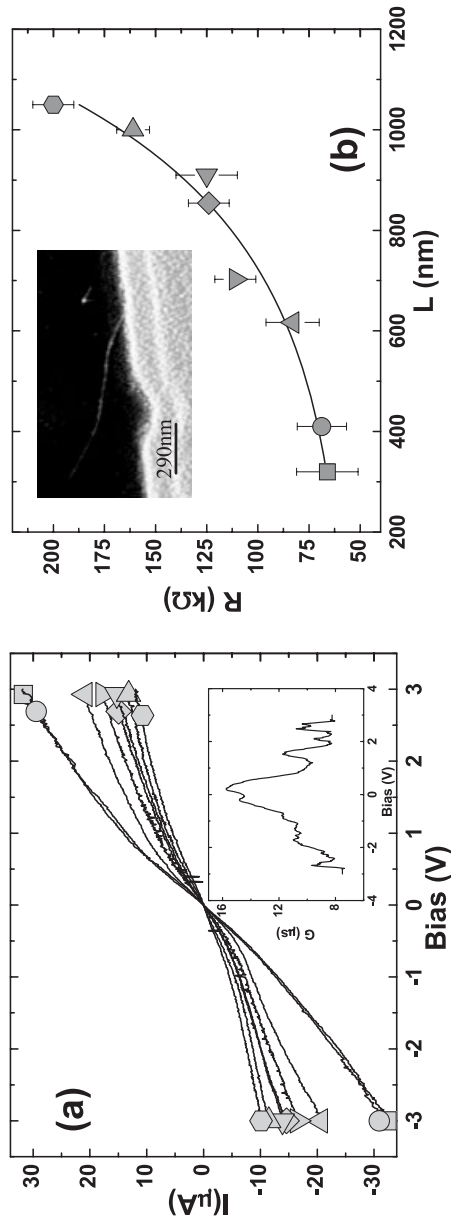


Fig. 12.11 (a) Several IV curves taken along the nanotube SWNT, 1.5 nm diameter, from the inset in (b). Inset to (a): for large voltages a saturation effect of the conductance is observed. (b) Low-voltage resistance vs. length of the nanotube from the inset shows a nonlinear behavior. From this plot a contact resistance of 54 $\text{k}\Omega$ is extrapolated. In (a) a symbol is assigned for each IV, and used in (b) to plot the experimental resistance data. Adapted from ref. 30.

that this dependence is intrinsic to each SWNT. The nonlinearity indicates that the electronic transport through the tube is neither ohmic nor completely ballistic. Each and every conducting wire that follows Ohm's law always presents a linear dependence of the resistance upon its length. Ohm's law is a consequence of dissipative transport caused by inelastic scattering (due to phonons, for instance). However, the experimental data describe a different situation, where each nanotube has its own nonlinear characteristic curve $R(L)$. This situation is compatible with a different explanation: in the absence of inelastic scattering the electrons may still suffer elastic scattering events with defects inside the conductor. In addition, the resulting effects due to elastic scattering are noticeable, assuming that the transport is coherent inside the nanotube. From the data of Fig. 12.11(b), it is concluded that the electron travels freely along the nanotube for 260 nm, which could be interpreted as the average distance between defects. Of course, ℓ is different for every nanotube, because each nanotube has a different number of defects. This hypothesis has been confirmed in experiments in which the density of defects of SWNTs is changed by Ar ion irradiation [32].

12.4.1.2 The Influence of Buckling on the Electrical Properties of SWNTs

As an additional application of this method, the conductance of a mechanically deformed SWNT was measured [33]. Depending on different factors, contact experiments with the SFM tip may produce plastic deformations in the SWNT shape. Figure 12.12(a) is an SFM topography image of an SWNT showing one of these modifications at point D. Whereas the differential resistance before point D saturates at large bias voltages, after point D it decreases with bias (see Figs. 12.12a and 12b). Therefore, by modifying the SWNT geometry, changes in the electrical transport properties of the nanotubes can be induced. This result extends a previous one [34] where a reversible drop in the conductance of a suspended metallic SWNT was induced by local deformations of the nanotube using a conventional SFM tip. In ref. 33 not only were resistance measurements performed, but also IVs. The IVs change from linear around 0 V (dark lines in Fig. 12.12b) before the deformation D, to nonlinear (gray lines in Fig. 12.12b) after the deformation D. In the inset (2) of Fig. 12.12(b), the differential conductance of all the IVs in Fig. 12.12(b) taken after modification D increases for high voltages. The IVs vary from being saturated before deformation, to nonsaturated after it. This suggests that the saturation of IVs is not related to the contact resistance, but to the particular structure of the nanotube. In addition, in inset (1) of Fig. 12.12b the behavior of the resistance at 0 V is presented, showing a sudden increase in the resistance precisely where the deformation D occurred. The closed angle ($\sim 90^\circ$) of this deformation indicates the buckling of the nanotube at D.

12.4.1.3 Radial Electromechanical Properties of SWNTs

In this experiment [35], a conductive AFM tip was again used as an electrode for the selected molecule. Only SWNTs exhibiting a linear dependence around 0 V and a drop in the conductance at high bias were considered. This behavior is typical of metallic nanotubes [31]. The experimental setup described in ref. 35 was able to

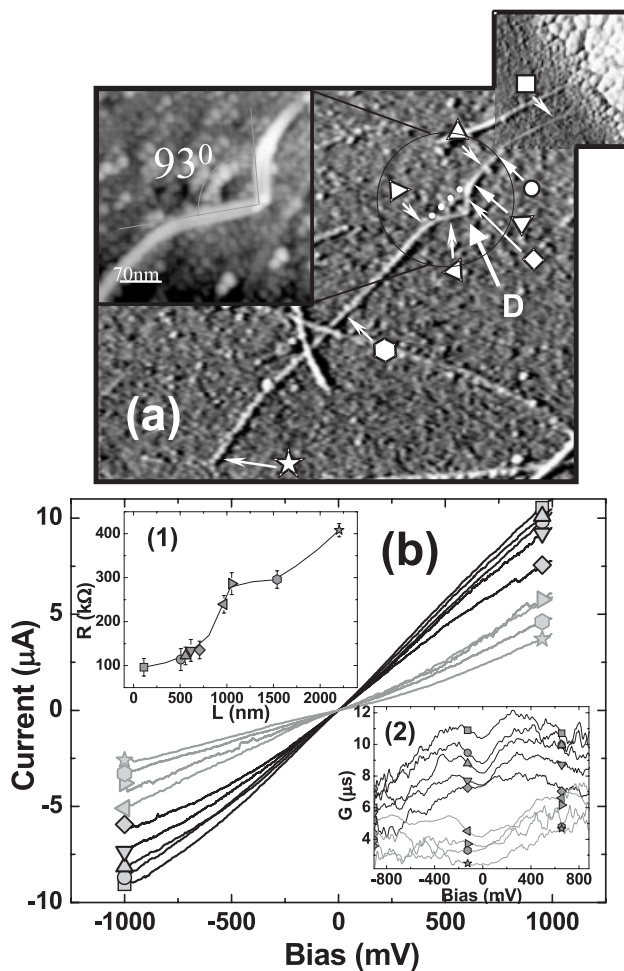


Fig. 12.12 SWNT deformation performed during a contact experiment with the SFM tip. (a) The SWNT image with the deformation “D.” The white dots show the previous SWNT shape. Observe the gold electrode in the upper right-hand corner. The spots where IV curves have been acquired are located by symbols

corresponding to the curves in (b) and insets (1) and (2). (b) Dark curves: IV plotted before deformation D; gray curves: IV plotted after D. Inset (1): the resistance near 0 V along the nanotube; inset (2): the differential conductance (dark and gray curves as above) [33].

record IV characteristics while the loading force was continuously increased [36]. The differential conductance was also acquired simultaneously as a function of the voltage and the loading force, using an AC lock-in amplifier technique.

The central point of this experiment was to obtain simultaneous maps of the differential conductance (color scale) and the normal force applied to the tube as a function of the bias voltage (V) and the piezoelectric elongation (z) along the direc-

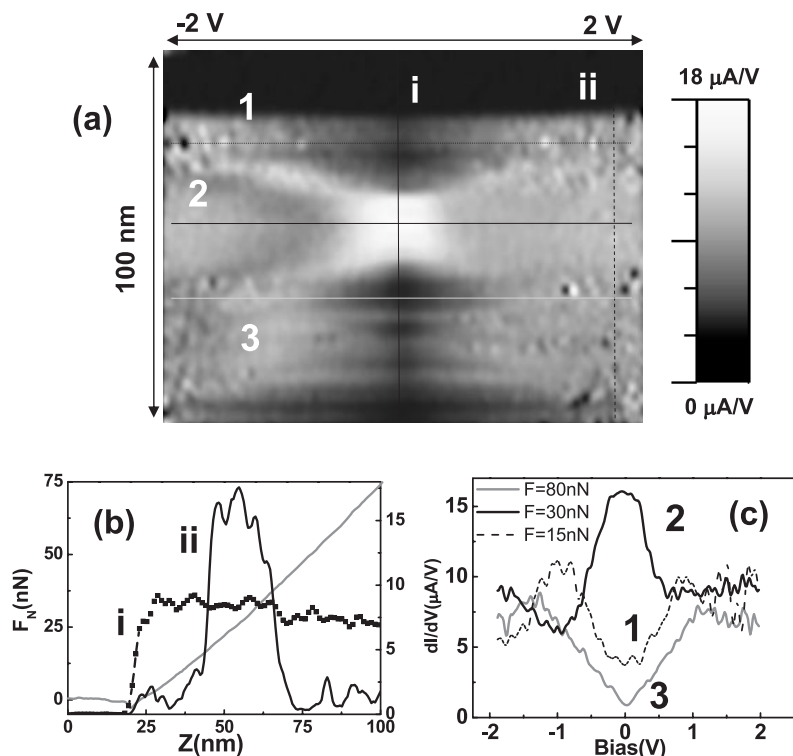


Fig. 12.13 (a) Differential conductance map $G(V, z)$ (color scale on the right) plotted as a function of the bias voltage (horizontal axis) and the piezo z displacement (vertical axis). The bias range was ± 2 V and the total z piezo displacement was 100 nm, starting from the feedback position. (b) Conductance as a function of the piezo z displacement. The

curves i and ii have been obtained along the vertical lines drawn in (a). The normal force applied to the SWNT is also plotted (gray curve). (c) Differential conductance as a function of the tip–SWNT bias voltage. The curves 1–3 were obtained along the horizontal lines drawn in (a). Adapted from ref. 35.

tion perpendicular to the sample for the loading cycle (Fig. 12.13a). In Fig. 12.13(a), while the tip is not in contact with the nanotube the conductance is zero (upper dark region). When the tip contacts the molecule an electrical current of several microamps starts to flow. To elucidate Fig. 12.13(a), several vertical profiles are drawn in Fig. 12.13(b): the gray line is the normal force, the black line is the low-voltage conductance (LVC), and the broken line is the high-voltage conductance (HVC). The LVC exhibits a minimum that tends to disappear as the molecule is loaded. For loading forces between 25 and 40 nN, this minimum disappears. Afterward the conductance drops to $2 \mu\text{A V}^{-1}$. However, the HVC does show a constant plateau caused by the mechanical contact from $z = 23$ nm to the end.

Experiments performed with two gold fixed electrodes [37] showed differential conductance similar to curve 2 of Fig. 12.13(c). This curve, obtained for a normal

force of 30 nN [35], was taken as the representative differential conductance for a nanotube in good contact and not strained. The conductance drop at high energies is now well understood in terms of electron–phonon interaction [31, 38]. According to this, the low-voltage minima in curves 1 and 3 of Fig. 12.13(c) are anomalies in the differential conductance of the nanotubes, but they have different origins. Curve 1 was obtained at a low loading force (15 nN) when the tip–nanotube contact was not well established. This was interpreted in terms of electrons passing from the tip to the molecule through a tunnel barrier. What is observed in curve 1 is the result of two processes: at low voltage the conductance tends to increase because of the increase in the conductance of a tunnel barrier [39] with the bias voltage, but at high voltage this tendency cannot be sustained any longer because the phonon–electron scattering produces a drop in conductance. The minimum observed in curve 3 appears at high loading forces (80 nN) and it is due to the radial strain (the relationship between the deformed and nondeformed diameter) of the carbon nanotube, which was estimated to be 0.7 [15]. The cage deformation produces a variation in the density of states of the nanotube, opening a gap and decreasing the low-voltage conductance. As the bias is increased the gap is overcome and the conductance tends to increase, but again the phonon interaction saturates the conductance.

12.4.1.4 Three Electrodes plus a Gate Voltage

The inset of Fig. 12.14(a) portrays another configuration [40] where the carbon nanotube is hooked between two planar electrodes and the tip is used as a third mobile electrode. While the gate voltage from silicon is used to change the Fermi level of the carbon nanotube, two measurement configurations can be used in this setup. In one, the source–drain bias is applied to the tip, while the drain electrode is connected to the current amplifier, and the left-hand electrode to a voltmeter (Fig. 12.14a). In the second, it is also possible to use one planar electrode as a voltage source–drain, while the other electrode is connected to a preamplifier. In this case, the tip is connected to a voltmeter and used to check the voltage drop along the carbon nanotube (Fig. 12.14b). From the conductance curve, 20 nm from the preamplifier electrode of Fig. 12.14(a) the minimum resistance is about 18 k Ω .

12.4.1.5 Contact Experiments on Single DNA Molecules

SWNTs are highly ordered mesoscopic systems, and can be considered as molecular crystals with a periodic structure. This is on the basis of the electrical transport properties of carbon nanotubes. Since the position of each and every single atom can be specified with just two numbers, they can be considered to have low complexity. As a consequence, the structuring capabilities of carbon nanotubes are reduced and it is difficult to envisage how a circuit based on them can be built on the bottom-up approximation. However, DNA represents the opposite concept of order, since it is a sequence of bases, and it stores a large amount of information. Mesoscopic transport theory dictates that weakly disordered one-dimensional systems (i.e., the electron mean free path ℓ is greater than the system length L ; $\ell/L > 1$) feature ballistic electronic transport. For increasing disorder (i.e.,

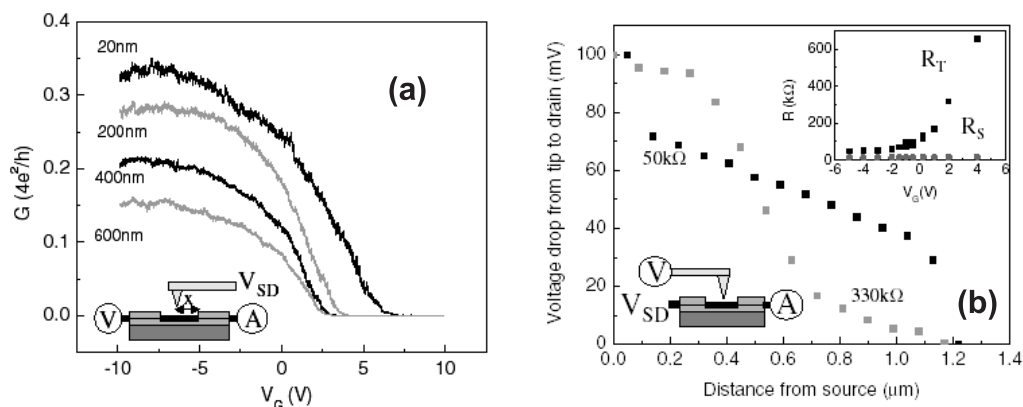


Fig. 12.14 (a) Three-electrode configuration Conductance vs. gate voltage, for different distances x between the tip and the drain ($x = 20, 200, 400, 600$ nm). $V_{tip} = 100$ mV. Inset: measurement configuration. The source–drain bias V_{SD} is applied to the tip, while the drain (right) electrode is connected to the current amplifier, and the left-hand electrode to a voltmeter. (b) Profile of the

voltage drop along the tube with $L = 1.2$ μm and $V_{SD} = 100$ mV. The two curves are for two different gate voltages, which correspond to total resistance R_T of 50 and 330 k Ω . Upper right inset: R_T and source contact resistance R_S (measured 70 nm from the lead) vs. gate voltage. Lower left-hand inset: measurement configuration. Adapted from ref. 40.

$\ell/L \ll 1$) the transport becomes first diffusive, and finally localized. According to this idea, natural DNA is probably not the best choice for a conductor [41]. On the contrary, DNA probably is the best choice for self-organizing a complex system like, for instance, a sophisticated nanocircuit [42].

However, during recent years several experimental studies have been published suggesting DNA as a molecular wire [43]. In order to address this issue, conductance AFM measurements on DNA [44] were carried out. Figure 12.15(a) shows, via FZ curves, a molecule partially covered by a gold electrode contacted with the metallic AFM tip at a selected spot. Then an IV was plotted at the maximum indentation point. The experiment was repeated at different distances from the edge of the gold electrode, as well as at different force thresholds.

The current sensitivity was 1 pA, and a bias voltage of up to 10 V was applied, without detecting any current. Therefore, it was concluded that the resistance of the molecule was at least 1 T Ω , and that the minimum value for the DNA resistivity ρ was $\sim 10^4$ Ω cm.

In order to avoid any spurious current, the minimum distance between the conductive tip and the gold electrode was set to 70 nm. After the contact experiments along the DNA, the conductance of the tip was checked by contacting the gold electrode carefully; contact resistances of about 30 Ω were found.

The experiments with carbon nanotubes explained above prove the conductivity of the tips and the feasibility of making electrical contacts between an SFM tip and long molecules. This absence of conductivity in DNA molecules was found even

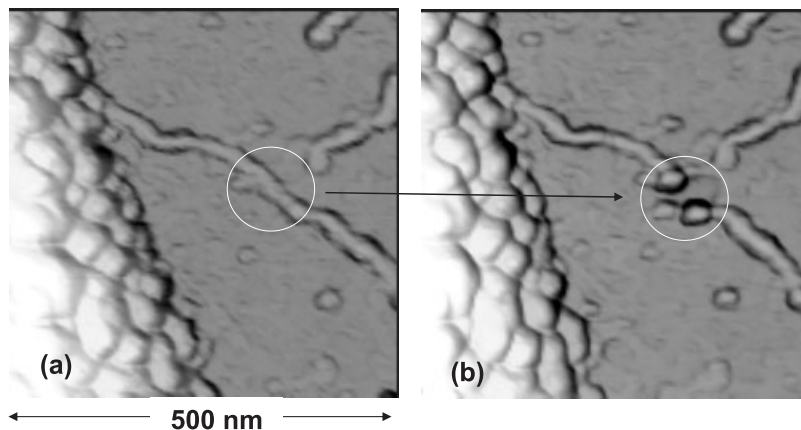


Fig. 12.15 (a) A single DNA molecule connected to a gold electrode. (b) The same molecule contacted by the tip (inside the circle) to measure the current, and cut at the place where the tip touches. No current outside the noise levels was measured at all.

when the tip broke the DNA molecules, as shown in Fig. 12.15. Figure 12.15(a) shows a single-stranded λ -DNA molecule before being cut. In Fig. 12.15(b) the same λ -DNA was divided in two pieces by the tip during an FZ. This experiment was also repeated for polyG–polyC [45] for different humidity conditions: again, negative results were obtained.

If we move from DNA conductivity single-molecule experiments to DNA network experiments [46], where the same SFM technique discussed above is used, some conductivity is found.

12.4.1.6 Electrical Maps of SWNTs

So far we have been considering experiments in which the electrical properties of the molecules are obtained via single FZs and IVs at certain spots on the molecules. In this section we will discuss other types of experiments in which current maps are taken simultaneously with the topography, thus obtaining the same number of data points as for the topography. In the pioneering experiment [22], the contact mode was used to perform electrical mapping of MWNTs using NbN-covered tips and getting minimum resistances of 150 k Ω on the MWNTs. However, for the case of other more delicate molecules like SWNT and DNA, the contact mode cannot be used since it bends or cuts the molecules. Thus other strategies have to be employed for the molecules which are prone to modification by the shearing forces of contact mode.

Otsuka et al. have proposed a technique called point-contact current-imaging atomic force microscopy (PCI-AFM) [47]. In this method, a topographic image is measured in NCDFM, and IV curves are obtained by establishing mechanical con-

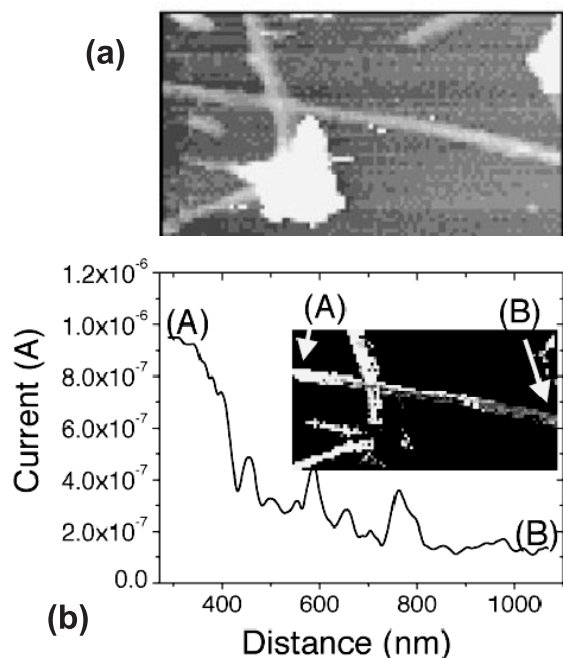


Fig. 12.16 Current maps for an SWNT. (a) Topographic image obtained in tapping mode. (b) Relationship between current and distance from electrode. This graph is plotted along the SWNT between (A) and (B) in the inset, which is the current image obtained by PCI-AFM. The current image was taken at a bias voltage of 2.0 V. Adapted from ref. 47.

tact with the tip during the consecutive interruption of NCDFM. On the basis of the spatially resolved IV measurements, a current image can be formed at a chosen bias voltage, getting simultaneously the topographic and the electrical map. In Fig. 12.16(a) a topographic image of an SWNT is shown, and in the inset of Fig. 12.16(b) it is possible to observe the current map at 2 V. The graph in Fig. 12.16b represents the electrical profile from point (A) to point (B) of the inset, showing a nonlinear decrease in the current with the nanotube length. The minimum resistance, when the tip is close to the gold electrode, is about $2 \text{ M}\Omega$. While one clear advantage of this method is the simultaneous acquisition of topography and electrical maps of SWNTs, we should comment on two drawbacks: first, the tip could wear out its metallic cover very rapidly since it is brought into contact at every topographic point; secondly, the velocity of data acquisition of a 128×128 point frame takes about 10 min, provided that it takes 0.04 s per point, as sketched in Fig. 1 of ref. 47.

12.4.1.7 Electrical Maps of V_2O_5 Nanofibers with Jumping Mode

Jumping mode (JM) is a true intermittent contact SFM scanning technique, where the topography is acquired from feedback on the cantilever deflection, as in contact

mode [48]. The lateral displacement is synchronized with the perpendicular one in such a way that it is performed when the tip-sample distance is a maximum. This avoids most of the shear forces between the tip and the sample. Current maps $I(X, Y)$ are made by monitoring the current flowing through the tip while it is in contact with the surface. It must be noted that each current map is performed at a fixed tip-sample bias voltage.

V_2O_5 nanowires [49] are ribbon-like structures with typical dimensions of 1.5 nm height, 10 nm width, and up to several microns length. It was carefully checked that JM does not modify V_2O_5 fibers. This is not the case for all types of molecular wires, such as single-walled carbon nanotubes or DNA [50]. The main reason for this difference is attributed to the shape and size of the objects (see figure 1(c) of ref. 51). A V_2O_5 fiber can be considered as a flat ribbon on the substrate, with a molecule-surface contact area which is typically seven times larger than in the case of SWNTs. Therefore the interaction between the V_2O_5 fiber and the substrate is strong enough to withstand the force exerted by the tip in JM. In contrast, carbon nanotubes and DNA molecules are thinner and roughly of cylindrical shape, resulting in a much lower interaction with the substrate than that of the V_2O_5 fibers. As in the SWNT case, it is only when the tip establishes contact with a fiber connected to the gold electrode that the electrical circuit is closed and a current passes through the tip. Inset (a) in Fig. 12.17 shows the topography of a couple of crossed V_2O_5 fibers connected to the gold electrode located at the upper right-hand end (outside the image region), and Fig. 12.17(b) is the current map when a bias voltage of 2 V is applied. In Fig. 12.17(c) a current profile along the dotted line in Fig. 12.17(b) presents a nonlinear variation of the current with the fiber length, plus an outstanding increment of the current at the crossing point of the two fibers. This increase in current just at the junction between the fibers indicates that the force applied by the cantilever does improve the electrical contact between them just at this place. As a consequence it is possible to conclude that the resistance between the fibers is negligible compared with 1 G Ω . An important drawback of this experiment is that the gold electrode cannot be imaged in JM, since the high adhesion between the tip and the sample removes the tip's gold coverage.

12.4.1.8 Using Tunneling Current to Obtain Current Maps of SWNTs

There have been several experiments performed to obtain current maps of SWNTs. One possible solution of the problem is to use a technique based on a tuning fork (TF): an SFM tip covered with tungsten carbide or doped diamond is attached to a vibrating quartz needle, so that topography images are taken in DF SFM DMS, and the tunneling current detected by the tip is monitored to build current maps of the surface, as shown in Fig. 12.18 [52]. When a bias of -1 V is applied to the tip, a maximum current of 35 pA is obtained on the SWNT rope, while the tunneling current is zero at the substrate. Although this method is very helpful toward resolving the connectivity of carbon nanotubes with the gold electrode, the high resistances found (30 G Ω) indicate that the tunnel barrier could mask the physical properties of the electrical transport of carbon nanotubes. Using a similar technique, Staderman et al. [53] obtained resistances of 20 G Ω .

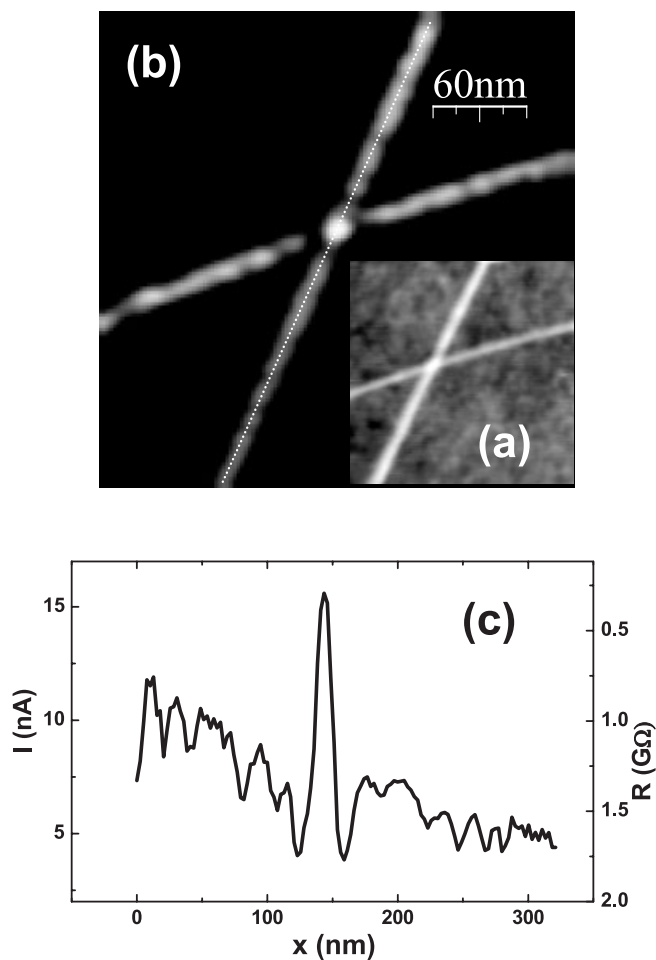


Fig. 12.17 (a) Current map for two crossing V_2O_5 nanofibers in JM at $V_{bias} = 2$ V. Inset: Simultaneous topography. (c) Current profile along the dotted line in (a). The current peak at 140 nm corresponds to the junction between the two fibers. Adapted from ref. 51.

12.5 Noncontact Experiments

So far, we have been discussing experiments in which the tip is an active tool in the electrical transport process, acting like a current transportation probe. However, in other kinds of electrical experiments with long molecules the tip can be used to probe electrostatic interactions. In conductance experiments the role of the contacts is always a problem. It is never clear whether the molecule is not a

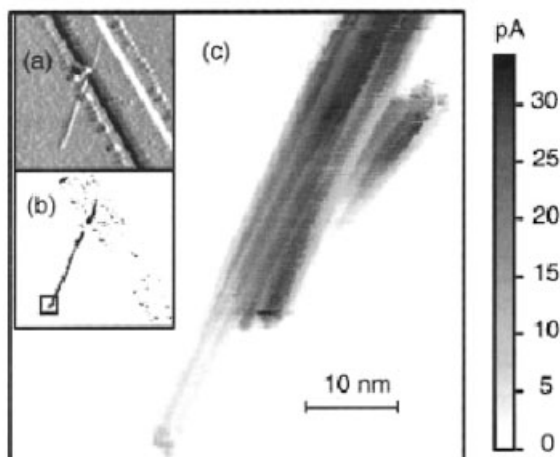


Fig. 12.18 High-resolution tunnel current image of an SWNT bundle contacted by an electrode on an otherwise insulating surface. Individual tubes in the bundle are clearly visible. The electrode is grounded, and the

AFM tip biased at -1 V. Top inset: topographic AFM image showing the bundle and the gold lead. Lower inset: Simultaneously acquired current image. Scan size in the inset is 850 nm. Adapted from ref. 52.

conductor, or whether the resistance of the contact is too high and it is disguising the real conductance of the molecule. Electrostatic interaction can be used to gain information about the intrinsic conductance properties of the molecule since it does not require electrical contact. When the AFM is operated in dynamic mode [54], it is possible to detect electrostatic interactions between the tip and the sample. Briefly, in this mode the tip is oscillated at its resonance frequency, and the feedback loop is engaged at a fixed value of the amplitude of the cantilever.

The electrostatic interaction has a long-range character and therefore it can be measured at large tip-sample distances where the van der Waals forces have already vanished. It is produced by the presence of localized charges or dipoles as well as from the polarization of the substrate due to an external electric field.

For a general case in electrostatic force microscopy (EFM), a bias voltage V is applied between a conductive tip and the sample, and the difference in voltage between the tip and the sample can be expressed as Eq. (10), where V_{dc} and V_{ac} are the DC and AC components respectively.

$$V = V_{dc} + V_{ac} \sin(\omega t) \quad (10)$$

Correspondingly the interaction force has three terms, which can be classified according to the frequency response (see Chapter 13) as given by Eqs. (11)–(13), where C is the local capacitance between tip and sample and z is the tip-sample distance.

$$F_{dc} = \frac{1}{2} \frac{\partial C}{\partial z} \left(V_{dc}^2 + \frac{1}{2} V_{ac}^2 \right) \quad (11)$$

$$F_{\omega} = \frac{\partial C}{\partial z} V_{ac} V_{dc} \quad (12)$$

$$F_{2\omega} = -\frac{1}{4} \frac{\partial C}{\partial z} V_{ac}^2 \quad (13)$$

While F_{dc} and F_{ω} depend on V_{dc} , $F_{2\omega}$ does not. This term is proportional to the square of the alternating potential V_{ac} , which is fixed during the experiment, and the derivative of the capacitance with respect to distance. This derivative changes with the sample topography, owing to variations in the tip–sample distance, and locally with the dielectric properties of the sample. The study of $F_{2\omega}$ will yield the dielectric properties of the sample provided that the probe–sample system geometry is constant along the surface. Interestingly, the second term, F_{ω} , is also proportional to the derivative of the capacitance and to the two potentials, V_{ac} and V_{dc} . Whereas V_{ac} is fixed during the experiment, V_{dc} may vary locally on the sample due to different chemical potential values at the sample surface. Correspondingly this voltage is a quantity to be measured. By the use of lock-in techniques, F_{ω} and $F_{2\omega}$ can be measured separately; depending on the mode of measurement being used, different sample properties will be extracted.

12.5.1

Carbon Nanotubes

EFM has been used to probe the voltage variation along SWNTs and MWNTs contacted between two electrodes [55]. Since the tip–sample distance is kept constant during the experiment and V_{ac} is constant, F_{ω} depends on the local dielectric properties (through C) and is proportional to the potential difference V_{dc} between the tip and the sample. Sometimes the changes in the capacity along the surface can be neglected and, as in this experiment, F_{ω} is considered proportional to the interaction potential V_{dc} ; so, by locking the normal force at a frequency ω , a map of the electrostatic force in newtons is obtained (see Fig. 12.19a), but not of the potential in volts. The profile along the carbon nanotube depicted in Fig. 12.19(b) shows an almost linear variation of the electrostatic force on the length, with some influence from the topography.

When the simplest case is analyzed, without applying AC voltage to the tip ($V_{ac} = 0$), the key physics is sustained by F_{dc} , which depends on the local variations of the capacitance C between the tip and the surface [Eq. (11)], and on the square of the difference of voltage between the tip and the sample V_{dc}^2 . The capacitance C depends not only on the geometry and the distance between tip and sample, but also on the surface dielectric constant ϵ just below the tip. This has to be taken into account when interpreting the electrostatic images: that is, a local change in the dielectric properties produces a variation in the force signal. The importance of the two parameters is different, depending on the experiment considered. For

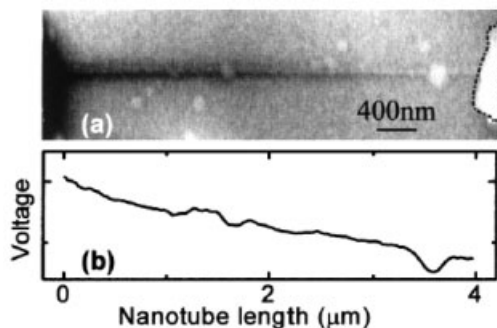


Fig. 12.19 (a) AC EFM image of an MWNT, diameter 9 nm. The resistance of the entire circuit was 42 k Ω . An AC bias of 150 mV was applied to the left-hand electrode; the IV

characteristic verified that this bias was within the linear response region. (b) AC EFM signal as a function of the nanotube length. Adapted from ref. 55.

example, if we have a network of SWNTs close to a gold electrode [56], the SWNTs connected to the gold electrode show a much higher interaction than those disconnected (Fig. 12.20a) via the V_{dc}^2 term of Eq. (11). When a voltage is applied to the tip this interaction produces an artifact on the topography which appears higher on the conducting parts of the sample (Fig. 12.20b). The conductive areas on a color map image “shine” and the spatial resolution is lost, as shown in Fig. 12.20(b). By means of the “shining” effect, it is possible to discriminate between molecules connected and unconnected to the gold electrode. Figure 20(a) shows a SFM topography image of the electrode border with several SWNTs connected to the gold with a bias of 0 V applied to the SFM tip. A label has been added to mark the position of some relevant nanotubes. In Fig. 12.20(b) a bias of 1.5 V is applied to the SFM tip. As a consequence of the electrostatic interaction, the topography image shows a blurring effect on the conductive areas of the surface connected to ground, i.e., the gold electrode and the connected nanotubes. Specifically, the nanotubes connected to the electrode show a higher and wider topography than those in Fig. 12.20(a). Nanotubes directly connected to the gold (nanotube 1 in Fig. 12.20(b)) and nanotubes connected to the gold via a second nanotube (nanotube 2 in Fig. 12.20(b)) show this blurring effect. Another case is that of electrically isolated nanotubes (like nanotube 3 in Fig. 12.20b), which do not show this effect.

The voltage applied to the tip induces the charges to flow from the ground to the nanotubes to screen the effect of the electrostatic field generated by the tip. This does not happen in the electrically isolated areas of the sample, such as the SiO₂ substrate or the isolated SWNT, e.g., nanotube 3 of Figure 21(b). This “shining” effect is explained by the way in which the electrostatic force does affect the topography image formation. The oscillation of the tip under the electrostatic force can be modeled by Eq. (14), where z is the distance between tip and sample, m is the effective cantilever mass, k the force constant, ω_0 the resonance frequency of the

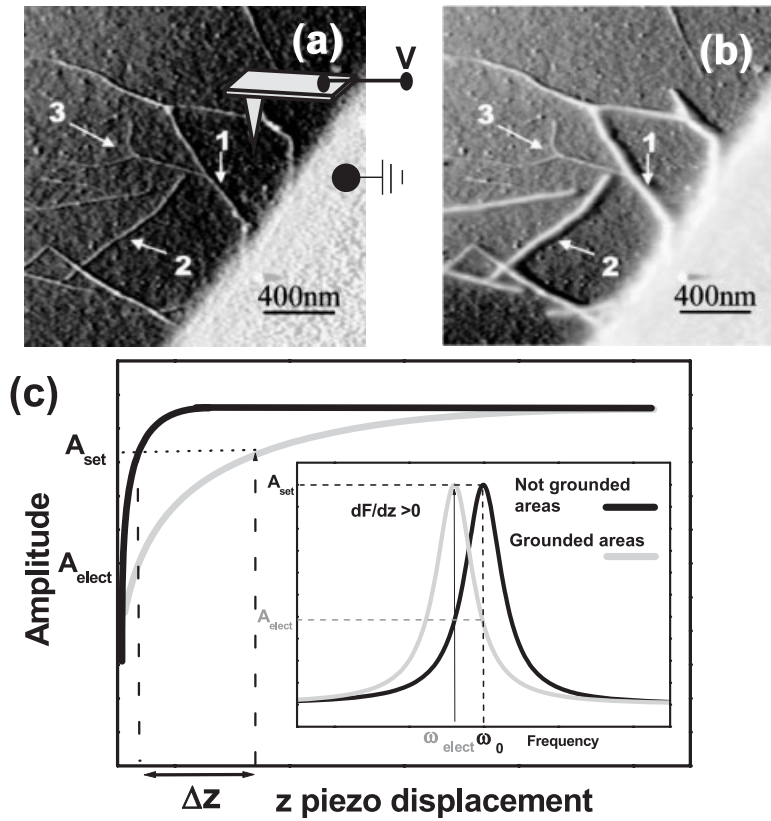


Fig. 12.20 (a) An area with SWNTs connected and unconnected to the gold while a voltage of 0 V is applied to the SFM tip. The connection of the tip is also shown. (b) A voltage of 1.33 V is applied to the tip in the same region of (a). Three different nanotubes are labeled. 1: directly connected to the gold; 2: connected via another nanotube; 3: unconnected. (c) Behavior of the oscillating amplitude versus piezo z displacement for insulating areas (black) and ground-connected areas (gray). Inset: change in the resonance frequency with the electrostatic interaction at a fixed distance from the sample. Adapted from ref. 56.

system, Q the quality factor, $F_0 \cos(\omega t)$ the cantilever driving force, and F_e the electrostatic force between tip and sample.

$$m\ddot{z} = -kz - \frac{m\omega_0}{Q}\dot{z} + F_0 \cos(\omega t) + F_e(z) \quad (14)$$

In the case of F_e being absent, the resonance peak of the amplitude is very close to ω_0 , the resonance frequency of the free system (see the inset of Fig. 12.20c). When $V_{tip} \neq 0$ and F_e is assumed to be linear for low-interaction regimes, the resonance frequency changes in $\Delta\omega \approx \omega_0/2k \times dF_e/dz$, where $\Delta\omega$ is negative because electro-

static forces are always attractive (Fig. 12.20c). Let us see how the topography is changed. When F_e is not present between the tip and the sample, the amplitude at which the topography images are taken is A_{set} (see Fig. 12.20c), but when F_e is present, the amplitude decreases to A_{elect} because of the shift on the resonance frequency (see inset of Fig. 12.20c). As a consequence the feedback loop moves the tip away from the surface to keep the amplitude constant. In this way the electrostatic force is originating an extra size in the topography, which is seen in Fig. 12.20(b). This extra height depends not only on the tip voltage, but also on the feedback parameters and amplitude set point.

12.5.2

Single DNA Molecules

One problem which could be attributed to the contact experiments on DNA discussed in Section 12.4.1.6 is the bad electrical contact between the tip and the DNA molecule, along with the DNA contact with the electrode. Noncontact EFM experiments similar to those of Section 12.5.1 have been performed in order to address not only the quality of the DNA electrical contacts, but also the ϵ value of the DNA [57]. DNA molecules and carbon nanotubes are co-adsorbed on mica in order to compare the electrostatic signal of both molecules with the same AFM tip. Figure 21(a) shows a SFM topographic image of a mica substrate with an SWNT and a DNA molecule partially covered by the gold electrode without (inset) and with bias voltage. Notice that while the SWNT appears higher and wider because of the presence of the electrostatic interaction, the DNA molecule remains unmodified. Therefore, no charges have passed from the gold electrode to the DNA, implying that DC conductivity in the DNA is negligibly small. It could be argued that the connection to the DNA molecule by means of an evaporated macroscopic electrode could modify its properties. Therefore, in a further experiment, a more gentle electrical contact to the DNA was established through an SWNT. The inset of Fig. 12.21(b) shows a DNA molecule connected to a carbon nanotube in contact with a macroscopic gold electrode. Fig. 12.21(b) is a topographic image of the same area but with a tip-sample bias voltage of 2 V. As expected, the SWNT is affected by the bias in the same way as in Fig. 12.20. In contrast, the DNA molecule remains unmodified, indicating no flow of electrons from the grounded electrode.

The previous experiments describe a situation where the molecules were contacted at just one end. Following a similar strategy it is possible to design experiments to measure electrostatic properties without contacting the molecules. Let us recall that the capacity term of Eq. (11) when just a DC voltage is applied to the tip does depend, once the tip-surface distance is kept constant, on the dielectric constant ϵ . For the situation of single molecules on an insulating surface, the V_{dc}^2 term of Eq. (11) does not contribute, since the lack of a grounding electrode causes the whole surface to float with respect to the tip, thus taking the tip voltage. This means that any contrast in the data should come from local variations of ϵ . Since ϵ is related to the ability of charges to move inside a material, i.e., to its polarization, its value should be related to its electrical conductivity. In this frame-

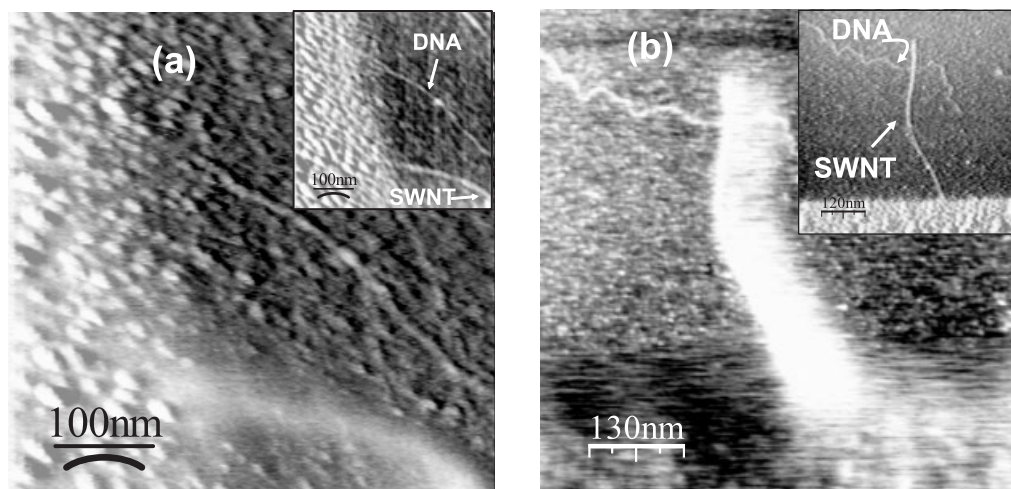


Fig. 12.21 Electrostatic response of DNA molecules. (a) With 1.33 V applied between tip and sample, only the SWNT shows the blurring effect. Inset: the 0 V bias topography of an SWNT and a DNA molecule connected to the

gold. (b) With a bias of 2 V applied, the nanotube does show blurring effects in the topography. Inset: gold-connected nanotube contacting a single DNA molecule at 0 V of bias. Adapted from ref. 57.

work, conducting materials should present $\epsilon \gg 1$ and insulating ones $\epsilon \sim 1$. Figure 22(a) shows an SFM topographic image of a DNA molecule parallel to an SWNT (upper molecule). Neither molecule is connected to any electrode. After this topographic image was recorded, the tip was lifted 100 nm above the mica substrate while oscillating at the free resonance frequency. A bias voltage of 1.6 V was then applied to the metal-covered tip. As the tip approached the surface while scanning over the SWNT and the DNA molecule, a monotonic decrease in the resonance frequency was observed because of the electrostatic force produced by the polarization of the insulating substrate [36]. Fig. 12.22(b) shows a frequency-shift profile taken along the broken line drawn in Fig. 12.22(a), with the tip positioned at 10 nm above the sample. Whereas a remarkable decrease in the resonance frequency appeared at the nanotube position, no signal above the noise level was detected when the tip was over the DNA molecule. Since the electrostatic force between tip and sample is basically produced by the effect of the polarization induced by the applied bias, the absence of a signal over the DNA molecule implies that the dielectric constant ϵ of the DNA and that of the substrate were similar. No significant contrast was detected over the DNA molecule at any bias voltage between ± 10 V. However, the SWNT is a good conductor and hence its ϵ value is very high. Thus, it presents a marked electrostatic signal with respect to the insulating substrate. This result is especially significant since it does not depend on any contact with the electrodes, since it demonstrates that the ability of DNA to carry charges inside is negligible compared with that of SWNTs.

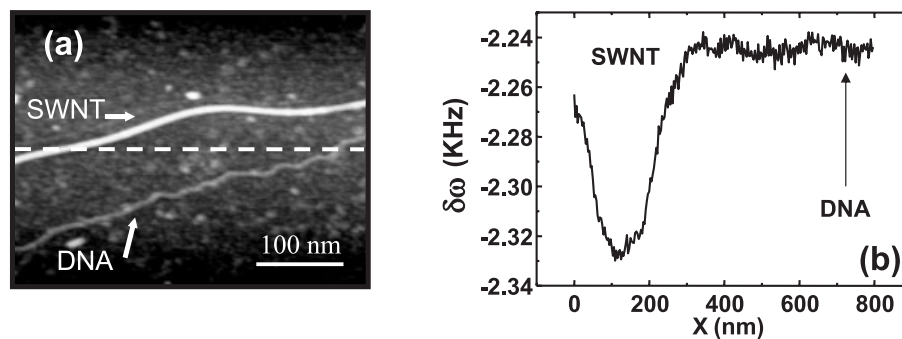


Fig. 12.22 Polarization of an SWNT and DNA. (a) Topographic image showing an SWNT and a DNA molecule adsorbed on mica. (b) Frequency-shift profile along the broken line in (a). Adapted from ref. 57.

Other authors [58] have used the Kelvin probe, confirming the previous results.

To conclude this chapter, the experiments performed on molecular wires are compiled in Table 12.2, which lists for each case the molecule used, the minimum resistance obtained, and the metallization of the tip. For every experiment in the

Table 12.2 Resistance of tip coatings, summarizing the main parameters of most of the experiments on molecular wires discussed in the chapter.

	Technique	Tip coating	Minimum resistance	Reference
SWNT	AFM	commercial platinum	2 M Ω	43
SWNT	vibrating quartz needle	tungsten carbide or doped diamond	30 G Ω	48
SWNT	tuning fork	Pt/Ir wire	20 M Ω	49
MWNT	AFM	NbN	0.15 M Ω	19
SWNT	AFM	chromium/gold	60 k Ω	26
SWNT	AFM	gold	18 k Ω	36
SWNT	AFM	chromium/gold	10 k Ω	29
λ -DNA	AFM	chromium/gold	1 T Ω	40
PolyGD DNA network	AFM	chromium/gold	50 M Ω	42

table it is possible to draw a general conclusion, that the gold-covered tips give the lowest resistances. The tuning fork experiments, although they do involve tunneling current, are included in the table for reference.

References

- 1 W. SHOCKLEY, J. BARDEEN, W. H. BRATTAIN, *Science* 1948, 108, 678–679.
- 2 J. KILBY, *IEEE Trans. Electron Devices* 1980, 27, 2176–2176.
- 3 G. E. MOORE, *Electronics* 1965, 38.
- 4 P. A. PACKAN, *Science* 1999, 285, 2079–2081.
- 5 S. DATTA, *Electronic Transport in Mesoscopic Systems* (Cambridge University Press, Cambridge, 1997).
- 6 J. I. PASCUAL, J. MENDEZ, J. GOMEZHERRERO, A. M. BARO, N. GARCIA, V. T. BINH, *Phys. Rev. Lett.* 1993, 71, 1852–1855.
- 7 Y. KONDO and K. TAKAYANAGI, *Phys. Rev. Lett.* 1997, 79, 3455–3458.
- 8 T. W. EBBESEN, H. J. LEZEC, H. HIURA, J. W. BENNETT, H. F. GHAEMI, T. THIO, *Nature* 1996, 382, 54–56.
- 9 G. BINNIG, H. ROHRER, *Helvetica Physica Acta* 1982, 55, 726–735.
- 10 J. TERSOFF, D. R. HAMANN, *Phys. Rev. Lett.* 1983, 50, 1998–2001.
- 11 J. I. PASCUAL, J. GOMEZ-HERRERO, C. ROGERO, A. M. BARO, D. SANCHEZ-PORTAL, E. ARTACHO, P. ORDEJON, J. M. SOLER, *Chem. Phys. Lett.* 2000, 321, 78–82.
- 12 E. BARRENA, S. KOPTA, D. F. OGLETREE, D. H. CHARYCH, M. SALMERON, *Phys. Rev. Lett.* 1999, 82, 2880–2883.
- 13 D. J. WOLD, C. D. FRISBIE, *J. Am. Chem. Soc.* 2000, 122, 2970–2971.
- 14 D. J. WOLD, C. D. FRISBIE, *J. Am. Chem. Soc.* 2001, 123, 5549–5556.
- 15 K. L. JOHNSON, *Contact Mechanics* (Cambridge University Press, Cambridge, 2001).
- 16 A. SALOMON, D. CAHEN, S. LINDSAY, J. TOMFOHR, V. B. ENGELKES, C. D. FRISBIE, *Advanced Materials* 2003, 15, 1881–1890.
- 17 X. D. CUI, A. PRIMAK, X. ZARATE, J. TOMFOHR, O. F. SANKEY, A. L. MOORE, T. A. MOORE, D. GUST, G. HARRIS, S. M. LINDSAY, *Science* 2001, 294, 571–574.
- 18 B. Q. XU, X. Y. XIAO, N. J. TAO, *J. Am. Chem. Soc.* 2003, 125, 16164–16165.
- 19 B. Q. XU, N. J. J. TAO, *Science* 2003, 301, 1221–1223.
- 20 B. Q. XU, X. L. LI, X. Y. XIAO, H. SAKAGUCHI, N. J. J. TAO, *Nano Letters* 2005, 5, 1491–1495.
- 21 S. IIJIMA, *Nature* 1991, 354, 56–58.
- 22 HONGJIE DAI, ERIC W. WONG, CHARLES M. LIEBER, *Science* 1996, 272, 523–526.
- 23 P. J. DE PABLO, E. GRAUGNARD, B. WALSH, R. P. ANDRES, S. DATTA, R. REIFENBERGER, *Appl. Phys. Lett.* 1999, 74, 323–325.
- 24 Y. MARTIN, C. C. WILLIAMS, H. K. WICKRAMASINGHE, *J. Appl. Phys.* 1987, 61, 4723–4729; Q. ZHONG, D. INNIS, K. KJOLLER, V. B. ELINGS, *Surf. Sci.* 1993, 290, L688–L692.
- 25 P. J. DE PABLO, M. T. MARTINEZ, J. COLCHERO, J. GOMEZ-HERRERO, W. K. MASER, A. M. BENITO, E. MUNOZ, A. M. BARO, *Advanced Materials* 2000, 12, 573–576.
- 26 C. M. MATE, R. ERLANDSSON, G. M. MCCLELLAND, S. CHIANG, *Surf. Sci.* 1989, 208, 473–486.
- 27 G. DRESSSELHAUS, P. C. EKLUND, M. S. DRESSSELHAUS, *Science of Fullerenes and Carbon Nanotubes* (Academic Press, San Diego, 1996).
- 28 J. COLCHERO, A. STORCH, M. LUNA, J. G. HERRERO, A. M. BARO, *Langmuir* 1998, 14, 2230–2234.
- 29 M. SALMERON, D. F. OGLETREE, C. OCAL, H. C. WANG, G. NEUBAUER, W. KOLBE, G. MEYERS, *Journal of Vacuum Science & Technology B* 1991, 9, 1347–

- 1352; J. M. SOLER, A. M. BARO, N. GARCIA, H. ROHRER, *Phys. Rev. Lett.* 1986, 57, 444–447.
- 30 P. J. DE PABLO, C. GOMEZ-NAVARRO, J. COLCHERO, P. A. SERENA, J. GOMEZ-HERRERO, A. M. BARO, *Phys. Rev. Lett.* 2002, 88, 36 804–36 808.
- 31 Z. YAO, C. L. KANE, C. DEKKER, *Phys. Rev. Lett.* 2000, 84, 2941–2944.
- 32 C. GOMEZ-NAVARRO, P. J. DE PABLO, J. GOMEZ-HERRERO, B. BIEL, F. J. GARCIA-VIDAL, A. RUBIO, F. FLORES, *Nat. Mater.* 2005, 4, 534–539.
- 33 P. J. DE PABLO, C. GOMEZ-NAVARRO, M. T. MARTINEZ, A. M. BENITO, W. K. MASER, J. COLCHERO, J. GOMEZ-HERRERO, A. M. BARO, *Appl. Phys. Lett.* 2002, 80, 1462–1464.
- 34 T. W. TOMBLER, C. W. ZHOU, L. ALEXSEYEV, J. KONG, H. J. DAI, L. LEI, C. S. JAYANTHI, M. J. TANG, S. Y. WU, *Nature* 2000, 405, 769–772.
- 35 C. GOMEZ-NAVARRO, P. J. DE PABLO, J. GOMEZ-HERRERO, *Advanced Materials* 2004, 16, 549–552.
- 36 C. GOMEZ-NAVARRO, A. GIL, M. ALVAREZ, P. J. DE PABLO, F. MORENO-HERRERO, I. HORCAS, R. FERNANDEZ-SANCHEZ, J. COLCHERO, J. GOMEZ-HERRERO, A. M. BARO, *Nanotechnology* 2002, 13, 314–317.
- 37 Z. YAO, C. DEKKER, P. AVOURIS, *Carbon Nanotubes* 2001, 80, 147–171.
- 38 J. Y. PARK, S. ROSENBLATT, Y. YAISH, V. SAZONOVA, H. USTUNEL, S. BRAIG, T. A. ARIAS, P. W. BROUWER, P. L. MCEUEN, *Nano Letters* 2004, 4, 517–520.
- 39 J. G. SIMMONS, *J. Appl. Phys.* 1963, 34, 1793–1803.
- 40 Y. YAISH, J. Y. PARK, S. ROSENBLATT, V. SAZONOVA, M. BRINK, P. L. MCEUEN, *Phys. Rev. Lett.* 2004, 92, 046401.
- 41 (a) E. BRAUN, Y. EICHEN, U. SIVAN, G. BEN-YOSEPH, *Nature* 1998, 391, 775–778; (b) R. GUCKENBERGER, M. HEIM, G. CEVC, H. F. KNAPP, W. WIEGRABE, A. HILLEBRAND, *Science* 1994, 266, 1538–1540.
- 42 K. KEREN, R. S. BERMAN, E. BUCHSTAB, U. SIVAN, E. BRAUN, *Science* 2003, 302, 1380–1382.
- 43 (a) H. W. FINK, C. SCHONENBERGER, *Nature* 1999, 398, 407–410; (b) D. PORATH, A. BEZRYADIN, S. DE VRIES, C. DEKKER, *Nature* 2000, 403, 635–638.
- 44 P. J. DE PABLO, F. MORENO-HERRERO, J. COLCHERO, J. G. HERRERO, P. HERRERO, A. M. BARO, P. ORDEJON, J. M. SOLER, E. ARTACHO, *Phys. Rev. Lett.* 2000, 85, 4992–4995.
- 45 In polyG–polyC DNA one strand is a chain of guanines and the other is a chain of cytosines.
- 46 L. T. CAI, H. TABATA, T. KAWAI, *Appl. Phys. Lett.* 2000, 77, 3105–3106.
- 47 Y. OTSUKA, Y. NAITOH, T. MATSUMOTO, T. KAWAI, *Japanese Journal of Applied Physics Part 2–Letters* 2002, 41, L742–L744.
- 48 P. J. DE PABLO, J. COLCHERO, J. GOMEZ-HERRERO, A. M. BARO, *Appl. Phys. Lett.* 1998, 73, 3300–3302.
- 49 J. LIVAGE, F. BETEILLE, C. ROUX, M. CHATRY, P. DAVIDSON, *Acta Materialia* 1998, 46, 743–750.
- 50 F. MORENO-HERRERO, P. J. DE PABLO, J. COLCHERO, J. GOMEZ-HERRERO, A. M. BARO, *Surf. Sci.* 2000, 453, 152–158.
- 51 C. GOMEZ-NAVARRO, P. J. DE PABLO, J. COLCHERO, Y. FAN, M. BURGHARD, J. GOMEZ-HERRERO, A. M. BARO, *Nanotechnology* 2003, 14, 134–137.
- 52 M. FREITAG, M. RADOSAVLJEVIC, W. CLAUSS, A. T. JOHNSON, *Physical Review B* 2000, 62, R2307–R2310.
- 53 M. STADERMANN, S. J. PAPADAKIS, M. R. FALVO, J. NOVAK, E. SNOW, Q. FU, J. LIU, Y. FRIDMAN, J. J. BOLAND, R. SUPERFINE, S. WASHBURN, *Physical Review B* 2004, 69, 45406.
- 54 P. J. DE PABLO, J. COLCHERO, M. LUNA, J. GOMEZ-HERRERO, A. M. BARO, *Physical Review B* 2000, 61, 14 179–14 183.
- 55 A. BACHTOLD, M. S. FUHRER, S. PLYASUNOV, M. FORERO, E. H. ANDERSON, A. ZETTL, P. L. MCEUEN, *Phys. Rev. Lett.* 2000, 84, 6082–6085.
- 56 P. J. DE PABLO, C. GOMEZ-NAVARRO, A. GIL, J. COLCHERO, M. T. MARTINEZ, A. M. BENITO, W. K. MASER, J.

- GOMEZ-HERRERO, A. M. BARO, *Appl. Phys. Lett.* 2001, 79, 2979–2981.
- 57 C. GOMEZ-NAVARRO, F. MORENO-HERRERO, P. J. DE PABLO, J. COLCHERO, J. GOMEZ-HERRERO, A. M. BARO, *Proc. Natl. Acad. Sci. USA* 2002, 99, 8484–8487.
- 58 (a) A. GIL, P. J. DE PABLO, J. COLCHERO, J. GOMEZ-HERRERO, A. M. BARO, *Nanotechnology* 2002, 13, 309–313; (b) C. H. LEI, A. DAS, M. ELLIOTT, J. E. MACDONALD, *Appl. Phys. Lett.* 2003, 83, 482–484.

13 Electronic Characterization of Organic Thin Films by Kelvin Probe Force Microscopy

Vincenzo Palermo, Matteo Palma, and Paolo Samorì

13.1 Introduction

“Smart” organic molecules with tailor-made properties are promising materials for the fabrication of novel cheap electronic devices such as flexible displays, chemical sensors, or large-area solar cells. Although a few of these devices have recently been introduced into the market, their workup still needs to be optimized for large-scale applications [1]. The performance of such devices can be improved by achieving full control over the supramolecular structure of the active organic components, and by unraveling and improving many other physicochemical properties of such architectures, such as their complex electronic structure, the peculiarities of which make it difficult in some ways to explore these materials by means of conventional surface-sensitive techniques, such as photoelectron spectroscopy. Moreover, a very delicate problem in the frame of electrical characterizations of organic materials is the tailoring of a metallic/organic interface, i.e., the formation of a reliable ohmic contact needed to electrically test the material under investigation. Therefore, unconventional methodologies are required to study, in a non-invasive way, the structural and electrical properties of soft materials across a wide range of length scales.

Scanning force microscopy (SFM) enables the mapping of surfaces and interfaces with a resolution that spans from hundreds of micrometers down to the nanometer scale [2–4]. The versatility of such methodology, which is also due to its applicability under different environmental conditions, makes it possible to gain insight both into structural and dynamic properties of thin films. In this way, inorganic, organic, and biological materials can be studied, even in their native environments.

While surface topography mapping by SFM is usually straightforward, the exploration of the chemical composition, as well as the quantitative investigation of different physicochemical properties of the surface, is more problematic [5]. On the other hand, scanning tunneling microscopy (STM) and scanning tunneling spectroscopy (STS) techniques are very powerful methodologies which possess a chemical sensitivity and can achieve a subnanometer resolution [6, 7]. Nevertheless,

their application is restricted to the first atomic layers of electrically conducting films. This therefore hinders their use to explore working electronic devices, which are usually made up of thick conductive layers alternating with highly insulating areas.

Recently a number of new SFM-based techniques exploiting electrically conducting probes have been developed [8]. The prime physical properties they measure are current flows, resistance, capacitance, electrostatic forces, charge distribution, surface potential, or voltage drops on sub-100 nm length scales. These new SFM adaptations, i.e., conducting probe SFM [9], scanning capacitance microscopy [10], electrostatic force microscopy [11], and Kelvin probe force microscopy [12], hold great promise for electronic characterization of materials, since they allow simultaneous high-resolution topographic imaging as well as electrical and electronic characterization. In this chapter we focus on the Kelvin probe force microscopy technique. Hitherto, this method has been coined with different acronyms such as KPFM, KPM, SKPM, KFM, or SKM. For the sake of simplicity, we will utilize KPFM hereafter.

KPFM does not measure a current flow, but rather it records the electrostatic force interaction between two objects, i.e., the tip and the sample. This measurement does not require a direct contact between the two objects [13], so KPFM is well suited for the study of fragile and soft samples such as organic materials. Further, its high-voltage resolution, being about a few millivolts, allows the study of surface potential distribution/differences of a variety of thin films, including those possessing poor conductive properties [14]. Being a noncontact and nondestructive method, it does not pose the risk of desorbing or removing even weakly bound species from the surface. In addition, it does not require particular sample treatments, such as exposure to high electric fields or beams of electrons or photons.

The Kelvin probe method is very versatile since, differently from other surface techniques, it can be employed to measure the work function of a wide range of materials under different experimental conditions, in a wide range of temperatures, pressures, environments, etc. [15]. The work function (ϕ ; see Section 13.2 for a proper definition) is a very sensitive parameter which can provide evidence for micro- and nanoscopic structural and chemical variations, including the presence of contaminants. Moreover, unlike many other methods, KPFM measurement of ϕ does not depend on an estimation of the electron reflection coefficient on the surface.

Besides the use of KPFM since the early 1990s to study inorganic semiconductors and conventional Si-based devices (see Section 13.5), a major effort has been addressed recently toward the exploitation of KPFM to characterize organic semiconductor-based materials and devices.

This review offers an introduction to the KPFM technique. Due to the extremely large number of studies performed with this method in many scientific disciplines and on a variety of materials, spanning from metals, to classical semiconductors, to organic and to biological materials, this contribution will be addressed mainly to the use of KPFM on organic films and will not treat extensively all the results obtained. Particular emphasis will be given to the theoretical background of this

method, to the “art” of collecting reproducible results with the highest possible resolution, and to the unraveling and elimination of artifacts from KPFM data.

After this introduction, the physics behind Kelvin probe force microscopy and the limitations of the technique are discussed in Section 13.2. Section 13.3 is focused to the interpretation of the signal in KPFM measurements. Section 13.4 provides a general description of the main differences in the electronic properties of conventional and organic semiconductors. This introduces Sections 13.5 and 13.6, which are addressed to the use of KPFM to study inorganic semiconductors and organic films, respectively. Section 13.7 highlights some successful applications of KPFM to working organic electronic devices. After a general discussion and conclusion, an appendix focuses in detail on some practical aspects of KPFM.

13.2 Kelvin Probe Scanning Force Microscopy

The Kelvin probe technique takes its name from William Thomson, also known as Lord Kelvin, who first introduced it in 1898 [16] to explain the formation of built-in contact potential differences in metals, which was previously observed by Alessandro Volta at the beginning of the 19th century. To describe this phenomenon, the concept of work function (ϕ) has to be introduced. In its simplest definition, ϕ is the minimal energy needed to remove an electron from the electronic ground state in a given material. In a metal ϕ can be described in terms of the free electron model [17]. It is usually defined as the difference in energy between an electron in the vacuum state and an electron at the Fermi energy of the metal (Fig. 13.1a).

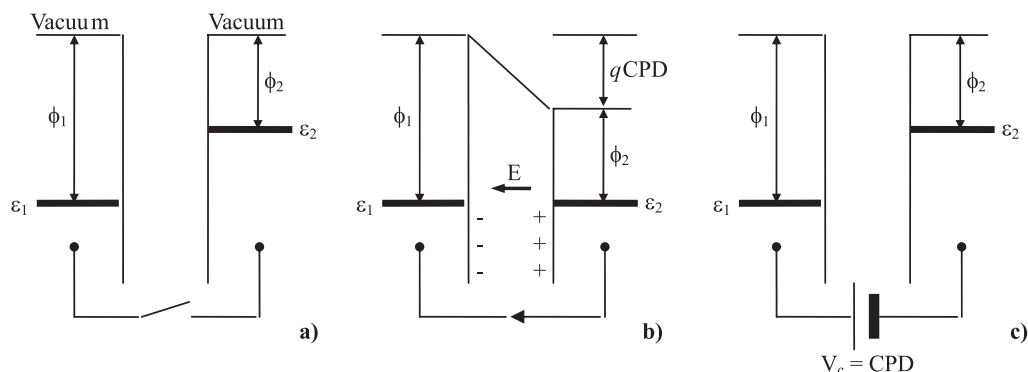


Fig. 13.1 Schematic diagram of Kelvin probe physics. (a) Two materials **1** and **2** with different work functions ϕ_1 and ϕ_2 , corresponding to the energy difference between Fermi level ϵ and vacuum level. (b) When the two materials are contacted

electrically, electrons flow from **2** to **1** until the Fermi levels are aligned, leading to a contact potential V_b . The charges present in the two materials causes an electric field E . (c) The electric field is removed by applying an external potential V_c which equals the contact potential.

In other types of materials, such as semiconductors or insulators, it can be regarded as the difference in energy between the vacuum level and the most loosely bound electrons inside the solid [18].

When two plates of a capacitor composed of different materials are wired electrically (Fig. 13.1b), electrons will flow from the material with the lower work function (weak electron binding, ϕ_2 in the figure) to the one with the higher work function (strong electron binding, ϕ_1 in Fig. 13.1), generating opposite charges on the capacitor plates and a contact potential difference (CPD) between the two materials. The presence of an electric field in the capacitor due to these charges can then be detected easily. An external potential V_c can indeed be applied to nullify this field. At equilibrium, the field is zero and the externally applied potential equals the contact potential difference, which corresponds to the difference between the two work functions (Fig. 13.1c). Thus, if the work function of the reference plate (ϕ_1) is known, the work function of the material under study can be determined as $\phi_2 = \phi_1 - qV_c$, where q is the elementary charge. Lord Kelvin realized this experimentally using a gold-leaf electroscope to measure the charge transfer upon electrical contact between two large, flat, polished discs of zinc and copper.

In 1932, Zisman improved the method by using a vibrating reference surface [19]. In this vibrating capacitor setup, the mechanical oscillation, at frequency ω , induces changes in the system capacitance and thus in the reference plate voltage. This change in capacitance induces a small alternating current, which can be easily detected. In fact a periodic vibration of the distance between the two plates at ω results in a current $i(t)$ given by Eq. (1), where V_c is the contact potential difference (CPD) and ΔC is the change in capacitance [12].

$$i(t) = V_c \omega \Delta C \cos(\omega t) \quad (1)$$

For the actual measurement of CPD, an additional voltage is applied between the two plates until the space in between becomes field-free and the current $i(t)$ goes to zero.

The classical Kelvin probe technique employing the Zisman concept has been used for macroscopic measurements of many materials, by tracking shifts in the contact potential due to changes in the work function of the sample surface and surface photovoltage effects [20, 21]. The electrical resolution attainable was very high, even down to ~ 1 mV. The major drawback was that the measured ϕ represented an average of the local work functions over the whole sample surface, so no detail on local ϕ variations on the sample's surface could be achieved.

A few years after the advent of scanning force microscopy, Kelvin probe force microscopy was developed by Wickramasinghe and coworkers [12]. In this setup the reference capacitor plate is a sharp, conductive SFM tip attached to a very flexible cantilever. The tip-sample interaction is highly localized, and potential differences between the tip and the sample can be detected by measuring the deflection of the cantilever due to electrostatic interactions, thus allowing ϕ to be measured with high spatial and electrical resolution.

In the Wickramasinghe KPFM setup [12], a conductive tip is scanned in noncon-

tact mode [3, 4] on a sample surface, following its topography. The principle is similar to the Kelvin method except that forces are measured instead of currents. An oscillating potential V_{ac} at frequency ω is applied to the tip during the scan. The tip interacts electrostatically with the surface, being attracted and repelled at the same frequency as V_{ac} . Thus an oscillation mode at a frequency ω appears on the cantilever. This oscillation is detected by the SFM photodiode, which sends a signal through a lock-in amplifier to isolate the oscillation mode at ω . The oscillation amplitude at frequency ω is proportional to the surface potential difference between the tip and the surface. Nevertheless this interaction could not be exactly quantified due to the complexity of the system dynamics and tip shape. Alternatively, qualitative 2D maps of the surface potential can be obtained with the technique called electrostatic force microscopy (EFM).

In order to obtain an exact measurement of the work function (ϕ) of the sample, an additional feedback loop is added. This loop applies a given DC offset potential voltage (V_{dc}) to the cantilever tip to minimize the electrostatic interaction between the tip and the surface (Fig. 13.2).

Both an AC and a DC voltage bias signal are then applied between the tip and the sample. In this case, the voltage between the tip and the sample can be expressed by Eq. (2), where $\Delta\phi$ is the contact potential (difference in work function

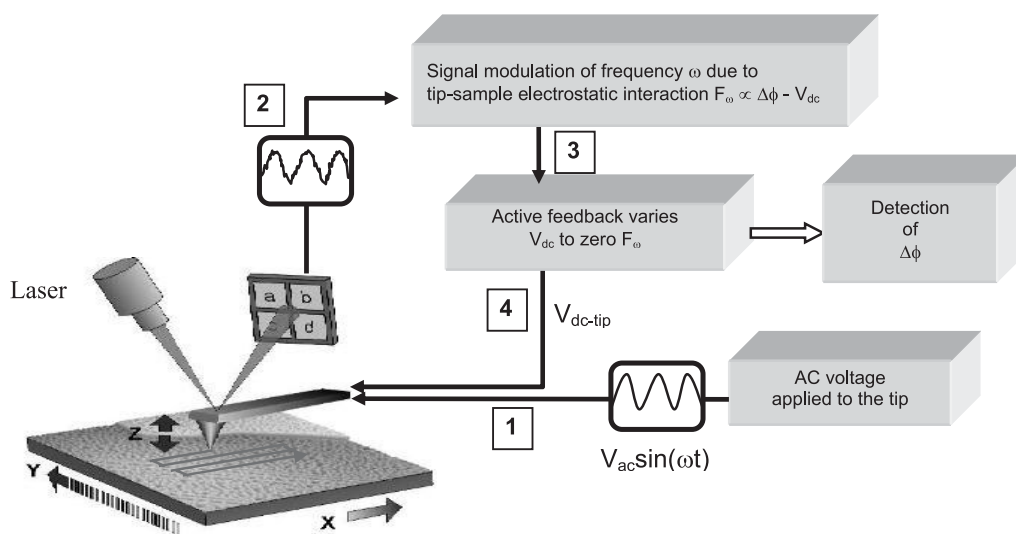


Fig. 13.2 KPFM apparatus. (1) An alternating voltage V_{ac} is applied to the tip with a frequency ω . (2) The electrostatic tip-sample interaction induces a mechanical oscillation of the cantilever at a frequency ω . (3) The cantilever oscillation at ω is isolated using a lock-in amplifier, and sent to a feedback circuit.

(4) The feedback tries to minimize F_{ω} (which is proportional to tip-sample interaction) by adding a V_{dc} voltage to the tip. A different setup is exploited in some cases, in which the external potential bias is applied directly to the sample.

between the tip and the sample), V_{dc} is the DC offset potential applied to the tip and V_{ac} and ω are the amplitude and frequency of the applied AC voltage signal, respectively.

$$\Delta V = \Delta\phi - V_{dc} + V_{ac} \sin(\omega t) \quad (2)$$

Equation (2) can be used to derive an expression for the electrostatic force F between the tip and the sample assuming a parallel-plate capacitor geometry (other geometries can be also considered, although they require more complicate models) [22]. The energy U in a parallel-plate capacitor can be expressed as in Eq. (3), where C is the local capacitance between the tip and the sample.

$$U = \frac{1}{2} C \Delta V^2 \quad (3)$$

The force is then the rate of change of the energy with tip–sample separation distance, Z [Eq. (4)], with components at DC given by Eq. (5) and at frequencies ω and 2ω by Eqs. (6) and (7) respectively.

$$F = -\frac{\partial U}{\partial z} = -\frac{1}{2} \frac{\partial C}{\partial z} \Delta V^2 = F_{dc} + F_{\omega} + F_{2\omega} \quad (4)$$

$$F_{dc} = -\frac{1}{2} \frac{\partial C}{\partial z} \left[(\Delta\phi - V_{dc})^2 + \frac{V_{ac}^2}{2} \right] \quad (5)$$

$$F_{\omega} = -\frac{\partial C}{\partial z} [(\Delta\phi - V_{dc}) \cdot V_{ac} \sin(\omega \cdot t)] \quad (6)$$

$$F_{2\omega} = \frac{1}{4} \frac{\partial C}{\partial z} [V_{ac}^2 \cos(2\omega \cdot t)] \quad (7)$$

Information on the electrical properties of the sample can be obtained by isolating and then analyzing separately each of these three different force signals, i.e., F_{dc} , F_{ω} , $F_{2\omega}$.

When the ω component of the electrostatic force interaction is zero, V_{dc} is equal to the difference in work function ($\Delta\phi$) between the tip and the sample surface ($V_{dc} = \Delta\phi$). Therefore a 2D quantitative map of $\Delta\phi$ can be obtained by monitoring the voltage V_{dc} applied by the feedback signal. If the work function of the tip is known, the work function of the sample can then be determined. The ϕ of the tip can be obtained easily by calibrating the setup making use of surfaces with known work functions. In essence KPFM exploits the first harmonic component (F_{ω}) of the electrostatic force interaction to determine the local work function on the sample surface.

Alternatively, as discussed in Section 13.3, the measurements can be performed

by employing the frequency modulation method (FM-KPFM) which uses the force gradient as a data set instead of the force.

Furthermore, the 2ω component of the force on the tip can provide information on the local dielectric properties through the capacitance gradient dC/dz . This signal can therefore be used to gain insight into surface defects or heterogeneities.

Two different KPFM modes are commonly employed. In one the Kelvin probe and the topographical signals are detected simultaneously at two different frequencies of oscillation of the tip. In the other one, a first scan collects the topographic signal while a second scan, performed at a higher tip–surface distance, records the Kelvin probe signal, in the so-called “lift mode.”

13.3

Interpretation of the Signal in KPFM Measurements

The interpretation of images collected by KPFM is quite complicated and requires the use of theoretical models. To correlate the effective surface potential distribution with the measured quantities, the KPFM setup can be modeled as a sample surface consisting of n ideally conducting electrodes of constant potential V_i and a tip of potential V_t [23]. As demonstrated by Stemmer and coworkers, the measured KPFM potential does not exactly match the surface potential of a given location; rather it is a weighted average of all the local potentials on the surface below the tip apex. The weighting factors of this average are the derivatives in z of probe–surface capacitances, expressed by Eq. (8), where V_{dc} is the voltage applied to the tip during the KPFM scan, V_i is the local surface potential at point i on the surface, and C'_{it} is the derivative of the capacitance versus distance between the tip and the point i on the surface.

$$V_{dc} = \frac{\sum_{i=1}^n (C'_{it} V_i)}{\sum_{i=1}^n (C'_{it})} \quad (8)$$

It is worth noting that the first harmonic component of the tip force, F_ω , depends only on the mutual capacitances between tip and surface C_{it} , and not on the mutual capacitances between different surface elements.

The surface is considered as an ensemble of capacitor plates of lateral dimensions Δx , Δy , and the V_{dc} measured by KPFM as a function of the capacitor location (x_i, y_i) can be expressed as Eq. (9) [23], with Eq. (10), where C'_{tot} is the derivative of the total capacitance between tip and surface [Eq. (11)] and x_t , y_t is the tip location.

$$V_{dc}(x_i, y_i) = \int_{-\infty}^{+\infty} \int_{-\infty}^{+\infty} h(x - x_i, y - y_i) V(x, y) dx dy \quad (9)$$

$$h(x - x_i, y - y_i) = \lim_{\Delta x, \Delta y \rightarrow 0} \left[\frac{C'(x_i - x_t, y_i - y_t)}{C'_{tot} \Delta x, \Delta y} \right] \quad (10)$$

$$C'_{tot} \equiv \sum_{j=-\infty}^{j=+\infty} \sum_{i=-\infty}^{i=+\infty} C'(x_i - x_t, y_j - y_t) \quad (11)$$

Equation (9) shows that the measured KPFM potential maps, i.e., $V_{dc}(x, y)$, are effectively 2D convolutions of the surface potential distribution $V(x, y)$ with the corresponding transfer function $h(x, y)$ that is defined by the tip's geometry.

Owing to the long-range nature of electrostatic interactions, contributions to the KPFM signal always derive from the interaction of the surface with (a) the apex of the SFM tip, (ii) the tip bulk, and even (c) the cantilever on which the tip is mounted. The cantilever contribution to the interaction is also relevant for a cantilever-sample distance of $\sim 15 \mu\text{m}$. Numerical simulations of KPFM on microscopic dots and sharp steps were performed to determine the influence of system geometry on KPFM resolution. Simple electrostatic calculations corroborated by experiments (Fig. 13.3) suggested that the effect of the cantilever dominates for tip-sample distances $z > 1000 \text{ nm}$, whereas it is very small for $z < 100 \text{ nm}$. As an example, Fig. 13.3(b) shows the influence of tip-sample distance on the error in measuring the sample bias (i.e., V_{peak} or V_{valley}) for two purposely made metallic

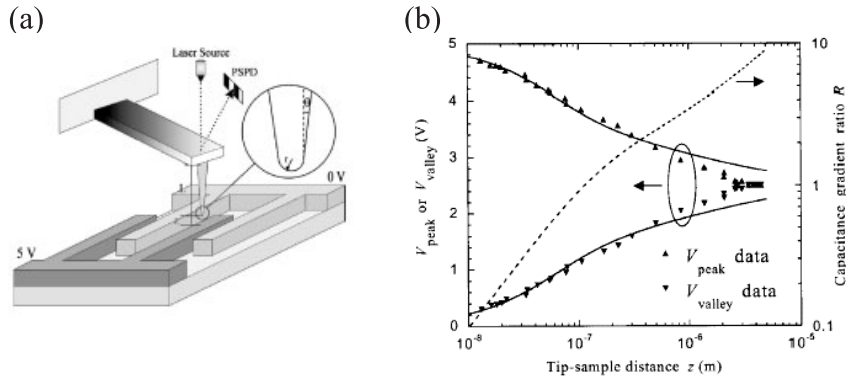


Fig. 13.3 (a) Schematic diagram of the scanning probe and the test structure used in ref. 24 to study the influence of tip-sample distance z on the measured potential. The test structure consisted of electrodes coming out alternately from each of two macroscopic metal pads which were biased to 0 and 5 V. The width of the electrodes as well as the spacing between them was $1.7 \mu\text{m}$. The tip was modeled as a hemisphere at the end of a truncated-conical part (shown magnified in the inset).

(b) Experimentally observed variations with z of V_{peak} (voltage measured over 5 V biased finger, shown as triangles) and V_{valley} (voltage measured over 0 V biased finger, shown as inverted triangles) are compared with theoretically calculated variations (shown by the two dark lines: the upper one for V_{peak} and the lower one for V_{valley}). The calculated ratio of the capacitance gradient of the cantilever to that of the tip, R , plotted against z is also shown by a broken line (with permission from [24]).

patterns [24]. Moreover, it reveals that the highest resolution can be obtained using tips with a high aspect ratio, with a cantilever as small as possible, and with a relatively large tip apex [24, 25].

More refined calculations are difficult, since electrostatic forces and the tip-sample capacitance depend both on the charge distribution and on the polarization of tip and sample, and these in turn are affected simultaneously by the potential difference and by the tip-sample distance [26].

In addition, the tip does not lie at a constant distance from the surface even when it follows at best the surface topography. This is due to the oscillation of the tip above the surface as driven by the piezo actuator in the noncontact mode. Consequently the tip-sample distance can vary continuously between 10 and 600 nm [27]. The electrostatic interaction changes during the oscillation, and it reaches a maximum at the lower end of the tip swing. The effect of oscillation on the electrostatic force can be dominant if wide oscillations and tips of large mass are used [27].

Different methods have been employed to reduce the effect of long-distance interactions on KPFM measurements. While the conventional KPFM setup uses amplitude modulation (AM) to detect the electrostatic force F , a possible way to reduce long-range electrostatic contributions experimentally is to measure instead the force gradient along the z axis:

$$\nabla F = \frac{\partial F}{\partial z}$$

The forces due to the interaction of the sample with both the cantilever and the cone of the tip vary only slowly in the proximity of the sample compared with the tip apex-sample interaction; therefore they can be separated. This is only correct when the oscillation amplitude of the tip is small compared with the range over which the potential varies significantly [28].

To measure the force gradient, one can use the frequency shift [26] or phase-shift [28–30] of the tip oscillation at ω . The corresponding techniques have been called FM-KPFM and EFM-phase, respectively.

In these measurements, the tip is oscillated during the lift scan as described in Section 13.2: the tip's resonant frequency and phase shift due to the electrostatic force gradient $\partial F/\partial z$ are probed. For small force gradients, the resonant frequency shift and phase shift are [29] given by Eqs. (12) and (13), where ω_0 is the resonant frequency, k is the spring constant, and Q is the quality factor of the cantilever.

$$\Delta\omega = \frac{\omega_0}{2k} \frac{\partial F}{\partial z} \quad (12)$$

$$\Delta\phi = \arcsin\left(\frac{Q}{k} \frac{\partial F}{\partial z}\right) \quad (13)$$

Since for a parallel-plate capacitor Eq. (14) holds, by combining Eqs. (12), (13), and

(14) the frequency and phase shift can be directly related to the potential difference ΔV by Eqs. (15) and (16) respectively.

$$\frac{\partial F}{\partial z} = -\frac{1}{2} \frac{\partial^2 C}{\partial z^2} (\Delta V)^2 \quad (14)$$

$$\Delta\omega = -\frac{\omega_0}{4k} \frac{\partial^2 C}{\partial z^2} (\Delta V)^2 \quad (15)$$

$$\Delta\phi = -\arcsin\left(\frac{Q}{2k} \frac{\partial^2 C}{\partial z^2} (\Delta V)^2\right) \quad (16)$$

This means that the phase and frequency shift are squared functions of the potential difference ΔV between the tip and the sample, and that the resolution of the technique is determined by the lateral variations of the gradient $\partial^2 C/\partial z^2$. The phase shift is always negative, because $\partial^2 C/\partial z^2$ is positive [29].

A simple analytical model describing tip–surface interactions has been also reported [25, 31]. A very precise estimation of $\partial C/\partial z$ components of the electrostatic interaction can be achieved by modeling the tip as a hemisphere and a truncated cone, in the study of relatively simple structures (spherical Au- and CdSe-based nanoparticles). The use of simple and regular structures, such as well-defined silicon dots, even enables determination by KPFM of the amount of charge present in a structure, right down to single electrons [25, 31].

A detailed experimental and theoretical study of the accuracy and resolution provided by the amplitude-sensitive method and the frequency-modulation method has been reported recently [32].

Comparing the two approaches, Zerweck and coworkers clearly proved that the frequency-modulation method is preferable in most applications because it provides much higher lateral resolution, it yields quantitative surface potential values on areas larger than the tip radius, and it is not significantly affected by variations in the tip–sample distance during topographic imaging [32].

When the Kelvin probe and the topography measurements are performed simultaneously, without making a second scan (i.e., lift mode), an inversion in the image contrast can occur, i.e., areas seem to have lower potential than the background in some cases and higher in others, even while a single image is being recorded. This is due to the contribution of non-electrostatic forces to the V_{dc} KPFM signal [33]. In order to separate the electrostatic force signal from the non-electrostatic forces signal efficiently, the amplitude of the AC bias in FM-mode KPFM must be relatively large [33].

KPFM measurements can be performed in a different way by applying the bias voltage $V(t) = |V_{dc}| + V_{ac} \sin(\omega t)$ directly to the sample, holding the tip at ground potential. However, an influence of the AC sample voltage on the measured contact potential has to be taken into account. This dependence can be explained by bias-induced band bending at the semiconductor surface [34].

13.4

Electronic Characterization of Organic Semiconductors

In a semiconductor, the combination of atomic orbitals leads to the formation of a conduction and a valence band, with a well-defined forbidden energy gap in the middle. Electrons are free to move throughout the solid in the extended electronic bands. This makes it possible to reach a thermal equilibrium leading to the Fermi level alignment and band-bending phenomena in the case of a metal–semiconductor contact. This can be described with the well-known Mott–Schottky model (Fig. 13.4b) [35].

Although the organic materials applied as active components in electronic devices are usually called organic semiconductors, their HOMO–LUMO gap is typically quite large, i.e., 2–3 eV. The concentration of thermally excited carriers is therefore extremely small, like those of an insulator. Consequently the formation of valence and conduction bands, thermal equilibrium, and thus Fermi-level alignment and band bending at the interfaces, cannot be assumed *a priori* since the HOMO–LUMO separation is usually much larger than the thermal energy. It is noteworthy that interfacial dipoles cannot be neglected for most organic/metal interfaces as the potential shift at the interface due to such dipoles sometimes reaches over 1 eV, in contrast to the assumption of the common vacuum level in the Mott–Schottky model (Fig. 13.4c) [36, 37].

Furthermore, the conventional techniques applied for band-bending measurement, such as ultraviolet (UPS) or X-ray photoelectron spectroscopy (XPS), cannot always be employed because of the high resistance of the organic materials, which leads to sample charging during the measurement. In contrast, Kelvin probe microscopy provides insight into the band bending on materials with poor electrical properties also [38].

In the case of an organic/metal interface, if the total number of available mobile carriers in the organic film is sufficiently large, there will be a charge redistribution near the interface within the reasonably short time of an experiment [39]. In the case of Fig. 13.4(a), for example, the work function of the metal is higher than that of the organic layer, and the electrons prefer to reside in the metal. As a result, some electrons may move from the organic layer to the metal, leading to the negative and positive charging of the metal and the organic layer, respectively. This charging decreases the affinity of the metal for the negatively charged electrons.

This flow and distribution of charge continues until the Fermi levels of the metal and that of the bulk of the organic layer are aligned. In such a redistribution of charges, the potential distribution at the interfacial region can be described by the Poisson equation, which expresses the relationship between the charge and potential distributions. As a result, a diffusion layer (known also as a depletion layer) with band bending is formed, characterized by a built-in potential V_{bi} in the organic film [35, 40, 41]. The thickness w of the diffusion layer depends on factors such as V_{bi} , the dielectric constant of the organic layer ϵ_r , and the spatial distribution of the available donor or acceptor levels [39]. In organic devices, band bending is closely related to the potential profile across the organic layer when an external

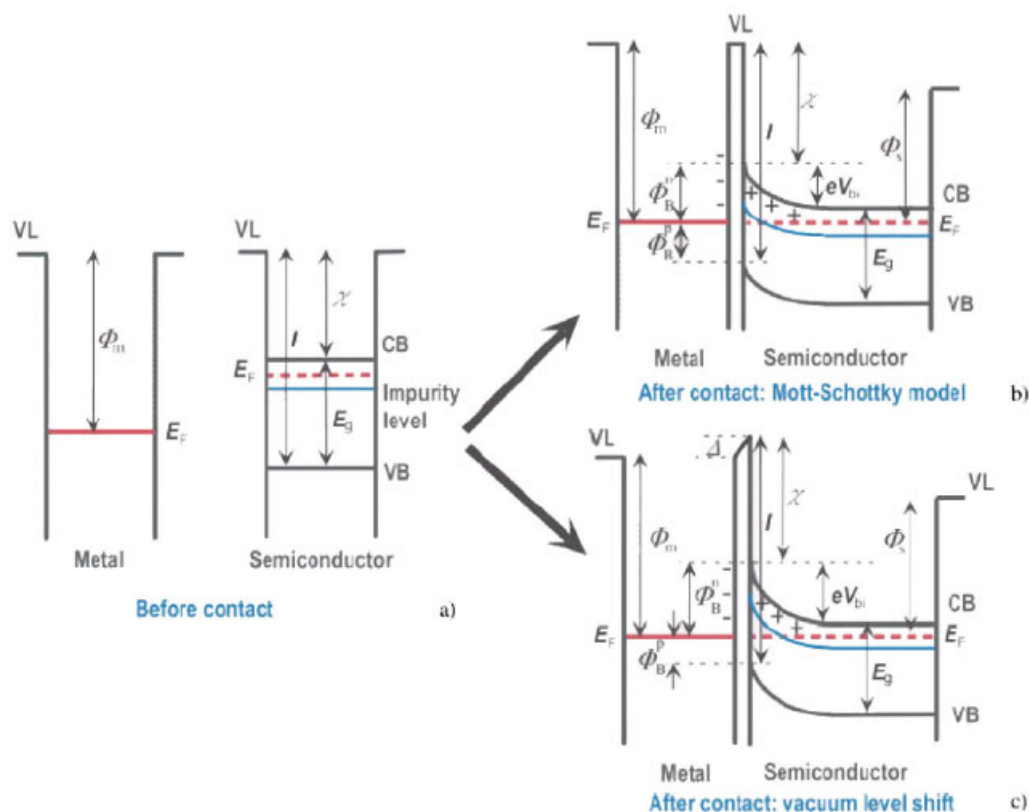


Fig. 13.4 Models for energy-level alignment at an organic semiconductor–metal contact: (a) Energy diagram before contact. (b) Mott–Schottky model, assuming vacuum-level alignment at the interface and band bending with Fermi-level alignment. (c) Realistic model including a vacuum-level shift at the interface. The barrier height for hole injection is $\phi_B^p = I - \phi_m^p$ for a p-type semiconductor, while for an n-type semiconductor it is $\phi_B^n = \phi_m^n - \chi$.

In the image, VL, CB, VB, E_F and E_g are the energy levels of the vacuum, conduction, and valence bands, the Fermi level, and the energy gap respectively; ϕ_m , ϕ_s , ϕ_b , and V_{bi} are the work functions of the metal and the semiconductor, the barrier height for n and p charge injection, and the built-in junction voltage; I and χ are the ionization energy and the electron affinity of the solid, respectively; Δ is the surface dipole (with permission from [37]).

electric field is applied, which promotes the redistribution of charges. Nevertheless, for a very thin layer of molecular material, nearly flat bands in the interfacial region are expected [39].

For metal–organic junctions, a dipole layer may be formed directly at the interface, originating from various sources such as charge transfer across the interface, redistribution of electron cloud, interfacial chemical reaction, and other types of rearrangement of electronic charge [42, 43]. Such interfacial dipole formation will cause an abrupt shift of the potential across the dipole layer [44], leading to a shift

of vacuum level (ΔVL) at the interface, as shown in Fig. 13.4(c). The value of Δ is determined by the magnitude of the dipole. This leads to the shift in VL in the organic layer on the right-hand side in Fig. 13.4, from that of the metal on the left-hand side. Although Nielsen pointed out the importance of such an interfacial dipole layer in 1974 [44], the experimental contributions to gain insight into such an issue have been very scarce. Consequently, this factor has often been neglected in the field of organic devices. On the other hand, this possible shift of the VL s is well known in the field of surface science [42, 43]. It is usually referred to as the change in the work function (or surface potential) of the metal [43]. For a better understanding of the origin of surface-dipole induced shifts of the vacuum level, it is indeed worth pointing out that the concept of vacuum level is not at all straightforward [39].

Usually the vacuum level is defined as the energy of an electron at rest at infinite distance from the sample, $VL(\infty)$, but for most measurements of electron affinity, ionization potential, and work function, the reference vacuum level is the energy of an electron just outside the sample, at a short distance from the surface, where the role played by the potential of the solid is not negligible [42, 45]. The effect of the solid on this vacuum level at the surface ($VL(s)$) is most convincingly demonstrated by the well-known dependence of the work function on the surface of a single crystal. Since the Fermi level is a common level inside the solid, this dependence is due to the energy difference of an electron just outside the solid, as shown in Fig. 13.5.

As the distance from the surface becomes larger, the energy of free electrons gradually converges to a common value, which corresponds to what we have called $VL(\infty)$. For a metal, the difference between the energies of $VL(\infty)$ and $VL(s)$ is mostly due to the surface dipole layer formed by the tailing of the electron cloud at the surface. For organic solids, the existence of a surface dipole layer comparable with that of a metal surface has not yet been thoroughly investigated experimentally. For the case of solids consisting of nonpolar molecules, one can expect a relatively small surface dipole [39].

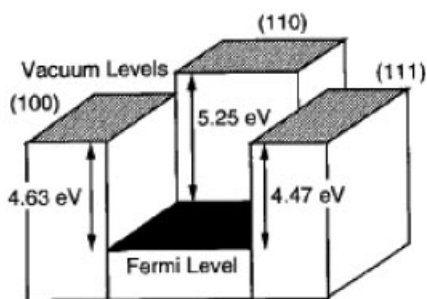


Fig. 13.5 Dependence of the work function of a tungsten single crystal on the crystalline surface considered. The energy of the vacuum level at the surface, i.e., $VL(s)$, is different for the (100), (110), and (111) surfaces (with permission from [39]).

Interestingly, Seki and coworkers studied the work function of various metals such as Ca, Mg, Cu, Ag, and Au when coated with a typical hole-injection layer, such as *N,N'*-bis(3-methylphenyl)-*N,N'*-diphenyl[1,1'-biphenyl]-4,4'-diamine (TPD) [46]. The change in the work function was analyzed by the Kelvin probe method and UPS up to a film thickness of 100 nm. The results showed that band bending leading to Fermi-level alignment is not achieved, at least for systems prepared and measured under UHV conditions.

Comparative studies of band bending in organic materials have been carried out on C₆₀ fullerene, TPD, and tris(8-hydroxyquinoline)aluminum(III) (Alq₃) thin films [37]. Gradual band bending was observed for C₆₀/metal interfaces, revealing a width of the space charge layer of about 100 nm. On the other hand, a flat band feature was detected for TPD/metal interfaces, probably because of their high purity. These results demonstrate that the model of band bending used in inorganic semiconductor interfaces is still valid for organic semiconductors although much thicker films are often necessary to achieve bulk Fermi-level alignment. For Alq₃/metal interfaces, a new type of band bending was observed where the energy levels changed as a linear function of the distance from the interface [37].

In inorganic semiconductors the surface states lie typically in the forbidden gap, and can pin the Fermi level at the surface, hindering band bending. For organic semiconductors, the surface states are usually outside the optical gap and thus pinning of surface states is less common [38]. Furthermore, even surface states associated with dangling bonds present at cleaved surfaces of inorganic semiconductors typically pin the Fermi level, and hinder any electrostatic measurement of the band structure in the bulk. These surface charges are generally absent in van der Waals-bonded organic materials, making KPFM particularly suitable for organic compounds [47].

It is important to point out that very often the KPFM method can be employed also to explore thin, almost insulating, organic films. When the null charge condition is achieved, the electric field E in the capacitor gap is zero and the vacuum level of the reference electrode coincides with the vacuum level of the sample even though charges may be induced both in the layer and at the surface region of the substrate on which the sample film is formed. Thus, the KPFM method correctly maps the surface potential distribution even when the sample is poorly conducting [37, 38].

13.5 KPFM of Conventional Inorganic Materials

KPFM measurements of the contact potential difference between different materials were performed for the first time by Wickramasinghe and coworkers [12]. The possibility of simultaneous topographical and electronic characterization on the nanometer scale was demonstrated in this way. In this set of experiments, several images of different metals such as gold, platinum, and palladium were taken in order to demonstrate the performance and reliability of the new technique. These

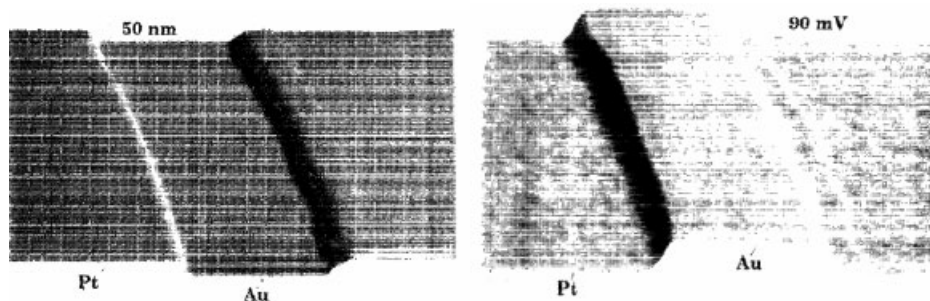


Fig. 13.6 Comparison of topographic and CPD images ($8 \mu\text{m} \times 6 \mu\text{m}$) of platinum on gold (with permission from [12]).

measurements were carried out in air using either gold-coated silicon or nickel chrome tips (Fig. 13.6).

KPFM also enabled detection of contaminations of metallic surfaces by carbon-based materials by tracking the ϕ value [48].

KPFM investigations were then extended to conventional semiconductors, such as silicon [49]. Dopant concentration profiles in two dimensions were studied at size scales below 100 nm. Such results were obtained using gold-coated and uncoated silicon tips, setting the V_{ac} frequency ω at one of the resonance frequencies of the cantilever. The measurements were stable and reproducible, albeit the quantitative determination of dopant concentration was not achieved. The error due to surface oxide charges present on the semiconductor surface was estimated to be below 50 mV [49].

In addition, KPFM, in combination with scanning capacitance microscopy (SCM), has been employed to detect the surface potential changes in a silicon p–n junction. In this combined measurement, KPFM has been used to map surface potential distributions while SCM has allowed the mapping of the charge carrier density (Fig. 13.7). Surface potential differences between the KPFM results and theoretical expectations were ascribed to the presence of oxide charges with a density of $\sim 10^{11} \text{ cm}^{-2}$ [50]. Surface-state pinning did not prevent KPFM measurements on p–n junctions, while the removal of adsorbed water improved the resolution [51].

Another very interesting application of KPFM has been the measurement of minority-carrier diffusion length in conventional semiconductors [52, 53]. The method is based on the study of the surface photo-induced voltage between the SFM tip and the surface of an illuminated semiconductor p–n junction. The photo-generated carriers diffuse to the junction and change the voltage difference between the tip and the sample, as a function of the horizontal distance from the p–n junction. The diffusion length L is then obtained by fitting the measured contact potential difference using the minority-carrier continuity equation. The method

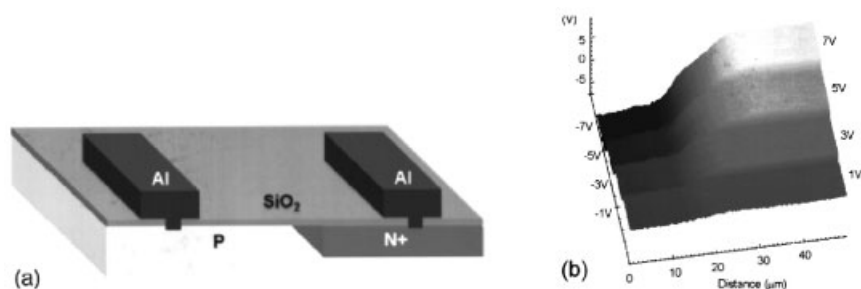


Fig. 13.7 (a) Schematic diagram of a model p-n junction diode with Al contacts from ref. 50. (b) Three-dimensional potential profiles measured with KPFM under various reverse bias conditions (1 V for n type and -1 V for p

type, 3 V for n type and -3 V for p type, 5 V for n type and -5 V for p type, and 7 V for n type and -7 V for p type) (with permission from [50]).

was applied to determine the electron diffusion length in GaP p-n and Schottky junctions (Fig. 13.8). The measured diffusion length was found to be $\sim 2 \mu\text{m}$, in good agreement with electron-beam induced current measurements (Fig. 13.9) [53].

KPFM measurements have been also performed on quantum dots [54, 55], quantum wells under illumination [56], laser diodes [57], nanotubes [58, 59], and chemically sensitive field-effect transistors [60]. This technique made it possible to measure the size dependence of the work function for different nanostructures

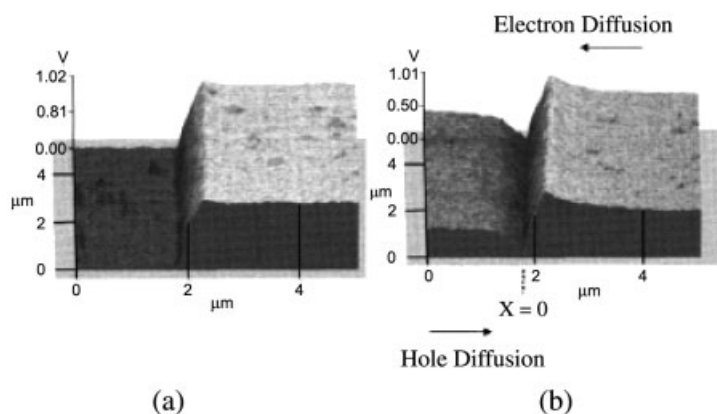


Fig. 13.8 Two-dimensional potential difference images of the cleaved GaP p-n junction (a) in the dark and (b) under super band-gap ($\lambda = 488 \text{ nm}$) illumination. The minority-carrier diffusion on both sides of the p-n junction can be observed clearly in (b) (with permission from [53]).

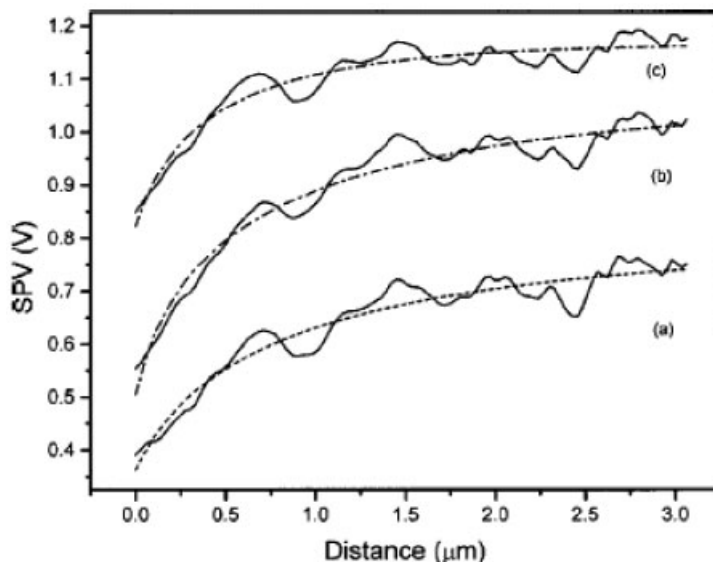


Fig. 13.9 Experimental (solid lines) and calculated (broken lines) surface photo-induced voltage profiles as a function of the distance from the edge of the p–n junction ($x = 0$) for three different light intensities: (a) $0.41 \mu\text{W}$, (b) $1.3 \mu\text{W}$, and (c) $4.1 \mu\text{W}$ at the output of the optical fiber (with permission from [53]).

such as multi-walled nanotubes [61], and the charging behavior of dots [55]. One of the most promising applications of KPFM is indeed its use on working devices, where the effect of current or light passing through the device can be observed on different areas of the device. Jiang and coworkers observed by KPFM the effect of illumination on charge generation and potential build-up on solar cells, performing the measurements jointly with macroscopic IV and CV characterizations [62, 63]. KPFM investigations on solar cells, which convey single and multiple layers of $\text{Cu}(\text{In,Ga})\text{Se}_2$ and GaInP_2 , showed a complex distribution of built-in electrical potential. In multi-component solar cells, selective charging of one of the different layers composing the cell can be obtained using light of a different wavelength. In this context, KPFM has been used recently with a higher resolution to study the fine structure of $\text{Cu}(\text{In,Ga})\text{Se}_2$ solar cells [64, 65] and CuGaSe_2 solar cells [66], by observing the effect of grain boundaries on charge generation and collection. It has been shown that KPFM enables observation of positively charged grain boundaries which are not visible in topography, and identification of the locations where the potential is lower than that of the grain bulk [64, 65]. By correlating the KPFM results with macroscopic measurements of photocurrents it was possible to identify the cell composition that gave the best device performance.

13.6

KPFM on Organic Monolayers, Supramolecular Systems, and Biological Molecules

KPFM explorations have been performed on a wide variety of ordered molecular architectures such as self-assembled monolayers (SAMs), Langmuir–Blodgett (LB) films, and even single molecules, with high lateral and voltage resolutions.

A classical SAM is one formed from solution by chemisorbing crystalline alkane-thiol monolayers on a metallic surface, e.g., a Au(111) crystal. The versatility of such a method makes it possible to form a variety of different monolayers with diverse chemical compositions and orientations [67–69]. KPFM has been employed to explore the electronic properties of phase-separated SAMs of different alkane-thiols on Au(111). This study revealed a dependence of the contact potential difference (CPD) on the molecular length. The measured CPD was found to increase linearly by either 9 mV (Fig. 13.10) [70] or 14 mV [71] for each CH₂ unit. This result was ascribed to the changing dielectric behavior of the hydrocarbon tail region.

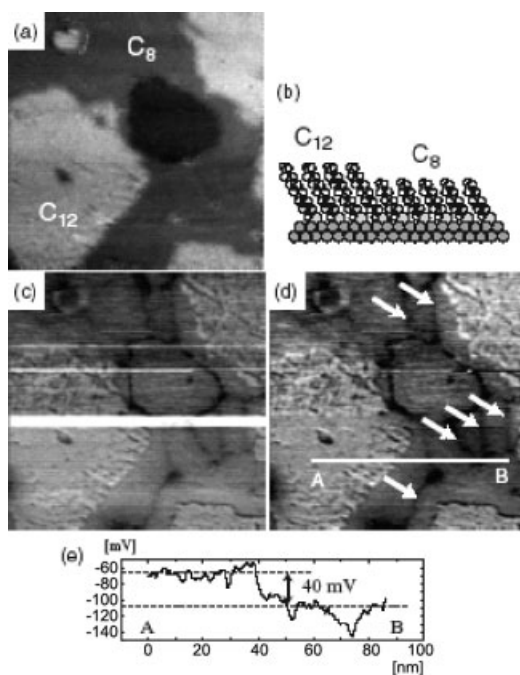


Fig. 13.10 (a) Noncontact SFM image of a C₈/C₁₂ phase-separated SAM (100 nm × 100 nm). (b) Schematic illustration of possible structure models of the C₈/C₁₂ phase-separated SAM. (c) Surface potential image obtained simultaneously with (a). (d) Filtered surface potential image, which reduced the effect of “tip changes” from (c); narrow

regions with lower SP (indicated by arrows) can be seen in the C₈ domains: these regions probably correspond to the domain boundaries of the C₈ domains, which are barely seen in the topographic image. (e) Cross-sectional plots taken on the unfiltered SP image (with permission from [70]).

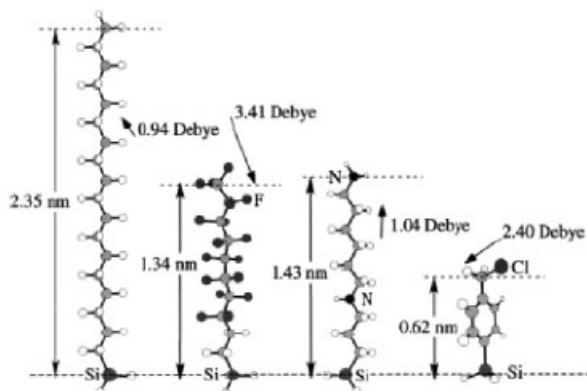


Fig. 13.11 Molecular structures and dipole moments for different molecular systems. From left to right: *n*-octadecyltrimethoxysilane (ODS), heptadecafluoro-1,1,2,2-tetrahydrodecyl-1-trimethoxysilane (FAS),

n-(6-aminohexyl)aminopropyltrimethoxysilane (AHAPS), and 4-(chloromethyl)phenyltrimethoxysilane (CMPS) (with permission from [73]).

In SAM of aromatic oligomers bearing a thiol end group, the molecular dipole is typically oriented downward, i.e., toward the surface. For this reason, a negative change in the surface potential distribution between the uncovered and the SAM-covered gold was observed [72]. For aromatic molecules the delocalization of the electron cloud is higher if compared with alkanethiols, and thus the decrease in surface potential, proportional to the molecular length, already saturates to a fixed value when three aromatic rings are attached to gold.

The surface potential difference between two different SAMs can be calculated to a good approximation from the molecular dipole moments of different molecules (Fig. 13.11) [73], according to Eqs. (17) and (18), where μ is the actual molecular dipole moment normal to the substrate, μ_0 is the molecular dipole moment in the absence of depolarizing effects, A is the area occupied by each molecule, ϵ is the dielectric constant, ϵ_0 is the permittivity of free space, α is the polarizability of a molecule, and n is the number of dipoles per unit area.

$$\Delta V_{SAM1-SAM2} = \frac{\left[\frac{\mu_{SAM1}}{(\epsilon_{SAM1} A_{SAM1})} - \frac{\mu_{SAM2}}{(\epsilon_{SAM2} A_{SAM2})} \right]}{\epsilon_0} \quad (17)$$

$$\mu = \frac{\mu_0}{(1 + 9\alpha \cdot n^{3/2})} \quad (18)$$

By using *ab-initio* calculations, the relationship between surface voltage, dipole moment, and work function (Eq. (19); e = electron charge) has been determined for SAMs with different chemical compositions supported on silicon (Figs. 13.11 and 13.12).

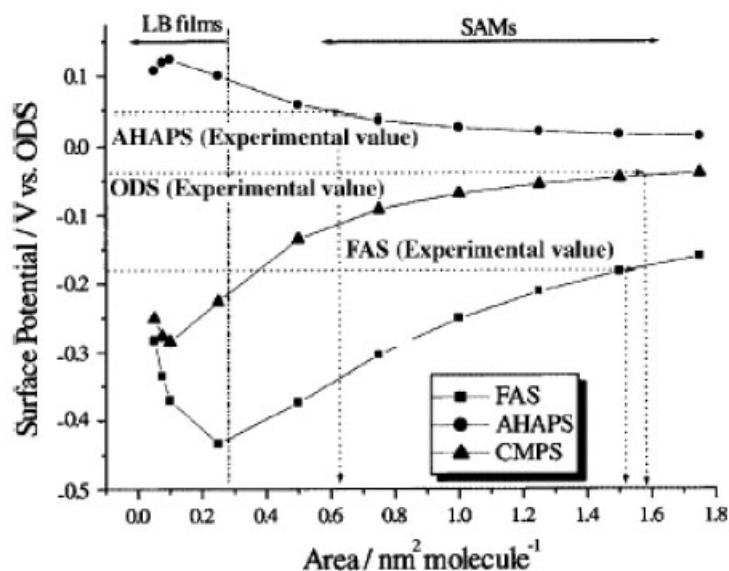


Fig. 13.12 Calculated surface potential for FAS-, AHAPS- and CMPS-SAMs vs. ODS-SAM in different molecular areas. The dotted lines are the experimental surface potential values measured by KPFM (with permission from [73]).

$$\Delta V_{\text{SAM1-SAM2}} = - \frac{[\phi(\text{SAM1}) - \phi(\text{SAM2})]}{e} \quad (19)$$

The comparison of calculated and measured surface potentials enabled determination of the surface density of the molecules for the different layers (Fig. 13.12). The measured differences in surface potential were related to the different energy and geometry of the HOMO and LUMO orbitals for each molecule (Fig. 13.13).

SFM and KPFM experiments on LB films of modified hexa-*peri*-hexabenzocoronenes (HBCs) made it possible to measure the effect of the molecular order on the electronic structure. The HBCs were found to arrange in the film in two different phases: one was characterized by a low-pressure packing in which the aromatic cores of the HBCs were stacked in order to maximize the overlap of the π orbitals; in the second, denser, phase the alkyl chains were organized in a crystalline fashion and the aromatic cores were separated by a larger distance, i.e., this phase is characterized by a lower overlap of the π orbitals. [74] The authors proposed that the electrons can be considered delocalized along the π stack of the former phase, while in the second case the electrons should be regarded as highly localized on the molecules since the coherence in the π stack is lost. When the two phases are brought into contact the more loosely bound electrons lying high in the “conduction” band of the low-pressure phase will be attracted by the more tightly bound molecular orbitals in the high-pressure phase. As a result a small number of elec-

ODS-molecule		FAS-molecule		AHAPS-molecule		CMPS-molecule	
HOMO	LUMO	HOMO	LUMO	HOMO	LUMO	HOMO	LUMO
Eigenvalue (hartree)							
-0.27729	0.05301	-0.34059	-0.07242	-0.20447	0.05042	-0.26128	-0.05405

Fig. 13.13 Schematic drawings of the HOMO and LUMO for the ODS, FAS, AHAPS and CMPS molecules, along with their eigenvalues (with permission from [73]).

trons will be funneled from the low- to the high-pressure domains. This will lead to slightly more positive low-pressure areas and slightly more negative high-pressure domains, as a p–n junction (Fig. 13.14). The measured potential difference of 20 mV between the high- and low-pressure phases is in good agreement with typical bandwidth values of π stacks [74].

Similar results were obtained by investigating the structural and electronic properties of different submicron-scale self-assembled architectures of a larger alkylated synthetic nanographene, consisting of 96 carbon atoms in the aromatic core (C₉₆C₁₂) [75]. Extended layers, percolated networks and broken patterns were grown from solutions at surfaces and successfully visualized by KPFM (Fig. 13.15) [76]. This study made it possible to determine the local ϕ value of the different π -conjugated nanostructures adsorbed on mica with a resolution below 10 nm and 0.05 eV. It revealed that the ϕ value depends strongly on the local molecular order at the surface, in particular on the delocalization of electrons in the π states, on the molecular orientation at surfaces, on the molecular packing density, on the presence of defects in the film, and on the different conformation of the aliphatic peripheral chains that might cover the conjugated core. These results were confirmed by comparing the KPFM-estimated local ϕ value of layers supported on mica, where the molecules are preferentially packed “edge-on” on the substrate, with the UPS microscopically measured ϕ of layers adsorbed on graphite, where the molecules should tend to assemble “face-on” at the surface. It appears that local ϕ studies are of paramount importance to an understanding of the electronic properties of active organic nanostructures [76].

KPFM has also been exploited to study complex biological architectures, such as DNA. Contact potential difference images revealed DNA strands oriented on Si

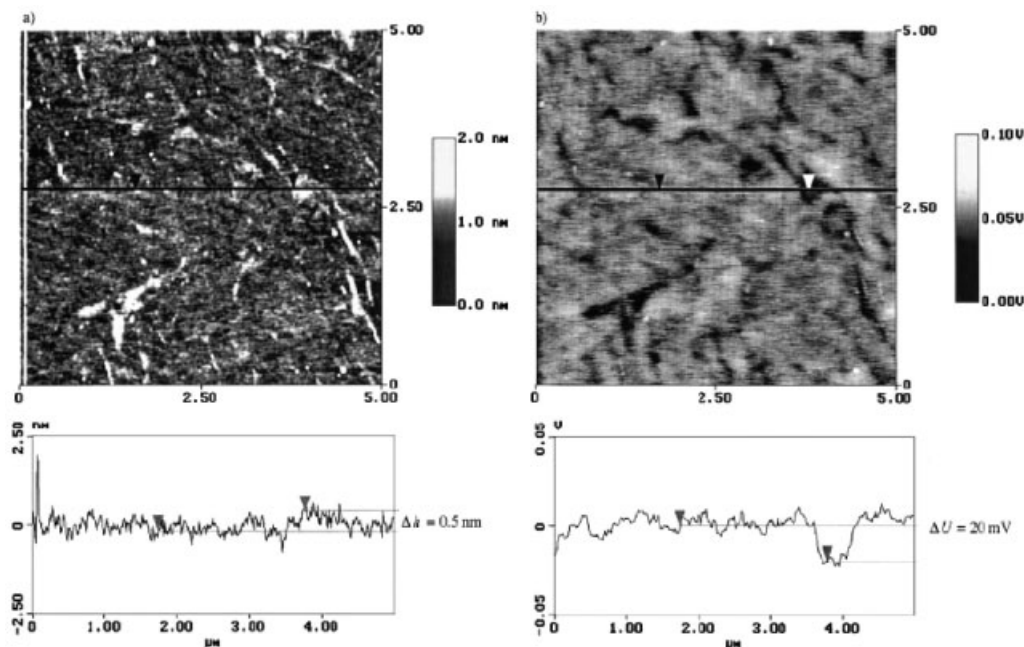


Fig. 13.14 (a) SFM tapping mode topography image of an LB monolayer of HBC transferred to a SiO_x at a mean area per molecule $A = 1 \text{ nm}^2$. A cross-section profile from the middle of the scan is also displayed, showing the height difference between the high-pressure and the low-pressure phases. The height difference is

ca. 0.5 nm (b) KPFM image showing the potential landscape of the same area as that shown in (a). The potential of the low-pressure phase is ca. 20 mV higher than the potential of the high-pressure phase, as can also be seen from the cross-section profile (with permission from [74]).

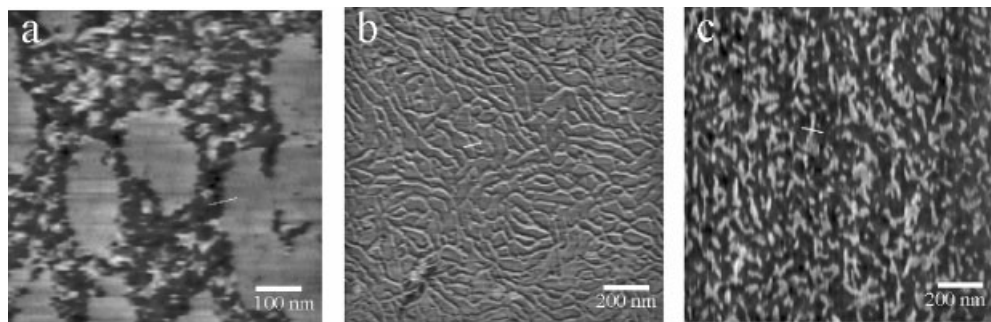


Fig. 13.15 KPFM image of C96-C12 architectures on mica: (a) layers; (b) network of fibers; (c) elongated agglomerates. Different profiles have been traced on the KPFM images

in order to estimate the local work function (not shown). A white line is shown in each image as an example of a location where the profiles were traced (with permission from [76]).

and glass substrates, recorded using a hexadecanethiol-modified gold tip, but without achieving a particularly high resolution [77].

KPFM also permits exploration of the dynamic properties of single molecules. As an example, the changes of potential in photosynthetic structural proteins during light harvesting were monitored with a minimal interference in the protein activity. This study was addressed to study biological nanometer-size supramolecular structures called photosystem I (PS I), which can be isolated and purified from green plants. By means of KPFM, measurement of exogenous photovoltages generated from single PS I reaction centers in a heterostructure composed of PS I, organosulfur molecules, and atomically flat gold were carried out [78].

The PS I adsorbs with a preferential orientation, keeping its electron acceptor center on the upside (away from the substrate). KPFM measurements performed in a helium atmosphere with the lift-off technique enabled quantification, with a remarkably high resolution, of the potential of this acceptor center. By irradiating the sample with visible light, the photosynthetic process triggers a photon-induced charge separation, biasing negatively the acceptor center. The bias shift, being ca. 1 V, can be easily measured in real time with KPFM. Furthermore, a 2D map of the protein surface potential was achieved with KPFM, providing information on the position of the acceptor center inside the protein. The results obtained are in good agreement with the known structural and energetic features of protein PS I measured by other techniques (Fig. 13.16) [78].

KPFM also granted insight into the photochemical behavior of chemisorbed organic layers at surfaces. Organosilane layers ($R-Si(OCH_3)_3$), where R can be either an aliphatic or an aromatic group, have been patterned on SiO_x wafers, and then decomposed using UV light. The surface potential difference between the nanopatterned irradiated and non-irradiated areas has been measured by KPFM [79]. The occurrence of a photo-oxidation of the methyl end groups transformed them to CHO and COOH, and the subsequent complete molecular decomposition of the organic monolayer led to changes in the surface potential, which were highlighted by KPFM, XPS, and lateral force microscopy. The change in surface potential in these systems is due to the variation of the molecular dipole moment, as confirmed by *ab-initio* calculations [80].

In a similar set of experiments, KPFM was able to monitor macroscopically the light-induced dipole moment changes due to *cis-trans* molecular rearrangement in SAMs of thiol azobenzenes on Au(111) [81].

A well-known class of molecules with a great potential for organic electronics applications are poly(thiophenes). KPFM studies provided unambiguous evidence for the dependence of the measured work function of the molecular material on the substrate type. Monolayers and bilayers of dimethylquinquethiophene supported on Pt and Ta substrates displayed a surface potential difference of 5.36 and 3.92 V, respectively. These values are quite similar to those of the underlying metals [82]. The difference in surface potential has been interpreted by assuming a charge transfer from the metal to the thiophene, and a reduction of the quinquethiophene LUMO due to image force interactions. The deposition on Pt of a second quinquethiophene layer led to an increase of 0.1 V in the measured potential. This was ex-

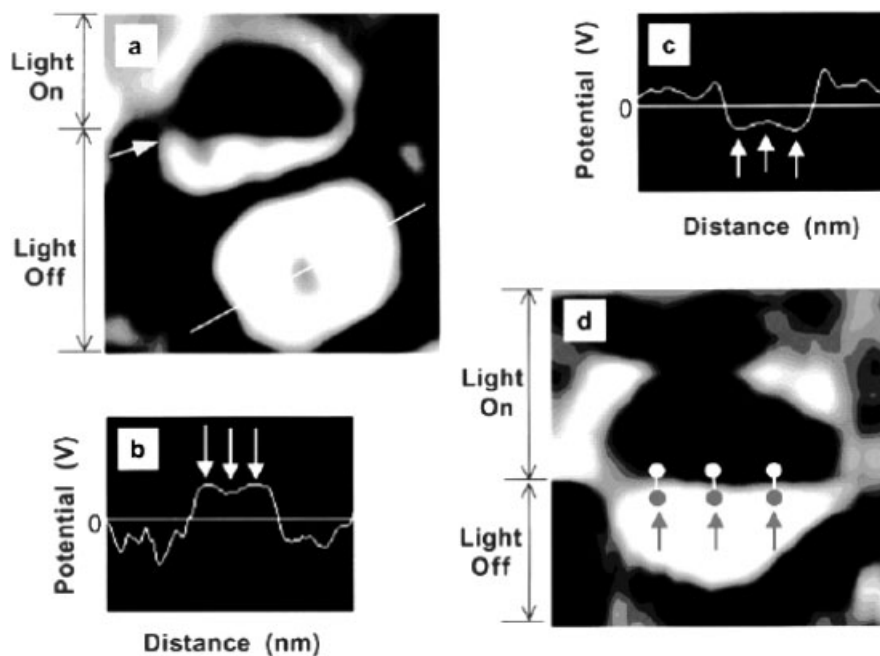


Fig. 13.16 KPFM images of individual PS I reaction centers and corresponding cross-sectional voltage–distance profiles. (a) View of two PS I reaction centers: the lower PS I was imaged entirely in darkness, whereas the upper PS I was imaged mostly in light. Note the abrupt change in electric potential for the upper PS I as the diode laser was switched off in mid-scan at the indicated location. (b) Light-

off voltage–distance profile along the indicated cross-sectional axis. (c) Light-on voltage–distance profile. (d) A single PS I was “bisected” in mid-scan by switching the diode laser off. Voltage difference measurements in light and darkness, indicated by the proximal dots, were taken at the peripheries and the center (with permission from [78]).

plained by an induced polarization due to the local electric field originating from the charges exchanged between the first layer and the metal. A decrease of the measured potential down to only 20 mV above the potential of the Pt background was observed upon irradiating the quinquethiophene with visible light. This behavior is due to transfer of photo-generated holes from the molecule to the substrate because of the local electric field [83].

13.7 KPFM on Organic Electronic Devices

KPFM, being a contactless technique, can be employed to explore in a noninvasive way the electronic and morphological behavior of working devices based on molecular organic materials or polymers. Understanding and controlling the relationship

between the electronic transport properties and the morphology of conducting organic layers is crucial for further development and exploitation of these materials, as many aspects, including their poor electronic properties due to the polycrystalline character of the organic thin films, often limit the overall performance of the device.

The tailoring of a metal/organic interface represents a fundamental issue in the study and optimization of working devices such as light-emitting diodes (LEDs), field-effect transistors (FETs), and solar cells. Extensive investigation revealed that the contact resistance at the metal/organic interface depends on many factors, including the work function of the metal, the ionization potential of the organic architecture, the effect of the diffusion layer, and the built-in potential at the interface [84]. Moreover, as was pointed out in Section 13.4, the metal/organic interface is quite a complex system as it involves controversial issues such as the vacuum-level shift, band bending, and formation of interface dipoles. KPFM allows one to follow potential differences at the interface between different components, providing two-dimensional maps of potential drops due to low-conductivity areas, short circuits, electrical defects, and phase separations.

Electrostatic force microscopy (EFM) made it possible to detect the current passing through an ultrathin polymer network of poly(hexylthiophene) (P3HT) deposited on SiO_x . This was performed by using a shadow mask to deposit Au nanoelectrodes separated by a gap of $4\ \mu\text{m}$ on the top of the P3HT self-assembled network. The potential drop between the two electrodes was recorded. The resolution attained allowed the network in the EFM image to be distinguished (Fig. 13.17), providing evidence for the good conducting properties of the organic architecture. On the other hand, the current passing through double-stranded DNA chains deposited between electrodes could not be detected by EFM, confirming the poor electrical conductivity of the DNA [85].

Sirringhaus, Friend, and coworkers performed a more quantitative investigation with KPFM by measuring the potential drop along the source/channel/drain inter-

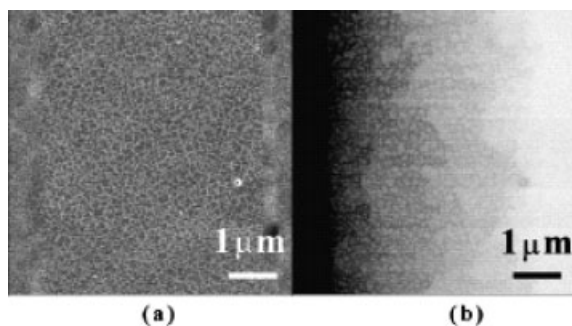


Fig. 13.17 Topography and EFM phase images for P3HT with a gold contact at each end. (a) Flattened topography image. (b) EFM phase map when a bias of 15 V was applied to the left-hand electrode (with permission from [85]).

faces in different organic-based transistors, while current was flowing through the device [47, 84, 86, 87]. The potential decay obtained in a 5.2 μm wide P3HT transistor allowed them to estimate the resistance of source and drain contacts, the charge mobility and the resistance of the polymer architecture, as well as the linear and nonlinear transistor operating ranges (Figs. 13.18 and 13.19) [47, 87].

The contact resistance at the P3HT/Au electrode interface is given by Eq. (20), where W is the channel width and I_d is the current passing through the device. Potential drops ΔV_s , ΔV_d at the source and drain interfaces were measured with KPFM.

$$R_C = W(\Delta V_s + \Delta V_d)/I_d \quad (20)$$

From the profile of the potential across the active layer, the field-effect mobility μ of the organic material was obtained using Eqs. (21) and (22), where V_g is the gate voltage.

$$I_D = eWn(x)\mu(V'_g, E)E(x) \quad (21)$$

$$E(x) = -\partial V(x)/\partial x \quad (22)$$

The density n of field-induced carriers is given by $en(x) = C_i V'_g$, while $V'_g = V(x) - V_g$ is the effective potential drop over the insulator, and C_i is the insulator capacitance. In the nonlinear mode ($V_d > V_g$) the density of accumulated charges decreases when going from source to drain, and the mobility decreases as well. This is a nice example of how the analysis of KPFM measurements allows complete characterization of electrical properties of an operating electronic device.

In a different set of experiments, the absolute work function value of the aforementioned P3HT has been estimated by KPFM, ultraviolet photoelectron spectroscopy, and photoemission electron spectroscopy, and compared with the work functions of the electrodes wiring the P3HT. In this case the organic material was deposited on a flexible substrate (i.e., paper) and wired using unconventional electrodes made of colloidal graphite and carbon black, patterned on the paper using a commercial plotter. The work functions measured in vacuum amounted to 3.8, 4.1, and 3.8 eV, for P3HT, graphite, and carbon black, respectively. This shows how the versatility and applicability of KPFM allow the study of unconventional working devices, in this case fabricated on an unusual substrate [88]. KPFM can also be used to explore charge transport through domain boundaries in polycrystalline organic layers. Channel potential drops in transistors based on a nematic glassy state polymer revealed that domain boundaries do not limit the charge transport [87]. It is rather the transport through the domains themselves that is the main obstacle to the current flow [87]. Qualitative KPFM measurements of potential drops at domain boundaries due to different molecular orientations have also been performed on very thin Langmuir–Blodgett polymer layers (Fig. 13.20) [89].

A detailed study on the importance of source–drain contacts in organic devices was recently reported by Frisbie and coworkers [90]. Surface potentials of operating

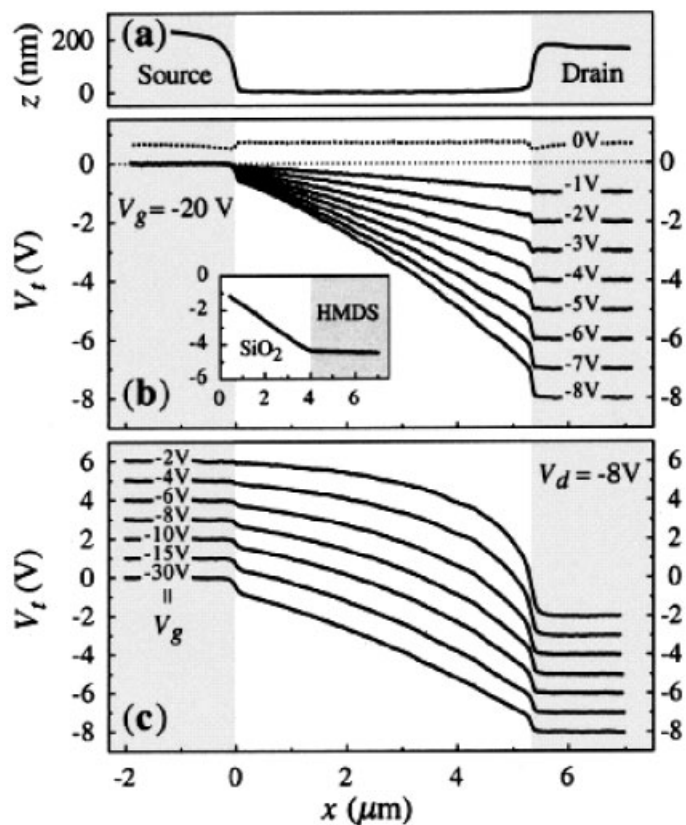


Fig. 13.18 KPFM of a P3HT thin-film field-effect transistor ($L = 5.2 \mu\text{m}$ channel length). Two-dimensional maps were recorded, but only profiles perpendicular to the channel are shown, since the conductivity of P3HT proved to be homogeneous. It is worth noting that interchanging the source and the drain did not change the results. (a) The channel between the source and the drain electrodes is seen clearly in the topographic profile. (x denotes the distance from the source). (b) Potential profiles acquired simultaneously with the topography at $T = 300 \text{ K}$. The gate voltage was kept constant at $V_g = -20 \text{ V}$ while the drain voltage V_d was decreased from -1 to -8 V in -1 V steps ($I_d = 3.9, 7.6, 11.0, 14.2, 17.2, 20.1, 22.8,$ and $25.4 \mu\text{A}$). $\Delta\Phi(x)$, i.e., the profile for $V_d = 0 \text{ V}$ (dotted line, offset by 0.5 V

for clarity), was subtracted from all profiles with $V_d \neq 0$. (c) Potential profiles as a function of gate voltage, where $V_d = -8 \text{ V}$ and $T = 165 \text{ K}$. (Profiles are offset by increasing 1 V steps. $I_d = 4010, 850, 334, 195, 97, 37,$ and 9 nA). Inset of (b): potential profile of an $L = 20 \mu\text{m}$ P3HT transistor with partially hexamethyldisilazane-covered SiO_2 interface ($V_g = -40 \text{ V}$, $V_d = -5 \text{ V}$, and $T = 300 \text{ K}$). The lateral electric field (i.e., $-\partial V_t/\partial x$) in the bare $-\text{SiO}_x$ region is 26 times larger than the value found in the HMDS region, indicating that the field-effect mobility of an HMDS-treated interface is ~ 20 times that of bare SiO_x , in excellent agreement with field-effect mobilities deduced from devices made of either bare or completely HMDS-treated SiO_x surfaces (with permission from [47]).

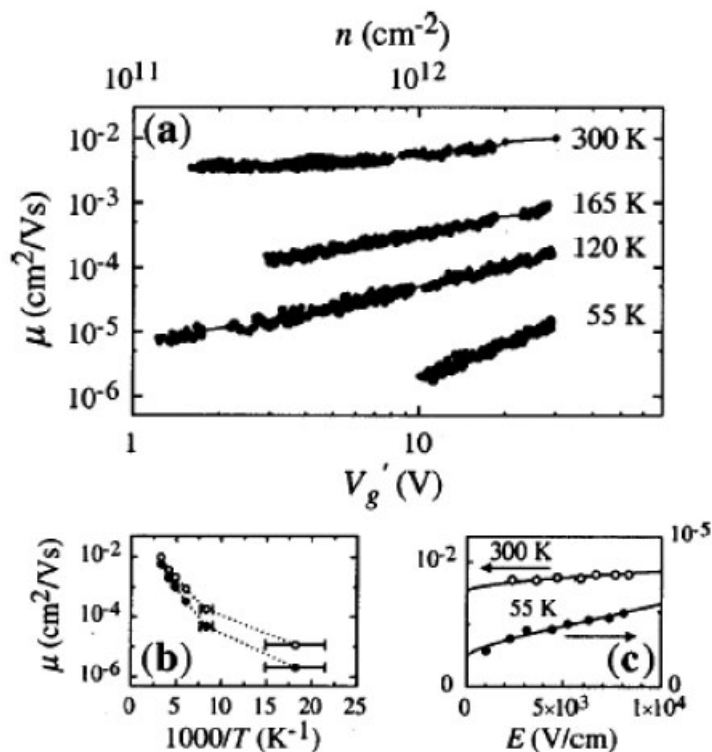


Fig. 13.19 Field-effect hole mobility of regioregular head-to-tail P3HT. (a) Dependence on effective gate voltage, i.e., carrier concentration. (b) Temperature dependence. Open and filled symbols represent data for potential gate $V'_g = 30$ V and 10 V,

respectively. (c) Dependence on lateral electric field ($V'_g = 20$ V). The continuous lines depict a fit with a Poole-Frenkel law: $\mu \propto \exp(B\sqrt{E/kT})$ with $B = 5 \times 10^{-5}$ eV $V^{-1/2}$ $\text{cm}^{-1/2}$ (with permission from [47]).

pentacene thin-film FETs with two different contact geometries (deposited above or beneath the active organic layer) were mapped by KPFM. The surface potential distribution was used to quantify the potential drops at the source and drain contacts. The bottom-contact FETs were contact-limited at large gate voltages, while the top-contact FETs were not contact-limited. In both geometries, the contact and the channel resistances decreased notably with the increasing (negative) gate bias but did not depend strongly on the drain bias. This study highlighted the potential of KPFM to monitor the charge transport bottlenecks in operating pentacene devices, and more generally to correlate the electrical behavior with the structure of the devices by comparing the surface potential with the topographic maps (Figs. 13.21 and 13.22).

An appropriate choice of the metallic electrode is needed, the resistance at the metal/organic interface being dependent on the metal type. For pentacene-based

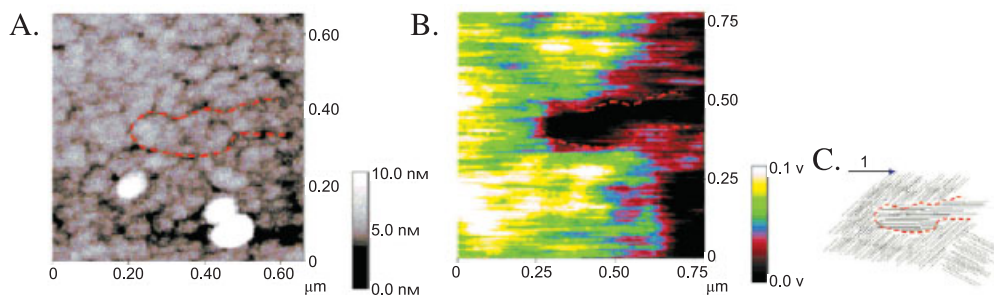


Fig. 13.20 (A) Tapping mode SFM topographical map of a Langmuir–Blodgett polymer monolayer. (B) EFM-measured potential map of the sample area visualized in (A). The structure (marked by a red line) that correlates with the domain seen in the EFM picture is clearly visible in the height profile. Other features such as the two dust particles (white areas in the height picture) can also be

distinguished in the EFM picture. (C) A model of how the polymer crystallites could be oriented in order to give rise to the potential map observed. Please note that the lines do not represent individual polymers, but are drawn to indicate the possible direction of the highly oriented polycrystallites, which form the “electronic” domains (with permission from [89]).

junctions, contacts with platinum showed a very small resistance compared with palladium and nickel [91].

A higher efficiency for Pt was also observed for a FET fabricated using a monolayer of methylquinque thiophene [92]. In this work the resistances in the channel

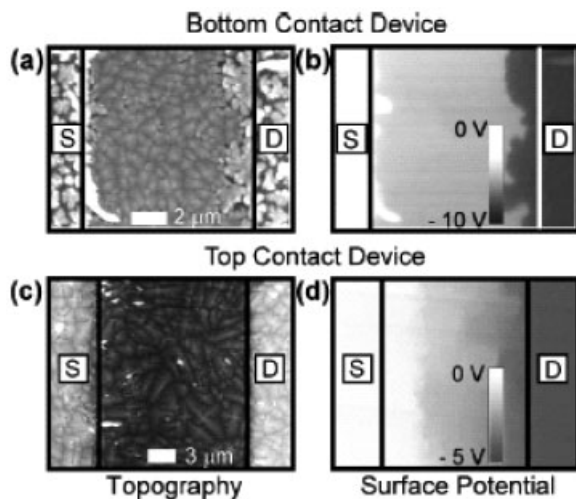


Fig. 13.21 (a), (c) Topographic and (b), (d) corresponding surface potential images for bottom-contact and top-contact thin-film FETs. Drain bias $V_D = -10$ V for (b), $V_D = -5$ V for (d) and gate bias $V_G = 0$ V for both cases.

Labels *S* and *D* indicate the source and drain electrodes, respectively. The solid vertical lines indicate the edge between the contacts and the conducting channel (with permission from [90]).

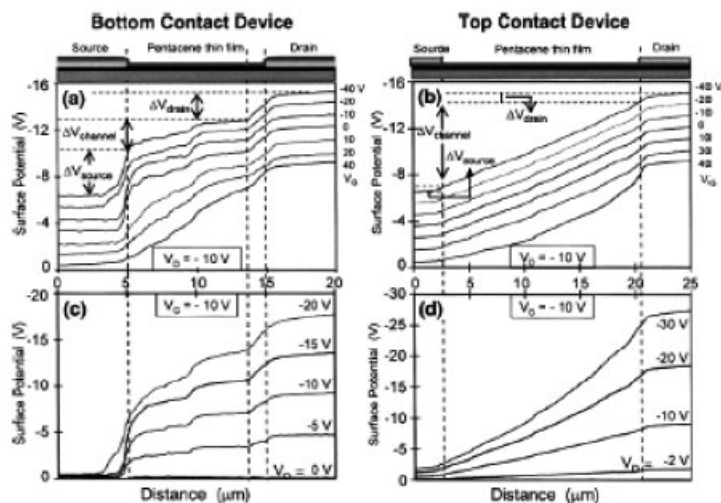


Fig. 13.22 (a), (c) A set of surface potential profiles for a bottom-contact thin-film FET, with a schematic of the device at the top for reference. For (a) $V_D = -10$ V and $V_G = 40$ to -40 V. The profiles are artificially offset for clarity of viewing. For (c) $V_G = -10$ V and $V_D = 0$ to -20 V. The channel length as defined by the lithography is $10\ \mu\text{m}$. The outer

broken lines indicate the edge between the contacts and the channel. (b), (d) A similar set of profiles for a top-contact FET. In this case, the channel length was $\sim 18\ \mu\text{m}$. The profiles in each device were taken at the same spot in the channel. Zero bias profiles are not subtracted from any of the data shown here (with permission from [90]).

and at the source/drain interfaces were measured. Despite the nominal thickness of a single layer of the active film, a uniform potential drop and high resistivity sites corresponding to interfaces and defects were clearly observed and discussed (Fig. 13.23) [92].

Nanotube-based transistors have recently attracted much interest. The electrical characterization of these devices has been quite complex, as the semiconducting nanotubes behave as p type or n type if they are measured in air or vacuum respectively. KPFM measurements on Au/nanotube/Au systems, using only semiconducting single-wall nanotubes, demonstrated that the p-type behavior in air is due to oxygen adsorption on the Au surface, creating a dipole layer and thus changing the Au work function. The dipole formation can be hindered by simple “passivation” of the Au surface using H_2S or alkanethiols [59].

Similarly to the case of inorganic solar cells, organic photovoltaic devices can also be studied with KPFM under illumination. Very recently, the surface potential of polymer heterojunction solar cells based on a blend of a poly(*p*-phenylenevinylene) (PPV) and fullerene has been measured. Under suitable conditions, the fullerenes segregate into a PPV matrix forming spherical clusters, which can be visualized by SFM. KPFM images of the blend showed that some clusters possess a higher work function and some a lower one with respect to the surrounding poly-

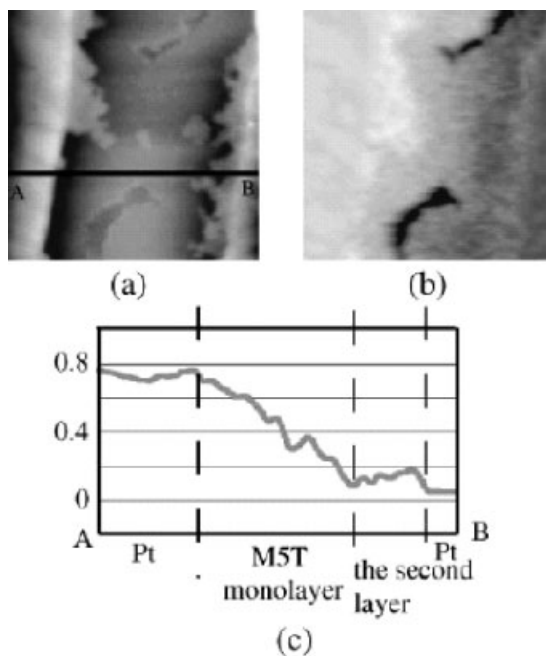


Fig. 13.23 Methylquinquethiophene monolayer partially covering the gap between ultrathin Pt electrodes (a) Topographic image and (b) surface potential image with 0.7 V DC voltage applied. (c) Surface potential line profile along A–B in (a) (with permission from [92]).

mer. SEM measurements revealed that the clusters with the lower work function are electron-rich fullerene aggregates directly exposed to the atmosphere, while those with the higher work function are covered by a thin layer of polymer. This thin layer limits photocurrent collection, and thus device efficiency [93].

KPFM measurements under dark and illuminated conditions have also been used to study qualitatively the charged-trap release in poly[(9,9-dioctylfluorene-2,7-diyl)-*alt*-phenylene-(*N*-(*p*-2-butylphenyl)iminophenylene)] (TFB). The surface density of charges is shown to decay slowly in the dark, due to the discharging of shallow traps, and reach a steady value, stable in time, due to deep-level traps which remain charged in the dark. Upon illumination the charge density, and thus the measured potential, quickly drop to zero. The discharging of traps takes place only with light having $\lambda < 450$ nm and it is faster if shorter wavelengths are used (Fig. 13.24) [87].

The use of KPFM to study working devices is not limited to steady-states conditions, but transient potentials can be measured as well with a time resolution of ~ 5 ms. The charging and discharging of the active organic layer of a transistor can be followed with KPFM while the applied gate voltage is varied. Changes in

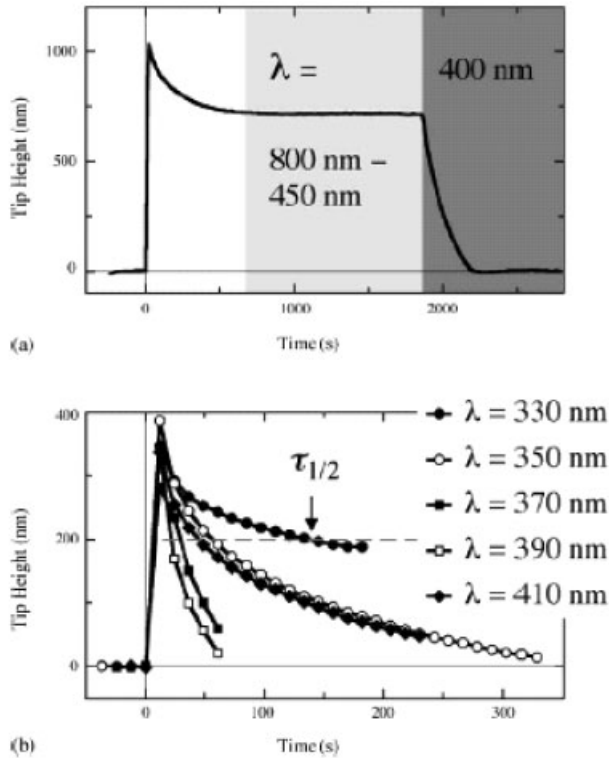


Fig. 13.24 Photon-assisted release of trapped charges in a TFB transistor. The measurements were recorded in the center of the transistor channel. (a) Only illumination with light of $\lambda < 450$ nm results in trap-release. (b) The process of trap-release depends critically on the wavelength of the incident light (with permission from [87]).

potential at each point of the active layer reveal an exponential decay, which depends on the dimensions of the device, on the final gate voltage, and on the field-effect mobility. Therefore KPFM also provides tools to measure field mobility in organic materials [86, 87].

The density of trapped charges in defects of organic layers can also be estimated by a KPFM-based approach [87]. The traps are first accumulated in the layer by applying a gate voltage greater than the turn-on voltage. Then the gate is brought below turn-on voltage. This drives all the mobile charges out of the layer, and leaves only trapped, immobile charges inside the organic architecture. The interaction of the tip with the charged defects can be used to measure charge density [87].

Unfortunately, the KPFM technique is not fast enough to detect shallow traps, which discharge too fast for KPFM detection. In principle, trap densities down to 10^9 cm^{-2} , corresponding to a change in tip potential of about 10 mV, can be resolved [87].

13.8

Conclusions and Future Challenges

This review has highlighted the potential of Kelvin probe force microscopy to gain insight simultaneously into the structural and electronic properties of functional surfaces and interfaces. The versatility of the technique makes it possible to perform measurements under different environmental conditions on different sample types, including metals and both inorganic and organic materials. Such explorations can be accomplished with resolutions of a few nanometers and some millivolts. This is of great importance, since it is well established that a solid surface possesses different properties from the bulk material. Equally importantly, there are many processes of technological significance which depend upon the use of solid surfaces and which may be improved in some way if the role of the surface and the interface could be fully understood. Beyond imaging, KPFM is a viable approach to obtaining new information concerning electrical and electronic properties of sample surfaces.

KPFM is a powerful technique for studying, in a noninvasive way, complex electronic phenomena in supramolecularly engineered systems and devices. The combination of such a methodology with external stimuli, e.g., light irradiation, opens new doors to the exploration of processes occurring in nature or in complex artificial architectures.

Unfortunately surface effects (e.g., dipole formation), as well as systematic errors due to the simple geometrical models that are often assumed to interpret tip-sample interactions, still affect KPFM measurements and data interpretation. Indeed, various approximations are sought whose complexity depends on the variables taken into account. Moreover, the different data that can be attained from the distinct KPFM signals still need to be fully unraveled. Combining these data, KPFM could acquire a wide knowledge of the overall electronic and electrical behavior of a sample surface: work function, capacitance, interface electronic behavior, and the concentration of mobile charge carriers can be determined in this way. Therefore, KPFM is a powerful technique not only for exploring the electronic (dynamic) properties of materials, but also for optimizing the design and performance of new devices based on organic semiconductor nanostructures.

Acknowledgements

We are grateful to Drs. Anna Maria Talarico and Susanna Morelli for enlightening discussions. We also express our gratitude to long-term collaborators for stimulating discussions and support: Professors Klaus Müllen (Mainz), Roeland J. M. Nolte and Alan E. Rowan (Nijmegen), Giovanni Marletta (Catania). Financial support from NMP-STREP ForceTool, the EU through the Marie Curie EST project SUPER, ESF-SONS-BIONICS and the bilateral program CNR-CNRS is gratefully acknowledged.

References

- 1 S. R. FORREST, *Nature* **2004**, 428, 911.
- 2 G. BINNIG, C. F. QUATE, C. GERBER, *Physical Review Letters* **1986**, 56, 930.
- 3 C. BUSTAMANTE, D. KELLER, *Physics Today* **1995**, 48, 32.
- 4 H. TAKANO, J. R. KENSETH, S.-S. WONG, J. C. O'BRIEN, M. D. PORTER, *Chemical Reviews* **1999**, 99, 2845.
- 5 P. SAMORÌ, *Journal of Materials Chemistry* **2004**, 14, 1353.
- 6 G. BINNIG, H. ROHRER, C. GERBER, E. WEIBEL, *Applied Physics Letters* **1982**, 40, 178.
- 7 J. K. GIMZEWSKI, C. JOACHIM, *Science* **1999**, 283, 1683.
- 8 D. A. BONNELL, R. SHAO, *Current Opinion in Solid State & Materials Science* **2003**, 7, 161.
- 9 T. W. KELLEY, E. L. GRANSTRÖM, C. D. FRISBIE, *Advanced Materials* **1999**, 11, 261.
- 10 J. R. MATEY, J. BLANC, *Journal of Applied Physics* **1985**, 57, 1437.
- 11 B. D. TERRIS, J. E. STERN, D. RUGAR, H. J. MAMIN, *Physical Review Letters* **1989**, 63, 2669.
- 12 M. NONNENMACHER, M. P. O'BOYLE, H. K. WICKRAMASINGHE, *Applied Physics Letters* **1991**, 58, 2921.
- 13 C. GOMEZ-NAVARRO, F. MORENO-HERRERO, P. J. DE PABLO, J. COLCHERO, J. GOMEZ-HERRERO, A. M. BARO, *Proceedings of the National Academy of Sciences of the United States of America* **2002**, 99, 8484.
- 14 L. E. CHERAN, M. E. MCGOVERN, M. THOMPSON, *Faraday Discussions* **2000**, 116, 23.
- 15 A. KIKUKAWA, S. HOSAKA, R. IMURA, *Review of Scientific Instruments* **1996**, 67, 1463.
- 16 L. KELVIN, *Philos. Mag.* **1898**, 46, 82.
- 17 H. M. ROSENBERG, *The Solid State*, Clarendon Press, Oxford, **1974**.
- 18 M. PRUTON, *Introduction to Surface Physics*, Oxford University Press, New York, **1994**.
- 19 W. A. ZISMAN, *Review of Scientific Instruments* **1932**, 3, 367.
- 20 L. KRONIK, Y. SHAPIRA, *Surface Science Reports* **1999**, 37, 1.
- 21 D. K. SCHRODER, *Measurement Science & Technology* **2001**, 12, R16.
- 22 Veeco Instruments, Inc., *Nanoscope IV Controller Manual*, **2002**.
- 23 H. O. JACOBS, P. LEUCHTMANN, O. J. HOMAN, A. STEMMER, *Journal of Applied Physics* **1998**, 84, 1168.
- 24 G. KOLEY, M. G. SPENCER, H. R. BHANGALE, *Applied Physics Letters* **2001**, 79, 545.
- 25 O. CHERNIAVSKAYA, L. CHEN, V. WENG, L. YUDITSKY, L. E. BRUS, *Journal of Physical Chemistry B* **2003**, 107, 1525.
- 26 J. COLCHERO, A. GIL, A. M. BARÓ, *Physical Review B* **2001**, 64, 245403.
- 27 T. TAKAHASHI, S. ONO, *Ultramicroscopy* **2004**, 100, 287.
- 28 A. GIL, J. COLCHERO, J. GOMEZ-HERRERO, A. M. BARÓ, *Nanotechnology* **2003**, 14, 332.
- 29 C. H. LEI, A. DAS, M. ELLIOTT, J. E. MACDONALD, *Nanotechnology* **2004**, 15, 627.
- 30 T. TAKAHASHI, T. KAWAMUKAI, *Ultramicroscopy* **2000**, 82, 63.
- 31 O. CHERNIAVSKAYA, L. CHEN, M. A. ISLAM, L. BRUS, *Nano Letters* **2003**, 3, 497.
- 32 U. ZERWEEK, C. LOPPACHER, T. OTTO, S. GRAFSTRÖM, L. M. ENG, *Physical Review B* **2005**, 71, 125424.
- 33 K. OKAMOTO, Y. SUGAWARA, S. MORITA, *Japanese Journal of Applied Physics Part 1 – Regular Papers Short Notes & Review Papers* **2003**, 42, 7163.
- 34 C. SOMMERHALTER, T. GLATZEL, T. W. MATTHES, A. JÄGER-WALDAU, M. C. LUX-STEINER, *Applied Surface Science* **2000**, 157, 263.
- 35 S. M. SZE, *Physics of Semiconductor Devices*, 2nd ed., Wiley, New York, **1981**.
- 36 H. ISHII, H. OJI, E. ITO, N. HAYASHI, D. YOSHIMURA, K. SEKI, *Journal of Luminescence* **2000**, 87–89, 61.
- 37 H. ISHII, N. HAYASHI, E. ITO, Y. WASHIZU, K. SUGI, Y. KIMURA, M. NIWANO, Y. OUCHI, K. SEKI, *Physica Status Solidi a – Applied Research* **2004**, 201, 1075.

- 38 M. PFEIFFER, K. LEO, N. KARL, *Journal of Applied Physics* **1996**, *80*, 6880.
- 39 H. ISHII, K. SUGIYAMA, E. ITO, K. SEKI, *Advanced Materials* **1999**, *11*, 605.
- 40 K. C. KAO, *Electrical Transport in Solids*, Pergamon, Oxford, **1981**.
- 41 M. SCHOTT, *Organic Conductors* (Ed.: J. P. FARGES), Marcel Dekker, New York, **1994**, p. 539.
- 42 D. P. WOODRUFF, T. A. DELCHAR, *Modern Techniques of Surface Science*, Cambridge University Press, Cambridge, **1986**.
- 43 J. HOELZEL, F. K. SCHULTE, H. WAGNER, *Surface State Surface Physics*, Springer, Berlin, **1979**.
- 44 P. NIELSEN, *Photogr. Sci. Eng.* **1974**, *18*, 186.
- 45 K. WANDELT, *Thin Metal films and Gas Chemisorption*, Elsevier, Amsterdam, **1987**.
- 46 K. SEKI, N. HAYASHI, H. OJI, E. ITO, Y. OUCHI, H. ISHII, *Thin Solid Films* **2001**, *393*, 298.
- 47 L. BÜRGI, H. SIRRINGHAUS, R. H. FRIEND, *Applied Physics Letters* **2002**, *80*, 2913.
- 48 A. ALESSANDRINI, U. VALDRÈ, *Philosophical Magazine Letters* **2003**, *83*, 441.
- 49 A. K. HENNING, T. HOCHWITZ, J. SLINKMAN, J. NEVER, S. HOFFMANN, P. KASZUBA, C. DAGHLIAN, *Journal of Applied Physics* **1995**, *77*, 1888.
- 50 G. H. BUH, H. J. CHUNG, C. K. KIM, J. H. YI, I. T. YOON, Y. KUK, *Applied Physics Letters* **2000**, *77*, 106.
- 51 A. DOUKKALI, S. LEDAIN, C. GUASCH, J. BONNET, *Applied Surface Science* **2004**, *235*, 507.
- 52 T. MEODED, R. SHIKLER, N. FRIED, Y. ROSENWAKS, *Applied Physics Letters* **1999**, *75*, 2435.
- 53 R. SHIKLER, N. FRIED, T. MEODED, Y. ROSENWAKS, *Physical Review B* **2000**, *61*, 11041.
- 54 T. YAMAUCHI, M. TABUCHI, A. NAKAMURA, *Applied Physics Letters* **2004**, *84*, 3834.
- 55 M. A. SALEM, H. MIZUTA, S. ODA, *Applied Physics Letters* **2004**, *85*, 3262.
- 56 A. CHAVEZPIRSON, O. VATEL, M. TANIMOTO, H. ANDO, H. IWAMURA, H. KANBE, *Applied Physics Letters* **1995**, *67*, 3069.
- 57 G. LÈVÊQUE, P. GIRARD, E. SKOURI, D. YAREKHA, *Applied Surface Science* **2000**, *157*, 251.
- 58 C. MAEDA, S. KISHIMOTO, T. MIZUTANI, T. SUGAI, H. SHINOHARA, *Japanese Journal of Applied Physics Part 1 – Regular Papers Short Notes & Review Papers* **2003**, *42*, 2449.
- 59 X. D. CUI, M. FREITAG, R. MARTEL, L. BRUS, P. AVOURIS, *Nano Letters* **2003**, *3*, 783.
- 60 R. GROVER, B. MC CARTHY, Y. ZHAO, G. E. JABBOUR, D. SARID, G. M. LAWS, B. R. TAKULAPALLI, T. J. THORNTON, D. GUST, *Applied Physics Letters* **2004**, *85*, 3926.
- 61 S. TAKAHASHI, T. KISHIDA, S. AKITA, Y. NAKAYAMA, *Japanese Journal of Applied Physics Part 1 – Regular Papers Short Notes & Review Papers* **2001**, *40*, 4314.
- 62 C.-S. JIANG, H. R. MOUTINHO, F. S. HASOON, H. A. AL-THANI, D. J. FRIEDMAN, J. F. GEISZ, Q. WANG, M. J. ROMERO, M. M. AL-JASSIM, *NCPV and Solar Program Review Meeting* **2003**, 870.
- 63 C.-S. JIANG, D. J. FRIEDMAN, J. F. GEISZ, H. R. MOUTINHO, M. J. ROMERO, M. M. AL-JASSIM, *Applied Physics Letters* **2003**, *83*, 1572.
- 64 C.-S. JIANG, R. NOUFI, K. RAMANATHAN, J. A. ABUSHAMA, H. R. MOUTINHO, M. M. AL-JASSIM, *Applied Physics Letters* **2004**, *85*, 2625.
- 65 C.-S. JIANG, R. NOUFI, J. A. ABUSHAMA, K. RAMANATHAN, H. R. MOUTINHO, J. PANKOW, M. M. AL-JASSIM, *Applied Physics Letters* **2004**, *84*, 3477.
- 66 S. SADEWASSER, T. GLATZEL, S. SCHULER, S. NISHIWAKI, R. KAIGAWA, M. C. LUX-STEINER, *Thin Solid Films* **2003**, *431*, 257.
- 67 A. ULMAN, *Introduction to Ultrathin Organic Films*, Academic Press, San Diego CA, **1991**.
- 68 G. E. POIRIER, *Chemical Reviews* **1997**, *97*, 1117.
- 69 E. DELAMARCHE, B. MICHEL, H. A.

- BIEBUYCK, C. GERBER, *Advanced Materials* **1996**, *8*, 719.
- 70 T. ICHII, T. FUKUMA, K. KOBAYASHI, H. YAMADA, K. MATSUSHIGE, *Nanotechnology* **2004**, *15*, S30.
- 71 J. LÜ, E. DELAMARCHE, L. ENG, R. BENNEWITZ, E. MEYER, H. J. GÜNTHERODT, *Langmuir* **1999**, *15*, 8184.
- 72 H. McNALLY, D. B. JANES, B. KASIBHATLA, C. P. KUBIAK, *Superlattices and Microstructures* **2002**, *31*, 239.
- 73 N. SAITO, K. HAYASHI, H. SUGIMURA, O. TAKAI, N. NAKAGIRI, *Surface and Interface Analysis* **2002**, *34*, 601.
- 74 N. REITZEL, T. HASSENKAM, K. BALASHEV, T. R. JENSEN, P. B. HOWES, K. KJAER, A. FECHTENKÖTTER, N. TCHEBOTAREVA, S. ITO, K. MÜLLEN, T. BJÖRNHOLM, *Chemistry – a European Journal* **2001**, *7*, 4894.
- 75 Z. TOMOVIC, M. D. WATSON, K. MÜLLEN, *Angewandte Chemie – International Edition* **2004**, *43*, 755.
- 76 V. PALERMO, M. PALMA, Z. TOMOVIC, M. D. WATSON, R. FRIEDLEIN, K. MÜLLEN, P. SAMORÌ, *ChemPhysChem* **2005**, *6*, 2371.
- 77 K. J. KWAK, S. YODA, M. FUJIIHARA, *Applied Surface Science* **2003**, *210*, 73.
- 78 I. LEE, J. W. LEE, A. STUBNA, E. GREENBAUM, *Journal of Physical Chemistry B* **2000**, *104*, 2439.
- 79 H. SUGIMURA, N. SAITO, N. MAEDA, I. IKEDA, Y. ISHIDA, K. HAYASHI, L. HONG, O. TAKAI, *Nanotechnology* **2004**, *15*, S69.
- 80 H. SUGIMURA, K. HAYASHI, N. SAITO, N. NAKAGIRI, O. TAKAI, *Applied Surface Science* **2002**, *188*, 403.
- 81 B. STILLER, G. KNOCHENHAUER, E. MARKAVA, D. GUSTINA, I. MUZIKANTE, P. KARAGEORGIEV, L. BREHMER, *Materials Science & Engineering C – Biomimetic and Supramolecular Systems* **1999**, *8–9*, 385.
- 82 K. UMEDA, K. KOBAYASHI, K. ISHIDA, S. HOTTA, H. YAMADA, K. MATSUSHIGE, *Japanese Journal of Applied Physics Part 1 – Regular Papers Short Notes & Review Papers* **2001**, *40*, 4381.
- 83 H. YAMADA, T. FUKUMA, K. UMEDA, K. KOBAYASHI, K. MATSUSHIGE, *Applied Surface Science* **2002**, *188*, 391.
- 84 L. BÜRGI, T. J. RICHARDS, R. H. FRIEND, H. SIRRINGHAUS, *Journal of Applied Physics* **2003**, *94*, 6129.
- 85 C. H. LEI, A. DAS, M. ELLIOTT, J. E. MACDONALD, *Applied Physics Letters* **2003**, *83*, 482.
- 86 L. BÜRGI, R. H. FRIEND, H. SIRRINGHAUS, *Applied Physics Letters* **2003**, *82*, 1482.
- 87 L. BÜRGI, T. RICHARDS, M. CHIESA, R. H. FRIEND, H. SIRRINGHAUS, *Synthetic Metals* **2004**, *146*, 297.
- 88 K. MÜLLER, A. GORYACHKO, Y. BURKOV, C. SCHWIERTZ, M. RATZKE, J. KÖBLE, J. REIF, D. SCHMEISSER, *Synthetic Metals* **2004**, *146*, 377.
- 89 T. HASSENKAM, D. R. GREVE, T. BJÖRNHOLM, *Advanced Materials* **2001**, *13*, 631.
- 90 K. P. PUNTAMBEKAR, P. V. PESAVENTO, C. D. FRISBIE, *Applied Physics Letters* **2003**, *83*, 5539.
- 91 J. A. NICHOLS, D. J. GUNDLACH, T. N. JACKSON, *Applied Physics Letters* **2003**, *83*, 2366.
- 92 T. MIYAZAKI, K. KOBAYASHI, K. ISHIDA, S. HOTTA, T. HORIUCHI, H. YAMADA, K. MATSUSHIGE, *Japanese Journal of Applied Physics Part 1 – Regular Papers Short Notes & Review Papers* **2003**, *42*, 4852.
- 93 H. HOPPE, T. GLATZEL, M. NIGGEMANN, A. HINSCH, M. C. LUX-STEINER, N. S. SARICIFTCI, *Nanoletters* **2004**, *5*, 269.
- 94 C. SOMMERHALTER, T. W. MATTHES, T. GLATZEL, A. JÄGER-WALDAU, M. C. LUX-STEINER, *Applied Physics Letters* **1999**, *75*, 286.
- 95 H. O. JACOBS, H. F. KNAPP, A. STEMMER, *Review of Scientific Instruments* **1999**, *70*, 1756.
- 96 H. SUGIMURA, Y. ISHIDA, K. HAYASHI, O. TAKAI, N. NAKAGIRI, *Applied Physics Letters* **2002**, *80*, 1459.
- 97 K. OKAMOTO, K. YOSHIMOTO, Y. SUGAWARA, S. MORITA, *Applied Surface Science* **2003**, *210*, 128.
- 98 H. SUGIMURA, K. HAYASHI, N. SAITO, O. TAKAI, N. NAKAGIRI, *Japanese Journal of Applied Physics Part 2* **2001**, *40*, L174.

- 99 N. SAITO, K. HAYASHI, H. SUGIMURA, O. TAKAI, *Langmuir* **2003**, *19*, 10 632.
- 100 K. OKAMOTO, Y. SUGAWARA, S. MORITA, *Applied Surface Science* **2002**, *188*, 381.
- 101 S. SADEWASSER, M. C. LUX-STEINER, *Physical Review Letters* **2003**, *91*, 266 101.
- 102 N. NAKAGIRI, H. SUGIMURA, Y. ISHIDA, K. HAYASHI, O. TAKAI, *Surface Science* **2003**, *532*, 999.

Appendix: Practical Aspects of KPFM

Despite the simplicity of the macroscopic, classical Kelvin probe technique, KPFM needs a relatively complex setup. A second electrical feedback loop must be added to the conventional noncontact SFM setup in order to apply the V_{ac} (expressed also as V_c) potential to the tip; a sinusoidal wave generator has to be used to apply the V_{ac} bias, and a lock-in amplifier is needed to detect the ω component of the tip-sample electrostatic force interaction, as shown in Fig. 13.2. The tip must be conductive, and connected to the loop circuit by an ohmic contact with a low resistivity. The right frequency ω_{el} must be chosen, and tip oscillation at ω_{el} must not interfere with the mechanical oscillation of the cantilever at ω_{topo} used for topography acquisition. In contrast, if a lift-off setup is used, the same resonance frequency can be employed for both topography and KPFM detection, even if the larger tip-sample distance can reduce lateral resolution. The calibration of the signal has to be performed, and the macroscopic contributions of the cantilever on which the tip is mounted to the electrostatic interaction must be taken into account.

Different kinds of KPFM setups and experimental parameters have been employed, as summarized in Table A13.1.

Even though KPFM is a technique based on electrostatic forces, and thus its resolution is limited by the long-range nature of these forces, a high spatial resolution can be attained. A surprising atomic resolution of individual Si and Sb atoms has been achieved in ultra-high vacuum, for example, using Si tips cleaned by Ar-ion bombardment (Fig. A13.1) [97].

A major limitation in resolution is due to the charges induced by the AC voltage needed for the Kelvin probe measurements [33]. The resulting “artifact” can be detected through the 2ω -signal [100]. The local effect of the electrostatic interactions can be so strong to influence even the topography measurement, introducing an error in the SFM height map [100, 101] and influencing the phase of the tip’s mechanical oscillation [28].

Another issue to be considered in KPFM experiments, in particular those on photoactive systems, is the effect of the laser light used to measure the SFM cantilever deflection; it can give rise to a significant photovoltage on the surface, and thus introduce a systematic error in the measurements [62, 63].

A useful procedure for KPFM calibration can be found in ref. 95, a report on a systematic study of KPFM resolution dependence on tip composition, AC signal phase, and loop gain parameters. Rapid changes in the KPFM signal along the slow scan axis can be observed due to variations in the ϕ value of the tip, as a con-

Table A13.1 Summary of representative KPFM experiments and details of the experimental conditions. The tip's material, cantilever spring constant, frequency used for topographic and electrical measurement and value of the AC voltage applied to the tip are listed.

Experiment	Tip material	Cantilever spring constant k [N m^{-1}]	Measurement frequency [KHz]		V_{ac} [V]	Ref.
			ω_{topo}	ω_{el}		
KPFM on organic transistors	Pt/Ir on Si	2.8	75	0.5	0.5	47
	Si	–	80	15	1	91
	Pt on Si	–	70	3	1	92
KPFM on inorganic solar cells	Si	3	70	350	0.1	66, 94
KPFM on metals	Au on Si	20	532	534	2	12
	Ni/Cr	10	83	85	–	–
	Si	–	250	250	–	95
KPFM on p–n junction	Au on Si	1.8	27.5	25	2	96
Carrier diffusion length measurements on p–n junction	Si	–	90	20	–	53
FM-KPFM on p–n junctions in vacuum	amorphous C on Si	–	34	195	–	15
2D surface dopant profiling	tungsten, Si Au on Si	–	90–500	100	–	49
Atomic-level KPFM on Si in UHV	ion-sputtered Si	35	167	1	1	97
KPFM on nanotubes	C nanotube	–	$29 + \xi^*$	$29 - \xi$	10	61
Hi-res KPFM on SAM	Pt/Ir on Si	30	300	1	2	70
KPFM on patterned SAM	Au on Si	–	27	25	2	98
KPFM on SAM	Au on Si	–	21	5	2	99
EFM on LB	Pt/Ir on Si	–	300	300	–	89
KPFM on DNA	Au on Si	1.6	24	–	–	77
EFM on nanocrystals	Pt/Ir on Si	1.2	65	0.4	3	25
Quantitative EFM on organics	Si	–	302	302	–	29
KPFM on nanodots	Cr on Si	1.8	24	–	10	55

*Where ξ is a small finite quantity.

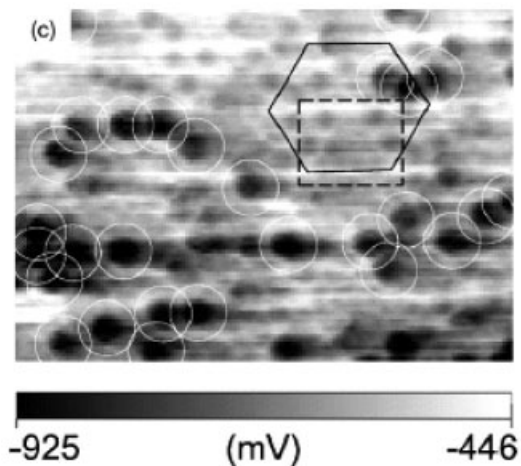


Fig. A13.1 CPD image of Sb atoms on Si(111) obtained with NC-SFM/KPFM. Scan size = $121 \times 85 \text{ \AA}^2$. Two kinds of adatoms can be distinguished (with permission from [97]).

sequence of material loss or acquisition [70]. Furthermore, the high resistance of the organic sample can lead to surface charging, with abrupt changes in the measured work function (Fig. A13.2) [64].

Since the KPFM requires a conductive tip, highly doped semiconductors or even metals are employed. The most widely used tips are made of silicon, either highly doped or coated with metals such as gold [49], gold and chromium [56], platinum [95], platinum/iridium [25, 48], or rhodium [55]. Carbon nanotube probes have also produced a good resolution in KPFM, due to their regular electronic structure and high conductivity [58, 61].

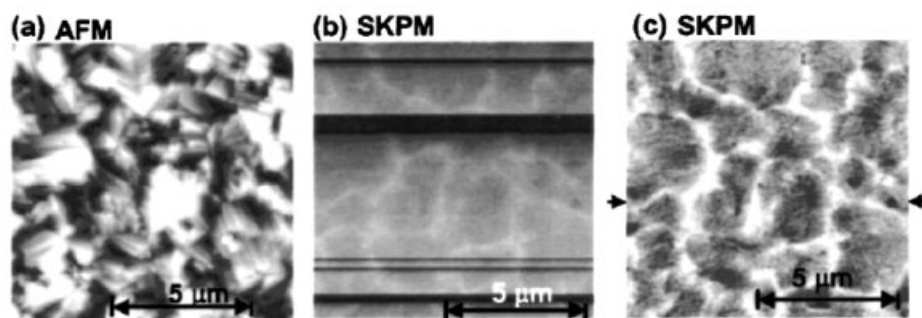


Fig. A13.2 (a) SFM and (b) corresponding KPFM image of CIS film with 0% Ga content; (c) The KPFM image of (b) after a background correction (with permission from [64]).

If coated tips are used, the metal coating often exhibits poor stability, and can be lifted off during the scan, leading to a change in the work function of the reference electrode during the measurement. An irregular metal coating on the tip can even induce a strong dependence of the measured potential on tip–sample distance z [34].

In the case of uncoated tips, a good ohmic contact is needed to apply the V_{ac} and V_{dc} voltage to the SFM silicon cantilever, otherwise a Schottky junction is obtained and asymmetries in the applied potential and band bending are observed. The optimization of the contact resistance between the silicon tip and the metallic tip holder has been achieved using an InGa alloy or a silver paste to make the contact ohmic [95]. In KPFM the tip–sample capacitance and the contact resistance define the time delay between the actual tip potential and the compensating, externally applied, potential. For the tips used in the experiment described in ref. 95, the total tip–sample capacitance was 0.6 fF at a 15 nm tip–sample separation, and the time constant $\tau = R \cdot C$ resulted ~ 1.3 ps using the silver paste. Thus the silver paste contact is sufficient for KPFM applications, since this time constant is much smaller than the periodicity of the AC driving voltage $1/\omega = 1/250$ kHz ~ 4 μ s ($\omega =$ resonance frequency of the cantilever). Other groups obtained good ohmic contacts and symmetric potential measurements simply by using highly doped silicon tips [34].

The great sensitivity of KPFM to the electronic structure of surfaces makes it very sensitive to contamination. Even atmospheric humidity can reduce KPFM resolution, forming an adsorbed water layer which shields the surface charge. This shielding is particularly great for hydrophilic surfaces and humid environments [96, 102]. In order to reduce this shielding effect, measurements can be performed under vacuum or in a sealed chamber saturated with an inert gas, e.g., N_2 , He, etc. Moreover, in measurements carried out in an air atmosphere, the presence of trapped surface charges can affect KPFM images at low humidity (10% r.h.). Such charging effects become less prominent at high humidity (80% r.h.) [95]. Finally, it should be taken into account that uncoated Si tips, when used in air, exhibit on the surface a layer of native oxide, which alters the work function of the tip. This problem can be solved by working under UHV. In such a case the oxide layer can be removed by ion bombardment, leading to an improvement in the spatial and voltage resolution [97].

Part III
Other SPM Methodologies

14 Scanning Electrochemical Microscopy Beyond Imaging

François O. Laforge and Michael V. Mirkin

14.1 Introduction

Scanning electrochemical microscopy (SECM; the same abbreviation is also used for the device, i.e., the microscope) is a powerful tool for studying structures and processes in micrometer- and submicrometer-sized systems [1]. SECM can probe electron, ion, and molecule transfer, and other reactions at solid/liquid, liquid/liquid, and liquid/air interfaces [2]. This versatility allows for the investigation of a wide variety of processes, from metal corrosion to adsorption to metabolism of single living cells, as discussed in Section 14.5 below.

SECM employs an ultramicroelectrode probe (“tip”) to collect electrochemical information while approaching or scanning the surface of interest (“substrate”). The substrate may also be biased and serve as a second working electrode. An ultramicroelectrode (UME) can be defined as an electrode with at least one dimension reduced to a microscopic size [3]. Many different types of UME can be fabricated, e.g., microband electrodes, cylindrical electrodes, microrings, and disk-shaped and hemispherical electrodes. For reasons that will become apparent later in the chapter, disk geometry is preferred for SECM tips, though other shapes are sometimes used [4]. UMEs offer important advantages for electroanalytical applications, including (a) a greatly diminished ohmic potential drop in solution and double-layer charging current; (b) the ability to reach a steady state in seconds or milliseconds, which facilitates the extraction of useful parameters from experimental data; and (c) a small size allowing one to do experiments in microscopic domains.

The precise positioning capability, which makes high spatial resolution possible, gives SECM an important edge over other techniques employing UMEs, such as cyclic voltammetry, AC voltammetry, or chronoamperometry [5]. In this way, the SECM can produce a microstructures on a substrate, visualize its topography, and probe its chemical reactivity on a micrometer or nanometer scale. At the same time, SECM differs from other SPM techniques in its applicability to quantitative measurements (e.g., kinetic ones) through well-developed and rigorous electrochemical theory. The nature of the tip and the way it interacts with the substrate determine what information can be obtained in an SECM experiment. We will first

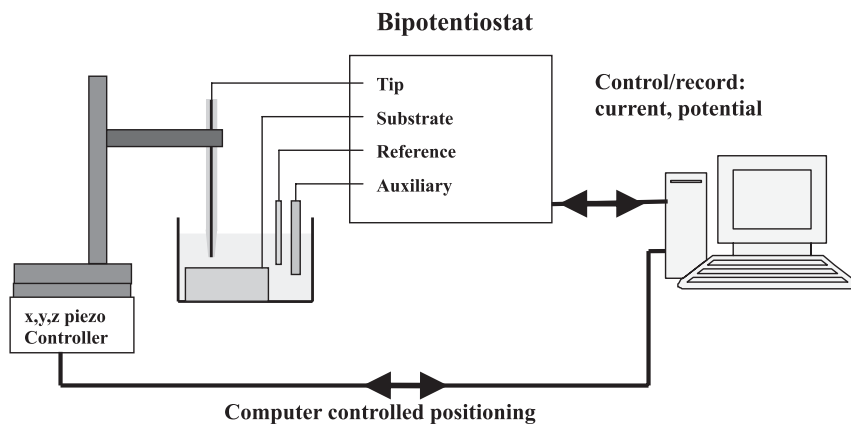


Fig. 14.1 Schematic diagram of the SECM instrument.

survey various modes of the SECM operation and their applicability to different types of measurements. Then, the SECM theory, approaches to data analysis, and some typical applications will be reviewed.

14.2 SECM Principle of Operation

Figure 14.1 is a schematic diagram of the basic SECM instrument employing an amperometric microprobe. A UME tip is attached to a 3D piezo positioner controlled by a computer, which is also used for data acquisition. A bipotentiostat (i.e., a four-electrode potentiostat) controls the potentials of the tip and/or the substrate versus the reference electrode and measures the tip and substrate currents. The SECM instrument is often mounted on a vibration-free optical table inside a Faraday cage to isolate it from environmental electromagnetic noise. With essentially the same setup, several SECM modes of operation can be realized, including feedback mode, tip generation/substrate collection (TG/SC) mode, and substrate generation/tip collection (SG/TC) mode.

14.2.1 Feedback Mode

In a feedback mode experiment, the tip is immersed in a solution containing a redox mediator (e.g., an oxidizable species, R). When a sufficiently positive potential is applied to the tip, the oxidation of R occurs via reaction (1) at a rate governed by the diffusion of R to the UME.

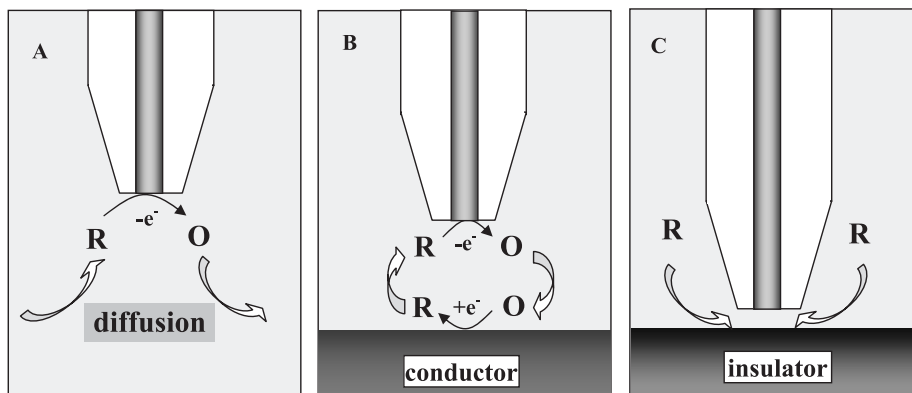


Fig. 14.2 Feedback mode of the SECM operation. (A) The UME tip is far from the substrate. (B) Positive feedback: species R is regenerated at the substrate. (C) Negative feedback: diffusion of R to the tip is hindered by the substrate.



If the tip is far (i.e., more than several tip diameters) from the substrate (Fig. 14.2A) the steady-state current, $i_{T,\infty}$, is given by Eq. (2), where F is the Faraday constant, n is the number of electrons transferred in the tip reaction, D and c are the diffusion coefficient and the bulk concentration of R, respectively, and a is the tip radius.

$$i_{T,\infty} = 4nFDca \quad (2)$$

When the tip is brought to within a few tip radii of a conductive substrate surface (Fig. 14.2B), the O species formed in reaction (1) diffuses to the substrate, where it may be reduced back to R in reaction (3).



This process produces an additional flux of R to the tip and hence “positive feedback”, i.e., an increase in tip current ($i_T > i_{T,\infty}$). The smaller the tip–substrate distance (d), the larger the tip current. When reaction (3) is rapid, $i_T \rightarrow \infty$ as $d \rightarrow 0$.

If the substrate is an inert electrical insulator, the tip-generated species, O, cannot react at its surface. At small d , $i_T < i_{T,\infty}$, because the insulator blocks diffusion of species R to the tip (“negative feedback”; Fig. 14.2C). The closer the tip to the insulator substrate, the smaller the i_T , with $i_T \rightarrow 0$ as $d \rightarrow 0$. Overall, the rate of mediator regeneration at the substrate determines the magnitude of the tip current, and conversely the measured dependence of i_T versus d (“approach curve”) provides information on the kinetics of the process at the substrate.

The rate of reaction (3) can be controlled by applying a suitable potential to the substrate by a potentiostat. Alternatively, the potential of a conductive substrate (E_s) may be determined by concentrations of redox species in solution without an external bias. For example, if the solution contains only the reduced form of the redox species, most of the substrate, which is usually much larger than the tip, is in contact with a solution of R. According to the Nernst equation, Eq. (4), in this case $E_s - E^\circ \ll 0$, where E° is the standard potential of the mediator.

$$E_s = E^\circ + \frac{RT}{nF} \ln \frac{c_O}{c_R} \quad (4)$$

14.2.2

Tip Generation/Substrate Collection

In the tip generation/substrate collection mode (TG/SC) experiment, the tip generates an electroactive species that diffuses across the tip-substrate gap to react at the substrate surface (Fig. 14.3). A TG/SC experiment includes simultaneous measurements of both tip and substrate currents (i_T and i_S). For a one-step heterogeneous electron transfer (ET) at steady state, these quantities are almost identical if d is not very large (the collection efficiency, i_S/i_T , is more than 0.99 at $d \leq 2a$). Under these conditions, the tip-generated species predominantly diffuse to the large substrate, rather than escaping from the tip-substrate gap. For a process with a coupled homogeneous chemical reaction, there may be large differences between i_S and i_T , and both quantities provide important kinetic information. If the

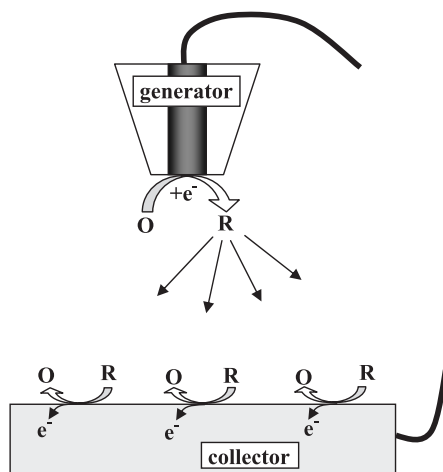


Fig. 14.3 Schematic representation of the TG/SC mode. The tip generates species R by reduction of O in solution; R diffuses toward the substrate and is reoxidized to O. Both tip and substrate currents are recorded.

reaction is slow, the process is diffusion-controlled, the i_T versus d curves follow the positive feedback theory, and $i_S/i_T \rightarrow 1$ at short separation distances. If the reaction is very fast, most species R get converted to electroinactive products before reaching the substrate; hence, there is a very low substrate current, and $i_S/i_T \rightarrow 0$. Between these two extreme cases, the homogeneous reaction kinetics can be determined by measuring the collection efficiency as a function of d [6].

14.2.3

Substrate Generation/Tip Collection Mode

Historically, the first SECM-type experiments were carried out to measure concentration profiles in the diffusion layer generated by a macroscopic substrate [7]. This type of measurement is now called substrate generation/tip collection (SG/TC). When the tip is moved through the thick diffusion layer produced by the substrate, the changes in i_T reflect local variations of the concentrations of redox species (Fig. 14.4). Ideally, the tip should not perturb the diffusion layer at the substrate. This is easier to achieve with a potentiometric tip, which is a passive sensor and does not change concentration profiles of electroactive species.

The collection efficiency in SG/TC mode is much lower than that in the TG/SC mode, and the steady state can be achieved only by using a micrometer-sized substrate. Other disadvantages of this mode are the high sensitivity to noise and the difficulty in controlling the tip/substrate separation distance.

Theoretical treatments for the SG/TC mode have been reported for a spherical cap or an embedded microdisk-shaped substrate that generates stable species and

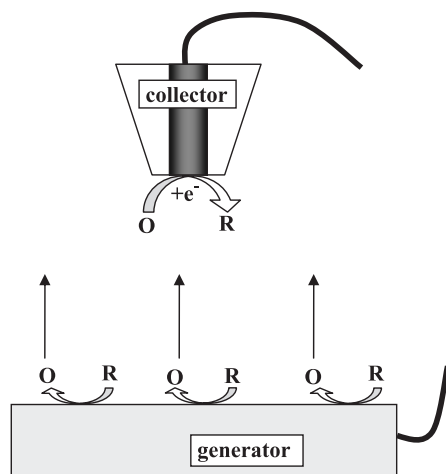


Fig. 14.4 Schematic representation of the SG/TC mode. O is electrogenerated at the substrate surface and collected at the tip. Both tip and substrate currents are recorded.

for a smaller tip collecting them [8]. This mode can be used for monitoring corrosion, enzymatic reactions, and other heterogeneous processes at the substrate surface.

14.3 Instrumentation

14.3.1

Tip

A typical SECM probe is an ultramicroelectrode sharpened to allow a closer approach to the substrate surface [9]. Several approaches to fabrication of SECM tips are available in the literature [1a, 10–13]. An established procedure involves heat sealing of a microwire or a carbon fiber in a glass capillary under vacuum and connecting it with silver epoxy to a larger copper wire on the back side. The sealed side of the probe is polished down to 50 nm alumina and then sharpened using coarse sandpaper to form a tip. The important parameters of the tip geometry are (1) the radius, a , of the conductive core; and (2) the total tip radius (i.e., the insulating sheath thickness plus the radius of the electroactive area), r_g . The dimensionless parameter $RG = r_g/a$ is normally not more than 10. This fabrication method does not require any expensive equipment, and it is widely used for the production of micrometer-sized tips.

Nanometer- and submicrometer-sized tips have been fabricated using different strategies. A simple way to produce nanometer-sized conical electrodes consists in etching a metal wire and then coating it with an insulator while leaving the apex exposed. For example, a Pt–Ir wire, diameter 125 μm , was etched in a solution of saturated CaCl_2 and HCl at about 20 V rms AC, then insulated by dipping the metal tip into molten Apiezon wax, and finally its very end was exposed using an STM [14]. Many types of coating have been tried, such as Apiezon wax [15], varnish [14b, 16], molten paraffin [17], silica coating [18], poly(α -methylstyrene) [19], polyimide [20], electropolymerized phenol [21], and electrophoretic paint [22].

Another fabrication method employs a micropipet puller [10]. Shao et al. [10a] used a laser puller to prepare glass-sealed Pt electrodes with radii ranging from 2 to 500 nm. They attempted to polish larger (>100 nm) electrodes and to characterize the tip geometry by a combination of SEM, steady-state voltammetry, and SECM; but the quality of the approach curves obtained was not high. A somewhat different approach to polishing of pulled submicrometer electrodes was proposed in ref. 10b. Recently, it was shown that a tip with a radius as small as ~ 15 nm can be polished on a lapping tape under video-microscopic control [10c]. The polished flat nanotips yield more reliable and reproducible data, and can be used for fast kinetic measurements.

The addition of an electromagnetic shield to the body of the tip can greatly reduce the stray capacitance. This is particularly useful for fast-scan voltammetry [23a] and high-frequency impedance experiments [23b].

14.3.2

Positioning

Similarly to other scanning probe microscopies, the SECM probe has to be moved in x , y , and z directions with a nanometer-scale precision. However, the travel distance required can be as long as a few hundred micrometers. Most SPM positioning devices are not suitable for such long scans. Also, a reasonable accuracy in the x and y directions has to be combined with a higher accuracy in z direction for the measurement of i_T-d curves. In one arrangement, inchworm motors are used for coarse traveling while a vertical PZT piezo pusher enables a finer control over short distances. Other combinations are possible, e.g., stepper motors for coarse positioning and close-loop positioners with optical encoders to control the distance precisely (this eliminates a backlash, but gives a slower response).

Unlike STM or AFM tips, which are sharp cones, a typical SECM tip is a conductive disk surrounded by a flat ring of insulating glass whose thickness is equivalent to several disk radii. Thus, the proper alignment of the tip with respect to the substrate surface is crucial. Unless the tip surface is flat and strictly parallel to the substrate plane, the insulator touches the substrate first and prevents the conductive disk from coming close to its surface. Special care must be given to the attachment of the tip to the translation stage and to mounting the substrate to facilitate the alignment.

14.3.3

Potentiostat

Many SECM experiments require the substrate to be biased. A bipotentiostat is used to control both the tip and the substrate potentials in Fig. 14.1. Unless transient measurements are to be made, the response of the bipotentiostat does not have to be fast. More importantly, it should be capable of measuring a broad range of current responses: a picoamp- (or even subpicoamp)-scale tip current, and a much higher current at a macroscopic substrate. For this reason, it is convenient to have several choices of preamplifiers/current-to-voltage transducers.

14.4

Theory

The quantitative SECM theory has been developed for various heterogeneous and homogeneous processes, and different tip and substrate geometries. In general, theoretical SECM dependencies can be generated by solving partial differential equations numerically. In some cases, analytical approximations allow easier generation of theoretical dependencies and analysis of experimental data. Several recent reviews focused on various aspects of the SECM theory [24]. Most of the theoretical results presented below concern SECM with a disk-shaped tip. The ap-

plications of non-disk tips (e.g., shaped as a cone or a spherical cap) are discussed in refs. [4] and [24c].

14.4.1

Analytical Approximations for Steady-State Responses

The solution of a diffusion problem for the most general case of two quasi-reversible ET processes occurring at the tip and substrate electrodes was obtained in the form of two-dimensional integral equations [25]. This solution applies to both transient and steady-state feedback experiments. Since transient SECM measurements are somewhat less accurate and harder to perform, most quantitative studies were carried out under steady-state conditions. The nonsteady-state SECM response depends on too many parameters to allow presentation of a complete set of working curves, which would cover all experimental possibilities. The steady-state theory is simpler and can often be expressed in the form of dimensionless working curves or analytical approximations.

14.4.1.1 Diffusion-Controlled Heterogeneous Reactions

The dimensionless steady-state current–distance curves were obtained numerically by Kwak and Bard [1b] for both insulating and conductive substrates assuming a diffusion-controlled mediator turnover, equal diffusion coefficients, and an infinitely large substrate (the current–distance curves for microscopic substrates can be found in ref. 25b).

More recently [13, 26], analytical expressions were derived for several RG values [Eqs. (5)–(7)]. Equation (5) with the parameter values listed in Table 14.1 fits within 1% the simulated dimensionless I_T – L data for a conductive substrate over the L interval from 0.04 to 10 (Fig. 14.5(a), upper curve) and for RG values between 1.1 and 10, where $L = d/a$ is the normalized tip/substrate distance.

$$I_T^C(L) = \frac{i_T}{i_{T,\infty}} = A + B/L + C \exp(D/L) \quad (5)$$

Table 14.1 Parameter values for Eq. (5).

RG	A	B	C	D
1.1	0.588 262 9	0.600 700 9	0.387 274 1	–0.869 822
1.5	0.636 836 0	0.667 738 1	0.358 183 6	–1.496 865
2.0	0.668 660 4	0.697 398 4	0.321 817 1	–1.744 691
10	0.744 993 2	0.758 294 3	0.235 304 2	–1.683 087
5.1	0.720 35	0.751 28	0.266 51	–1.620 9

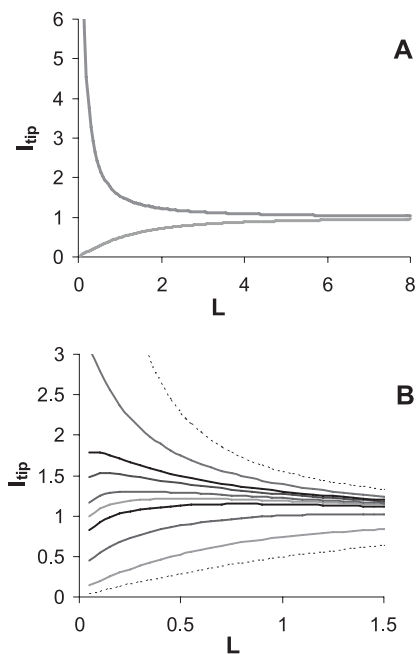


Fig. 14.5 Simulated SECM current vs. distance curves. (A) Pure positive (upper curve) and negative (lower curve) feedback. (B) Finite kinetics at the substrate. The κ values are, from bottom to top, 0.1, 0.4, 0.8, 1, 1.2, 1.6, 2.0, and 4.0. The lower and upper broken curves represent the insulator and conductor limits, respectively. (Adapted with permission from ref. 25b. Copyright 1992, American Chemical Society.)

For an insulating substrate, Eq. (6) with the parameter values listed in Table 14.2 is similarly accurate (Fig. 14.5(a), lower curve) over the same ranges of L and RG values.

$$I_T^{ins}(L) = \frac{i_T}{i_{T,\infty}} = \frac{1}{A + B/L + C \exp(D/L)} + \frac{EL}{F + L} \quad (6)$$

Another expression for the negative feedback is Eq. (7) [26b], with the parameter values listed in Table 14.3.

$$I_T^{ins}(L) = 1/[k_1 + k_2/L + k_3 \exp(k_4/L)] \quad (7)$$

Although Eq. (7) is not valid for small tip–substrate distances ($L \geq 0.2$ for all RG values, and $L \geq 2$ for RG = 1.11) it can be useful for $2 < RG < 10$, and for larger RG values that are unavailable in Table 14.2.

Table 14.2 Parameter values for Eq. (6).

RG	A	B	C	D	E	F
1.1	1.167 516 4	1.030 998 5	0.380 085 5	-1.701 797	0.346 376 1	0.036 741 6
1.5	1.003 595 9	0.929 427 5	0.402 260 3	-1.788 572	0.283 262 8	0.140 159 8
2.0	0.783 857 3	0.877 792	0.424 841 6	-1.743 799	0.163 843 2	0.199 390 7
10	0.457 182 5	1.460 423 8	0.431 273 5	-2.350 667	-0.145 437	5.576 895 2

By fitting an experimental current–distance curve to the theory [Eqs. (5)–(7)], one can determine the zero tip–substrate separation point ($L = 0$), which in turn allows the determination of L values essential for any quantitative SECM measurement.

If a small (submicrometer) tip is to be used in quantitative measurements, it is important to show that the metal surface is not recessed into the insulator. On the other hand, a recessed tip may be produced intentionally, e.g., for single-molecule detection [27]. Fan et al. [27b] simulated the approach curves for a recessed tip with the radius of the circular hole in the insulator equal to the disk radius. An analytical approximation for recessed tips with a hole in the insulator sheath which is different from the disk radius is also available [10a], though it has not been verified by comparison with simulated data.

The SECM feedback transients (i.e., tip current versus time dependencies for tip–substrate distances comparable with the tip radius) for a diffusion-controlled process were simulated and analyzed in ref. 28.

Table 14.3 Parameter values for Eq. (7).

RG	k_1	k_2	k_3	k_4	Error [%]	Validity range
1002	0.132 19	3.371 67	0.821 8	-2.347 19	<1.0	0.3–20
100	0.279 97	3.054 19	0.686 12	-2.759 6	<1.0	0.4–20
50.9	0.305 12	2.620 8	0.667 24	-2.669 8	<1.0	0.4–20
20.1	0.355 41	2.025 9	0.628 32	-2.556 22	<1.0	0.4–20
15.2	0.373 77	1.851 13	0.613 85	-2.495 54	<1.0	0.4–20
10.2	0.404 72	1.601 85	0.588 19	-2.372 94	<1.0	0.4–20
8.13	0.426 76	1.460 81	0.568 74	-2.285 48	<1.0	0.4–20
5.09	0.486 78	1.177 06	0.512 41	-2.078 73	<1.0	0.2–20
3.04	0.604 78	0.860 83	0.395 69	-1.894 55	<0.2	0.2–20
2.03	0.761 79	0.609 83	0.238 66	-2.032 67	<0.15	0.2–20
1.51	0.904 04	0.427 61	0.097 43	-3.230 64	<0.7	0.2–20
1.11	-1.465 39	0.272 93	2.456 48	8.995E-7	<1.0	2–20

14.4.1.2 Finite Kinetics at the Tip or Substrate

For finite heterogeneous kinetics at the tip and diffusion-controlled mediator regeneration at the substrate, an approximate Eq. (8) was obtained for I_T at any tip potential, assuming uniform accessibility of the tip surface (i.e., the current density is uniform over the entire tip surface) [29].

$$I_T(E, L) = \frac{0.68 + 0.78377/L + 0.3315 \exp(-1.0672/L)}{\theta + 1/\kappa} \quad (8)$$

Here $I_T(E, L) = i_T/i_{T, \infty}$, $\theta = 1 + \exp[nf(E - E^{o'})]D_O/D_R$, $\kappa = k^o \exp[-\alpha nf(E - E^{o'})]/m_O$, k^o is the standard rate constant, E is the tip potential, $E^{o'}$ is the formal potential, α is the transfer coefficient, and $f = F/RT$ (where F is the Faraday constant, R is the gas constant, and T is temperature), and the effective mass-transfer coefficient for SECM is given by Eq. (9).

$$m_O = 4D_O \frac{0.68 + 0.78377/L + 0.3315 \exp(-1.0672/L)}{\pi a} = \frac{i_T(L)}{\pi a^2 n F c} \quad (9)$$

One can see from Eq. (9) that at $L \gg 1$, $m_O \sim D/a$ (as for a microdisk electrode alone), but at $L \ll 1$, $m_O \sim D/d$, which is indicative of the thin-layer cell (TLC) type behavior. By decreasing the tip-substrate distance, the mass-transport rate can be increased sufficiently for quantitative characterization of fast ET kinetics, while preserving the advantages of steady-state methods, i.e., the absence of problems associated with ohmic drop, adsorption, and charging current.

At constant L , Eq. (8) describes a quasi-reversible steady-state tip voltammogram (if kinetics are fast, $\kappa \rightarrow \infty$, and Eq. (8) reduces to one for a Nernstian tip voltammogram). Such a curve can be obtained by scanning the potential of the tip while the substrate potential is held constant. More recent simulations [36] have shown that Eq. (8) is not very accurate and may yield underestimated k^o values. Equation (10) is a significantly better approximation, where $\kappa = \pi k^o a \exp[-\alpha n F (E - E^{o'}) / RT] / (4D_O I_T^c)$ and $I_T^c(L)$ is the normalized tip current for the same L and the diffusion-controlled positive feedback at a conductive substrate, as defined by Eq. (5).

$$I_T(E, L) = \frac{0.78377}{L(\theta + 1/\kappa)} + \frac{0.68 + 0.3315 \exp(-1.0672/L)}{\theta \left[1 + \frac{\pi}{\kappa \theta} \frac{2\kappa\theta + 3\pi}{4\kappa\theta + 3\pi^2} \right]} \quad (10)$$

The current-distance curves for an irreversible heterogeneous reaction occurring at the substrate while the tip process is diffusion-controlled can be calculated from Eqs (11) [30a], where I_T^c and I_T^{ms} are given by Eqs. (5) and (6), respectively, and I_S is the kinetically controlled substrate current; $\Lambda = k_f d/D$, k_f is the heterogeneous rate constant (cm s^{-1}), and $F(L, \Lambda) = (11/\Lambda + 7.3)/(110 - 40L)$.

$$I_T(L) = I_S \left(1 - \frac{I_T^{ins}}{I_T^c} \right) + I_T^{ins} \quad (11a)$$

$$I_S = \frac{0.78377}{L(1 + 1/\Lambda)} + \frac{0.68 + 0.3315 \exp(-1.0672/L)}{1 + F(L, \Lambda)} \quad (11b)$$

Figure 14.5(b) shows the family of I_T versus L working curves calculated from Eqs. (11a) and (11b) for different values of $\kappa = k_f a / D$. Equations (11a) and (11b) fit the numerical results within $\sim 1\text{--}2\%$ over the L interval from 0.1 to 1.5 and $-2 \leq \log \kappa \leq 3$.

The radius of the portion of the substrate surface participating in the SECM feedback loop can be evaluated as $r \cong a + 1.5d$ [25b]. Thus, at small tip–substrate separations (e.g., $L \leq 2$), a large substrate behaves as a virtual UME of a size comparable with that of the tip electrode. The SECM allows local kinetics to be probed on a small portion of the macroscopic substrate with all of the advantages of microelectrode measurements [3].

Although Eq. (11) was derived for one-step heterogeneous ET reactions, it was shown to be applicable to more complicated substrate kinetics (e.g., liquid/liquid interfacial charge transfer [30], ET through self assembled monolayers [31], and mediated ET in living cells [32]). The effective heterogeneous rate constant obtained by fitting experimental approach curves to Eq. (11) can be related to various parameters which determine the rates of those processes, as discussed in the references cited.

14.4.1.3 SG/TC Mode

Unlike feedback mode of the SECM operation, where the overall redox process is essentially confined to the thin layer between the tip and the substrate, in SG/TC experiments the tip travels within a thick diffusion layer produced by the large substrate. A consistent theoretical treatment was proposed only for a steady-state situation when a small substrate (a microdisk or a spherical cap) generates or consumes the species of interest. The concentration of such species can be measured by an ion-selective (potentiometric) microprobe as a function of the tip position. The concentration at any point can be related to that at the source surface. For a microdisk substrate the dimensionless expression is Eq. (12) [33].

$$c(R, Z)/c(0, L) = \frac{2}{\pi} \tan^{-1} \left[\frac{2}{R^2 + Z^2 - 1 + \sqrt{(R^2 + Z^2 - 1)^2 + 4Z^2}} \right]^{1/2} \quad (12)$$

A somewhat more complicated expression was derived to relate the concentration distribution in the diffusion layer to the flux at the source or sink surface [8b].

One can also evaluate the relative change in the rate of a heterogeneous reaction at the substrate by measuring the concentration of the reaction product at the tip. In this setup, the tip is positioned at a fixed distance from the substrate, and the time dependence of concentration is measured. This simpler approach is based on the proportionality between the heterogeneous reaction rate and the product

concentration. It is most useful when the substrate flux cannot be measured directly (e.g., when the substrate reaction is not an electrochemical process) [34].

Martin and Unwin developed quantitative treatment for amperometric SG/TC experiments with the separation distance of the same order of magnitude as the tip radius [35]. Although the chronoamperometric current at a macroscopic substrate does not exhibit any steady state, the collection current at the tip electrode at long times reaches a stable, time-independent value. The time-dependent theory for a diffusion-controlled process was illustrated by a number of three-dimensional concentration profiles and working curves covering a range of experimental conditions.

14.5 Applications

14.5.1

Heterogeneous Electron Transfer

The kinetics of electron transfer is of primary importance for most electrochemical applications, ranging from fuel cells and batteries to biosensors to solar cells to molecular electronics. An important advantage of SECM for heterogeneous kinetic measurements is the high mass-transfer rate, allowing one to study fast reactions under steady-state conditions.

14.5.1.1 Electron Transfer Kinetics at Solid/Liquid Interfaces

The first application of SECM to study ET kinetics at the substrate surface was reported by Bard et al. [25b], who measured the rate of irreversible oxidation of Fe^{2+} at the glassy carbon (GC) electrode. Using the feedback mode, Fe^{3+} was reduced at the carbon fiber tip in 1 M H_2SO_4 electrolyte solution [Eq. (13a)], and Fe^{2+} was oxidized at the GC substrate [Eq. (13b)].



The tip was biased at the potential at which the reduction of Fe^{3+} was diffusion-controlled. By changing the substrate potential over a wide range, the oxidation rate constant, k_f could be varied by several orders of magnitude. The current-distance curves obtained at different substrate potentials (Fig. 14.6A) reflect the gradual change in substrate behavior between a “perfect” conductor, when all the Fe^{2+} species coming from the tip are reoxidized at the substrate (upper curve), and an insulator, when the substrate reaction rate is immeasurably slow (lower curve). The whole family of I_T - L curves given in Fig. 14.6(A) was fitted to the theory and yielded Butler-Volmer-type potential dependence of the rate constant (Fig. 14.6B) with the kinetic parameter values, $k^\circ = 2 \times 10^{-5} \text{ cm s}^{-1}$ and $\alpha = 0.69$, in good agreement with literature data.

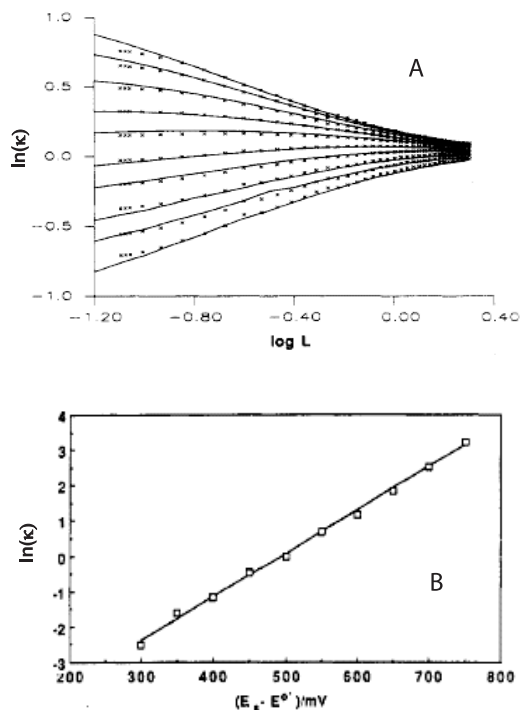


Fig. 14.6 (A) SECM log (current–distance) curves for the $\text{Fe}^{\text{III}}/\text{Fe}^{\text{II}}$ system (\times). The tip electrode (carbon fiber, $5.5\ \mu\text{m}$ radius) was held at a potential of $-600\ \text{mV}$, while the GC substrate electrode was held at various potentials, 300 – $750\ \text{mV}$, positive relative to the formal potential (with $50\ \text{mV}$ increments). The solid curves are the corresponding best theoretical fits to the data, obtained with various normalized rate constant values (indicated in B). (B) Plot of normalized rate constant κ versus substrate overpotential ($E_s - E^\circ$). (Reprinted with permission from ref. 25b. Copyright 1992, American Chemical Society.)

The approaches developed for studies of simple, one-step ET kinetics at a uniformly reactive substrate were later extended to investigate more complicated systems that could involve multistep processes and parallel reaction pathways. For example, in a recent study of ET at self-assembled monolayers (SAMs) [31], SECM was used to measure independently the rates of ET mediated by monolayer-attached redox moieties and direct ET through the film, as well as the rate of the bimolecular ET reaction between the attached and dissolved redox species. The SAMs were assembled on the evaporated-gold electrodes from a solution containing a mixture of *n*-alkylthiol and ferrocenyl-alkanethiol. Several different situations were considered (Fig. 14.7): the monolayer either contained redox centers (Fig. 14.7A) or simply acted as a blocking layer (Fig. 14.7B). In case (A), ET occurred via a bimolecular reaction between dissolved redox species generated at the tip (R) and redox centers attached to the SAM (M^+), which was followed by the electron

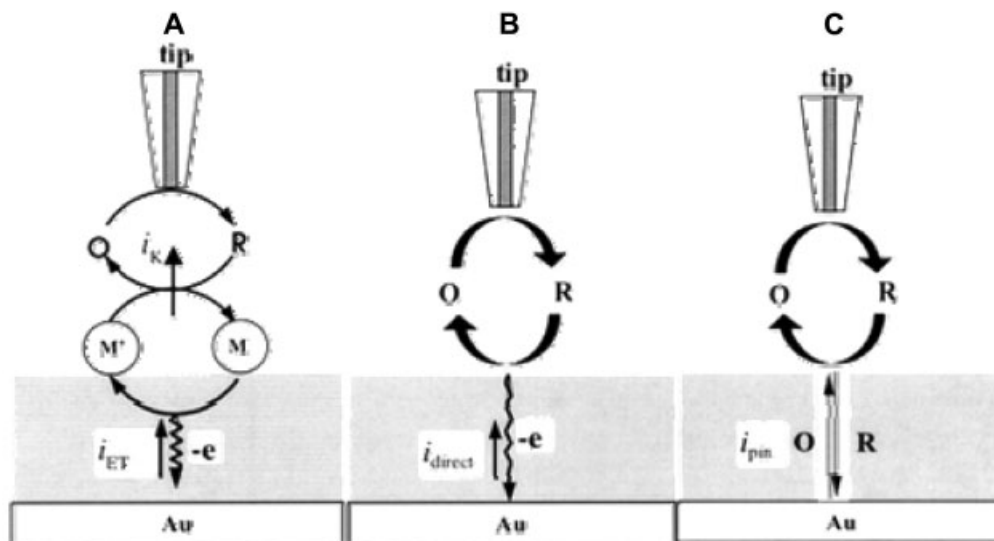


Fig. 14.7 Schematic view of the processes involved in the SECM measurements of ET across an electroactive SAM: (A) mediated ET; (B) direct electron tunneling through the monolayer; (C) ET through pinholes. (Reprinted with permission from ref. 31. Copyright 2004, American Chemical Society.)

tunneling; but in case (B) it occurred by direct tunneling between the dissolved species, R, and the electrode. Finally, the charge transfer may occur through pinhole defects in the film (Fig. 14.7C). The possibility of measuring the rates of all of these processes and analyzing the combinations of different competing pathways for the long-distance ET was demonstrated. The upper limits for the electron tunneling and bimolecular rate constants measurable by the technique developed were given as $\sim 10^8 \text{ s}^{-1}$ and $\sim 5 \times 10^{11} \text{ mol}^{-1} \text{ cm}^3 \text{ s}^{-1}$, respectively.

Kinetic parameters for very fast oxidation of ferrocene in acetonitrile were determined by fitting steady-state tip voltammograms to Eq. (8) [36]. The reproducible standard rate constant value ($3.7 \pm 0.6 \text{ cm s}^{-1}$) was obtained at different tip-substrate distances. While the mass transfer rate increased with a decrease in the tip-substrate separation, the heterogeneous rate constant and transfer coefficient remained constant within the range of experimental error. In this way, one can check the validity of the experimental results and the reliability of the kinetic analysis.

14.5.1.2 Liquid/Liquid ET Kinetics

Heterogeneous charge-transfer reactions at the liquid/liquid and liquid/membrane interfaces, e.g., electron-transfer, and simple and facilitated ion transfers (ITs), are of fundamental importance for many biological and technological systems. The experimental problems that are typical for kinetic measurements at the metal/elec-

trolyte interface are even more severe in the case of an interface between two immiscible electrolyte solutions (ITIES). With the SECM, one can separate interfacial ET quantitatively from IT processes and minimize resistive potential drop and double-layer charging effects, which hampered previous studies of charge-transfer reactions at the ITIES [37]. One of the motivations for SECM studies was to check the applicability of conventional ET theories to this system.

When SECM is used to probe ET at the ITIES, a UME tip is placed in the upper liquid phase (e.g., organic solvent) containing one form of the redox species (e.g., the reduced form, R_1). With the tip held at a sufficiently positive potential, R_1 reacts at the tip surface to produce the oxidized form of the species, O_1 . When the tip approaches the ITIES, the mediator can be regenerated at the interface via the bimolecular redox reaction between O_1 in the organic phase (o) and R_2 in the aqueous phase (w) [Eq. (14)] and i_T increases with a decrease in d (positive feedback).



The kinetics of such a reaction can be evaluated from approach curves.

In most SECM experiments, a nonpolarizable ITIES was poised by the concentrations of the potential-determining ion providing a constant driving force for the ET process [37, 38]. The interfacial charge transfer is a multistep process. Under SECM conditions, the following four stages of the overall process may influence the tip current (Fig. 14.8): organic mediator diffusion between the tip and the ITIES; interfacial reaction [Eq. (14)]; diffusion of R_2 in the bottom phase; and charge compensation by IT. The electric current across the ITIES (i_S) caused by this multistage serial process can be expressed as Eq. (15) [30a], where i_T^C , i_{ET} , i_d , and i_{IT} are the characteristic limiting currents for the above four steps, respectively.

$$\frac{1}{i_S} = \frac{1}{i_T^C} + \frac{1}{i_{ET}} + \frac{1}{i_d} + \frac{1}{i_{IT}} \quad (15)$$

Any of those steps can be rate-limiting, but the concentration of R_2 is usually made high enough to exclude the possibility of diffusion limitations in the bottom phase. By using sufficiently high concentrations of the common ion (e.g., ClO_4^-) in both phases, one can ensure that IT is also fast. Under these two conditions, the two last terms in Eq. (15) are negligible, and Eq. (15) is essentially reduced to Eq. (11). The effective heterogeneous rate constant can be obtained by fitting experimental I_T - L curves to the latter equation [30a]. Barker et al. [39] carried out extensive simulations and described the effect of diffusion in the bottom phase on the shape of the approach curve. This theory can be useful when the ratio of the mediator concentrations in the bottom and the top phases cannot be sufficiently large to make the third term in Eq. (15) negligible.

Tsionsky et al. [38] studied the electron transfer between zinc porphyrin dissolved in the organic phase and different aqueous redox species (e.g., $\text{Ru}(\text{CN})_6^{4-}$, $\text{Fe}(\text{CN})_6^{4-}$, or V^{2+}) at the water/benzene interface. The results were in agreement with the main predictions of existing ET theory. The effective heterogeneous rate

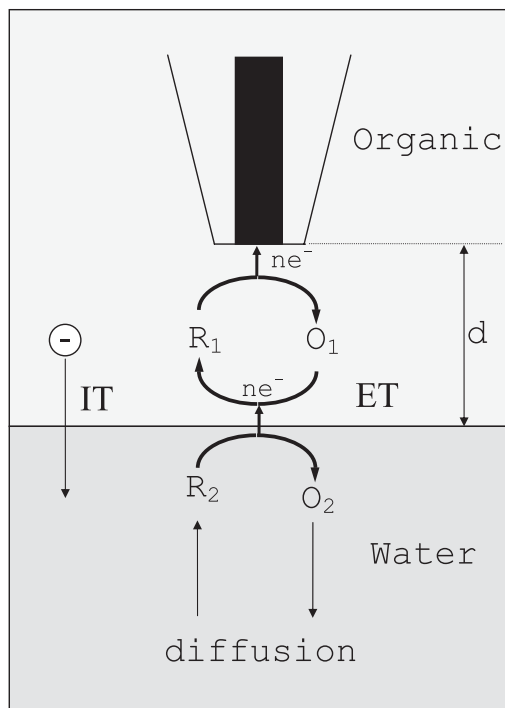


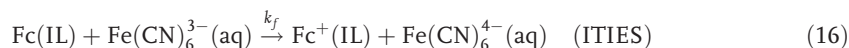
Fig. 14.8 Schematic diagram of ET at the liquid/liquid interface under SECM conditions. Electroneutrality is maintained by transfer (IT) of the common ion (shown as an anion) across the interface.

constant of ET reaction between ZnPor^+ and $\text{Ru}(\text{CN})_6^{4-}$ evaluated from the i_T - d curves was directly proportional to the concentration of $\text{Ru}(\text{CN})_6^{4-}$ in aqueous solution, and the $\log k_f$ versus $\Delta_w^\circ\phi$ dependence (Tafel plot) was linear with a transfer coefficient of $\alpha = 0.5$. Similar approaches were used to probe other ET reactions [40].

SECM studies of the ITIES can also be carried out at an externally biased polarizable ITIES [41]. In this case the applied interfacial voltage should be within the polarization window, where almost no current flows across a macroscopic liquid/liquid interface. The tip reaction changes the concentrations of redox species in a microscopic volume near the phase boundary and induces a small current across a micrometer-sized portion of the ITIES. An advantage of such an approach is in a potentially wider range of interfacial voltages available for the ET study (as compared with those at a nonpolarizable interface). The main disadvantage is the possibility of concurrent ion-transfer reactions being induced by the external voltage.

Recently [42], the ET was probed at the ITIES formed between water and a hydrophobic ionic liquid (IL), 1-octyl-3-methylimidazolium bis(trifluoromethylsulfo-

nyl)imide. Ferrocene was dissolved in the ionic liquid and ferrocyanide in the aqueous phase. The tip was immersed in the aqueous phase. Ferricyanide, electrogenerated at the tip, diffused toward the interface, where it was reduced by ferrocene [Eq. (16)].



The interfacial potential drop at the nonpolarizable ITIES was controlled by varying the concentration of either the cation or the anion of the ionic liquid in the aqueous phase. The kinetics of interfacial ET followed the Butler–Volmer equation, and the measured bimolecular rate constant was much larger than that obtained at the water/1,2-dichloroethane interface.

Interfacial ET reactions between monolayer protected gold clusters (MPCs) dissolved in 1,2-dichloroethane and aqueous redox species were also studied by SECM [43]. The heterogeneous rate constant was measured for ET between organic, soluble Au₃₈ clusters and an aqueous IrCl₆²⁻ oxidant [43b]. The Au cluster cores, protected with a shell of phenylethylthiolate ligands, were sufficiently small ($d \sim 1.1$ nm) to exhibit molecule-like redox activity. Accordingly, the evaluation of the rate constant at the nonpolarizable liquid/liquid interface was accomplished by the approach discussed above, which was originally developed for bimolecular ET reactions between conventional redox entities.

14.5.2

Experiments Employing Nanoelectrodes

Most SECM experiments published to date have employed micrometer-sized UME tips. Such probes are easy to fabricate from commercially available microwires, and to polish in order to ensure accuracy and reproducibility of their electrochemical responses. However, smaller tips offer important advantages for various applications such as kinetic measurements, high-resolution studies of biological systems, or single-molecule experiments.

The fabrication of nanoelectrodes is challenging because of the difficulties in controlling and characterizing the electrode geometry. Ideally, the electrode surface should be polishable to ensure the reproducibility of the data obtained with the same tip. Most nanotips reported to date have been conical and not polishable. Such tips are not very useful for feedback mode experiments. They were mostly employed in single-molecule experiments, for thin film penetration, and as SECM-AFM tips.

In a single-molecule experiment, Fan and Bard [27] used a Apiezon wax-sealed Pt/Ir tip of ~ 15 nm diameter. The active tip area was slightly recessed into the insulating sheath, so that, at small tip–substrate distances, solution was trapped in a nanometer-sized wax pocket between two electrodes. When such a tip was held at ~ 10 nm from the indium–tin oxide substrate, the picoamp-range tip current exhibited slow (of the order of tens of seconds) fluctuations. The shape of the current–time response was markedly different from that measured at the same

tip far from the substrate and from the tunneling current between the tip and the substrate observed with no electroactive species present in solution. Although the signal was noisy, the tip current reproducibly showed peaks of 0.7 and 1.4 pA corresponding to the trapping of one and two electroactive molecules respectively, and periods of essentially zero average current between them. When the tip potential was swept linearly, the stochastic process produced well-defined steady-state voltammograms with the half-wave potential expected for the redox mediator employed.

Nanometer-sized tips can be used to penetrate a microstructure, e.g., a submicrometer-thick polymer film containing fixed redox centers or loaded with a redox mediator, and extract spatially resolved information (i.e., a depth profile) about concentrations, and kinetic and mass-transport parameters [44]. With the tip inside the film, relatively far from the underlying conductor or insulator, solid-state voltammetry at the tip can be carried out similarly to conventional voltammetric measurements in solution. At smaller distances, the tip current either increases or decreases depending on the rate of mediator regeneration at the substrate. If the film is homogeneous and not very resistive, the current–distance curves are similar to that obtained in solution. In this way, the kinetic parameters, diffusion coefficient value, and formal potential for $\text{Os}(\text{bpy})_3^{2+}$ oxidation in Nafion were extracted from steady-state voltammograms at a nanometer-sized conical tip [44a]. Direct measurements of the film thickness ($2180 \pm 50 \text{ \AA}$) have also been carried out by recording the tip current as the tip was moved from solution into a polymer phase and was ultimately brought into contact with the underlying metal. For poly(vinylferrocene), the depth profile of film resistance was obtained by scanning the tip across a layer 300 nm thick [44b].

Several groups have been working on the development of SECM-AFM techniques [45a]. Figure 14.9 shows two different kinds of SECM-AFM probes. The first type (Fig. 14.9A), called a conducting-AFM probe (C-AFM), can be used to ac-

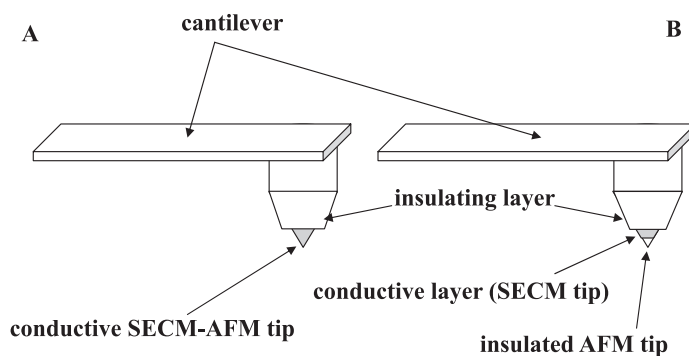


Fig. 14.9 (A) Conducting and (B) nonconducting SECM-AFM tips. (A) The SECM and the AFM tips are made from the same conducting material. (B) The AFM tip is insulated to prevent direct electrical contact with the conductive substrate surface.

quire information about the reactivity of a nonconductive substrate. The probe in Fig. 14.9(B) is suitable for conductive substrates: the insulation of the AFM tip prevents direct electrical contact between its conductive core and the substrate. Nonconductive crystal dissolution [46] have been studied with C-AFM probes. The probe was first used amperometrically to induce crystal dissolution (see Section 14.5.3) and the resulting changes in topography were imaged in the AFM regime. Diffusion through single nanoscale pores has also been probed by a C-AFM tip [47].

The SECM-AFM combination is most useful for imaging substrates of complex topography and variable reactivity. When the tip is scanned laterally above the substrate, the image obtained reflects both the topography of the substrate and the distribution of its chemical reactivity. This makes the data interpretation difficult if no *a priori* information on the substrate topography is available. By maintaining a constant distance between the substrate and the electroactive part of the tip in the AFM contact mode, the electrochemical information can be deconvoluted from the substrate topography.

Modern nanofabrication techniques, e.g., electron beam lithography (EBL) and focused ion beam (FIB) lithography, have been used to produce AFM-SECM nanotips. Kranz et al. [45b] employed a nonconductive SECM-AFM electrode to study enzyme activity in the AFM contact mode. They obtained deconvoluted images of the activity and the topography of a micropatterned sample with immobilized enzyme spots.

14.5.3

Surface Reactions: Corrosion and Dissolution of Ionic Crystals

SECM is well suited for high-resolution studies of metal corrosion in aqueous environments. The studies reported have been mostly focused on (a) detection of small pits and pit precursors, i.e., electrochemically active sites on which pits nucleate in the course of an experiment; (b) monitoring concentration profiles of the corrosion participants and products; and (c) the use of the tip to induce the pit formation. Below, there are a few examples of such studies.

The precursor sites for pit formation on the surface of oxide-covered titanium foil were first detected using SECM by Casillas et al. [48]. The feedback mode of SECM was used to visualize a few microscopic domains of intense faradic activity. The tip process was the reduction of Br_2 to Br^- , and Br_2 was regenerated via electrooxidation of bromide on the TiO_2 surface. After determining the positions of the active sites, the pits on the surface were nucleated by application of a more positive potential to the substrate. It was found for the first time that the pit nucleation occurs preferentially at surface sites of high electrochemical activity. The values determined for the typical active-site diameter (about 10–50 μm) and density (about 20–30 sites per cm^2) showed that active sites represent only a small fraction ($\sim 0.04\%$) of the TiO_2 surface. Higher-resolution maps and more information about conductivity of the oxide film on titanium were obtained later by using the combination of SECM with conducting AFM [49].

Wipf [50a] used SECM to initiate and image active corrosion pits on stainless steel and aluminum samples. Chloride ions were produced at a tip through the reduction of trichloroacetic acid [Eq. (17)].



The electrogenerated Cl^- ions initiated a single corrosion pit at the substrate surface. The recorded substrate current spikes were consistent with initiation, growth, and repassivation of such pits. The probability of successful pit generation was shown to decrease with the increase in the passivating layer growth time [50b]. The pitting precursor sites in the passive layer were also detected and ascribed to defects associated with grain boundaries. The presence of pitting precursors was correlated with current fluctuations at the tip observed before passive layer breakdown occurred. A similar observation was made by Zhu and Williams for type 304 stainless steel corrosion in dilute chloride solutions [51].

The oxidizable product of iron corrosion (presumably Fe^{2+}) can be collected at the tip [51]. In this way, the spatial distribution of the corrosion current was mapped by scanning the tip over the growing pit. Corrosion of pure iron was also monitored using the GC mode of SECM [52]. By applying suitable potentials to the tip, the concentration profiles of species participating in the surface oxidation reaction could be determined independently. Fe^{2+} ions generated by the oxidation of iron metal were oxidized to Fe^{3+} at +0.6 V versus Ag/AgCl while O_2 was reduced at -0.7 V.

An original SG/TC scheme was used by Janotta et al. [53] in their study of the corrosion of protected zinc-selenium waveguides in harsh acidic environments. To detect corrosion sites due to cracks in the diamond-like carbon coating of the waveguide they used a Au/Hg amalgamated UME and performed anodic stripping voltammetry in OSG/TC mode [54], leading to very sensitive detection levels of the corrosion products.

Like metal corrosion, the initial stage of dissolution of ionic solids involves the formation of a microscopic pit. These processes are of importance in biology (bone resorption and remodeling) and environmental science (calcite, mineral dissolution). Previously, dissolution kinetics has been deduced from bulk concentration changes, e.g., in stirred suspensions. The SECM allows direct monitoring of the interfacial undersaturation as well as measurements at single crystal surfaces with micrometer spatial resolution [55].

The investigation of dissolution of ionic solids by SECM is based on the use of the UME tip to oxidize or reduce the species of interest in solution near the crystal surface [55]. If this species is one of the crystal components, the depletion of its concentration in the solution gap between the tip and the substrate induces crystal dissolution. Similarly to the induced desorption experiments, this process produces an additional flux of electroactive species to the tip. The rate of the substrate reaction in this case is given by Eq. (18) [55a], where j is the flux of dissolving species, k_n is the rate constant, n is the reaction order, and σ is the undersaturation produced by the tip reaction.

$$j = k_n \sigma^n \quad (18)$$

In this way, heterogeneous reaction rates were measured and reaction orders determined for dissolution of different salts, e.g., the (100) face of copper sulfate pentahydrate [55a] and the (010) face of potassium ferrocyanide crystal [55b].

The spatial distribution of dissolution activity can also be imaged by scanning the SECM tip over the surface. Macpherson and Unwin [55c] mapped the dissolution rate around a single pit on the surface of potassium ferrocyanide trihydrate. An increase in tip current near the edge of the pit indicated that the local dissolution rate there was more rapid than for the planar surface. Higher spatial resolution, sufficient to observe directly the unwinding of screw dislocations on the surface, was achieved using a combined AFM/SECM probe where the dissolution was initiated on the SECM scale by the faradic tip current, but with simultaneous AFM imaging of the KBr crystal surface [46]. The same group obtained more detailed information on the surface processes involved in dissolution of calcite by using the combined SECM-AFM technique [55g].

14.5.4

Biological Systems

14.5.4.1 Single-Cell Measurements

The applications of SECM to studies of biological cells include topographic imaging of living cells, mapping concentration profiles and fluxes of various biologically important substances in the proximity of immobilized cells, and feedback mode investigations of redox reactivity and transmembrane charge-transfer processes [56].

Tsionsky et al. [57] used SECM to study the leaves of a plant, *Tradescantia fluminensis*. They imaged the topography and probed the photoelectrochemistry of single guard cells. Liebetrau et al. [58a] used SECM in the negative feedback mode to image living neurons (PC12). They were able to monitor the growth of narrow (1–2 μm wide) neurites after the addition of nerve growth factor to the medium to induce PC12 differentiation into neuron phenotypes (Fig. 14.10). This work also showed that SECM combined with traditional voltammetric and amperometric techniques can help elucidate neurotransmitter dynamics. In a later report from the same group [58b], a major improvement in the image quality was achieved using the constant-impedance mode of imaging.

Matsue's group mapped oxygen fluxes at the cell surface associated with respiration of various kinds of cells and photosynthesis [59]. By measuring the rate of oxygen consumption, the authors addressed a number of biomedical problems, from drug sensitivity of cancer cells [60a] to viability of a bovine embryo [60b] to mitochondrial respiration in neuronal cells [60c].

The feedback mode of the SECM operation was used to noninvasively probe the redox activity of individual mammalian cells [32a,b] and purple bacteria [32c]. Both oxidized and reduced forms of a hydrophobic redox mediator (e.g., menadione) used in such experiments must be capable of crossing the cell membrane and shuttling the charge between the tip electrode and the intracellular redox centers

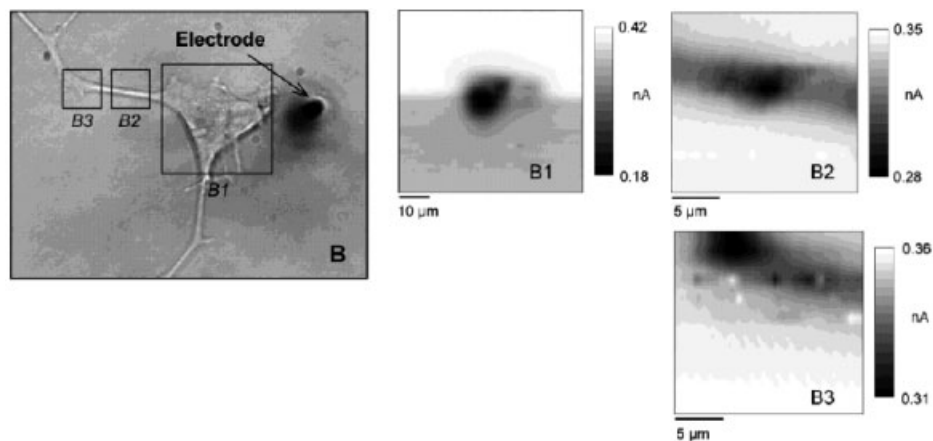


Fig. 14.10 Optical and electrochemical images of differentiated PC12 cells. SECM images were obtained using a polymer-insulated flame-etched carbon fiber tip. The redox mediator was 1.0 mM $\text{Ru}(\text{NH}_3)_6^{3+}$. (Reprinted with permission from ref. 58a. Copyright 2003, American Chemical Society.)

(Fig. 14.11). The possibilities of measuring the rate and investigating the pathway of transmembrane charge transfer were demonstrated. Mechanistic analysis [32b] showed that, depending on properties of the mediator (e.g., formal potential, ionic charge, and hydrophobicity), the main factor limiting the overall charge-transfer rate can be the membrane transport, the availability of intracellular redox agents, or the driving force for the ET reaction, i.e., the difference between the intracellular redox potential and the formal potential of the mediator. Kinetic parameters were determined for the different steps of the charge-transfer process.

By this approach, significant differences were detected in the redox responses given by immotile, untransformed human breast epithelial cells and metastatic breast cancer cells. The kinetic data obtained were used to identify the experimental conditions, such as the nature and concentration of the redox mediator, which would maximize the detection of metastatic cells in a field of normal breast cells and in tissue samples [32d].

Two papers by Mauzeroll et al. [61] addressed cytotoxicity of menadione and the expulsion of its product – menadione-*S*-glutathione conjugate – by export pumps. The uptake of menadione, a toxic molecule for yeast cells, is accompanied by its active expulsion from the cell after being complexed by glutathione. From the results of flux measurements and numerical simulation, it was concluded that the rate of expulsion of the conjugate from yeast cells was limited by the uptake of menadione [61a]. A similar approach was used to characterize the cytotoxicity of menadione on hepatocytes [61b].

SECM was also used to study transport processes across the nuclear envelope. Guo and Amemiya [62] studied the molecular transport facilitated by nuclear pore

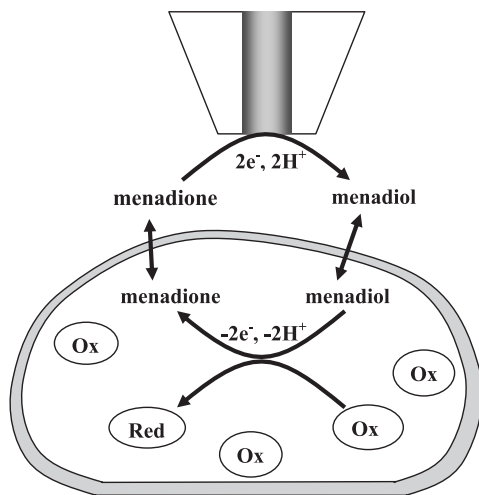


Fig. 14.11 Schematic representation of the SECM feedback across the living cell membrane. The mediator regeneration inside the cell proceeds via bimolecular ET between reduced mediator species (menadiol) and cell-bound redox moieties (Ox).

complexes (NPCs) in an intact nucleus of *Xenopus laevis* oocytes (Fig. 14.12A). The NPC is a 60–120 MDa complex made of 30 or more distinct proteins. Small molecules can diffuse passively through it. The partitioning of redox species X across the nuclear envelope [Eq. (19)] was characterized by obtaining approach curves and chronoamperograms (Fig. 14.12B). From such experiments performed with different mediators, the authors concluded that the nuclear envelope permeability is very high, and most NPCs on the nucleus are open. Estimates were obtained for the single-channel flux and the NPC diameter.



The most recent efforts have been aimed at using nanometer-sized UMEs and nanopipet-based probes for high-resolution studies of mammalian cells [63]. It was also shown that amperometric nanopipet probes allow quantitative intracellular measurements inside living cells. The use of a tip about 1000 times smaller than the cell greatly minimizes the damage to the cell membrane and may facilitate sub-cellular level studies of biologically relevant charge-transfer processes.

14.5.4.2 Redox Enzymes

The recent SECM studies of immobilized enzymes focused on two areas: measuring the catalytic enzyme activity, and micropatterning the surface with enzymes. The use of two SECM-based approaches – generation/collection and feedback

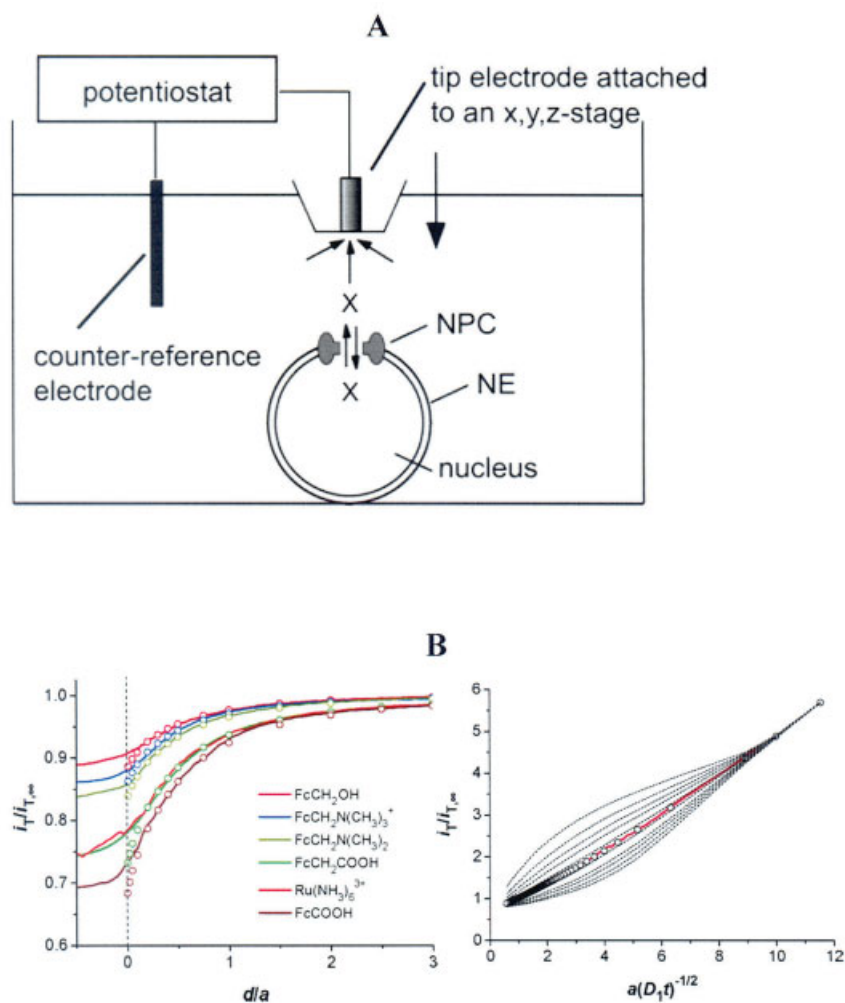


Fig. 14.12 (A) Schematic representation of SECM experiments on the intact nucleus (not to scale). X is a redox molecule. (B) Left: normalized experimental approach curves at the nuclear envelope obtained with a Pt tip, 10 μm diameter, and different redox mediators (solid lines). The circles represent simulated results for freely permeable membranes. Right: normalized chronoamperometric data (solid red line) with tip positioned at 0.95 μm from the nuclear envelope. The potential was stepped from 0 to 450 mV; the mediator was 2.5 mM ferrocenecarboxylic acid. The open circles represent the best theoretical fit. (Reprinted with permission from ref. 62. Copyright 2005, American Chemical Society.)

mode measurements – to probe redox enzymes (oxidoreductases) is illustrated in Fig. 14.13. The feedback mode is more appropriate for high-activity enzymes with high surface coverage. The GC mode is more sensitive and can be employed when the enzyme kinetics is too slow for feedback measurements.

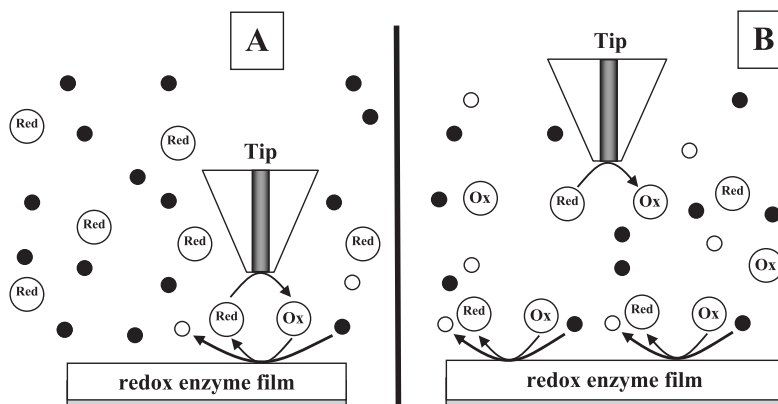


Fig. 14.13 Feedback and GC mode SECM measurements of enzyme kinetics. (A) Feedback mode: locally electrogenerated mediator is reduced by glucose (•) at the substrate surface; the reaction is catalyzed by glucose oxidase. (B) GC mode: the reduced

form of the mediator is produced continuously by the enzyme-catalyzed reaction at the substrate and collected at the tip. The tip probes the concentration profile of reduced mediator species.

The earliest example of the feedback mode application is the study of catalytic oxidation of β -D-glucose to D-glucono- δ -lactone inside a micrometer-thick layer of immobilized glucose oxidase (GO), by Pierce et al. [64a]. The oxidized form of the mediator produced by the diffusion-controlled tip reaction was reduced on the substrate surface by GO. Zero-order enzyme-mediator kinetics was established, and similar apparent heterogeneous rate constants were measured for several mediators, indicating saturation with respect to both substrate and mediator. A similar approach was used to observe the localized reaction of GO in the pores of track-etched polycarbonate membranes and membrane-bound NADH-cytochrome *c* reductase in rat liver mitochondria [64b].

The activity of immobilized alcohol dehydrogenase was probed and modified by changing the local pH [65]. The tip was positioned close to the enzyme film and used to increase the local pH by reducing water and producing hydroxide ions. A significant increase in enzyme activity was observed at higher pH. The opposite effect, i.e., local inactivation of the immobilized enzyme (diaphorase) by chlorine or bromine species electrogenerated at the tip, has also been reported [66].

In a more recent study of the catalytic behavior of horseradish peroxidase (HRP), Zhou et al. [67] immobilized HRP on glass using two methods. In the first, the enzyme was immobilized by crosslinking on a glass slide with a copolymer. When placed in the buffer solution, the film swelled to form a hydrogel. In the second method, the same copolymer and avidin were co-immobilized on the glass slide and biotin-labeled HRP was conjugated with the avidin of the film. The experiment was done in solution containing H_2O_2 and benzoquinone mediator. Hydroquinone

was electrogenerated at the tip and catalytically reoxidized to benzoquinone by HRP in the presence of H_2O_2 . This process produced positive SECM feedback. By varying the avidin loading of the film, the maximum feedback current was shown to be a linear function of the HRP surface concentration, and a detection limit of 7×10^5 HRP molecules within an area of $7 \mu\text{m}$ diameter was demonstrated.

The SECM was also used to fabricate and analyze micrometer-sized enzymatic structures on surfaces, which are potentially useful in the design of miniaturized biosensors. Wittstock and Schuhmann described the preparation and imaging of micrometer-sized spots of GO on Au [68]. First, the SECM tip was used to produce micrometer-sized defects in a self-assembled monolayer of dodecylthiolate on Au. Then, cystamine dihydrochloride was adsorbed on the bare Au spots and used to anchor periodate-oxidized GO covalently via Schiff-base chemistry. H_2O_2 generated at the substrate was collected by the Pt tip in the SG/TC mode. Another approach to enzyme micropatterning was developed by Shiku et al. [69], who scanned a micropipet dispenser above the surface to create an array of $20 \mu\text{m}$ -sized solution droplets on a glass slide, from which micrometer-sized spots of active HRP were formed. The most recent application of the SECM to localized enzyme (GO) immobilization involved direct microspotting of polypyrrole–biotin films [70].

The use of SECM to optimize the efficiency of “wired” enzyme electrodes has been reported [71]. In wired enzyme electrodes the enzymes are immobilized within a conductive polymer on the electrode surface. The electrode efficiency depends on the concentration of an enzyme in the polymer film and the ability of the matrix to recycle the enzyme by reducing/oxidizing it and shuttling the electrons to the electrode surface. Combinatorial screening techniques with the use of SECM can reduce the time and material expended in the optimization process. Fernandez et al. [71] produced arrays of enzymatic spots on the glassy-carbon substrate surface. Each spot contained two enzymes – bilirubin oxidase (BOD) and laccase – and the composition of the mixture was varied systematically within the array. Using the GC mode, a gold UME tip biased to produce O_2 from water was scanned above the enzymatic array. The authors found the optimal weight ratio for the two enzymes at which the oxygen reduction rate was close to the diffusion limit (Fig. 14.14). They repeated the experiment using a rotating disk electrode arrangement with the same mixture ratios and found agreement between the two methods, although SECM measurements were ten times faster and required $\sim 100\,000$ times less material.

14.5.5

Surface Patterning

The SECM can be used to fabricate microstructures on surfaces by deposition of metals or other solids or by etching of the substrate. Two different approaches have been used, the direct mode [72] and the feedback mode [73]. Typically, in direct mode the tip held in close proximity to the substrate acts as a working electrode (in deposition reactions) or as the counter-electrode (in etching processes). The direct deposition of a metal is illustrated in Fig. 14.15 [72, 74, 75]. A thin

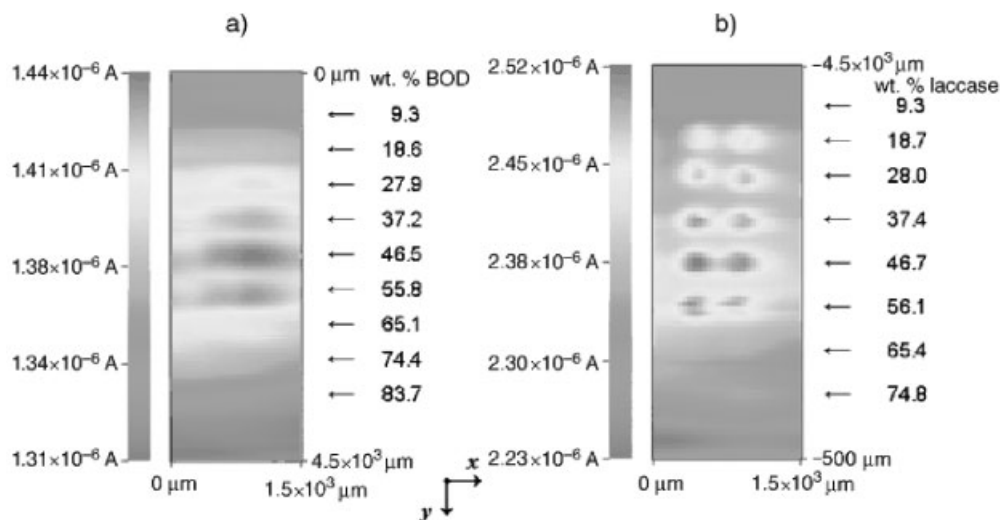


Fig. 14.14 SECM images of "wired" enzyme arrays containing spots with different polymer/enzyme ratios. (a) BOD (6.9 wt.% crosslinker) in pH 7.2 phosphate buffer, $i_T = -161$ nA, $E_s = 0.3$ V versus Ag/AgCl; b) laccase (6.5 wt.% crosslinker) in pH 5.0 citrate buffer, $i_T = -240$ nA, $E_s = 0.4$ V versus Ag/AgCl. (Reprinted with permission from ref. 71. Copyright 2004, Wiley-VCH.)

film of an ion-exchange polymer (e.g., Nafion or polyvinylpyridine, PVP) is coated on the substrate surface, which is then immersed in a solution of the metal ion to be reduced. The metal of interest is either in the cationic form, e.g., Ag^+ or Cu^+ (with Nafion, a cation-exchanger) or in the anionic form, e.g., AuCl_4^- or PdCl_4^- (with PVP, an anion-exchanger). The film-covered substrate is then removed from the metal-ion solution, placed in the SECM, and scanned in air, as shown in Fig. 14.15(A). In this application, the conical tip need not be insulated, and the resolution is determined by the extent of tip penetration into the film, which can be controlled by monitoring the current and keeping it constant. A lower tip current corresponds to a smaller depth of penetration and a smaller area of deposited metal.

The deposition of Ag in a Nafion film is illustrated in Fig. 14.15(B). The W tip was moved in the desired pattern at 90 nm s^{-1} scan rate across the Nafion/ Ag^+ surface while maintaining a constant current of 0.5 nA. Lines as narrow as $0.3 \mu\text{m}$ were produced by this procedure. Similar lines could be produced by deposition of Au or Pd in polymer films. Interestingly, the deposited lines did not get broader during the scan, showing that the electrodeposition process was confined to the tip-substrate gap. By changing the polarity of the tip, direct metal deposition on the substrate, presumably with oxidation of water in the polymer occurring at the tip, is possible. Patterns of metals such as Au deposited in polymer films using this technique have been suggested as possible masks for X-ray lithography [74, 75]. A similar approach has also been used to deposit polyaniline by oxidation of

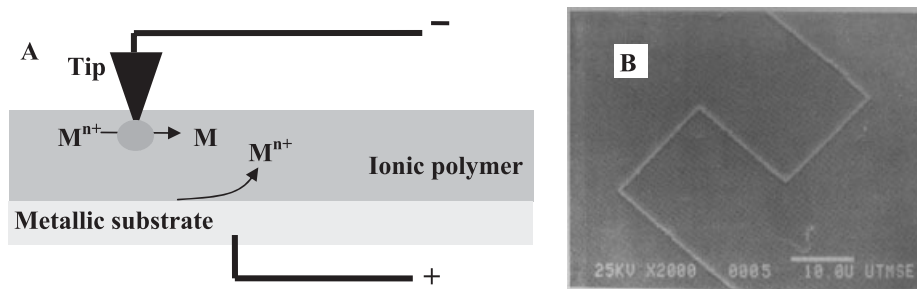


Fig. 14.15 (a) Schematic diagram of direct mode metal deposition. Metallic ions are reduced at the tip, and oxidation occurs at the substrate/polymer interface. (b) SEM picture of a pattern of silver lines deposited in a Nafion film. (Reprinted with permission from ref. 72. Copyright 1988, The Electrochemical Society.)

aniline on a Pt substrate covered with a Nafion film, with the tip acting as the cathode [76].

More recently, Forouzan and Bard [77] used the thin water layer (10–15 Å) that condenses on a mica substrate in a humid atmosphere for direct mode deposition of silver. This water layer acted as the solution phase, and the faradic current was returned through a gold contact on the mica surface. Silver ions, which had been preaccumulated in the mica matrix by soaking a freshly cleaved mica substrate in silver nitrate solution, were reduced at the negatively biased STM-type tip to form submicrometer-sized rectangular patterns.

Direct etching of a metal substrate (e.g., Cu) covered with a Nafion film was accomplished by biasing the substrate at a positive potential versus the tip [74]. In this case, a mediator such as MV^{2+} was introduced into the film and reduced at the tip. The etching resolution attainable by this technique is lower than that for the deposition at the tip because the electric field distribution yields a lower current density at the substrate than at the tip. The same is true for deposition on the substrate.

The resolution attainable in direct deposition and etching depends on a number of factors: the tip size, the depth of penetration, the tip current, and the scan rate. The faster scan rates tend to yield smaller features. However, fast scanning across the surface produces a higher contribution from the charging current. Typical maximum scan speeds applied are about 500 nm s^{-1} . Instrumental factors, e.g., vibration damping, feedback response, and temperature control, are also important to high resolution, as are the reactions at the tip and substrate.

For the feedback mode surface patterning, the tip reaction is selected to generate a species that induces the desired reaction at the substrate, i.e., deposition or etching (Fig. 14.16). For example, a strong oxidant such as Br_2 , generated at the tip, can etch the area of the substrate, e.g. GaAs, directly under the tip (Fig. 14.16B) [78]. Clearly, a small tip size and a close tip–substrate spacing are required for high resolution. The regeneration of the mediator at the substrate yields positive feedback

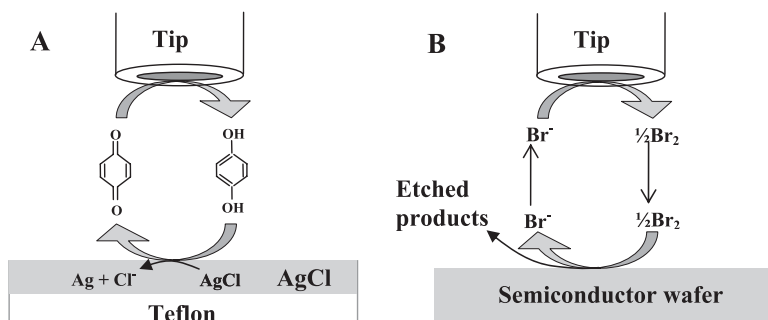
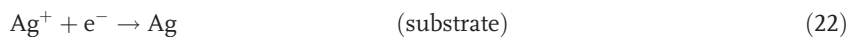
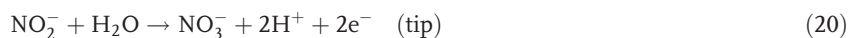


Fig. 14.16 Schematic representation of feedback mode deposition and etching experiments. (A) “Chemical development” of silver on an AgCl film. (B) Etching of a semiconductor with bromine.

current. Thus, the usual approach curves can be employed to estimate the tip–substrate distance.

In the feedback mode metal deposition reactions, the tip-generated species reacts with a thin film of metal precursor on the substrate surface [79]. For example, Au or Pd were electrodeposited in PVP films containing AuCl_4^- or PdCl_4^{2-} by generating a suitable reductant (e.g., $\text{Ru}(\text{NH}_3)_6^{2+}$) at the tip. Shohat and Mandler [80] developed a method to “focus” the diffusion field of the reductant under the tip in order to narrow the region of metal deposition. $\text{Ag}(\text{NH}_3)_2^+$ served as metal precursor, the gold substrate was biased at a moderate negative potential, so that aqueous silver could be reduced but not $\text{Ag}(\text{NH}_3)_2^+$. The tip generated H^+ ions by oxidizing nitrite [Eq. (20)], and the increased local acidity shifted the dissociation of the diamminesilver complex [Eq. (21)]. Aqueous silver ions generated by the latter reaction were reduced at the substrate [Eq. (22)].

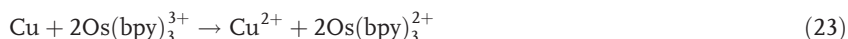


The addition of ammonia to the solution made the silver pattern narrower by complexing aqueous silver immediately outside the reaction zone. This effect was given the name of a “chemical lens.”

One of the advantages of the feedback mode deposition is that the substrate need not be a conductor. Heinze and coworkers used the above method for the deposition of silver lines on both conducting substrates [81] and a smooth Teflon surface [82]. Benzoquinone served as mediator and the AgCl film was “chemically developed” during the SECM scanning by local reduction with electrogenerated dihy-

droquinone (Fig. 14.16A). The film was grown further by “physical development” according to the photographic process.

Etching is carried out in the feedback mode by generating an appropriate oxidant (etchant) [72]. For example, Cu was etched by generating $\text{Os}(\text{bpy})_3^{3+}$ at the tip by reaction (23).



The tip was held at a positive potential, so there was no tendency to plate Cu on the tip, which could be a problem for direct mode etching. Moreover, since the substrate was maintained at a more negative potential, no copper oxidation occurred far from the tip.

The feedback mode has also been used to study the mechanism of semiconductor (GaAs) etching by using different electrogenerated oxidants, varying the pH, and contrasting the behavior of n type, p type, and intrinsic GaAs [83]. This study indicated that etching occurred only when the tip-generated oxidant was sufficiently strong to inject a hole into the valence band of GaAs. By using different mediators and noting the onset of positive feedback, the location of the valence band edge could be estimated. Zu et al. [84] used the confined etchant layer technique (CELT) – conceptually similar to “chemical lens” – technique to etch silicon (Fig. 14.17).

A different SECM-based approach was used to form a fluorescent micropattern in an ionically conductive polymer (Flemion) film [85]. In this application, the fluorescer, Rhodamine-6G (R-6G), and a quencher, MV^{2+} , were introduced in a thin film of Flemion formed on the Pt substrate. The characteristic R-6G fluorescence was completely quenched under these conditions. However, when the concentration of MV^{2+} was depleted locally by reduction at the tip, the fluorescence of R-

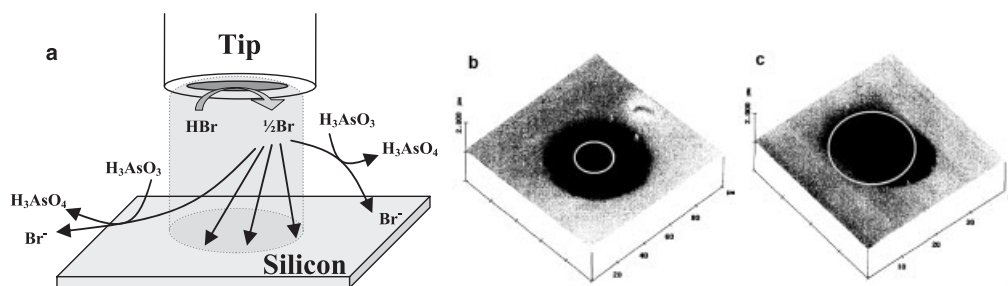


Fig. 14.17 (a) CELT scheme. Br_2 electro-generated at the tip is reduced to Br^- by H_3AsO_3 outside the tip/substrate gap. (b) and (c) AFM maps of the n type Si(111) surface after 10 min of etching in a solution consisting of 5 mM HBr, 0.5 M H_2SO_4 and 0.5 M HF with a carbon fiber tip, diameter 20 μm . (c) The

same etching conditions as in (b) but with the addition of 50 mM H_3AsO_3 . The yellow circle indicates the size of the electroactive area of the tip. The imaged area is larger in (b) than (c). (Adapted with permission from ref. 84. Copyright 1998, Elsevier.)

6G at this position was observed. Thus the tip could be used to write a fluorescent pattern in the Flemion layer with a resolution at least as fine as 0.5 μm .

Acknowledgements

The support of our research in SECM by the National Science Foundation (CHE-0315558) is gratefully acknowledged.

References

- 1 (a) BARD, A. J.; FAN, F.-R. F.; KWAK, J.; LEV, O. *Anal. Chem.*, **1989**, *61*, 132. (b) KWAK, J.; BARD, A. J. *Anal. Chem.*, **1989**, *61*, 1221.
- 2 BARD, A. J.; MIRKIN, M. V. (Eds.). *Scanning Electrochemical Microscopy*; Marcel Dekker: New York, **2001**.
- 3 (a) WIGHTMAN, R. M.; WIPF, D. O. in *Electroanalytical Chemistry*, Vol. 15; BARD, A. J., Ed.; Marcel Dekker: New York, **1988**; p. 267. (b) AMATORE, C. in *Physical Electrochemistry: Principles, Methods, and Applications*; RUBINSTEIN, I., Ed.; Marcel Dekker: New York, **1995**; p. 131.
- 4 (a) MIRKIN, M. V.; FAN, F.-R. F.; BARD, A. J. *J. Electroanal. Chem.* **1992**, *328*, 47. (b) ZOSKI, C. G.; LIU, B.; BARD, A. J. *Anal. Chem.* **2004**, *76*, 3646.
- 5 BARD, A. J.; FAULKNER, L. R. *Electrochemical Methods, 2nd ed.*, Wiley: New York, **2001**.
- 6 (a) UNWIN, P. R.; BARD, A. J. *J. Phys. Chem.* **1991**, *95*, 7814. (b) ZHOU, F.; UNWIN, P. R.; BARD, A. J. *J. Phys. Chem.* **1992**, *96*, 4917. (c) ZHOU, F.; BARD, A. J. *J. Am. Chem. Soc.* **1994**, *116*, 393. (d) TREICHEL, D. A.; MIRKIN, M. V.; BARD, A. J. *J. Phys. Chem.* **1994**, *98*, 5751. (e) UNWIN, P. R.; BARD, A. J.; DEMAILLE, C. J. *J. Phys. Chem.* **1996**, *100*, 14137.
- 7 (a) ENGSTROM, R. C.; WEBER, M.; WUNDER, D. J.; BURGESS, R.; WINQUIST, S. *Anal. Chem.* **1986**, *58*, 844. (b) ENGSTROM, R. C.; MEANEY, T.; TOPLE, R.; WIGHTMAN, R. M. *Anal. Chem.* **1987**, *59*, 2005. (c) ENGSTROM, R. C.; WIGHTMAN, R. M.; KRISTENSEN, E. W. *Anal. Chem.* **1988**, *60*, 652.
- 8 (a) DENUAULT, G.; TROISE-FRANK, M. H.; PETER, L. M. *Faraday Discuss. Chem. Soc.* **1992**, *94*, 23. (b) HORROCKS, B. R.; MIRKIN, M. V.; PIERCE, D. T.; BARD, A. J.; NAGY, G.; TOTH, K. *Anal. Chem.* **1993**, *65*, 1213. (c) WEI, C.; BARD, A. J.; NAGY, G.; TOTH, K. *Anal. Chem.* **1995**, *67*, 1346. (d) WEI, C.; BARD, A. J.; KAPUI, I.; NAGY, G.; TOTH, K. *Anal. Chem.* **1996**, *68*, 2651. (e) KLUSMANN, E.; SCHULTZE, J. W. *Electrochim. Acta* **1997**, *42*, 3123.
- 9 FAN, F.-R. F.; DEMAILLE, C. In *Scanning Electrochemical Microscopy*; BARD, A. J.; MIRKIN, M. V., Eds.; Marcel Dekker: New York, **2001**; p. 75.
- 10 (a) SHAO, Y.; MIRKIN, M. V.; FISH, G.; KOKOTOV, S.; PALANKER, D.; LEWIS, A. *Anal. Chem.* **1997**, *69*, 1627. (b) KATEMANN, B. B.; SCHUHMANN, W. *Electroanalysis* **2002**, *14*, 22. (c) SUN, P.; MIRKIN, M. V., *J. Am. Chem. Soc.*, submitted.
- 11 SLEVIN, C. J.; GRAY, N. J.; MACPHERSON, J. V.; WEBB, M. A.; UNWIN, P. R. *Electrochem. Commun.* **1999**, *1*, 282.
- 12 KRANZ, C.; FRIEDBACHER, G.; MIZAIKOFF, B.; LUGSTEIN, A.; SMOLINER, J.; BERTAGNOLLI, E. *Anal. Chem.* **2001**, *732*, 2491.
- 13 MIRKIN, M. V.; FAN, F.-R. F.; BARD, A. J. *J. Electroanal. Chem.* **1992**, *328*, 47.
- 14 (a) LIU, H.-Y.; FAN, F.-R. F.; LIN, C. W.; BARD, A. J. *J. Am. Chem. Soc.*

- 1986, 108, 3838. (b) GEWIRTH, A. A.; CRASTON, D. H.; BARD, A. J. *J. Electroanal. Chem.* **1989**, 261, 477.
- 15 (a) NAGAHARA, L. A.; TUNDAT, T.; LINDSAY, S. M. *Rev. Sci. Instrum.* **1989**, 60, 3128. (b) WIECHERS, J.; TWONEY, T.; KOLB, D. M.; BEHM, R. J. *J. Electroanal. Chem.* **1988**, 248, 451.
- 16 VITUS, C. M.; CHANG, S. C.; WEAVER, M. J. *J. Phys. Chem.* **1991**, 95, 7559.
- 17 ZHANG, B.; WANG, E. *Electrochim. Acta* **1994**, 39, 103.
- 18 ZHAO, G.; GIOLANDA, D. M.; KIRCHOFF, J. R. *Anal. Chem.* **1995**, 67, 2592.
- 19 PENNER, R. M.; HEBEN, M. J.; LEWIS, N. S. *Anal. Chem.* **1989**, 61, 1630.
- 20 SUN, P.; ZHANG, Z.; GUO, J.; SHAO, Y. *Anal. Chem.* **2001**, 73, 5346.
- 21 POTJE-KAMLOTH, K.; JANATA, J.; JOSSOWITZ, M. *Ber. Bunsen-Ges. Phys. Chem.* **1990**, 93, 1480.
- 22 (a) SLEVIN, C. J.; GRAY, N. J.; MACPHERSON, J. V.; WEBB, M. A.; UNWIN, P. R. *Electrochem. Commun.* **1999**, 1, 282. (b) BACH, C. E.; NICHOLS, R. J.; BECKMANN, W.; MEYER, H. J. *Electrochem. Soc.* **1993**, 40, 1281. (c) ZU, Y.; DING, Z.; ZHOU, J.; LEE, Y.; BARD, A. J. *Anal. Chem.* **2001**, 73, 2153.
- 23 (a) WIPF, D. O.; MICHAEL, A. C.; WIGHTMAN, R. M. *J. Electroanal. Chem.* **1989**, 269, 15. (b) ALPUCHE-AVILES, M. A.; WIPF, D. O. *Anal. Chem.* **2001**, 73, 4873.
- 24 (a) MIRKIN, M. V. in *Scanning Electrochemical Microscopy*; BARD, A. J.; MIRKIN, M. V., Eds.; Marcel Dekker: New York, **2001**; p. 145. (b) ARCA, M.; BARD, A. J.; HORROCKS, B. R.; RICHARDS, T. C.; TREICHEL, D. A. *Analyst* **1994**, 119, 719. (c) BARD, A. J.; FAN, F.-R. F.; MIRKIN, M. V. in *Electroanalytical Chemistry*, Vol. 18; BARD, A. J., Ed.; Marcel Dekker: New York, **1993**; p. 243. (d) BARD, A. J.; FAN, F.-R. F.; PIERCE, D. T.; UNWIN, P. R.; WIPF, D. O.; ZHOU, F. *Science* **1991**, 254, 68.
- 25 (a) MIRKIN, M. V.; BARD, A. J. *J. Electroanal. Chem.* **1992**, 323, 29. (b) BARD, A. J.; MIRKIN, M. V.; UNWIN, P. R.; WIPF, D. O. *J. Phys. Chem.* **1992**, 96, 1861.
- 26 (a) SHAO, Y.; MIRKIN, M. V. *J. Phys. Chem. B* **1998**, 102, 9915. (b) AMPHLETT, J. L.; DENUAULT, G. *J. Phys. Chem. B* **1998**, 102, 9946.
- 27 (a) FAN, F.-R. F.; BARD, A. J. *Science* **1995**, 267, 871. (b) FAN, F.-R. F.; KWAK, J.; BARD, A. J. *J. Am. Chem. Soc.* **1996**, 118, 9669.
- 28 BARD, A. J.; DENUAULT, G.; FRIESNER, R. A.; DORNBLASER, B. C.; TUCKERMAN, L. S. *Anal. Chem.* **1991**, 63, 1282.
- 29 MIRKIN, M. V.; BARD, A. J. *Anal. Chem.* **1992**, 64, 2293.
- 30 (a) WEI, C.; BARD, A. J.; MIRKIN, M. V. *J. Phys. Chem.* **1995**, 99, 16033. (b) TSIONSKY, M.; BARD, A. J.; MIRKIN, M. V. *J. Phys. Chem.* **1996**, 100, 17881. (c) TSIONSKY, M.; BARD, A. J.; MIRKIN, M. V. *J. Am. Chem. Soc.* **1997**, 119, 10785.
- 31 LIU, B.; BARD, A. J.; MIRKIN, M. V.; CREAGER, S. E. *J. Am. Chem. Soc.* **2004**, 126, 1485.
- 32 (a) LIU, B.; ROTENBERG, S. A.; MIRKIN, M. V. *Proc. Natl. Acad. Sci. U.S.A.* **2000**, 97, 9855. (b) LIU, B.; ROTENBERG, S. A.; MIRKIN, M. V. *Anal. Chem.* **2002**, 74, 6340. (c) CAI, C.; LIU, B.; MIRKIN, M. V.; FRANK, H. A.; RUSLING, J. F. *Anal. Chem.* **2002**, 74, 114. (d) FENG, W.; ROTENBERG, S. A.; MIRKIN, M. V. *Anal. Chem.* **2003**, 75, 4148.
- 33 (a) SCOTT, E. R.; WHITE, H. S. *Anal. Chem.* **1993**, 65, 1537. (b) BATH, B. D.; LEE, R. D.; WHITE, H. S.; SCOTT, E. R. *Anal. Chem.* **1998**, 70, 1047.
- 34 (a) TROISE FRANK, M. H.; DENUAULT, G. *J. Electroanal. Chem.* **1993**, 354, 331. (b) TROISE FRANK, M. H.; DENUAULT, G. *J. Electroanal. Chem.* **1994**, 379, 405. (c) HORROCKS, B. R.; MIRKIN, M. V. *J. Chem. Soc. Faraday Trans.* **1998**, 94, 1115.
- 35 MARTIN, R. D.; UNWIN, P. R. *Anal. Chem.* **1998**, 70, 276.
- 36 MIRKIN, M. V.; RICHARDS, T. C.; BARD, A. J. *J. Phys. Chem.* **1993**, 97, 7672.
- 37 For reviews of the electrochemistry of ITIES, see: (a) GIRAULT, H. H.; SCHIFFRIN, D. J. in *Electroanalytical*

- Chemistry, Vol. 15; BARD, A. J., Ed.; Marcel Dekker: New York, 1989; p. 1. (b) GIRAULT, H. H. in *Modern Aspects of Electrochemistry*, Vol. 25; BOCKRIS, J. O'M.; CONWAY, B. E.; WHITE, R. E., Eds.; Plenum Press: New York, 1993; p. 1. (c) VOLKOV, A. G.; DEAMER, D. W. (Eds.). *Liquid-Liquid Interfaces. Theory and Methods*; CRC Press: Boca Raton, 1996.
- 38 (a) TSIONSKY, M.; BARD, A. J.; MIRKIN, M. V. *J. Phys. Chem.* **1996**, *100*, 17 881. (b) TSIONSKY, M.; BARD, A. J.; MIRKIN, M. V. *J. Am. Chem. Soc.* **1997**, *119*, 10 785.
- 39 BARKER, A. L.; UNWIN, P. R.; AMEMIYA, S.; ZHOU, J.; BARD, A. J. *J. Phys. Chem. B* **1999**, *103*, 7260.
- 40 (a) BARKER, A. L.; GONSALVES, M.; MACPHERSON, J. V.; SLEVIN, C. S.; UNWIN, P. R. *Anal. Chim. Acta* **1999**, *385*, 223. (b) ZHANG, J.; UNWIN, P. R. *Langmuir* **2002**, *18*, 1218. (c) CANNAN, S.; ZHANG, J.; GRUNFELD, F.; UNWIN, P. R. *Langmuir* **2004**, *20*, 701.
- 41 ZHANG, Z.; YUAN, Y.; SUN, P.; SU, B.; GUO, J.; SHAO, Y.; GIRAULT, H. H. *J. Phys. Chem. B* **2002**, *106*, 6713.
- 42 LAFORGE, F. O.; KAKIUCHI, T.; SHIGEMATSU, F.; MIRKIN, M. V. *J. Am. Chem. Soc.* **2004**, *126*, 15 381.
- 43 (a) QUINN, B. M.; LILJEROTH, P.; RUIZ, V.; LAAKSONEN, T.; KONTTURI, K. *J. Am. Chem. Soc.* **2003**, *125*, 6644. (b) GEORGANOPOULOU, D. G.; MIRKIN, M. V.; MURRAY, R. W. *Nano Letters* **2004**, *4*, 1763.
- 44 (a) MIRKIN, M. V.; FAN, F.-R. F.; BARD, A. J. *Science* **1992**, *257*, 364. (b) FAN, F.-R. F.; MIRKIN, M. V.; BARD, A. J. *J. Phys. Chem.* **1994**, *98*, 1475.
- 45 (a) GARDNER, C. E.; MACPHERSON, J. V. *Anal. Chem.* **2002**, *74*, 577A. (b) KRANZ, C.; KUENG, A.; LUGSTEIN, A.; BERTAGNOLLI, E.; MIZAIKOFF, B. *Ultramicroscopy* **2004**, *100*, 127. (c) DOBSON, P. S.; WEAVER, J. M. R.; HOLDER, M. N.; UNWIN, P. R.; MACPHERSON, J. V. *Anal. Chem.* **2005**, *77*, 424. (d) BURT, D. P.; WILSON, N. R.; WEAVER, J. M. R.; DOBSON, P. S.; MACPHERSON, J. V. *Nano Letters* **2005**, *5*, 639.
- 46 (a) MACPHERSON, J. V.; UNWIN, P. R.; HILLIER, A. C.; BARD, A. J. *J. Am. Chem. Soc.*, **1996**, *118*, 6445. (b) JONES, C. E.; MACPHERSON, J. V.; UNWIN, P. R. *J. Phys. Chem. B* **2000**, *104*, 2351.
- 47 MACPHERSON, J. V.; JONES, C. E.; BAKER, A. L.; UNWIN, P. R. *Anal. Chem.* **2002**, *74*, 1841.
- 48 (a) CASILLAS, N.; CHARLEBOIS, S.; SMYRL, W. H.; WHITE, H. S. *J. Electrochem. Soc.* **1993**, *140*, L142. (b) CASILLAS, N.; CHARLEBOIS, S.; SMYRL, W. H.; WHITE, H. S. *J. Electrochem. Soc.* **1994**, *141*, 636.
- 49 BOXLEY, C. J.; WHITE, H. S.; GARDNER, C. E.; MACPHERSON, J. V. *J. Phys. Chem. B* **2003**, *107*, 9677.
- 50 (a) WIPF, D. O. *Colloid Surf. A* **1994**, *93*, 251. (b) STILL, J. W.; WIPF, D. O. *J. Electrochem. Soc.* **1997**, *144*, 2657.
- 51 ZHU, Y.; WILLIAMS, D. E. *J. Electrochem. Soc.* **1997**, *144*, L43.
- 52 BASTOS, A. C.; SIMOES, A. M.; GONZALEZ, S.; GONZALEZ-GARCIA, Y.; SOUTO, R. M. *Electrochem. Commun.* **2004**, *6*, 1212.
- 53 JANOTTA, M.; RUDOLPH, D.; KUENG, A.; KRANZ, C.; VORABERGER, H. S.; WALDHAUSER, W.; MIZAIKOFF, B. *Langmuir* **2004**, *20*, 8634.
- 54 CIANI, I.; DANIELE, S.; BRAGATO, C.; BALDO, M. A. *Electrochem. Commun.* **2003**, *5*, 354.
- 55 (a) MACPHERSON, J. V.; UNWIN, P. R. *Phys. Chem.* **1994**, *98*, 1704. (b) MACPHERSON, J. V.; UNWIN, P. R. *Phys. Chem.* **1994**, *98*, 11 764. (c) MACPHERSON, J. V.; UNWIN, P. R. *Phys. Chem.* **1995**, *99*, 3338. (d) MACPHERSON, J. V.; UNWIN, P. R. *Phys. Chem.* **1995**, *99*, 14824. (e) MACPHERSON, J. V.; UNWIN, P. R. *Phys. Chem.* **1996**, *100*, 19 465. (f) UNWIN, P. R.; MACPHERSON, J. V. *Chem. Soc. Rev.* **1995**, *24*, 109. (g) JONES, C. E.; UNWIN, P. R.; MACPHERSON, J. V. *Chemphyschem.* **2003**, *4*, 139.
- 56 (a) HORROCKS, B. R.; WITTSTOCK, G. in *Scanning Electrochemical Microscopy*; BARD, A. J.; MIRKIN, M. V., Eds.; Marcel Dekker: New York, **2001**; p. 445. (b) ROTENBERG, S. A.; MIRKIN, M. V. *J. Mammary Gland Biol. and Neoplasia* **2004**, *9*, 375.

- 57 TSIONSKY, M.; CARDON, Z. G.; BARD, A. J.; JACKSON, R. B. *Plant Physiol.* **1997**, *113*, 895.
- 58 (a) LIEBETRAU, J. M.; MILLER, H. M.; BAUR, J. E.; TAKACS, S. A.; ANUPUNPISIT, V.; GARRIS, P. A.; WIPF, D. O. *Anal. Chem.* **2003**, *75*, 563. (b) KURULUGAMA, R. T.; WIPF, D. O.; TAKACS, S. A.; PONGMAYTEEGUL, S.; GARRIS, P. A.; BAUR, J. E. *Anal. Chem.* **2005**, *77*, 1111.
- 59 YASUKAWA, T.; KAYA, T.; MATSUE, T. *Electroanalysis* **2000**, *12*, 653.
- 60 (a) TORISAWA, Y.-S.; KAYA, T.; TAKII, Y.; OYAMATSU, D.; NISHIZAWA, M.; MATSUE, T. *Anal. Chem.* **2003**, *75*, 2154. (b) SHIKU, H.; SHIRAISHI, T.; OHYA, H.; MATSUE, T.; ABE, H.; HOSHI, H.; KOBAYASHI, M. *Anal. Chem.* **2001**, *73*, 3751. (c) TAKII, Y.; TAKOH, K.; NISHIZAWA, M.; MATSUE, T. *Electrochim. Acta* **2003**, *48*, 3381.
- 61 (a) MAUZEROLL, J.; BARD, A. J. *Proc. Natl. Acad. Sci.* **2004**, *101*, 7862. (b) MAUZEROLL, J.; BARD, A. J.; OWHADIAN, O.; MONKS, T. J. *Proc. Natl. Acad. Sci.* **2004**, *101*, 17582.
- 62 GUO, J.; AMEMIYA, S. *Anal. Chem.* **2005**, *77*, 2147.
- 63 CAI, C.; SUN, P.; MIRKIN, M. V., in preparation.
- 64 (a) PIERCE, D. T.; UNWIN, P. R.; BARD, A. J. *Anal. Chem.* **1992**, *64*, 1795. (b) PIERCE, D. T.; BARD, A. J. *Anal. Chem.* **1993**, *65*, 3598.
- 65 O'BRIEN, J. C.; SHUMAKER-PARRY, J.; ENGSTROM, R. C. *Anal. Chem.* **1998**, *70*, 1307.
- 66 SHIKU, H.; TAKEDA, T.; YAMADA, H.; MATSUE, T.; UCHIDA, I. *Anal. Chem.* **1995**, *67*, 312.
- 67 ZHOU, J.; CAMPBELL, C.; HELLER, A.; BARD, A. J. *Anal. Chem.* **2002**, *74*, 4007.
- 68 (a) WITTSTOCK, G.; SCHUHMAN, W. *Anal. Chem.* **1997**, *69*, 5059. (b) WITTSTOCK, G.; HESSE, R.; SCHUHMAN, W. *Electroanalysis* **1997**, *9*, 746.
- 69 SHIKU, H.; MATSUE, T.; UCHIDA, I. *Anal. Chem.* **1996**, *68*, 1276.
- 70 EVANS, S. A. G.; BRAKHA, K.; BILLON, M.; MAILLEY, P.; DENUAULT, G. *Electrochem. Commun.* **2005**, *7*, 135.
- 71 FERNANDEZ, J. L.; MANO, N.; HELLER, A.; BARD, A. J. *Angew. Chem. Int. Ed.* **2004**, *43*, 6355.
- 72 CRASTON, D. H.; LIN, C. W.; BARD, A. J. *J. Electrochem. Soc.* **1988**, *135*, 785.
- 73 MANDLER, D.; BARD, A. J. *J. Electrochem. Soc.* **1989**, *136*, 3143.
- 74 HÜSSER, O. E.; CRASTON, D. H.; BARD, A. J. *J. Vac. Sci. Technol. B* **1988**, *6*, 1873.
- 75 HÜSSER, O. E.; CRASTON, D. H.; BARD, A. J. *J. Electrochem. Soc.* **1989**, *136*, 3222.
- 76 WUU, Y.-M.; FAN, F.-R. F.; BARD, A. J. *J. Electrochem. Soc.* **1989**, *136*, 885.
- 77 FOROUZAN, F.; BARD, A. J. *J. Phys. Chem. B* **1997**, *101*, 10876.
- 78 MANDLER, D.; BARD, A. J. *J. Electrochem. Soc.* **1990**, *137*, 2468.
- 79 MANDLER, D.; BARD, A. J. *J. Electrochem. Soc.* **1990**, *137*, 1079.
- 80 SHOCHAT, I.; MANDLER, D. *J. Electrochem. Soc.* **1994**, *141*, 995.
- 81 BORGWARTH, K.; RICKEN, C.; EBLING, D. G.; HEINZE, J. *Ber. Bunsenges Phys. Chem.* **1995**, *99*, 1421.
- 82 HER, C.; BORGWARTH, K.; RICKEN, C.; EBLING, D. G.; HEINZE, J. *Electrochim. Acta* **1997**, *42*, 3065.
- 83 MANDLER, D.; BARD, A. J. *Langmuir* **1990**, *6*, 1489.
- 84 ZU, Y.; XIE, L.; MAO, B.; TIAN, Z. *Electrochim. Acta* **1998**, *43*, 1683.
- 85 SUGIMURA, H.; UCHIDA, T.; SHIMO, N.; KITAMURA, N.; MASUHARA, H. *Ultramicroscopy* **1992**, *42*, 468.

Part IV
Theoretical Approaches

15 Theory of Elastic and Inelastic Transport from Tunneling to Contact

Nicolas Lorente and Mads Brandbyge

15.1 Introduction

The purpose of this chapter is to give a succinct review of recent advances in the field of conductance calculations. In particular, the emphasis is put on the similarities and differences between conductance properties in the tunneling regime and in the contact regime. The experimental innovations in this field have been many in the last two decades. In the case of the tunneling regime, the scanning tunneling microscope (or microscopy) (STM) has permitted imaging of atomic structures on surfaces [1]. More recently, the contact regime has been studied thoroughly by different techniques, from STM-based techniques where an STM tip was brought into contact with a surface atom [2, 3], to break junctions [4] and atom-sized wires [5]. These experiments allow an enhanced control over the characteristics of the conduction region, showing properties unique to the atomic-scale transport. In this chapter we summarize the main techniques and concepts to deal with these different transport regimes.

Transport in these regimes usually takes place in the presence of inelastic processes. Since the late 1960s, inelastic effects in metal–insulator–metal systems have attracted much attention both experimentally [6, 7] and theoretically [8, 9]. Recently, however, inelastic effects have been revealed with the STM [10]. This has allowed the chemical identification of a species under an STM tip by detecting its vibrational signature in the tunneling conductance (see Chapter 4). The equivalent type of effect was revealed in the high-conductance regime in 2002. Agraït and coworkers [11, 12] were able to measure the excitation of the localized vibrations of an atomic chain when electronic current was flowing through it. In the present chapter, we include the theoretical treatment of inelastic effects both in the low-conductance or tunneling and in the high-conductance or contact regimes. These theories allow us to analyze, interpret, and understand the signature of vibrations in the conductance, as well as the physics controlling the different inelastic processes.

15.2 Theory of Tunneling Conductance

15.2.1

Introduction

There are many excellent reviews devoted to the evolution of simulations and theories dealing with the STM, e.g., the review article by Tsukada et al. [13], the multi-author book edited by Wiesendanger and Güntherodt [14], and the more recent review articles by Hofer and coworkers.

Ref. [13] gives a clear idea of the status of theory at the beginning of the 1990s. There were several approaches, ranging from simplified Hamiltonians treated in a tight-binding like formalism, to more elaborate treatments of solving the electron's wavefunction in the presence of the surface–tip potential. In this review, there is a clear account of different ways of using Bardeen's approach in order to calculate realistically the full surface–tip problem. The biggest limitation then, compared with the present day, was the computer power available. Nevertheless the main concepts and methods were largely established.

The book edited by Wiesendanger and Güntherodt [14] contains many interesting contributions, clarifying concepts and showing what could be achieved in the mid-1990s, but it was in the early part of 2000 that the new developments in computers and in *ab-initio* calculations permitted the evaluation of realistic STM images, as is vividly narrated in refs. 15 and 16.

Part of the achievement of more recent approaches [15–17] lies in the simplicity and accuracy of Bardeen's approximations as compared with more exact but complex treatments. This reason leads us to give a brief account of Bardeen's approach in Section 1.2.2.

15.2.2

Tunneling Calculations with Bardeen's Transfer Hamiltonian

In order to calculate the conductance in a tunneling junction, one can in principle adopt a scattering approach. This is currently being used by a number of groups [18, 19]. In the calculation of the tunneling transmission they use a scattering formalism to calculate the transmission matrix. In scattering theory one needs extended states, with correct asymptotic behavior infinitely far from the tunneling junctions. This turns out to be difficult to achieve numerically.

The first approaches used localized basis sets and in particular an extended Hückel description of the electronic structure. This makes it possible to perform the calculation because of the finite number of matrix elements to be calculated, at the price of reducing the accuracy of the calculation. Cerda has developed new codes using an efficient extended Hückel algorithm, and high-performing tunneling codes that are publicly available [20]. The same group have described an *ab-initio* implementation with a plane wave basis set, but the calculations remain limited to relatively small systems [19].

Landauer's formalism (see Section 15.4) originates in scattering theory and can be used as a framework for the study and calculation of STM images [18]. Indeed, it can give us the formal language to define the relationship between the underlying electronic structure and an STM image. Nevertheless, Landauer's formalism is not commonly used for the calculation of STM images. The reason lies in the numerical difficulties associated with it. Transmissions in tunneling are small, and the calculations employ large and small numbers that render good numerical accuracy difficult to obtain.

However, we can make use of the smallness of transmission by using a perturbation-like approach: Bardeen's transfer Hamiltonian. The electron current is calculated by means of Eq. (1),

$$I = -\frac{2\pi e}{\hbar} \sum_{v,\mu} (f_L(\varepsilon_v))(1 - f_R(\varepsilon_\mu)) \times \left| \hbar \int_S \vec{J}_{v,\mu} \cdot d\vec{S} \right|^2 \delta(\varepsilon_\mu - \varepsilon_v) \quad (1)$$

where f_L and f_R are the Fermi distributions for the left- and right-hand electrodes respectively, and v and μ are the respective electronic states of the electrodes. The modulus squared of the flux of the operator J refers to the flux of some sort of current density through a fictitious surface S that divides the L and R regions originating in the electrodes. This density current does not correspond to any electron density current, but it is just mathematically analogous to a density current evaluated onto a mixed set of left and right wavefunctions [Eq. (2)].

$$\vec{J}_{v,\mu} = \frac{\hbar}{2mi} (\psi_{\mu,R}^* \vec{\nabla} \psi_{v,L} - \psi_{v,L} \vec{\nabla} \psi_{\mu,R}^*) \quad (2)$$

Due to this mixing of left and right states, Eq. (2) does not correspond to a true current density. Ideally, the limit between the two regions, as described by the integration surface, is where the mutual interaction between electrodes is already negligible.

Bardeen's approach is accurate in typical STM constant-current conditions and can be used with high-performing codes using plane waves. Hofer and Redinger [21] have implemented Bardeen's approach using *ab-initio* results for both tip and substrate with excellent results in different systems [16]. Recently, a series of combinations of atomic basis sets and efficient algorithms have boosted the calculation of STM images by using Bardeen's approach [17]. The agreement and *ab-initio* character of these simulations permit the systematic exploration of geometries and other factors in the obtainment of STM constant-current images. In particular, the authors of ref. 17 have created a computational tool that can evaluate the properties of a real STM tip in comparison with the STM image that is obtained experimentally. The main advantage of this procedure is its execution speed, which permits evaluation of STM images with different tips as experiments are performed.

Bardeen's approach can be used as starting points for other approximations. Chen [22] has shown that one can expand the wavefunctions of the tip in spherical

harmonics centered on some “center” of the tip apex and increase the accuracy of the calculation by including higher spherical harmonics. This permits rationalization of the effect of the tip’s electronic structure on the STM images.

The first term of Chen’s approach is to keep the s-wavefunction of the electronic wavefunction of the full tip. This is the Tersoff and Hamann approximation. Tersoff and Hamann [23] show that in this case the conductance of the tunneling junction is proportional to the local density of states (LDOS) of the substrate:

$$\frac{\partial I}{\partial V} \propto \sum_{\mu} |\psi_{\mu}(\mathbf{r}_0)|^2 \delta(E_F - \varepsilon_{\mu})$$

The LDOS is an electronic density weighted by the number of electronic states about the Fermi energy. This is indeed an appealing result. It tells you that if the tip’s electronic structure is symmetric enough and originates basically in a point, then the STM image contains information on only the electronic structure of the substrate at the Fermi energy.

Tersoff and Hamann’s approach stirs mixed feelings. It is very simple and attractive, but it rises questions of accuracy. It is known that it cannot account for the corrugation of clean metal surfaces. It fails in giving a tip–surface distance scale with corrugation corresponding to those observed experimentally. However, it has been shown [24, 25] that in the case where an important local electronic structure exists (such as near an adsorbate), it gives results that contain all the experimental information. This is notably the case for molecules chemisorbed on metal surfaces.

15.2.3

Extension of the Bardeen Approach to the Many-Body Problem

The Bardeen approach has been extended to take into account the many-body structure of the electronic wavefunction in a metal, [26–29]. The greatest advantage of using Green’s functions is that by slightly complicating the formulation, one has access to inclusion of many-body effects which turn out to be fundamental in inelastic transport. The tunneling current can be expressed then by Eq. (3).

$$I(V) = \frac{2e^2}{\hbar\pi} \left(\frac{\hbar^2}{2m} \right)^2 \int_{E_F}^{E_F+eV} d\omega \operatorname{Tr}(\{\vec{\nabla}_1 - \vec{\nabla}_1\} \operatorname{Im} G_T^r(\mathbf{r}_1, \mathbf{r}_2, \omega) \times \{\vec{\nabla}_2 - \vec{\nabla}_2\} \operatorname{Im} G_S^r(\mathbf{r}_2, \mathbf{r}_1, \omega)) \quad (3)$$

This equation should be interpreted in the following way. The current depends on the voltage through the limits of the integration over the Green’s function energies ω . The Green’s functions are retarded ones. The trace, Tr , includes a surface integration over a fictitious surface in the region of no interaction between tip (T) and sample (S), and we calculate the flux of the nabla operators through this surface [28]. This is the extension to Green’s functions of the Bardeen approach where

the flux of nabla operators acting on the two-electrode wavefunctions is calculated over the fictitious surface. The nabla operators act on the coordinate that their sub-index denotes and on the Green's function to which the arrow points. If there is no Green's function, we make use of the cyclic property of the trace, and rotate the nabla and Green's function so there is no ambiguity about where the nabla operators act. From now on atomic units will be used unless otherwise stated ($\hbar = m_e = e = 1$).

The substitution of single-particle Green's functions (and in equilibrium) leads naturally to the customary Bardeen formula [28]. The Green's functions for the tip are given in Eq. (4),

$$G_T^{a(r)}(\mathbf{r}, \mathbf{r}', \omega) = \sum_m \frac{\psi_m(\mathbf{r})\psi_m^*(\mathbf{r}')}{\omega - \varepsilon_m - (+)i\delta} \quad (4)$$

where the $a(r)$ superscript refers to the advanced or retarded Green's function, given by an imaginary infinitesimal $-(+)\delta$ respectively. For the tip's single-electron wavefunctions we are using Latin subindices, $\psi_m(\mathbf{r})$. The Green's functions for the sample are described by Eq. (5).

$$G_S^{a(r)}(\mathbf{r}, \mathbf{r}', \omega) = \sum_\lambda \frac{\psi_\lambda(\mathbf{r})\psi_\lambda^*(\mathbf{r}')}{\omega - \varepsilon_\lambda - (+)i\delta} \quad (5)$$

Now one can introduce the electron–vibration coupling into Eq. (4) by using many-body Green's functions. These functions can be evaluated with Dyson's equation. Even in the case where a local vibration is assumed, and when the one-electron structure is well known, Dyson's equation cannot be solved. This will be the aim of the sections devoted to inelastic transport theory.

15.3

Theory of Inelastic Processes in Electron Transport

Inelastic processes take place when the electron current excites vibrations of the atomic constituents of either the contacts or the electrodes. When the bias voltage corresponds to electron energies smaller than the quantum of vibration, the propagating electron cannot yield its energy to the vibration. Let us assume that the temperature is very low (less than 10 K) such that the probability of finding the vibrator in an excited state is negligible. In this case the electron will not gain energy from the vibrator but will cede its energy. In order to yield its energy the final state of the electron has to be empty; in other words, the final channel must be open. The only way of opening the channel is when the bias voltage energy is larger than the quantum of vibration. In this case the electron can excite the vibration and continue its propagation in an electronic state above the Fermi level of the second electrode: the vibration opens a new channel.

At this stage the tunneling regime is easily distinguished from the contact regime. In the first case, the phase space increase due to the opening of a channel leads to an increase of the conductance. This conductance increase has been used to detect the vibrations of single molecules under an STM tip [10]. In the contact regime, the interaction is a scattering event that impedes the electron motion, and an increase of the electron reflection or backscattering by the vibration is expected, as discussed further in Section 15.5. Hence, a drop in conductance is the signal recorded in controlled vibration excitation in the contact regime [11, 12].

15.3.1

Linear Model for the Electron–Vibration Coupling

In order to treat inelastic effects due to the excitation of vibrations (phonons in extended systems) we need first to understand what is the coupling or interaction giving rise to the possibility of exciting the nuclear dynamics via the electronic dynamics. Typical treatments linearize the full Hamiltonian and retain the first term that contains both electronic and nuclear degrees of freedom. Let $\{\vec{R}\}$ be the ensemble of nuclear coordinates and $\{\vec{r}\}$ the corresponding electronic ones; hence we would like to find the contribution to the Hamiltonian that contains both sets. In order to simplify, let us assume that the excitation of vibrations scarcely varies the ground-state nuclear coordinates, so we can just look for the change of the Hamiltonian when a small change in coordinates, $\delta\{\vec{R}\}$, is effected. Then we can expand the full Hamiltonian to linear order in the nuclear coordinates, as in Eq. (6),

$$\hat{H} \approx \hat{H}_0 + \delta\hat{H} = \hat{H}_0 + \frac{\partial\hat{H}}{\partial\vec{R}} \cdot \delta\vec{R} \quad (6)$$

where we are implicitly assuming a summation over all nuclei, and the gradient with respect to the nuclear coordinates is explicitly given by

$$\nabla\hat{H} = \frac{\partial\hat{H}}{\partial\vec{R}}$$

This gradient is evaluated at the relaxed position of the nuclei. It is mandatory that the nuclear coordinates are fully relaxed; otherwise the electron–vibration perturbation, $\delta\hat{H}$, will include contributions coming from the Hellmann–Feynman forces on the nuclei, and will not correspond to the vibration of the system. The gradient includes only electronic coordinates. We have then factorized an otherwise complicated electron–vibration interaction into a factor containing only electronic coordinates (the gradient of \hat{H}) and a factor containing nuclear ones (the variation of the nuclear coordinates $\delta\vec{R}$). We can now use different linear combinations of nuclear coordinates to represent the different modes or phonons of our system and express the above coupling in terms of normal coordinates. These normal coordinates can be quantized with the creation and annihilation operators of the normal modes \hat{b}

and \hat{b}^\dagger in order to obtain the final expressions, Eq. (8), expressed for a local mode Q and the electronic energy eigenvalue basis μ , and Eq. (41) expressed in a local-electron basis.

In order to evaluate inelastic effects on a quantitative level, the electron–vibration coupling must be evaluated as accurately as possible from first principles. This turns out to be possible using customary DFT implementations. However, it is interesting to understand the approximations and the meaning of the equations that are actually involved in order to give a numerical coupling. Since this analysis is quite complex the interested reader can find it in Appendix B.

15.3.2

Tunneling Regime

Hence, as we just saw, newly open channels in the tunneling regime lead to an increase in the electron current. The infinite electron reservoirs act as pressurized containers: whenever an electron can leak from the reservoir, it will. Hence the increase of final electron channels leads to an increase of the electron current.

The picture just given is not accurate. It actually depends on what type of coupling exists between the vibrator and the flowing electrons. Caroli et al. [9] give a complete account of the different scenarios leading to a rich variety of behaviors of the current with the excitation of localized vibrations. In their analysis of metal–insulator–metal junctions they consider different types of coupling by the situation where the vibrator (molecular impurity) lies within the junction. If the impurity lies inside the insulator layer, then the above picture turns out to be correct: the vibrational excitation is an opening of a new channel and the current increases. If the impurity is in contact with one of the electrodes, the case is much more complex, and particular details on the impurity–metal interaction need to be taken into account. The reason behind this classification is that the electron–vibration scattering in the insulator layer is a one-electron process equivalent to the electron–molecule scattering problem. In contact with the metal, many-body features appear. The states are multielectronic and the vibration mixes them efficiently. The simple channel-opening picture is no longer valid. As a matter of fact, Caroli et al. [9] show that the current can actually decrease.

Davis [8] showed very interesting results where the defining parameter of the type of electron–vibration coupling was the distance of the vibrator to the metal contacts. He reached some conclusions along the lines of the more systematic description by Caroli et al. [9], namely, that the main many-body effect is the antisymmetry of the many-body wavefunction. In order to take this antisymmetry into account, he considered Slater determinants of the one-electron wavefunctions, and then applied perturbation theory to the electron–vibration interaction. The effect of the electron–vibration coupling is to mix up the electronic states: the states of the full Hamiltonian contain the electron and vibration coordinates. One way of putting this mixing is to claim that *virtual* phonons are emitted and reabsorbed. This is a description that comes from perturbation theory in which electrons and vibrations are treated separately and they are mixed gradually through perturbation theory. Indeed, what it means is that the actual ground state contains vibration

contributions that one cannot neglect. These contributions are very efficient in mixing two-electron coordinates with the vibration coordinates in the full-system wavefunction.

By measuring the change in conductance over the vibration threshold, inelastic electron tunneling spectroscopy (IETS) gives information on the localized vibrations of the STM junction. Hence there are two processes: electron propagation and vibration excitation. IETS-STM is performed at low temperatures (typically below 10 K) and at low currents (in the nanoamp range). These are conditions that allow an identification of vibration excitation by single electrons: the vibrator is probably in its ground state and the time between electrons is much longer than the lifetime of the vibrations.

A perturbation theory approach seems to be justified due to the smallness of the electron–vibration coupling, and the dynamics of the process (excitation and de-excitation) is considerably simplified by the above experimental conditions.

In the existing literature on inelastic effects in tunneling, there are two approaches to describe the vibration excitations: approaches that compute the probability of vibration excitation by an electron current, and approaches that compute the change in conductance by vibration excitation. In the first case the accent is put on the description of the excitation, the change in conductance being a secondary process. In the second case, the conductance description is emphasized.

15.3.2.1 Approaches Based on Scattering Theory

The process of vibrational excitation is described in great detail in these approaches. The underlying idea is to calculate transition times (or excitation rates) and from here to obtain the contribution to the current coming from the inelastic process. A current can be seen as the product of a transition time between electrodes and the charge of the electron. In this way, these theories expect that the inelastic contribution to the current to be the rate of vibration excitation multiplied by the charge of the electron. In the tunneling regime these theories turn out to be good approximations, because electron transport can be understood as single-electron conduction events, where the static electronic structure is not strongly modified by transport itself.

Persson and Baratoff [30] have been the first to estimate the inelastic contribution to the current by using a scattering-like approach. They show that fundamental aspects of the transport problem can be taken into account only if the propagation of the electron is treated on the same level as the vibration excitation. Similar approaches are those by Gata and Antoniewicz [34] and Spataru and Budau [35]. All of these approaches start by writing a Newns–Anderson type Hamiltonian, Eq. (7).

$$\begin{aligned}
 H = & \varepsilon_a c^\dagger c + \sum_{k_{L,R}} \varepsilon_{k_{L,R}} c_{k_{L,R}}^\dagger c_{k_{L,R}} + \sum_{k_{L,R}} [V_{a,k_{L,R}} c^\dagger c_{k_{L,R}} + H.c.] + \hbar\Omega \left(b^\dagger b + \frac{1}{2} \right) \\
 & + \sum_{\mu,v} V_{\mu,v} c_\mu^\dagger c_v (b^\dagger + b)
 \end{aligned} \tag{7}$$

The first term of Hamiltonian (7) refers to the molecular orbital a ; it is just the energy of the corresponding level when the state a is populated (this is the meaning of the creation and annihilation couple $c^\dagger c$). The second term refers to the extended electron states in the left, k_L , and right, k_R , electrodes. The third term is the coupling between the molecular and electrode states, given by the matrix element. H.c. stands for hermitian conjugate. Hence, this term sets the width of the molecular resonance in contact with the electrode continua. The fourth term is the corresponding vibrational Hamiltonian for the local vibration of single frequency. The creation and annihilation operators of one quantum of vibration are denoted b^\dagger and b respectively. The last term is the electron–vibration coupling $V_{\mu,\nu}$ where μ and ν designate any electronic states of the full system. This term makes it possible for an electronic transition to be induced by a vibrational one, and vice versa. This term has been thoroughly expounded in the Appendix B.

These theories assume that there is an electronic state, a , of the molecular adsorbate that will be populated and will induce the vibration excitation. This process is usually called resonance scattering because the active electronic state becomes a resonance in presence of the electrode's continuum of states. In the gas-phase formulation [31, 32] a negative ion resonance is formed. This negative ion has a different geometrical conformation from the neutral molecule, so when the ion resonance decays into the neutral molecule, the molecule is left in a vibrationally excited state of the neutral molecule. This process is very efficient in producing the coherent multiple excitations of molecular modes [33]. However, it is quite different from what the above theories using Eq. (7) try to model. Indeed, the residence time of an electron in a chemisorbed molecular resonance is orders of magnitude smaller than the typical times involved in any vibrational quantity. This is different from the negative-ion resonance excitation in the gas phase, where the resonance lifetime is of the order of the vibrational period.

The above approaches estimate the excitation rate by using either second-order perturbation theory [30] or a re-summation to all orders in perturbation theory [34, 35]. In order to be able to sum the infinite series of perturbation theory, refs. 34 and 35 use an orthogonal basis-set of the model Hamiltonian (7), which leads to neglect of the mixing of electronic states in the electrode due to the molecular vibration. Despite the more approximate treatment of ref. [30], this coupling is not neglected. The outcome is that refs. 34 and 35 neglect many-body effects that explain the decrease of conductance in certain systems as Persson and Baratoff predicted in the case of IETS–STM [30] and Davis [8] in the case of insulator–metal junctions.

15.3.3

Approaches Based on Conductance Calculations

More directly, these approaches focus on the measured quantity: the conductance. There are two main groups of theories. One is based on a tight-binding description of the transport processes [36–38]. This approach allows for a complete calculation of transport in the presence of vibrations and interacting with them. In this way,

the effect of temperature (through phonon population, i.e., degree of excitation of the vibrations) and multiple excitations is taken into account. The inclusion of multiple electronic channels permits them to go beyond the above resonance models: the molecule can have several orbitals contributing to the conductance and to the coupling with its vibrations [38]. Emberly and Kirczenow [39] have included explicitly the effect of exchange in the evaluation of inelastic transport in the above approach. As we saw above, the effect of exchange is fundamental to understand the decrease in conductance when a vibration is excited (i.e., a phonon is emitted).

The other type of theory uses nonequilibrium Green's functions. Green's functions are more tractable in a localized basis set, such as the one corresponding to a tight-binding description [9].

There exists real-space or extended-basis descriptions that have the advantage of building upon accurate results from plane-wave calculations of the electronic structure [40]. Nevertheless, electronic structure calculations based on localized basis sets can become as accurate and predictive as plane-wave based results [41]. Transport calculations are easier to perform in localized basis sets; hence *ab-initio* localized basis codes is turning out to be the best tool [42]. In Section 15.4, we give a brief account of this type of calculation.

When a tunneling calculation is undertaken, many simplifications render the task easier than a complete transport calculation. Here we will assume that the current and thus the conductance are proportional to the density of states (spectral function) of the leads (here, tip and substrate). This is tantamount to using some perturbational scheme on the electron transmission amplitude between tip and substrate. This is what Bardeen's transfer Hamiltonian achieves. The main advantage of this approximation is that one can use the electronic structure calculated by some standard way, for example plane-wave codes, and use perturbation theory to account for the inelastic effect. In ref. 43, a description of the Bardeen approximation in the context of inelastic tunneling is given; in Section 15.3.5 we undertake a summary of the presentation in ref. 43.

15.3.4

Inelastic Approach Based on Bardeen's Approximation

The local vibration is introduced perturbatively. The perturbing Hamiltonian becomes Eq. (8),

$$\hat{H}_1 = \sum_{\mu, \nu} v'_{\mu, \nu} \hat{c}_{\mu}^{\dagger} \hat{c}_{\nu} \delta Q (\hat{b}^{\dagger} + \hat{b}) \quad (8)$$

where we have assumed a simple mode with root mean square displacement given by $\delta Q = \sqrt{\hbar/(2M\Omega)}$ with Ω the vibration frequency of the localized mode, and M the reduced mass associated with the vibration. δQ can be easily generalized to local modes of many atoms; see for example ref. 44. The locality of the mode is

expressed by the absence of coordinates of the harmonic creation and destruction operators \hat{b}^\dagger and \hat{b} . The harmonic approximation allows us to evaluate $v_{\mu, \nu}$ easily through the derivative of the effective one-electron potential [Eq. (9)],

$$\hat{v}'(\mathbf{r}) = \left\langle \frac{\partial \hat{H}_1(\mathbf{r}, Q)}{\partial Q} \right\rangle \quad (9)$$

with the angle brackets denoting averaging over the harmonic oscillator states. We will call $v = v' \delta Q$ the electron–vibration coupling. Please refer to Appendix B for a more complete account of the electron–vibration coupling in the adiabatic approximation.

Perturbation theory is performed on the Green’s functions appearing in Eq. (3). Two remarks are important: (a) we use a local theory where the tunneling electron is not dressed by the electron–vibration interaction; hence we can keep first-order perturbation theory, contrary to the treatment of polaron transport, where resummations to all orders are needed; (b) the locality and weakness of the perturbation also means that the tunneling is basically a one-particle problem through two equilibrium many-body reservoirs; hence we can use equilibrium Green’s functions theory. The locality and the equilibrium assumptions are totally justified in the usual conditions of IETS–STM, where the currents and excitation probabilities set a time between excitation events much longer than the vibrational lifetime. The molecule is thus relaxed between inelastic electrons. Nevertheless this theory is based on nonequilibrium Green’s functions (NEGFs) [9].

Let us define the following correlation function [9] $G^>(\mathbf{r}, \mathbf{r}', t')$ for the sample by Eq. (10),

$$G_S^>(\mathbf{r}, \mathbf{r}', \omega) = -i2\pi \sum_{\lambda} (1 - f_{\lambda}) \psi_{\lambda}(\mathbf{r}) \psi_{\lambda}^*(\mathbf{r}') \delta(\omega - \varepsilon_{\lambda}) \quad (10)$$

where $f_{\lambda} = n_F(\varepsilon_{\lambda})$ is the Fermi distribution for the eigenvalue of the equilibrium Hamiltonian with eigenfunction $\psi_{\lambda}(\mathbf{r})$.

Perturbation theory is easily implemented using NEGF [9]. The first contribution to the perturbed correlation function is [9]: $\delta G_S^> = \delta G_{ine}^> + \delta G_{ela}^>$, with the right-hand terms described by Eqs. (11) and (12).

$$\delta G_{ine}^>(\mathbf{r}, \mathbf{r}', \omega) = \iint d\mathbf{r}_1 d\mathbf{r}_2 G^r(\mathbf{r}, \mathbf{r}_1, \omega) \Sigma^>(\mathbf{r}_1, \mathbf{r}_2, \omega) G^a(\mathbf{r}_2, \mathbf{r}', \omega) \quad (11)$$

$$\begin{aligned} \delta G_{ela}^>(\mathbf{r}, \mathbf{r}', \omega) = & \iint d\mathbf{r}_1 d\mathbf{r}_2 (G^>(\mathbf{r}, \mathbf{r}_1, \omega) \Sigma^a(\mathbf{r}_1, \mathbf{r}_2, \omega) G^a(\mathbf{r}_2, \mathbf{r}', \omega) \\ & + G^r(\mathbf{r}, \mathbf{r}_1, \omega) \Sigma^r(\mathbf{r}_1, \mathbf{r}_2, \omega) G^>(\mathbf{r}_2, \mathbf{r}', \omega)) \end{aligned} \quad (12)$$

Equation (11) yields the purely inelastic contribution and Eq. (12) gives the elastic one. Let us consider the explicit form of the self-energies [9]:

$$\begin{aligned}
\Sigma^>(\mathbf{r}_1, \mathbf{r}_2, \omega) &= iv(\mathbf{r}_1)v(\mathbf{r}_2) \int \frac{d\omega'}{2\pi} D^>(\omega - \omega') G^>(\mathbf{r}_1, \mathbf{r}_2, \omega') \\
&= -i2\pi v(\mathbf{r}_1)v(\mathbf{r}_2) \sum_{\lambda} (1 - f_{\lambda}) \psi_{\lambda}(\mathbf{r}_1) \psi_{\lambda}^*(\mathbf{r}_2) \delta(\omega - \Omega - \varepsilon_{\lambda}), \quad (13)
\end{aligned}$$

The advanced (retarded) self-energies are then given by Eq. (14), and

$$\begin{aligned}
\Sigma^a(\mathbf{r}_1, \mathbf{r}_2, \omega) &= v(\mathbf{r}_1)v(\mathbf{r}_2) \sum_{\lambda} \psi_{\lambda}(\mathbf{r}_1) \psi_{\lambda}^*(\mathbf{r}_2) \\
&\times \left\{ \frac{1 - f_{\lambda}}{\omega - \Omega - \varepsilon_{\lambda} - i\delta} + \frac{f_{\lambda}}{\omega + \Omega - \varepsilon_{\lambda} - i\delta} \right\} \quad (14)
\end{aligned}$$

the retarded self-energy is simply the complex conjugate of Eq. (14). It is easy to see why the current is divided into elastic and inelastic. The advanced and retarded self-energies, Eq. (14), do not include the exchange of a quantum of vibration in the energy balance of the process. While $\Sigma^>$ [Eq. (13)] includes the phonon in the delta of energy conservation, a quantum is transferred only in the inelastic term, Eq. (11).

We can make contact with the tunneling current by substituting the above equations in Eq. (3), and by using

$$G^>(\mathbf{r}_1, \mathbf{r}_2, \omega) = 2i(1 - n_F(\omega)) \text{Im} G^r(\mathbf{r}_1, \mathbf{r}_2, \omega)$$

The change in conductance due to the purely inelastic contribution of the sample, Eq. (11), is given by Eq. (15),

$$\begin{aligned}
\delta\left(\frac{dI}{dV}\right)(\omega) &= \frac{1}{i\pi} \iint d\vec{S}_1 d\vec{S}_2 \cdot (\{\vec{V}_1 - \vec{V}_1\} \text{Im} G_T^r(\mathbf{r}_1, \mathbf{r}_2, \omega) \\
&\times \{\vec{V}_2 - \vec{V}_2\} \delta G_S^>(\mathbf{r}_2, \mathbf{r}_1, \omega)) \quad (15)
\end{aligned}$$

where $\omega = \varepsilon_F + eV$ and we have replaced the trace by the surface integrations.

Let us first evaluate the inelastic contribution. After some simple algebra, we obtain Eq. (16),

$$\begin{aligned}
\delta\left(\frac{dI}{dV}\right)_{ine}(\omega) &= \frac{\pi}{2} \sum_{m, \lambda} (1 - f_{\lambda}) \\
&\times \left| \iint d\vec{S} \cdot (\delta\psi_{\lambda} \vec{V} \psi_m^* - \psi_m \vec{V} \delta\psi_{\lambda}^*) \right|^2 \delta(\varepsilon_m - \omega) \delta(\omega - \Omega - \varepsilon_{\lambda}) \quad (16)
\end{aligned}$$

and the perturbed sample wavefunction is given by Eq. (17).

$$\delta\psi_\lambda = \sum_\mu \psi_\mu \frac{\langle \mu|v|\lambda \rangle}{\varepsilon_\lambda - \varepsilon_\mu + i\delta} \quad (17)$$

The inelastic contribution, Eq. (16), presents a threshold with the voltage at the vibration frequency. The origin of the threshold is the Fermi factor $(1 - f_\lambda)$. By using the conservation of energy given by the δ functions of Eq. (16) we see that at zero temperature there is a sharp onset at $eV = \hbar\Omega$. As the temperature increases, the Fermi distribution function smears out and the threshold is less sharp. Other temperature effects are absent from the Eq. (17), since the phonon distribution function used in Eq. (14) did not take into account a phonon equilibrium population different from zero. As the voltage is ramped up, the change in conductance given by Eq. (16) is rather discontinuous, as corresponds to the sharp threshold just discussed. This translates into a second derivative of the current that presents a peak at the voltage matching the frequency of the vibration.

In order to evaluate the total change of conductance across the vibrational threshold, we can neglect the frequency dependence in the so-called quasi-static approximation. In this case $\omega \approx \varepsilon_F$ and Eq. (16) simplifies to Eq. (18):

$$\Delta \left(\frac{dI}{dV} \right)_{ine} = \frac{\pi}{2} \sum_{m,\lambda} \left| \int d\vec{S} \cdot (\delta\psi_\lambda \vec{\nabla} \psi_m^* - \psi_m \vec{\nabla} \delta\psi_\lambda^*) \right|^2 \delta(\varepsilon_F - \varepsilon_m) \delta(\varepsilon_F - \varepsilon_\lambda) \quad (18)$$

If just the s-wave contribution about a “center” of the tip is kept, Bardeen’s equation gives the Tersoff and Hamann approximation [23], which simplifies to a change of conductance that is proportional to the change in the LDOS due to the perturbation of the wavefunction [40]:

$$\delta \frac{dI}{dV} \propto \sum_\lambda |\delta\psi_\lambda(\vec{r}_0)|^2 \delta(\varepsilon_\lambda - \varepsilon_F)$$

The interpretation of this equation and of Eq. (16) is that the strength of the inelastic contribution is given by the modulation of the tunneling amplitude due to the vibration.

The elastic contribution is more complicated. The contribution is given by substituting Eq. (19),

$$\begin{aligned} \delta G_{ela}^>(\mathbf{r}_1, \mathbf{r}_2, \omega) &= -i \cdot 2\pi \sum_{\lambda,\mu,\nu} (1 - f_\lambda) \sum_{\lambda,\mu,\nu} (1 - f_\lambda) \frac{\psi_\lambda(\mathbf{r}_1) \psi_\nu^*(\mathbf{r}_2)}{\omega - \varepsilon_\nu - i\delta} \langle \lambda|v|\mu \rangle \langle \mu|v|\nu \rangle \\ &\times \left\{ \frac{1 - f_\mu}{\omega - \Omega - \varepsilon_\mu - i\delta} + \frac{f_\mu}{\omega + \Omega - \varepsilon_\mu - i\delta} \right\} \delta(\omega - \varepsilon_\lambda) + c.c. \quad (19) \end{aligned}$$

in Eq. (15). The corresponding expression cannot be factored as in the case of Eq. (16). Nevertheless we can explore the main features of the elastic contribution. At a given positive or negative voltage bias only one of the two terms f_μ or $(1 - f_\mu)$ sur-

vives. The corresponding denominator gives two contributions, a logarithmic divergence with a characteristic Fano-like profile, and a delta-like function. The integration across the vibrational threshold largely cancels the logarithmic divergence and only the delta function survives. The quasi-static approximation gives an expression (20) formally identical to the inelastic one except in that there is a minus sign multiplying Eq. (18). The change in the wavefunction to be used in the new expression is proportional to the imaginary part of Eq. (17).

$$\delta\psi_\lambda = \sqrt{2\pi} \sum_\mu \psi_\mu \langle \mu | v | \lambda \rangle \delta(\varepsilon_\lambda - \varepsilon_\mu) \quad (20)$$

The study of the lineshape of the second derivative of the current is more difficult, due to the appearance of Fano-like profiles in the elastic contribution. However, the total change across the vibrational threshold is very simple to evaluate and formally identical to the purely inelastic contribution. The main feature of the elastic contribution is that it is purely negative. This is an important consequence of this theory; the change in conductance is a mixture of positive (inelastic) and negative (elastic) contributions. Eventually, the change in conductance can be negative [45], contrary to the standard one-particle intuition [7]. A comprehensive analysis of the second-derivative lineshape has been performed for model systems using nonequilibrium Green's functions, and a thorough analysis on the different types of profiles can be found in refs. 46, 47, and 82.

The application of Tersoff and Hamman-type approximations leads to the equations of ref. 40; for a brief account see Chapter 4.

15.4 Elastic High-Transmission Regime

Soon after the invention of the STM it was realized that the instrument could be useful not only in the tunneling limit but also in the case where the tip is in direct contact with the substrate surface or adsorbates. In 1987, Gimzewski and Möller studied the transition from tunneling to point contact in a scanning tunneling microscope (STM) [2]. At a tip-sample distance corresponding to a resistance of the order $0.1G_0$ (the quantum of conductance is $G_0 = 2e^2/h = 1/(12.9 \text{ k}\Omega)$) they observed a sudden discontinuity in the current, and the resistance of the junction dropped to $\approx 10 \text{ k}\Omega$. This signified a “jump-to-contact” [55] and contact formation between tip and sample [67]. After these initial studies the properties of the atomic-scale metal contacts has been under intensive studies, and it has been realized that small chains of metal atoms bridging the electrodes can be formed and manipulated [81]. It is now known that the electronic valence structure plays a crucial role for the conductance of these systems, in contrast to conductance at the macro scale. In particular, contacts of single-valence metals (Au, Na, etc.) exhibit “quantized conductance,” i.e., preferred conductance values around integers of G_0 ,

whereas atomic metal contacts with higher valence do not [81]. Recently a device involving this quantization has been put forward [56].

The STM offers information about the sample surface prior to and after the contact formation. Especially, in the case of molecular contacts [57] the conductance depends strongly on bonding geometry, and this method gives important information. Further information may be obtained by measuring the force mediated by the contact [58, 59]. However, the structure of the contacts themselves is not known. To this end first-principles theory may give useful insights.

Shortly after the experiments by Gimsewski and Möller the conductance of atomic contacts was investigated theoretically by Lang [60] using DFT combined with scattering theory, and Ferrer et al. [61] used the empirical one-orbital tight-binding method combined with nonequilibrium Green's functions (NEGFs). The use of the combined DFT and NEGF methods has gained popularity in recent years in the study of atomic-scale contacts. This methodology has so far mostly yielded results in reasonable agreement with experiments on atomic metal contacts; however, in the case of molecular contacts there is limited correspondence between experiments and theory [62]. In this section, we will give a brief account of the method and discuss a few applications to the elastic transport properties of atomic metal contacts.

15.4.1

The Orbital-Based DFT-NEGF Method

The strong coupling limit poses some challenges for the theoretical method on several points. Firstly, the coupling of the contact region to the electrodes cannot be treated in perturbation theory since there are strong chemical bonds between all regions, rather than tunnel barriers [67]. Secondly, there is no obvious way to divide the system into, e.g., two electrode parts such as “tip” and “sample”, as is done in the tunnel perturbation approach. One way to deal with the latter problem is to use an atomic orbital basis set (Eq. (21), in which the orbital index α runs over all orbitals on all atoms in the system) to expand the wavefunctions.

$$\psi_{\mu}(\mathbf{r}) = \sum_{\alpha} \phi_{\alpha}(\mathbf{r}) c_{\alpha}^{\mu} \quad (21)$$

When the basis functions $\phi_{\alpha}(\mathbf{r})$ have a finite range in space this enables one to divide space (Hilbert space) into separate pieces chosen for computational convenience, and calculate the electronic current between these pieces. Since this system is neither isolated nor periodic one cannot use the normal periodic boundary conditions which are a standard ingredient in electronic structure calculations. This situation, combined with the nonperturbative nature, can be tackled within the DFT by calculating the exact scattering states [63]. Another popular approach is to use nonequilibrium Green's functions (NEGFs) [64, 65]. As with the scattering approach, with the NEGF method one can obtain the electronic current, density, and potential at a finite applied voltage. Furthermore the NEGF method facilitates

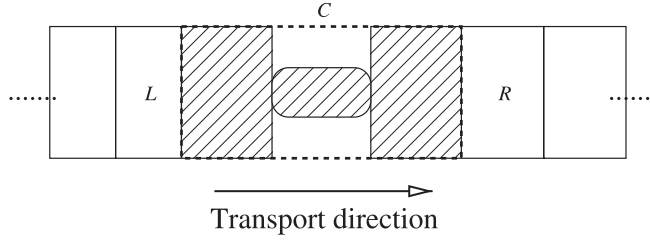


Fig. 15.1 Schematic picture of the division of the system into a central contact (C), and ideal left (L) and right (R) electrode regions.

the inclusion of interactions such as the electron–phonon coupling, as described in Section 15.5.

Below, we will briefly sketch the combined DFT-NEGF approach [42] we have used in the strong coupling regime, and then go through some illustrative applications. Recently a similar method has been used to study the contact formation in STM [68]. Detailed reviews covering several related methods can be found in refs. 69 and 70.

We consider the following system setup (Fig. 15.1): a left semi-infinite electrode (L), a contact region (C), and a right semi-infinite electrode (R). We use an atomic orbital basis set with a finite range as implemented in the SIESTA DFT code [71]. This basis enables us to split space into these regions. (The fact that these basis functions has an overlap $\langle \phi_\alpha | \phi_\beta \rangle = \mathbf{S}_{\alpha,\beta}$ has to be taken into account but does not alter the fundamental ideas; see, e.g., ref. 42 for further details.) The electrode regions L and R are chosen to have a perfect layer structure with a potential converging to the bulk values; i.e., all disturbances in the C region are assumed to be screened out here. There is no orbital overlap or interaction *directly* between L and R regions. In the setup in Fig. 15.1, the Hamiltonian matrix takes the form of Eq. (22),

$$\mathcal{H} = \begin{pmatrix} \mathbf{H}_L & \mathbf{V}_L & 0 \\ \mathbf{V}_L^\dagger & \mathbf{H}_C & \mathbf{V}_R \\ 0 & \mathbf{V}_R^\dagger & \mathbf{H}_R \end{pmatrix}, \quad (22)$$

where the \mathbf{H}_R is a semi-infinite tri-diagonal matrix

Likewise for \mathbf{H}_L , Eq. (23) applies.

$$\mathbf{H}_R = \begin{pmatrix} \mathbf{h}_R & \mathbf{v}_R & 0 & \cdots \\ \mathbf{v}_R^\dagger & \mathbf{h}_R & \mathbf{v}_R & 0 & \cdots \\ 0 & \mathbf{v}_R^\dagger & \mathbf{h}_R & \mathbf{v}_R & \ddots \\ \vdots & \ddots & \ddots & \ddots & \ddots \end{pmatrix} \quad (23)$$

The intralayer (\mathbf{h}) and interlayer (\mathbf{v}) Hamiltonians are identical to the corresponding Hamiltonians for the semi-infinitely repeated layer structure for the L or R electrodes, and can be calculated once and for all using periodic boundary conditions. The electron density, $n(\mathbf{r})$, is obtained through Eq. (24) via the density matrix, $\mathbf{D}_{\alpha\beta}$,

$$n(\mathbf{r}) = \sum_{\alpha,\beta} \phi_{\alpha}(\mathbf{r}) \mathbf{D}_{\alpha\beta} \phi_{\beta}(\mathbf{r}) \quad (24)$$

which again is related to the retarded Green's function matrix, \mathbf{G} [Eq. (25)] by Eq. (26),

$$\mathbf{G}(E) = (E + i\delta - \mathcal{H})^{-1} \quad (25)$$

$$\mathbf{D} = \int \frac{dE}{2\pi} n_F(E - E_F) i[\mathbf{G}(E) - \mathbf{G}^{\dagger}(E)] \quad (26)$$

This latter equation is *only* true in *equilibrium* when no voltage is applied between left and right electrodes. We return to the nonequilibrium situation shortly.

We note that obtaining \mathbf{G} involves the inversion of an *infinite* matrix, which is not practical! On the other hand, all interesting properties take place within the C region since here the electron density and potential differ from the bulk values in the electrodes (i.e., the matrix elements differ from the values in $\mathbf{h}_{L,R}$). So we basically want to consider finite matrices involving this region. For orbitals *inside* the C region we can in fact write this part of \mathbf{G} exactly as an inversion of a *finite* matrix, as in Eq. (27),

$$\mathbf{G}_{CC}(E) = [E + i\delta - \mathbf{H}_C - \boldsymbol{\Sigma}_L(E) - \boldsymbol{\Sigma}_R(E)]^{-1} \quad (27)$$

where the so-called (one-electron) self-energies, $\boldsymbol{\Sigma}_{L,R}$, fully take into account the coupling of the C region to the L and R . The self-energies can be calculated exactly; due to the perfect semi-infinite layer structure of the electrodes, which translates into a tri-diagonal semi-infinite matrix, we can formally write Eq. (28),

$$\mathbf{H}_R = \begin{pmatrix} \mathbf{h}_R & \mathbf{v}_R \\ \mathbf{v}_R^{\dagger} & \mathbf{H}_R \end{pmatrix} \quad (28)$$

We can obtain its inverse restricted to the first R unit cell, \mathbf{g}_R , by an efficient iterative procedure [72],

$$(E + i\delta - \mathbf{H}_R)^{-1} = \begin{pmatrix} \mathbf{g}_R(E) & \cdots \\ \vdots & \ddots \end{pmatrix}, \quad (29)$$

where we do not specify the other elements (marked by “ \cdots ”).

With this at hand, and similarly for L , we can using simple algebra solve the matrix equations (25), (27), and find Eq. (30),

$$\Sigma_L(E) = \mathbf{V}_L^\dagger \mathbf{g}_L \mathbf{V}_L, \quad \Sigma_R(E) = \mathbf{V}_R^\dagger \mathbf{g}_R \mathbf{V}_R \quad (30)$$

Roughly speaking, the real part of $\Sigma_{L,R}$ describes the change in energy levels in region C due to the bond formation with the L, R electrodes, whereas the imaginary part describes the decay (inverse lifetime) of electronic states located inside region C . This latter “escape rate” is directly related to the electron transport and is denoted by Eq. (31),

$$\Gamma_L(E) = i[\Sigma_L(E) - \Sigma_L^\dagger(E)] \quad (31)$$

and likewise for R .

Using these and Eq. (27) we can also write Eq. (32) for the density matrix, which specifies the density inside region C ,

$$\mathbf{D} = \int \frac{dE}{2\pi} n_F(E - E_F) [\mathbf{G}\Gamma_L\mathbf{G}^\dagger(E) + \mathbf{G}\Gamma_R\mathbf{G}^\dagger(E)] \quad (32)$$

where we have assumed all matrices (orbital indices) now due to the “self-energy trick” are restricted to the C region only, and discarded the “ CC ” labels.

One can show [42] that the first/second term in Eq. (32) corresponds to the electron density in region C due to the filling of scattering states originating in the left/right electrode. In equilibrium these scattering states are filled to the common Fermi level $E_F^L = E_F^R = E_F$. Out of equilibrium this is not the case: in this case there is a voltage drop and a difference in the filling of the scattering states and the two terms in Eq. (32) acquire a different Fermi function:

$$\mathbf{D} = \int \frac{dE}{2\pi} n_F(E - E_F^L) [\mathbf{G}\Gamma_L\mathbf{G}^\dagger](E) + n_F(E - E_F^R) [\mathbf{G}\Gamma_R\mathbf{G}^\dagger](E) \quad (33)$$

In the language of NEGF this is written in terms of the so-called “lesser” or electron distribution Green’s function [64, 65], as in Eq. (34),

$$\mathbf{D} = \int \frac{dE}{2\pi} (-i\mathbf{G}^<(E)), \quad \mathbf{G}_{\alpha\beta}^<(t) = i\langle \hat{c}_\alpha^\dagger(t) \hat{c}_\beta \rangle \quad (34)$$

This describes how the charge density in region C responds to the external battery with voltage V making the chemical potentials differ in the two electrodes, $E_F^L - E_F^R = eV$. The two electrodes are still assumed to be described by their bulk quantities as in Eq. (23), except for a constant shift in the potential zero and Fermi energy. Thus it is assumed that the current has spread out and the change in density due to the nonequilibrium is screened in the L, R regions. In the DFT method we calculate the electronic density and potential in a self-consistent cycle but now us-

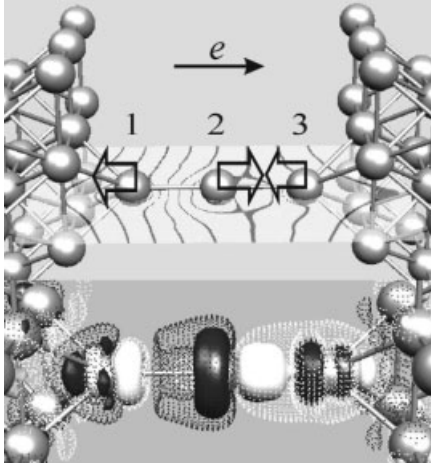


Fig. 15.2 Atomic gold wire connecting (100) electrodes. (a) The contours indicate the voltage drop, i.e., change in one-electron potential, \mathcal{V} from 0 V to 1 V ($\mathcal{V}_{1V}(\mathbf{r}) - \mathcal{V}_{0V}(\mathbf{r})$). The arrows indicate the direction of the forces on the atoms due to the nonequilibrium.

(b) Isodensity surfaces for the *change* in density from 0 V to 1 V. Dark is deficit and white is extra electron density. The solid (dotted) surfaces correspond to $\pm 5 \times 10^{-4} e \text{ \AA}^{-3}$ ($\pm 2 \times 10^{-4} e \text{ \AA}^{-3}$). From ref. 73.

ing the expression in Eq. (33) for the electron density inside C . This enables us to calculate the voltage drop in a current-carrying device, which in the case of a strong contact is a nontrivial quantity which does not only include the response of the electrons due to the electric potential but also the effect of the nonequilibrium filling.

An illustration of this is shown in Fig. 15.2, where an atomic gold wire three atoms long is considered connecting two (100) electrodes with $E_F^L - E_F^R = 1$ eV. The voltage is not dropping linearly across the wire but mainly in the bond between atoms 1 and 2. The reason for the asymmetry can be traced back to the fact that the wire loses electronic charge with the applied voltage and becomes slightly more positive with bias. The nonequilibrium situation changes the electron density in the atomic bonds and will lead to forces and structural changes. The voltage drop has been analyzed for molecular conductors [80, 74].

In the case of no interactions beyond the mean-field potential (e.g., electron-phonon; cf. Section 15.5) the conductance can be cast in the Landauer-Büttiker [75] form, Eqs. (35) and (36),

$$G = G_0 \int dE (n_F(E - E_F^L) - n_F(E - E_F^R)) \text{Tr}[t^\dagger t](E) \quad (35)$$

$$= G_0 \int dE (n_F(E - E_F^L) - n_F(E - E_F^R)) T_{\text{Tot}}(E) \quad (36)$$

where the transmission amplitude matrix involves the decay rates to the left and right electrodes and the matrix elements of the retarded Green's function between orbitals connecting L and R [76]:

$$\mathbf{t} = (\mathbf{\Gamma}_R)^{1/2} \mathbf{G} (\mathbf{\Gamma}_L)^{1/2} \quad (37)$$

The transmission itself depends on the applied voltage through the change in the self-consistent potential landscape in the C region (i.e., the change in \mathbf{H}_C in Eq. (22) with applied voltage) and the rigid potential shifts of the electrodes relative to each other. An equivalent and popular way to write the conductance is Eq. (38):

$$G = G_0 \int dE (n_F(E - E_F^L) - n_F(E - E_F^R)) \text{Tr}[\mathbf{\Gamma}_R \mathbf{G} \mathbf{\Gamma}_L \mathbf{G}^*] \quad (38)$$

Contrary to the weak coupling/tunneling situation, the total transmission, $T_{\text{Tot}}(E)$, can take values greater than 1 corresponding to several transmitting channels. This can be investigated using the so-called transmission eigenchannels [77, 78],

$$T_{\text{Tot}}(E) = \sum_n \tau_n(E) \quad (39)$$

which correspond to a basis change of scattering states so that \mathbf{t} becomes diagonal with values $0 \leq \tau_n \leq 1$ in the diagonal.

By plotting the corresponding scattering states at a particular energy, one can get information on what orbitals contribute to the conduction. As an example, in Fig. 15.3 we consider a platinum atomic wire where two highly transmitting channels exist for that particular atomic configuration. From the plots of these two channels it is qualitatively seen how the d orbitals enter these: the first channel has an angular momentum $m = 0$ character and involves d_{z^2} orbitals on the wire atoms while the second channel involves higher angular momentum d orbitals. (Note that the left–right symmetry is broken since we consider scattering states originating in the right electrode.)

In the case of atomic gold wires the d electrons do not participate significantly in the conduction, which is mainly carried by a single channel consisting of zero angular momentum states around the wire axis (mainly 6s). The 6s orbitals have a greater range and larger ss matrix elements compared to the d orbitals. The effect of this can be seen in the big variation of the conductance with interatomic distances in Pt compared to Au [79], but also in the I – V characteristics.

To illustrate this latter effect we consider in Fig. 15.4 a comparison between simplified gold and platinum single-atomic contacts. For Au the transmission at zero bias is dominated by a single, broad channel of mainly 6s character resulting from the strong coupling of these orbitals. For almost constant channel transmissions within the voltage window, and without a change of the transmission behavior with voltage, we anticipate from Eqs. (39) and (36) a quite linear I – V . This turns

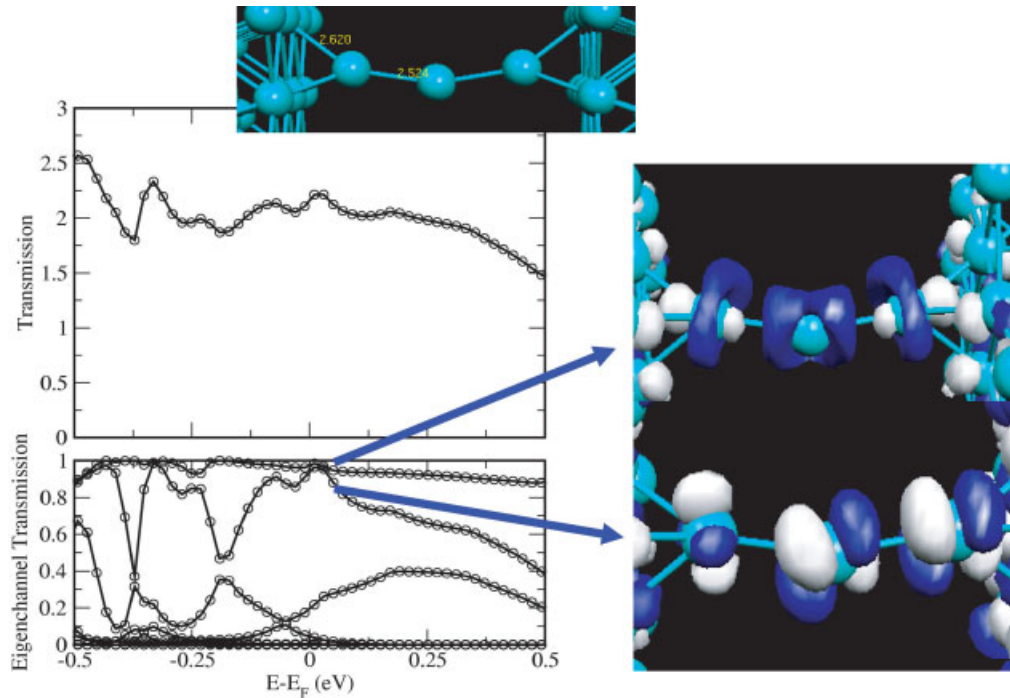


Fig. 15.3 The total transmission and eigenchannel transmissions for a platinum wire (at zero voltage). The scattering states corresponding to the two highest transmitting channels at the Fermi energy are shown. These

clearly involve d orbitals of different character (the color indicates the phase of the wavefunction). The channel involving d_{z^2} orbitals (upper) has least variation in eigenchannel transmission with energy.

out to be the case since we find that the change in channel behavior with bias below a couple of volts is very minor for Au. This is in contrast to Pt. Here we find four channels with significant contributions and a much stronger variation with energy for zero bias. Note that the d_{yz} , d_{zx} channels are degenerate while the d_{xy} and $d_{x^2-y^2}$ channels are split due to the symmetry of the (100) electrodes. Additionally the s and d_{z^2} channels at certain energies split into two contributing channels. From the strong variation with energy and rich structure we do not anticipate a linear I - V and furthermore we cannot expect the channel structure to be independent of bias: indeed for finite bias we find that a significant change in the $\{d_{yz}, d_{zx}, d_{xy}, d_{x^2-y^2}\}$ -derived channels, which become less transmitting and downshifted in energy, whereas the broader s-derived channel is not prone to the shift in potential.

Thus we find that the reason for the decrease in conductance with bias for Pt is the significant participation of the d electrons in the transport: the d electrons are more easily scattered by the voltage-induced potential, which in this case is of the same order of magnitude as the strength of the coupling to the electrodes. The

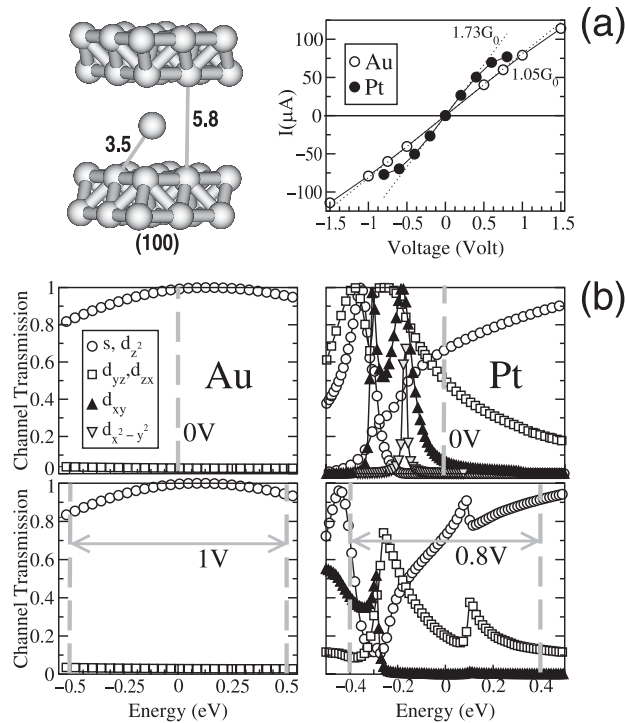


Fig. 15.4 Comparison of the I - V characteristics of a simplified Au and Pt single-atom contact. The z direction is defined to be perpendicular to the electrode surfaces. (a) Atomic structure (atom-surface distance shown in Å) of a single-atom contact of Au and Pt between (100) electrodes, and corresponding I - V . (b) Eigenchannel

decomposition of the total transmission through the atoms for Au for 0 V and 1 V (left panels) and Pt for 0 V and 0.8 V (right panels). The channels are labeled by their main orbital components (z is the direction perpendicular to the electrode surfaces). The gray broken lines indicate the voltage window. From ref. 79.

same argument goes for the variation with atom-electrode distance. Here it is essentially the d contributions which decrease as the distance increases.

15.5 Inelastic High-Transmission Regime

Inelastic effects in the contact regime are qualitatively different from those in the tunneling case. The main difference is the out-of-equilibrium character of transport in the contact regime. In this case the conductance is high, and electron transport must be described without use of the equilibrium electronic structure. The consequences are that the simplifications leading to a computable but accurate ac-

count of inelastic effects in the tunneling regime are not applicable any longer. In particular, in the steady state, the oscillator will reach an equilibrium with the electron current when the vibrational excitation rate is equilibrated by the de-excitation one. This will lead to an average phonon population different from zero, allowing the heating of the conduction region.

Despite these difficulties, there has been some progress recently, in particular steered by the experimental progress in the field of electron transport and molecular electronics. Part of the experimental progress has again been led by the study of conductance of single-atomic gold wires (or chains) [11]. By recording the conductance of the wire against the displacement of the tip, it was possible to determine the approximate length as well as the level of strain of the wire. The data show distinct drops of conductance at different tip–substrate voltages, leading to the conclusion that the conducting electrons were backscattered from wire vibrations. The onset of the drops was assumed to coincide with natural vibration frequencies of the wire at certain sizes and strains. An experimental result is shown in Fig. 15.5 from ref. 12 involving four stages of wire strain. We note especially the following features: (a) a single primary conductance drop of the order of $0.01G_0$ corresponding to a vibrational quantum of $\hbar\Omega \sim 10\text{--}20$ meV; (b) mode softening with strain; and (c) the increased vibrational signal with strain. In the molecular case, the inelastic signal has been measured in the high-transmission limit for a hydrogen molecule in a Pt break junction [66].

This type of experiment gives valuable additional information about the nature of the contacts. Steered partly by the experimental findings, there is an increasing

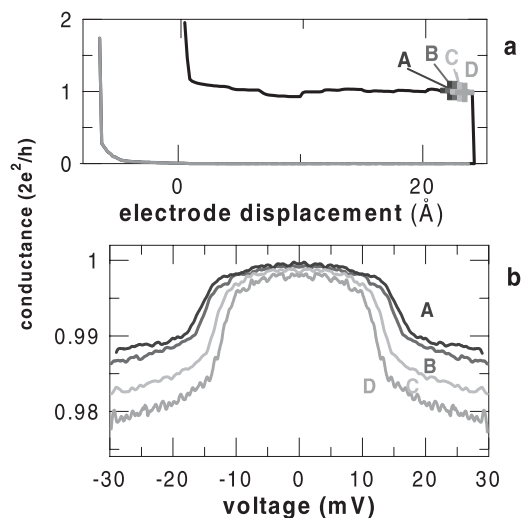


Fig. 15.5 Experimental results from ref. 12. (a) Measured conductance at fixed bias as the atomic wire is being pulled. (b) Differential conductance from (a) vs. voltage. The increase in the separation between the electrodes for each of the successive curves A, B, C, D, is 0.5 Å. The experiment was performed at $T = 4.2$ K.

interest in the theoretical modeling of the electron–vibration processes in electron transport. A first theoretical approach has been taken by several groups [50, 51] where they apply a Fermi golden rule to evaluate the rate of phonon excitation by the electron current. The electron–vibration interaction can be treated numerically exactly [52] when one neglects the electron occupation and assumes a single-particle picture. The many-particle features involve the Pauli principle, taking into account the occupations and especially the change in occupations in the presence of electron current in the scattering processes. This is also taken into account in the NEGF approach; however, it can only be solved in terms of partial summation of the perturbative series as discussed below. This approach has recently been applied to atomic-scale conductors by Asai [53] using Hückel theory for the electronic structure, and Frederiksen et al. [54] using DFT. It is this latter method which we briefly review below.

Again the theory is based on DFT and takes as the starting point the system setup and electronic Hamiltonian in Eq. (22). We employ the standard adiabatic approximation and consider the atomic positions as a parameter in the electronic Hamiltonian. We restrict the atomic motion to the central region C , use the harmonic approximation, and determine the normal vibrational modes (λ) and their frequencies (Ω_λ) for selected atoms embedded in region C , denoted by the small displacements, Q_λ . We can choose a C region large enough so that only \mathbf{H}_C will depend on the atomic motion around the equilibrium positions, and to lowest order we have Eq. (40),

$$\mathbf{H}_C(Q) \approx \mathbf{H}_C(0) + \sum_\lambda \frac{\partial \mathbf{H}_C}{\partial Q^\lambda} \cdot Q^\lambda \quad (40)$$

or explicitly quantizing the harmonic motion, Eq. (41),

$$\mathbf{H}_C(Q) \approx \mathbf{H}_C(0) + \sum_\lambda \mathbf{M}^\lambda (\hat{b}_\lambda^\dagger + \hat{b}_\lambda) \quad (41)$$

The coupling matrices for each mode, \mathbf{M}^λ , are equivalent to the electron–vibration coupling potential v of Section 15.3.4. They can be calculated in the atomic orbital basis set using finite differences [83]. In Section 15.3.4, the eigenstate basis set was used instead. Thus all modes and parameters (Ω_λ , Q_λ , \mathbf{M}^λ), can be determined using DFT without using fitting parameters. The NEGF method is especially ideal for a systematic treatment of the nonequilibrium situation in combination with interactions beyond the mean-field approximation, as employed, e.g., by DFT. It is possible to go to infinite order in the perturbing \mathbf{M}^λ using the self-consistent Born approximation (SCBA) [64, 82]. The self-consistency of this approximation to the many-body system provides the theory with current conservation, which of course is important when the electronic current is a primary quantity under investigation.

As an example of the method, we consider its application to the inelastic transport in gold wires four atoms long, just before rupture. The typical force mediated

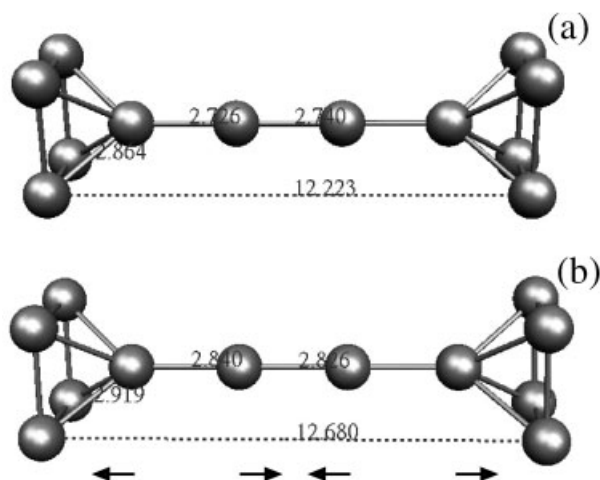


Fig. 15.6 Geometry of a four-atom gold wire under two different states of stress corresponding to an electrode separation of (a) $L = 12.22 \text{ \AA}$ and (b) $L = 12.68 \text{ \AA}$. The gold electrodes are modeled by perfect (100) surfaces. The alternating bond length (ABL)

modes, which cause the inelastic scattering, are shown schematically below each structure, together with mode energies Ω_i and reduced conductance drop $\Delta G/G(0 \text{ V})$. The displayed interatomic distances are measured in \AA units.

by the wire at fracture is 1.5 nN [58]. We consider in Fig. 15.6 two stages of strain corresponding to electrode separations of $L = 12.22 \text{ \AA}$ and $L = 12.68 \text{ \AA}$ corresponding to forces of about 0.5 nN and 1.5 nN. In the results displayed in Fig. 15.7 the phonon occupation is kept constant (almost zero) corresponding to the experimental temperature $T = 4 \text{ K}$, i.e., in a situation where the vibration is losing all its energy obtained from the electronic current to an external source such as phonons in the electrodes (the damping is not included in the dynamics of the oscillator, which is valid when the damping rate is much smaller than the vibrational frequency). The results of the calculation reproduce the main features of the experiments: (a) a single main conductance drop is observed; (b) the order of magnitude of the conductance drop; (c) the mode softening; and (d) the increased phonon signal with strain. A frequency shift with elongation ($\Delta\Omega/\Delta L = 7 \text{ meV \AA}^{-1}$) corresponding to a softening of the bonds in the wire is also in accordance with the experiments.

The fact that only a single main drop is observed can be traced back to the symmetry of the electronic states at the Fermi level. These states are mainly composed of s orbitals (see Fig. 15.7) as discussed in the previous section. The symmetry dictates that this state mainly couples to longitudinal vibrations where the bond length is alternating inside the wire.

A closer look at the experimental results in Fig. 15.5 show a slight slope of the conductance versus voltage after the onset of the vibrational excitation. This can be explained as being due to heating of the vibrations caused by the electronic excitation. We can take the opposite limit, assuming that there is no external damping

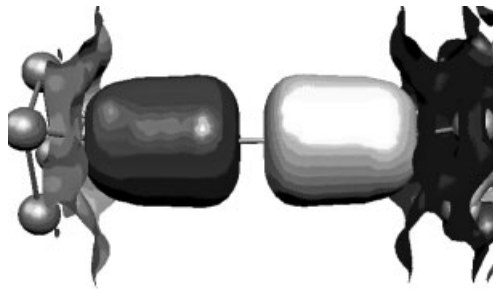
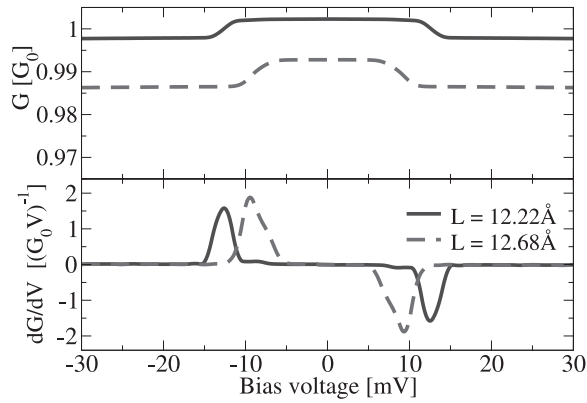


Fig. 15.7 Differential conductance and its derivative for the four-atom gold wire at two different tensions in the case where the oscillators are externally damped ($N_\lambda \approx 0$). All modes are included in this calculation. Below, the state at E_F responsible for the transport is shown (similar for both chain lengths).

mechanism (e.g., phonons in the electrodes) keeping the occupation fixed. In this case the vibration can only lose energy to electronic excitations and the number of phonons is determined by the excitation and de-excitation due to the coupling to the electronic degrees of freedom. For a given bias voltage we can use the fact that the system is in a steady state and we require that the net power into the vibration must be zero. The power can be obtained using the NEGF as well [54]. This in turn puts a restriction on N_λ . For simplicity we include only the most important mode. The idea is illustrated in Fig. 15.8, where the power balance for different fixed-mode occupations is shown. For low bias and finite phonon excitation we will have energy transfer from the phonon subsystem to the electrons: i.e., vibrational damping due to the electron–hole pair excitation. For increasing voltage, each power curve crosses the abscissa at one particular point (marked with a dark circle) corresponding to power balance between the electronic and phonon subsystems: hence the crossing point sets the occupation at the corresponding bias

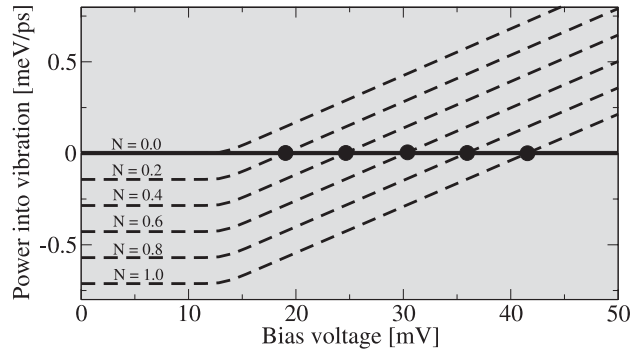


Fig. 15.8 Net power transferred from the electrons to the phonon mode vs. bias voltage for different (fixed) occupations N . The data shown here for $L = 12.22 \text{ \AA}$ are representative for both geometries.

voltage when we assume a steady state. At a voltage $V = 55 \text{ mV}$ the occupation is found to be the same as if the mode was occupied according to a Bose–Einstein distribution with temperature $T = 300 \text{ K}$. The conductance calculation is shown in Fig. 15.9(a). Compared with the externally damped results (Fig. 15.7), the notable differences are a slightly larger drop as well as a finite slope in the conductance beyond the onset of inelastic scattering. This increase in backscattering with voltage beyond the threshold is simply due to the fact that the probability of emitting a phonon and thus of backscattering increases with an increasing number of phonons present. Quantitatively we find a slope (dG/dV) which is only slightly larger than detected for relatively long atomic gold wires. Including the damping due to the coupling to electrode phonons, one can expect that the typical damping conditions lead to conductance curves between those in Figs. 15.7 and 15.9(a). However, measurements are the closest to the externally undamped limit, which suggests that such mechanisms are weak and that the mode “heating” is a significant element.

15.6 Conclusions and Outlook

The modeling and understanding of transport on the atomic scale has experienced enormous progress over the last decade. The possibility to understand the electronic conduction properties of ensembles of a few atoms has reached unprecedented accuracy in ballistic conductance. However, atomic motion cannot be neglected in many situations of electronic transport, in particular when temperature effects are to be accounted for. The progress of present-day experimental techniques has permitted isolation at low temperature of the effect of a few vibrational

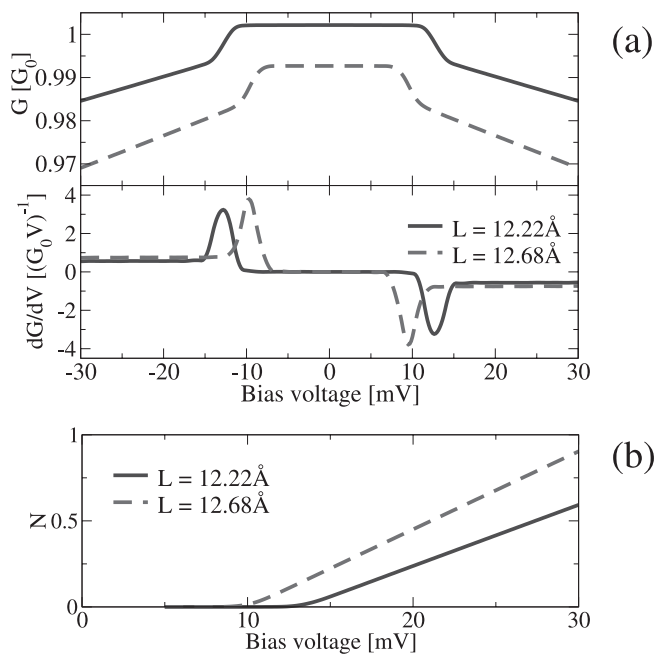


Fig. 15.9 (a) Differential conductance and its derivative for the four atom gold wire at two different tensions in the externally undamped limit. Only the most important mode is included in this calculation. (b) Mode occupation N vs. bias voltage.

modes and a few vibrational quanta on the electronic transport, furnishing a privileged framework for the comprehension and development of theoretical tools. In this chapter we first addressed the tunneling regime in which a single vibration is excited once in a chemisorbed molecule. This particular case has yielded a new field of activity in the study of surface science by permitting the chemical analysis of surfaces via their single-molecule vibrational spectra.

Indeed tunneling represents a very adequate framework in to enhance the effect of vibrations. This is due to the extremely low transmission probabilities of the electron through the insulating gap, the vacuum in the case of STM studies. When the transmission becomes high, the study of vibrations becomes more difficult. In the contact regime with transmissions of the order of 1, the conductance is several orders of magnitude larger than in the tunneling case. A first consequence is that the current can drive the vibrational degrees of freedom out of equilibrium by continuously exciting the vibrational modes of the conducting structure. A good theory needs to include dissipative effects to be able to equilibrate the power injected in the nuclear motion. Indeed, this chapter shows how to achieve this in the case of the very precise experimental situation of vibrational excitation of monoatomic gold chains by an electronic current.

The good agreement with the available experimental data for this particular system shows that strategies combining traditional transport calculations with *ab-initio*-like electron structure calculations are fundamental for understanding the actual physical processes. The simulations presented here have permitted us to understand the role of external strain on the vibrations and their coupling to the electronic current. The first experimental data seemed to indicate that electron transport was highly selective by only exciting one type of vibration which underlined the role of symmetry of the vibrations and quantum states in atomic-scale conduction. The calculations have made it possible to go beyond these analyses, and to show that in certain situations several modes can contribute, emphasizing the quantal aspects of the transport process.

Yet, these calculations are among the first in a series of improvements and developments needed in the field of realistic transport simulations. In order to give a succinct idea of the developments to come, we would like to emphasize the role of temperature in electronic transport, in particular via the delicate balance between exciting and de-exciting vibrations that are subjected to a high external temperature such as is the case in microelectronic applications. It is then mandatory to develop efficient numerical schemes that can solve the coupled Keldysh–Dyson equations for both the electronic and nuclear degrees of freedom. Of concern is the case when perturbational schemes are not valid, such as in vibronic tunneling and in polaronic transport. We think that the coming years will see many activities concerning these problems and full simulation codes will appear, allowing the accurate description of nanoelectronic devices under working conditions.

Acknowledgements

We thank Thomas Frederiksen for the figures and calculations of Section 15.5. We also acknowledge interesting discussions with H. Ueba, J. I. Pascual, M. Persson, R. Rurali, M. Paulsson and A.-P. Jauho.

References

- 1 G. BINNING, H. ROHRER, Ch. GERBER, E. WEIBEL, *Appl. Phys. Lett.* **40**, 178 (1982); *Phys. Rev. Lett.* **49**, 57 (1982).
- 2 J. K. GIMZEWSKI, R. MÖLLER, *Phys. Rev. B* **36**, 1284 (1987).
- 3 L. OLESEN, M. BRANDBYGE, M. R. SØRENSEN, K. W. JACOBSEN, E. LÆGSGAARD, I. STENSGAARD, F. BESENBACHER, *Phys. Rev. Lett.* **76**, 1485 (1996).
- 4 C. J. MULLER, J. M. VAN RUITENBEEK, L. J. DE JONGH, *Phys. Rev. Lett.* **69**, 140 (1992).
- 5 M. BRANDBYGE, J. SCHIØTZ, M. R. SØRENSEN, P. STOLTZE, K. W. JAKOBSEN, J. K. NØRSKOV, L. OLESEN, E. LÆGSGAARD, I. STENSGAARD, F. BESENBACHER, *Phys. Rev. B* **52**, 8499 (1995).
- 6 C. B. DUKE, *Tunneling in Solids*, Suppl. 10 of *Solid State Physics*, edited by F. SEITZ, D. TURNBULL, Academic Press, New York, USA, 1969.

- 7 P. K. HANSMAN, *Phys. Rep.* **30**, 145 (1977).
- 8 L. C. DAVIS, *Phys. Rev. B* **2**, 1714 (1970).
- 9 C. CAROLI, R. COMBESCOT, P. NOZIÈRES, D. SAINT-JAMES, *J. Phys. Part C Solid State Physics* **5**, 21 (1972).
- 10 B. C. STIPE, M. A. REZAEI, W. HO, *Science* **280**, 1732 (1998).
- 11 N. AGRAÏT, C. UNTIEDT, G. RUBIO-BOLLINGER, S. VIEIRA, *Phys. Rev. Lett.* **88**, 216 803 (2002).
- 12 N. AGRAÏT, C. UNTIEDT, G. RUBIO-BOLLINGER, S. VIEIRA, *Chem. Phys.* **281**, 231 (2002).
- 13 M. TSUKADA, K. KOBAYASHI, N. ISSHIKI, H. KAGESHIMA, *Surf. Sci. Rep.* **13**, 265 (1991).
- 14 R. WIESENDANGER, H.-J. GÜNTHERODT (eds.), *Scanning Tunneling Microscopy III*, Springer Series in Surface Science, Berlin (1996).
- 15 W. A. HOFER, *Prog. Surf. Sci.* **71**, 147 (2003).
- 16 W. A. HOFER, A. S. FOSTER, A. L. SLUTER, *Rev. Mod. Phys.* **75**, 1287 (2003).
- 17 O. PAZ, I. BRIHUEGA, J. M. GÓMEZ-RODRÍGUEZ, J. M. SOLER, *Phys. Rev. Lett.* **94**, 56 103 (2005).
- 18 J. CERDA, M. A. VAN HOVE, P. SAUTET, M. SALMERON, *Phys. Rev. B* **56**, 15 885 (1997).
- 19 S. CORBEL, J. CERDA, P. SAUTET, *Phys. Rev. B* **60**, 1989 (1999).
- 20 <http://www.icmm.csic.es/jcerda/>.
- 21 W. A. HOFER, J. REDINGER, *Surf. Sci.* **447**, 51 (2000).
- 22 C. J. CHEN, *Phys. Rev. B* **42**, 8841 (1990); *Phys. Rev. Lett.* **65**, 448 (1990).
- 23 J. TERSOFF, D. R. HAMANN, *Phys. Rev. Lett.* **50**, 1998 (1983); *Phys. Rev. B* **31**, 805 (1985).
- 24 F. OLSSON, M. PERSSON, N. LORENTE, L. J. LAUHON, W. HO, *J. Phys. Chem.* **106**, 8169 (2002).
- 25 F. OLSSON, N. LORENTE, M. PERSSON, *Surf. Sci.* **522**, L27 (2003).
- 26 A. ZAWADOWSKI, *Phys. Rev.* **163**, 341 (1967).
- 27 J. A. APPELBAUM, W. F. BRINKMAN, *Phys. Rev.* **186**, 464 (1969).
- 28 J. B. PENDRY, A. B. PRÊTRE, B. C. H. KRUTZEN, *J. Phys. Condens. Mat.* **3**, 4313 (1991).
- 29 J. LI, W.-D. SCHNEIDER, R. BERNDT, O. BRYANT, S. CRAMPIN, *Phys. Rev. Lett.* **81**, 4464 (1998).
- 30 B. N. J. PERSSON, A. BARATOFF, *Phys. Rev. Lett.* **59**, 339 (1987).
- 31 W. DOMCKE, L. S. CEDERBAUM, *Phys. Rev. A* **16**, 1465 (1977).
- 32 J. P. GUAYACQ, *Dynamics of Negative Ions*, World Scientific, Singapore (1987).
- 33 G. P. SALAM, M. PERSSON, R. E. PALMER, *Phys. Rev. B* **49**, 10 655 (1994).
- 34 M. A. GATA, P. R. ANTONIEWICZ, *Phys. Rev. B* **47**, 13797 (1993).
- 35 C. SPATARU, P. BUDAU, *J. Phys. Condens. Mat.* **9**, 8333 (1997).
- 36 J. BONCA, S. A. TRUGMAN, *Phys. Rev. Lett.* **75**, 2566 (1995).
- 37 N. MINGO, K. MAKOSHI, *Surf. Sci.* **438**, 261 (1999).
- 38 N. MINGO, K. MAKOSHI, *Phys. Rev. Lett.* **84**, 3694 (2000).
- 39 E. G. EMBERLY, G. KIRCZENOW, *Phys. Rev. B* **61**, 5740 (2000).
- 40 N. LORENTE, M. PERSSON, *Phys. Rev. Lett.* **85**, 2997 (2000).
- 41 J. M. SOLER, E. ARTACHO, J. D. GALE, A. GARCIA, J. JUNQUERA, P. ORDEJON, D. SANCHEZ-PORTAL, *J. Phys. Condens. Mat.* **14**, 2745 (2002).
- 42 M. BRANDBYGE, J.-L. MOZOS, P. ORDEJÓN, J. TAYLOR, K. STOKBRO, *Phys. Rev. B* **65**, 165 401 (2002).
- 43 N. LORENTE, *Appl. Phys. A – Mater. Sci. Proc.* **78**, 799 (2004).
- 44 N. LORENTE, R. RURALI, H. TANG, *J. Phys. Condens. Mat.* **17**, S1049 (2005).
- 45 J. R. HAHN, H. J. LEE, W. HO, *Phys. Rev. Lett.* **85**, 1914 (2000).
- 46 T. MII, S. G. TIKHODEEV, H. UEBA, *Surf. Sci.* **502–503**, 26 (2002).
- 47 T. MII, S. G. TIKHODEEV, H. UEBA, *Phys. Rev. B* **68**, 205 406 (2003).
- 48 A. I. YANSON, G. RUBIO-BOLLINGER, H. E. VAN DEN BROM, N. AGRAÏT, J. M. VAN RUITENBEEK, *Nature (London)* **395**, 783 (1998).
- 49 L. H. YU, Z. K. KEANE, J. W. CISZEK,

- L. CHENG, M. P. STEWART, J. M. TOUR, D. NATELSON, *Phys. Rev. Lett.* **93**, 266 802 (2004).
- 50 M. J. MONTGOMERY, J. HOEKSTRA, T. N. TODOROV, A. P. SUTTON, *J. Phys. Condens. Mat.* **15**, 731 (2003).
- 51 Y.-C. CHENG, M. ZWOLAK, M. DI VENTRA, *Nano Lett.* **4**, 1709 (2004).
- 52 H. NESS, A. J. FISHER, *Phys. Rev. Lett.* **83**, 452 (1999).
- 53 Y. ASAI, *Phys. Rev. Lett.* **93**, 246 102 (2004).
- 54 T. FREDERIKSEN, M. BRANDBYGE, N. LORENTE, A.-P. JAUHO, *Phys. Rev. Lett.* **93**, 256 601 (2004).
- 55 J. B. PETHICA, A. P. SUTTON, *J. Vac. Sci. Technol. A* **6**, 2490 (1988).
- 56 K. TERABE, T. HASEGAWA, T. NAKAYAMA, M. AONO, *Nature* **433**, 47 (2005).
- 57 Y. Q. XUE, S. DATTA, S. HONG, R. REIFENBERGER, J. I. HENDERSON, C. P. KUBIAK, *Phys. Rev. B* **59**, R7852 (1999).
- 58 G. RUBIO-BOLLINGER, S. R. BAHN, N. AGRAÏT, K. W. JACOBSEN, S. VIEIRA, *Phys. Rev. Lett.* **87**, 26 101 (2001).
- 59 X. D. CUI, A. PRIMAK, X. ZARATE, J. TOMFOHR, O. F. SANKEY, A. L. MOORE, T. A. MOORE, D. GUST, G. HARRIS, S. M. LINDSAY, *Science* **294**, 571 (2001).
- 60 N. D. LANG, *Phys. Rev. B* **36**, 8173 (1987).
- 61 J. FERRER, A. MARTÍN-RODERO, F. FLORES, *Phys. Rev. B* **38**, 10 113 (1988).
- 62 A. NITZAN, M. RATNER, *Science* **300**, 1384 (2003).
- 63 N. D. LANG, *Phys. Rev. Lett.* **55**, 230 (1985).
- 64 H. HAUG, A.-P. JAUHO, *Quantum Kinetics in Transport and Optics of Semiconductors*, Springer-Verlag, Berlin, 1996.
- 65 S. DATTA, in *Electronic Transport in Mesoscopic Systems*, edited by H. AHMED, M. PEPPER, A. BROERS, Cambridge University Press, Cambridge, UK, 1995.
- 66 R. H. M. SMIT, Y. NOAT, C. UNTIEDT, N. D. LANG, M. C. VAN HEMERT, J. VAN RUITENBEEK, *Nature* **419**, 906 (2004).
- 67 W. HOFER, A. FISHER, *Phys. Rev. Lett.* **91**, 36 803 (2003).
- 68 J. BLANCO, C. GONZALEZ, P. JELINEK, J. ORTEGA, F. FLORES, R. PEREZ, *Phys. Rev. B* **70**, 85 405 (2004).
- 69 A. PECCHIA, A. DI CARLO, *Rep. Prog. Phys.* **67**, 1497 (2004).
- 70 D. BOWLER, *J. Phys. Condens. Mat.* **16**, R721 (2004).
- 71 J. M. SOLER, E. ARTACHO, J. D. GALE, A. GARCIA, J. JUNQUERA, P. ORDEJÓN, P. SANCHEZ-PORTAL, *J. Phys. Condens. Mat.* **14**, 2745 (2002).
- 72 M. LOPEZ-SANCHO, J. LOPEZ-SANCHO, J. RUBIO, *J. Phys. F* **14**, 1205 (1984).
- 73 M. BRANDBYGE, K. STOKBRO, J. TAYLOR, J. L. MOZOS, P. ORDEJÓN, *Phys. Rev. B* **67**, 193 104 (2003).
- 74 N. D. LANG, P. AVOURIS, *Nano Lett.* **3**, 737 (2003).
- 75 M. BÜTTIKER, Y. IMRY, R. LANDAUER, S. PINHAS, *Phys. Rev. B* **31**, 6207 (1985).
- 76 J. C. CUEVAS, A. L. YEYATI, A. MARTÍN-RODERO, *Phys. Rev. Lett.* **80**, 1066 (1998).
- 77 T. MARTIN, R. LANDAUER, *Phys. Rev. B* **45**, 1742 (1992).
- 78 M. BRANDBYGE, M. R. SØRENSEN, K. W. JACOBSEN, *Phys. Rev. B* **56**, 14 956 (1997).
- 79 S. K. NIELSEN, M. BRANDBYGE, K. HANSEN, K. STOKBRO, J. M. VAN RUITENBEEK, F. BESENBACHER, *Phys. Rev. Lett.* **89**, 66 804 (2002).
- 80 J. TAYLOR, M. BRANDBYGE, K. STOKBRO, *Phys. Rev. Lett.* **89**, 138 301 (2002).
- 81 N. AGRAÏT, A. L. YEYATI, J. M. VAN RUITENBEEK, *Phys. Rep.* **377**, 81 (2003).
- 82 M. GALPERIN, M. A. RATNER, A. NITZAN, *J. Chem. Phys.* **121**, 11 965 (2004).
- 83 M. HEAD-GORDON, J. C. TULLY, *J. Chem. Phys.* **96**, 3939 (1992).
- 84 L. D. LANDAU, E. M. LIFSHITZ, *Quantum Mechanics*, 3rd. edn., Pergamon Press, Oxford, 1991.
- 85 R. M. MARTIN, *Electronic Structure*, Cambridge University Press, Cambridge, UK, 2004, p. 482.

Appendix A

In this appendix we give a brief derivation of Bardeen's approximation in order to facilitate access to the approximations and physics contained in it.

We divide the space into two parts. Each will be described by a Hamiltonian and its states, the left-hand side by:

$$\left(-\frac{\hbar^2 \nabla^2}{2m} + V_L \right) \psi_{\mu,L} = \varepsilon_{\mu,L} \psi_{\mu,L}$$

and the right-hand one by:

$$\left(-\frac{\hbar^2 \nabla^2}{2m} + V_R \right) \psi_{\nu,R} = \varepsilon_{\nu,R} \psi_{\nu,R}$$

The total Hamiltonian takes into account the perturbation that the two contacts exert on each other, hence

$$\hat{H} = -\frac{\hbar^2 \nabla^2}{2m} + V_L + V_R + \Delta V$$

The Bardeen approach only needs three approximations:

- we can neglect the overlap between left and right states
- the left potential cannot cause transitions in the right states, and vice versa
- we can neglect all mutual interaction in the transmission matrix elements ΔV .

The rest of the approach develops on keeping the first contribution to tunneling. Some authors have included more conditions to reach Bardeen's results. In what follows we will reproduce Bardeen's results just by making use of the above conditions.

The first step is to show that we can write a Fermi's golden rule-like expression for the transition rate of a left state into right states. This is conceptually different from Fermi's golden rule, where the initial and final states diagonalize the same unperturbed Hamiltonian.

We proceed along the lines of Fermi's golden rule demonstration (see any quantum mechanics textbook, e.g., ref. 84). We expand a wavepacket in left and right states, and use Schrödinger's equation under the full Hamiltonian:

$$\psi(\mathbf{r}, t) = \sum_{\nu} a_{\nu}(t) \psi_{\nu,R}(\mathbf{r}) e^{-i\varepsilon_{\nu} t/\hbar} + \sum_{\mu} a_{\mu}(t) \psi_{\mu,L}(\mathbf{r}) e^{-i\varepsilon_{\mu} t/\hbar}$$

Hence we get Eq. (A1)

$$\begin{aligned}
& \sum_v i\hbar \frac{da_v}{dt} \psi_{v,R}(\mathbf{r}) e^{-i\varepsilon_v t/\hbar} + \sum_\mu i\hbar \frac{da_\mu}{dt} \psi_{\mu,L}(\mathbf{r}) e^{-i\varepsilon_\mu t/\hbar} \\
&= \sum_\mu (V_L + \Delta V) a_v(t) \psi_{v,R} e^{-i\varepsilon_v t/\hbar} + \sum_\mu (V_R + \Delta V) a_\mu(t) \psi_{\mu,L} e^{-i\varepsilon_\mu t/\hbar}. \quad (\text{A1})
\end{aligned}$$

The boundary conditions are that initially the wavepacket is prepared on a left state:

$$\psi(\mathbf{r}, t=0) = a_0(t) \psi_{0,L}(\mathbf{r}) e^{-i\varepsilon_0 t/\hbar}$$

and the final state is a right one $\psi_{\alpha,R}$. So we will project Schrödinger's equation on this final state to give Eq. (A2).

$$\begin{aligned}
& i \cdot \hbar \frac{da_\alpha}{dt} e^{-i\varepsilon_\alpha t/\hbar} + \sum_\mu i\hbar \frac{da_\mu}{dt} \langle \alpha, R | \mu, L \rangle e^{-i\varepsilon_\mu t/\hbar} \\
&= \sum_\mu \langle \alpha, R | V_L + \Delta V | v, R \rangle a_v e^{-i\varepsilon_v t/\hbar} + \sum_\mu \langle \alpha, R | V_R + \Delta V | \mu, L \rangle a_\mu e^{-i\varepsilon_\mu t/\hbar} \quad (\text{A2})
\end{aligned}$$

The above approximations lead us to neglect the terms on $\langle \alpha, R | \mu, L \rangle$ and $\langle \alpha, R | V_L + \Delta V | v, R \rangle$.

The probability of finding the wavepacket on the final state α is

$$P_{0 \rightarrow \alpha} = |\langle \psi(\mathbf{r}, t) | \alpha, R \rangle|^2 = |a_\alpha(t)|^2$$

By trivially solving the previous differential equation we find:

$$P_{0 \rightarrow \alpha} = \left| \frac{e^{i(\varepsilon_\alpha - \varepsilon_0)t/\hbar} - 1}{\varepsilon_\alpha - \varepsilon_0} \right|^2 |\langle \alpha, R | V_R + \Delta V | 0, L \rangle|^2$$

The transition rate is the speed of variation of the transmission probability:

$$\frac{1}{\tau} = \sum_\alpha \frac{dP_{0 \rightarrow \alpha}}{dt}$$

This leads to a Fermi golden rule-like expression in the long time and continuum limits (i.e., see [84]):

$$\frac{1}{\tau} = \frac{2\pi}{\hbar} \sum_\alpha |\langle \alpha, R | V_R + \Delta V | 0, L \rangle|^2 \delta(\varepsilon_\alpha - \varepsilon_0)$$

We need to evaluate the matrix element. In order to achieve this we restrict the integration to the right hemi-space; this is justified by the short range of both the

potential and the wavefunctions, and we neglect the mutual action of both electrodes:

$$\langle \alpha, R | V_R + \Delta V | 0, L \rangle \approx \langle \alpha, R | V_R | 0, L \rangle_R$$

If we use:

$$\langle \alpha, R | V_L | 0, L \rangle_R \approx 0$$

then we can write:

$$\langle \alpha, R | V_R + \Delta V | 0, L \rangle \approx \langle \alpha, R | V_R | 0, L \rangle_R + \langle 0, L | V_L | \alpha, R \rangle_R$$

A common expression is to use the kinetic energy operator instead of the potential one:

$$V_R | \alpha, R \rangle = \left(-\frac{\hbar^2 \nabla^2}{2m} - \varepsilon_\alpha \right) | \alpha, R \rangle$$

and

$$V_L | 0, L \rangle = \left(-\frac{\hbar^2 \nabla^2}{2m} - \varepsilon_0 \right) | 0, L \rangle$$

So finally:

$$\begin{aligned} \langle \alpha, R | V_R + \Delta V | 0, L \rangle &\approx \left\langle \alpha, R \left| -\frac{\hbar^2 \nabla^2}{2m} - \varepsilon_\alpha \right| 0, L \right\rangle_R + \left\langle 0, L \left| -\frac{\hbar^2 \nabla^2}{2m} - \varepsilon_0 \right| \alpha, R \right\rangle_R \\ &= \int_R -\frac{\hbar^2}{2m} \vec{\nabla} \cdot [\psi_{\alpha, R} \vec{\nabla} \psi_{0, L}^* - \psi_{0, L} \vec{\nabla} \psi_{\alpha, R}^*] d^3 r \\ &= \hbar i \int_S \vec{J}_{\alpha, 0} \cdot d\vec{S} \end{aligned}$$

Using the transmission rate, $1/\tau$, we can calculate the current in Bardeen's approximation: just by noting that the current is the transmitted charge per unit time, we recover expression (2).

Appendix B

The electron–vibration coupling can be obtained from the adiabatic or Born–Oppenheimer approximation. This statement is far from being obvious. Intuitively, one could think that the adiabatic approximation misses fundamental aspects of the nuclear dynamics leading to the electron–vibration coupling.

Let us first state the adiabatic approximation. Here we will use the same notation as ref. 85. This approximation is the general framework for all of the electronic structure calculations. It is based on the division of the full Hamiltonian into the nuclear kinetic energy T_N and the rest of the Hamiltonian, H_{el} , which includes electron–nucleus interactions. Hence,

$$\hat{H} = \hat{T}_N + \hat{H}_{el}$$

The full solution of the Schrödinger equation is

$$\hat{H}\Psi_s(\{\vec{r}, \vec{R}\}) = E_s\Psi_s(\{\vec{r}, \vec{R}\})$$

The full solution can be expanded in different ways, in particular on functions exclusively of the nuclear coordinates $\{\vec{R}\}$, given that:

$$\Psi_s(\{\vec{r}, \vec{R}\}) = \sum_i \chi_{s,i}(\{\vec{R}\})\psi_i(\{\vec{r}\}; \{\vec{R}\})$$

where $\psi_i(\{\vec{r}\}; \{\vec{R}\})$ are eigenfunctions of the electronic Schrödinger equation:

$$\hat{H}_{el}\psi_i(\{\vec{r}\}; \{\vec{R}\}) = E_i(\{\vec{R}\})\psi_i(\{\vec{r}\}; \{\vec{R}\})$$

In this equation $\{\vec{R}\}$ are not variables but just parameters. The ensemble of eigenvalues of this equation for the different $\{\vec{R}\}$ defines the potential energy surface (PES).

The solution of the full Schrödinger equation can be re-expressed by projecting it on the electronic eigenfunctions $\psi_i(\{\vec{r}\}; \{\vec{R}\})$. This yields

$$[T_N + E_i(\{\vec{R}\}) - E_s]\chi_{s,i}(\{\vec{R}\}) = -\sum_{i'} C_{ii'}\chi_{s,i'}(\{\vec{R}\})$$

where $T_N = -\frac{1}{2}(\sum_J \nabla_J^2/M_J)$, with J the index running over the nuclear coordinates and $\hbar = 1$, and the matrix elements are given by $C_{ii'} = A_{ii'} + B_{ii'}$, with

$$A_{ii'} = \sum_J \frac{1}{M_J} \langle \psi_i(\{\vec{r}\}; \{\vec{R}\}) | \nabla_J | \psi_{i'}(\{\vec{r}\}; \{\vec{R}\}) \rangle \nabla_J$$

and

$$B_{ii'} = \sum_J \frac{1}{M_J} \langle \psi_i(\{\vec{r}\}; \{\vec{R}\}) | \nabla_J^2 | \psi_{i'}(\{\vec{r}\}; \{\vec{R}\}) \rangle$$

The electronic equation is solved to find the PES and then, in the adiabatic approximation, the nuclear wavefunctions are solved, assuming that $C_{ii'} = 0$ giving

$\chi_{s,i}^{ad}$. This approximation is reasonable when the nuclear dynamics belongs to a timescale very different from the electronic one, which is justified in total energy calculations by the large mass mismatch between electrons and nuclei. In this approximation there is no electron–vibration coupling. Hence the justification of our intuitive fears.

But it is possible to approximate an interaction that couples the electronic and nuclear coordinates by looking at how the different adiabatic nuclear states are coupled by the $C_{ii'}$ terms.

Hence the coupling is

$$\langle \chi_{s'i}^{ad} | C_{ii'} | \chi_{si'}^{ad} \rangle = \langle \chi_{s'i}^{ad} | A_{ii'} | \chi_{si'}^{ad} \rangle$$

where we have assumed that $s'i \neq si'$ such that the term in B does not contribute. By doing so, we are going to place ourselves in the case of electron–vibration interactions in solids or solid surfaces, where there is a continuum of electronic states, and we are interested in studying the vibrational transitions, s' to s , while changing the adiabatic electronic state from i to i' . If we substitute the expression for $A_{ii'}$ we obtain

$$\langle \chi_{s'i}^{ad} | C_{ii'} | \chi_{si'}^{ad} \rangle = \sum_J \frac{1}{M_J} \langle \psi_i(\{\vec{r}\}; \{\vec{R}\}) | \nabla_J | \psi_{i'}(\{\vec{r}\}; \{\vec{R}\}) \rangle \langle \chi_{s'i}^{ad} | \nabla_J | \chi_{si'}^{ad} \rangle$$

This last expression can be further simplified by using:

- the Hellmann–Feynman theorem stating that

$$\langle \psi_i(\{\vec{r}\}; \{\vec{R}\}) | \nabla_J | \psi_{i'}(\{\vec{r}\}; \{\vec{R}\}) \rangle = \frac{\left\langle \psi_i(\{\vec{r}\}; \{\vec{R}\}) \left| \frac{\partial H_{el}}{\partial \vec{R}_J} \right| \psi_{i'}(\{\vec{r}\}; \{\vec{R}\}) \right\rangle}{E_{i'}(\{\vec{R}\}) - E_i(\{\vec{R}\})}$$

which is an exact result, and

- the evolution of the nuclear coordinate operators in the absence of external electromagnetic fields:

$$\frac{1}{M_J} \nabla_J = [\vec{R}_J, \hat{H}^{ad}]$$

Finally,

$$\begin{aligned} & \langle \chi_{s'i}^{ad} | C_{ii'} | \chi_{si'}^{ad} \rangle \\ &= \sum_J \frac{E_s^{ad} - E_{s'}^{ad}}{E_{i'}(\{\vec{R}\}) - E_i(\{\vec{R}\})} \langle \chi_{s'i}^{ad} | \vec{R}_J | \chi_{si'}^{ad} \rangle \cdot \left\langle \psi_i(\{\vec{r}\}; \{\vec{R}\}) \left| \frac{\partial H_{el}}{\partial \vec{R}_J} \right| \psi_{i'}(\{\vec{r}\}; \{\vec{R}\}) \right\rangle \end{aligned}$$

The fraction can be approximated by one due to energy conservation during elec-

tronic transitions in the solid, since the energy gained by the nuclei is equal to the energy spent in the electronic transition. This is definitely not so in the molecular case. Here, we have neglected the possibility of level crossings, which can be rather common; hence the above derivation should be taken as a qualitative justification of using the adiabatic approximation with Eq. (6).

We recover Eq. (6) by identifying \hat{H}_0 with the above electronic Hamiltonian for the relaxed nuclear positions, and the linear coupling coincides with the above expression.

This last result shows that the adiabatic approximation implies only linear coupling between the adiabatic nuclear wavefunctions in the presence of transition between the adiabatic electronic states. In the derivation presented here we have solely made use of the adiabatic approximation, and nowhere has an expansion or linearization of the equations been effected.

16

Mechanical Properties of Single Molecules: A Theoretical Approach

*Pasquale De Santis, Raffaella Paparcone, Maria Savino,
and Anita Scipioni*

16.1 Introduction

Proteins are involved in a wide spectrum of biological functions as a result of their structural polymorphism and conformational versatility, due to their large chemical dispersion along the polypeptide chain. Contrarily, the chemical homogeneity of the nucleotide residues along the DNA double helix restricts the structural variance to slight sequence-dependent deformations of the B-DNA structure. These can be amplified, however, and produce superstructures when phased with the DNA helical periodicity which are relevant for the molecular mechanisms that control the functional organization of the genome.

Although DNA is iconized as a straight double helix, it does not exist in this canonical form in nature. Instead, DNA *in vivo* continuously interacts with different molecules as the proteins become involved in replication, transcription, repair, and regulation processes; furthermore, it constantly transforms between packed and unpacked architectures, into chromatin and other higher-order structures. Interactions and thermal fluctuations make it bend, twist and writhe, and loop dynamically in a variety of structural changes during these processes.

Such structural and dynamic deviations from the monotonous regularity of the straight canonical B-DNA are not localized, however: rather, they are diffused on tracts of the DNA chain and are intrinsic properties of the sequence. These sequence-dependent features can be recognized and amplified by protein binding and play a relevant part in the management of the gene information the sequence contains. This is particularly evident in the case of sequence-dependent DNA–histone octamer association in the nucleosome, which governs the packaging and the superstructural organization of the genome as well as the gene regulation [1]. Here, DNA is wrapped around a protein core and bent to a much greater extent than is normally observed for free DNA in solution. DNA bending of the magnitude observed in such tight packaging requires substantial changes in both the external and the internal geometry of the double helix. Bending is implicated not only in DNA packaging, but also in DNA looping between sequences that are line-

arly distant from each other. This mechanism is known to be important for the regulation of gene expression [2, 3]. In addition, a fraction of DNA in the cell frequently exists as a circular rather than a linear form and topological constraints may force the DNA double helix to adopt a higher-order writhing with an associated higher energy than the corresponding relaxed form.

An important part of the DNA information content is not localized on the codogenic regions but appears to be associated with the superstructures and mechanical properties of relatively long DNA tracts. In fact, many processes involving DNA occur on a scale that is neither truly molecular nor truly macroscopic. They span a large range of length scales, from the local changes of the DNA structure (1 nm) to the size of tertiary structures of DNA architectures (100 nm).

To explain such a variety of phenomena in terms of the laws of physical chemistry, it is necessary to model DNA at these length scales using the scaffold provided by the DNA structure and base sequence to bridge molecular and macroscopic properties.

In the present post-genomic era, DNA sequences with billions of informational elements are currently accumulating in the data banks. Consequently, the need to translate the linear information of the base sequences into functional elements is becoming more and more crucial. Therefore, several authors have focused their attention on the mechanical properties of DNA resulting from static and dynamic effects produced on the nanoscale by concerted sequence-dependent deviations from the canonical B-DNA structure.

16.2 DNA Curvature

The first hypothesis about the existence of macroscopic deviations from the B-DNA canonical structure was proposed to explain the aberrant electrophoretic behavior of some DNA sequences in the 1970s [4–6]. After analyzing the nucleotide sequence of some eukaryotic DNAs, Trifonov and Sussman [7] found a weak periodicity of certain dinucleotide steps along the sequence, with a period close to the DNA helical repeat. They suggested that these dinucleotide steps produce sequence-dependent “wedge angles” between base-pair planes and that the observed periodicity reflects the anisotropic flexibility of the DNA molecule. Two years later, Marini et al. advanced the concept of the static bend as a sequence-dependent DNA property, as a result of investigations on the electrophoretic anomalies of a kinetoplast DNA tract of *Leishmania tarentolae* [8]. Afterwards, Wu and Crothers localized the bend in that DNA tract, by introducing the electrophoresis gel permutation assay. It consists in localizing the minimum of the retardation plot of cyclically permuted DNA tracts, obtained by single restrictions on the tandem dimer of the tract considered [9].

Systematic investigations about the origin of DNA curvature were carried out by Hagerman [10] and Koo et al. [11], by the anomalies of polyacrylamide gel electrophoresis, quantified by the retardation factors, the ratio between the apparent and

actual base-pair numbers, associated to biosynthetic multimeric oligomers. Koo et al. advanced the hypothesis that deviations from linearity should occur at the interface between the normal B-DNA structure and a structural variant of the double helix characterizing AA repeating stretches longer than three base-pairs [11].

Later, several authors proposed models to describe the curvature in terms of the local deviations of the different dinucleotide steps from the canonical B-DNA structure. Different wedge angles between consecutive base-pairs were adopted for each dinucleotide step. When summing up along a DNA sequence, the associated wedge angles, if in phase with the helix periodicity, produce an effective curvature large enough to be detected macroscopically. These models generally assume that the wedge angles are dependent only upon nearest-neighbor interactions [12–16]. They were reviewed recently by Crothers [17], who verified that their effectiveness in predicting intrinsic DNA curvature was in good agreement with the experiments. It is worth noting that, in spite of the rather large differences characterizing the different proposals for the dinucleotide step wedge angles, the curvature resulting from their integration over DNA tracts is similar.

However, since the first evidence of DNA anomalous electrophoretic mobility, large amounts of other experimental data have shown that many DNAs are curved or exhibit tracts with preferential bendability. Many different experimental methods have been used to this purpose, such as light scattering [18, 19], ligase-catalyzed cyclizations [20], flow dichroism [21], transient electric birefringence [22, 23] and transient electric dichroism [24, 25]. However, in order to derive the DNA curvature all these methods need suitable models for interpreting the data, which can affect the results. In addition, the statistical analysis of X-ray crystal structures of a large pool of double-stranded oligonucleotides provided estimates of the deviations from the canonical B-DNA structure associated with the different dinucleotide steps [15, 16].

Finally, recent progress in the direct visualization of DNA tracts allows the mapping of the curvature and flexibility of DNAs in terms of sequence and their structural changes by analyzing the digitized images [26–29] of single DNA molecules as well as the time course of their dynamics [30]. The statistical analysis of a number of molecule images large enough to obtain reliable results could bring information on both the sequence-dependent intrinsic curvature and the flexibility of DNA tracts on nanometric scales in relatively long sequences.

This chapter gives an overview of recent research on the mechanical properties of the DNA molecule on the nanometric scale. On this scale the DNA chain behaves like an elastic rod, and the sequences of local twisting and bending produce its superstructure and control its dynamics. These mechanical properties vary according to the base-pair distribution along the sequence and these variations play an important role in the biological function of that DNA tract.

This chapter also reviews the different modeling of DNA proposed by various authors, to relate the single-molecule DNA mechanics with its experimental manifestation. Particular attention is devoted to those models suitable to map the curvature and flexibility as a function of the sequence from the statistical analysis of the scanning force microscopy (SFM) images.

16.3 DNA Flexibility

A long B-DNA molecule may be simply described as a moderately flexible elastic rod. The flexibility of the chain is generally described by the persistence length P , which is defined as the distance over which two segments of the chain remain directionally correlated. Recent investigations have provided evidence that not only the curvature but also the elastic modulus of DNA are strongly dependent on nucleotide sequence, so that an implementation of the classical Kirchhoff rod-like model, generally adopted to simulate the elastic behavior of DNA chains, is required.

Among the models proposed to describe the elastic behavior of DNA, we will briefly illustrate those in which DNA is considered unsharable and inextensible.

Base-pair modeling takes the nucleotide step as the fundamental unit, and employs semi-empirical force constants to evaluate the stiffness of bending and torsion increments between adjacent base-pairs. These force constants were assumed to depend primarily on the physicochemical properties of individual dinucleotide steps, and to a lesser extent on the DNA sequence context in which they are embedded. For a random DNA sequence the value of persistence length determined by most experimental methods is ≈ 50 nm or 145 bp for B-DNA. However, since the chemical and physical features of the 10 possible dinucleotide steps are sensitively different, like the intrinsic curvature the flexibility of DNA is also a sequence-dependent property [15, 16, 31].

In such discrete modeling of the DNA mechanics, the molecule is usefully imagined to be smeared out to form a continuous elastic rod characterized by bending and twisting moduli to take advantage of the classical elasticity theory [32]. In the case where bending and twisting stiffness are considered to be constant along the length of the rod, closed-form analytical solutions are sometimes available: for example, an exact analytical solution of Kirchhoff's equations of mechanical equilibrium can be obtained for the supercoiling of knotted and unknotted circular DNA. In continuum modeling, the stiffness can easily be made to vary in a prescribed manner along the rod, and the intrinsic curvature can be introduced: but then solutions naturally become harder to obtain. We recently proposed an alternative theoretical treatment [33].

Hoffman has exploited the variational structure of the elastic rod model to derive new methods that can identify the stable equilibrium configurations of inextensible and unsharable elastic rods [34]. Tobias considered the statistical dynamics of small rings of DNA under thermal fluctuations. He showed that increasing the intrinsic curvature of the rods can broaden the writhe distribution, a result related to the stability properties of the circular equilibrium configuration of the elastic rings [35]. Balaeff et al. (2004) extended the classical continuum model to account for sequence-dependent intrinsic twists and curvatures, anisotropic bending rigidities, electrostatic force interactions, and overdamped Brownian motion in a solvent [36].

Alternatively, a numerical technique was developed in which the system that has

been smeared out and modeled as a continuum is conceptually chopped up into finite elements (finite element analysis). White and Bauer used finite element analysis to study the writhing of the DNA molecule under torsional stress. They showed that the manner of this writhing depends critically on the distribution of the intrinsic curvature along the DNA axis and on the precise location at which the applied rotation is introduced [37].

Furthermore, since DNA may be regarded as an extended negatively charged polyanion, its physical properties, curvature, and flexibility, in particular, are also controlled by the ionic strength. Bending and flexibility of DNA are strongly affected by its immediate ionic environment. At very low ionic strength (for example less than 0.01 M NaCl) the repulsive forces between negative charges on the phosphates of the backbone act to oppose bending and thus impart rigidity [38]. Neutralization of these charges by cations thus decreases the persistence length [39]. These effects depend on the nature of the cation. Monovalent cations are less effective than multivalent ones, such as Mg^{2+} . They cause reduction in bending stiffness, enhancing the close packing of DNA. As an extreme manifestation, polyamines or hexammonium cobaltic ions produce DNA toroids [40–42].

Although the behavior of a long DNA molecule may be well approximated by treating it as an isotropically bendable rod, the magnitude and directionality of the local stiffness of a DNA molecule are particularly relevant for circular DNAs. The ratio of the twist modulus to the bending modulus is an important factor that controls the equilibrium topoisomer distributions for DNA minicircles [43] as well as their writhing transitions.

In fact, estimates of the intrinsic parameters and elastic constants of DNA derived from base-pair configurations observed in X-ray crystal structures indicate that these quantities are strongly dependent on nucleotide sequence [15, 16]. In addition, the statistical analysis of crystallographic data shows that coupling between bending and twisting is particularly strong for AA, AC, and AT base-pair steps [16].

If DNA is considered to be unshearable and inextensible, the rod mechanics may then be characterized entirely by one twisting and two bending force constants. Therefore, the deformation energy, U , can be generally considered to be proportional to the geometric deviations δ_1^2 , δ_2^2 and δ_3^2 from the reference configuration adopting the simplest possible dependence consistent with a quadratic energy [Eq. (1)].

$$U = \frac{1}{2} \int (b_1 \delta_1^2 + b_2 \delta_2^2 + C \delta_3^2) ds \quad (1)$$

For a homogeneous rod-like chain the apparent force constants quantify the bending rigidities: $b_1 = EI_2$ and $b_2 = EI_1$, where E is the Young's modulus and I_1 and I_2 the principal moments of inertia. For an isotropic circular cross-section $I_1 = I_2 = I = \pi a^4/4$ (a is the radius of the cross-section). In the case of DNA, the bending rigidities are usually assumed to be isotropic; $b_1 = b_2 = b = kTP/\ell$, where k is Boltzmann constant, T is the absolute temperature, and P/ℓ is the persistence length in monomer unit lengths, (for B-DNA $\ell = 0.34$ nm and $P \approx 50$ nm), char-

acterizing the orientational correlation in the rod-like chain. It should be noted that the persistence length is defined only for isotropic rods; it characterizes the cylindrically averaged bending, when $b_1 \neq b_2$.

The twisting rigidity is similarly defined as $C = GJ$, where G is the shear modulus and $J = \pi a^4/2$ is the polar moment of inertia of the rod. C is generally defined in terms of the twisting persistence length: $C = kTP_{tw}/\ell$, ($P_{tw} \approx 70$ nm for B-DNA).

For a real DNA chain, such force constants, b and C , are sequence-dependent. Compared with bending and twisting, shearing and stretching deformations are usually negligible.

Brownian twisting and bending motions of the rod are the result of colliding molecules surrounding the DNA in solution, and are assumed to be overdamped by Stokesian viscous drag forces. At the thermodynamic equilibrium the action of the stochastic force and torque vanish on average, and the rod-like dynamics satisfies the fluctuation–dissipation relationship.

The electrostatic interactions of the charged rod representing the DNA polyanionic chain with its surroundings are also implicated in the thermodynamic equilibrium as well as in dynamic fluctuations of the rod. They originate from both the rod self-interaction term and the interactions between the rod and other charges present in solution, taking into account the Debye screening factor due to the effect of counter-ions in the DNA environment [36].

In most cases relevant to DNA mechanics, the electrostatic terms can be ignored except in the neighborhood of self-intersections, which are particularly important in supercoiled forms.

16.4 The Worm-Like Chain Model

The classical theory for describing DNA conformations on nanometric scale is the worm-like chain model (WLC), initially proposed by Kratky and Porod [44] and later revisited by various authors [45–47]. In this model the stiffness of the chain is represented by its persistence length, which can be interpreted as the distance over which the memory of any initial orientation of the polymer persists. It is the correlation integral between the direction of pairs of tangent unit vectors to the profile of the curved DNA tract separated by the curvilinear distance $s'-s$ [Eq. (2)].

$$P = \langle \mathbf{u}(s) | \mathbf{u}(s') \rangle \quad (2)$$

A limitation of the initial WLC model was the assumption of intrinsically straight homogeneous polymers whose thermal fluctuations are quantified as deviations from the straight line. However, DNA almost always contains curved regions, which can strongly affect the persistence length. The intrinsic bent regions contribute to the experimentally measured persistence length (P_a) with a term denoted as

the static persistence length (P_s), whereas thermal fluctuations contribute with the dynamic persistence length (P_d). The three contributions are related by Eq. (3), as initially proposed by Trifonov et al. [48] and later checked by Schellman and Harvey [49].

$$\frac{1}{P_a} = \frac{1}{P_s} + \frac{1}{P_d} \quad (3)$$

Such a relationship can be obtained as the sum of the angular dispersions of the unit vectors along the curvilinear DNA profile due to both the static curvature and the dynamic fluctuations under the hypothesis of their mutual independence [50].

Scanning force microscopy (SFM) and electron microscopy (EM) have the advantage of directly observing the DNA molecules when absorbed onto supporting surfaces. However, the interaction with such surfaces could introduce artifacts in the measurements. First of all, during adsorption DNA molecules are transformed from a three-dimensional (3D) into a two-dimensional (2D) object. EM techniques require the drying and staining of the samples. In addition, the finite size of the tip used in SFM experiments and the image processing restrict the derivation of the structural features within the range of the experimental resolution.

Two extreme cases were reported – those in which the molecules freely equilibrate on the surface, before being trapped in a particular conformation; or the molecules adhere without having equilibrated on the substrate, resembling the actual 3D conformations [51]. In the latter case, the conformations of the molecules reflect the history of their approach to the surface and it is therefore difficult to distinguish between intrinsic conformations and those induced upon adsorption. In the case of the molecules that freely equilibrate on the surface, it is possible to have an ensemble of 2D conformations which can be related to the actual 3D DNA structures, as will be described in Sections 16.5 and 16.11.

16.5 DNA Persistence Length in Two Dimensions

Given a polymer chain with a persistence length P in the framework of first-order elasticity, the energy U required to bend two adjacent segments of length ℓ by an angle θ is provided by Eq. (4), where $b = kTP/\ell$ is the apparent bending force constant [52].

$$U = \frac{kTP}{2\ell} \theta^2 = \frac{b}{2} \theta^2 \quad (4)$$

Therefore, in two dimensions, according to the Central Limit theorem, the probability of having a certain bend angle follows a Gaussian distribution [Eq. (5)].

$$p(\theta)_{2D} = \sqrt{\frac{P}{2\pi\ell}} \exp\left(-\frac{P}{2\ell} \theta^2\right) \quad (5)$$

This equation permits one to calculate the mean-square end-to-end distance of the polymer by Eq. (6), where L is the contour length.

$$\langle R^2 \rangle_{2D} = 4PL \left(1 - \frac{2P}{L} \left(1 - \exp\left(-\frac{L}{2P}\right) \right) \right) \quad (6)$$

The comparison with the classical equation of Kratky and Porod [44], in three dimensions, shows that the mean-square end-to-end distance of a molecule which freely equilibrates on a surface has an apparent persistence length of twice that found in three dimensions.

However, DNA almost always contains curved regions and tracts with different flexibility, dependent on the sequence, which can strongly affect the persistence length. It was therefore necessary to extend the WLC model to these cases.

Therefore, in two dimensions, considering static bend β , located at a certain distance d from one end of a polymer, a possible generalization (7) of Eq. (6) was proposed [53] which could be approximated, when both d and $(L - d)$ are greater than $2P$, to Eq. (8).

$$\langle R_\beta^2 \rangle = 4PL \left\{ 1 - \frac{P}{L} \left[\left(1 - \exp\left(-\frac{d}{P}\right) \right) + \left(1 - \exp\left(-\frac{L-d}{P}\right) \right) - \cos \beta \left(1 - \exp\left(-\frac{d}{2P}\right) \right) \left(1 - \exp\left(-\frac{L-d}{2P}\right) \right) \right] \right\} \quad (7)$$

$$\langle R_\beta^2 \rangle \approx 4PL \left(1 - \frac{P}{L} (2 - \cos \beta) \right) \quad (8)$$

Equation (7) can be extended to the case where N coplanar bends are present [53]. Therefore, averaging the end-to-end distance of a statistically significant number of molecules observed in SFM maps represents a way to obtain the average persistence length and the corresponding bending force constant of DNA tracts.

16.6

A Model for Predicting the DNA Intrinsic Curvature and Flexibility

According to the classical formulation by Landau and Lifshitz [52], the curvature of a space line is defined as the derivative dt/ds of the tangent vector, \mathbf{t} , along the line, s . Its modulus is the inverse of the curvature radius and its direction is that of the main normal to the curve. In the case of DNA, the line corresponds to the helical axis and the curvature is a vectorial function of the sequence. It represents the angular deviation between the local helical axes of the n th and $(n + 1)$ th helix turns centered on the n th and $(n + 1)$ th dinucleotide step, respectively. Actually, the DNA curvature is a superstructural sequence-dependent property, which is continuously changed by the thermal energy of the environment.

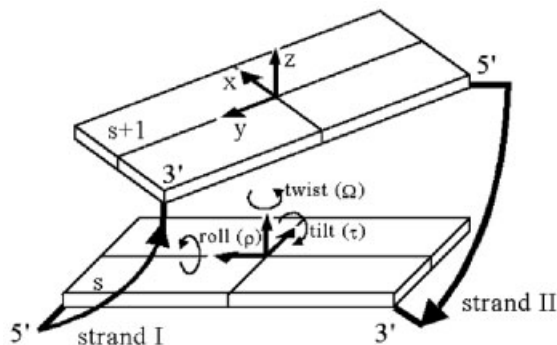


Fig. 16.1 Orientational parameters of the base-pair average plane in a dinucleotide step.

Sequence-dependent DNA curvature can be conveniently represented by a complex function of the sequence number, n [Eq. (9)].

$$\mathbf{c}(n, t) = \frac{1}{v} \sum (\mathbf{d}(s) + \delta(s, t)) \exp\left(\frac{2\pi i s}{v}\right) = \mathbf{c}(n) + \chi(n, t) \quad (9)$$

Here $\mathbf{d}(s) = (\rho - i\tau)$ is the intrinsic deviation from the canonical B-DNA structure of the s th dinucleotide step in terms of its roll, ρ , and tilt, τ , angles (Fig. 16.1), and $\delta(s, t)$; the corresponding stochastic deviations, $\mathbf{c}(n, t)$ is the DNA curvature per base-pair, calculated as the sum of the dinucleotide step deviations over recurrent turns of the double helix and assigned to the central base-pair of the n th turn, at time t ; $\chi(n, t)$ represents the dynamic curvature fluctuations at the n th base-pair position at time t ; v is the helical average periodicity of the n th turn, evaluated from the local twist angles, Ω .

$\mathbf{c}(n, t)$ is equal to the sum of a static intrinsic contribution, $\mathbf{c}(n)$, and a dynamic contribution, $\chi(n, t)$, whose time-average is obviously zero. Therefore, the time-average or the ensemble-average curvature simply corresponds to the intrinsic curvature of the DNA sequence.

Summing up the roll and tilt local deviations in the complex plane approximates the pertinent product of the rotation matrices and conveniently defines the curvature of the helical axis that occurs only when the distribution of the local deviations contains a harmonic component with the helix periodicity. All the other components affect the DNA structure locally, but their effects cancel and do not produce superstructural modifications of the chain.

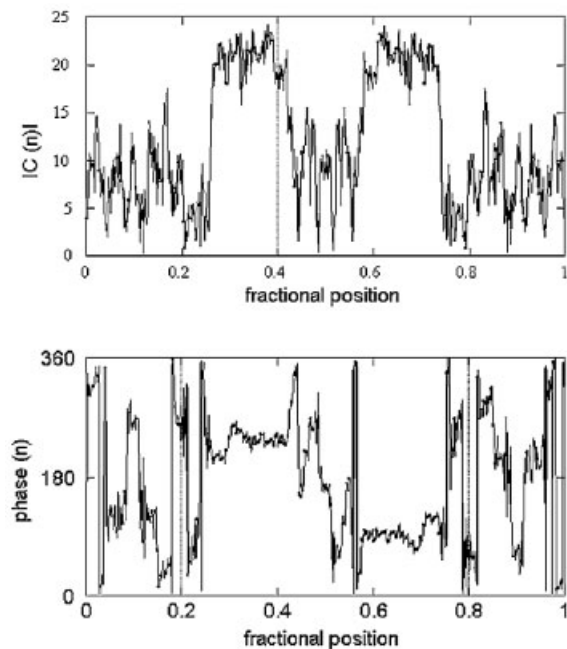
Roll, tilt, and twist angles for each dinucleotide step were proposed by different authors [12–16] on the basis of the interpretation of gel electrophoretic anomalies of DNA tracts or X-ray crystal structure averages of double-stranded oligonucleotides. Table 16.1 reports the set we first obtained by minimizing the conformational energy of the different dinucleotide steps and later refined to optimize the agreement with gel electrophoresis data of a large pool of DNA tracts [12, 13].

Table 16.1 Roll (ρ), tilt (τ), and twist (Ω), angles for each dinucleotide step.

ρ, τ, Ω [°]	A	T	G	C
T	8.0, 0.0, 34.5	-5.4, 0.5, 36.0	6.8, -0.4, 34.1	2.0, 1.7, 34.6
A	-5.4, -0.5, 36.0	-7.3, 0.0, 35.3	1.0, -1.6, 34.4	-2.5, -2.7, 33.7
C	6.8, 0.4, 34.1	1.0, 1.6, 34.4	4.6, 0.0, 33.5	1.3, 0.6, 33.1
G	2.0, -1.7, 34.6	-2.5, 2.7, 33.7	1.3, -0.6, 33.1	-3.7, 0.0, 33.3

As curvature is a complex function, it can be represented in terms of modulus, which quantifies the local angle of bending, and in terms of phase, namely the direction in which the bending points. As an example, Fig. 16.2 illustrates the intrinsic curvature $C(n)$ diagram of an 898 bp palindromic construct obtained from the highly curved *Crithidia fasciculata* DNA tract [29].

While the main determinants of DNA curvature are generally recognized, the evaluation of DNA flexibility in terms of the sequence still remains an open prob-

**Fig. 16.2** Diagrams representing the curvature modulus ($|C(n)|$, in degrees per turn of double helix) and the corresponding phase (in degrees) of the 898 bp tail-to-tail palindromic DNA containing the highly curved region of *Crithidia fasciculata*.

lem. Thus, different authors consider the same dinucleotide steps to be either flexible or alternatively rigid. In fact the dispersion of the orientational parameters from X-ray crystal structures of double-helix oligonucleotides with different sequences produces a scale of flexibility in which the AA/TT step belongs to the rigid class while GG/CC and GC/GC dinucleotides result as being more flexible [15, 16]. Other authors proposed different flexibility scales based on the thermodynamic stability of the double helix, and related to the differential stacking energy of the dinucleotide steps or their melting temperature differential contributions [54–56]. These appear to be in good agreement with the SFM data, as will be discussed in Section 16.11.

16.7

Mapping Sequence-Dependent DNA Curvature and Flexibility from Microscopy Images

Electron microscopy and scanning force microscopy are unique techniques, which provide information on both the images of individual molecules and their population. In addition, SFM is capable of following the time evolution of single-molecule shapes. The data obtained from these techniques were explained by using either static or dynamic models of the behavior of DNA in solution. The static models are focused on time-averaged conformations, i.e., on static intrinsic curvature, the dynamic models on dynamic contributions, i.e., on the flexibility that characterizes the deformability about those averaged structures.

SFM makes it possible to image the conformations of DNA single molecules deposited from a solution in water on a mica substrate. The observation of single molecules can give a deeper insight into the way the base sequence determines the local intrinsic curvatures and drives the elastic response to thermal energy, provided that the base sequence of the imaged DNA can be assigned at any position along the chain in all the images.

In general, when the curvature of a DNA molecule is measured in a micrograph, we never know which end we start with. In order to remove this uncertainty, the strategy of palindromic constructs was adopted recently [27–29]. In a palindromic molecule, the sequence is the same reading from either end, and no uncertainty exists about the sequence orientation. Furthermore, the curvature profile of a population of palindromic DNA molecules should reflect the dyad symmetry of the sequence, if the number of molecules analyzed is great enough, and if the equilibration conditions are satisfied.

A different approach had been adopted previously by Theveny and Revet [57], who produced several EM images of linearized *pBR322* DNA molecules, obtained by different restriction enzymes and labeled by a streptavidin–ferritin–biotin complex. The authors underlined how curvature maps, when superimposed two at a time, showed many similarities, proving that, despite dynamic fluctuations of the single molecules and the deformation effects due to the adsorption on a 2D surface, the intrinsic features of the DNA sequence were largely conserved. Finally, the authors compared the experimental average curvature maps with the results

from four different theoretical models [11, 13, 14]. They found that all the theoretical sets of data showed very comparable features, which enabled correct prediction of the principal curved regions along the pBR322 tracts.

16.8

The Ensemble Curvature and the Corresponding Standard Deviation for a Segmented DNA

The curvature profiles along the contour of each DNA molecule can be evaluated from the digitation of each DNA image. The non-uniform sequence of local curvatures associated with the DNA images is transformed into a uniform curvature distribution along the contour of the molecules via Fourier transform operations. The intrinsic curvature is the statistical average of the curvature at the n th sequence position. However, the segmental nature of the DNA traces on a surface, due to the resolution power of the SFM, requires a definition of the segmental curvature, $C_m(n)$, which represents the angular deviation of the local helical axes separated by m base-pairs (see Fig. 16.3). Accordingly, $\langle C_m(n) \rangle$ represents the ensemble-average segmental intrinsic curvature and is equivalent to half of the intrinsic curvature of $2m$ bp, $C(n, 2m)$. Adopting a first-order elasticity model for DNA axis deformations, the 2D ensemble-average dispersion of the segmental curvature, $\langle C_m^2(n) \rangle - \langle C_m(n) \rangle^2$, depends on the thermal fluctuations of $2m$ bp (see Fig. 16.3).

Therefore, setting $C(n, 2m) - \langle C(n, 2m) \rangle = \chi$ and $B = \frac{b(n)}{2kT}$, Eq. (10) is obtained.

$$\langle \chi^2 \rangle = \frac{1}{Q} \int_{-\infty}^{\infty} \chi^2 \exp\left(-\frac{B}{2m} \chi^2\right) d\chi = \frac{m}{B} \quad (10)$$

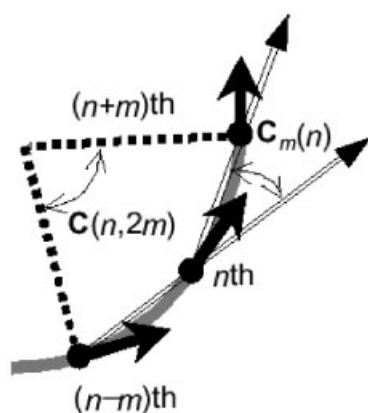


Fig. 16.3 Schematic representation of the segmental curvature, $C_m(n)$, at the sequence position n . The dark arrows represent the helix axis directions at the $(n - m)$ th, n th, and $(n + m)$ th sequence positions. $C_m(n)$ is the

angle between the two virtual segments, which corresponds to the angular deviation of the local helical axes pertinent to the nucleotide steps separated by $2m$ bp.

In this equation, Q is the pertinent canonical partition function:

$$Q = Q(n, 2m) = \int_{-\infty}^{\infty} \exp\left(-\frac{B}{2m}\chi^2\right) d\chi$$

The integration limits up to $+\infty$ and $-\infty$ are introduced to solve the integrals analytically; in any case, they are inessential because of the rapid convergence of the integrands.

Considering that the curvatures refer to a $2m$ bp DNA tract, they are two times the corresponding values experimentally detectable for a segmented chain (see Fig. 16.3); therefore, Eq. (11) results for the segmental curvature dispersion, which is simply dependent on the DNA rigidity function $b(n)$.

$$\langle C_m^2(n) \rangle - \langle C_m(n) \rangle^2 = \frac{\langle \chi^2 \rangle}{4} = \frac{mkT}{2b(n)} \quad (11)$$

It should be noted that, in three dimensions, the curvature is a complex function and the integration has to be done in the complex plane. As a result the curvature dispersion will be double that of the 2D case.

Contrarily, the average curvature modulus $\langle |C_m(n)| \rangle$, which some authors adopted to characterize the 2D DNA structure in EM as well as in SFM images, depends on both the static and the dynamic curvature contributions. Setting $C = C(n, 2m)$, the average curvature modulus for a $2m$ bp segment is given by Eq. (12).

$$\begin{aligned} \langle |C| \rangle &= \frac{1}{Q} \int_{-\infty}^{\infty} |C| \exp\left(-\frac{B}{2m}\chi^2\right) d\chi \\ &= \left| \frac{1}{Q} \int_{-\infty}^{\infty} C \exp\left(-\frac{B}{2m}\chi^2\right) d\chi - 2 \frac{1}{Q} \int_{-\infty}^0 C \exp\left(-\frac{B}{2m}\chi^2\right) d\chi \right| \end{aligned} \quad (12)$$

By simple substitutions and expansion to the second order, considering that curvatures of interest are small, we obtain a compact formulation (13) valid for curvatures up to 0.6 rad.

$$\langle |C(n, 2m)| \rangle = \left[\frac{2}{\pi} \left(\langle C(n, 2m) \rangle^2 + \frac{2mkT}{b(n)} \right) \right]^{1/2} \quad (13)$$

Considering that the average curvature modulus we obtained refers to a $2m$ bp DNA tract, it is two times the corresponding value experimentally detectable for a segmented chain (see Fig. 16.3), as is expressed in Eq. (14).

$$\langle |C_m(n)| \rangle = \frac{\langle |C(n, 2m)| \rangle}{2} = \left[\frac{2}{\pi} \left(\langle C_m(n) \rangle^2 + \frac{mkT}{2b(n)} \right) \right]^{1/2} \quad (14)$$

This result clearly points out that the average curvature modulus depends on two

terms: one corresponds to the intrinsic segmental curvature and the other represents the sequence-dependent flexibility of the chain. The differential flexibility function along the sequence can be obtained only for an intrinsically straight DNA, where the static curvature is zero.

The corresponding standard deviation can be obtained easily by considering that, from Eq. (11),

$$\langle C_m^2(n) \rangle = \langle C_m(n) \rangle^2 + \frac{m}{B}$$

Equation (15) follows.

$$SD(|C_m(n)|) = [\langle C_m^2(n) \rangle - \langle |C_m(n)| \rangle^2]^{1/2} = \left[\left(\frac{\pi - 2}{\pi} \right) \left(\langle C_m(n) \rangle^2 + \frac{mkT}{2b(n)} \right) \right]^{1/2} \quad (15)$$

Therefore, the ensemble curvature modulus and the corresponding standard deviation are expected to be proportional because they contain the same dependence from both the static and the dynamic curvature contributions. This proportionality, theoretically predicted, was experimentally verified for all the DNA molecules we investigated [28–30]. Moreover, it can be adopted as an internal gauge of the existence of the thermodynamic equilibrium of the DNA molecule ensemble on the mica surface.

16.9

The Symmetry of Palindromic DNA Images

A curve in space can be fully described by its local-curvature amplitudes and phases. The averaged shape of a palindromic DNA is characterized by a dyad axis, which relates the two halves of the molecule. This statistical dyad symmetry persists also when the molecules are flattened on a crystal surface such as mica in SFM images. However, only two alternative directions of the dyad axis are allowed: parallel or perpendicular to the surface plane. In the former case the ensemble-average curvature of the molecule is a symmetric function. In the latter case the two curved halves have average curvatures opposite in sign; that is, the curvature is an antisymmetric function. We called these symmetry species C-like shapes and S-like shapes (or S*, the asterisk indicating the mirror image across the surface plane), respectively, because they are isomorphous with these figures. The curvatures of the antisymmetric halves will be oppositely signed and retain the same signs independently of the direction of whichever end is chosen as the starting point of the molecule. In fact, the two faces of the S and S*-shaped molecules are mutually prochiral and expose complementary sequences to the crystal surface. In the case of C-shaped molecules, the two faces are equivalent because one half of a face exposes a sequence complementary to that of the other half. This also implies

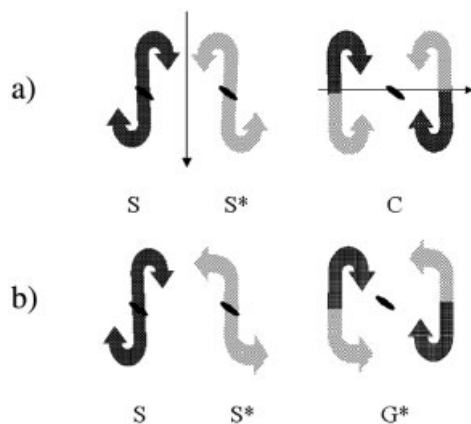


Fig. 16.4 Pictorial representation of the tail-to-tail DNA palindromic construct. In this scheme, the DNA is drawn as a directional curved ribbon. The two opposite DNA faces, characterized by complementary base sequences, are indicated with two different shades of gray. The DNA sequence of the tract used to build the dimers is read in the

direction of the arrow. Two situations are illustrated: (a) the interactions with the mica surface change the curvature independently of the sequence; (b) the changes are sequence-dependent. The dyad axes perpendicular and parallel to the mica surface, which characterize the intramolecular and intermolecular symmetry, are indicated.

that the two faces of the C-shaped molecules are indistinguishable and belong to the same symmetry species. Figure 16.4(a) illustrates the symmetry relationship of the palindromes. Here, the presence of dyad axes parallel or perpendicular to the surface is indicated with standard symmetry group symbols. Besides the intramolecular dyad axis, the one referring to the two alternative modes of DNA flattening onto the surface is indicated also. The presence of a dyad perpendicular to the surface (such as between the C and C* forms) indicates that they are indistinguishable because they correspond to reading the same DNA image starting from the two alternative ends.

However, the possible presence of differential interactions with the surface of the two DNA faces, characterized by complementary base sequences, could change this symmetry as illustrated pictorially in Fig. 16.4(b). Such differential interactions could change the curvature and the flexibility, i.e., the intrinsic mechanical properties of DNA. As a consequence both the S and S* shapes retain the dyad axis and the intrinsic antisymmetry of the curvature functions, but their shapes and the related curvatures are no longer equivalent because they interact with the surface with complementary and chemically different sequences. The same effect is found for the C shapes, which lack their intrinsic dyad parallel to the surface and which we now call G shapes, accordingly. In this case also, the G and G* forms are indistinguishable. It is interesting to note that if the same DNA tracts are bridged head-to-head, forming different palindromic constructs, instead of tail-to-tail, the symmetry relations hold but the faces of the molecules are interchanged with those

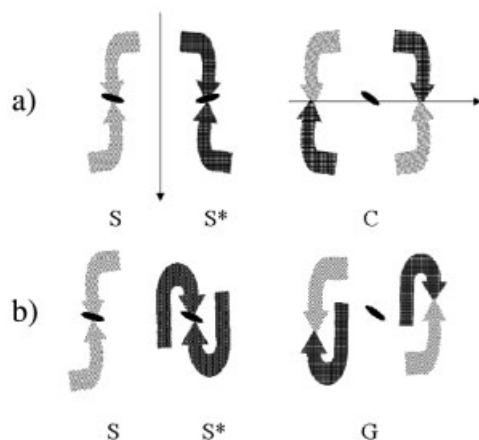


Fig. 16.5 Pictorial representation of the head-to-head DNA palindromic construct. The direction of the DNA tract is reversed with respect to that of Fig. 16.4; accordingly, the base sequences toward the observer are interchanged with those that are complementary.

complementary to them, as illustrated in Fig. 16.5. All the situations illustrated pictorially in Figs. 16.4 and 16.5 are transformed into the corresponding curvature diagrams reported in Fig. 16.6.

16.10

Experimental Evidence of DNA Sequence Recognition by Mica Surfaces

We collected a large pool of SFM images (about 1500) of two palindromic DNA constructs containing the curved tract of *Crithidia fasciculata*, bridged head-to-head and tail-to-tail to obtain two palindromic dimers [29]. The curvature functions were obtained from the SFM images, as already described in Section 16.8. As is evident in the SFM map, the thermal energy causes a high variability of the shapes of the molecules (see Fig. 16.7). Therefore, the dyad symmetry is fulfilled as a statistical property of the molecular ensemble. Similar sigmoidal shapes were obtained for the curvature profiles of both dimers, but with opposite signs as expected (see Fig. 16.8). This result has to be interpreted as the evidence that the surface preferentially binds one of the two faces of the curved DNA tracts. In fact, a nondifferential adhesion should result in equivalent populations of the prochiral forms on the surface, so that their contribution to the average curvature would cancel out. Furthermore, the opposite curvature profiles of the two dimers are an expected result due to the opposite sequence directions in the two palindromes, as already illustrated in Figs. 16.4 and 16.5.

A deeper analysis obtained by grouping the DNA images in the three symmetry

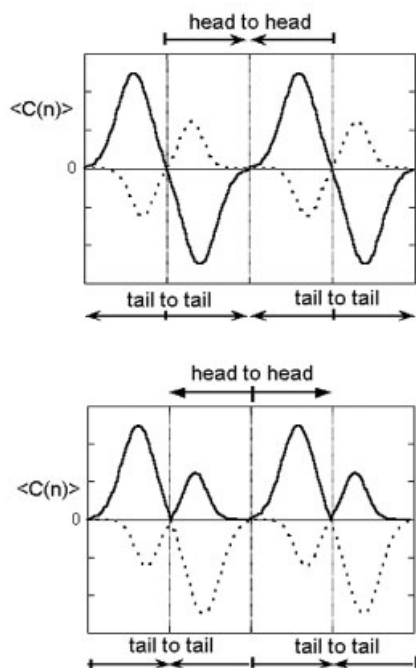


Fig. 16.6 Curvature profiles of the S, S*, G, and G* symmetry classes of tail-to-tail and head-to-head palindromic dimers corresponding to the pictorial representations of Figs. 16.4(b) and 16.5(b). Note the inversion

of the curvature signs of the two halves of the molecules when the tail-to-tail dimer is formally transformed into the head-to-head dimer.

classes S, S*, and G allows the evaluation of the differential prochiral recognition by the mica surface. The prochiral ratio S/S^* reaches the value of $\frac{1}{2}$ in the head-to-head dimer of *Crithidia fasciculata* and, coherently, approximately the reciprocal value in the tail-to-tail dimer. In addition, the comparison between the curvature functions of the two DNA halves shows very significant curvature deviations as a result of differential sequence–mica interactions (see Fig. 16.9). Therefore, the differential adhesion of DNA to mica not only privileges one face of a curved DNA tract with respect to the other one, but also modifies its curvature differently and significantly, as described pictorially in Figs. 16.4 and 16.5.

This result was not due to an incomplete ensemble averaging. The symmetrical shape of the sequence-dependent curvature profiles and the cross-equivalence of the halves of the G and S forms showed that the ensemble sampled is statistically relevant for this system. In addition, for both the populations of DNA molecules examined, the experimental local curvature modulus along the chain was found to be proportional to the corresponding standard deviation, as predicted theoretically [see Eqs. (14) and (15)].

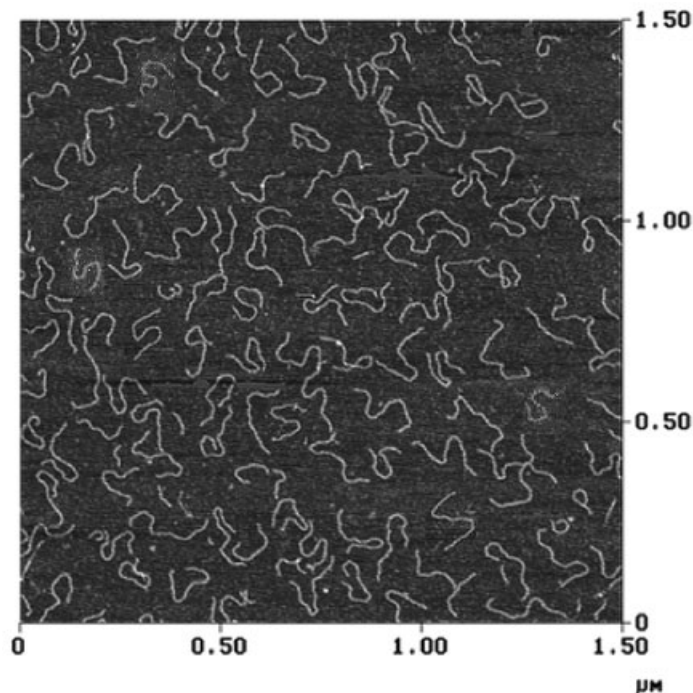


Fig. 16.7 SFM images showing a sample of DNA traces of the tail-to-tail palindromic dimer. The images were obtained by operating in tapping mode on mildly dehydrated DNA.

This prochiral recognition effect is expected to be general for any curved DNA molecule; the same evidence was obtained from the analysis of the average local curvatures of other DNA palindromic dimers [27, 28].

16.11

Comparison between Theoretical and Experimental DNA Curvature and Flexibility

The analysis of the theoretical curvature profile of the tail-to-tail *Crithidia fasciculata* palindrome (see Fig. 16.2) indicates the presence of two highly curved planar tracts in phase contrast, which results in an S-shaped superstructure. It is characterized by a strong asymmetry in the distribution of A and T nucleotide steps in the direction perpendicular to the plane of curvature [29]. The symmetry relationships with the SFM S-shaped forms imply that the dimer preferentially exposes the T-rich face of the curved tracts to the mica surface. To achieve this preferential adhesion due to the inversion of the curved sequence, the head-to-head palindrome is forced to assume the opposite prochiral shape (see Fig. 16.8).

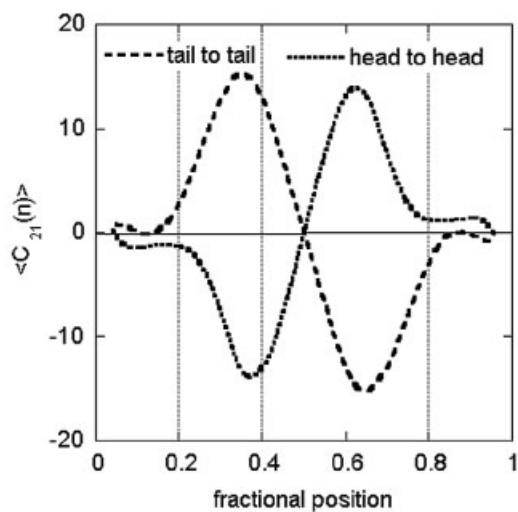


Fig. 16.8 SFM ensemble-average curvature profiles of the head-to-head and the tail-to-tail DNA palindromic dimers. The inversion of sequence direction results in an inversion of curvature sign.

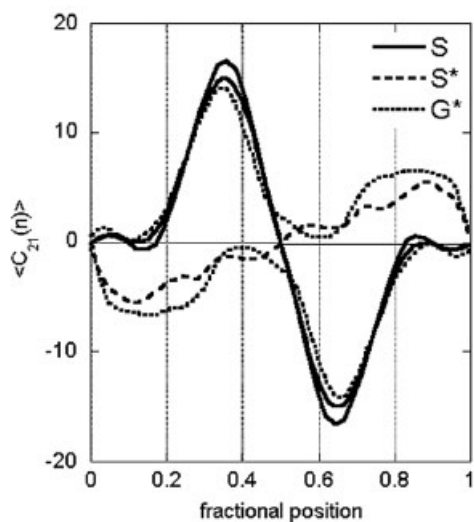


Fig. 16.9 SFM ensemble-average curvature profiles of the tail-to-tail DNA palindromic dimer after shape classification. For this representation, the G species have been separated into two subclasses with positive or negative global curvature.

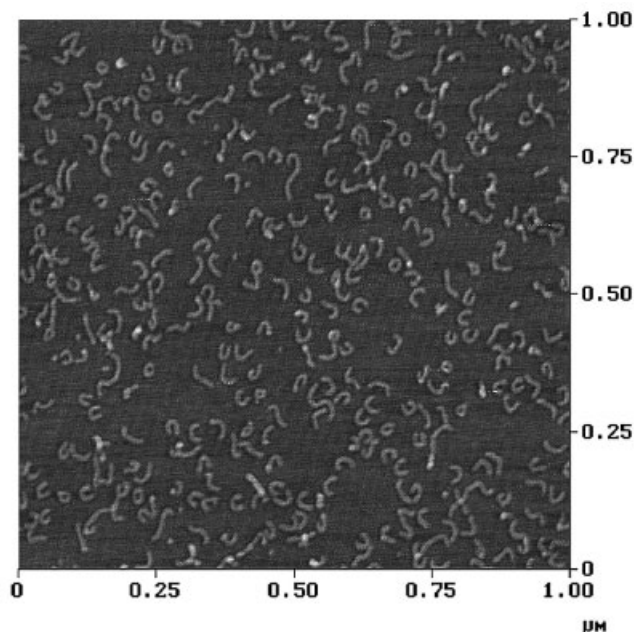


Fig. 16.10 SFM images of a sample of 212 bp highly curved *Crithidia fasciculata* DNA molecules. The images were obtained by operating in tapping-mode on mildly dehydrated DNA.

The comparison between the ensemble average curvature as evaluated from the SFM image statistical analysis and that theoretically predicted for both the *Crithidia fasciculata* palindromes is satisfactory [29]. However, the curvature profile of the SFM experimental curvature appears to be halved with respect to the theoretical profile. We have recently obtained the same finding for the SFM images of the isolated 212 bp most curved tract of *Crithidia fasciculata* (see Fig. 16.10). This is in contrast with the EM images of the same tract as reported earlier by Griffith et al., who showed a higher curvature in agreement with that theoretically predicted [58].

According to the symmetry analysis previously described, we suggest that the interactions with the mica surface and/or the effects of the protocol, which requires rinsing the sample with pure water and drying it, generally reduce the curvature. This effect is sequence-dependent, as comparison of the curvature profiles of the S and the S* shapes indicates. In fact, the A-rich face is more influenced than the T-rich face by adhesion to the mica-surface (A. Scipioni, S. Pisano, A. Bergia, M. Savino, B. Samori, P. de Santis, sequence-dependent DNA recognition by an inorganic crystal in the nanoscale. *Chembiochem*, submitted).

It is interesting that the time-averaged curvature profile obtained from the statistical analysis of DNA images in liquid cells, as in the case of pBR322 reported in Section 16.12, appears to agree with the theoretical prediction instead [30].

It is worth noting that significant differences were also detected between EM and

SFM images of supercoiled DNAs. Generally, the writhing number of SFM images is reduced with respect to that of EM images, which, however, agrees with that resulting from topological experiments in solution [59–61]. Therefore further investigations are required to clarify how mica surface, ionic strength, and experimental protocols affect DNA superstructures.

The profile of the experimental standard deviation of the curvature correlates with the frequency of AT+AA+TA+TT dinucleotide steps along the DNA sequences and not with the frequency of GC+GG+CC+CG dinucleotide steps [27, 28]. This finding strongly supports the hypothesis that A/T-rich sequences are generally more flexible than G/C-rich sequences [31]. Moreover, it suggests that the sequence determinants of the DNA curvature should be strictly correlated with those of DNA flexibility; that is, the static and dynamic curvatures are monotonic functions of the sequence.

To relate this finding to physical properties associated to the sequence, we adopted the flexibility scale proposed some years ago, based on the thermodynamic stability of B-DNA [31].

In fact, the profile of the standard deviation of the curvature obtained by the SFM images agrees with the profile of the normalized local “pre-melting” absolute temperatures, $T_m/\langle T_m \rangle$, evaluated by averaging the Gotoh and Tagashira [62] dinucleotide step contributions over recurrent tracts of 21 bp [28]. This ratio is equivalent to the corresponding normalized bending force constants, if first-order elasticity is assumed for the base-pair libration (θ) up to the pre-melting temperatures, where the curvature fluctuations reach the critical amplitude that nucleates the melting transition.

The experimental persistence length along the sequence is closely reproduced by the linear function of the melting temperature in Eq. (16), where $P(n)$ is in nanometers (see Fig. 16.11).

$$P(n) = 350 \frac{T_m(n)}{\langle T_m \rangle} - 300 \quad (16)$$

Travers recently proposed a similar function of the melting temperature [56]. Such a linear dependence of the DNA stiffness on the melting temperature can be explained by assuming an anharmonic energy contribution that is negligible at room temperature but important near the melting temperature. Thus, the bending energy per nucleotide step is given by Eq. (17), in which the second energy term simulates the cooperativity of the helix–coil transition in DNA (submitted).

$$kT = \frac{1}{2} b \langle \theta^2 \rangle + A \langle \theta^4 \rangle \quad (17)$$

The satisfactory agreement between the profile of the SFM experimental persistence length and that evaluated by Eq. (16) indicates that the normalized melting temperatures can be adopted as a measure of the sequence-dependent DNA stiffness.

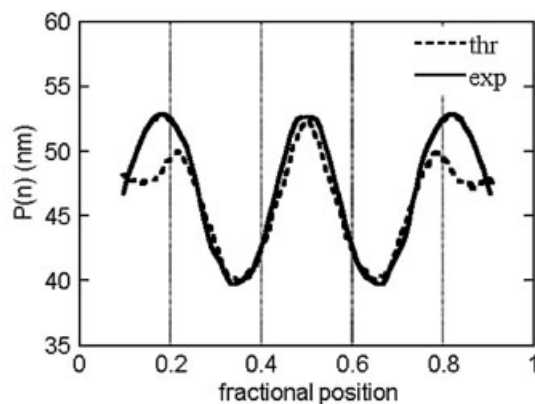


Fig. 16.11 Comparison between the profile of the persistence length obtained from the experimental standard deviation of the SFM images of the *Crithidia fasciculata* tail-to-tail dimer (“exp”) with that evaluated from the normalized melting temperatures by means of Eq. (16) (“thr”).

16.12

Sequence-Dependent DNA Dynamics from SFM Time-Resolved DNA Images

DNA can be represented as a topologically conditioned elastic chain continuously fluctuating in solution under the thermal perturbations by the molecular environment.

The possibility offered by SFM to follow the dynamics of a single DNA molecule in real time opens another direct way to study the large-scale mechanical properties of DNA along the sequence. Time-averaging of the SFM images could provide the determination of both the static and dynamic contributions to the curvature as a function of the sequence, leaving only its alternative directions to be found. In addition, working on a single molecule guarantees that all the single-time curvature profiles refer to the same sequence with the same orientation.

This new approach to the study of DNA superstructure could address the issue of the large-scale dynamics of a DNA, in particular when the environment severely damps its motions.

Both the intrinsic curvature and the flexibility along the sequence are found to be in satisfactory agreement with the theoretical predictions confirming the results previously obtained by analyzing a large ensemble of static DNA molecules. Accordingly, the ergodicity of the local dynamics, corresponding to fluctuations around the equilibrium (intrinsic) curvature, was verified on the basis of the expected constant ratio [see Eqs. (14) and (15)] between the time-average curvature modulus and the corresponding standard deviation (see Fig. 16.12). Contrarily, the global shape of the DNA molecule shows a non-ergodic behavior and a time evolution far from the equilibrium.

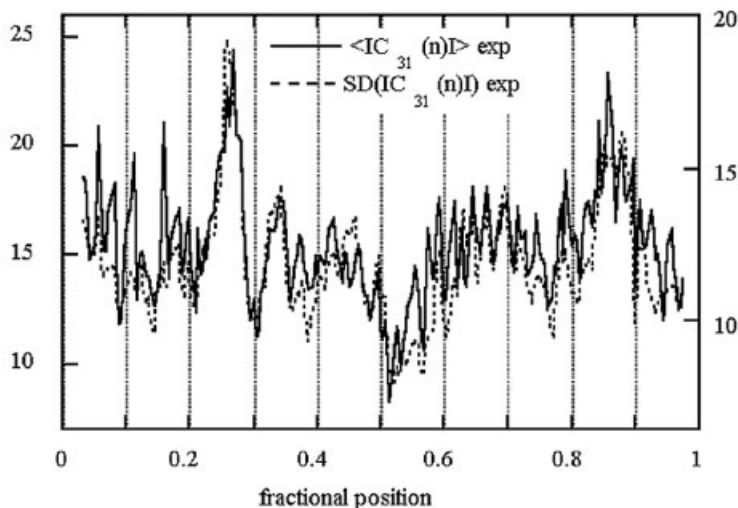


Fig. 16.12 Comparison between the profiles of the experimental time-average curvature modulus ($\langle |C'_{31}(n)| \rangle$) and the corresponding standard deviations (SD) obtained from the SFM images of a linearized pBR322 single molecule.

The motion of two 4360 bp linear DNA molecules, obtained by cutting the circular pBR322 DNA in two different positions, was monitored by SFM images in liquid cells for a few hours [30]. The superimposition of DNA traces shows that the global shapes of the two molecules are very different. The average squared end-to-end distances for the two molecules would correspond to apparent 3D persistence lengths of 10 and 80 nm. This is a consequence of the different conformational histories of the two molecules, which appear not to equilibrate on the surface during the time of the experiment. As shown earlier [30], the proportionality between the average curvature modulus and its standard deviation monitors the conformational equilibrium of the DNA chains (see Section 16.8). This relationship, found for an equilibrium statistical ensemble, should hold if the two DNA molecules have an ergodic behavior during the time of the experiment. We have found that this proportionality holds for DNA tracts up to 60–70 bp and progressively deviates for longer tracts [30], which proves the expected ergodicity of the microscopic dynamics according to the principle of microscopic reversibility. However, some memory of the starting DNA shapes is still conserved for large-scale dynamics. This raises the important question of whether the structural transformations involving DNA can be considered among the thermodynamic equilibrium states. This is not true for the dynamics of the whole pBR322 molecule on the mica surface in a time interval of several hours. In the case of very much longer genomic DNAs, the problem of the apparent conservation of the DNA architecture appears to be even more dramatic.

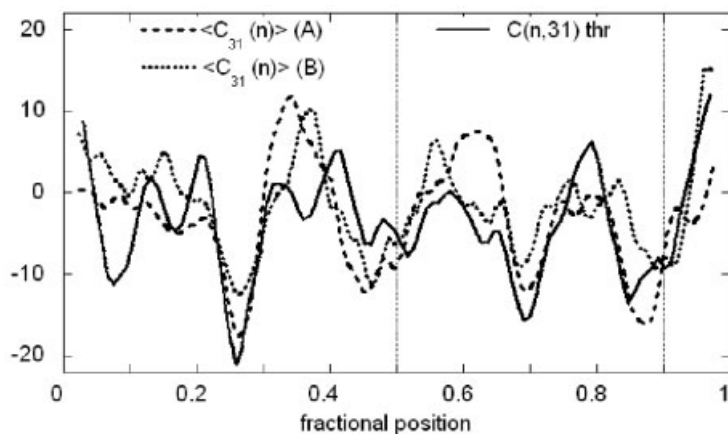


Fig. 16.13 Comparison between the time-averaged curvature profiles of two pBR322 molecules after the cyclic permutation of one with respect to the other to maximize the correlation function, with the predicted curvature profile.

A careful study of the average time curvature of the two molecules has shown that the small-scale curvatures measured are in satisfactory agreement with the sequence-dependent local curvatures that can be predicted theoretically for linearized pBR322.

Figure 16.13 illustrates the comparison between the experimental and theoretical curvature profiles for the two molecules. The theoretical curvature profile was calculated using the dinucleotide step orientational parameters reported in Table 16.1, and cyclically permuted to maximize the correlation with the experimental profile. As a result, the sequence of the two molecules was identified.

The evaluation of the standard deviation of the curvature allows the calculation of an average 3D persistence length of 48 nm. This is in good agreement with the accepted value for B-DNA and confirms the local ergodicity of the DNA chains in the conditions of the experiment.

16.13 Conclusions

The implication of DNA curvature and flexibility in mechanisms that govern biological processes such as replication, transcription, and chromatin organization appears to involve large-scale static and dynamic sequence effects and certainly requires further investigation. Different approaches have been proposed in the literature to modeling the mechanical properties of DNA in relation to the sequence. SFM offers the best opportunity to investigate the mechanical behavior of DNA single molecules in this connection.

In this chapter we discuss some theoretical issues concerning the DNA curvature and flexibility, which are the main determinants of the DNA static and dynamic behavior on a nanometric scale, and we analyze critically methods for obtaining these properties from SFM images. Finally, we report strong evidence of sequence recognition effects by crystal surfaces where DNA is adsorbed [29]. Such effects could be brought into play for the design of self-assembling nanostructures.

Acknowledgements

This work was supported by: “Progetto 60% Ateneo” of Università “La Sapienza”, 2003–2004; Progetti di Interesse Nazionale, MIUR, 2003–2005; and Istituto Pasteur, Fondazione Cenci–Bolognetti.

References

- 1 R. D. KORNBERG, *Annu. Rev. Biochem.* **1977**, *46*, 931–954.
- 2 K. MATTHEWS, *Microbiol. Mol. Biol. Rev.* **1992**, *56*, 123–136.
- 3 R. SCHLEIF, *Annu. Rev. Biochem.* **1992**, *62*, 199–223.
- 4 K. DANNA, D. NATHANS, *Proc. Natl. Acad. Sci. USA* **1971**, *68*, 2913–2917.
- 5 K. DANNA, D. NATHANS, *Proc. Natl. Acad. Sci. USA* **1972**, *69*, 3097–3100.
- 6 J. E. MERTZ, P. BERG, *Proc. Natl. Acad. Sci. USA* **1974**, *71*, 4879–4883.
- 7 E. N. TRIFONOV, J. L. SUSSMAN, *Proc. Natl. Acad. Sci. USA* **1980**, *77*, 3816–3820.
- 8 J. C. MARINI, S. D. LEVENE, D. M. CROTHERS, P. T. ENGLUND, *Proc. Natl. Acad. Sci. USA* **1982**, *79*, 7664–7668.
- 9 H. M. WU, D. M. CROTHERS, *Nature* **1984**, *308*, 509–513.
- 10 P. J. HAGERMAN, *Nature* **1986**, *321*, 449–450.
- 11 H. S. KOO, H. M. WU, D. M. CROTHERS, *Nature* **1986**, *320*, 501–503.
- 12 P. DE SANTIS, A. PALLESCHI, S. MOROSETTI, M. SAVINO, *Structures and Dynamics of Nucleic Acids, Proteins and Membranes*, eds. E. CLEMENTI, S. CHIN, Plenum Press, New York, **1986**.
- 13 P. DE SANTIS, A. PALLESCHI, M. SAVINO, A. SCIPIONI, *Biochemistry* **1990**, *29*, 9269–9273.
- 14 A. BOLSHOY, P. MCNAMARA, R. E. HARRINGTON, E. N. TRIFONOV, *Proc. Natl. Acad. Sci. USA* **1991**, *88*, 2312–2316.
- 15 A. A. GORIN, V. B. ZHURKIN, W. K. OLSON, *J. Mol. Biol.* **1995**, *247*, 34–48.
- 16 W. K. OLSON, A. A. GORIN, X.-J. LU, L. M. HOCK, V. B. ZHURKIN, *Proc. Natl. Acad. Sci. USA* **1998**, *95*, 11 163–11 168.
- 17 D. M. CROTHERS, *Proc. Natl. Acad. Sci. USA* **1998**, *95*, 15 163–15 165.
- 18 Z. KAM, N. BOROCHOV, H. EISENBERG, *Biopolymers* **1981**, *20*, 2671–2690.
- 19 E. S. SOBEL, J. A. HARPST, *Biopolymers* **1991**, *31*, 1559–1564.
- 20 D. SHORE, J. LANGOWSKI, R. L. BALDWIN, *Proc. Natl. Acad. Sci. USA* **1981**, *78*, 4833–4837.
- 21 V. RIZZO, J. SCHELLMAN, *Biopolymers* **1981**, *20*, 2143–2163.
- 22 J. G. ELIAS, D. EDEN, *Macromolecules* **1981**, *14*, 410–419.
- 23 P. J. HAGERMAN, *Biopolymers* **1981**, *20*, 1503–1535.
- 24 S. DIEKMANN, W. HILLEN, B. MORGENEYER, R. D. WELLS, D. PÖRSCHKE, *Biophys. Chem.* **1982**, *15*, 263–270.
- 25 D. PÖRSCHKE, *Biophys. Chem.* **1991**, *40*, 169–179.
- 26 G. MUZARD, B. THEVENY, B. REVET, *EMBO J.* **1990**, *9*, 1289–1298.
- 27 G. ZUCCHERI, A. SCIPIONI, V. CAVALIERE, G. GARGIULO, P. DE

- SANTIS, B. SAMORÌ, *Proc. Natl. Acad. Sci. USA* **2001**, *98*, 3074–3079.
- 28 A. SCIPIONI, C. ANSELMi, G. ZUCCHERI, B. SAMORÌ, P. DE SANTIS, *Biophys. J.* **2002**, *83*, 2408–2418.
- 29 B. SAMPAOLESE, A. BERGiA, A. SCIPIONI, G. ZUCCHERI, M. SAVINO, B. SAMORÌ, P. DE SANTIS, *Proc. Natl. Acad. Sci. USA* **2002**, *99*, 13 566–13 570.
- 30 A. SCIPIONI, G. ZUCCHERI, C. ANSELMi, A. BERGiA, B. SAMORÌ, P. DE SANTIS, *Chem. Biol.* **2002**, *9*, 1315–1321.
- 31 C. ANSELMi, G. BOCCHINFUSO, P. DE SANTIS, M. SAVINO, A. SCIPIONI, *Biophys. J.* **2000**, *79*, 601–613.
- 32 M. LE BRET, *Biopolymers* **1984**, *23*, 1835–1867.
- 33 C. ANSELMi, G. BOCCHINFUSO, P. DE SANTIS, M. FUÀ, M. SAVINO, A. SCIPIONI, *J. Phys. Chem. B* **1998**, *102*, 5704–5714.
- 34 K. A. HOFFMAN, *Phil. Trans. R. Soc. Lond. A* **2004**, *362*, 1301–1314.
- 35 I. TOBIAS, *Phil. Trans. R. Soc. Lond. A* **2004**, *362*, 1387–1402.
- 36 A. BALAEFF, C. R. KOUDELLA, L. MAHADEVAN, K. SCHULTEN, *Phil. Trans. R. Soc. Lond. A* **2004**, *362*, 1355–1371.
- 37 J. H. WHITE, W. R. BAUER, *Phil. Trans. R. Soc. Lond. A* **2004**, *362*, 1335–1353.
- 38 T. ODIJK, *J. Polym. Sci.* **1977**, *15*, 477–483.
- 39 C. G. BAUMANN, S. B. SMITH, V. A. BLOOMFIELD, C. BUSTAMANTE, *Proc. Natl. Acad. Sci. USA* **1977**, *94*, 6185–6190.
- 40 S. M. KLIMENKO, T. I. TYKHCHOENENKO, V. M. ANDRE'EV, *J. Mol. Biol.* **1967**, *23*, 523–533.
- 41 K. E. RICHARDS, R. C. WILLIAMS, R. CALENDAR, *J. Mol. Biol.* **1973**, *78*, 255–259.
- 42 L. C. GOSULE, J. A. SCHELLMAN, *Nature* **1976**, *259*, 333–335.
- 43 D. S. HOROWITZ, J. C. WANG, *J. Mol. Biol.* **1984**, *173*, 75–91.
- 44 O. KRATKY, G. POROD, *Rec. Trav. Chim. Pays-Bas Belg.* **1949**, *68*, 1106–1124.
- 45 L. D. LANDAU, E. M. LIFSHITZ, *Statistical Physics*, Pergamon Press, London, **1958**.
- 46 P. J. FLORY, *Statistical Mechanics of Chain Molecules*, John Wiley & Sons, New York, **1969**.
- 47 J. A. SCHELLMAN, *Biopolymers* **1974**, *13*, 217–226.
- 48 E. N. TRIFONOV, R. K.-Z. TAN, S. C. HARVEY, *Structure and Expression*, vol. 3, eds. W. K. OLSON, M. H. SARMA, R. H. SARMA, M. SUNDARALINGAM, Adenine Press, Schenectady, NY, **1988**.
- 49 J. A. SCHELLMAN, S. C. HARVEY, *Biophys. Chem.* **1995**, *55*, 95–114.
- 50 P. DE SANTIS, M. FUÀ, A. PALLESCHI, M. SAVINO, *Biophys. Chem.* **1995**, *55*, 261–271.
- 51 C. RIVETTI, M. GUTHOLD, C. BUSTAMANTE, *J. Mol. Biol.* **1996**, *264*, 919–932.
- 52 L. D. LANDAU, E. M. LIFSHITZ, *Theory of Elasticity*, Pergamon Press, Oxford, **1970**.
- 53 C. RIVETTI, C. WALKER, C. BUSTAMANTE, *J. Mol. Biol.* **1998**, *280*, 41–59.
- 54 P. J. HAGERMAN, *Annu. Rev. Biophys. Biophys. Chem.* **1988**, *17*, 265–286.
- 55 A. V. SIVOLOB, S. N. KRAPUNOV, *J. Mol. Biol.* **1995**, *247*, 918–931.
- 56 J. VIRSTEDT, T. BERGE, R. M. HENDERSON, M. J. WARING, A. TRAVERS, *J. Struct. Biol.* **2004**, *148*, 66–85.
- 57 B. THEVENY, B. REVET, *Nucleic Acids Res.* **1987**, *15*, 947–958.
- 58 J. GRIFFITH, M. BLEYMAN, C. A. RAUCH, P. A. KITCHIN, P. T. ENGLUND, *Cell* **1986**, *46*, 717–725.
- 59 B. SAMORÌ, I. MAZZALUPO, G. ZUCCHERI, *Scanning Microsc.* **1996**, *10*, 953–960.
- 60 Y. L. LYUBCHENKO, L. S. SHLYAKHTENKO, *Proc. Natl. Acad. Sci. USA* **1997**, *94*, 496–501.
- 61 J. W. PAVLICEK, E. A. OUSSATCHEVA, R. R. SINDEN, V. N. POTAMAN, O. F. SANKEY, Y. L. LYUBCHENKO, *Biochemistry* **2004**, *13*, 10 664–10 668.
- 62 O. GOTOH, Y. TAGASHIRA, *Biopolymers* **1981**, *20*, 1033–1042.

Index

a

abalone shells 342
 absolute chirality 4, 6
 absolute configuration 4, 24
 acetylene 80, 90
 achiral 14, 16f, 20, 23f, 26, 28
 achirally functionalized tip 32
 acid–base titration 298
 active™ Pen array 162
 adamantane 334
 additives 305
 adenine 25f
 adhesion 208
 – forces 288
 adiabatic 504
 adsorbate
 – double layer 40f, 44ff
 – monolayer 38ff
 adsorbed organic molecules 121
 affinity 252
 AFM (atomic force microscope) tip
 – diameter 147
 – electrochemical DPN 159
 – functionalization 277
 – ink 148
 – resolution 147
 – Si 147
 – unconventional DPN 158
 alcohol 21, 22, 26
 alkanethiol 363
 – matrix 114
 – molecules 129
 – monolayer 360
 alkanethiol-type SAMs 112
 aluminum 115
 amino acid 6
 3'-aminopropyltrimethoxysilane 157
 ammonia molecule 90
 amplitude modulation (AM) 185, 398

 – mode 192, 194
 analytical approximations 439, 440
 anchoring of a molecule 69
 anodic oxidation 104, 115
 anomalous surface diffusion 170
 anthracene 20
 anthraquinone 48ff
 approach–retract 202
 – curves 176, 196–200, 202, 204
 APS monolayer 119, 120
 array of
 – AFM tips 105
 – dots 111
 – oligomer molecules 114
 – silicon oxide lines 116
 aspirin 295
 assembly 19
 atomic force microscope (AFM) 29, 208, 315,
 323, 327
 – amplitude modulation (AM-AFM) 192
 – cantilever array chips 105
 – force experiments 255
 atomic gold wires 490
 attractive interaction 187, 197
 average curvature 520, 523, 530
 average time curvature 531

b

B-DNA 511
 – structure 508, 510, 516
 ballistic 355
 band bending 399, 400, 403
 Bardeen's approximation 502
 Bardeen's transfer Hamiltonian 473
 barrier 254
 Bell 326, 348
 bending energy 528
 bending force constant 514, 528
 benzene 85
 benzylic amide rotaxanes 109

- bilayer template patterns 124
- biochemical recognition 136
- biochips 133
- biomembrane force probe (BFP) 263, 317, 327
- biosensors 133, 157, 459
- biotin 250
- block copolymers 175f, 198ff, 303
 - blends 101
- blocking 332
- bonds 324
 - cooperative 329
 - in parallel 329
 - in series 329
- Bootstrap Monte Carlo 260
- Born–Oppenheimer approximation 504
- bovine carbonic anhydrase II 134
- break junctions 356
- built-in potential V_{bi} 400
- 2-butanol 129, 131
- c**
- cadherins 267
- canonical partition function 520
- cantilever 210
- cantilever arrays 102
- capillary forces 282, 287
- carbon monoxide 80
- carbon nanotubes 114, 281, 356, 366
- carboxylic acid 4, 6, 23, 125f
- catalysis 6
- catalytic probe lithography 128
- catalytic probe nanolithography 126
- catalytic writing 127
- cells 454–456
- change in conductance 89
 - negative (elastic) 484
 - positive (inelastic) 484
- characteristic distance 110
- charge transfer 393, 401, 412
 - complexes 49ff, 346f
- chemical contrast 281
- chemical field-effect transistor (Chem-FET) 51
- chemical force microscopy (CFM) 31f, 276
 - inverted 301
- chemical lens 462f
- chemical sensitivity 277
- chemically modified tips 286
- chemisorbed 4, 6, 8, 26
- chemisorption 4
- chiral
 - discrimination 32
 - recognition 297
 - resolution 16
- chirality 4f, 12ff, 20
- cholesterol 295
- clusters 17, 18
- co-conformations 109
- coadsorption 25
- coalescence of domains 114
- cocrystals 26
- CODYMode 217
- colloidal particles 277
- complex viscosity 190
- complexation constants 335
- compositional mapping 301
- concentration profiles 452, 453
- conductance calculations 471
- conductance drop 493
- conductance properties
 - contact regime 471
 - tunneling regime 471
- conductance transition 104, 105
- conducting-AFM probe (C-AFM) 451
- confined etchant layer (CELT) 463
- conformational energy 516
- conformational molecular switch 67
- conformations of DNA 518
- conglomerate 12, 20, 21
- conjugated materials 116
- conjugated molecules 38ff, 101
- conjugated polymers 101
 - films 106
- constant deflection mode 211
- constant force 255
- constant height mode 62, 210
- constructive nanolithography (CNL) 121
- contact
 - electrical 369
 - mechanical 369
- contact force 155
- contact mechanics
 - Hertzian modeling 218
 - models incorporating adhesion 223
 - Sneddon's extensions 222
- contact-mode 157
- contact potential 394
- contact potential difference (CPD) 392f, 403f, 407
- cooperative failure 259
- coordinative bonds 321
- copolymers 178
- corrosion 452, 453
- covalent bonds 317
- covalent surface bonding 147
- Crithidia fasciculata* DNA tract 517
- crossover force 327

- crown ethers 322, 336
- crystallization 101
- C₁₀S monolayer 130, 132
- C₁₈S nanoislands 130–132
- Cu-tetra[(3,5-di-*tert*-butyl)phenyl]porphyrin (TBPP) 56
- curvature
 - diagrams 523
 - functions 524
 - maps 518
 - modulus 524
 - profiles 519ff
- curved DNA 524f
- β -cyclodextrin (β CD) 330f
- cyclopentanone 128

- d**
- 3D protein nanostructures 134
- damping coefficient γ_{int} 191ff
- damping 188
 - signal 186
- dangling bonds 403
- dendrigrfts 184
- deposition 460, 461
 - constant 151
 - of metals 459
 - rate 150f
- Derjaguin–Muller–Toporov model (DMT) 224ff, 283
- dewetting polymer blends 235
- diastereomeric 6, 9
- diblock copolymers 179, 181
- differential interactions with the surface 522
- diffusion 253
- diffusion layer 400, 437, 444
- diffusion-limited aggregation (DLA) 170
- diffusion model 167
- diiiodooctadecan-1-ol 21
- dimethoxyanthracene 49f
- dinucleotide step 511, 515f, 518, 528
- dinucleotide step deviations
 - roll, tilt, and twist angles 516
- dip-pen nanolithography (DPN) 102
 - automated lithography software 146
 - basic mechanism 144
 - bonding 149
 - dots 151
 - ink deposition rate 146
 - inks 149
 - integrated system 162
 - lines 151
 - resolution 154
 - solution coating 150
 - substrate 149
 - vapor coating 150
 - writing speed 150
- dipole layer 401f, 419
- dipole moment 408, 412
- direct patterning 102
- dispersive van der Waals forces 295
- dissipated energy 188, 190
- dissipative interactions 187
- distribution 257
- disulfides 278f
- DNA 134, 356, 374, 384, 410, 414
 - architecture 530
 - double-stranded (ds) 135f
 - ds-plasmid molecules 135
 - EFM 414
 - faces 522
 - FETs 417
 - images 519
 - mechanics 509, 513, 529
 - molecule ensemble 521
 - palindromic dimers 525
 - DNA curvature 509, 515, 517ff, 524f, 528, 532
 - bending 510
 - sequence-dependent intrinsic 510, 515
 - twisting 510
 - DNA flexibility 517
 - flexibility scale 528
 - persistence length 528
 - DNA sequence 511
 - nearest-neighbor interactions 510
 - DNA structure
 - dinucleotide steps 509
 - DNA helical repeat 509
 - superstructure 528
 - dodecanethiol 113f
 - 1-dodecylamine (DDA) 170
 - doped polypyrrole (PPY) 158
 - drive frequency ω 195
 - drop-casting 110
 - Dupré’s work of adhesion 224
 - dynamic curvature 520
 - curvature fluctuations 516
 - dynamic force spectroscopy 251, 258
 - dynamic mechanical analysis (DMA) 213
 - dynamic modes 175, 195, 211
 - dynamic persistence length 514

- e**
- effective modulus K 222
- effective radius R 222
- eigenfrequencies 212
- Einstein 253
- elastic contribution 90

- elastic response to thermal energy 518
 - elastic rod 511
 - elastic scattering quantum chemistry (ESQC) 63
 - elasticity 324, 340
 - elasto-mechanical forces 208
 - elastomer 304
 - electrochemical forces 208
 - electrochemical oxidation 121
 - electrochemical reduction 121
 - electron acceptor 47ff
 - electron beam lithography 104, 143
 - electron donor 47ff
 - electron microscopy (EM) 514, 518
 - images 527, 528
 - π -electron stacking 322
 - electron transfer (ET) 445, 447
 - electron tunneling 447
 - electronic contact
 - effect on the standing wave patterns 72
 - increased tunneling signal 71
 - electronic transport 355
 - electrostatic force microscopy (EFM) 380, 391, 394, 414
 - enantiomers 4ff, 22ff
 - enantioselectivity 28
 - end-to-end distances 530
 - energy barriers 328
 - ensemble-average curvature 516
 - profile 527
 - modulus 521
 - ensemble thermodynamics approaches 315
 - entropic contributions 294
 - enzymes 456, 457, 458, 459
 - equilibrium 252
 - statistical ensemble 530
 - ergodicity 529, 531
 - error 260
 - ester-terminated alkanethiolate monolayer 128
 - etching 459, 461, 463
 - etching resist patterning 162
 - Euler's gamma 168
 - Evans 325, 326, 328, 348
- f**
- far-from-equilibrium 327
 - FAS (heptadecafluoro-1,1,2,2-tetrahydrodecyl-1-trimethoxysilane) 116
 - feedback 441, 442, 456
 - circuits 155
 - mode 434, 435
 - Fermi level 400, 402, 403
 - fibronectin 267
 - field-effect devices 114
 - field-effect transistors (FETs) 405, 414
 - field evaporation 104
 - field-induced desorption 102
 - field-induced oxidation 114
 - finite kinetics 441, 443
 - first-order elasticity model 514, 519, 528
 - flexibility 529, 532
 - bending force constant 515
 - end-to-end distance 515
 - persistence length 515
 - flexibility of DNA 509
 - bending force constants 512
 - bending stiffness 512
 - elastic constants of DNA 512
 - persistence length 512
 - fluorescent nanoparticles 119
 - focused ion beam lithography 104
 - force–displacement measurements 282
 - force–distance curve (FDC) 214
 - force modulation mode 213
 - force titration 299, 306
 - force–volume mode 217
 - formal potential 443
 - fractal-like patterns 170
 - frequency modulation (FM) 185, 192
 - frequency modulation method (FM-KPFM) 396, 399
 - frequency shifts 187, 495
 - friction anisotropy 292
 - friction force microscopy (FFM) 217
 - friction forces 285, 291, 293
 - fullerene 80
- g**
- GaAs 115
 - gate dielectric 122
 - Ge 115
 - gel electrophoretic anomalies 516
 - Gibbs free energy 335, 484
 - goat anti-rabbit IgG 134
 - gold
 - Au(111) 111f
 - clusters 102
 - nanoclusters 117, 124, 126
 - nanoparticle 117ff
 - single-atomic contacts 490
 - Gordon Moore 355
 - Green's functions 474
- h**
- H-bonds 316, 320, 338
 - harmonic oscillator 186
 - heat dissipation 355

- helicenes 8
 - helix-coil transition 528
 - helix periodicity 516
 - heptanol 26
 - Hertz 368
 - Hertz theory 283
 - Hertzian deformation 360
 - Hertzian model 131
 - heterogeneous rate constant 443
 - heterogeneous reactions 440
 - heterogeneous surfaces 301
 - heterogeneous systems 303
 - hexa-*peri*-hexabenzocoronene 38ff
 - hexadecanoic acid 23
 - histidine 344
 - HMDS 119
 - hole-burning process 104f
 - TCNQ 104, 346
 - HOMO- and LUMO-derived resonances 83
 - HOMO-LUMO-gap 37ff
 - HOMO-LUMO-splitting 43ff
 - homochiral 14, 19
 - Hooke's law 325
 - HOPG (highly oriented pyrolytic graphite) 368
 - horseradish peroxidase (HRP) 120
 - protein adsorption 120
 - Hummer-Szabo model 328, 348
 - hybrid architectures 135
 - hybrid devices 144
 - hybrid molecular electronic (HME) device 54
 - hydrocarbon contamination 149
 - hydrodynamic forces 208
 - hydrogen-bond 317, 319
 - hydrogen-bonding 6, 12, 14, 23–25, 31
 - hydrolysis 127
 - hydrophobic recovery 308
 - hyperbranched polymers 176, 182
- i**
- inclusion complexes 330
 - indentation depth 202
 - inelastic effects
 - change in conductance 89
 - high-conductance 471
 - low-conductance 471
 - inelastic electron tunneling spectroscopy (IETS) 77
 - inelastic electron tunneling spectroscopy with STM (IETS-STM) 478
 - change in conductance across the threshold of a vibrational excitation 78
 - inelastic channel 78
 - inelastic fraction 79
 - inelastic processes 475
 - information storage 103, 111
 - InGaAs quantum dots 115
 - inorganic nanostructures 115
 - integrated DPN system 162
 - interaction
 - with the substrate 68
 - with the surface 522
 - interface between two immiscible electrolyte solutions (ITIES) 448f
 - interface dipole 49f
 - interfacial free energies 293
 - intermittent contact 175, 185, 189, 195, 202
 - mode 211
 - internal mechanics
 - deformation 63
 - motion 63
 - intracellular redox centers 454f
 - intramolecular hydrogen bonds 109
 - intramolecular mechanics 63
 - intrinsic curvature 516–519, 529
 - bending modulus 511f
 - segmental 521
 - twist modulus 512
 - inverse photoemission spectra 82
 - inverted CFM 301
 - ion transfers 447
 - ionic liquid (IL) 449
 - IPrDMA-I-TCNQ crystal surface 105
 - isophthalic acid 26
- j**
- Johnson-Kendall-Roberts model (JKR) 224ff, 283, 289, 295, 300
 - jumping mode (JM) 211, 217
- k**
- Kelvin probe force microscopy (KPFM) 117f, 391, 393
 - Kramers 253, 325, 326
 - Kratky and Porod 513, 515
 - Kuhn length 340, 341
- l**
- lamellar polymer crystals 292
 - Landauer 360
 - Landauer-Büttiker 489
 - Landauer's formalism 473
 - landscape 254, 258
 - Langmuir-Blodgett (LB) 29
 - film 284
 - layers 275
 - large-scale dynamics 530
 - of DNA 529

- lateral diffusion of molecules 166
- lateral force microscopy 151
- lateral forces 285, 366
- length scales of transport phenomena 116
- lifetime
 - at zero force 326
 - bond 326
- Lifshitz theory 284, 295
- lift mode 396
- ligand exchange 124
- ligand–receptor bonds 316
- light-emitting diodes 108
- linearization of the full Hamiltonian 476
- liquid crystals 8, 20
- liquid neck 208
- liquid/solid interface 9
- loading dynamics 349
- loading rate 255, 327, 328, 330f, 334, 336, 345
- local anodic oxidation 114
- local density of states (LDOS) 88, 474
- local electrochemical oxidation 122
- local electrochemical reduction 124
- local electrooxidation 122
- local electroreduction 122
- local mechanical properties 176
- local oxidation 114, 116f
 - nanolithography 114f
 - of silicon 121
- lock-in techniques 80
- low-density polyethylene (LDPE) 291
- low-temperature scanning tunneling microscopy (LT-STM)
 - manipulation 55
 - submolecular imaging 55
- lysozyme 134

- m**
- macrocycle 109f
- manipulation
 - lateral manipulation 58
 - vertical manipulation 58
- manipulation modes
 - pulling mode 58
 - pushing mode 60
 - sliding mode 60
- manipulation signal 58
- many-body structure 474
- many-body wavefunctions 89
- mass-transfer coefficient 443
- Maugis–Dugdale model (MD) 224ff
- mechanical contribution 198, 205
- mechanical instabilities 187
- mechanical plowing 129
- mechanical properties of DNA 509, 529
 - curvature 522, 531
 - flexibility 522, 531
- MEH-PPV film 107
- melting temperature 518
 - pre-melting temperatures 528
- membrane transport 455
- memory storage 104
- 16-mercaptohexadecanoic acid (MHA) 150, 153, 164
- 3'-mercaptopropyltrimethoxysilane (MPTMS) 157
- mesogenic molecules 107
- metallic silver nanoparticles 124
- metal–ligand 18
 - interactions 321
- metalloproteins 133
- metal–organic junctions 401
- metal–organic superstructures 20
- MHP Br 134
- mica surface 521, 524, 527f, 530
 - preferential adhesion 525
- micelles 181
- microfabrication 142
- microphase separation 202
- microstructures 459
- Millipede chip 105f, 157
- mirror image 6, 8, 17, 20, 22
- mirror symmetry 16, 31
- mode 457
- modified freely jointed chain 340
- modular polymers 343
- molecular
 - actuators 105
 - bonding to the substrate 166
 - chains 66
 - diffusion 114, 146
 - diodes 47ff
 - dynamics 260
 - electronics 36ff, 47ff, 74, 355
 - nanostructures 135
 - recognition mechanism 163
 - rectifiers 47ff
 - simulation 260
 - transistor 47ff
 - transport 166
 - vibrations 77
 - wires 357, 364
- molecular lander (C₉₀H₉₈)
 - long rigid polyaromatic mainboard 56
 - TBP spacer groups 56
- molecular molds to metallic nanostructures 70
- molecule–metal bonding 16

- monolayer 14, 119, 122
 - monolayer of imines 128
 - monolayer protected gold clusters (MPCs) 450
 - monomer protein 133
 - monomolecular electronics 51, 54
 - Monte Carlo 263
 - Mott–Schottky model 400
 - multiple bonds 328
 - multiple-DNA inks 158
 - multiple-ink patterning 154
 - multiple interactions 251
 - multiple-pen writing strategy 155, 163
 - multiple transition states 258
- n**
- N*-(6-acetylthiolhexyl)pyridinium bromide (MHP Br) 134
 - N*-biphenylthiol (*N*-BPT)–Au 112
 - n*-octadecyltrichlorosilane (OTS) monolayers 122
 - nanoassembly 163
 - nanoelectrochemical pattern 123
 - nanoelectrodes 450
 - nanofabricated patterns 111
 - nanofibers 29
 - nanografting 128f, 131, 134
 - nanoindentations 213
 - nanoparticles 101, 115
 - nanopatterns 119
 - nanophase segregation 49
 - nanorecording 104
 - nanorubbing 107f
 - nanoscale chemistry 276
 - nanoscale DMA 213
 - nanoscale molecular barrow 66
 - nanoscale water condensation 168
 - nanoshaving 129
 - nano-sized architectures 136
 - nanostuctures 109
 - nanotube 135
 - metallic 369
 - resistance 369
 - strain 374
 - NBMN-pDA 104
 - near-equilibrium 327
 - negative 441
 - negative feedback 441
 - negative-ion resonance 479
 - nematic liquid crystals 107
 - N*–H stretch 93
 - Ni nitrilotriacetate 344
 - niobium 115
 - nitronaphthalene 17
 - nonacosan-10-ol 23
 - noncontact mode 211, 391, 398
 - nonadecyltrichlorosilane (NTS) 126
 - nonequilibrium Green's functions (NEGFs) 480, 485
 - non-ergodic behavior 529
 - nonresonant modes 211
 - nonspecific 251
 - normal forces 282
 - nucleation 110
- o**
- 1-octadecanethiol 146, 162, 165
 - octadecanethiol monolayer 133
 - on gold 130
 - octadecanethiol SAM 290
 - octadecanol 22
 - octadecylsiloxane (ODS) 166ff
 - octadecyltrichlorosilane (OTS) 117
 - in bicyclohexyl (BCH) 123
 - monolayer 125
 - SAM 117
 - octadecyltriethoxysilane layer on mica (OTE/mica) 130f
 - odd/even effect 24
 - ODS-SAM 116ff
 - oligonucleotide 258, 262
 - oligo-*p*-phenylene-vinylene enantiomers 12
 - oligothiophenes 42f
 - opening of a new channel 477
 - optical lever technique 210
 - organic field-effect transistors 108, 122
 - organic molecular beam deposition (OMBD) 114
 - organic nanostructures 116
 - organic semiconductors 391f, 400, 403, 422
 - organic thin films 102
 - organosilane molecules 119
 - organosilane template pattern 125
 - organosiloxane surface assemblies 128
 - oscillating cantilever 197
 - OTE/mica 131
 - oxide dot array 118
 - oxidoreductases 457
 - oxygen 88, 90
- p**
- palindromic DNA
 - constructs 517, 522f
 - dyad symmetry 518
 - statistical dyad symmetry 521
 - palladium-coated tip 128
 - patterned SAMs 301
 - patterning organic nanostructures 101

- pentacene 110
 - persistence length 183, 513, 530
 - elastic modulus of DNA 511
 - force constants 511
 - stiffness of bending 511
 - twisting stiffness 511
 - PFM, see pulsed force mode
 - phase images 196
 - phase imaging 151, 285
 - phase separation 176f
 - phenyl benzoate 14
 - photoemission 82
 - photolithography 106, 142
 - photomask 143
 - resist 143
 - resolution 143
 - UV light 143
 - photonic crystal
 - physisorption 6, 26
 - pi-pi-interactions 41ff
 - pits 452, 453
 - plasmid DNA molecules 136
 - p–n junctions 404, 410
 - PNBN 105
 - nanostructures 105
 - point contact 484
 - poly(dimethylsiloxane) 308
 - poly[2-methoxy,5-(2'-ethylhexoxy)-1,4-phenylenevinylene] (MEH-PPV) 107
 - poly(methyl methacrylate) (PMMA) 231ff, 303
 - polymer films 105, 213
 - polydimethylsiloxane (PDMS) 161
 - polyethyleneimine 305
 - polymer blends 176, 177, 203, 303
 - poly(phenylene vinylene) (PPV) 106f
 - polypropylene 304, 305
 - polystyrene 303
 - position-sensitive detector (PSD) 210
 - positive feedback 443, 448
 - precursor molecules 159
 - primary interactions 319
 - prochiral forms 523
 - prochiral recognition 525
 - sequence–mica interactions 524
 - prochiral 14, 20, 25
 - prochiral shape 525
 - protein G 134
 - protein molecules 120
 - protein–protein interactions 134
 - proteins 133, 267, 412
 - pseudo-racemate 12
 - pulsed force mode (PFM) 208, 211, 213ff
 - adhesion 235
 - biological samples 242
 - chemically modified tips 239
 - CODYMode 242
 - data evaluation 229
 - elastic potential energy 227ff
 - electric double layer 239
 - electrostatic forces 228
 - force curves 227ff
 - hydrodynamic forces 228
 - hysteresis 227ff, 233
 - indentation depth 231
 - in liquids 239
 - plastic deformation 227ff
 - remanent plastic deformations 232
 - temperature-dependence 235
 - thermal oscillations 227ff
 - tip creeps 233
 - van der Waals forces 228
 - very thin layers 239
 - viscoelastic processes 227ff
 - pyrene 43
- q**
- quality factor 194ff
 - quantitative measurements 198
 - quantum of conductance 484
- r**
- rabbit IgG 134
 - racemate 12, 14, 18, 20, 21
 - racemic conglomerate 14, 16, 21
 - racemic mixtures 12, 23, 25, 29, 32
 - radical molecule, 3-nitrobenzal malonitrile and 1,4-phenylenediamine (NBMN-pDA) 104
 - random nucleation 114
 - rate constant 448
 - reading/writing data by SPnL 105
 - receptor–ligand bonds 325
 - recrystallization 110
 - redox enzymes 456
 - redox potential 121
 - regioregular polythiophene (P3HT) 108
 - registration 154
 - reorganization 109
 - of molecular species 166
 - process 111
 - replacement lithography 112
 - replacement nanolithography 112
 - repulsive interaction 187, 195
 - repulsive regime 196, 202f
 - resonance frequency 195
 - shift 186f
 - resonant mechanism for excitation 81

- resonant modes 211f
- resonant tunneling 37f
- resorc[4]arene cavitands 335
- RG 438, 441
- RNA 256
- rod-like chain 512f
- rod-like dynamics 513
- rod-like model 511
- rosettes 31
- rotaxanes 105f, 109f
 - thin films 110
- roughening 103, 110
- rupture 324
 - force libraries 349
 - forces 317, 325, 341
- ruthenium(II) complexes 344

- s**
- SAM, see self assembly monolayers
- scale of flexibility 518
- scanning catalytic probe lithography (SCPL) 126, 127
- scanning electrochemical microscopy (SEM) 433
 - SECM-AFM 454
 - – tips 451
- scanning force microscopy (SFM) 358, 510, 514, 518, 529
 - images 521, 523, 527–530, 532
 - – statistical analysis 527
- scanning near-field optical microscopy (NSOM) 107
- scanning probe microscopy (SPM) 208, 275
- scanning probe nanolithography (SPnL) techniques 101, 135
- scanning tunneling microscopy (STM) 4, 11, 22, 77, 357
 - molecular adsorbates 37f
 - nanolithography 104
 - replacement lithography 113
 - solid/liquid interface 36ff
- scanning tunneling spectroscopy
 - molecular adsorbates 37f
 - solid/liquid interface 36ff
- scanning tunneling techniques
 - vacuum vs. solid/liquid 40f
- scissors modes 93
- secondary interactions 319
- segmental curvature 519
- segmental curvature dispersion
 - DNA rigidity function 520
- selectins 267
- selection rules 88

- self-assembled 6, 8, 12, 24, 102, 126, 136
 - OTS monolayer 123
 - supramolecular 6
- self-assembly monolayers (SAMs) 111f, 119, 124, 129ff, 146, 278ff, 286, 292, 332f, 334, 339, 446, 459
 - carbon nanotube tip 148
 - DPN stamp tip 161
 - electrodeposited carbon tip 148
 - molecules 148
 - substrates 148
- self-assembling nanostructures 532
- self-assembly of Au nanoclusters 125
- self-consistent Born approximation (SCBA) 494
- self-doped sulfonated polyaniline (SPAN) 158
- self-excitation modes 211
- self-organization 30, 101f, 109, 136
 - molecular nanostructures 109
 - molecules 55
- semi-infinite layer structure 487
- semiconductors 391–393, 400, 403f
- sequence-dependent DNA curvature 516
- sequence-dependent flexibility 521
- sequence-dependent intrinsic twists and curvatures 511
- sequence-dependent property 511, 515
- sequence recognition 532
- sequential unfolding 343
- sexithienyl (T6) molecules 110, 116
- sharp onset 483
- shift of the resonance frequency 194
- SIESTA DFT code 486
- silane molecules 119
- silicon 115, 231ff
- silicon nitride 115
- simulations 472
- single gold colloidal particles 117, 119
- single molecules 54, 355
- single-molecule force spectroscopy (SMFS) 297, 323, 325
- single oxidized dot 119
- single-stranded DNA (ssDNA) 133f
- single walled carbon nanotubes (SWNTs) 369
 - current 376
 - maps 376
 - plastic deformations 371
 - radial electromechanical properties 371
- sinusoidal drive 214
- sinusoidal modulation 215ff
- SiO_x templates 116
- Smoluchowski 253

- soft materials 195, 205
 - solar cells 406, 419
 - solid solutions 12
 - solvent exclusion 294
 - spacer 323, 336
 - stiffness 349
 - spectrin 267
 - spontaneous resolution 12
 - spring constant 251
 - π -stacking 31
 - stacking energy 518
 - standard rate constant 443
 - standing wave patterns 70
 - static bend β 515
 - static curvature 514, 521
 - static modes 210
 - static persistence length 514
 - statistical analysis 510
 - steered molecular dynamics (SMD) 262
 - stiffness of the chain 513
 - stoppers 109
 - streptavidin 250
 - streptavidin/biotin 263
 - styrene–butadiene rubber (SBR) 231ff
 - substrate generation/tip collection (SG/TC)
 - mode 434, 437, 444, 445
 - superstructures
 - DNA architectures 509
 - DNA bending 508
 - DNA looping 508
 - DNA packaging 508
 - supramolecular 16, 17, 20, 29, 30
 - assemblies 101
 - interactions 315, 318
 - polymers 317, 341, 342
 - surface chemical functionalization 122
 - surface chemical reactions 300
 - surface differential interactions 522
 - surface energy 288
 - surface free energy 294
 - surface local oxidation 121
 - surface local reduction 121
 - surface nano-oxidation 115
 - surface potential 391, 394, 397, 399, 402–404
 - surface restructuring 28
 - surface states 403
 - surface-templated assembly process 165
 - symmetry selectivity 91
- t**
- T6 molecules 117
 - tapping 211
 - tapping mode 150, 157, 175, 196
 - tartaric acid 16
 - TBDMS SAMs bis(*tert*-butyldimethyl-
siloxyundecyl) disulfide 127f
 - template growth 116f
 - template pattern 111
 - template structure 119
 - terephthalic acid 11
 - Tersoff and Hamann 88, 474
 - tetracyanoquinodimethane (TCNQ) 346
 - tetramethylphenylenediamine (TMPD) 346
 - theoretical curvature profile 531
 - thermal actuation mechanism 162
 - thermal fluctuations 251
 - thermomechanical writing 105
 - thermoplastic elastomers 179, 198
 - thin-film growth 101
 - thin-layer cell 443
 - thiol-modified DNA molecules 157
 - thiols 131, 278
 - thiol-top-functionalized silane monolayer
(TFSM) 124
 - bound silver ions 124
 - template 125
 - three-point contact model 6
 - time-average curvature 529
 - profile 527
 - time evolution of single-molecule
 - dynamic fluctuations 518
 - time-averaged conformations 518
 - time-of-flight secondary-ion mass spectrometry
(ToF-SIMS) 275
 - tip
 - Au-coated 360
 - contact 365
 - metallization 358
 - modification 278, 286
 - tip functionalization 280, 316
 - tip generation/substrate collection (TG/SC)
 - mode 434, 436
 - tip-induced nanoelectrochemical reduction 124
 - tip-induced water meniscus 115
 - tip–sample forces 293
 - titanium 115
 - titin 267, 342
 - topographic 199, 205
 - transfer coefficient 443
 - transition state 253
 - transmission eigenchannels 490
 - triangular modulation 214f
 - trichlorosilane 280
 - triethoxysilane 280
 - trimesic acid 18
 - trimethoxysilylpropyl-diethylenetriamine
(DETA) 158

trimethylsilyl (TMS) 119
tris(hydroxyquinoline)-Al^{III} 110
tunneling current 451
– second derivative 79
tunneling transmission 472
tunnel junctions 114
twisting rigidity 513

u

ultra high vacuum (UHV) 8, 25, 26, 28
ultramicroelectrode 433, 438
umbrella or inversion mode 93
unbinding force 327
unfolding 259
2-ureido-4[1H]pyrimidinone 338

v

vacuum level 393, 402
vacuum state 392
velocity 255
vesicles 181
Vicker's indenter 223
virtual phonons 477
viscous processes 187

V₂O₅ nanofibers
– electrical maps 377

w

water meniscus 114, 161
water-soluble precursor 124
wetting 101
wetting/dewetting transitions 103, 110
Wickramasinghe 393, 403
William Thomson 392
work function 391f, 400, 402, 405
working curves 444
worm-like chain model (WLC) 513, 515
worm-like cylindrical brush 182
worm-like micelles 182
write information 110
write-once-read-many (WORM) 104
writhe distribution 511
writhing of DNA 512
writhing transitions 512
writing
– automated 141
– pen 141